# Polymer drug dispersions: understanding structure and dynamics

**Lucy Elizabeth Hawarden**
**School of Pharmacy**
**University of East Anglia**

**April 2015**

Thesis submitted to the School of Pharmacy, University of East Anglia
in fulfilment of the requirement for the degree of Doctor of Philosophy.

*Dedicated to my parents who, through everything*
*they have done, have made this possible.*

## Acknowledgements

Those that have witnessed the study of a PhD will know that it is not an individual pursuit. I know personally that there are a number of people without whom this project would simply not have been possible. To all those that have enriched my learning within university life, or suitably distracted from me it at times of need (!), I offer a heart-felt thank you.

I am eternally grateful to my supervisor Yaroslav Z. Khimyak for the opportunity to work alongside him and for his continued support. Along the way he has offered assistance ranging fully from all things scholarly to simple support and reassurance. My thanks also go to my industrial supervisor, Sarah Nicholson, who has also always offered fantastic advice and support. Without the guidance of my supervisors, this project would simply not have had the direction and drive that was needed.

There are a number of people who have come and gone from our 'NMR family' in my time in the Khimyak group, and it has been a pleasure working alongside every single one of them. In Andrea, Paul, Cate, Karol and Susana, I know that I have found friends for life. I look forward to seeing the fruits of your work, knowing that you are all exceptionally gifted individuals. I feel blessed that with all of you, I have found true friendship outside of the bounds of the office.

Thank you to all of the staff at both the University of East Anglia and the University of Liverpool as well as those at Bristol-Myers Squibb that have helped me along the way. A special note goes to Colin MacDonald at UEA for constant aid and support whilst dealing with complex and temperamental equipment. To BMS in general, I thank you for choosing to invest in my future and for the continued opportunity beyond my PhD. To Jon Brown, thank you for allowing me so much freedom and time to complete my thesis.

There are a number of other students I have come into close contact with at UEA and Liverpool, and I wish all of you well in your continued work. I have always felt completely welcomed into the wider community of university life. A special thank you must go to Inese for dropping everything multiple times to kindly run experiments for me, even when on the opposite side of the continent. You have always gone above and beyond what I have asked of you and that is sincerely appreciated.

I am very thankful that throughout my time studying, I have found myself alongside close friends to help me escape from academia. This has remained true despite moving across the country to a new city mid-way through my studies. Thank you to Catherine, Jen, Jenna, Sarah and Sarah my oldest friends from school; and the girls of Darby Road. Thanks to Krissy and Colin (from the basement!) for keeping me supplied with chicken wine. Finally, huge thanks go to Claire and Lewie, for ensuring that I have always had wonderful people to relax and enjoy myself with. I look forward to many weekends between Norwich and Liverpool in the future! Again, I feel I have made some friends for life as a consequence of my travelling.

As an aside to my association with BMS, I have been fortunate to know Mike Tobyn and his wonderful family; Sally, Joe, Ben, Ted and Meg. Your company has made the regular trips back to Liverpool an absolute pleasure.

Thank you to Steve for dedicating your time to reading and making corrections; your help is very much appreciated. Thank you to Terry and Lesley for all your moral support and for dropping everything in my time of need.

Thank you to Emma, who has always remained close despite being on the other side of the Atlantic. Knowing that you are on a similar journey and that you are always truly interested

in my work is a powerful motivator.

To Pete, thank you firstly for your techie help with writing my thesis; you have helped without complaint on SO many occasions and I couldn't have done it without you; but also for your continued support throughout the whole of my PhD. You were quick to encourage me to undertake the role and have constantly reminded me of my ability to excel in it. Thanks also for keeping me company in the lab on so many occasions when experiments have forced me to be there late into the night, and throughout the almost endless days and nights of writing my thesis!

And finally, I thank my family; Mum, Dad, Grandma, Amy, Andrew and Raj. Each of you have always enforced the idea that I can achieve anything I want and that has been a vital belief that has carried me forward at times. I know that I can turn to any one of you when in need as I have tested that during the last four years. I also truly appreciate that you are not only family but my closest friends and I look forward to having time available again to spend with you.

**Abstract**

Poor physical stability is a limiting factor in the pharmaceutical development of APIs. Amorphous drugs are attractive due to increased dissolution; however can unpredictably revert to the thermodynamically stable crystalline form. Accurate prediction of molecular level physical stability would be advantageous. Research surrounding stability prediction is evolving; but challenging, including thermodynamic, molecular and kinetic factors.

This study focussed on gaining a molecular level understanding of the structure and dynamics of amorphous dispersions using three model drugs. We aimed to develop solid-state NMR methods to provide invaluable information on molecular mobility; to ultimately use NMR for the prediction of crystallisation outcomes from stability studies, leading to quicker prediction of potential storage issues, since mobility is a key factor affecting stability in the amorphous state.

VT solid-state NMR was used to probe differences in local mobility between drug and polymer; and to monitor polymorphic transitions/crystallisation in high loaded dispersions. Methodologies were verified using additional physicochemical approaches.

We demonstrated:

- Differences in local mobility of drug/polymer dependent on model system and drug loading.
- Miscibility detection down to 2 nm, including important temperature dependent observations. VT relaxation curves could become important visual tools for quantification of drug loading and prediction of miscibility during initial development.
- VT NMR was a useful tool for quick and accurate prediction of high temperature stability study outcomes
- Insight into crystallisation of pharmaceuticals in formulation, demonstrating mapping complex phase transitions in high loaded dispersions
- Detection of different dynamic features of tolbutamide, including the identification of motional processes responsible for the detection of its structural transitions

VT solid-state NMR has provided a significant quantity of data surrounding the mobility and stability of our systems of study. These methods provide us with a valuable characterisation 'toolkit' for probing molecular mobility in solid dispersions, therefore aiding the prediction of potential long term stability issues.

# Glossary

$\tau_c$ Correlation time.

**API** Active Pharmaceutical Ingredient.

**BPP/KT** Bloembergen Purcell Pound / Kubo Tomita theory.

**C-K** Couchman-Karasz equation.

**CP/MAS** Cross polarisation magic angle spinning.

**CSA** Chemical shift anisotropy.

**DRS** Dielectric Relaxation Spectroscopy.

**DSC** Differential scanning calorimetry.

$\mathbf{E}_A$ Activation energy.

**FFA** Flufenamic Acid.

**FWHH** Full width half-height.

**G-T** Gordon-Taylor equation.

**G-T/K-B** Gordon-Taylor/Kelley-Bueche equation.

**IMC** Indomethacin.

**mDSC** Modulated temperature DSC.

**NMR** Nuclear magnetic resonance.

**PVP** Polyvinylpyrrolidone.

**PVP-VA** Polyvinylpyrrolidone-co-vinylacetate.

**PXRD** Powder X-ray diffraction.

**RTP** Room temperature and pressure.

$\mathbf{T}_{1\rho}$ Spin lattice relaxation time in the rotating frame.

$\mathbf{T}_1$ Spin lattice relaxation time.

$\mathbf{T}_2$ Spin-spin relaxation time.

$\mathbf{T}_g$ Glass transition temperature.

$\mathbf{T}_K$ Kautzmann temperature.

$\mathbf{T}_m$ Melting point.

**TLB** Tolbutamide.

**VT** Variable temperature.

**WISE** WIdeline SEparation.

# Contents

# List of Figures

# List of Tables

# Chapter 1

# Introduction

To put this thesis into context, the literature covered in this chapter highlights the important topics associated with the study of pharmaceutical amorphous solid dispersions. The formulation of solid dispersions of amorphous drugs with polymers is a technique employed in the pharmaceutical industry to improve the dissolution rate of crystalline APIs, and stability of amorphous APIs. The ultimate aim of successful formulation is to prepare a **fully amorphous**, **fully miscible** drug/polymer system which remains **physically stable** upon storage for the full shelf-life duration. The literature included in this chapter will explore these three areas, describing the importance, relevance and characterisation techniques employed to investigate each one. The important role solid-state NMR has played to date in the understanding of molecular mobility and physical stability of solid dispersions will also be discussed.

## 1.1 Amorphous and Crystalline Active Pharmaceutical Ingredients (APIs)

Knowledge of the amorphous form is of paramount importance when determining the solid-state physical and chemical properties of many pharmaceuticals. The word 'amorphous' is from the Greek 'a morphé,' meaning without shape [16]. An amorphous material can simply be defined as a disordered non-crystalline solid [59] which lacks the long range three-dimensional order of the crystalline form. Molecules in amorphous materials characteristically have *some* short-range chemical and topological order with near neighbours, but an overall more randomly disordered molecular structure [16]. A crystal can be defined as 'a solid body having a characteristic internal structure and enclosed by symmetrically arranged plane surfaces, intersecting at definite and characteristic angles' [60]. Therefore, crystalline APIs exhibit ordered three-dimensional structures, with repeated unit cells providing long range order and high physical stability. The difference in structure between amorphous and crystalline solids can be seen in figure 1.1.

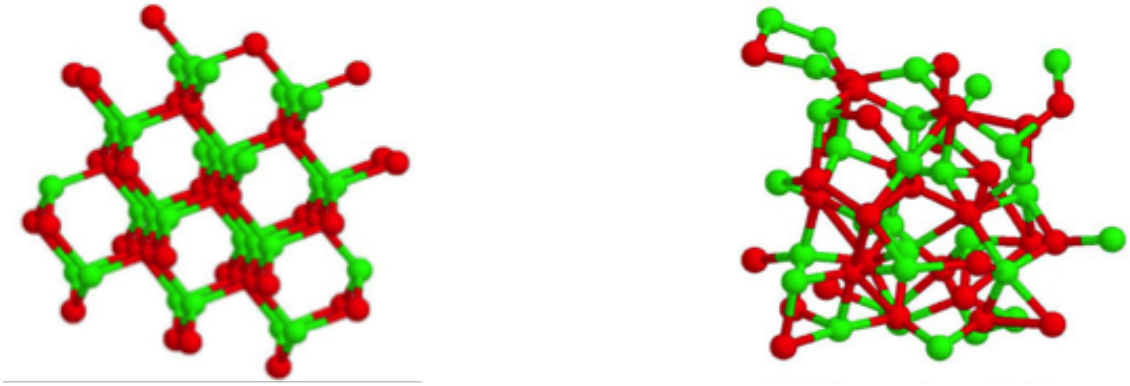

**Figure 1.1:** Structural differences between crystalline and amorphous materials, adapted from [15]

O'Donnell and Woodward [61] recently reported that an estimated 70 % of pipeline APIs

are poorly water soluble. Poor aqueous solubility is therefore currently one of the biggest hurdles for the pharmaceutical industry in the development of oral formulations [62]. The formulation of low solubility crystalline APIs in the amorphous form is a popular technique used to greatly improve dissolution rate and bioavailability [17, 63, 64]. Mullins and Macek [65] first demonstrated improved dissolution of APIs with the formation of amorphous novobiocin. Haleblian *et al.* [66] further demonstrated the lack of long range order in a number of amorphous APIs, which led to improved dissolution rates. Common methods of producing amorphous materials are highlighted in figure 1.2. The method of preparation and sample history are important factors for amorphous materials, as the amorphous state does not have a tightly defined energy, therefore the different dynamic and energetic properties can be affected by the method of preparation and the sample history [51]. For example, Fukuoka *at al.* [67] found that melt cooled indomethacin remained amorphous for two years at room temperature, whereas milled indomethacin showed evidence of crystallisation after two months of storage.

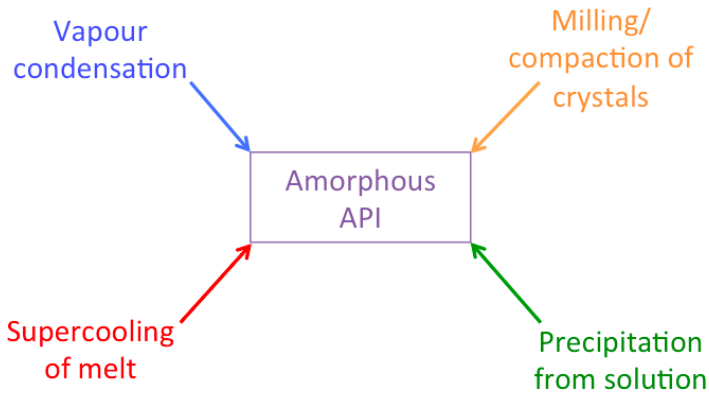


**Figure 1.2:** Schematic representation of common methods of producing amorphous pharmaceutical materials, adapted from [16]

It was later demonstrated that amorphous APIs lack the stability of the crystalline form due to their thermodynamically metastable nature, resulting from a higher enthalpy, entropy and Gibbs free energy [67–71]; and greater molecular mobility [51]. This leads to the likelihood of physical instability [62, 72], with formulations tending towards crystallisation, accelerated by environmental factors such as temperature or humidity [73]. Knowledge and understanding of the amorphous form is therefore of paramount importance when determining the solid-state physical and chemical properties of many pharmaceuticals.

## 1.2 Amorphous Solid Dispersions

Amorphous solid dispersions are defined as 'dispersions of one or more active ingredients in an inert and hydrophilic carrier or matrix in the solid state, prepared by melting or solvent method' [74] and provide molecular level mixing of drug and polymer [17].Polymers have

been found to be highly effective in stabilising amorphous pharmaceuticals through formulation as amorphous solid dispersions [68, 75–79]. Van den Mooter *et al.* [80] found that physical mixing of amorphous ketoconazole (KET) and polyvinylpyrrolidone (PVP) did not prevent crystallisation, but formulating the drug and polymer into a solid dispersion was a highly effective way to prevent crystallisation, and therefore improve physical stability. Yoshioka *et al.* [81] additionally demonstrated that inhibition of crystallisation of amorphous indomethacin (IMC) in the absence of polymer required storage temperatures of *ca.* 50 K below $T_g$, whereas in the presence of as little as 5 % PVP, crystallisation of IMC was inhibited at room temperature, with significant inhibition occurring with the presence of 20 % polymer. Widely used polymer examples include polyethylene glycol (PEG), hydroxypropylmethylcellulose (HPMC) [41, 82], hydroxypropylmethylcellulose-acetyl succinate (HPMC-AS) [83], polyvinylpyrrrolidone (PVP) [77–79, 84, 85] and polyvinylpyrrolidone-co-viynlacetate (PVP-VA) [79]. Preparation of an amorphous solid dispersion enables the drug to retain the favourable dissolution profile of the amorphous form, whilst improving physical stability through the prevention of crystallisation [77].

The overall formulation aim is to reduce the transformation of amorphous to crystalline material through inhibition of nucleation and crystal growth within the system [80]. Different stability mechanisms have been frequently discussed in the literature in recent years [62], with current understanding highlighting: 1) increased $T_g$ of the mixture with high $T_g$ polymers, through an anti-plasticising effect; 2) reduced molecular mobility of the amorphous drug; and 3) stability through specific drug/polymer interactions as important factors [62, 78, 80, 86]. Hydrophilic polymers have also been shown to improve both wetting and dissolution rate of amorphous APIs [78]. Additionally, amorphous solid dispersions can provide advantages for the pharmaceutical industry in early formulation development by improving drug exposure to APIs with low aqueous solubility [87, 88]; and by slowing the release of highly soluble APIs in extended-release preparations [88–90]. Common formulation methods include solvent evaporation [91], spray drying [92], cryo-milling [51], hot melt extrusion (HME) [17,93], nano-solid suspension formation *via* controlled precipitation [94] and solvent-free supercritical fluid processing [95].

Despite the numerous literature examples of successful stabilisation of amorphous drugs with polymers, there are still relatively few commercial solid dispersions available [96–99]. This is likely due to the lack of understanding of the structure and dynamics of amorphous solid dispersions, and how these factors relate to improved dissolution rate and physical stability [17]. Accurate prediction of physical stability on a molecular level would be a great advantage. Research in the field of predicting physical stability is active and evolving; but is a challenging topic, which includes overlapping considerations of thermodynamic, molecular and kinetic factors [100]. Additionally, very few techniques are able to probe miscibility at a molecular level, particularly in solid solutions as they require nanoscale detection limits [19],

leading to limitations of the use of a number of commonly used characterisation techniques. The ability to accurately predict physical stability of amorphous solid dispersions would be of great advantage to the pharmaceutical industry and therefore knowledge of how changes in the local molecular mobility of amorphous materials leads to reduced physical stability is of paramount importance.

### 1.2.1 Classification of amorphous solid dispersions

Solid dispersions are classified by a number of terms, depending on the level of mixing (or miscibility) between drug and polymer. This ranges between 'ideal' systems of molecular level dispersions (often termed solid or glass solutions), which are fully miscible, and intimately mixed [88, 101]; to phase separated systems containing nano or micro domains [17, 102]. Phase separation in an amorphous solid dispersion generally occurs due to the presence of both amorphous and crystalline API, leading to the formation of domains in the polymer matrix [11, 88], which are not always evenly distributed [103]. The successful formation of solid/glass solutions is most likely to fulfil the sought after characteristics of a **fully miscible, fully amorphous, physically stable** solid dispersion, offering beneficial high aqueous dissolution rate with the lowest possibility of phase separation [88, 104–106]. Phase separation, or heterogeneity of solid dispersions can occur during formulation, handling and storage, and results in complex systems, which are often difficult to characterise [107]. Both solubility and miscibility of the API in the chosen polymer help to determine the maximum drug loading level of an amorphous solid dispersion, above which the likelihood of phase separation and/or crystallisation increases [108, 109] as at high drug loading levels, amorphous solid dispersions can become metastable. It is therefore crucially important to understand the factors contributing to the crystallisation of materials from the amorphous state [17, 74]. Figure 1.3 outlines the important physicochemical properties associated with amorphous dispersions, and the differences in phase separation behaviour associated with introduction of stress (e.g increased temperature, humidity or mechanical stress).

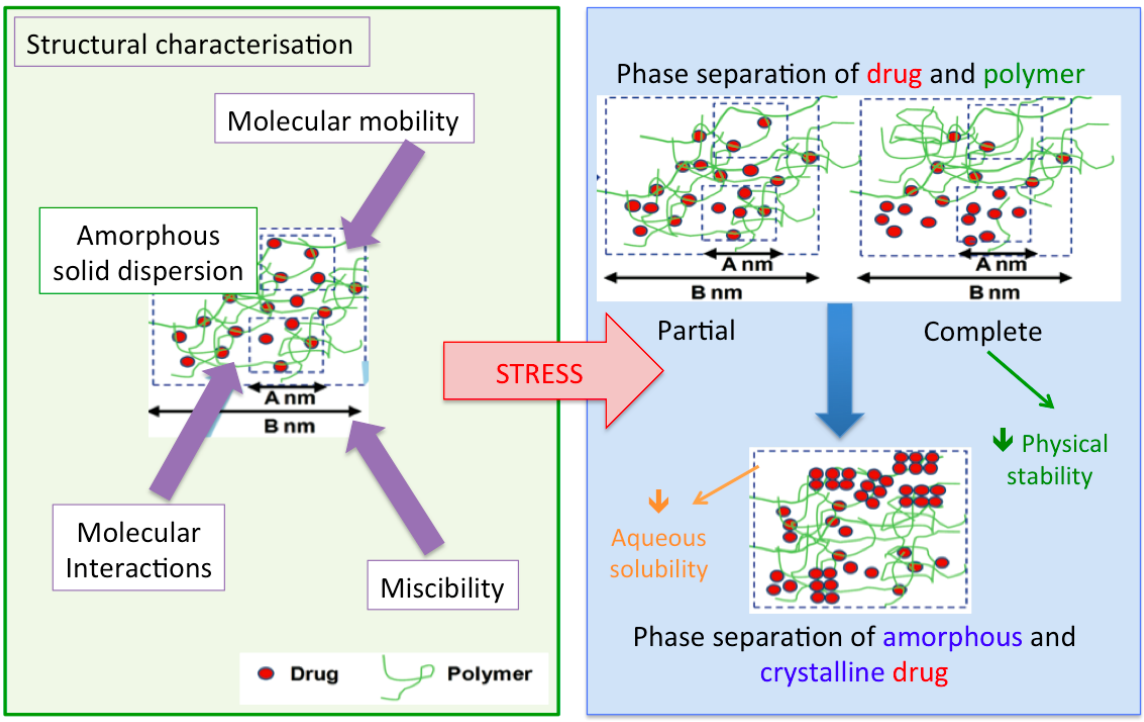


**Figure 1.3:** Scheme to understand the important physicochemical properties of amorphous solid dispersions, with a demonstration of the outcomes of exposure of these systems to stress, for example increased temperature, humidity or mechanical stress. Adapted from [17]

## 1.3 Glass transition temperature ($T_g$)

$T_g$ is a physical property of solid amorphous systems. It describes a kinetic event which results in the change of the thermodynamic properties of the material as it moves from a hard 'glassy' to a soft 'rubbery' state [18,110]. In the field of amorphous pharmaceutical systems, $T_g$ is generally regarded as the most important indicator of physical stability [61], as it describes a major change in the properties of amorphous materials [29]. The $T_g$ can provide local structural information, reflecting the chemical and physical stability of amorphous materials [111]. A fully miscible dispersion should have a $T_g$ value which is intermediate between the individual components, (i.e drug and polymer). The theoretical $T_g$ value of 'ideally mixed' amorphous solid dispersions can be predicted using a number of equations, including the Gordon-Taylor (G-T) [112], Gordon-Taylor/Kelley-Bueche (G-T/K-B) [113] and Couchman-Karasz (C-K) [114], which are discussed in further detail in chapter 2.

There is no widely accepted definition of $T_g$, but it is generally defined as the 'temperature of onset of the heat capacity increase during heating' [16]. The $T_g$ can be measured using differential scanning calorimetry (DSC), with the midpoint of the transition calculated as the $T_g$ temperature. Figure 1.4 highlights the change in specific volume and enthalpy as a function of temperature for a typical liquid. The transition between the glassy and crystalline states is often described with the aid of such diagrams. Upon cooling, a liquid can either:

[18, 115, 116]

- Crystallise at $T_m$: $\rightarrow$ first order phase transition associated with a sharp reduction in volume/enthalpy; *OR*
- Cool below $T_m$ without crystallisation: $\rightarrow$ formation of a 'supercooled' liquid, with a change in volume/enthalpy which follows the liquid equilibrium line.

Further cooling of the supercooled liquid results in a change in slope gradient, at temperature $T_g$. At this point, the 'glassy' material is in a non-equilibrium state which is accompanied by an *increase* in viscosity and a *decrease* in molecular mobility. The change in the properties of the systems results in the enhancement of the thermodynamic properties. The enhanced thermodynamic properties account for the increased dissolution rate of the amorphous material as compared to the crystalline form [18, 115, 116].

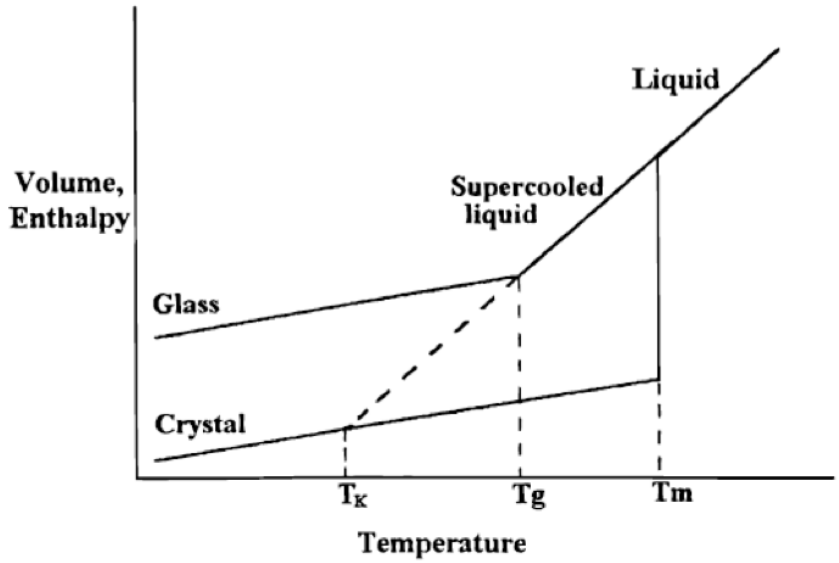


**Figure 1.4:** Specific volume/enthalpy vs. Temperature for a liquid which can both crystallise and form a glass, where $T_m$ = melting point, $T_g$ = glass transition temperature and $T_K$ = Kautzmann temperature, adapted from [18]

### 1.3.1 Molecular Mobility around $T_g$

Current literature places a large emphasis on molecular motions as the main factor affecting physical stability [117, 118], but the interpretation of dynamic phenomena in amorphous solids is difficult due to the presence of molecular motions on different timescales. At temperatures around $T_g$ molecular motions are very slow, sometimes taking minutes to hours for a molecule to reorientate [116]. In the supercooled rubbery state, the average timescale of molecular motions is $< 100$ s, with a viscosity around $10^{12}$ Pa $s^{-1}$ [116]. The timescale of molecular motion dramatically increases as the material is cooled towards $T_g$ [118], with further cooling resulting in the loss of *kinetic* equilibrium, leading to a change in the temperature dependence of specific volume and enthalpy: the

experimentally observed $T_g$ (figure 1.4). Below $T_g$, the material exists in a thermodynamically unstable glassy state, where the timescale of molecular motions is hugely reduced, with viscosities of $> 10^{12}$ Pa $s^{-1}$ [16, 116, 119].

There are two main types of molecular mobility which are described in association with the $T_g$ for amorphous materials: global mobility and local mobility, which are described in terms of $\alpha$-relaxation and $\beta$-relaxation times respectively [100]. Global mobility ($\alpha$ relaxations) describes the motions associated with the glass transition temperature. These motions are more widely studied, and are thought to be directly related to physicochemical stability. Local mobility ($\beta$ relaxations) describes the molecular mobility below the $T_g$, thought to be slower intramolecular motions, resulting from restricted rotation around bonds, such as motions of polymer side chains. They have lower activation energies, and are thought to be precursors to $\alpha$ relaxation [100, 117, 118]. Local mobility is currently not directly characterised, but measured by extrapolation from the data above $T_g$ [100].

Molecular mobility of amorphous materials is often expressed as it's reciprocal: the relaxation time ($\tau$). Relaxation in amorphous materials may result from a number of processes, including enthalpic relaxation [69], volume relaxation [69], dielectric relaxation [120] or spin-lattice relaxation [4]. Molecular mobility is often indirectly measured using DSC above and below the $T_g$, through estimation of $\tau$ using a number of equations including Kohlrausch-Williams-Watts (K-W-W) [102, 121], Adam Gibbs (AG) [100] and Vogel–Tammann–Fulcher (VTF) [100]. However, techniques such as dielectric relaxation spectroscopy, and solid-state NMR spectroscopy can provide a **direct** measure of the molecular mobility of an amorphous material [100]. It is generally thought that crystallisation is restricted to the region above $T_g$, as diffusional processes required for nucleation cannot occur below this temperature [59]. Local mobility obviously plays an important role in physical stability and it is therefore important to increase understanding of $\beta$ relaxations. The understanding of the molecular mobility around and below the $T_g$ value of amorphous solid dispersions therefore plays an important role in providing vital information about physical stability during formulation development.

Studies of amorphous materials have found that storage temperature greatly influences rate and occurrence of crystallisation [68, 81, 122] which highlights that $T_g$ can help to dictate the optimal storage conditions for an amorphous system as it represents the border between an area of high and low molecular mobility [74]. Storing an amorphous material close to, or above $T_g$ ultimately allows increased molecular mobility, reduced physical stability and eventual crystallization. The general 'rule of thumb' is that storage at temperatures of $T_g$ - 50 K (the 'Kautzmann temperature' ($T_K$) [69, 116]) molecular mobility is virtually non-existent, therefore crystallisation should not occur in an amorphous system [61, 64, 69, 100, 123]. However, as molecular mobility can still occur below $T_g$, crystallization may still occur upon product storage [123]. There are many examples of studies where $T_g$ measurements

have proved an inaccurate stability predictor as nucleation or crystallisation has still occurred at temperatures well below $T_g$ [68, 124]. For example nifedipine has a $T_g$ of 319 K, but has been shown to crystallise at temperatures as low as 40 K below this [125], extremely close to $T_K$. Additionally, many amorphous APIs exhibit low $T_g$ temperatures, therefore storage at $T_K$ is not realistically achievable for patients outside the laboratory setting.

## 1.4 Polymorphism of crystalline APIs

The investigation of physical stability of amorphous solid dispersions often requires the characterisation of crystalline forms of the API, as detection of crystallisation from the amorphous state is employed as a measure of reduced physical stability, particularly in accelerated stability studies. It is widely known that many APIs exist in multiple crystalline forms, or polymorphs [126]. Polymorphism describes the ability of a crystalline material to exist as more than one crystalline structure, each with a different molecular arrangement due to differences in packing and/or molecular conformation [127].

McCrone [128] was first to highlight why polymorphism was particularly important from a pharmaceutical perspective. He outlined two main factors which were imperative for full understanding of polymorphism, both of which are mainly still somewhat of a mystery today. The main question he asked was "What are the factors which determine what particular crystal form will be generated from vapour, liquid or solution when the thermodynamic phase region of the solid-state is entered?" [129]. This question remains largely unanswered to date. Understanding the polymorphic behaviour of pharmaceutical APIs is of paramount importance, as different polymorphs display different physicochemical properties (e.g. melting point, morphology) which can affect physical and chemical stability and bioavailability (table 1.1) [48, 126, 130].

**Table 1.1:** Properties which can differ between polymorphic forms [48]

| **Thermodynamic** | **Kinetic** | **Packing** | **Surface** | **Mechanical** |
|---|---|---|---|---|
| Melting temperature | Dissolution rate | Density | Surface free energy | Hardness |
| Enthalpy, entropy, heat capacity | Solid state reaction rates | Conductivity | Interfacial tensions | Tensile strength |
| Free energy | Physical/chemical stability | Morphology | Habit | Compactability |
| | Rate of nucleation | Colour | | Flow properties |

The literature is littered with examples of polymorphic issues, ranging from the photographic industry, to food additives, and the pharmaceutical industry [129]. Whether an API exists in different polymorphic or solvated crystal forms is still a huge part of pharmaceutical research [77]. It is fundamentally important to determine knowledge of this information about the compound, as the different thermodynamic properties of these forms can have a massive effect further along the manufacturing process on the properties of the drug during storage and handling [16]. It is well known that polymorphism can affect the final quality of

a drug product and is recognised by regulatory authorities as an issue [131]. The European Medicines Agency ICH Q6A test specifications of new drug substances and products contains guidelines of how to identify, monitor and control polymorphic forms of new drugs products, including both solvation and hydration products as pseudopolymorphs [33]. These properties must be identified in early stage drug development, to prevent major problems later in the drug development process and once the drug is available as a treatment.

One well documented pharmaceutical example of the outcomes of lack of understanding of polymorphism during the development process is that of ritonavir, an antiretroviral medication first marketed by Abbott Laboratories [132]. It was originally available on the market in 1996 as an oral semi-solid capsule, with ritonavir in ethanol/water based solutions. Guidelines state that when a drug is formulated in the solution state, polymorph control has little scientific rationale. Only one polymorphic form (form I) was identified during development [132]. However, in 1998, reduced oral bioavailability of the marketed dosage form was highlighted and was found to be due to a polymorphic transformation to the lower energy, more stable polymorph form II [133]. This seriously threatened supply of an extremely important, lifesaving treatment. The oral capsule was completely removed from the market and re-formulated as form II in a refrigerated gelcap, to prevent the polymorphic transition to form I occurring [132]. Later, three more forms including two solvates and one unsolvated form were discovered by high-throughput screening [133].

Polymorphic transitions occur to increase the system stability, through changes to free energy. Polymorphic relationships are commonly described by energy-temperature (E-T) phase diagrams. Thermodynamically, polymorphic transitions can be categorised as monotropic or enantiotropic. In monotropic systems, an irreversible transformation between polymorphs occurs to produce the more stable polymorph at a particular temperature. In an enantiotropic system, a reversible phase transition can occur between polymorphs, which is dependent on temperature [129]. In general, the 'rules' of polymorphism are based upon Frankheim's princlples [48, 129, 134], which ultimately conclude that polymorphic transitions are dependent on relative polymorphic stability:

- The most stable polymorph has the lowest free energy
- The transition between forms (A and B) is distinguished by a specific transition temperature
- Under specific experimental conditions, only one polymorph can have the highest stability: known as the *thermodynamically stable form*
- Additional polymorphs are referred to as *metastable* forms. Metastable polymorphs can lower their free energy in order to convert to the more stable form
- An increase in temperature ultimately leads to the formation of the more stable form, as described by Ostwald's rule of steps [135]

APIs can be at risk of polymorphic transitions throughout pharmaceutical processing procedures, for example during wet granulation, which is commonly used to formulate oral dosage forms [136]. Polymorphic transitions can occur through dissolving in solvents, through changes in temperature during manufacture and drying, or changes in mechanical stress, e.g. during milling [137]. Polymorphic relationships are therefore important to understand for new pharmaceutical solids, firstly to identify the best candidate to take forward into development; and secondly to fully predict the behaviour of the API throughout formulations development and manufacturing [48].

.

## 1.5 Monitoring the physical stability of amorphous solid dispersions

In the pharmaceutical industry, API and formulation stability is monitored through the use of accelerated stability studies, as part of quality and performance monitoring during drug development, clinical trials and beyond into the life-cycle of the drug [19]. Throughout the stability study, the formulation is monitored for changes in physical stability under a range of conditions, including increased temperature and humidity. Ultimately, stability studies are used to predict the shelf-life, and necessary storage conditions of the formulation. The important regulatory guidelines for APIs and formulations are outlined in figure 1.5.

| Guideline | Physical stability criteria and requirements |
|---|---|
| ICH Q1A(R2) | Appearance, physical attributes and functionality test (e.g., color, phase separation, resuspendability, caking, hardness, dose delivery per actuation, pH, dissolution) |
| ICH Q1B | Drug substance: any changes in physical properties (e.g., appearance, clarity, or color of solution)<br><br>Drug product: any changes in physical properties (e.g., appearance, clarity or color of solution, dissolution/disintegration for dosage forms, such as capsules) |
| ICH Q1E | Phase separation of a semi-solid dosage form occurs at the accelerated condition; testing at the intermediate condition should be performed |

**Figure 1.5:** Regulatory (ICH) guidelines, adapted from [19]

A recent review of physical stability of pharmaceutical formulations by Guo *et al.* [19] highlighted that changes in physical stability, as compared to chemical stability of APIs, and oral formulations are more difficult to quantify, with extrapolations from accelerated stability conditions often found to be unreliable in relation to ambient conditions. FDA recalls throughout 2011 to 2013 were mostly related to oral formulations [19]. Therefore, it

is of great importance to understand the physical/chemical mechanisms which result in physical instability of such systems.

## 1.6 Characterisation of amorphous solid dispersions

A wide range of techniques are available for the characterisation of amorphous materials, including differential scanning calorimetry (DSC) [102, 138], powder X-ray diffraction (PXRD) [139], microscopic (scanning electron microscopy (SEM), optical microscopy) and spectroscopic techniques; including Raman [140], FT-infrared (IR) [71] and solid-state nuclear magnetic resonance (NMR) [17, 88]. These techniques are often combined to provide a more complete understanding of the physical properties of an amorphous system, including thermal behaviour, physical stability, drug/polymer interactions crystallisation behaviour and miscibility information [62, 107].

### 1.6.1 Differential Scanning Calorimetry (DSC)

Differential scanning calorimetry (DSC) is an established thermal analysis technique for the estimation of stability of amorphous materials through the measurement of $T_g$ and detection of thermal events relating to crystallisation and melting [29]. DSC is also commonly used to detect miscibility of individual components within amorphous solid dispersions, where the observation of a single $T_g$ indicates miscibility with a domain size detection limit of *ca.* 20 - 30 nm [17, 88]. Comparing experimental $T_g$ values of solid dispersions with theoretical predictions based on the Gordon-Taylor equation [112] additionally provides information regarding the miscibility and interactions between drug and polymer components within the system [62].

Many previous studies have focused on DSC to characterise amorphous solid dispersions, mainly to confirm the formation and stability of an amorphous material through observation of $T_g$ [74] and to detect the miscibility of drug and polymer within the dispersion [69, 84, 141]. Molecular mobility has also been investigated with DSC, for example: Van den Mooter *et al.* [80] used modulated temperature DSC (mDSC) to investigate the molecular mobility of pure amorphous ketoconazole below $T_g$; and Zhou *et al.* [125] who used a similar method for ritonavir and nifedipine by analysing thermodynamic quantities and molecular relaxation time constants. DSC can also provide thermodynamic information including enthalpy, entropy and free energy of crystallisation measurements, demonstrated using felodipine and nifedipine by Marsac *et al.* [102].

Additionally, DSC studies are very commonly employed during initial characterisation of amorphous solid dispersions. A comprehensive review by Baird and Taylor [138] outlined the major uses of DSC for analysis of amorphous solid dispersions, and should be referred

to for further information. Van den Mooter *et al.* [80] investigated the miscibility of ketoconazole/PVP dispersions, and found that PVP prevented crystallisation by forming a compatible blend highlighted by a single $T_g$ value, which gradually increased with increasing polymer content. Drug/polymer interactions were also detected in a number of dispersions, including ketoprofen with poly(lactic-co-glycolic acid) (PLGA) where the polymer acted as a plasticizer, forming hydrogen bonds between carboxylic acid and carbonyl groups along the polymer backbone [142]. Aso *et al.* [143] additionally used DSC to estimate the stability of solid dispersions (nifedipine and phenobarbital with PVP) by probing molecular mobility at various temperatures, finding that molecular mobility of the amorphous drug was reduced in the presence of PVP. Song *et al.* [62] recently demonstrated a strong intermolecular ionic interaction between lapatinib and HPMC-P amorphous solid dispersions through deviation of experimental and predicted $T_g$ values of up to 40 K.

In summary, DSC methods are useful characterisation techniques as they can provide important information regarding the *bulk* properties of amorphous systems, but are lacking in their ability to provide the detailed structural, dynamic and molecular level information required for full understanding of amorphous solid dispersions [88].

### 1.6.2 Powder X-Ray Diffraction (PXRD)

Powder X-ray diffraction is mainly used for the detailed study of crystalline materials, but can be useful when studying amorphous solid dispersions to confirm the amorphous nature (or absence of crystalline material) through the presence of a broad halo pattern [88,129,144]. However, it is difficult to extract further information from the often featureless pattern [17]. PXRD is a useful technique to track the crystallisation of amorphous drugs, particularly in larger scale stability studies [139], however it is not always suitable due to the lower detection limit as compared to other techniques [145]. PXRD can also be used to investigate the polymorphic behaviour following crystallisation of amorphous materials, particularly in high drug loaded dispersions. More recently, PXRD methods have been extended for amorphous solid dispersions to investigations with pair-distribution functions (PDF-PXRD), which are able to provide some additional structural information [139, 144].

### 1.6.3 Vibrational spectroscopy

In the field of pharmaceutical solids, vibrational spectroscopy is more commonly applied to investigate crystalline APIs, with the most commonly used techniques being infrared (IR) and Raman spectroscopy [146]. For amorphous solid dispersions, IR spectroscopy can provide detailed information regarding drug-polymer specific interactions, for example hydrogen bonding, which are thought to be important as a stabilisation mechanism of these systems [146].

The Zografi group [71, 84] found that Indomethacin and PVP interact in solid dispersions through drug-polymer hydrogen bonding, using IR and Raman spectroscopy. Other studies have employed similar techniques to detect hydrogen bonding in dispersions of nifedipine/PVP, ketoprofen/PVP and droperidol/PVP [146]. Additionally confocal Raman microscopy has been widely employed to study amorphous solid dispersions, for example in assessing homogeneity of diflusinal/PVP [147] and ebselen/PVP-VA systems [148]. These techniques are extremely useful in providing qualitative information on intermolecular interactions, but do not allow the acquisition of direct information regarding proximity and molecular conformations in more complicated multicomponent systems. [17].

### 1.6.4 Dielectric Relaxation Spectroscopy (DRS)

Dielectric relaxation spectroscopy (DRS) has been used in a number of studies to study molecular mobility around $T_g$ [17], including with amorphous aspirin, ibuprofen, quinidine [149] and indomethacin [150] systems. The molecular mobility probed using this technique is often in the MHz - GHz range [146], and therefore motions on a different timescale to those measured through solid-state NMR spectroscopy. However, DRS has not been widely employed for the study of amorphous solid dispersions [146].

### 1.6.5 Solid-state Nuclear Magnetic Resonance (NMR)

The following discussion provides a brief overview of the range of solid-state NMR methods which have been employed for the characterisation of amorphous pharmaceuticals. For more detailed information, a number of excellent literature examples of recent developments in solid-state NMR techniques, especially regarding the characterisation of amorphous solid dispersions should be referred to: Paudel *et al.* [17] 'Structural and Dynamic Properties of Amorphous Solid Dispersions: The Role of Solid-State Nuclear Magnetic Resonance Spectroscopy and Relaxometry' ; Vogt [146] 'Solid-State Characterisation of Amorphous Dispersions' ; Pham *et al.* [88] 'Analysis of Amorphous Solid Dispersions Using 2D Solid-State NMR and $^1$H $T_1$ Relaxation Measurements' and Geppi *et al.* [151] 'Solid-State NMR studies of Pharmaceutical Systems.'

Throughout pharmaceutical development of a particular dosage form, solid-state characterisation is essential to understand as much as possible about the individual components, and about how they interact once fully formulated. Solid-state NMR can provide detailed molecular level structural information of multicomponent pharmaceutical formulations, encompassing amorphous, polymorphs, hydrates, co-crystals and solvates [17, 88]. Additional information about multicomponent systems can also be obtained including molecular dynamics, domain morphology and miscibility [152], drug-polymer inter and intra-molecular interactions, crystallisation and

polymorphism [17, 130, 153], and local dynamics *via* relaxation studies [41]. Variable temperature solid-state NMR is a valuable tool for prediction of the physical stability of drugs in formulations [101]. Graeser *et al.* [100] found that DSC was a limited technique to predict stability of amorphous systems below $T_g$, but that solid state NMR could provide a direct measure of global and local mobility, but has had limited exploitation in the field of amorphous pharmaceutical systems [100].

Koga *et al.* [154] investigated molecular mobility above and below $T_g$ of a stable amorphous CCK2 receptor antagonist (AG-041R) using variable temperature $^{1}$H-$^{13}$C CP/MAS NMR kinetics, finding that smaller functional groups (methyl) were mobile at lower temperatures, but carbonyls were restricted by interactions and therefore had low molecular mobility below $T_g$; and $^{2}$H-NMR was used to investigate the molecular reorientations around the $T_g$ of supercooled and glassy aspirin [155]. $^{1}$H-$^{13}$C CP/MAS NMR methods have been used to investigate interactions of drug and polymer and dispersion homogeneity between ketoprofen and PVP [156]; and the prediction of recrystallisation behaviour of troglitazone in a solid dispersion with PVP [145]; $^{1}$H-$^{13}$C CP/MAS NMR and $^{13}$C{$^{1}$H} MAS NMR have been used to investigate the local dynamic behaviour of ibuprofen/Eudragit dispersions [157], ketoprofen/PEO dispersions [30] and IMC/cyclodextrin systems [158]. Schantz *et al.* (2008) [159] used VT $^{1}$H-$^{13}$C CP/MAS NMR and $T_{1\rho}{}^{H}$ times to investigate molecular mobility and interactions in blends of paracetamol and citric acid, to help understand physical instability in such systems.

Solid-state NMR relaxation studies, mainly involving the detection of $T_1{}^{H}$ and $T_{1\rho}{}^{H/C}$ have been employed to investigate the molecular mobility and intermolecular interactions of solid dispersions, including for nifedipine and phenobarbital/PVP dispersions [160], where changes in local mobility were linked with stability of amorphous dispersions; and nifedipine in amorphous solid dispersions with PVP and HPMC where analysis was successfully used to determine domain size and therefore polymer-drug miscibility [152]. Aso *et al.* [161] used kinetic studies to look at the relationship between crystallization rate and molecular mobility measured with $^{1}$H $T_1$, $T_{1\rho}$ and $T_2$ relaxation times of a number of amorphous drugs. Additionally, VT studies ($^{1}$H MAS alongside $^{13}$C $T_1$ times) to monitor phase transition and molecular mobility of a blend of ketoprofen/POLYOX highlighted the changes in mobility detected in the blend as compared to the pure amorphous drug [162]; and multivariate analysis of solid-state $^{13}$C MAS NMR has additionally been used to investigate differences in the physical stability of troglitazone/PVP dispersions prepared *via* different methods [145].

Tobyn *et al.* [78] pooled information from modulated DSC, FT-IR, Raman and solid state NMR ($^{1}$H MAS NMR and variable contact time (VCT) CP/MAS NMR kinetics) to study an investigative drug compound formulated with PVP which confirmed the presence of stabilising hydrogen bonding interactions between the drug and polymer, and found that similar interactions were present in the both the crystalline and amorphous forms as

intermolecular bonds. Pham *et al.* [88] carried out an excellent study focusing on determining detailed structural information using a large number of amorphous drug/polymer dispersions, prepared using different methods, using 2D solid-state NMR approaches. They particularly focused on $^{1}$H-$^{1}$H, $^{1}$H-$^{13}$C and $^{1}$H-$^{19}$F HETeronuclear CORrelation (HETCOR) NMR to identify the presence of intimately mixed solid solutions. Molecular mobility was not reported in the extensive study, although this was highlighted as another important area for which solid-state NMR can be extremely useful, as mobility is often correlated with physical stability of amorphous solid dispersions [88].

Additionally, the detection of miscibility and phase separation of solid dispersions is a vital part of formulation development, as successful formulation of miscible drug/polymer amorphous dispersions is crucial for maintaining acceptable physical stability during manufacture and storage of pharmaceuticals [62, 108]. The miscibility of solid dispersions has traditionally been studied using differential scanning calorimetry (DSC), where a single $T_g$ value (intermediate between the $T_g$s of the individual components) is thought to indicate molecular level homogeneity [78, 106, 108, 163], with a detection limit of 20-30 nm [46, 164–166]. However, the detection of miscibility using DSC has been shown to be unreliable [144]. The use of NMR spin-lattice relaxation times ($T_{1\rho}{}^{H}$ and $T_1{}^{H}$) in the solid-state has proven to be extremely useful in providing additional information about the miscibility and phase separation of solid dispersions, with differences in $T_{1\rho}{}^{H}$ times allowing estimation of much smaller domains than with DSC; with a demonstrated detection down to *ca.* 2 nm in size [46, 62, 88].

Differences in the physical stability and behaviour of amorphous systems are often related to very subtle changes in the local structure and mobility [17]. Solid state NMR is a versatile and non-destructive technique which can probe on a local molecular level, providing information about the molecular environments, dynamics, correlations and mobility to provide molecular level information on the structure and dynamics of solid dispersions [100]. The available literature provides evidence that it could be an extremely powerful tool to understand and predict the physical stability of polymer-stabilised amorphous systems, but is an area that needs utilising further [101]. Solid-state NMR is an invaluable technique and should be employed in combination with other well established solid-state characterization methods such as DSC and PXRD, in other to maximise the understanding of the structure and physical stability of solid amorphous dispersions [101].

## 1.7 Selection of model amorphous drug compounds

A systematic literature review was carried out, with the aim of choosing three model amorphous drugs with a range of different stabilities; and one polymer which would be compatible for the formulation of amorphous solid dispersions. The choice of model

compounds was based upon rationale used in previous large scale studies of amorphous solid dispersions (see table 1.2). Pham *et al.* [88] analysed a number of amorphous solid dispersions using 2D solid-state NMR and $^{1}$H $T_1$ relaxation measurements. Bhugra *et al.* [167] analysed a number of pure amorphous drugs using DSC and dielectric relaxation spectroscopy to probe molecular mobility below $T_g$.

**Table 1.2:** Summary of rationale of drug choice in two large scale studies

| Rationale from Pham et al. (2010) [88] | | Rationale from Bhugra et al. [167] | |
|---|---|---|---|
| Paracetamol | Simple molecule, extensively studied | Nifedipine | H-bonding comparison (stronger in crystalline state) |
| Diflusinal | Fluorinated drug allowed for $^{19}$F NMR analysis | Felodipine | H-bonding comparison (stronger in amorphous state) |
| IMC | Small molecule but with greater structural complexity | IMC | Wealth of information available |
| Telithromycin | High molecular weight, not yet studied | Ketoconazole | High heat of fusion |
| Voriconazole | Large complex molecule, not yet studied | Flopropione | High heat capacity change at $T_g$ |

Using a similar rationale, model amorphous compounds were chosen by highlighting desirable properties and parameters to study, gradually ruling out unsuitable compounds. The drugs were ranked according to the number of desirable properties including: $T_g$ and $T_m$ values; amount of information available in the literature; the presence of alternative magnetic nuclei present; range of functional groups; separation of chemical shifts between drug and chosen polymer in $^{13}$C NMR spectra; range of molecular weight, and complexity of structures.

Indomethacin (IMC) was chosen as the starting point for the investigation of drug-polymer systems, alongside flufenamic acid (FFA) and tolbutamide (TLB) as the remaining model amorphous materials. All three were formulated as amorphous solid dispersions with PVP-VA, which was the chosen polymer.

### 1.7.1 Indomethacin (IMC)

IMC was chosen as the initial investigative compound as it has been widely formulated and studied both as amorphous drug and as an amorphous dispersion [29, 71, 77, 84]. There is a wealth of information available in the literature, with studies being carried out using a variety of techniques including solid-state NMR, PXRD, DSC, FT-IR, Raman and dielectric relaxation spectroscopy. The first reporting of the success of using a solid dispersion to stabilise amorphous IMC was reported by Imaizumi *et al.* in 1983 [168], where the IMC solid dispersion was found to remain amorphous for 6 months of storage at 313 K. Many studies have since found that the physical stability of IMC at room temperature is greatly improved when formulated as an amorphous dispersion with a polymer, due to the formation of hydrogen bonds between the drug and polymer [77, 84, 91], despite the high level of molecular mobility of amorphous IMC observed below its $T_g$ value [150]. IMC is a small molecule non-steroidal anti-inflammatory pain killer which is poorly soluble in water leading to a limited oral bioavailability, and exhibits predictable polymorphism [29, 77, 130]. Two polymorphic forms with known structures [31, 130] are widely recognised as $\alpha$ and

$\gamma$ [169]. Form $\gamma$ is stable under ambient conditions, with a melting point of 433 - 434 K [29] and form $\alpha$ is metastable with a melting point of 425 - 427 K [31].

### 1.7.2 Flufenamic Acid (FFA)

FFA is another non-steroidal anti-inflammatory drug and is part of the fenamates drug class, used to treat rheumatoid and osteoarthritis. It was chosen as part of this study as it has a simple structure which contains a $CF_3$ group, which can be utilised through $^{19}F$ MAS NMR. $^{19}F$ is an ideal magnetic nucleus to study as it has 100 % natural abundance and a high gyromagnetic ratio and can be utilised to assess drug molecular mobility as almost all pharmaceutical excipients do not contain fluorine but many drug products do [41]. FFA is reported to have extremely poor solubility (0.0067 mg/ml at 298 K in water [170]), alongside the rest of the fenamate compounds. Compared with IMC, there are few literature studies where FFA has been formulated as an amorphous dispersion and studied *via* solid-state NMR. Additionally, FFA exhibits rich polymorphism and has nine known polymorphic forms, eight of which have solved crystal structures [39]. Lopez-Meijas *et al.* recently solved the structures six of these polymorphs, meaning FFA has a record number of structurally characterized polymorphs in the Cambridge Structural Database (CSD) [39]. Amorphous FFA is thought to have a lower stability than IMC. No amorphous material has been formed under common conditions [131], so no value for the $T_g$ of the pure amorphous material is known in the literature. However, 80/20 drug/polymer dispersions with PVP and HPMC have been studied and the $T_g$ temperatures were calculated as 296 and 288 K respectively [41].

### 1.7.3 Tolbutamide (TLB)

Tolbutamide (TBM) is a potassium channel blocker for the management of type II diabetes. It is poorly water-soluble (0.11 mg/ml at 298 K in water for form I [170]) and has a low bioavailability [171]. The reported $T_g$ for TLB is 278 K, therefore TLB has low physical stability at ambient temperatures [100], as compared to IMC and FFA. Graeser *et al.* [100] demonstrated that amorphous TBM was stable at 258 K after 30 days storage, but unstable at ambient temperatures. TLB is a very flexible molecule, with seven rotatable bonds, leading to different arrangements of the butyl chain, and therefore interesting polymorphism. TLB has six reported polymorphic forms (forms $I^L$, $I^H$, II-V) [42–44, 172–174], with its ability to crystallize into different forms due to the flexibility of the rotatable alkyl bonds [42]. Form $I^H$ has the highest melting point, and is the most stable form at high temperatures. TLB has been studied as a solid dispersion with PVP [175] and PEG-4000 [176], but such studies focused on techniques such as DSC, PXRD and molecular dynamics, with solid-state NMR very rarely employed as a technique for characterisation of TLB in the amorphous form. Solid-state NMR is an ideal technique to investigate the local mobility of this molecule: how

local mobility changes upon formulation as an amorphous solid dispersion with polymer will provide an interesting study perspective.

### 1.7.4 Choice of polymer

Polymers are able to stabilise amorphous pharmaceuticals through an anti-plasticizing effect, ideally raising the $T_g$ value of the amorphous form sufficiently to prevent crystallisation across the temperature range experienced by the formulation during manufacturing and storage [177, 178]. Interactions between the drug and polymer and reduction of molecular mobility of the amorphous form can improve physical stability and product shelf life by preventing crystallisation [179]. It is therefore important to understand how well the various components mix, and the types of interactions present within the system [179]. Polyvinylpyrollidone-vinyl acetate (PVP-VA) was chosen as the polymer to carry forward in the study as studies have been carried out but it is not overly published in the literature. It has previously been studied in a solid dispersion with IMC (prepared *via* solvent evaporation) which used DSC and FT-IR to look at drug polymer interactions in relation to crystallisation [84] and Sun *et al.* [85] found that IMC is actually soluble in this polymer. Zhao et al. [180] also predicted the miscibility of IMC and PVP-VA using the Flory-Huggins theory and found that PVP-VA did inhibit the crystallisation of IMC, especially at higher polymer loading levels.

## 1.8 Aims of the Project

The overall aim of this project was to characterise the local structure and dynamics of three amorphous solid dispersions (IMC, FFA and TLB; with PVP-VA), and correlate this with outcomes of physical stability. We focused on exploiting the huge potential of solid-state NMR as a tool to probe the local molecular environment of such dispersions, aiming to unify the knowledge gained with other commonly used characterisation techniques.

In order to achieve this goal, we aimed to develop solid-state NMR methodologies to understand important factors contributing to the successful formulation of solid dispersions, in terms of being **fully amorphous**, **fully miscible** and **physically stable** upon storage; and relate them to local structure and dynamics. We focused on using variable temperature solid-state NMR techniques, as literature investigations are limited in this area; to enhance understanding of molecular motions on different timescales, aiming to identify key parameters, methodology and information to aid the prediction of physical stability. To ultimately use NMR to enable the prediction of crystallisation outcomes from standard stability studies could pave the way to enable the quicker identification of potential storage issues, since molecular mobility of amorphous dispersions is a key factor affecting their physical stability.

Characterisation of amorphous dispersions using a 'one technique' approach is limiting: drug/polymer systems can be very complex, and therefore require a multicomponent characterisation approach to provide information from a number of different perspectives.

Characterisation was performed on a bulk level using more traditional techniques (DSC and PXRD), with local molecular level information provided *via* solid-state NMR and monitored throughout a 12 week accelerated stability study. We concurrently characterised the dispersions with a number of variable temperature solid-state NMR techniques, which provided a sensitive probe of changes in local mobility. By correlating the traditional and variable temperature characterisation across a range of systems we therefore aimed to obtain a clearer understanding of the mobility and stability behaviour within these systems.

# Chapter 2

# Characterisation

This chapter summarises the principles and theory behind the various techniques used to characterise the three model drug systems of IMC, FFA and TLB; both as amorphous materials, crystalline polymorphs and amorphous solid dispersions of varying drug loading levels. The techniques described are common across all results chapters. The experimental conditions used for each technique are discussed in chapter 3.

## 2.1 Nuclear Magnetic Resonance (NMR) spectroscopy

### 2.1.1 Basic NMR principles [1–4]

Nuclear Magnetic Resonance (NMR) spectroscopy relies upon interactions between a nucleus exhibiting a magnetic moment ($\overrightarrow{\mu}$), and an external magnetic field ($\overrightarrow{B}$), and is a powerful analytic technique providing detailed information about chemical structure and dynamics. Magnetic moment occurs in nuclei which possess the intrinsic property angular momentum, often referred to as nuclear spin. Nuclei can be thought of small bar magnets, as any charged body in motion is associated with a magnetic field. The magnetic moment of a nucleus (equation 2.1) is directly proportional to the spin quantum number ($I$) and gyromagnetic ratio ($\gamma$), which is a constant dependent on nucleus type.

$$\overrightarrow{\mu} = \gamma \hbar I \tag{2.1}$$

where $\hbar$ is Plank's constant divided by $2\pi$. To be magnetically active, a nucleus must have a spin quantum number ($I$) $\neq 0$, (e.g. $I = \frac{1}{2}$, 1, $\frac{3}{2}$, 2, $\frac{5}{2}$...).

Angular momentum is a vector quantity, and is related to spin quantum number through equation 2.2:

$$\overrightarrow{I}^2 = (I(I+1)\hbar^2) \tag{2.2}$$

Without the presence of an external magnetic field ($B_0$), magnetic moments are orientated randomly, with all orientations ($2I + 1$) having the same energy. Upon application of an external magnetic field, magnetic moments will align at an angle either **with** ('spin-up') or **against** ('spin-down') $B_0$. The two spin states are separated by $\Delta$E, as outlined in figure 2.1 (termed the Zeeman effect), which depends on the strength of the interaction between the nucleus, and the magnetic field.

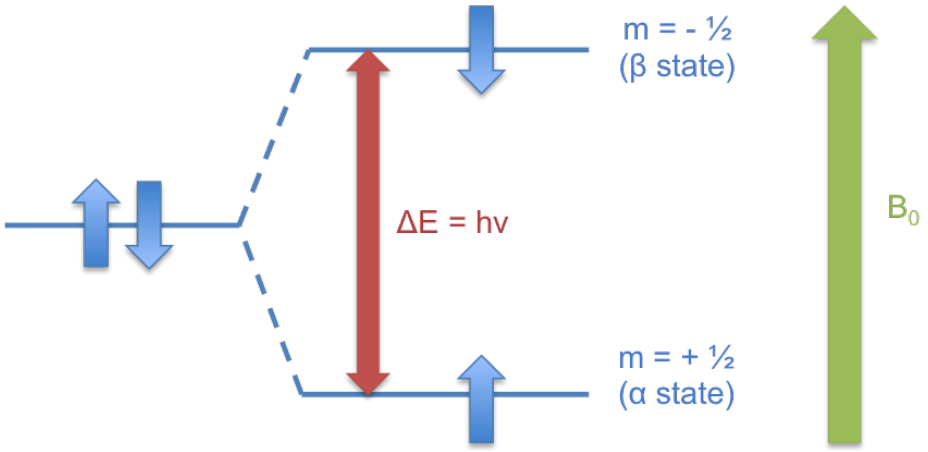


**Figure 2.1:** Relative energy levels of spin $\frac{1}{2}$ nucleus, showing the two magnetic spin states (m = magnetic quantum number) with increasing $B_0$, adapted from [1, 5]

In the presence of an external magnetic field, the magnetic moment rotates about $B_0$, at an angular velocity, known as the Larmor frequency:

$$\omega_0 = -\gamma B_0 \tag{2.3}$$

Electromagnetic radiation (radiofrequency ($rf$) pulses), oscillating at a specific frequency, are applied in NMR to measure the energy difference of the Zeeman effect. This frequency, applied close to the Larmor frequency of the nucleus of interest is therefore dependent on both the observation nucleus and external magnetic field. At a particular magnetic field strength, the Larmor frequency occurs in the radiofrequency region of the electromagnetic spectrum. For example, for a $^1$H nucleus in a 9.4 T external magnetic field, $\Delta$E between the two spin states is measured to be 400 MHz, which is the Larmor frequency of protons at this $B_0$.

### 2.1.2 Bulk Magnetisation [1, 4]

We have so far discussed the interactions of a single spin, with the external magnetic field. Analysis of actual sample with NMR spectroscopy involves a much larger number of spins, which of course must be taken into consideration. If multiple nuclear spins are placed into an external magnetic field ($B_0$), thermal equilibrium will be established through equation 2.4, the Boltzmann distribution.

$$\frac{n(+\frac{1}{2})}{n(-\frac{1}{2})} = exp^{(\frac{\Delta E}{kT})} \tag{2.4}$$

where n represents the population of the spin states, k is Boltzmann's constant, T is absolute temperature.

For example, using equation 2.4 to calculate the population of spin states in an external magnetic field of 9.4 T, an extremely small excess of *ca.* 50 $\alpha$ spins in every **million** spins, as compared to $\beta$ spins exists. This excess of $\alpha$ spins leads to a net magnetization in parallel alignment along the z axis, termed the **bulk** magnetisation ($M_0$). $M_0$ is represented in figure 2.2, which outlines the 'vector model' analogy.

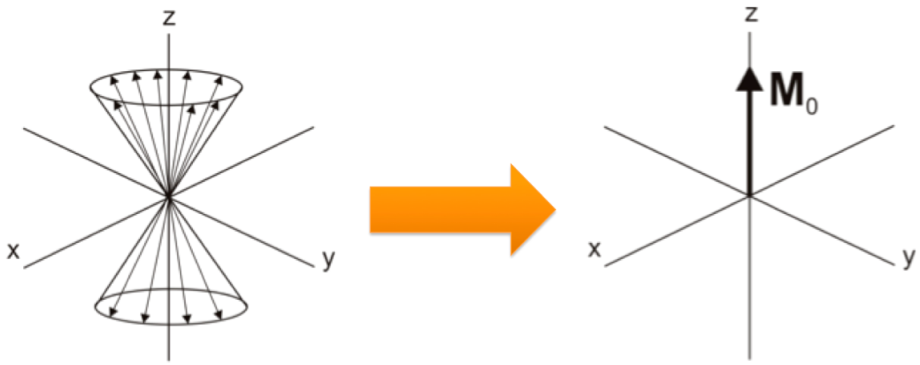


**Figure 2.2:** Vector model of bulk magnetisation (collection of spin- $\frac{1}{2}$ nuclei), where the Boltzmann distribution leads to bulk magnetisation ($M_0$) parallel to $M_0$, adapted from [20, 21]

As previously outlined, applying an *rf* pulse (*via* a coil) at the Larmor frequency leads to spin excitation. The magnetic field of the applied *rf* field is termed $B_1$. For the bulk magnetisation, the individual magnetisation vectors are still precessing at the Larmor frequency (around the applied field). To aid understanding, the rotating frame of reference is used as a simplified descriptive model for pulsed NMR experiments.

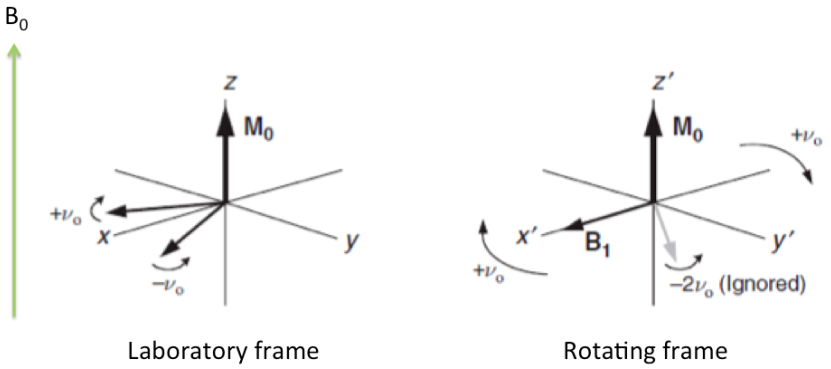


**Figure 2.3:** Representations of the laboratory and rotating frames of reference, adapted from [20, 21]

In the laboratory frame, the x, y and z axes are viewed as being static; whereas in the rotating frame, the whole frame rotates at the *rf* frequency ($\nu_0$), with $B_1$ and $M_0$ stationary, and perpendicular to each other. The rotating frame model therefore removes the time dependency.

### 2.1.3 Chemical Shift [1–5]

As previously discussed, the resonant frequency of a nucleus is dependent upon both the gyromagnetic ratio, and the strength of $B_0$. To obtain one single frequency signal for each particular magnetically active nucleus would not be particularly useful. In reality, the NMR frequency is sensitive to the environment of a nucleus in a molecule, which arises through differences in the electron distribution.

This effect occurs because the external magnetic field influences the chemical environment, causing surrounding electrons to circulate in their atomic orbitals, resulting in small local magnetic fields ($B$). I.e. the local field experienced by the nucleus is actually different to the external magnetic field. The induced motion can be compared to a wire with a current passing though, which generates a small (local) magnetic field, in the opposite direction to $B_0$, and shields the nucleus from its surrounding electrons and external magnetic field. The effect of the local magnetic field gives rise to differences in the frequencies detected, dependent on chemical environment, hence NMR is particularly useful in the characterisation and identification of molecules.

The local field (B) is slightly smaller than the the external magnetic field ($B_0$), and is calculated using equation 2.5:

$$B = B_0 - B' = B_0(1 - \sigma) \tag{2.5}$$

where $\sigma$ is the shielding constant. In molecules, as compared to a single atom, the electron distribution becomes much more complex. The electron distribution depends upon neighbouring atoms, and can be affected by a number of different factors including hydrogen bonding, electronegativity and unpaired electrons. The effects of shielding changes the resonance frequency of the nucleus, resulting in a chemical shift value ($\delta$). Experimentally, chemical shift is measured in ppm, showing the difference in resonance frequency between the particular nucleus ($\nu$) and a reference nucleus ($\nu_{ref}$), commonly tetramethylsilane (TMS).

$$\delta = 10^6(\frac{\nu - \nu_{ref}}{\nu_{ref}}) \tag{2.6}$$

### 2.1.4 Solid-state NMR [4, 6, 7]

Solids and liquids show completely different behaviour in terms of their nuclear spin interactions. In solution-state NMR, fast molecular motions average out the majority of the nuclear spin interactions, resulting in narrow, isotropic chemical shifts. In solids however, atoms and molecules are more likely to be rigid, therefore do not experience

random tumbling. The reduction in molecular mobility leads to additional anisotropic (orientation dependent) nuclear spin interactions, resulting in broadening of linewidths.

Nuclei in a magnetic field experience many different types of interactions, and can be described using Hamiltonian operators ($\hat{H}$). $\hat{H}$ represents the energy in the system, and generally provide a quantum mechanical description of the interactions between a nuclear spin and a local magnetic field.

$$\hat{H} = \overrightarrow{I} \cdot \mathbf{A} \cdot \overrightarrow{B} \tag{2.7}$$

where **A** represents the *orientation* dependence of the interaction (with respect to the x,y,z axes) and $\overrightarrow{B}$ is the magnetic field. The spin Hamiltonian (equation 2.8) provides a quantum mechanical description of all possible interactions between nuclear spins, with each interaction contributing to the properties of linewidths in NMR.

$$\hat{H}_{TOTAL} = \hat{H}_z = \hat{H}_{CSA} + \hat{H}_D + \hat{H}_Q + \hat{H}_J \tag{2.8}$$

where:

- $\hat{H}_z$ = Zeeman Hamiltonian
- $\hat{H}_{CSA}$ = Chemical Shift Anisotropy Hamiltonian
- $\hat{H}_D$ = Dipolar coupling Hamiltonian
- $\hat{H}_Q$ = Quadrupolar coupling Hamiltonian
- $\hat{H}_J$ = J-coupling Hamiltonian

For an isotropic liquid, the orientation dependent interactions ($\hat{H}_{CSA}$, $\hat{H}_D$ and $\hat{H}_Q$) are averaged out through fast molecular motions. However these interactions result in significant broadening of solid-state NMR linewidths. In order to overcome these orientation dependent factors, and therefore achieve higher resolution solid-state NMR spectra, a number of methodologies must be applied. In solids, the $\hat{H}_J$ becomes negligible, as J-coupling interactions in the solid-state are so small. Additionally, the quadrupolar coupling Hamiltonian ($\hat{H}_Q$) is only relevant for nuclei with $I > \frac{1}{2}$, which were not observed in this research. The Zeeman interaction is the strongest, and therefore most important interaction in NMR. However, this interaction in the solid-state is very similar to the liquid-state. Therefore, a detailed description of the only the important anisotropic nuclear spin interactions, ($\hat{H}_{CSA}$ and $\hat{H}_D$) and the methods employed to overcome the resulting spectral broadening are discussed below.

A summary of the interactions, and relative magnitudes in both the solid and liquid state can be seen in figure 2.4.

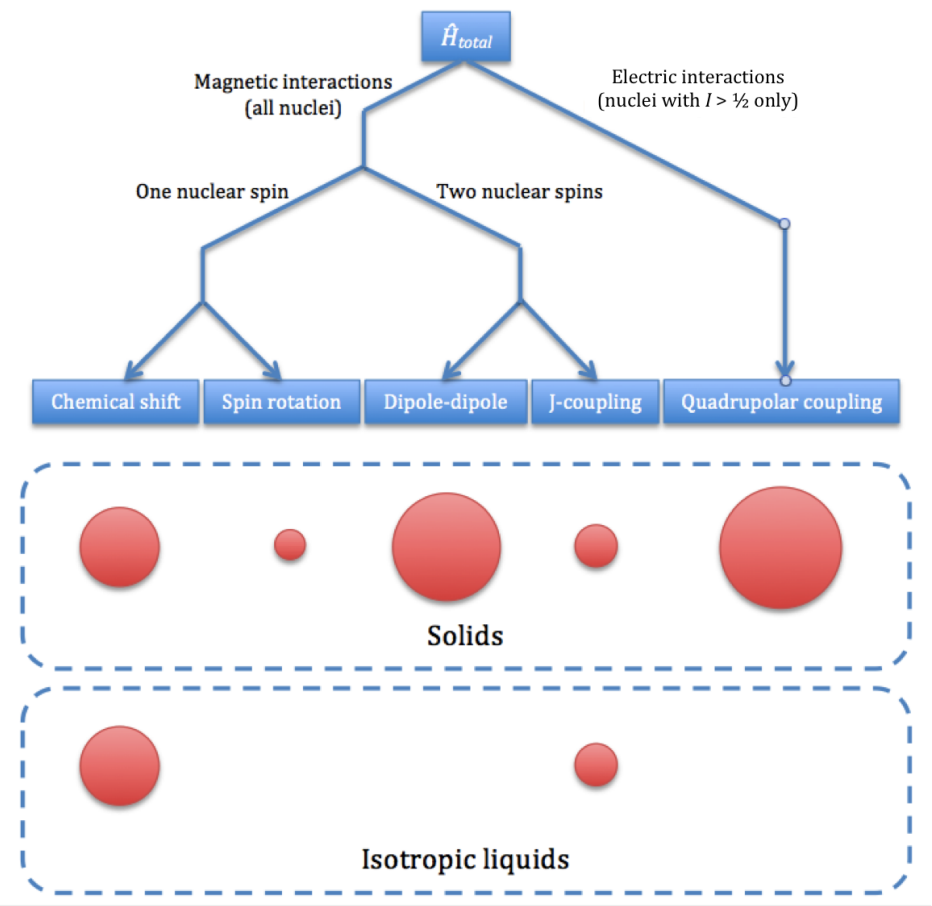


**Figure 2.4:** Summary of the organisation of the spin Hamiltonian interactions, with relative magnitudes represented by circle area, adapted from [7]

#### 2.1.4.1 Chemical Shift Anisotropy ($\hat{H}_{CSA}$) [4, 6, 7]

Chemical shift describes the change in frequency of a nucleus, arising from the effect of induced motions of electrons by the external magnetic field ($B_0$) on the local magnetic field (B). Chemical Shift Anisotropy (CSA) originates from the orientation dependence effect of a molecule, with respect to external magnetic field ($B_0$). This is due to electron distribution around a nucleus often being non-spherical, assumed to be an elongated ellipsoid stretched along bonds. In the liquid-state, anisotropy is averaged out to zero by fast molecular motions, therefore a single isotropic value of chemical shift is observed for each nuclear environment. In the solid-state however, the molecule can adopt a range of different orientations (with respect to $B_0$). The shielding interaction experienced by each orientation is therefore slightly different as well, resulting in small variations of chemical shift, and therefore and therefore a much broader peak (figure 2.5).

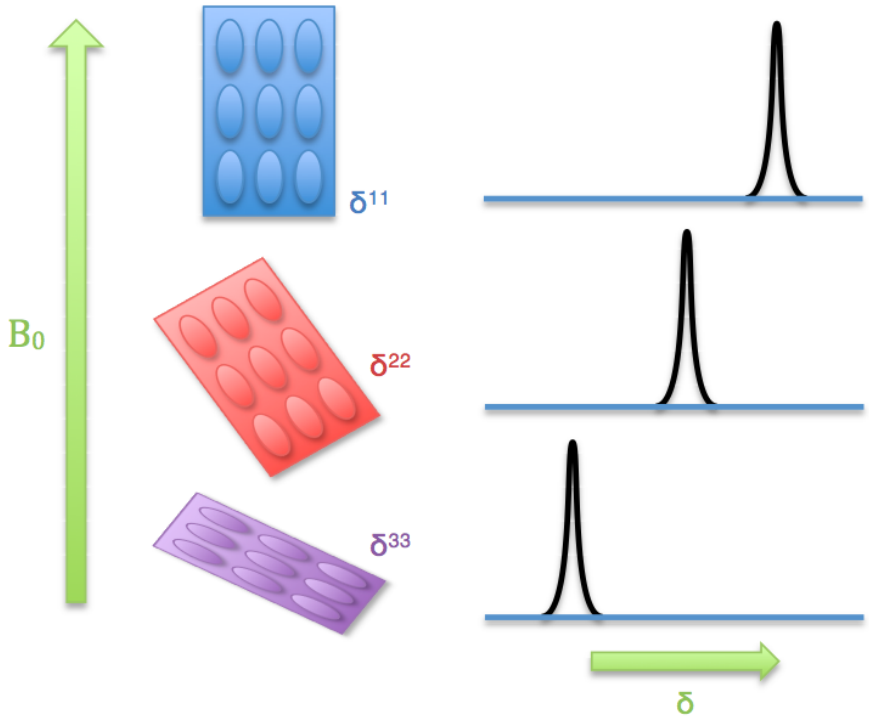


**Figure 2.5:** Orientation dependence of chemical shift of a solid, with respect to the external magnetic field, adapted from [5, 6]

To further understand CSA, the chemical shift Hamiltonian must be analysed (equation 2.9):

$$\hat{H}_{CSA} = \gamma B_0 I_z[\delta_{iso} + \frac{1}{2}\delta_{CSA}(3cos^2\theta) - 1)] \tag{2.9}$$

where $\theta$ = angle of the molecular orientation (with respect to external magnetic field). $\delta_{iso}$ (equation 2.10) and $\delta_{CSA}$ (equation 2.11) describe the isotropic chemical shift, and the magnitude of the CSA respectively.

$$\delta_{iso} = (\delta_{11} + \delta_{22} + \delta_{33})/3 \tag{2.10}$$

$$\delta_{CSA} = \delta_{iso} - \delta_{33} \tag{2.11}$$

where $\delta_{11}$ is the least shielded (has the largest influence on the chemical shift), and $\delta_{33}$ is the most shielded (has the smallest influence on the chemical shift) component. In reality in solids, there are many more possible orientations than the three principle values described in equation 2.10, which leads to the presence of a broadened powder pattern, as outlined in figure 2.6.

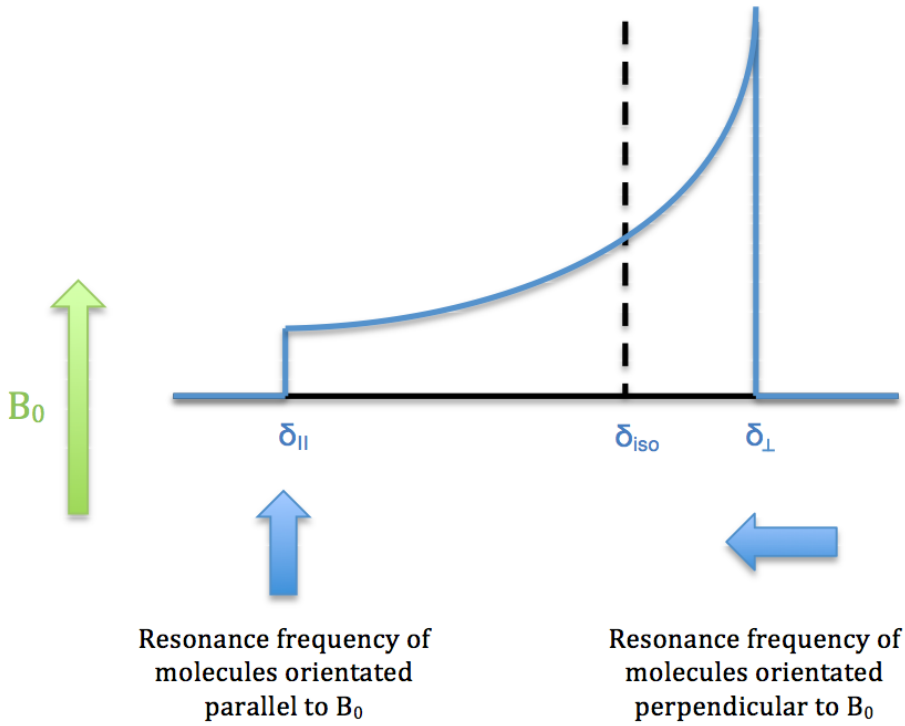


**Figure 2.6:** Powder pattern of a molecule with axial symmetry, adapted from [4]

The anisotropic component of $\hat{H}_{CSA}$ contains a geometric term (3 $\cos^2\theta$ - 1) which can be eliminated through Magic Angle Spinning (MAS), described alongside other techniques for eliminating the effect of CSA in section 2.1.4.3.

### 2.1.4.2 Dipolar Coupling ($\hat{H}_D$) [3, 4, 7]

Dipolar coupling (often termed dipole-dipole couplings) occurs due to interactions of nuclear spins with each other. This can occur through interactions between like (*homo*nuclear, I-I) spins; or unlike (*hetero*nuclear, I-S) nuclei. Dipolar coupling is a through-**space** interaction, which leads to significant line broadening in solids. Methods employed in solid-state NMR to help to reduce broadening though dipolar coupling are outlined in section 2.1.4.3.

**2.1.4.2.1 Homonuclear dipolar coupling** Homonuclear dipolar coupling arises from the interaction between two like-spins (for example $^1$H and $^1$H), when close enough in space. The homonuclear dipolar Hamiltonian is described by equation 2.12:

$$\hat{H}_{DD} = (\frac{\mu_0}{4\pi}\frac{1}{2}\frac{\gamma_i\gamma_j\hbar}{r_{ij}^3})2\hat{I}_{iz}\hat{I}_{jz} - \frac{1}{2}[\hat{I}_{1+}\hat{I}_{2-} + \hat{I}_{1-}\hat{I}_{2+}](3cos^2\theta_{ij} - 1) \tag{2.12}$$

where $I_i$ and $I_j$ are like-spins, $r_{ij}$ is the distance between the two nuclei, $\mu_0$ is the permability of free space, $\gamma$ is the gyromagnetic ratio of each spin (j and k).

The dipolar coupling Hamiltonian is extremely complex, and beyond the scope necessary here. However, to relate the Hamiltonian equation to common nuclei, such as $^{1}$H and $^{13}$C, we can split the equation into three main terms. This helps to understand the effect of dipolar coupling on the resulting NMR spectra (figure 2.7)

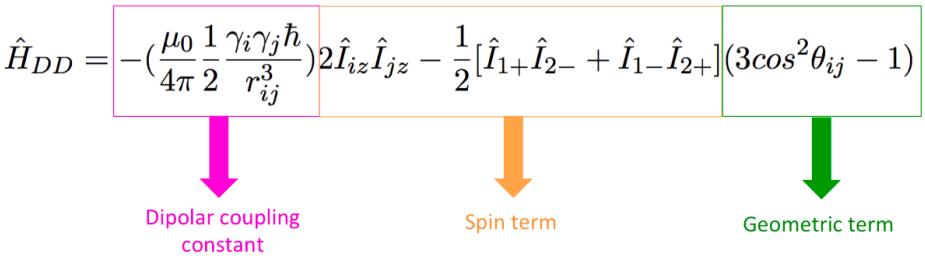


**Figure 2.7:** Demonstration of the three important terms of the dipolar coupling Hamiltonian

From this, it becomes clearer that:

1. Dipolar coupling constant is dependent on gyromagnetic ratio and distance between spins.
2. Spin term represents the energy conserving 'flip-flop' transition between two like spins, commonly referred to as spin diffusion. This term is dependent on the abundance of the spin.
3. Geometric term describes the orientation dependent broadening effect, and was previously seen in the $\hat{H}_{CSA}$. Reduction of the broadening effect will be discussed in section 2.1.4.3.

The resonance frequency of the two-like spins is similar, therefore they are able to undergo 'flip-flop' transitions, described by the spin term of the homonuclear dipolar Hamiltonian. This transition is an energy conserving process where one spin flips to a higher energy state, whilst the other spin flips to a lower energy state, through a change of spin angular momentum (figure 2.8). The 'flip-flop' transition is commonly referred to as spin diffusion, and will be discussed further in chapter 4.

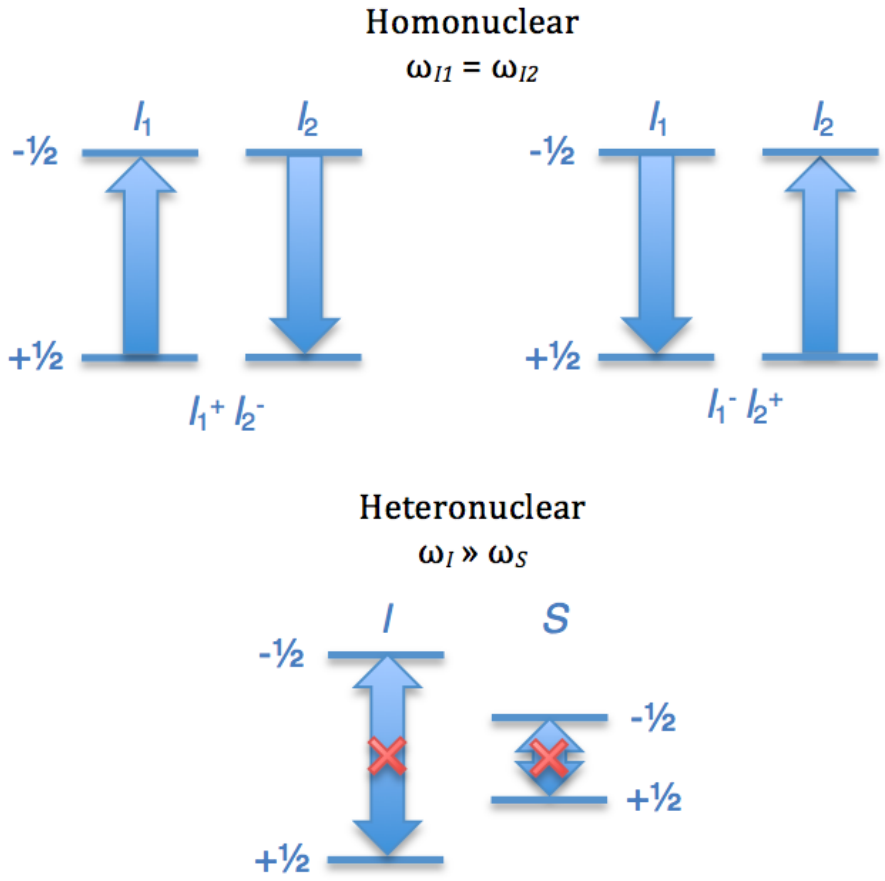


**Figure 2.8:** Diagramatic representation of flip-flop transition between homonuclear spins, adapted from [5, 6]

Therefore, in summary, important properties of the dipolar coupling interaction include:

- **Dipolar coupling constant**: The magnitude of the interaction is proportional to the gyromagnetic ratio ($\gamma$), therefore higher $\gamma$ nuclei (e.g. $^{1}$H) will display much stronger homonuclear dipolar coupling as compared to lower gamma nuclei (e.g, $^{13}$C or $^{29}$Si)
- **Dipolar coupling constant**: Distance between nuclei determines the strength of dipolar coupling, (D is *inversely* proportional to $r^3$), making it highly distance dependent. Nuclei with higher abundance (e.g. $^{1}$H or $^{19}$F) are more likely to be close in space than low abundance nuclei (e.g. $^{13}$C or $^{15}$N), and have stronger dipolar coupling interactions
- **Geometric term**: The dipolar coupling Hamiltonian contains the orientation dependence term ($3\cos^2\theta$-1), which leads to broadening of the spectra, and can be reduced through MAS

Dipolar couplings can be seen in the solid-state spectrum as a 'Pake Doublet' (figure 2.9).

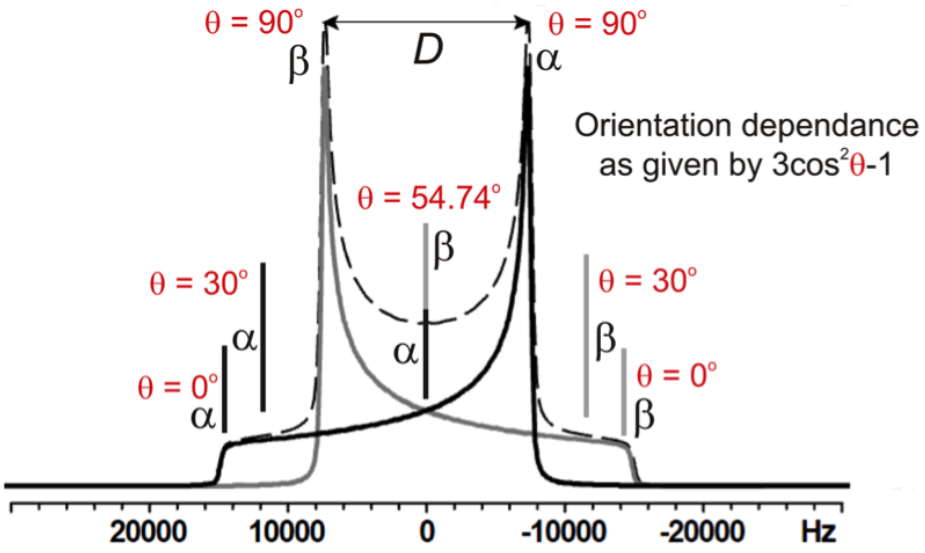


**Figure 2.9:** Powder pattern (Pake doublet) of two spin $\frac{1}{2}$ nuclei experiencing homonuclear dipolar coupling, adapted from [6]

The two sub-spectra arise from the different spin states ($\alpha$, or $\beta$), with molecular orientations where $\theta$ is between 0 and 90 deg. The peak intensities correspond to the number of crystallites adopting the particular orientation, hence the highest intensity peak is observed when $\theta$ is perpendicular to $B_0$. The splitting of the Pake-doublet is equal to D (dipolar coupling constant). When the sample is placed at $\theta = 54.74, ^\circ$ known in solid-state NMR as the 'magic angle' the frequency is unaffected by dipolar couplings (see section 2.1.4.3).

**2.1.4.2.2 Heteronuclear dipolar coupling** Heteronuclear dipolar coupling occurs due to the interaction between unlike spins that are close in space. Using NMR terminology, the unlike spins are labelled I (abundant spin, e.g. $^1$H) and S (rare spin, e.g. $^{13}$C). In the presence of a magnetic field, Zeeman splitting occurs for each spin, resulting in alignment of the I and S spins either spin-up, or spin-down, with respect to $B_0$). Each spin also experiences a local magnetic field, which can affect the magnetic field of close proximity neighbouring spins.

The heteronuclear dipolar coupling for unlike ($\hat{I}$,$\hat{S}$) spins is described by the following Hamiltonian:

$$\hat{H}_{DD} = (\frac{\mu_0}{8\pi}\frac{1}{2}\frac{\gamma_I\gamma_S\hbar}{r_{IS}^3})2\hat{I}_z\hat{S}_z(3cos^2\theta_{IS} - 1) \tag{2.13}$$

It has a very similar form to the homonuclear Hamiltonian, but with a reduced spin term. This is because the energy saving spin-diffusion process can not occur in unlike spins, as the resonant frequencies are too different (figure 2.8). Again, the coupling strength is dependent on $\gamma$, and distance between spins.

#### 2.1.4.3 Techniques used in solid-state NMR to improve resolution

A number of clever methodologies have been developed as the field of solid-state NMR study has progressed, in order to compensate for the strong anisotropic interactions described above 2.8.

**2.1.4.3.1 Magic Angle Spinning (MAS) [4, 6]** The Hamiltonians describing homonuclear and heteronuclear dipolar coupling and chemical shift anisotropy all contain the same geometric component: (3 $\cos^2$ $\theta$ - 1). This orientation dependent term can be averaged out in the solid-state, by spinning the sample at an angle of 54.74 ° with respect to $B_0$. The 'magic angle' results in the anisotropy of the interaction averaging to zero, ((3$\cos^2\theta$-1) = 0). This effectively removes the orientation dependence of the Hamiltonians, giving an isotropic chemical shift in the NMR spectrum.

For MAS to effectively remove interactions, the MAS frequency needs to be at least 3 times greater than the interaction itself. In the case on strong interactions (for example $^1$H-$^1$H dipolar interactions), this can be difficult to achieve. Removal of $^1$H-$^1$H dipolar interactions requires extremely fast spinning rates (*ca.* 80 kHz), which requires extremely specialist fast MAS probes. However, $^1$H-$^{13}$C heteronuclear dipolar interactions can be removed more easily, with spinning rates of *ca.* 10 kHz sufficient to remove the spectral broadening of these interactions.

**2.1.4.3.2 Decoupling [3,4,6]** For strong interactions, which are not effectively averaged out through Magic Angle Spinning, decoupling will likely be employed to further improve spectral resolution.

High power heteronuclear decoupling techniques use multiple high power radiofrequency (*rf*) pulse sequences, at the resonant frequency of the I (abundant) spin to further average the effects of dipolar coupling, during acquisition of the free induction decay (FID) of the S (less abundant) spin. The *rf* irradiation results in the I spins rapidly switching between the $\alpha$ (spin-up) and $\beta$ (spin-down) states, at a rate determined by the decoupling power. To fully average the coupling interactions to zero, the rate of transition must be greater than the heteronuclear decoupling strength. This method, known as continuous radio-frequency wave (CW) decoupling [181] is not commonly used, as it results in sample heating during long acquisition times. Higher sophistication decoupling pulse sequences have since been developed, for example Two Phase Pulse Modulation (TPPM), which employs two high power pulses which differ in phase (between 10 and 70 °) [182]; and SPINAL-64 [183]. The effect of molecular mobility on heteronuclear decoupling is discussed in more depth in chapter 4.

The successful application of homonuclear dipolar decoupling is much harder to achieve, due

to the additional spin term (describing the flip-flop transitions of spin diffusion) present in the $\hat{H}_D$. Homonuclear decoupling techniques are based upon multiple pulse sequences, which contain sections where the dipolar coupling Hamiltonian has no effect on the magnetisation. Acquisition of magnetisation during one of the sections, results in improved resolution in the NMR spectrum. Commonly used decoupling sequences include Frequency-Switched-Lee-Goldburg (FSLG) [184] and Decoupling Using Mind Boggling Optimisation (DUMBO) [185].

**2.1.4.3.3 Cross-Polarisation [4,8,9]** Cross-Polarisation (CP)/MAS NMR experiments are commonly used to enhance signal-to-noise ratios and reduce the acquisition time of low $\gamma$, low sensitivity nuclei, such as $^{13}$C and $^{15}$N.

The cross-polarisation pulse sequence is based upon a magnetisation transfer step, which occurs through the tendency of magnetisation to move from highly polarised spins $\rightarrow$ less polarised spins, when the spins are in close contact. This CP step is analogous to the heat flow associated with thermal transfer from hot to cold objects in thermal contact. In section 2.1.4.2.1, we discussed the energy conserving 'flip-flop' transitions of like spins, and highlighted that such transitions do not occur for heteronuclear spin pairs. However, the application of *rf* pulses can essentially bridge the energy gap of the unlike resonance frequencies, leading to the transfer of magnetisation between the heteronuclear spins. For this to occur, the contact condition must adhere to the Hartmann-Hahn matching condition [186], described in equation 2.14:

$$\gamma_I B_1^I = \gamma_S B_1^S \tag{2.14}$$

where $\gamma_I$, $\mathrm{B}_I$ and $\gamma_S$ $\mathrm{B}_S$ are the gyromagnetic ratios and *rf* pulses applied to the I and S spins respectively.

To fulfil the Hartmann-Hahn condition, the simultaneous application of two continuous *rf* pulses, each one at the resonance frequency of either the I or the S spin must take place. Application of an *rf* pulse will result in the precession of magnetisation about the xy-plane, with the rate of precession dependent on both the frequency, and amplitude of the applied field. The application of the two fields, results in the precession of the I and the S spins about a particular axis. When these rotation frame frequencies are *equal*, the Hartmann-Hahn condition is said to be met, and an energy conserving dipolar contact occurs between the I and S spin, which in turn allows the polarisation transfer between the spins.

The pulse sequence of a typical $^1$H-$^{13}$C CP/MAS NMR experiment can be seen in figure 2.10. The pulse sequence involves a $\pi/2$ pulse, which flips proton magnetisation into the xy plane, followed by the application of simultaneous RF fields to the I and S spins, for a period ($\tau_{CP}$), followed by the detection of S spins, during which the I spins are decoupled, as described previously.

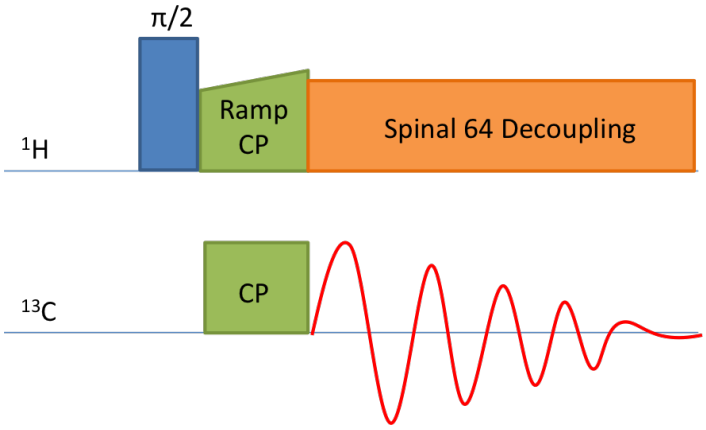


**Figure 2.10:** Pictorial representation of $^{1}$H-$^{13}$C CP/MAS NMR pulse sequence

### 2.1.5 Probing mobility using solid-state NMR [4, 7]

Solid-state NMR provides a number of techniques for characterisation of molecular mobility characterisation, and is able to probe dynamics on different time and length scales (figure 2.11). The effects of motions on nuclear spins are dependent on the three nuclear spin timescales: **relaxation, spectral and Larmor**. All timescales are also dependent on the sample, and on physical parameters such as temperature and strength of external magnetic field [7].

The techniques available to probe molecular mobility in solid-state NMR range from cross-polarisation based experiments, to the measurement of a number of different relaxation times. Chapter 4 outlines the main applications of solid-state NMR for the detection of different motional regimes in pharmaceutical solids. To aid understanding of these techniques, nuclear relaxation will be briefly introduced below.

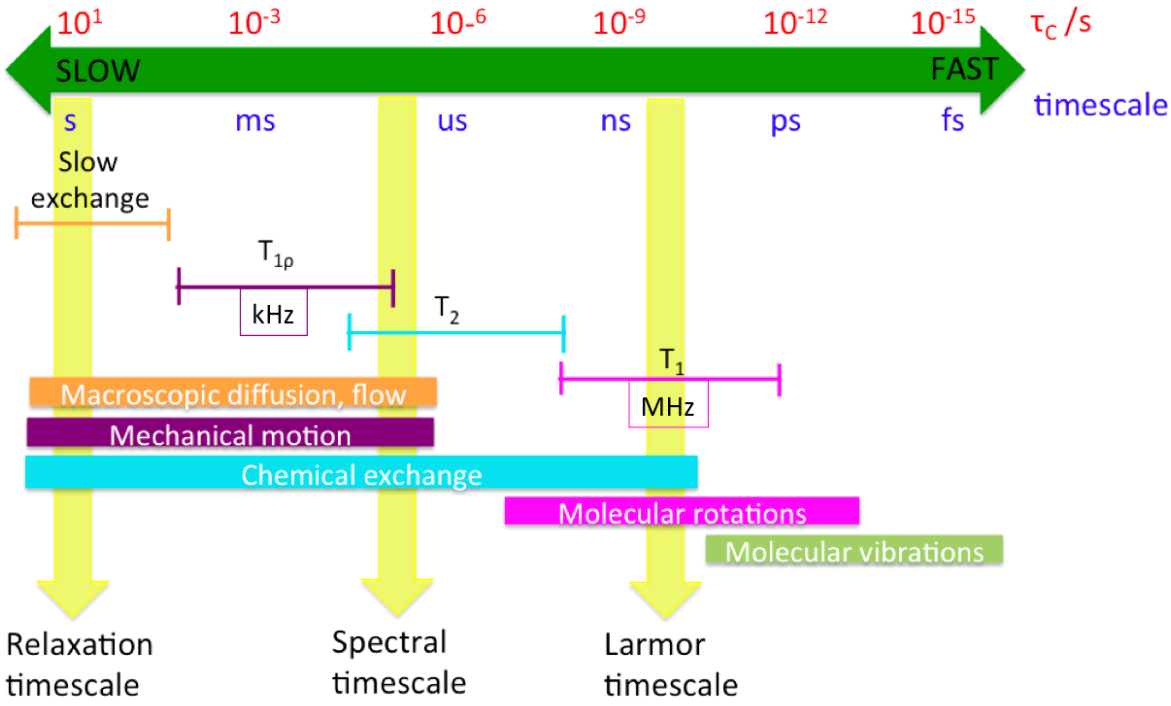


**Figure 2.11:** The motional timescales of NMR: physical processes and NMR relaxation methods, adapted from [7]

### 2.1.6 NMR Relaxation [4, 7]

At equilibrium, the populations of energy levels are predicted by the Boltzmann distribution. Following the application of an *rf* pulse, equilibrium is disturbed, and the energy level populations deviate from equilibrium positions, often generating spin coherence. The nature of the coherence is dependent on the magnitude of the pulse. A $\pi$ pulse (180 °) will invert the spin population along the z-axis; whilst a $\pi/2$ pulse (90 °) will transfer spins into the observable xy-plane.

Following perturbation from the application of an *rf*-pulse, magnetisation will re-establish equilibrium, through the process of nuclear spin relaxation. This occurs *via* one of two relaxation pathways: spin-lattice relaxation, or spin-spin relaxation; through interaction of the spins with the thermal environment (figure 2.12).

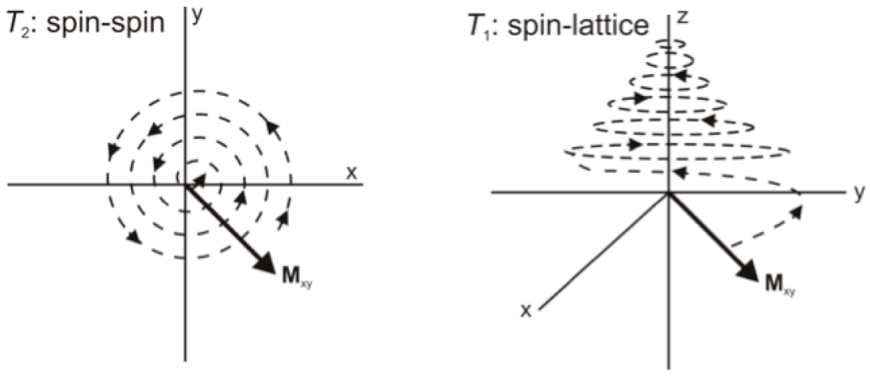


**Figure 2.12:** NMR relaxation pathways following a $\pi/2$ pulse: magnetisation decay through $T_2$ relaxation (viewed looking down the z-axis) and re-establishment of magnetisation through $T_1$ relaxation, adapted from [20, 21]

Spin-spin relaxation (also referred to as transverse, or $T_2$ relaxation) occurs through coherence decay. This occurs through the energy exchange between $\alpha$ and $\beta$ spin states (*via.* through-space dipole-dipole interactions), which results in loss of coherence **without** a net change in energy, which eventually, though repetition will drive overall (net) magnetisation back to zero.

Spin-lattice relaxation (also referred to as longitudinal, or $T_1$ relaxation) involves the movement of spins back to the Boltzmann distribution, through loss of heat energy from the spins to the surroundings (or the 'lattice'). The loss of energy is so small, it is undetectable in the bulk sample. The $T_1$ relaxation mechanism mainly occurs though dipole-dipole interactions, which are strongly dependent on molecular motion. This occurs as follows: for example for nuclei with $I = \frac{1}{2}$, relaxation occurs due to fluctuations in the local environment, or local magnetic field, which are induced by thermal molecular motion. These fluctuations are influenced by the surrounding nuclei which are close in space, through dipolar coupling. However, additional pathways, such as chemical shift anisotropy, quadrupolar relaxation and spin rotation do exist, but will not be discussed further.

Spin-lattice relaxation was employed in this study as the main technique to explore the molecular mobility of the three model amorphous systems, therefore spin-spin relaxation will not be discussed further.

#### 2.1.6.1 Measurement of spin-lattice ($T_1$) relaxation [8]

The recovery of the z-magnetisation ($M_z$) back to thermal equilibrium (governed by the Boltzmann distribution) follows an exponential decay, as described by the Bloch equation (equation 2.15 [8]):

$$\frac{dM_z(t)}{dt} = \frac{M_z(t) - M_0}{T_1} \tag{2.15}$$

where $M_0$ is the magnetisation at thermal equilibrium, and $T_1$ is the time constant. Bloch theory assumes first order kinetics are followed. Following the application of a $\pi/2$ pulse, the $T_1$ time, at time t, is described by:

$$M_z = M_0[1 - e^{\frac{t}{T_1}}] \tag{2.16}$$

$^1$H $T_1$ relaxation times were measured using an inversion recovery pulse sequence (see chapter 3). In this sequence, a $\pi$ pulse is applied to first invert the magnetisation. A delay ($\tau$) is then allowed, during which magnetisation relaxes, followed by a $\pi/2$ pulse to measure the remaining z-magnetisation after time, $\tau$. The delay is varied, which allows the peak intensities to be measured as a function of $\tau$.

#### 2.1.6.2 Spin-lattice relaxation in the rotating frame

$T_1$ relaxation in the rotating frame ($T_{1\rho}$) is sensitive to slower molecular motions, as compared to $T_1$. Investigation of ${T_{1\rho}}^H$ allowed us to probe the motions associated with backbone polymer chain motions [29, 161], thought to reflect the overall 'freeing up' of local mobility as temperature conditions change, especially through the $T_g$ [187]. These motions occur on a kHz timescale (ms – $\mu$s) at the frequency of rotating frame, determined by the $B_1$ field. ${T_{1\rho}}^H$ relaxation provides a sensitive probe of local mobility, giving a snapshot of molecular level changes within the systems which is particularly important below, and around $T_g$.

The measurement of ${T_{1\rho}}^H$ involves the use of the spin-locking pulse sequence, first devised by Schaefer *et al.* [188], . $^1$H relaxation times are measured through the acquisition of $^{13}$C spins, following a cross-polarisation transfer step between $^1$H and $^{13}$C nuclei. Using this method, the $^{13}$C magnetisation relaxes in the rotating frame, during the spin-locking time period ($\tau$). Peak intensities, as a function of spin-lock time are fitted in a similar way to $T_1$ (see chapter 2).

## 2.2 Other characterisation techniques used in the study of pharmaceutical compounds

### 2.2.1 Differential Scanning Calorimetry (DSC) [10, 11]

Differential Scanning Calorimetry measures the uptake of thermal energy by a sample during monitored changes in temperature. The energy uptake of the sample is compared to an empty reference pan in order to determine and identify thermal transitional events.

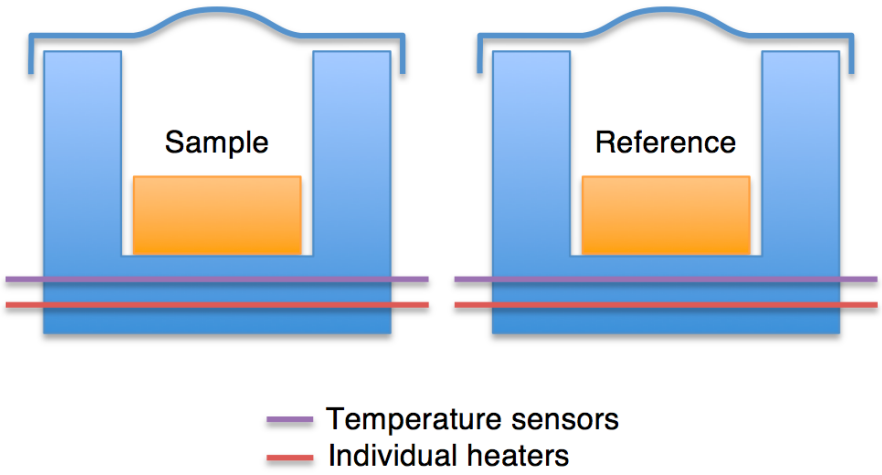


**Figure 2.13:** Schematic representation of the experimental set-up of Differential Scanning Calorimetry (DSC), adapted from [22]

The sample and reference pans are separately heated at the same linear rate, within a specified temperature range. As the reference is an empty pan, the heating rates between sample and reference will be different, with the difference representing the energy uptake of the sample. Isothermal conditions are maintained through calculation of the additional energy absorbed (endothermic) and released (exothermic) by the sample as compared to the reference. The calculated energy differences provide useful information on specific thermal events, including glass transitions ($T_g$), crystallisation ($T_c$) and melting ($T_m$) (figure 2.14).

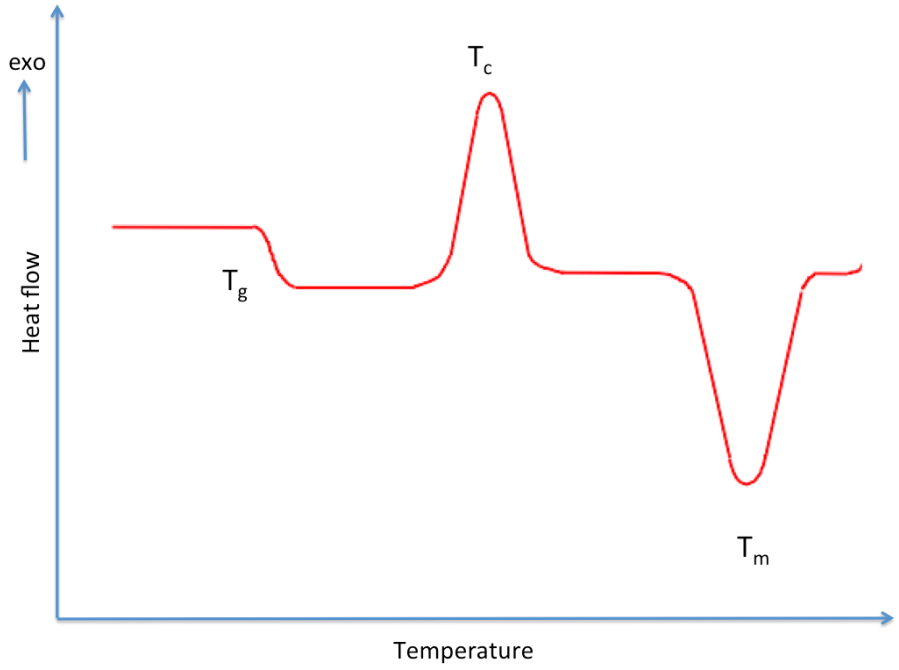


**Figure 2.14:** Example DSC curve, highlighting the glass transition temperature ($T_g$), exothermic crystallisation event ($T_C$) and endothermic melt ($T_m$), adapted from [23]

A miscible amorphous solid dispersion should have a $T_g$ value which is intermediate between

the individual components, i.e drug and polymer. This theoretical $T_g$ value of 'ideally mixed' amorphous solid dispersions can be predicted using a number of equations, including the Gordon-Taylor (G-T) [112], Gordon-Taylor/Kelley-Bueche [113] and Couchman-Karasz [114]. The G-T equation (equation 2.17)) is based upon free volume theory, and assumes that individual components are miscible, and that their free volumes are additive.

$$T_{gmix} = \frac{w_1 T_{g1} + k w_2 T_{g2}}{w_1 + k w_2} \tag{2.17}$$

where $w_1$ and $w_2$ are the weight fractions of the two components, and $T_{g1}$ and $T_{g2}$ are the respective $T_g$ values. k is a constant related to the ratio of free volume, and is calculated using the Simha-Boyer rule (equation 2.18) [189].

$$k \approx \frac{\rho_1 T_{g2}}{\rho_2 T_{g1}} \tag{2.18}$$

where $\rho_1$ and $\rho_2$ are the true densities of the individual components.

The Gordon-Taylor/Kelley-Bueche equation (G-T/K-B) is a slight variation on the original equation, where k represents a measurement of interaction between the components, rather than ratio of free volume (equation 2.19) and $\Delta C_p$ is the change in heat capacity at $T_g$ [112, 113, 190].

$$k \approx \frac{\Delta C_{p2}}{\Delta C_{p1}} \tag{2.19}$$

Additionally, the Couchman-Karasz equation (equation 2.20) is also used to predict the $T_g$ of miscible systems, and is based on a more classical thermodynamic approach, which takes into account the combined entropy of mixing of the individual components [62, 114, 179, 191].

$$lnT_g = \frac{(w_1 \Delta C_p lnT_g)_1 + (w_2 \Delta C_p lnT_g)_2}{(w_1 \Delta C_{p1}) + (w_2 \Delta C_{p2})} \tag{2.20}$$

For amorphous dispersions, significant deviation of $T_g$ between experimental and predicted values can potentially indicate differences in intermolecular interactions between components (both drug/drug and drug/polymer) [190]. Conversely, lack of deviation from predicted values indicates 'ideal' mixing with the absence of specific drug/polymer interactions [192]. Molecular interactions can affect the $T_g$ value of the system as follows:

- Negative deviation from predicted value: interactions between like species (e.g drug/drug interactions) dominate [192–194]
- No deviation from predicted value: indicates ideal mixing between phases, with a lack of specific drug-polymer interactions [190].

- Positive deviation from predicted value: interactions between different species (i.e drug/polymer interactions) dominate [192–194].

### 2.2.2 Powder X-ray Diffraction [12–14]

Powder X-ray Diffraction (PXRD) is a technique employed to characterise materials with an ordered three-dimensional structure, for example crystalline pharmaceutical APIs. A crystal can be defined as 'a solid body having a characteristic internal structure and enclosed by symmetrically arranged plane surfaces, intersecting at definite and characteristic angles' [60].

The repeating array of atoms in a crystal, or scattering centres, can be detected through X-Ray Diffraction if the scattering centres are separated by a particular distance (d) which is comparable to the X-Ray wavelength ($\lambda$), giving rise to interference between the scattered X-rays (figure 2.15. In the case of ordered structures, interference maxima and minima occur, which results in a diffraction pattern. In a typical X-Ray diffraction experiment:

1. A cathode ray tube is used to generate X-rays
2. The resulting X-rays are then filtered, resulting in a monochromatic beam
3. This beam is directed at the sample of interest
4. Diffraction rays are collected through the detector
5. The basis of the diffraction pattern is formed due to the angle between the incident and diffraction rays

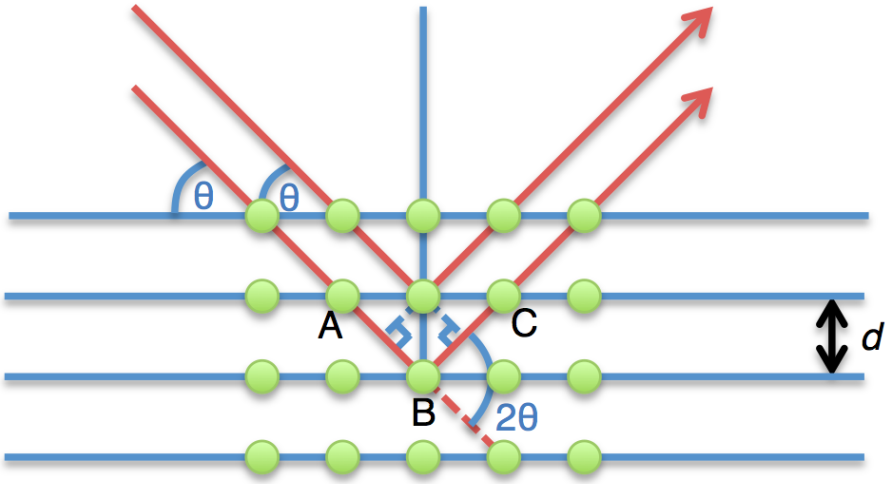


**Figure 2.15:** Example of X-ray diffraction, resulting in reflections at angle $\theta$, adapted from [12]

To emerge as a single beam, reflected beams must arrive in phase with one another, known as constructive interference through satisfaction of Bragg's Law (equation 2.21).

$$n\lambda = 2dsin\theta \tag{2.21}$$

where $n$ is the order of the beam, $\lambda$ is the wavelength of the X-ray beam, d is the distance between adjacent planes (d-spacings) and $\theta$ is the angle of incidence of the X-ray beam. d spacings are calculated using known values of $\theta$ and $\lambda$.

Characteristic diffraction patterns can be collected for each crystal structure, due to differences in the arrangement of atoms within the crystal lattice. There are two mains techniques which employ X-ray diffraction: single crystal X-ray diffraction and powder X-ray diffraction (PXRD). Single crystal XRD is mainly used for precise determination of unit cell parameters, to solve crystal structures. It can provide information regarding cell dimensions, atom positions, bond lengths and bond angles [195]. Powder XRD, which was the technique employed in this thesis, analyses a solid powder sample to obtain a unique characteristic 'fingerprint' X-ray diffraction pattern, where peaks represent constructive interference by atoms in the crystal lattice. This technique enables the identification of different crystalline materials, including identification of different polymorphs of crystalline pharmaceuticals [196].

# Chapter 3

# Experimental

## 3.1 Materials

Indomethacin ($C_{19}H_{16}ClNO_4$), Flufenamic Acid ($C_{14}H_{10}F_3NO_2$), Tolbutamide ($C_{12}H_{18}N_2O_3S$), methanol, ethanol and acetonitrile were purchased from Sigma Aldrich, UK. PVP-VA (polyvinylpyrollidone-vinylacetate) (Kollidon VA 64) was purchased from BASF chemicals, Germany.

### 3.1.1 Amorphous drug preparation

Amorphous IMC was produced *via* the quench cool method by melting the crystalline drug in an aluminium pan in an oven to 453 K, holding at this temperature for 5 minutes, followed by immediate quench-cooling in liquid nitrogen (adapted from [29, 84]). Amorphous FFA was prepared using the same method carried out in a cold room to minimise crystallisation, due to the low stability at ambient temperature. Attempts to form amorphous TLB were unsuccessful, due to the low $T_g$ of *ca.* 278 K. The fresh samples were lightly ground in a pestle and mortar and stored at 203 K. Analysis by Differential Scanning Calorimetry (DSC), Powder X-ray Diffraction (PXRD) and solid-state NMR confirmed the amorphous nature.

### 3.1.2 Preparation of amorphous solid dispersions

Amorphous Solid Dispersions were prepared using a solvent evaporation technique adapted from [71, 84]. $\gamma$-IMC, form I FFA and form $I^L$ TLB were formulated with PVP-VA in the following drug/polymer wt. ratios: 80/20, 70/30, 60/40, 50/50, 40/60, 30/70, 20/80 and 10/90. This was achieved by dissolving 8 g (total weight) of lightly mixed drug/polymer in a minimum volume of methanol at ambient temperature. Ethanol and acetonitrile were additionally used to prepare 80/20 IMC/PVP-VA dispersions to study the effect of solvent on crystallisation. The solvent was removed under vacuum at 323 K using a rotary evaporator, rotating at 8 rpm. The resulting powder was lightly ground in a pestle and mortar and stored at 203 K.

### 3.1.3 Preparation of crystalline polymorphic forms

The purchased IMC was confirmed to be $\gamma$-form through DSC and PXRD [50]. $\alpha$-IMC was formed by dissolving *ca.* 250 mg of $\gamma$-IMC in methanol in a round bottom flask. The solvent was removed under vacuum at 323 K using a rotary evaporator set at 8 rpm. The resulting powder was lightly ground in a pestle and mortar and stored at 203 K.

The purchased FFA was confirmed to be form I through DSC and PXRD [197]. Form III was prepared according to the method by Lopez-Mejias *et al.* [39]: 50 mg was dissolved in

1 ml of EtOH, and heated to 358 K. The resulting solution was allowed to cool to ambient temperature, where it was stored until crystals formed.

The purchased TLB was confirmed to be form $I^L$ through DSC and PXRD [42, 172]. Form II was prepared according to the method by Thirunahari *et al.* [42]: 1.2 g of purchased TLB was dissolved in 10 g acetonitrile at ambient temperature. 5 ml of water was slowly pipetted into the solution without stirring, where it was left until crystals formed. Form $I^H$ was prepared *in situ* in the NMR rotor, by heating the purchased form $I^L$ above 311 K [43].

Analysis by DSC, PXRD and solid-state NMR confirmed the successful formation of the different polymorphic forms.

## 3.2 Methods

### 3.2.1 Differential Scanning Calorimetry

All DSC measurements were performed using a Q 2000 MTDSC instrument (TA Instruments, Newcastle, DE, US). Indium, tin and n-octadecane were used as calibration standards. Standard TA crimped 100 $\mu$L aluminium pans were used for all experiments. The sample weights were between 2-5 mg (crystalline samples) and 5-10 mg (amorphous and solid dispersion samples) and a nitrogen purge of 50 mL/min was used for all experiments.

Experiments for each API were carried out within the following temperature ranges, to cover all glass transition, crystallisation and melting events for each system: IMC (283 - 493 K); FFA (253 - 463 K); TLB (243 - 463 K).Standard experiments on all crystalline API were carried out using a heating rate of 5 K/min. Modulated DSC experiments were carried out on all amorphous API and amorphous solid dispersions with a heating rate of 2 K/min with a modulation of $\pm$ 0.5 K every 60 seconds. This was repeated three times, using a heat-cool-reheat cycle, with an isotherm of 1 minute at each temperature extreme. The initial heating run was not taken into account for $T_g$ calculations, but was performed to remove thermal history of the materials. Analysis was performed on all samples using TA Instruments Universal Analysis 2000 software (TA Instruments, Waters LCC).

### 3.2.2 Powder X-ray Diffraction

PXRD patterns were acquired with an ARL$^{TM}$ XTRA Powder Diffractometer (Thermo Fisher Scientific Inc., Waltham, MA, US), using Cu K$\alpha$ radiation ($\lambda = 1.541$ $\mathring{A}$) in the $2\theta$ range between 3 and 60 °. All samples were analysed with a step size of 0.01 ° and a scanning rate of 1.2 s per step.

### 3.2.3 *In situ* PXRD at variable temperature *

The PXRD experiments at elevated temperature were performed using a Bruker AXS D8 Discover powder diffractometer (Bruker AXS GmbH, Germany) equipped with an MRI temperature chamber. Copper K$\alpha$ radiation ($\lambda$ = 1.5418 $\AA$) was used in the experiments. Data were collected using a flat sample (depth of 0.8 mm) holder in the Bragg–Brentano geometry. The X-ray diffraction measurements were performed at various temperatures (293, 313, 333, 353, 363, 373 K). Diffraction patterns were recorded with a 0.02 ° step size and a scan speed of 0.2 s per step in the 2$\theta$ range from 3 to 40 ° for FFA samples.

* - VT PXRD run by Inese Sarcevica, Department of Chemistry, University of Riga, Latvia. The author acknowledges Inese, and thanks her for her invaluable help and advice with these experiments.

### 3.2.4 Accelerated stability study

Amorphous dispersions of IMC/PVP-VA and FFA/PVP-VA and TLB/PVP-VA (20/80, 40/60, 50/50, 60/40, 70/30 and 80/20 wt. ratios) were monitored over a period between 8 - 14 weeks under the following storage conditions: room temperature 0% RH; room temperature 75 % RH; 313 K; 333 K. The high-drug loading dispersions were additionally stored at extreme temperature conditions (353 - 373 K) to further investigate crystallisation.

Each sample was monitored for evidence of crystallisation every two weeks using modulated DSC, PXRD and solid-state NMR.

### 3.2.5 Solid-state NMR

All solid-state NMR spectra were acquired at 9.4 T using a Bruker AVANCE III WB solid-state spectrometer operating at 400.23, 376.30 and 100.64 MHz for $^{1}$H $^{19}$F and $^{13}$C respectively. The chemical shifts of $^{1}$H and $^{13}$C are referenced with respect to external TMS, whilst $^{19}$F was referenced to external PTFE. Samples were spun at an MAS rate of 10.0 kHz using 4 mm diameter zirconia rotors with a 4 mm $^{1}$H/X/Y triple resonance probe.

#### 3.2.5.1 One dimensional magic angle spinning (MAS)

$^{1}$H and $^{19}$F single pulse MAS NMR experiments were acquired using a simple pulse program shown in figure 3.1. $^{19}$F signal was achieved through tuning the $^{1}$H channel to the Larmor frequency of $^{19}$F.

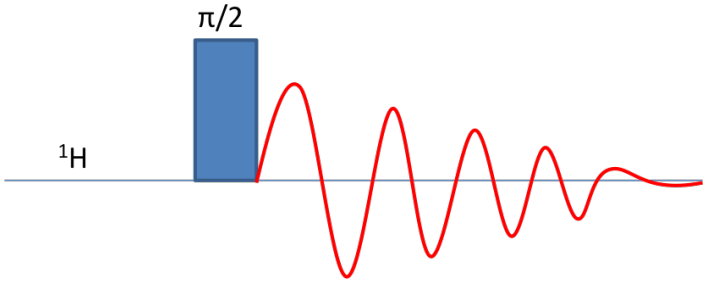


**Figure 3.1:** Representation of the single pulse MAS NMR experiment

$^{1}$H MAS NMR spectra were acquired using a $\pi/2$ pulse length of 2.60 $\mu$s at an MAS rate of 10.0 kHz and recycle delay of 10 s. $^{19}$F MAS NMR ($^{1}$H coupled) were acquired with a $\pi/2$ pulse length of 3.62 $\mu$s at 10.0 kHz and a recycle delay of 6 s.

#### 3.2.5.2 $^{1}$H-$^{13}$C Cross Polarisation Magic Angle Spinning NMR ($^{1}$H-$^{13}$C CP/MAS NMR)

All $^{1}$H-$^{13}$C CP/MAS NMR experiments were acquired using a ramp amplitude $^{1}$H pulse shape with SPINAL-64 [183] heteronuclear decoupling applied during the acquisition (figure 3.2).

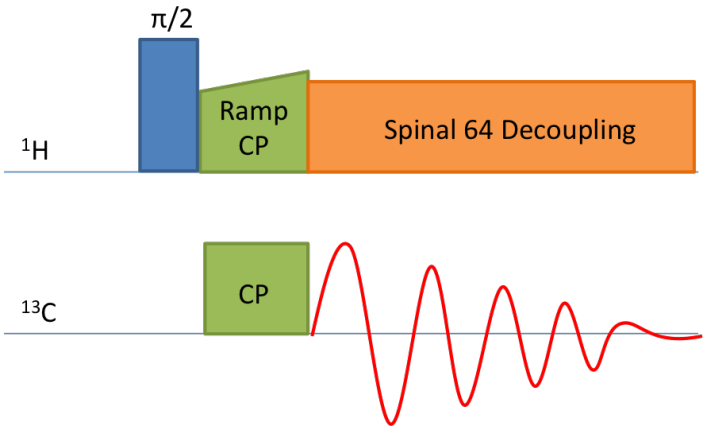


**Figure 3.2:** Representation of $^{1}$H-$^{13}$C CP/MAS NMR pulse sequence

All spectra were acquired at a MAS rate of 10.0 kHz, with an optimised $^{1}$H $\pi/2$ pulse length of 3.0 $\mu$s, contact time of 2.0 ms and a pulse delay of 10 s for IMC and TLB and 15 s for FFA. $^{1}$H *rf* decoupling field of 78 kHz was applied during acquisition. The Hartmann-Hahn matching conditions were set using hexamethylbenzene (HMB). Typically 512 scans were accumulated for crystalline materials and 1024 scans for amorphous materials.

### 3.2.5.3 Dipolar dephasing with Non-Quaternary Suppression (NQS)

The dipolar dephasing $^{1}$H-$^{13}$C CP/MAS NMR pulse sequence is a spectral editing method, which allows the distinction between protonated and quaternary carbons. This method relies on differences in the strength of heteronuclear dipolar interactions in different functional groups. The inclusion of a dephasing delay ($\tau_{DD}$) between the CP step and acquisition allows the $^{13}$C magnetisation to evolve under the influence of the dipolar interactions. The pulse sequence is shown in figure 3.3.

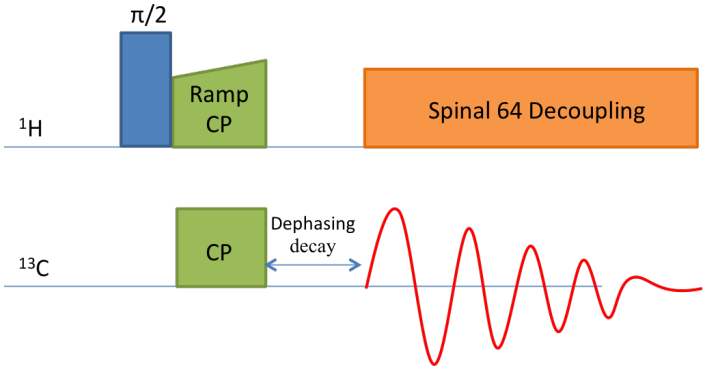


**Figure 3.3:** Representation of $^{1}$H-$^{13}$C CP/MAS NMR dipolar dephasing (NQS) pulse sequence

We used this pulse sequence for Non-Quaternary suppression (NQS), which allows the detection of quaternary carbons, whilst excluding -CH and -$CH_2$ functional groups. NQS was achieved through setting the dephasing delay to 40 $\mu$s. All other parameters were the same as in the standard $^{1}$H-$^{13}$C CP/MAS NMR above.

### 3.2.5.4 Single pulse $^{13}$C with high power $^{1}$H decoupling ($^{13}$C{$^{1}$H} MAS NMR)

$^{13}$C{$^{1}$H} MAS NMR experiments were carried out at using an optimised $^{13}$C $\pi/3$ pulse of 2.3 $\mu$s and a recycle delay of 30 s. Typically 1024 scans were accumulated.

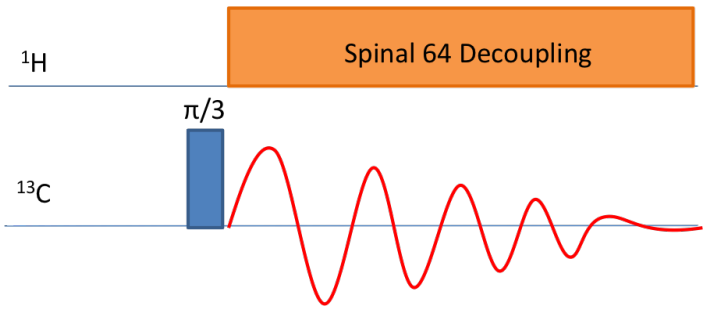


**Figure 3.4:** Representation of $^{13}$C{$^{1}$H} MAS NMR pulse sequence

SPINAL-64 heteronuclear decoupling [183] was applied during acquisition, with an $^{1}$H *rf* decoupling field of 89 kHz. Chemical shift values were referred to that of TMS.

#### 3.2.5.5 Two dimensional $^{1}$H-$^{13}$C WIdeline SEparation (WISE)

WIdeline SEparation (WISE) experiments in solid-state NMR are used to correlate information on local mobility with chemical structure [198]. The 2D WISE spectrum (figure 3.5) combines the $^{1}$H wideline spectral patterns with each of the $^{13}$C chemical shifts acquired through $^{1}$H-$^{13}$C CP/MAS NMR, which enhances spectral resolution. The widths of $^{1}$H are indicative of the strength of $^{1}$H-$^{1}$H homonuclear dipolar coupling, which in turn depends on mobility, with more rigid structures having wider lines.

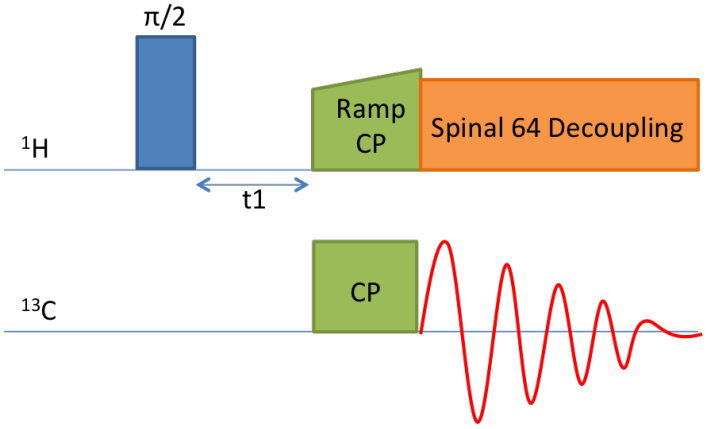


**Figure 3.5:** Representation of $^{1}$H-$^{13}$C 2D WISE pulse sequence

$^{1}$H-$^{13}$C WISE spectra were acquired for amorphous IMC, IMC/PVP-VA dispersions and PVP-VA at an MAS rate of 10 kHz, with a $^{1}$H $\pi/2$ pulse length of 3.0 $\mu$s and a pulse delay of 10 s. SPINAL-64 heteronuclear decoupling [183] was employed during $t_2$ with an *rf* field strength of 83 kHz. 128 - 256 increments were recorded during $t_1$, and 512 scans were accumulated. A fixed contact time of 200 $\mu$s was used to limit $^{1}$H spin diffusional effects, as longer contact times would lead to a lack of distinction between $^{13}$C sites through equilibration of $^{1}$H magnetisation.

#### 3.2.5.6 Spin-lattice relaxation

**3.2.5.6.1 Spin-lattice relaxation in the laboratory frame ($T_1$)** $T_1$ relaxation experiments were collected using the standard inversion-recovery (IR) pulse sequence for both $^{1}$H and $^{19}$F nuclei (figure 3.6).

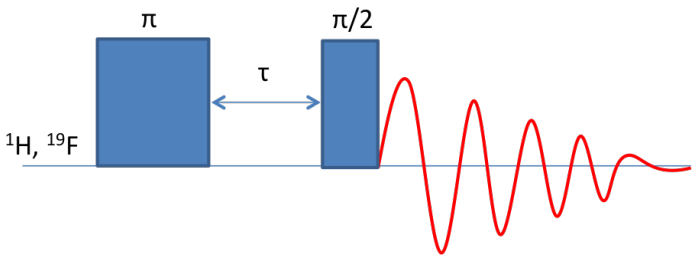


**Figure 3.6:** Representation of inversion recovery (IR) pulse sequence

A $\pi$ pulse (5.2 $\mu$s for $^{1}$H and 7.2 $\mu$s for $^{19}$F) rotated magnetisation into the -z plane, followed by an evolution period of time $\tau$, with a final $\pi/2$ pulse to rotate remaining magnetisation into the - xy plane for acquisition. 15 experiments were carried out with $\tau$ set between 0.01 to 20 ms for both $^{1}$H and $^{19}$F. Peak intensities were plotted as a function of delay time ($\tau$), and fitted with exponential equation 3.1:

$$M_z(t) = M_{0z}(1 - 2exp(-\frac{t}{T_1})) \tag{3.1}$$

where t is the delay time, and $M_z(t)$ is the net magnetisation along z at this time.

**3.2.5.6.2 Spin-lattice relaxation in the rotating frame ($T_{1\rho}{}^{H}$: Variable spin-lock)** $T_{1\rho}{}^{H}$ relaxation times in the rotating frame were measured using a modified CP sequence (based on figure 3.2) with an additional spin-locking pulse (figure 3.7).

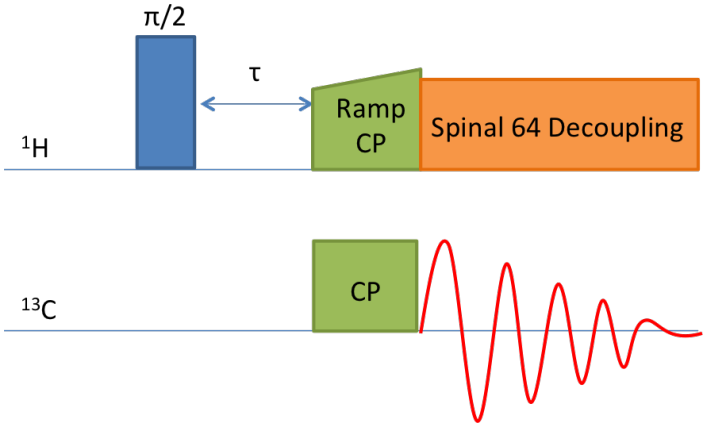


**Figure 3.7:** Representation of the $T_{1\rho}{}^{H}$ spin locking pulse sequence

Before the CP step, $^{1}$H magnetisation was locked along the y axis for a variable time ($\tau$) between 0.01 and 30 ms using a spin-locking pulse. During this delay time, the $^{1}$H magnetisation evolves under the effect of the homonuclear dipolar interaction. This results in a difference in the peak intensity dependent on $^{1}$H relaxation efficiency in the rotating frame. A spin-locking field of 78 kHz was employed during $\tau$. The contact time was fixed to 2 ms, delay time to 10 s (IMC and TLB) and 15 s for FFA, at an MAS rate of 10 kHz.

To obtain a $T_{1\rho}$ decay curve, 15 experiments were carried out with $\tau$ set between 0.01 and 30 ms. Peak intensities were plotted as a function of spin-lock time, and fitted with exponential equation 3.2:

$$M(t) = \sum M_{0i} exp(-\frac{t}{T_{1\rho i}}) \tag{3.2}$$

where t is the spin lock time, and *M(t)* is the peak intensity at this time.

The indirect detection of $T_{1\rho}{}^{H}$ *via* $^{13}C$ leads to higher resolution $^{13}C$ spectra compared to $^{1}H$. Measurements also highlight the volume averaged property of $T_{1\rho}{}^{H}$ (through spin diffusion - see chapter 4), allowing detection of homogeneity within a sample.

### 3.2.6 Data Processing

The NMR spectra were acquired and processed using Bruker Topspin 3.1.7 analysis software. All spectra were fitted with 60 Hz line broadening, unless otherwise stated. Further processing was carried out with Origin 9.0, including fitting of $T_1$ decays and deconvolution. $T_{1\rho}$ fits were achieved with Bruker Dynamics Centre (version)

### 3.2.7 Variable temperature

Variable temperature measurements were typically performed between 253 K and 373 K at 10 - 20 K intervals. Temperature control was accomplished with a Bruker BCU II chiller unit, and through heating the bearing gas within the probe *via* a probe filament. Prior to acquisition, packed rotors were spun for 30 minutes to equilibrate sample temperature.

## 3.3 Solution-state NMR

Solution-state NMR experiments were conducted on a Bruker Avance I 500 MHz NMR spectrometer equipped with a 5 mm TXI actively shielded Z-gradient high resolution probe, operating at 499.68 MHz for $^{1}H$ and 125.65 MHz for $^{13}C$. $^{1}H$, $^{13}C$, 2D $^{1}H$-$^{1}H$ COSY and 2D $^{1}H$-$^{13}C$ HSQC NMR spectra were collected.

To gain further resolution, FFA solution-state $^{1}H$, $^{1}H$-$^{1}H$ COSY and 2D J-resolved NMR spectra were acquired using a Bruker Avance III 800 MHz NMR spectrometer, operating at 800.23 MHz for $^{1}H$ and 201.22 MHz for $^{13}C$, equipped with an HCN Inverse triple resonance z-gradient probe.

Samples were prepared to a final API concentration of 0.05 M in 600 $\mu$l aliquots of $CD_3OD$.

For assignment purposes, the following pulse sequences were utilised:

- $^{1}$H single $\pi/2$ pulse of length 7.87 $\mu$s (IMC), 6.71 $\mu$s (FFA) and 7.99 $\mu$s (TLB), and delay time of 2.0 s.
- $^{13}$C{$^{1}$H} NMR: $\pi/2$ pulse of length 11.25 $\mu$s, delay time of 2.0 s and WALTZ-16 decoupling
- $^{1}$H-$^{1}$H COSY: $^{1}$H pulse of length 7.77 $\mu$s (at 500 MHz) and $^{1}$H pulse of length 9.05 $\mu$s (at 800 MHz)
- $^{1}$H-$^{13}$C HSQC: $^{1}$H pulse of length 7.77 $\mu$s, and $^{13}$C pulse of length 11.25 $\mu$s, with GARP decoupling
- J-resolved: $^{1}$H pulse of length 9.05 $\mu$s (at 800 MHz)

# Chapter 4

# Detection of mobility in solid-state NMR

Solid-state NMR provides a number of techniques for characterisation of molecular mobility, and is able to probe dynamics on different time and length scales (figure 4.1). The effects of motions on nuclear spins are dependent on the three nuclear spin timescales: **relaxation, spectral and Larmor**. All timescales are also dependent on the sample, and on physical parameters such as temperature and strength of external magnetic field [7].

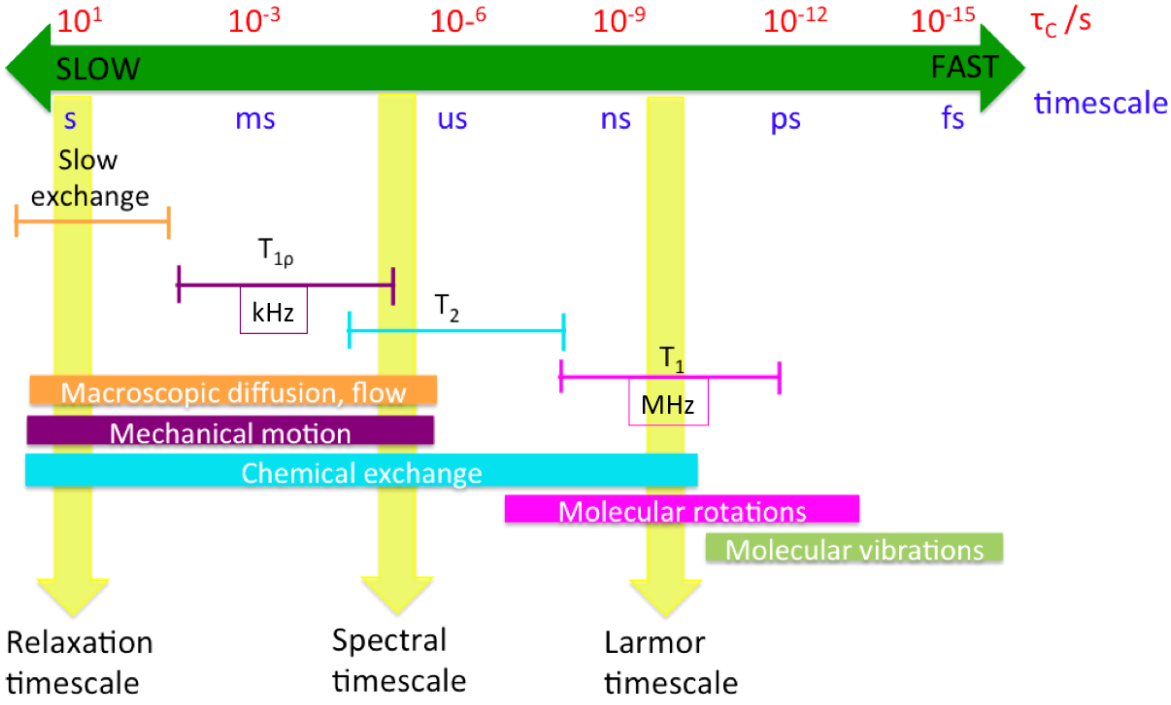


**Figure 4.1:** The motional timescales of NMR: physical processes and NMR relaxation methods, adapted from [7]

The solid-state NMR methods described below are common to all three drug/polymer systems studied (chapters 5 to 7) across a range of temperatures. For the benefit of the reader, the main applications of solid-state NMR for the detection of different motional regimes in pharmaceutical solids are outlined below.

## 4.1 $^{13}$C Magic Angle Spinning (MAS) NMR

Both $^{1}$H-$^{13}$C CP/MAS NMR and $^{13}$C{$^{1}$H} MAS NMR (high-power decoupling) techniques were used to acquire $^{13}$C spectra throughout this study, with variable temperature experiments allowing a further probe of the mobility [199]. This often leads to the detection of a difference in mobility of individual drug and polymer components within dispersions.

### 4.1.1 $^{1}$H-$^{13}$C Cross Polarisation(CP)/MAS NMR and mobility

CP/MAS NMR experiments are commonly used to enhance signal-to-noise ratios and reduce the acquisition time of low sensitivity nuclei, such as $^{13}$C and $^{15}$N. CP/MAS also provides a building block for numerous more complex pulse programmes, such as 2D correlation techniques (HETCOR) [4]. During the contact time period, upon fulfilment of Hartmann-Hahn conditions, proton magnetisation in the rotating frame relaxes back to the lattice at a rate of $T_{1\rho}{}^{H}$s. At the same time, $^{13}$C signal is acquired through transfer of magnetisation from $^{1}$H to $^{13}$C spins *via* heteronuclear dipolar couplings, at a rate of $T_{CP}$ s [4,24,199] (figure 4.2). The efficiency of polarisation transfer is therefore highly dependent on the strength of $^{1}$H -$^{13}$C dipolar interactions and the number of protons involved in transfer. The $^{1}$H-$^{13}$C dipolar interactions depend on the distance between carbon and proton nuclei, orientation with respect to external magnetic field *and* local molecular motion [24, 25, 199].

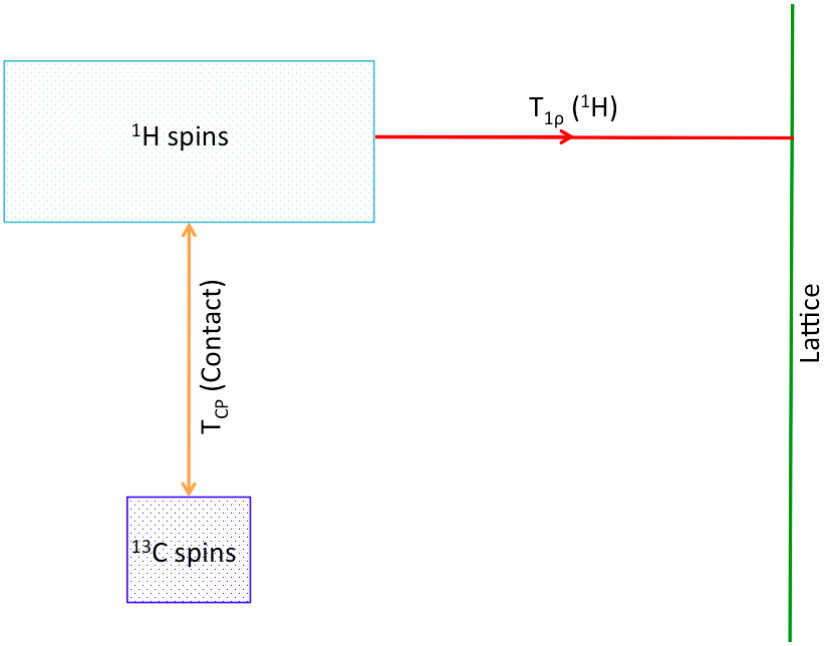


**Figure 4.2:** Representation of Cross Polarisation dynamics during contact time, adapted from [24]

In an extreme case, if $T_{1\rho}{}^{H}$ is too short, the loss of magnetisation into the lattice can occur faster than cross-polarisation, leading to absence of signal from the acquired spectrum altogether [24]. $T_{1\rho}{}^{H}$ is temperature dependent (see section 4.4.2) therefore if structural or motional heterogeneity exists between regions of a sample i.e. between drug and polymer components within a solid dispersion, $T_{1\rho}{}^{H}$ times may change drastically with temperature, allowing the discrimination between drug and polymer components. This effect can be observed both directly by calculating $T_{1\rho}{}^{H}$ times *via* spin-locking experiments, and indirectly through monitoring $^{13}$C resonances with CP/MAS NMR.

#### 4.1.1.1 Detection of mobility through $^{1}$H-$^{13}$C dipolar coupling: intermediate timescale motions

Intermediate motions can affect the cross-polarisation transfer efficiency *via* the motional modulation of $^{1}$H-$^{13}$C dipolar interactions [28, 199] ($^{1}$H-$^{13}$C dipolar interactions *ca.* 20-30 kHz [2]), leading to a reduction in signal intensity [200]. Reduction in signal intensity of CP/MAS spectra is often seen as a disadvantage of the technique, but this loss of signal can provide important information about changes in the local dynamics of the sample [28], which more traditionally have been studied *via* CP-kinetics build up curves [184].

Two early literature examples of the loss of signal in $^{1}$H-$^{13}$C CP/MAS NMR spectra of polyethylene, compared with the $^{13}$C{$^{1}$H} MAS NMR spectra are shown in figure 4.3.

For both polyethylene samples, additional $^{13}$C resonances are present in the $^{13}$C{$^{1}$H} MAS NMR as compared to the $^{1}$H-$^{13}$C CP/MAS NMR. This is due to loss of signal in the $^{1}$H-$^{13}$C CP/MAS NMR spectrum through motional averaging of dipolar interactions, leading to reduced cross-polarisation efficiency. Fyfe *et al.* [25] (figure 4.3 A) attributed the additional peak in the $^{13}$C{$^{1}$H} MAS NMR spectrum to a more mobile amorphous region. Harris [24] (figure 4.3 B) saw the same effect in end groups of polyethylene chains, with much greater intensity peaks present in the $^{13}$C{$^{1}$H} MAS spectrum, again attributing the loss of CP signal to higher mobility of amorphous chain regions.

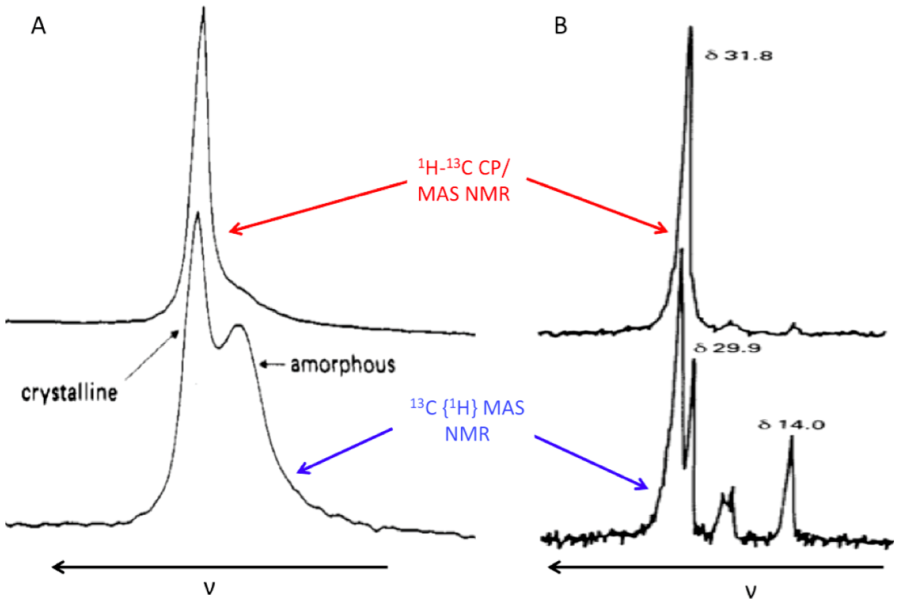


**Figure 4.3:** A) CP/MAS (contact time = 1.5 ms; recycle delay = 2 s) and $^{13}$C{$^{1}$H} MAS NMR (SPE) (delay = 20 s) $^{13}$C spectra of semi-crystalline polyethylene [25] and B) CP/MAS (contact time = 1 ms; recycle delay = 1.25 s) and $^{13}$C{$^{1}$H} MAS NMR SPE (delay = 11 s) $^{13}$C spectra of lower molecular weight polyethylene wax [24]

#### 4.1.1.2 The effect of $^{1}$H-$^{1}$H spin diffusion on CP/MAS NMR spectra

$^{1}$H-$^{1}$H spin diffusion also plays a significant role in the efficiency of $^{1}$H-$^{13}$C CP/MAS NMR, and can provide information on homogeneity of drug and polymer in solid dispersions. Spin diffusion is a property of $^{1}$H-$^{1}$H homonuclear dipolar interactions, and involves the exchange of spin energy between protons *via* flip-flop transitions (see chapter 3 for further explanation). Classical CP theory (named the I-S model) assumes that the $^{1}$H-$^{1}$H spin diffusion is sufficiently rapid to communicate between all protons in the system, which means all protons will behave in the same manner and will act as the source of polarisation [8]. Therefore if efficient spin diffusion can take place across the $^{1}$H pool, we will observe homogenous relaxation behaviour across all carbon sites. If the average domain size of a particular component of a system is below 6 nm, $^{1}$H-$^{1}$H spin diffusion averages out $T_{1\rho}{}^{H}$ differences, and we observe one common relaxation time across all sites [2, 46]; for larger domains, we might observe a difference in cross-polarisation efficiency due to inefficient spin diffusion, leading to differences in $T_{1\rho}{}^{H}$ times between components, i.e. drug and polymer within a dispersion. The I-S model of CP-kinetics is usually used to describe functional groups with weaker heteronuclear, and moderate to strong homonuclear dipolar interactions, for example quaternary carbons [8, 201].

### 4.1.2 $^{13}$C{$^{1}$H} MAS NMR and mobility

$^{13}$C{$^{1}$H} MAS NMR, often referred to as SPE (Single Pulse Excitation), or DP (Direct Polarisation) involves a direct excitation of $^{13}$C spins, combined with high power proton decoupling to remove $^{1}$H-$^{13}$C dipolar interactions. It is mainly used for quantitative analysis, where the area under each peak represents the number of carbon atoms within that particular environment, similar to peak integration in solution-state NMR [24]. As the delay time between pulses must be long enough to allow full relaxation to equilibrium, $^{13}$C{$^{1}$H} MAS NMR experiments are often very time consuming, especially for solids with long $T_{1}{}^{C}$ times [200]. The main effect of mobility on the acquisition of $^{13}$C{$^{1}$H} MAS NMR spectra is through motional modulation of the heteronuclear decoupling step, which leads to the reduction of spectral resolution.

#### 4.1.2.1 Detection of mobility through interference with heteronuclear decoupling: faster intermediate timescale motions

Motions on a similar timescale to the $^{1}$H *rf* decoupling field (usually between 50 - 100 kHz, and *ca.* 89 kHz in our $^{13}$C{$^{1}$H} MAS NMR experiments) can reduce the effectiveness of heteronuclear dipolar decoupling [26, 28, 200]. This manifests as line broadening of carbon signals within both $^{1}$H-$^{13}$C CP/MAS NMR and $^{13}$C{$^{1}$H} MAS NMR spectra [25]. Reduction in decoupling efficiency results from molecular motions modulating heteronuclear decoupling

through partial uncoupling of protons from the field [202]. Zhang *et al.* [203] varyied the decoupling strength to prove the observed broadening was indeed due to the interference of heteronuclear decoupling. Therefore, if particular motions are site specific within a sample, this experimental 'flaw' can be used as an identification and characterisation tool.

### 4.1.3 Manifestation of faster isotropic motions in solid-state $^{13}$C MAS NMR

Faster motions, an increased motional timescale compared to the previously discussed intermediate motions (i.e. $>$ 1000 kHz) can also be detected in the solid-state, particularly with variable temperature $^{1}$H-$^{13}$C CP/MAS and $^{13}$C$\{^{1}$H$\}$ MAS NMR experiments. With increasing temperature, line narrowing can be observed due to the presence of faster motions, which partially average both heteronuclear and homonuclear dipolar interactions to a value lower than the MAS frequency (10 kHz in our case). This leads to the presence of narrow isotropic peaks in the solid-state spectrum. This phenomenon has previously been observed for aliphatic chain motions of poly(vinyl methyl ether) (PVME) polymers [26] and methyl rotations in amorphous simvastatin [28]. The effect of chain motion on the linewidth of peaks in the $^{13}$C$\{^{1}$H$\}$ MAS NMR spectrum of PVME in PS/PVME blends can be seen in figure 4.4.

Additionally, even faster isotropic motions (i.e. equivalent to a 'liquid-like' environment, with $\tau_c < 0.01$ $\mu$s) can lead to the complete loss of $^{1}$H-$^{13}$C CP/MAS NMR signals, leading to the complete loss of signal intensity in the spectrum. These faster motions affect $^{1}$H-$^{13}$C CP/MAS NMR spectra through interference with the cross-polarisation transfer step, and do not affect signals of $^{13}$C$\{^{1}$H$\}$ MAS NMR spectra, instead fast motions would lead to the observation of sharp $^{13}$C resonances through direct excitation spectra [24, 204].

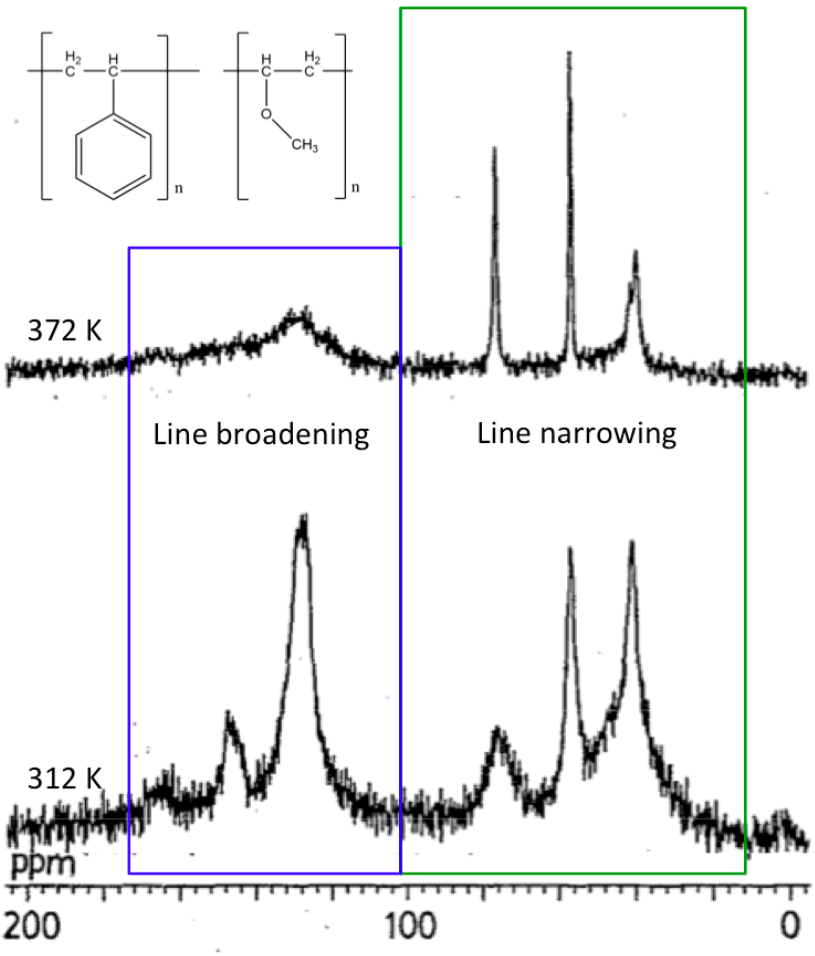


**Figure 4.4:** $^{13}C\{^{1}H\}$ MAS NMR spectra for PS/PVME (50/50) polymer blend, at 312 and 372 K, adapted from [26]

### 4.1.4 The combined use of $^{1}H$-$^{13}C$ CP/MAS NMR and $^{13}C\{^{1}H\}$ MAS NMR for investigation of molecular motion

The combined use of both $^{13}C$ MAS NMR techniques can result in a greater understanding of the molecular motion of pharmaceutical solids, through identification of different mobility regimes across a range of NMR timescales [204]. This approach allows discrimination between different regions of the sample, for example between drug and polymer in a solid dispersion. Changes in mobility will manifest themselves in different ways within the acquired carbon spectra. A variety of molecular motions, including phenyl ring flips and alkyl chain rotations can affect the $^{13}C$ linewidth [200], with this method being particularly sensitive to intermediate motions (10 kHz to 1 MHz), which are on the timescale of the NMR experiments [28, 184, 199]. Using the combined approach, we were able to differentiate between the molecular mobility of drug and polymer within solid dispersions of IMC (chapter 5), FFA (chapter 6) and TLB (chapter 7).

A literature example of the range of motional effects which are possible to observe with variable temperature $^{1}H$-$^{13}C$ CP/MAS NMR is shown in figure 4.5 [27, 205]. Here we see a

variety of line widths of the methyl resonance (C-3), as it undergoes temperature dependent rotation:

- Fast mobility: at increased temperature the methyl resonance is sharp, with narrow linewidth, due to rapid motional averaging of fast isotropic motion
- Intermediate mobility: maximum broadening is seen at 106 K where the methyl resonance is no longer visible, as the rate of motion equals the $^{1}$H decoupling frequency leading to reduced effectiveness. The methylene and methine carbon signals remain present.
- Slow mobility: at low temperature, the methyl resonance is present once more, as the reduced mobility allows the reduction of line width by effective decoupling of C-H dipolar interactions.

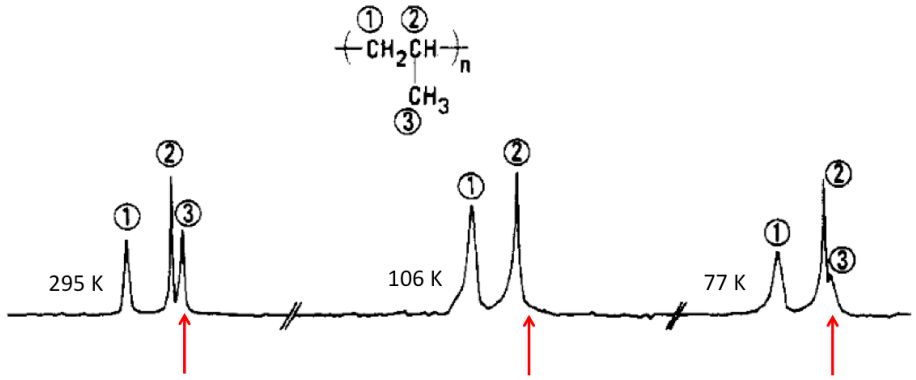


**Figure 4.5:** Variable temperature CP/MAS spectra of isotactic polypropylene, highlighting the change in the methyl resonance (red arrows, resonance 3) compared to methylene and methine carbon signals [27]

A number of studies have been reported, where different motional regimes have been highlighted through VT $^{1}$H-$^{13}$C CP/MAS NMR and $^{13}$C{$^{1}$H} MAS NMR experiments. Our group reported changes in local motions of drug/PLGA films dependent on drug loading levels. With increasing temperature, line broadening of carbonyl and aliphatic resonances was observed in CP/MAS experiments, due to reduced decoupling efficiency from increased backbone motions in the mid-kHz range (20 % drug loaded dispersion). Within a more rigid system (10 % film) no change in linewidth with increasing temperature was observed [202]. Nunes *et al.* [28] recently undertook a VT $^{1}$H-$^{13}$C CP/MAS study on amorphous simvastatin and found significant line broadening and loss of signal intensity with increasing temperature, for the majority of $^{13}$C peaks. This was attributed to an intermediate motional regime interfering with decoupling. Line narrowing of the peak corresponding to the ester tail, due to faster motions averaging both homonuclear and heteronuclear dipolar coupling was also highlighted. They found that having multiple frequency regimes within one system resulted in increased configurational entropy, leading to increased physical stability (with respect to crystallisation).

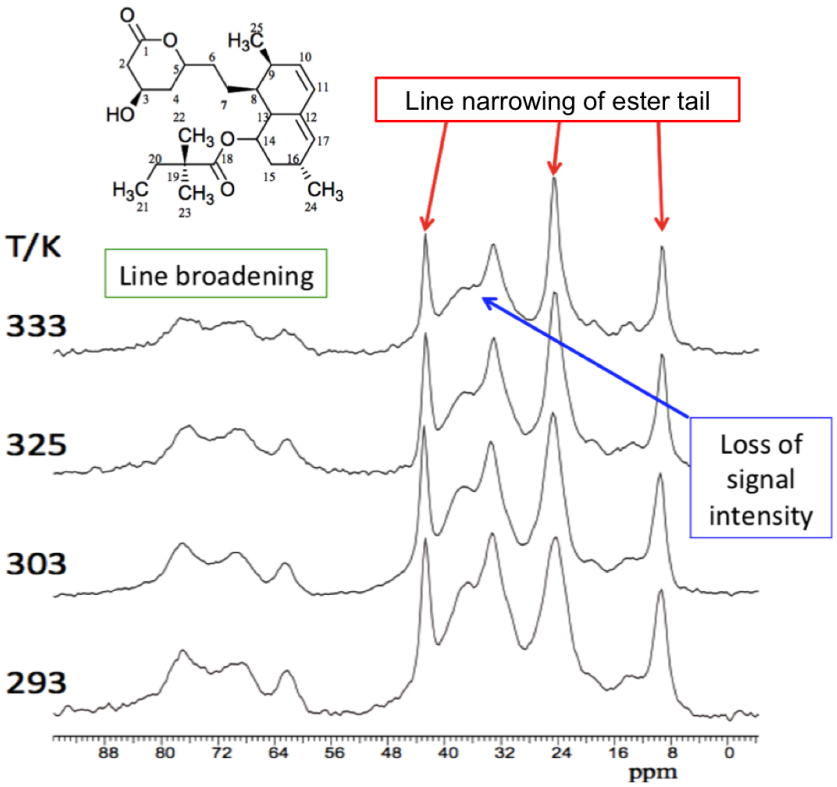


**Figure 4.6:** Variable temperature $^{1}$H-$^{13}$C CP/MAS NMR spectra of amorphous simvastatin, adapted from [28]

Carignani *et al.* [206] also used VT $^{1}$H-$^{13}$C CP/MAS NMR as part of an investigation on the different motional regimes present in the ibuprofen Na $^{+}$ salt. Again, significant line broadening of the aromatic carbon peaks upon heating occurred, which was attributed to interference with the decoupling field from the phenyl-$\pi$ ring flip, occurring on the intermediate timescale. Schantz *et al.* [159] carried out VT direct polarisation ($^{13}$C{$^{1}$H} MAS NMR) experiments on amorphous blends of paracetamol and citric acid with a decoupling field strength of 83 kHz (comparable to our own experiments). Here, linewidth broadening with increasing temperature was observed, due to motional interference with the decoupling field. They determined that because both components displayed the same mobility behaviour, this was a miscible system, with the dominant mobility identified as whole molecule $\alpha$-relaxation motions. Above a specific temperature, line narrowing (with 'liquid-like' resolution) of all peaks was identified, due to rapid molecular motions, above the intermediate regime. Carignani *et al.* identified methyl and isobutyl motional rotation as being on a faster ($>$ 1000 kHz) timescale, and investigated through VT $T_1{}^H$ experiments, which are on the MHz timescale [206].

## 4.2 $^1$H MAS NMR

$^1$H MAS NMR is very sensitive to both structure and molecular motions: increased molecular mobility leads to line narrowing of the $^1$H resonances. Sufficiently fast molecular motions can lead to the averaging of strong $^1$H-$^1$H dipolar interactions, responsible for the characteristic 'broad hump' appearance of $^1$H MAS NMR spectra in the solid-state (see chapter 2) [29, 30, 59]. Although it is more difficult to distinguish between drug and polymer peaks, especially at lower temperatures where amorphous materials have extremely broad $^1$H spectra, increased molecular motion can become apparent through monitoring the change in linewidth with increasing temperature. Sharp resonances, more comparable to a solution-state spectrum, indicate a higher mobility state [59].

Schachter *et al.* [30] investigated the mobility of ketoprofen/PEO blends by using VT $^1$H MAS. They found that with increasing temperature, significant line narrowing occurred whilst the blend was still in the solid state, before melting (figure 4.7 B). Apperley *et al.* [29] carried out static VT $^1$H experiments on amorphous indomethacin and nifedipine. They also showed rapid narrowing of the $^1$H peaks with increasing temperature, attributed to increased molecular mobility leading to averaging out $^1$H-$^1$H dipolar interactions (figure 4.7 A). Carpentier *et al.* [59] used VT $^1$H MAS NMR to monitor crystallisation and polymorphism of amorphous IMC. Firstly, when IMC was in the glassy state ($T < T_g$), a broad $^1$H spectrum was seen. With increasing temperature, they observed the metastable $\alpha$ polymorph ($T > T_g$) with line narrowing due to fast molecular motion, attributed to a cooperative motion identified *via* dielectric relaxation spectroscopy.

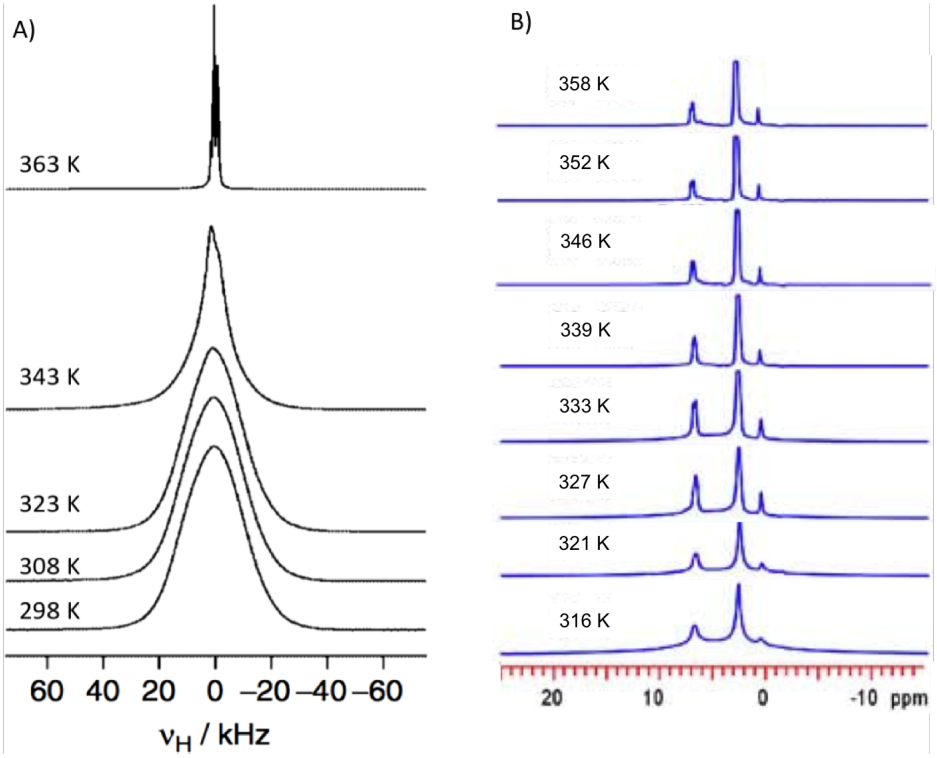


**Figure 4.7:** A) Static VT $^1$H NMR spectra of amorphous IMC [29] and B) VT $^1$H MAS NMR spectra of ketoprofen/PEO blends [30]

As seen in chapter 2, increased molecular mobility leads to line narrowing within the spectra due to the partial cancellation of homonuclear dipolar couplings between $^1$Hs. In the solution state, interactions average to zero, which leads to the high resolution/narrow linewidth observed in solution-state $^1$H spectra. Increased molecular motion in the solid-state can therefore become very obvious through monitoring the change in linewidth with increasing temperature.

## 4.3 $^{19}$F MAS NMR

$^{19}$F is a very attractive nucleus in NMR due to its large gyromagnetic ratio and high natural abundance, and therefore quick experimental time. Linewidth (quantified through measurement of Full Width Half-Height (FWHH) can be monitored: smaller FWHH values indicate the increased mobility of an isotropic 'liquid-like' environment, due to averaging of homonuclear dipolar interactions, in a similar way to VT $^1$H MAS NMR. Changes in mobility can additionally be determined through monitoring the change in the intensity and distribution of spinning sidebands within the spectra.

Chemical Shift Anisotropy (CSA) originates from the orientation dependence effect of chemical shift, with respect to external magnetic field ($B_0$) and is determined by non-spherical electron distribution around a nucleus. In liquids, anisotropy is averaged out to zero by fast molecular motion, therefore a single isotropic value of chemical shift is

observed. In solids, molecules orientate in a wide variety of directions, resulting in slight differences to chemical shift, and therefore a much broader peak. The anisotropic shielding tensor contains a geometric component ($3\cos^2\theta$ - 1), which is averaged through MAS to zero, essentially removing the orientation dependence resulting in a narrow isotropic chemical shift (see chapter 2 for further explanation). However, if the MAS rate is not sufficient to fully achieve such averaging, spinning sidebands on either side of the main isotropic peaks are observed, separated by the MAS frequency. The reduction, or disappearance of spinning sidebands in $^{19}$F MAS spectra, as a result of increasing temperature, would indicates higher molecular mobility within the system.

$^{19}$F MAS NMR is becoming increasingly important as a characterisation tool of pharmaceuticals. Currently 20 - 25 % of pipeline active pharmaceutical ingredients (APIs) contain one or more $^{19}$F atoms [207]. Additionally, very few pharmaceutical excipients contain $^{19}$F atoms, therefore $^{19}$F MAS NMR becomes a highly sensitive characterisation tool for solid dispersions, allowing the monitoring of API without the complication of drug/excipient peak overlap, even for highly diluted systems [207]. Brus *et al.* [207] used $^{19}$F MAS NMR combined with factor analysis to successfully characterise a number of solid forms of atorvastatin, including polymorphs and amorphous materials, by monitoring changes in chemical shift values. The same group went on to investigate the changes in the molecular arrangement of atorvastatin when formulated as a dispersion with PVP using $^{19}$F MAS NMR alongside multivariate analysis [208]. Pham *et al.* [88] studied a number of pharmaceutical systems using $^{19}$F MAS NMR. Firstly, $^{19}$F-$^{13}$C CP/MAS and $^{1}$H-$^{19}$F HETCOR experiments were used to compare dispersions of diflusinal/PVP and voriconazole/PVP to show interactions between the drug and polymer. They also measured $^{19}$F detected $^{1}$H $T_1$ times for dispersions of voriconazole/PVP to investigate phase separation. Abraham *at al.* [209] used $^{19}$F-$^{13}$C 2D HETCOR NMR as a tool for molecular structure investigation of the crystalline drug avagacestat, and solid dispersions with HPMC-AS; and were able to determine proximities between fluorine and carbon of up to 8 Å. Aso *et al.* [41] assessed the feasibility of $^{19}$F-NMR for the investigation of molecular mobility within FFA/PVP and FFA/HPMC solid dispersions, using variable temperature spin-lattice relaxation, and concluded that it was a useful measure for the assessment of physical stability. $^{19}$F MAS NMR has additionally been used to determine the amount of crystalline content within dispersions of AMG 517/HPMC-AS [210], for polymorph identification of crystalline casopitant [211], and for the characterisation of amorphous and crystalline forms of an $M_3$ receptor antagonist with increasing temperature [212].

## 4.4 Detection of molecular mobility in the solid-state with spin-lattice relaxation

It is important to note at this point, that the measurement of molecular mobility and discussion of relaxation in this thesis will refer to the measurement of spin-lattice relaxation through solid-state NMR. A discussion of different measures of relaxation, associated with molecular mobility in the amorphous state above and below $T_g$ was provided in chapter 1, section 1.3.1.

NMR relaxation time measurements in the solid-state allow motions across a range of timescales to be investigated, including faster motions on a MHz timescale (*i.e.* methyl group rotations), with ${T_1}^{H/C}$, and slower backbone motions on a kHz timescale with ${T_{1\rho}}^{H/C}$ times (figure 4.1). We investigated the ${T_{1\rho}}^{H}$, ${T_1}^{H}$ and ${T_1}^{F}$ relaxation of various amorphous systems, which enabled us to probe a range of motions. ${T_1}^{H}$ was used to probe faster MHz timescale relaxation of crystalline drugs, and all solid dispersions, with ${T_1}^{F}$ providing an additional analysis tool of $^{19}$F containing FFA/PVP-VA dispersions.

Investigation of ${T_{1\rho}}^{H}$ allowed us to probe the slower motions, namely those associated with backbone polymer chain motions [29, 161], thought to reflect the overall 'freeing up' of local mobility as temperature conditions change [187]. These motions occur on a kHz timescale (ms – $\mu$s) at the frequency of rotating frame, determined by the spin-lock field ($\omega_1 = 78$ kHz in this case). ${T_{1\rho}}^{H}$ relaxation provides a sensitive probe of local mobility, giving a snapshot of molecular level changes within the systems which is particularly important below, and around $T_g$. The timescale of molecular motions changes dramatically on cooling, with much slower dynamics occurring near and below $T_g$.

The ${T_{1\rho}}^{H}$ relaxation times give an indication of the molecular motions in the solid state, and are influenced by dipolar coupled nuclei and therefore structural rigidity [28, 46]. The spin-lock relaxation pulse sequence enables an estimation of ${T_{1\rho}}^{H}$ relaxation time associated with $^{13}$C peaks, allowing us to monitor the mobility of both the drug and the polymer components of the systems. ${T_{1\rho}}^{H}$ is a volume property, averaged over a distance of *ca.* 2 - 5 nm [8, 46], which allows a tool for the study of miscibility within drug/polymer systems. Single $^1$H relaxation times across each chemical site would indicate good miscibility within the system, due to efficient $^1$H-$^1$H spin-diffusion occurring in the solid state [46] (see section 4.4.2).

### 4.4.1 Temperature Dependence

When studying relaxation times, it is important to take into account the temperature dependence, in order to link relaxation behaviour with the mobility and dynamics of the system. Relaxation times display a typical dependence on temperature, as shown in figure

4.8. Spin-lattice relaxation times ($T_1{}^H$ and $T_{1\rho}{}^H$) are *highly* dependent on temperature, passing through minima as different motional processes lead to relaxation [24]. It is therefore important to determine the temperature dependence of relaxation times in order to determine which motional regime the relaxation time belongs.

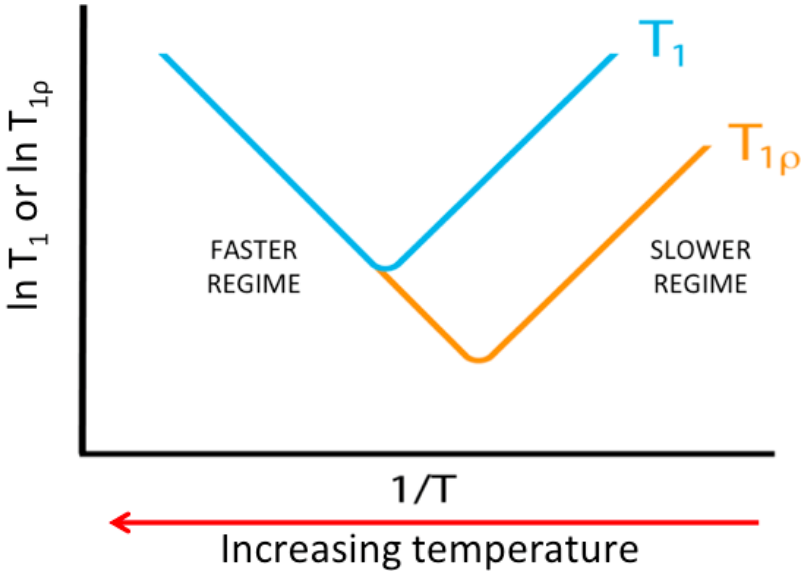


**Figure 4.8:** Typical temperature dependence of spin-lattice relaxation time

When studying molecular motions using VT relaxation, we must determine which side of the minimum the particular relaxation time is placed. On the slower regime side, the relaxation time will decrease with increasing temperature; on the faster regime side, the relaxation time will increase with increasing temperature [28, 161, 202, 213].

Activation energies ($E_A$) for the particular motional regime probed on kHz ($T_{1\rho}{}^H$) or MHz ($T_1{}^H$) timescales can be calculated using a simple Arrhenius expression (equation 4.1),

$$\frac{1}{T_{1(\rho)}} \propto \exp^{(\frac{E_A}{RT})} \tag{4.1}$$

By plotting ln $T_{1(\rho)}{}^H$ against the reciprocal of temperature, a slope equal to -$E_A$/RT can be used to calculate activation energy. A positive gradient would indicate the presence of motions on the slow side of the temperature dependence curve, and a negative gradient a faster motional regime [213]. To characterise the types of motions further, the correlation time ($\tau_c$) can be calculated from $T_{1\rho}/T_1{}^H$ using equations 4.2 and 4.3. $\tau_c$ is the average time it takes for a molecule with random molecular tumbling to progress through one radian [214], which therefore enables us to calculate the rate of molecular motion [213], by applying BPP/KT theory, which provides a relationship between $\tau_c$ and $T_{1\rho}{}^H/T_1{}^H$ [28, 215–218].

$$\frac{1}{T_{1\rho}} = \frac{3}{10r^6}\gamma^4\hbar^2[\frac{\frac{5}{2\tau_c}}{(1+\omega_0^2\tau_c^2)} + \frac{\tau_c}{(1+4\omega_0^2\tau_c^2)} + \frac{\frac{3}{2\tau_c}}{(1+4\omega_1^2\tau_c^2)}] \tag{4.2}$$

$$\frac{1}{T_1} = \frac{3}{10r^6}\gamma^4\hbar^2[\frac{\tau_c}{(1+\omega_0^2\tau_c^2)} + \frac{4\tau_c}{(1+\omega_0^2\tau_c^2)}] \tag{4.3}$$

where r is internuclear distance, $\gamma$ is gyromagnetic ratio, $\hbar$ is reduced Plank's constant, $\omega_0$ is Larmor frequency and $\omega_1$ is frequency of *rf* pulse. This gives us a way to link relaxation rate, internuclear distance, resonance frequency and spectral density functions of molecular motion by taking into account the effect of molecular motion on local field disturbance [214]. Variable temperature relaxation studies are therefore useful as they can provide both quantitative and qualitative information, which gives us a measure of changes in local mobility (within the kHz timescale) for both drug and polymer.

### 4.4.2 Detecting miscibility with relaxation times

The detection of miscibility through analysis of spin-lattice relaxation times was originally developed to detect polymer mixing within blends [219, 220] and has been since utilised for the detection of phase separation between drug and polymer components of amorphous solid dispersions [46,88,152]. Spin-lattice relaxation is a volume averaged property, due to efficient spin-diffusion in the solid-state [152]. The length scale of mixing of the components of interest can therefore be estimated *via* solid-state NMR. If the individual components (for example drug and polymer), are closer in space than the length scale of $^1$H-$^1$H spin diffusion, then the transfer of magnetisation is highly efficient [46]. This results in one common relaxation time between components, which is a weighted average of the expected individual values [221].

The length scale of spin diffusion is measured using equation 4.4. Here, the maximum range of $^1$H-$^1$H spin diffusion effects can be estimated from the diffusion path length ($L$) during the spin-lattice relaxation time period ($t$), for both $T_1$ and $T_{1\rho}$ times.

$$L = \sqrt{6Dt} \tag{4.4}$$

where D represents the spin diffusion coefficient (equation 4.5), calculated from the distance between protons ($l_0$) and the spin-spin relaxation time ($T_2$).

$$D = \frac{\langle l_0^2 \rangle}{T_2} \tag{4.5}$$

Typically, D is assumed to be $10^{-12}$ cm$^2$ s$^{-1}$ in studies of polymers [221] and drug/polymer dispersions [152]. Using this value of D, and assuming typical ${T_1}^H$ (1 - 5 s) and ${T_{1\rho}}^H$ (5 - 50 ms) relaxation times, the effective spin-diffusion lengths (L) are shown to be approximately 24 - 55 nm (${T_1}^H$) and 2 - 6 nm (${T_{1\rho}}^H$). By taking the difference of spin-lattice relaxation times between the two components of interest ($\Delta{T_1}^H$ and $\Delta{T_{1\rho}}^H$) the following three outcomes are possible [46, 62, 88]:

- $\Delta T_1{}^H > 0$ indicates domains of $> 55$ nm
- $\Delta T_1{}^H = 0$, but $\Delta T_{1\rho}{}^H > 0$ indicates miscibility on the 6 - 24 nm length scale
- $\Delta T_{1\rho}{}^H = 0$ indicates miscibility on the 2 - 6 nm length scale (domains of $< 2$ nm)

Differences in the relaxation times ($\Delta T_{1\rho}{}^H$ and $\Delta T_1{}^H$) of drug and polymer components have been used previously to provide information on miscibility and domain sizes in nifedipine/PVP dispersions [46, 152] and mefenamic acid/EUDRAGIT® dispersions [86].

# Chapter 5

# Variable Temperature Studies of Indomethacin

IMC has been extensively studied with a range of characterisation methods, and has been demonstrated to successfully form amorphous solid dispersions with PVP [71, 77] and PVP-VA [84]. Here we chose to use IMC as a 'proof of concept' comparison to other less studied molecules (flufenamic acid and tolbutamide) with lower $T_g$ values, to illustrate the capabilities of solid-state NMR methods used to characterise dispersions. Although there is a large volume of literature surrounding IMC, there is still a lack of information regarding the mobility of IMC formulated as amorphous dispersions at increased temperatures, and crystallisation from high drug loaded dispersions.

DSC has been previously used to investigate molecular mobility below $T_g$: a number of studies found that IMC experienced significant molecular mobility ($\alpha$ and $\beta$ relaxation) at temperatures up to 65 K below $T_g$ [69, 222]. The same group also used DSC to find evidence of nucleation of $\alpha$ IMC at temperatures 55 K below $T_g$ which provides evidence for nucleation in the $\beta$-relaxation region [223]. Matsumoto *et al.* [84] studied a variety of weight ratio IMC/PVP and IMC/PVP-VA dispersions, using DSC and FT-IR to investigate drug polymer interactions in relation to crystallisation from the amorphous state. They found that both polymers interacted with IMC through hydrogen bonding, eliminating the carboxylic dimer interaction required for the nucleation and growth of the $\gamma$-crystalline form. They additionally found that 5 % PVP content prevented crystallisation of IMC at 303 K over the 20 week storage period. Other studies have used dielectric relaxation spectroscopy to look at the molecular mobility of supercooled IMC, finding that high molecular mobility of amorphous IMC was observed below $T_g$, which was linked to reduced physical stability [150].

The amorphous form of IMC has been found to crystallise from the amorphous state under storage at 303 K within a few weeks, however inhibition of crystallisation was been observed for over 6 months when the storage temperature was reduced to 277 K [68], although storage near refrigeration temperatures is not always practical and room temperature storage would be more desirable [84]. Apperley *et al.* [29] characterised the amorphous form using variable temperature relaxation studies ($T_{1\rho}{}^H$ and $T_1{}^H$), variable temperature $^{13}C$ and $^1H$ MAS NMR. Karmwar *et al.* [224] also investigated the effect on the stability of amorphous IMC of the method of manufacture, finding that recrystallisation was different for each method, with quench cooled samples ranking as most stable. Carpentier *et al.* [59] combined dielectric relaxation spectroscopy with $^1H$ NMR spectroscopy to investigate the molecular mobility of both the amorphous and crystalline forms ($\gamma$ and $\alpha$) of IMC [59].

A handful of solid-state NMR studies have also investigated IMC/PVP solid dispersions. Guilbaud *et al.* [77] studied the functional group mobility with and without polymer using $^{13}C$ and $^1H$ relaxation time measurements, at ambient temperature. They found that solid-state NMR was able to demonstrate the stabilisation of the amorphous drug by reducing guest mobility. Brettmann *et al.* [225] used $T_1{}^H$ and $T_{1\rho}{}^H$ times to detect miscibility of electrospun IMC/PVP dispersions at two drug loadings, following storage at 313 K for 6 months, finding

that the dispersions remained homogenous over this time period. Additionally, Pham *et al.* [88] used advanced 2D $^{1}$H-$^{13}$C CP MAS HETeronuclear CORrelation (CP-HETCOR) and $^{1}$H double quantum (DQ) correlation experiments to characterise the structures in terms of drug/polymer intermolecular interactions; and $T_1{}^H$ times to study phase separation of the solid dispersions. Again, no phase separation was detected in these systems with this method.

## 5.1 Crystalline Indomethacin

Indomethacin is known to exhibit polymorphism, with two monotropic forms ($\gamma$ and $\alpha$) most widely studied within the literature. $\gamma$-IMC is the most thermodynamically stable form under ambient conditions, with a melting point of 432 - 434 K and enthalpy of fusion ($\Delta H_f$) of 109.5 J·g$^{-1}$ [51]. $\alpha$-IMC is a frequently occurring metastable form, with a melting point of 426 - 428 K and $\Delta H_f$ of 103.5 J·g$^{-1}$ [51]. The crystallographic information of both polymorphs is shown in table 5.1.

**Table 5.1:** Crystallographic data of $\gamma$ and $\alpha$-IMC, adapted from [31, 49]

| | $\gamma$ | $\alpha$ |
|---|---|---|
| Crystal system | triclinic | monoclinic |
| Space group | *P-1* | $P2_1$ |
| $a$ (Å) | 9.295(2) | 5.4616(16) |
| $b$ (Å) | 10.969(1) | 25.310(9) |
| $c$ (Å) | 9.742(1) | 18.152(7) |
| $\alpha$ (°) | 69.38(1) | 90 |
| $\beta$ (°) | 110.79(1) | 94.38(3) |
| $\gamma$ (°) | 92.78(1) | 90n |
| V (Å$^3$) | 869.8 | 2501.8 |
| Z/Z' | 2/1 | 6/3 |
| CSD Code | INDMET | INDMET02 |

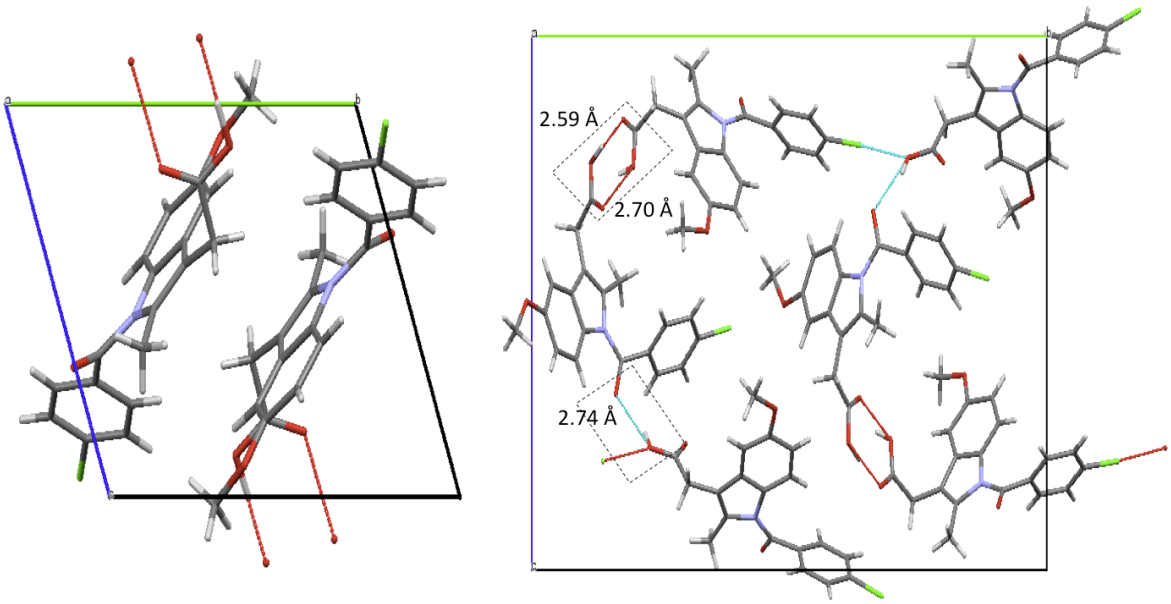


**Figure 5.1:** Crystal structures of $\gamma$ and $\alpha$-IMC as viewed along the $a$ axis, extracted from the Cambridge Structural Database (structure references INDMET and INDMET02). The hydrogen-bonding of both polymorphs is highlighted

$\gamma$ and $\alpha$-IMC exhibit differences in hydrogen bonding in their crystal structures (figure 5.1 and 5.2). The lattice of $\gamma$-IMC is stabilised through carboxylic acid hydrogen-bonded dimers of equivalent molecules in the unit cell, with H-bond length of 1.604 Å [31]. The three asymmetric unit molecules of $\alpha$-IMC exist as trimers, with two molecules (molecules 1 and 2) forming a hydrogen-bonded carboxylic acid dimer similar to $\gamma$-IMC, but with different length H-bonds; with an additional bonding motif between the amide carbonyl of the carboxylic acid dimer (molecule 2) and a carboxylic acid group of an additional molecule (molecule 3). [31].

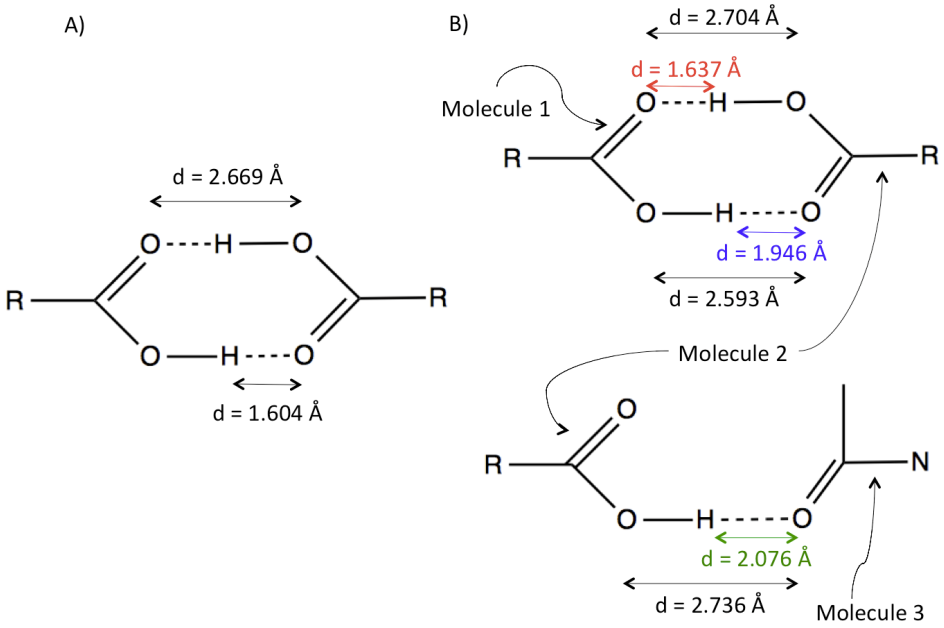


**Figure 5.2:** Hydrogen bonding in A) $\gamma$-IMC and B) $\alpha$-IMC [31]

The ambient temperature $^{1}$H-$^{13}$C CP/MAS NMR spectra of $\gamma$ and $\alpha$-IMC are shown in figure 5.3. Peak splitting patterns of solid-state spectra can provide information regarding the number of crystallographically non-equivalent molecules within the lattice structure. For example, $\gamma$-IMC has one molecule within the asymmetric unit, therefore single, narrow peaks are seen in the $^{13}$C spectrum [29]. $\alpha$-IMC can be identified from the $^{13}$C spectrum due to the splitting of each resonance into three [226], representing the positions of the three non-equivalent molecules in the asymmetric unit [31].

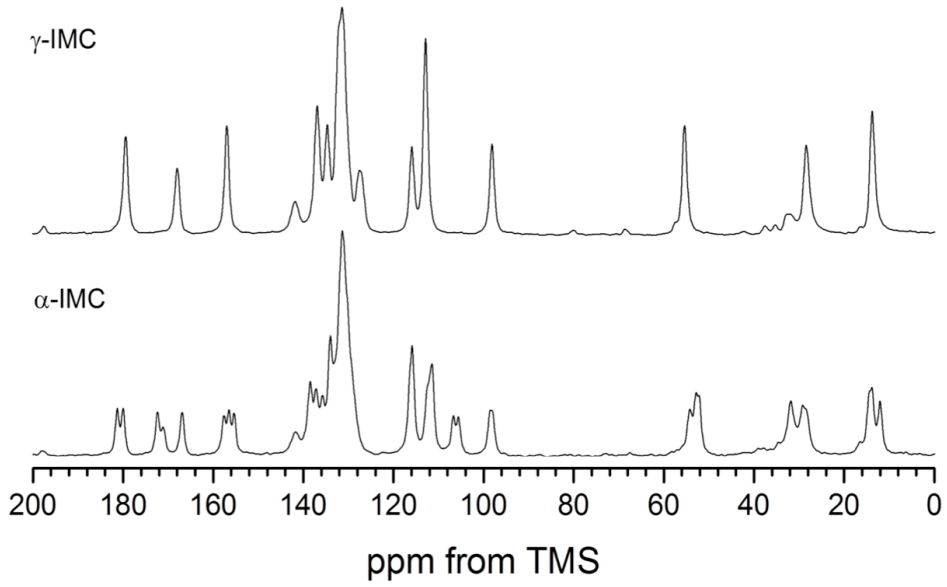


**Figure 5.3:** Experimental $^{1}$H-$^{13}$C CP/MAS NMR spectra of $\gamma$ and $\alpha$-IMC, recorded at an MAS rate of 10 kHz

Borka [50] described four forms of IMC, using a different naming system: Form I ($\gamma$), form II ($\alpha$), form III ($\beta$) and form IV ($\delta$), although the $\beta$ and $\delta$ forms were not further studied until more recently [51, 53]. Despite IMC being so extensively characterised as a model drug, new polymorphs are still being discovered. Surwase *et al.* recently reported three new polymorphic forms of IMC, named $\varepsilon$ (found to be the same form as a previously unnamed polymorph reported by Lin *et al.* [227]), $\zeta$ and $\eta$ isolated from amorphous suspensions of IMC and characterised using PXRD, DSC and FT-IR [52]. From solution concentration profiles at 273 K, they predicted the stability order to be $\varepsilon < \zeta < \eta < \alpha$. A summary of the melting points of all described polymorphs is shown in table 5.2.

**Table 5.2:** $T_m$ values (K) of Indomethacin polymorphs adapted from [50–53]. * Form $\varepsilon$ too unstable for analysis, transforming to $\alpha$ upon drying; ** Formed *via* desolvation from methanolate form [53]

| **Form** | **$T_m$ (K)** |
|---|---|
| $\alpha$ (II) | 426 - 428 |
| $\beta$ (III) | 421 |
| $\gamma$ (I) | 432 - 434 |
| $\delta$ (IV) ** | 407 |
| $\varepsilon$ | N/A * |
| $\zeta$ | 415 |
| $\eta$ | 427 |

## 5.2 Initial Characterisation of Amorphous IMC, and IMC/PVP-VA solid dispersions

Amorphous IMC and IMC/PVP-VA solid dispersions were initially characterised using modulated DSC, PXRD and $^{1}$H-$^{13}$C CP/MAS NMR. The solid dispersions were confirmed to be amorphous by the single $T_g$ values (figure 5.4), traditionally taken as an indication of miscible, single phase systems ( [69]), with domain sizes undetectable at less than 30 nm in size [164, 165]. $T_g$ values of the dispersions were intermediate between those of pure amorphous IMC and PVP-VA, as expected from the Gordon-Taylor relationship [112], and increased with increasing polymer content, indicating the anti-plasticising property of PVP-VA. This relationship has been demonstrated previously for dispersions of IMC/PVP [29, 77]. Ideal $T_g$ values of the dispersions were calculated using the Gordon-Taylor/Kelley-Bueche (G-T/K-B) and Couchman-Karasz (C-K) equations (equations 2.17 with 2.19 and 2.20 - see chapter 3), and can be seen in figure 5.4.

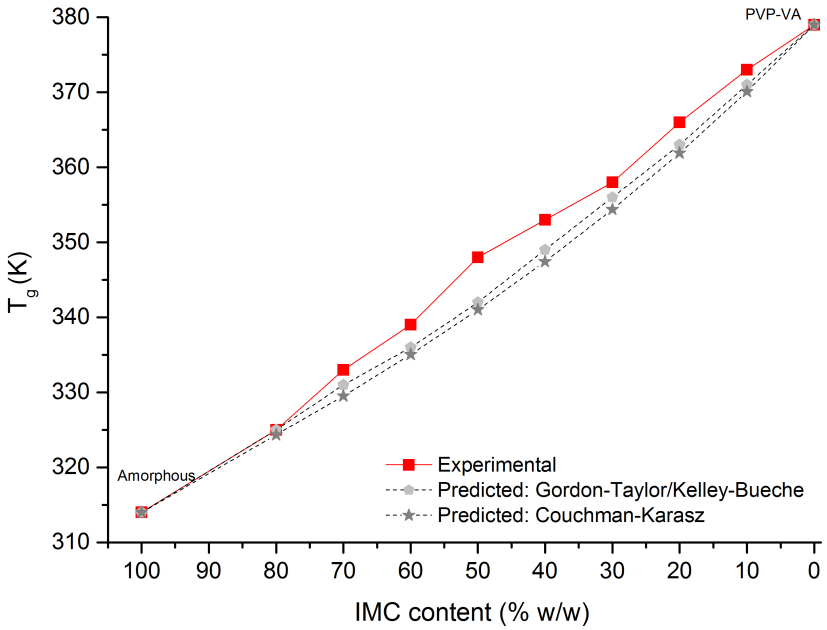


**Figure 5.4:** Glass transition temperatures for IMC/PVP-VA dispersions at different drug loadings, compared to values predicted by the Gordon-Taylor/Kelley-Bueche (G-T/K-B) and Couchman-Karasz (C-K) equations

A very slight positive deviation from predicted $T_g$ was observed for the IMC/PVP-VA dispersions, which was greatest for the mid drug loadings between 40 to 60 wt. %. This indicates the possible dominance of drug/polymer interactions [192–194]. IMC has been previously shown to interact with PVP *via* hydrogen bonds between the IMC hydroxyl and PVP carbonyl groups [71]. However, the maximum deviation (*ca.* 6 K), is negligible in this case. In previous studies, deviations of ± 5 K were considered to be good agreement for 'ideal' mixing [78]. Examples of positive deviation from predicted values have been encountered in the literature for solid dispersions: Song *et al.* [62] found large positive deviations in dispersions of lapatanib/HPMC-P, with intermediate loadings (40 - 60 wt. % drug) displaying the largest deviation, with experimental $T_g$ values over 40 K higher than predicted. This was found to be due to specific ionic interactions between drug and polymer, additionally detected *via* $^{15}N$ solid-state NMR. Gupta *et al.* [190] additionally found positive deviation in celecoxib/PVP dispersions, which again was most significant for intermediate loading dispersions. Considerable deviations are more likely at intermediate content, as these dispersions experience the greatest difference in free volume of each component upon mixing.

Amorphous indomethacin was produced *via* the quench cool method [29,70]. Upon heating, the $T_g$ was observed at *ca.* 314 K, which is in agreement with literature $T_g$ values [77]. This was followed by crystallisation (*ca.* 378 K) and subsequent melting of $\alpha$-IMC (425 K) and $\gamma$-IMC (433 K) (figure 5.5). This behaviour is in agreement with previous literature DSC studies on the crystallisation of amorphous IMC [32].

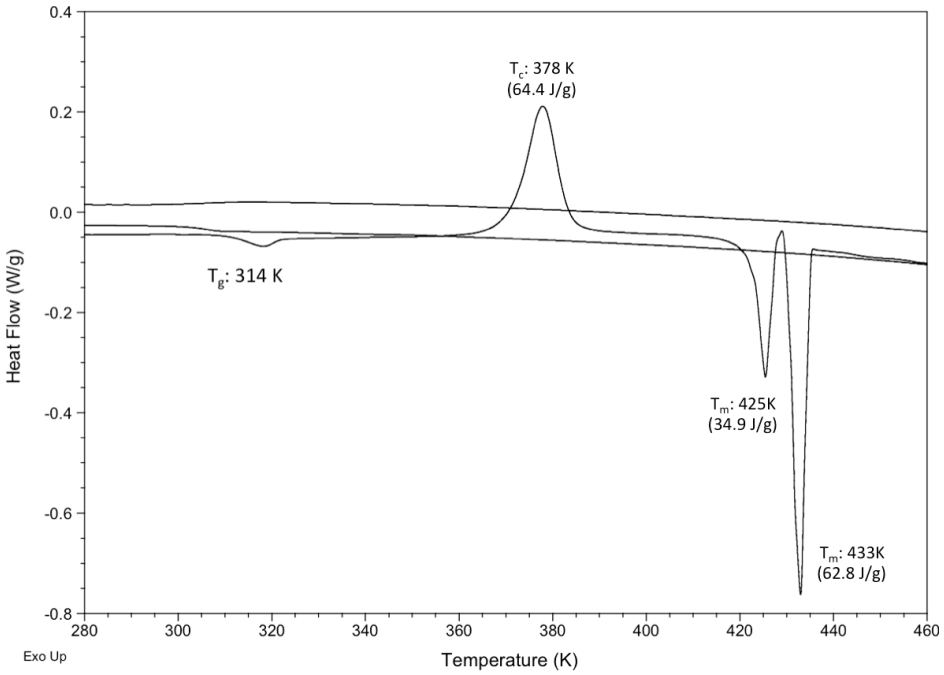


**Figure 5.5:** Modulated DSC curve (heat → cool → reheat cycle) for amorphous IMC prepared *via* quench cooling

The initial DSC heating cycle of the 80/20 and 70/30 IMC/PVP-VA dispersions indicates that they appear to contain a small amount of crystalline drug (figure 5.6). The melting endotherms were not preceded by a crystallisation event, indicating the possible presence of small seeds of crystalline material upon formulation, which melted at high temperatures. In previous studies of solid dispersions where two melting endotherms have been identifed, the lower temperature event is attributed to melting of a drug/polymer solid solution, formed through the dissolution of drug in the polymer upon heating [90, 148]. The higher temperature endotherm is thought to occur due to the melting of residual crystalline API formed during manufacture [190]. The presence of single endotherms in DSC curves of drug/polymer dispersions has been attributed to either solid solution formation, or dissolution of the drug in polymer upon heating, [228].

Two melting endotherms are present in the DSC curve of the 80/20 IMC/PVP-VA dispersion. The higher temperature endotherm at *ca.* 429 K in the 80/20 dispersion likely indicates the presence of a small amount of residual $\alpha$-IMC ($T_m$ = 426 – 428 K [31]). The quantity of crystalline drug can be approximated according to [229]:

$$\%crystallinity = (\frac{\Delta H_{disp}}{\Delta H_{\alpha} \times W}) \times 100 \tag{5.1}$$

where $\Delta H_{disp}$ is the enthalpy of fusion of the $\alpha$-IMC in the dispersion, $\Delta H_{\alpha}$ the enthalpy of fusion for pure $\alpha$-IMC and W the weight fraction of API in the dispersion. This equation has previously been used to quantify the % crystallinity of physical mixtures and solid dispersions of ibuprofen/PVP-CL and ibuprofen/MCC [229, 230].

The known melting enthalpy ($\Delta H_f$) of pure $\alpha$-IMC is 91 $J \cdot g^{-1}$ [59, 231, 232]. Therefore the residual content of $\alpha$-IMC in the 80/20 dispersion is calculated to be 2.1 %. For the 70/30 IMC/PVP-VA dispersion, the small single melting endotherm *ca.* 410 K is likely due to dissolution of the drug [90] rather than the presence of residual crystalline IMC.

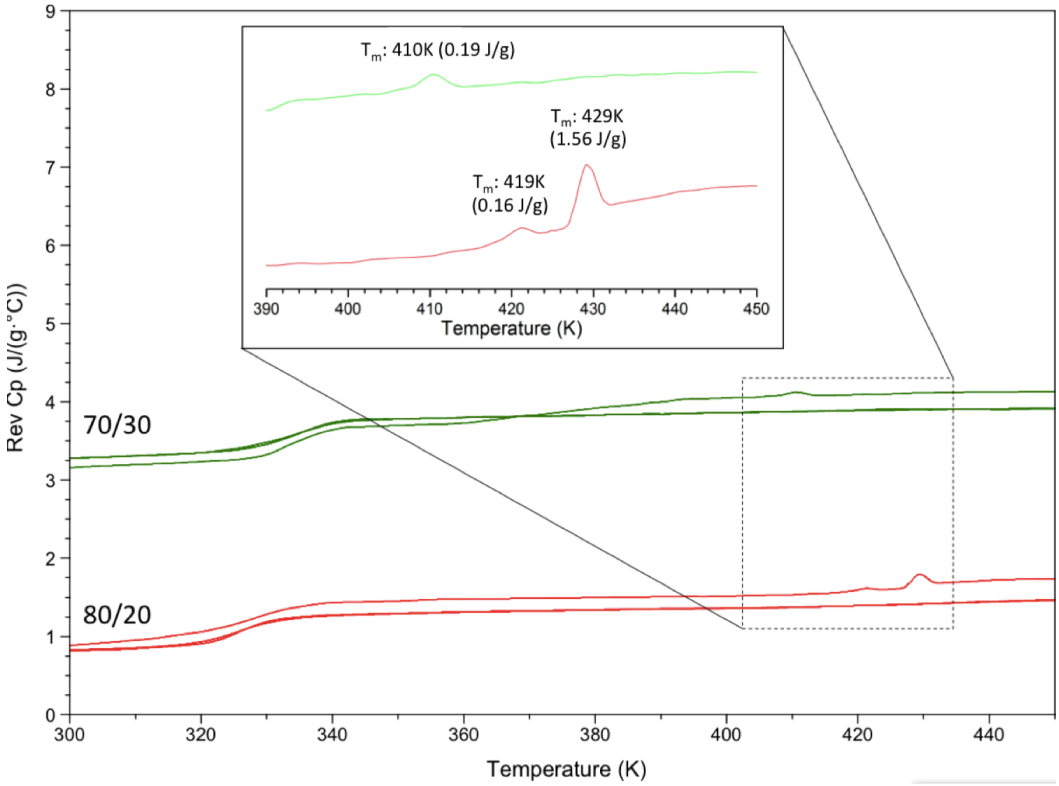


**Figure 5.6:** Modulated DSC heat capacity curve of IMC/PVP-VA 80/20 (red) and 70/30 (green) dispersions with melting peaks highlighted inset, for heat → cool → reheat cycles * $\Delta H_f$ calculated from heat flow vs. temperature curves

PXRD patterns indicated that all dispersions were fully amorphous (figure 5.7). The small amount of crystalline seeds identified in the DSC curves for the 80/20 and 70/30 dispersions are therefore below the detection limit of PXRD.

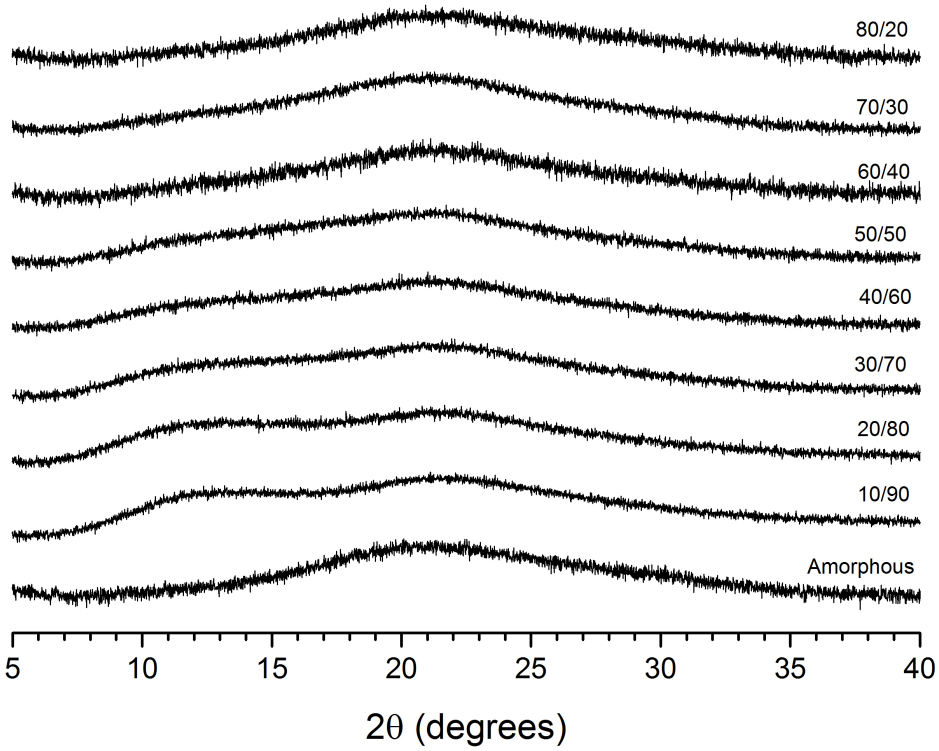


**Figure 5.7:** PXRD patterns of all IMC/PVP-VA dispersions

The $^{1}$H-$^{13}$C CP/MAS NMR spectra (figure 5.8) confirm that amorphous IMC was obtained *via* quench cooling of IMC melt. The amorphous IMC displays broad $^{13}$C resonances compared to narrow peaks of the crystalline IMC spectra. For example the FWHH of the $CH_3$ (C-11) peak (*ca.* 56 ppm) are 104.6 and 367.4 Hz for $\gamma$-IMC and amorphous IMC respectively. Broadening of peaks for amorphous materials is due to the lack of long range order, leading to a wider range of possible orientations of molecules, and an increased number of magnetically non-equivalent carbon atoms compared to the well defined repeating unit cell in crystalline structures. The full assignments of the $^{13}$C chemical shifts of amorphous IMC [70, 77], $\gamma$-crystalline IMC [29, 130, 233], $\alpha$-IMC [130, 226] and PVP-VA [148] have been reported previously. From figure 5.8 it can also be seen that amorphous IMC has an additional carbonyl peak at *ca.* 172 ppm, comparable to $^{13}$C spectrum of $\alpha$-IMC, which is attributed to an additional H-bonding motif between the amide carbonyl and carboxylic acid groups [31, 130, 226]. This is in agreement with the IR and Raman spectroscopic data presented by Taylor and Zographi [71], where two hydrogen bonding mechanisms in amorphous IMC were demonstrated: 1) carboxylic acid hydrogen-bonded dimers, similar to $\gamma$-IMC, were the dominant mechanism; 2) additional hydrogen bonding between the carbonyl and carboxylic acid groups, similar to the $\alpha$-IMC was also observed.

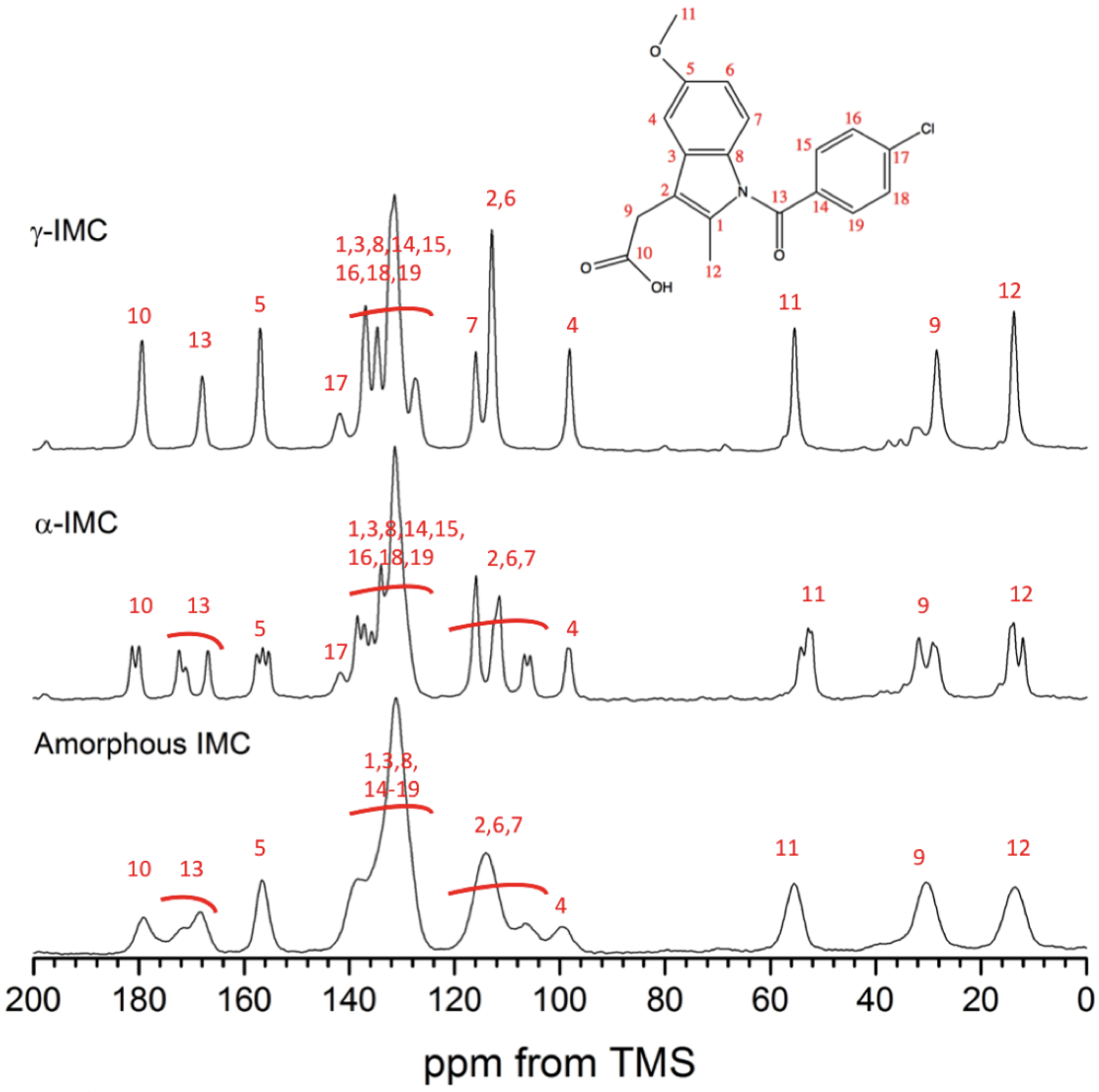


**Figure 5.8:** Experimental $^{1}$H-$^{13}$C CP/MAS NMR spectra of $\alpha$-IMC, $\gamma$-IMC and amorphous IMC, recorded at an MAS rate of 10 kHz

Figure 5.9 and table 5.3 show the assignment of chemical shifts to IMC, PVP-VA, or both drug and polymer within the IMC/PVPVA 40/60 dispersion. The main $^{13}$C peaks of IMC affected by overlapping with PVP-VA are the carbonyl resonances (C-10, C-13) masked by the lines from the carbonyl polymer peaks (C-D, C-I) and the IMC $CH_2$ group (C-9) masked by aliphatic polymer chain carbons (C-G, C-H). However, all aromatic peaks of IMC are unaffected by the PVP-VA. This peak separation allowed us to independently monitor changes to both components of the dispersion during variable temperature NMR investigations. The carbonyl region also provided additional information about changes in H-bonding during phase transitions and recrystallization.

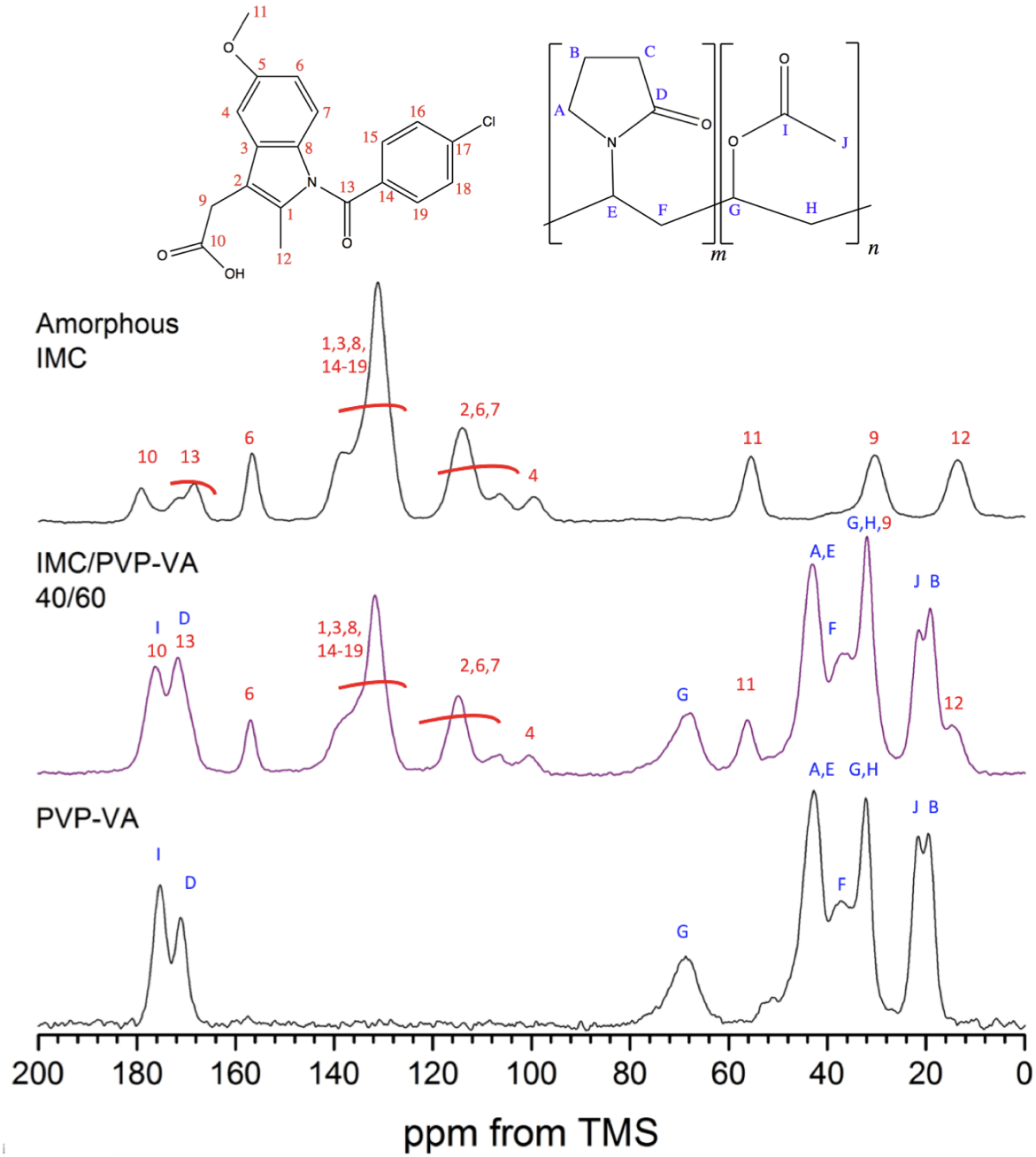


**Figure 5.9:** $^{1}$H-$^{13}$C CP/MAS NMR spectra with full peak assignments for IMC/PVP-VA 40/60 solid dispersion compared to amorphous IMC and PVP-VA recorded at an MAS rate of 10 kHz

**Table 5.3:** $^{13}$C Chemical Shift Assignments of IMC and PVP-VA (based on the 40/60 IMC/PVP-VA dispersion)

| Chemical Shift (ppm) | IMC | PVP-VA |
|---|---|---|
| 175.9 | 10 | I |
| 171.3 | 13 | D |
| 156.8 | 5 | |
| 131.7 | 1,3,8, 14-19 | |
| 115.0 - 107.2 | 2,6,7 | |
| 101.5 | 4 | |
| 68.0 | | G |
| 56.2 | 11 | |
| 42.9 | | A,E |
| 36.9 | | F |
| 32.0 | 9 | G,H |
| 21.4 | | J |
| 19.2 | | B |
| 13.8 | 12 | |

The change in the intensities of the drug/polymer peaks in the $^{1}$H-$^{13}$C CP/MAS NMR spectra reflect the ratio of the two components within each dispersion (figure 5.10). For the dispersions with the highest drug loading (80/20 and 70/30) an additional carbonyl shoulder peak at *ca.* 172 ppm is present, likely due to hydrogen bonding between the amide carbonyl and a carboxylic acid, as seen in amorphous and $\alpha$-IMC [31, 71]. This could be due to the presence of increased IMC/IMC over IMC/PVP-VA interactions at high drug loading, or could indicate the presence of a small amount of $\alpha$-IMC, identified in the 80/20 dispersion through DSC.

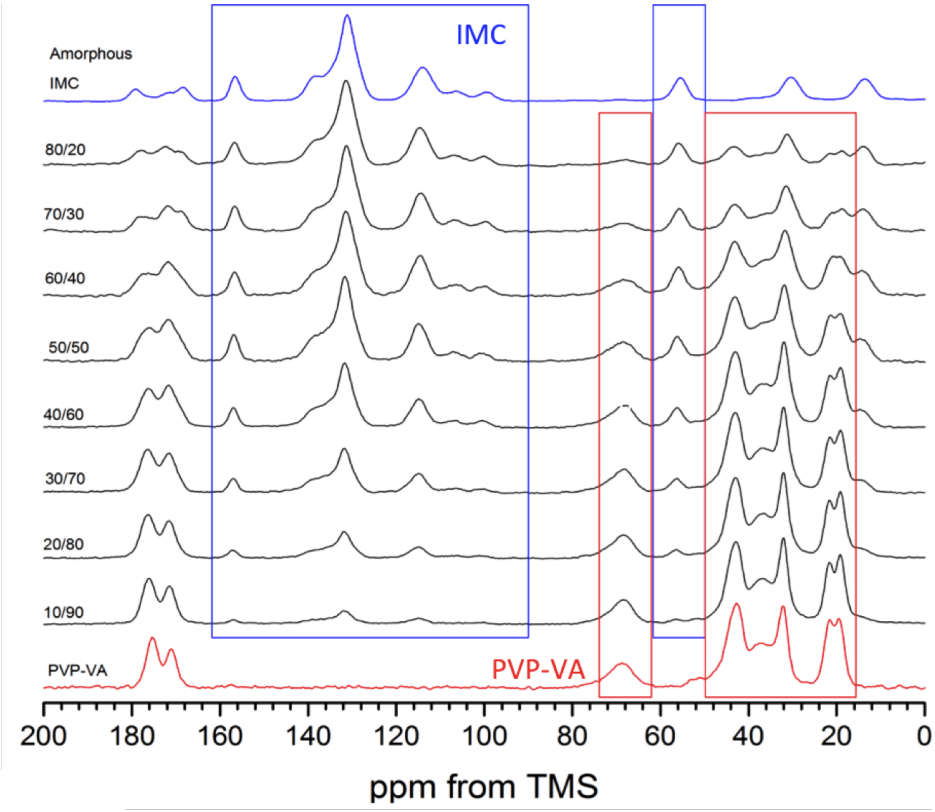


**Figure 5.10:** $^{1}$H-$^{13}$C CP/MAS NMR spectra for amorphous dispersions of various drug loadings, recorded at an MAS rate of 10 kHz

### 5.2.1 Correlating local mobility with chemical structure using WIdeline SEparation (WISE) NMR

WIdeline SEparation (WISE) experiments in solid-state NMR are used to correlate information on local mobility with chemical structure [198, 234]. The 2D $^{1}$H-$^{13}$C WISE spectrum shows the $^{1}$H wideline spectral patterns associated with each of the $^{13}$C chemical shifts. The widths of $^{1}$H are indicative of the strength of $^{1}$H-$^{1}$H homonuclear dipolar coupling, with more rigid structures displaying wider lines in the WISE projections. WISE NMR was originally developed to correlate structure and mobility during characterisation of poly(styrene)-poly(siloxane) polymer blends [234] and has since been utilised to investigate local mobility of a variety of co-block polymers [235, 236], biopolymers [198] and encapulation of an amorphous decapeptide in PLGA [202].

The WISE spectra and measured FWHHs of amorphous IMC, PVP-VA and dispersions with drug loadings of 20, 40 and 80 wt. % are shown in table 5.4 and figure 5.11. In the mid-loading dispersion (40/60), the FWHH of IMC and PVP-VA are similar to those measured for the individual components, suggesting formulation at this drug/polymer ratio has little effect on the local mobility of amorphous IMC and PVP-VA. The mixing of similar wt. ratios of drug and polymer therefore does not seem to disrupt the $^{1}$H-$^{1}$H dipolar coupling network of either component. However, in formulations where the content

of one component is much greater than the other, we see changes in local mobility. With excess IMC (80/20 IMC/PVP-VA dispersion), the local mobility of the drug is unaffected, but narrowing of the polymer peaks is observed, indicating an increased local mobility of the polymeric matrix. Enhanced local mobility of polymer was previously reported by Guilbaud *et al.* [202] with higher drug content of AZD/PLGA formulations. With excess PVP-VA (20/80 IMC/PVP-VA dispersion), broadening of drug **and** polymer widelines are observed, indicating a restriction of overall local mobility and an increase in $^{1}$H-$^{1}$H dipolar coupling for both components of the dispersion. The carbonyl widelines ($^{13}$C $\delta$ = 176 and 171 ppm) provide information on the overall strength of the dipolar coupling in the system, as carbonyl functionalities do not have directly attached protons. The broadening of these widelines in the 20/80 dispersion indicates a change to the local proton population, in comparison with pure PVP-VA, and could be an indication of interactions between drug and polymer [237].

**Table 5.4:** $^{1}$H full width half height (FWHH) in Hz of the main $^{13}$C chemical shifts of amorphous IMC, PVP-VA and 20/80, 40/60 and 80/20 IMC/PVP-VA dispersions, extracted from wideline spectral patterns of WISE spectra at 293 K. Assignment of I = IMC peak; P = PVP-VA peak; – unable to measure FWHH due to low intensity peak

| **Assignment** | **$^{13}$C (ppm)** | **FWHH (Hz)** | | | | |
|---|---|---|---|---|---|---|
| | | Amorphous | 80/20 | 40/60 | 20/80 | PVP-VA |
| I and P | 176 | – | 627 | 788 | 1183 | 874 |
| I and P | 171 | – | 552 | 636 | 1082 | 633 |
| I | 131 | 679 | 684 | 676 | 1104 | |
| I | 115 | 758 | 762 | 743 | 1047 | |
| P | 43 | | – | 1001 | 1527 | 1186 |
| P | 32 | | 975 | 1073 | 1450 | 1140 |
| P | 21 | | 652 | 627 | 1102 | 879 |
| P | 19 | | 663 | 756 | 1295 | 778 |
| I | 13 | 628 | 629 | 648 | 1159 | |

The WISE spectra highlighted differences in local mobility of IMC and PVP-VA dependent on drug loading levels upon formulation of amorphous solid dispersions. These changes will be further investigated with variable temperature solid-state NMR techniques.

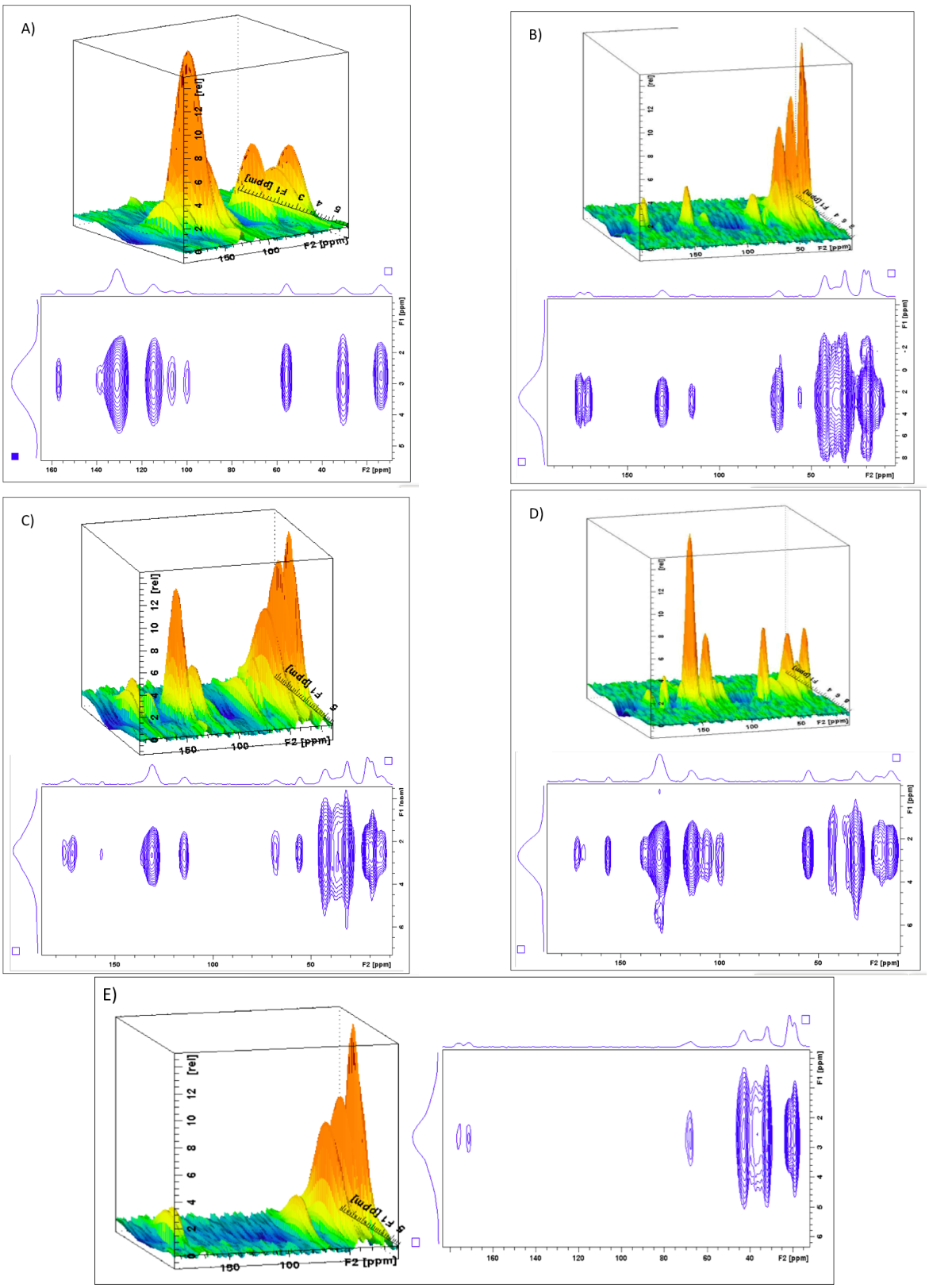


**Figure 5.11:** $^{1}$H-$^{13}$C WISE NMR spectra (1D and 2D projections) for A) Amorphous IMC, B) 20/80 IMC/PVP-VA, C) 40/60 IMC/PVP-VA, D) 80/20 IMC/PVP-VA and E) PVP-VA

## 5.3 Variable temperature NMR studies of IMC

$^{1}$H-$^{13}$C CP/MAS NMR spectra of amorphous IMC and the IMC/PVPVA dispersions were acquired across a range of temperatures to probe their stability by monitoring crystallisation and changes in mobility.

### 5.3.1 Detection of crystallisation at high temperatures

Crystallisation was investigated by monitoring changes in $^{13}$C spectra with increasing temperature, above and below $T_g$, as changes in mobility around and below $T_g$ have been linked with changes in physical stability. It was thought previously that storing an amorphous material at the Kautzmann temperature ($T_g$ – 50 K) would be sufficient to indefinitely stabilise it [69]. However, studies have shown that changes in mobility can occur, leading to instability, even at very low temperatures [123].

When amorphous IMC was heated from 298 to 373 K the $^{13}$C CP/MAS NMR spectra indicated the onset of crystallisation by 353 K, well above the $T_g$ of 315 K (figure 5.12). The peaks became narrower and more defined with increasing temperature, and with chemical shifts and splitting characteristic of the $\alpha$-polymorph [31, 130]. Detailed comparison of the spectra indicates full crystallisation of the amorphous IMC at temperatures above 353 K. There were no changes observed in the spectra around and below the $T_g$. A comparison of the spectra upon cooling highlights that $\alpha$-IMC was still present, indicating a permanent crystallisation event from amorphous to $\alpha$-IMC occurred.

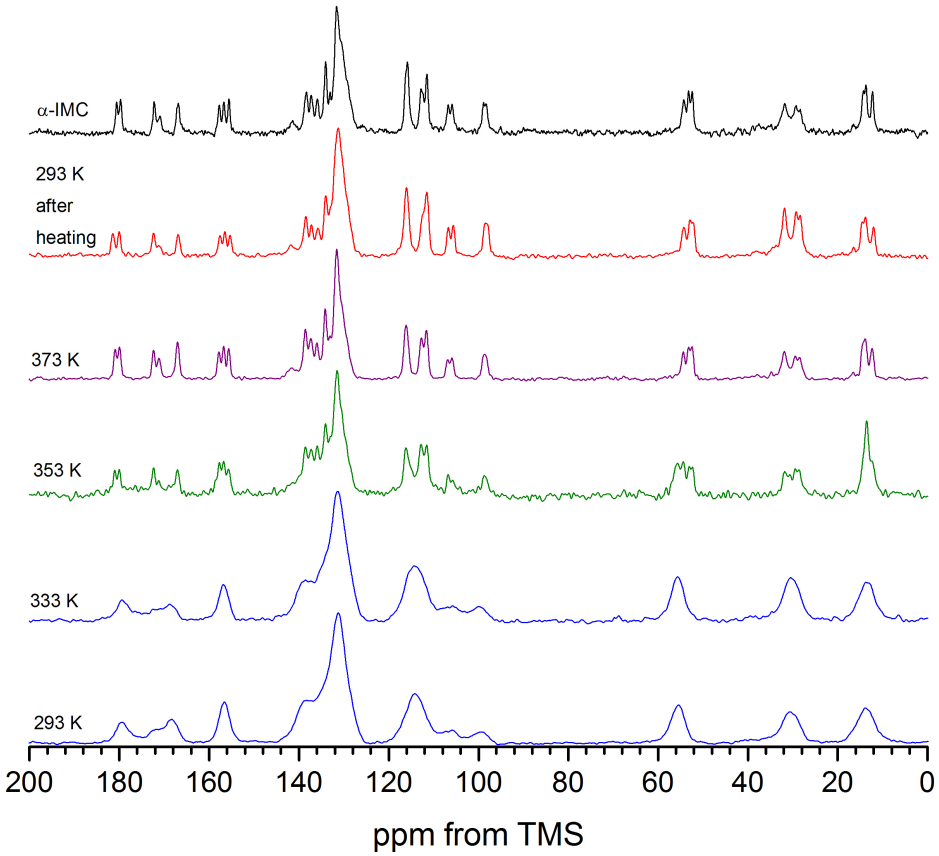


**Figure 5.12:** $^{1}$H-$^{13}$C CP/MAS NMR spectra of amorphous IMC recorded at different temperatures between 293 K and 373 K, with comparison spectrum of $\alpha$-IMC (373 K), at an MAS rate of 10 kHz

This extends work by Apperley *et al.* [29], who heated amorphous IMC to 353 K under MAS conditions, but found the results 'relatively uninformative' with some line narrowing around 343 K and increased resolution at 353 K but with no specific polymorph identified [29, 238]. Upon cooling, their sample appeared more amorphous than crystalline, therefore line narrowing was attributed to increased molecular mobility rather than recrystallisation [238].

In our case, the crystallization above $T_g$ is in agreement with previous stability studies of amorphous IMC. Yoshioka *et al.* [68] found that crystallisation to the more stable $\gamma$-form occurred at storage temperatures below $T_g$, but at higher temperatures (above $T_g$) crystallisation to the metastable $\alpha$-form predominated. Andronis and Zographi [32] further studied the polymorphic phase selectivity of IMC and found that the $\alpha$-polymorph was more likely to crystallise at higher temperatures due to a lower free energy difference between crystalline and amorphous forms ($\Delta G_v$), faster nucleation and growth rate, and lower activation energy of crystallisation compared to the $\gamma$-polymorph at elevated temperatures (figure 5.13). At 353 K, where we observed crystallisation from amorphous IMC to the $\alpha$-form, the activation energy of crystallisation for $\alpha$-IMC is lower than that for the $\gamma$-polymorph. These findings were in agreement with Stranski's proposal that at a specific temperature, the nucleated phase will be the phase with the lowest free energy

barrier of formation. Crystallisation to $\gamma$-IMC, occurred at lower temperatures, particularly around $T_g$, where $\gamma$-IMC has a lower activation energy for recrystallization.

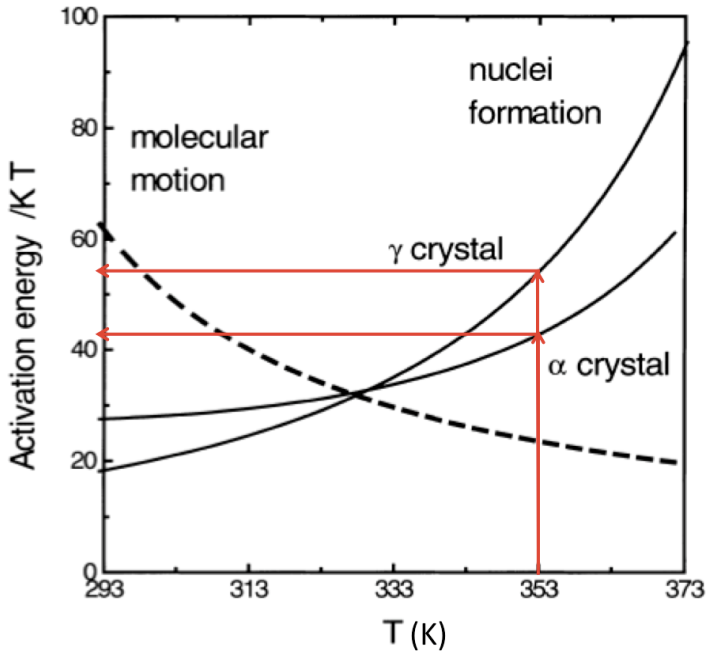


**Figure 5.13:** Energy-temperature diagram to summarise activation energies for: free energy barrier to nucleation ($\Delta$G) of $\alpha$ and $\gamma$-IMC; and viscosity of dry amorphous IMC (dotted line), adapted from [32]

The crystallisation of amorphous IMC (prepared *via* melt quench) to different polymorphs has been studied under a variety of conditions. In addition to high temperature heating, the metastable $\alpha$-polymorph was found to recrystallise preferentially at high humidity (above 43 % RH) [124], under dissolution conditions (phosphate buffer at 37 °C, and a water-ethanol (50 % w/w) solution) from amorphous IMC moulded into compacts during the melt quench process [73, 239]; and from amorphous suspensions in 0.1 M aqueous media at 298 K [52]. As discussed above, the room temperature $^{13}$C NMR spectra of both amorphous IMC and $\alpha$-IMC contained an additional carbonyl shoulder peak, attributed to H-bonding motifs between -COOH and –N-C=O groups [31]. This could be an indication that the H-bonding within the amorphous system is similar to the $\alpha$-polymorph, with an extra H-bond occurring between amide and carboxyl carbonyl groups.

The variable temperature $^{1}$H-$^{13}$C CP/MAS NMR spectra of PVP-VA (data not shown) showed no major changes with regards to chemical shifts and line widths, but some loss of intensity was observed for the peaks at 17, 42 and 19 ppm indicating a slight increase in mobility leading to loss of CP signal. The carbonyl peak was still present in the spectrum after heating and cooling, confirming chemical stability.

### 5.3.2 Detection of changes in mobility of IMC/PVP-VA dispersions at high temperatures using $^{13}$C VT NMR

The IMC/PVP-VA dispersions proved an excellent system to probe mobility by evaluating the loss of signal intensity and line broadening with increasing temperature (outlined in chapter 4), due to separation of drug and polymer peaks.

The VT $^{13}$C NMR spectra for IMC/PVP-VA 20/80 dispersion (figure 5.14 A) and 30/70 dispersion (data not shown) illustrate changes in mobility of the dispersions. The CP spectra show loss of signal intensity of the IMC peaks (especially the aromatic peaks at *ca.* 131.7 and 115.0 ppm) with increasing temperature up to 373 K. This indicates an increased mobility of the drug within the dispersion on an intermediate timescale, affecting C-H dipolar interactions during the CP transfer step. This effect was especially pronounced above the $T_g$ of 367 K. The mobility on this timescale is likely to be dominated by the chlorobenzyl aromatic ring of IMC, as a previous study on the motions of amorphous IMC highlighted this functional group as being crucial for changes in local mobility [59]; although we did see loss of signal intensity across all IMC peaks. The carbonyl resonance at 171 ppm (IMC: C-13 and PVP-VA: C-D) also showed a loss of signal intensity, likely from the drug contribution to these overlapping peaks. There was little change in the polymer peaks on heating, indicating its lower mobility in comparison to the drug on the observed timescale. There were no significant changes to the $^{1}$H-$^{13}$C CP/MAS spectra recorded at 293 K before and after heating to 373 K.

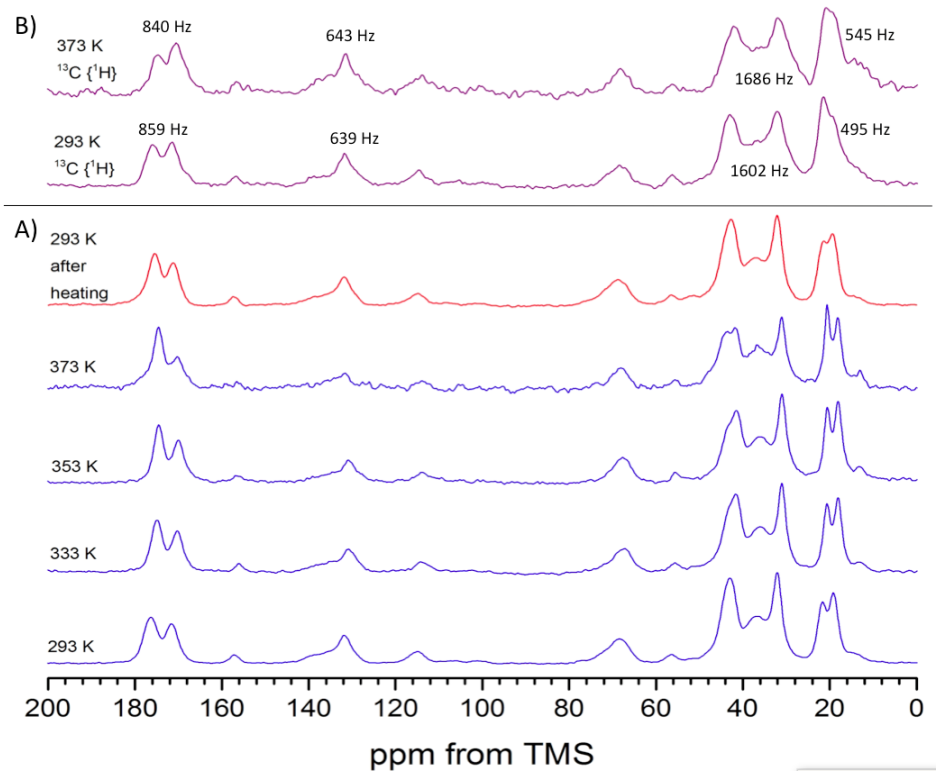


**Figure 5.14:** A) $^{1}$H-$^{13}$C CP/MAS NMR spectra of IMC/PVP-VA 20/80 dispersions recorded at different temperatures between 293 and 373 K, and upon cooling back to 293 K (red spectrum); B) $^{13}$C{$^{1}$H} MAS NMR spectra of IMC/PVP-VA 20/80 dispersions recorded at 293 and 373 K, with FWHH values (Hz) for the main resonances

There is no significant change to the FWHH or intensity for all resonances in the $^{13}$C{$^{1}$H} spectra of the 20/80 dispersion with increasing temperature (figure 5.14 B). This indicates that the observed mobility of IMC is on the intermediate timescale, but is not fast enough to affect the efficiency of the heteronuclear decoupling of the $^{1}$H-$^{13}$C CP/MAS or $^{13}$C{$^{1}$H} MAS NMR experiments.

The VT CP/MAS spectra for the IMC/PVP-VA 40/60 dispersion (figure 5.15) showed no major changes to either the drug or polymer peaks upon heating to 373 K and subsequent cooling to 293 K. This suggests that both drug and polymer components have similar lower mobility than that observed for the drug component of the 20/80 dispersion, even above the $T_g$ of 353 K. This indicates the presence of a homogenous system with restricted mobility on a kHz timescale. The miscibility of the mid-loaded dispersions is further demonstrated in section 5.4. The lower mobility of the 40/60 and 50/50 dispersions could possibly be due to steric hindrance within the system. This has been previously demonstrated in polymer systems, where Takegoshi *et al.* [26] found that at ratios of 50/50 PS/PVME copolymer blends, the freedom of local motion of one component was restricted by steric hindrance of the other. A previous study by our group also found that at a certain drug/polymer ratio, no change in line broadening with increasing temperature indicated a more rigid system [202]. The increased number of drug/polymer hydrogen bonding sites within the 40/60 and 50/50 solid dispersions could also contribute to the decreased mobility of the systems, compared

to the lower concentration solid dispersions [180].

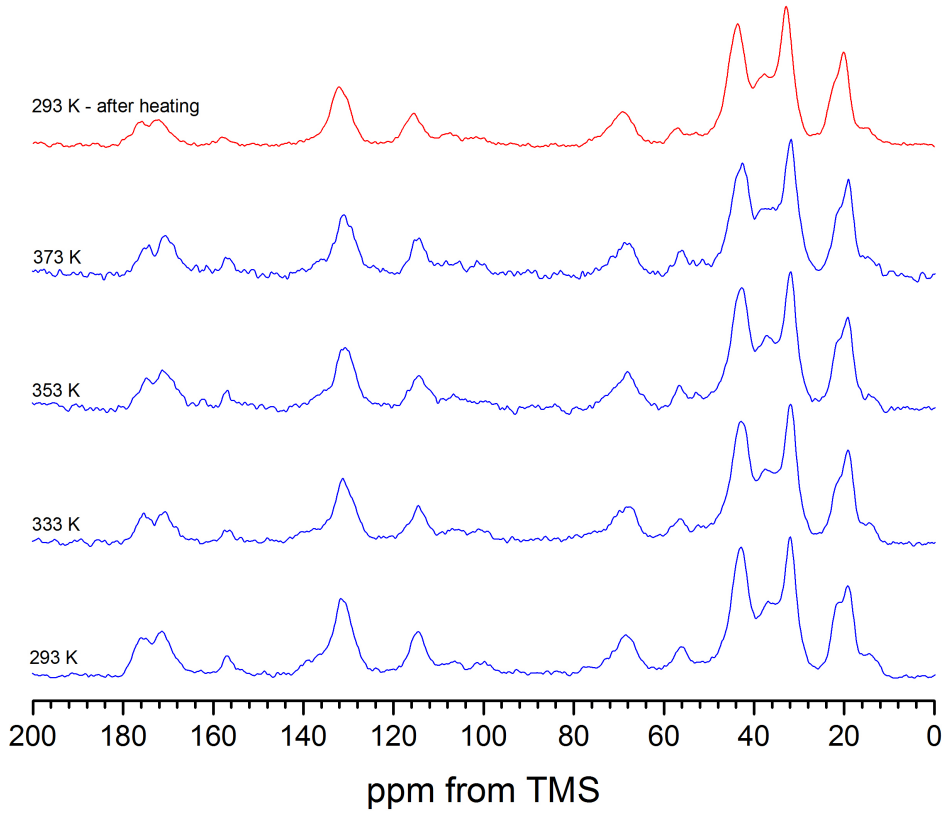


**Figure 5.15:** $^{1}$H-$^{13}$C CP/MAS NMR spectra of IMC/PVP-VA 40/60 dispersion recorded at different temperatures between 293 K and 373 K, and upon cooling back to 293 K (red spectrum), at an MAS rate of 10 kHz. Similar results were observed for the 50/50 dispersion (data not shown)

Further analysis of the $^{1}$H-$^{13}$C CP/MAS NMR spectra suggests that for the 20/80 dispersion, the area of the main drug peak (*ca.* 131 ppm) at 373 K is 54 % of the same peak at 298 K for the 20/80 dispersion (figure 5.16); compared to only a 12 % reduction in peak area for the 40/60 dispersion. For the main polymer peak (*ca.* 42 - 31 ppm) there is no change in peak area with increasing temperature across all dispersions.

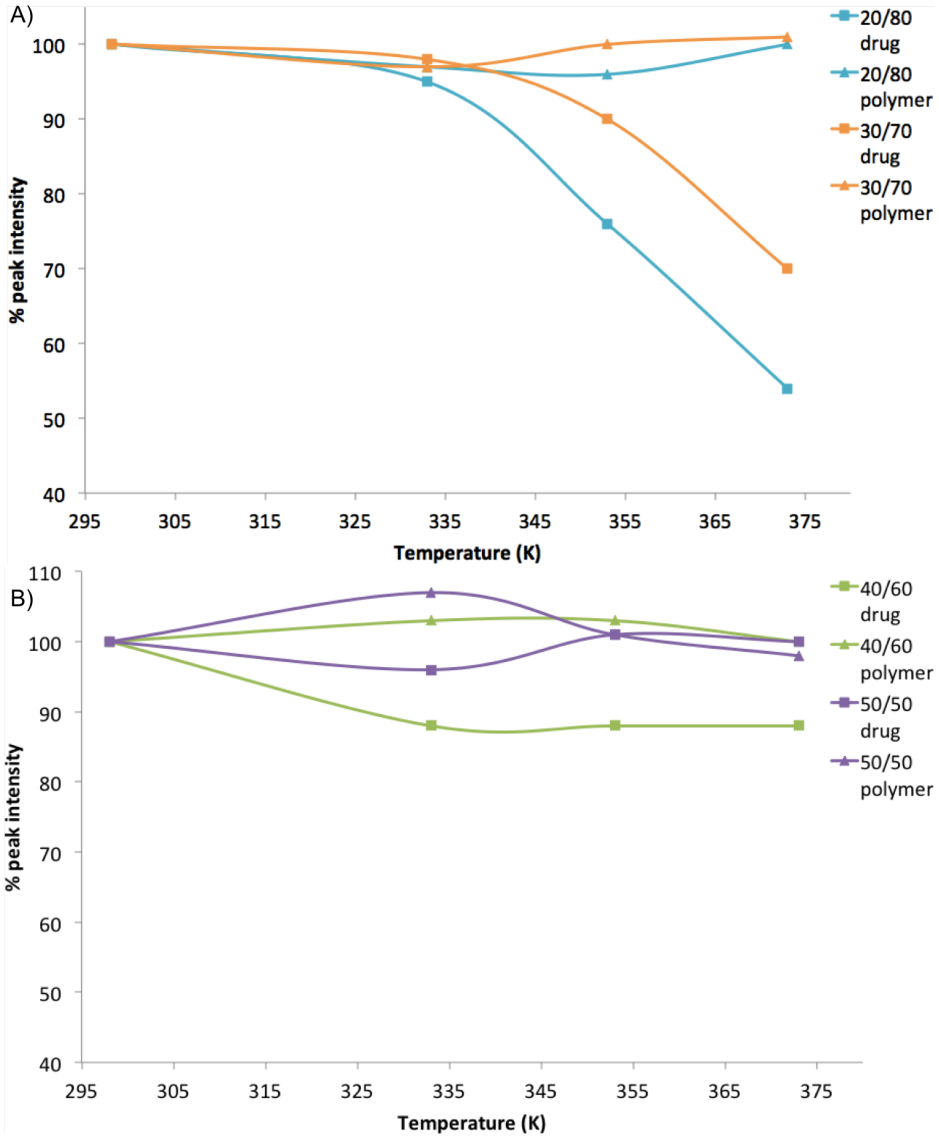


**Figure 5.16:** Changes in peak area of the CP/MAS spectra for A) IMC/PVP-VA 20/80 and 30/70 dispersions with increasing temperature and B) 40/60 and 50/50 dispersions. Integrals of the predominant drug (*ca.* 131 ppm) and polymer (*ca.* 42 - 31 ppm) resonances are shown. Percentages were calculated by determining the reduction in integral values at each temperature compared to the initial measurement at 293 K, using Topspin analysis software

The VT $^{1}$H-$^{13}$C CP/MAS NMR spectra for IMC/PVP-VA 60/40 dispersion (figure 5.17) illustrate changes in mobility with increasing temperature. Upon heating from 293 to 353 K, there were no major changes to either the drug or polymer peaks. However at 373 K, we see significantly broadened $^{13}$C signals, which is particularly obvious for the aromatic IMC signals at *ca.* 131 and 115 ppm. This indicates a large increase in mobility on the intermediate timescale, of both drug and polymer in the dispersion, *ca.* 35 K above the $T_g$ of 339 K. The drug and polymer signals were all visible in the $^{13}$C{$^{1}$H} spectrum at 373 K (figure 5.17 - green spectrum), but significant broadening was also observed. This indicates both drug and polymer are mobile at higher kHz frequencies (*ca.* 90 kHz) than the 20/80 dispersion at the same temperature, therefore modulating the heteronuclear decoupling of both the $^{1}$H-$^{13}$C

CP/MAS and $^{13}C\{^{1}H\}$ MAS NMR pulse sequences. There were no significant changes to the $^{1}H$-$^{13}C$ CP/MAS spectra recorded at 293 K before and after heating to 373 K (figure 5.17 - red spectrum).

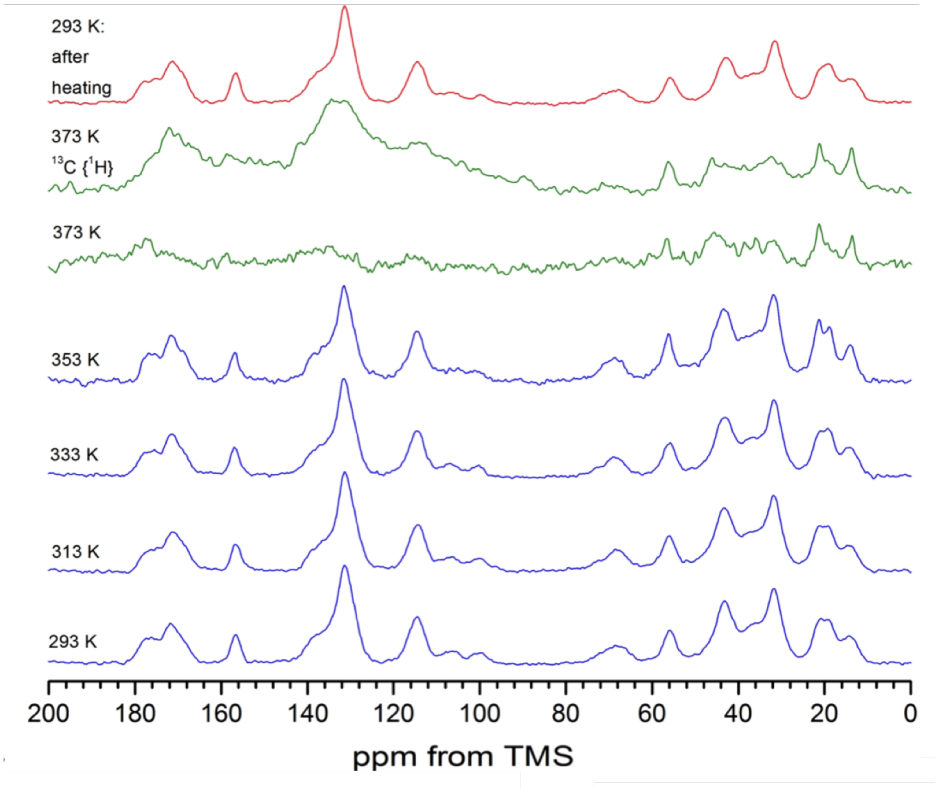


**Figure 5.17:** $^{1}H$-$^{13}C$ CP/MAS NMR spectra of 60/40 IMC/PVP-VA dispersion recorded at different temperatures between 293 and 373 K, at an MAS rate of 10 kHz

An increased level of the drug (IMC/PVP-VA 80/20 dispersion) lead to another change in mobility regime. As the 80/20 dispersion was heated through the $T_g$ (*ca.* 325 K), two different motional phenomena were detected (figure 5.18 - 333 K). Significant line broadening and loss of signal intensity occurred for the main aromatic IMC peaks (*ca.* 115, 131, 138, 156 ppm), with FWHH at 131 ppm increasing from 470 Hz to 998 Hz, indicating an increase in molecular motions on the intermediate timescale. Additionally line *narrowing* of the methyl groups of both drug and polymer (*ca.* 13 ppm (IMC: C-12), 19 ppm (PVP-VA: C-B), and 56 ppm (IMC: C-11)) occurred, indicating increased mobility on a faster timescale [26,28]. The changes in mobility at *ca.* 333 K are likely due to the reorganisation and phase separation of the drug molecules within the polymer during the initial stages of IMC crystallisation.

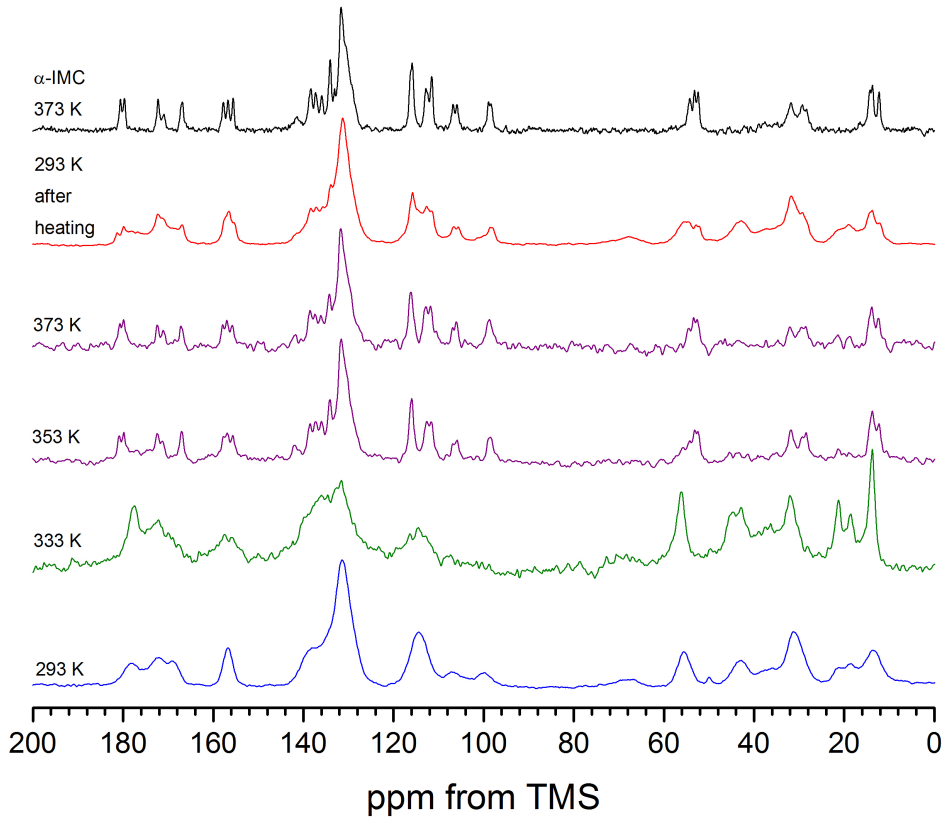


**Figure 5.18:** $^{1}$H-$^{13}$C CP/MAS NMR spectra of amorphous IMC recorded at different temperatures between 293 and 373 K, at an MAS rate of 10 kHz. A comparison of pure $\alpha$-IMC at 373 K is included for comparison

At temperatures of 353 K and above, apparent crystallisation to the $\alpha$-polymorph was observed, identified in the spectra by the characteristic peak splitting [31, 130], which is in agreement with DSC results. Increasing temperature resulted in the absence of all PVP-VA resonances in the spectra, either through loss of signal intensity, or through dramatic line broadening effects. The higher mobility of the polymer compared to drug at high temperatures indicates a possible phase separation, which is further explored in section 5.4.

The $^{1}$H-$^{13}$C CP/MAS NMR spectrum of pure $\alpha$-IMC has been shown to exhibit temperature dependence: with increasing temperatures (up to 343 K), Masuda *et al.* reported downfield shifts of resonances for C-5, C-11 and C-12 due to movement of the methoxy and methyl side groups [226]. Here we observe the same temperature dependence of $\alpha$-IMC present within the 80/20 dispersion (figure 5.19). At 373 K, slight downfield shifts of a number of carbon resonances occurred, with the spectrum of the 80/20 dispersion comparable to that of pure $\alpha$-IMC at the same temperature. This provides strong evidence for the crystallisation of amorphous IMC to the $\alpha$-polymorph, which is the expected polymorphic transition from amorphous IMC above $T_g$ [68]. We also observed one upfield shift of a carbonyl group of IMC (C-10) in both pure $\alpha$-IMC and the 80/20 dispersion at 373 K, which was not discussed in previous literature, and may be due to the presence of hydrogen bonding between drug and polymer.

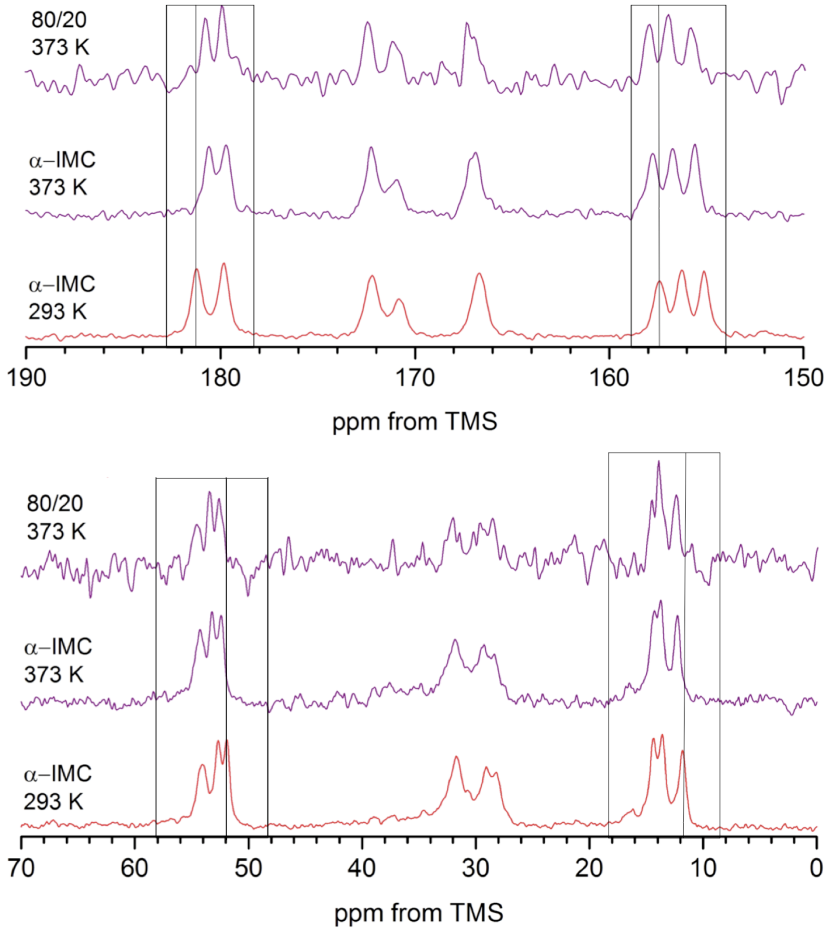


**Figure 5.19:** $^{1}$H-$^{13}$C CP/MAS NMR spectra for 80/20 dispersion and $\alpha$-IMC at 373 K: zoomed in on the C-10 carbonyl (*ca.* 179.8 - 180.7 ppm), C-5 aromatic (*ca.* 157.9 - 155.7 ppm), C-11 methoxy (*ca.* 54.4 - 52.7 ppm) and C-12 methyl (*ca.* 13.9 - 12.3 ppm) regions, with a comparison to $\alpha$-IMC at 293 K to highlight chemical shift differences at high temperatures. Line broadening = 20 Hz

Following heating to 373 K, the 80/20 dispersion was cooled gradually to 293 K within the rotor (figure 5.20). Slight broadening of the IMC peak at *ca.* 115 ppm (aromatic C-2,6,7) was observed but the majority of IMC peaks could still be assigned to $\alpha$-IMC, suggesting a permanent crystallisation from amorphous to $\alpha$-IMC at high temperatures. The polymer peaks reappeared upon cooling, due to reduction of polymer mobility (figure 5.18).

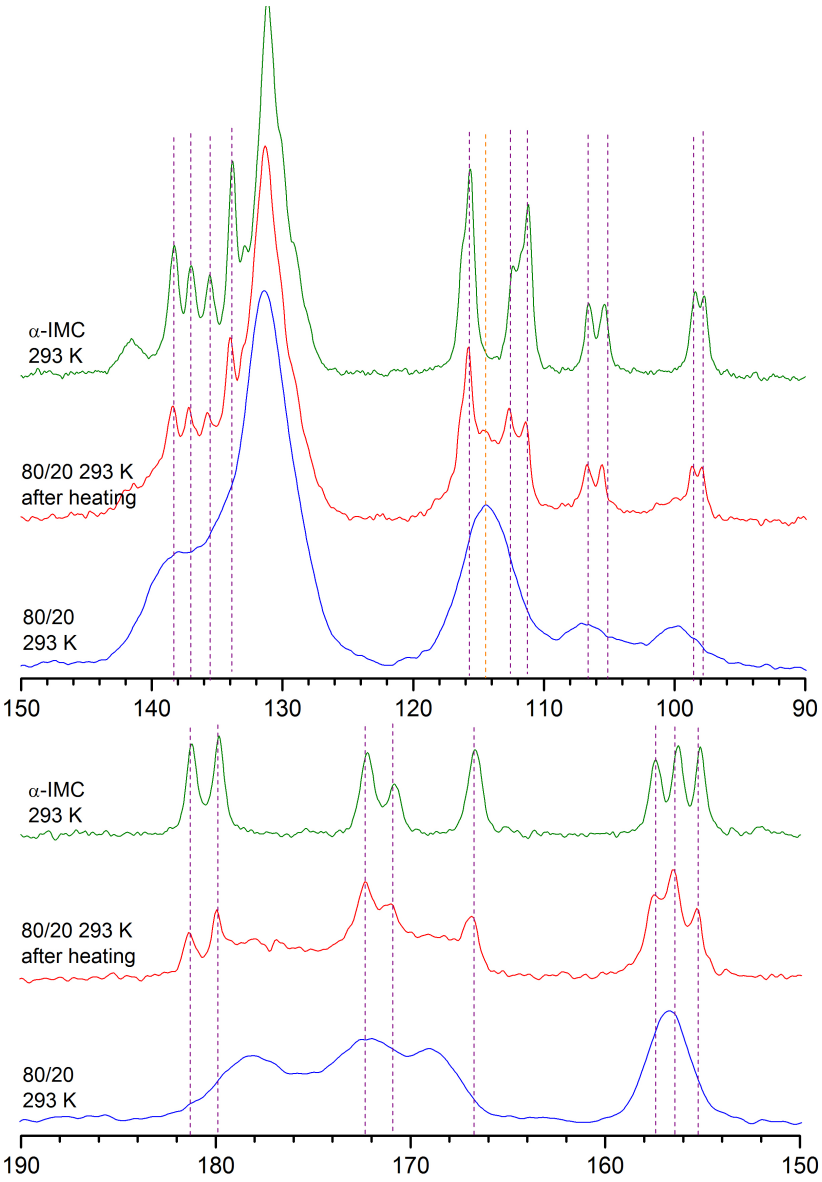


**Figure 5.20:** $^{1}$H-$^{13}$C CP/MAS NMR spectra for 80/20 dispersion before and after heating, compared to α-IMC. Purple dashed lines indicate the presence of α-IMC, with the orange dashed line *ca.* 115 ppm indicating amorphous IMC. Line broadening = 20 Hz

### 5.3.3 Detection of changes in the mobility of IMC/PVP-VA dispersions at high temperatures with VT $^{1}$H MAS NMR

To investigate the mobility of the IMC/PVPVA dispersions further, variable temperature $^{1}$H NMR studies were carried out. $^{1}$H solid-state NMR is very sensitive to molecular motions, where fast molecular mobility leads to line narrowing within the spectra, as discussed in chapter 4. Although it is harder to distinguish between drug and polymer peaks, increased mobility can become very obvious through monitoring the change in linewidth with increasing temperature. The VT $^{1}$H MAS NMR spectra show differences in the mobility of the dispersions dependent on drug content: higher IMC content lead to narrower resonances with increasing temperature indicating an increase in fast molecular

motions *ca.* 373 K (figures 5.21 and 5.22). Only small changes in resolution and chemical shift values occurred for the 20/80 and 40/60 dispersions with increasing temperature, indicating a lower mobility. The broad $^{1}$H peaks are dominated by the strong $^{1}$H-$^{1}$H dipolar interactions of drug and polymer. The VT $^{1}$H spectra of the 60/40 dispersion showed some increased mobility by 373 K, which was also seen in the VT $^{1}$H-$^{13}$C CP/MAS NMR spectrum at the same temperature. For the 80/20 dispersion a dramatic reduction in linewidth occurred, with peaks of much higher resolution observed *ca.* 373 K.

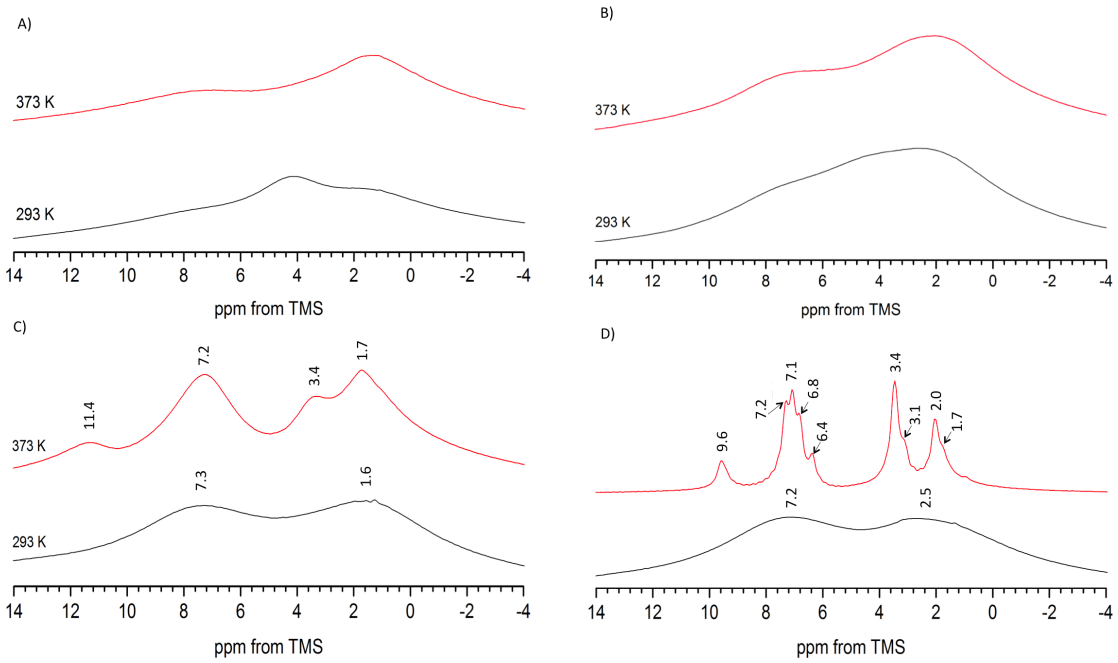


**Figure 5.21:** Variable temperature $^{1}$H MAS NMR spectra for A) 20/80, B) 40/60, C) 60/40 and D) 80/20 IMC/PVP-VA dispersions, measured at an MAS rate of 10 kHz, between 293 and 373 K

The 80/20 and 60/40 dispersions at 373 K have comparable chemical shifts values, with the 80/20 dispersion displaying increased peak resolution (figure 5.22 A)), indicating the formation of a similar chemical environment *ca.* 373 K. Resonances for all IMC protons can be identified in the 80/20 dispersion, indicating the presence of a highly dynamic state. The broader peaks seen at 373 K in the 60/40 dispersion represent a less mobile state, with incomplete averaging of homonuclear dipolar interactions between protons.

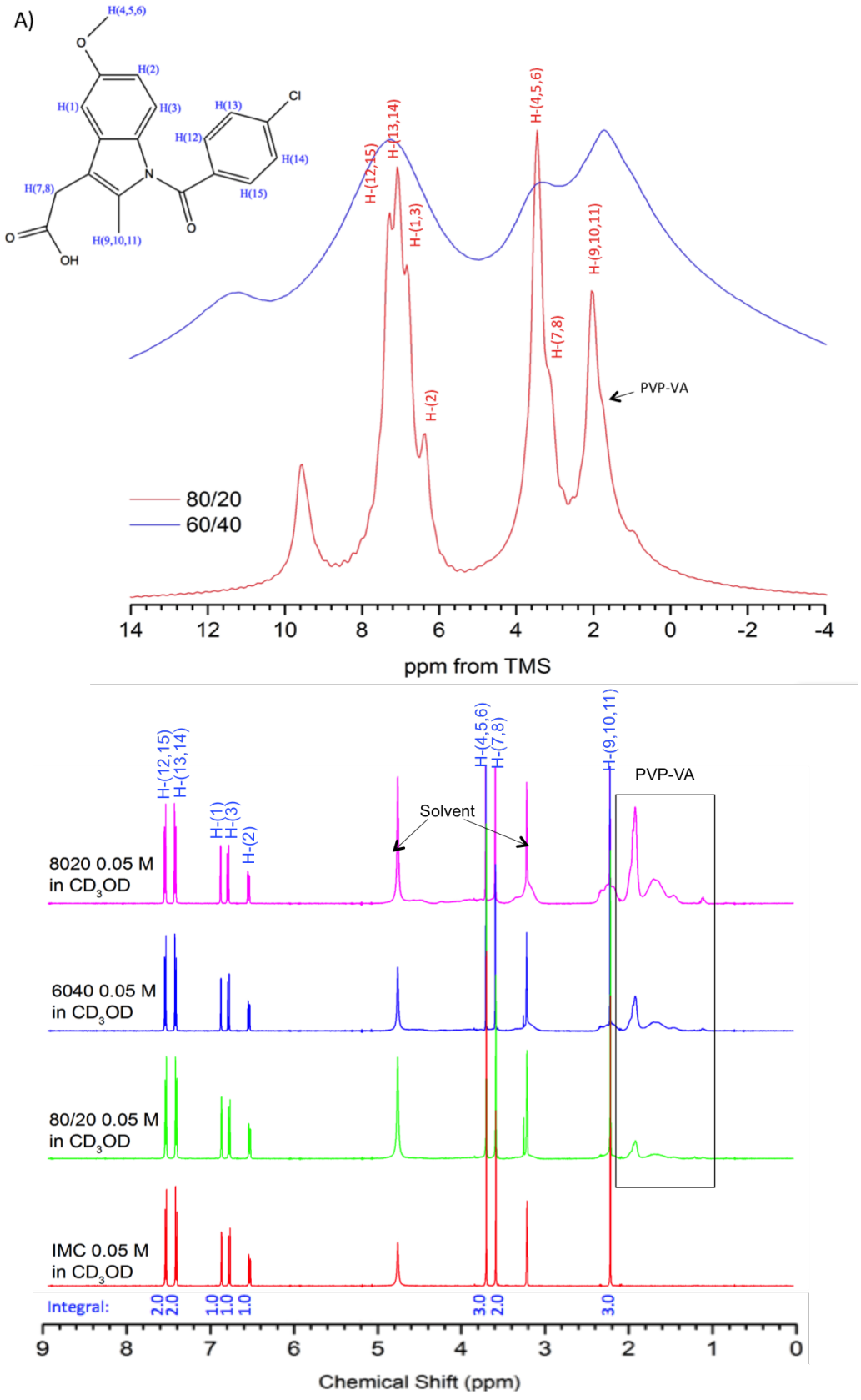


**Figure 5.22:** A) High temperature (373 K) $^{1}$H MAS NMR spectra for 80/20 and 60/40 IMC/PVP-VA dispersions (MAS = 10 kHz) with full chemical shift assignment; B) Solution-state $^{1}$H spectra (295 K) for different IMC/PVP-VA dispersions and IMC alone dissolved in $CD_3OD$ (0.05 M)

Assignment of the $^1$H peaks was based on the integral and J-coupling values of the solution-state $^1$H NMR spectrum (figure 5.22 B), alongside previous literature assignments of IMC [240, 241]. There is an upfield shift (between 0.1 and 0.4 ppm) for the majority of $^1$H signals of the 80/20 dispersion at 373 K from the solution to the solid state (table 5.5). In the solution state, the PVP-VA protons are only visible in a small broad peak at *ca.* 1.9 ppm, due to the high molecular weight, but this still allows identification of the polymer within the dispersion in the solid state at high temperature. The additional $^1$H peak at *ca.* 9.6 ppm (80/20) and 11.3 ppm (60/40) indicates the presence of hydrogen bonding within the system. The lack of $^1$H resonances in the hydrogen bonding region of the solution-state spectrum indicates the absence of bonding interactions in solution.

**Table 5.5:** Solution and solid-state experimental $^1$H chemical shifts for IMC and PVP-VA. Solution-state taken from IMC/PVP-VA 40/60 dissolved in $CD_3OD$ at 0.05 M (298 K) and solid-state from 80/20 IMC/PVP-VA dispersion at 373 K, MAS = 10 kHz

| $^1$H | $\delta$ (ppm) Solution at 298 K | | $\delta$ (ppm) MAS at 373 K | $\Delta\delta$ (ppm) |
|---|---|---|---|---|
| | multiplicity | J-coupling (Hz) | | |
| 12,15 | 7.6 (d) | 8.5 | 7.3 | 0.3 |
| 13,14 | 7.5 (d) | 8.3 | 7.1 | 0.4 |
| 1 | 6.9 (d) | 2.4 | 6.8 | 0.1 |
| 3 | 6.8 (d) | 9.1 | 6.8 | 0.0 |
| 2 | 6.6 (dd) | 2.6, 9.1 | 6.4 | 0.2 |
| 4,5,6 | 3.7 (s) | – | 3.4 | 0.3 |
| 7,8 | 3.6 (s) | – | 3.4 | 0.2 |
| 9,10,11 | 2.2 (s) | – | 2.0 | 0.2 |
| PVP-VA | 1.9 | – | 1.7 | 0.2 |

Apperley *et al.* [29] carried out static VT $^1$H experiments on amorphous indomethacin. They showed significant narrowing of the $^1$H peaks with increasing temperature, attributed to increased molecular mobility averaging out $^1$H-$^1$H dipolar interactions. At *ca.* 383 K, the indomethacin peaks broadened again, due to the reduced molecular mobility associated with a recrystallisation event [29]. Carpentier *et al.* [59] studied pure amorphous IMC *via* VT $^1$H MAS NMR. They also observed line narrowing due to fast molecular motion ($>$ 1000 kHz - chapter 4) averaging dipolar interactions at temperatures higher than $T_g$ - this effect was attributed to a cooperative motion identified with dielectric relaxation spectroscopy. At *ca.* 403 K, a broad component to the curve due to recrystallisation to the $\alpha$-polymorph was detected. Subsequently, this component disappeared at 420 K, close to the $T_m$ of $\alpha$-IMC [59]. In contrast to the measurements carried out for pure amorphous IMC, we did not observe a subsequent broadening in the $^1$H MAS spectrum for the 80/20 dispersion at 373 K, despite seeing strong evidence for the crystallisation of $\alpha$-IMC in the $^1$H-$^{13}$C CP/MAS spectra. Our observations therefore indicate that the $^1$H MAS NMR spectrum of the dispersions at high

temperature is dominated by an additional mobile phase, possibly containing amorphous IMC and polymer, which cannot be detected at high temperature using $^{1}$H-$^{13}$C CP/MAS NMR. We can postulate that the $\alpha$-IMC detected at 373 K within the 80/20 dispersion, is due to small crystallites formed within a mobile polymer environment, which remain in the dispersion upon cooling.

### 5.3.4 Effect of solvent on crystallisation of high drug loaded dispersions

The dispersions discussed so far were formulated *via* solvent evaporation with methanol. To investigate the effect of solvent on crystallisation behaviour from high drug loaded dispersions, 80/20 dispersions were additionally formulated using ethanol and acetonitrile.

In section 5.3.2, we demonstrated that amorphous IMC crystalllised to $\alpha$-IMC in the 80/20 dispersion formulated *via* solvent evaporation from methanol. Upon preparation from acetonitrile, the same behaviour was observed, with $\alpha$-IMC crystallising from amorphous IMC in the 80/20 dispersion *ca.* 333 K (figure 5.23 A)). The 80/20 dispersion prepared from ethanol displayed different crystallisation behaviour: *$\gamma$-IMC* formed from the amorphous component of the dispersion, again *ca.* 333 K (figure 5.23 B)). High polymer mobility was observed at temperatures $\geq$ 353 K in both dispersions, which is comparable to the original 80/20 dispersion (formulated from methanol). Upon cooling back to 293 K, crystalline material was detected in both dispersions (80/20 from acetonitrile and ethanol), indicating permanent crystallisation of $\alpha$ and $\gamma$-IMC respectively.

These results are in agreement with literature surrounding IMC crystal growth in solution, assuming behaviour from supersaturated solutions. Slavin *et al.* [33], Okumura *et al.* [35] and Lohani *et al.* [34,242] undertook a number of studies on the crystallisation of IMC from a wide range of solvents and found that the resulting polymorphic form of IMC was dependent on the nature of the solvent, degree of supersaturation and temperature. The expected crystallisation outcomes for IMC in methanol, ethanol and acetonitrile are summarised in figure 5.24). Additionally, in the solid state, amorphous indomethacin has been found to recrystallise to the $\gamma$ polymorph at temperatures below $T_g$ and the $\alpha$ polymorph above $T_g$ [68].

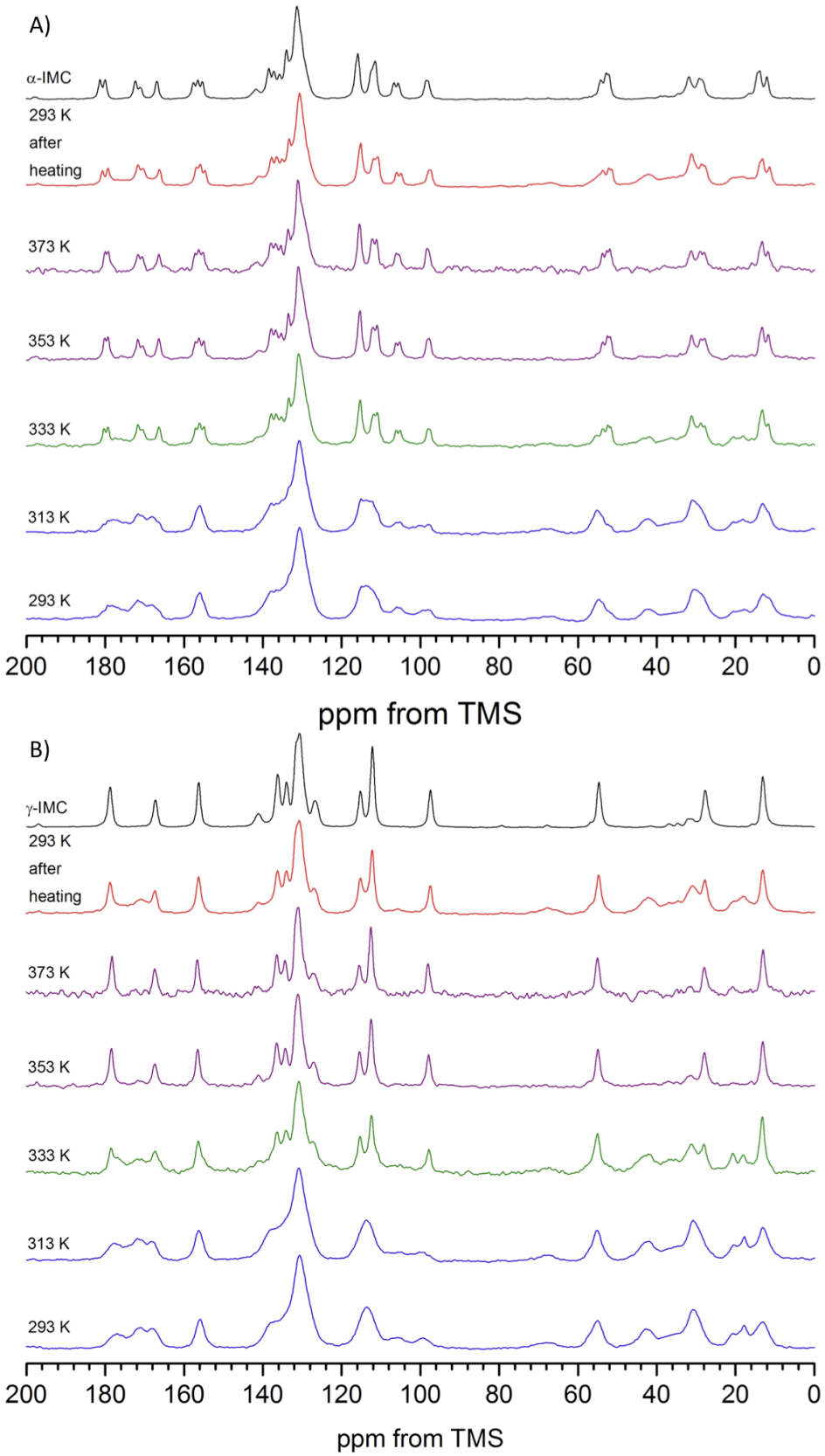


**Figure 5.23:** $^{1}$H-$^{13}$C CP/MAS NMR spectra of IMC/PVPVA 80/20 dispersion prepared *via* solvent evaporation of A) acetonitrile (comparison to $\alpha$-IMC) and B) ethanol (comparison to $\gamma$-IMC). Recorded at temperatures between 293 and 373K and upon subsequent cooling to 293K (MAS = 10 kHz)

$\alpha$-IMC was the expected polymorph to crystallise from methanol and acetonitrile at **high**

supersaturation, with crystallisation of $\gamma$-IMC occurring from ethanol solutions at **low** supersaturation. However, Okumura *et al.* found that at room temperature and pressure (RTP), in supersaturated solutions of IMC dissolved in ethanol, the $\alpha$ polymorph was formed, but at higher temperatures the $\gamma$ polymorph was obtained [35].Therefore, if we assume behaviour from supersaturated solutions, we see the expected outcome from methanol and acetonitrile of $\alpha$-IMC. It is possible that the temperature effect is dominant, therefore $\gamma$-IMC is formed, as described by Okumura [35] .

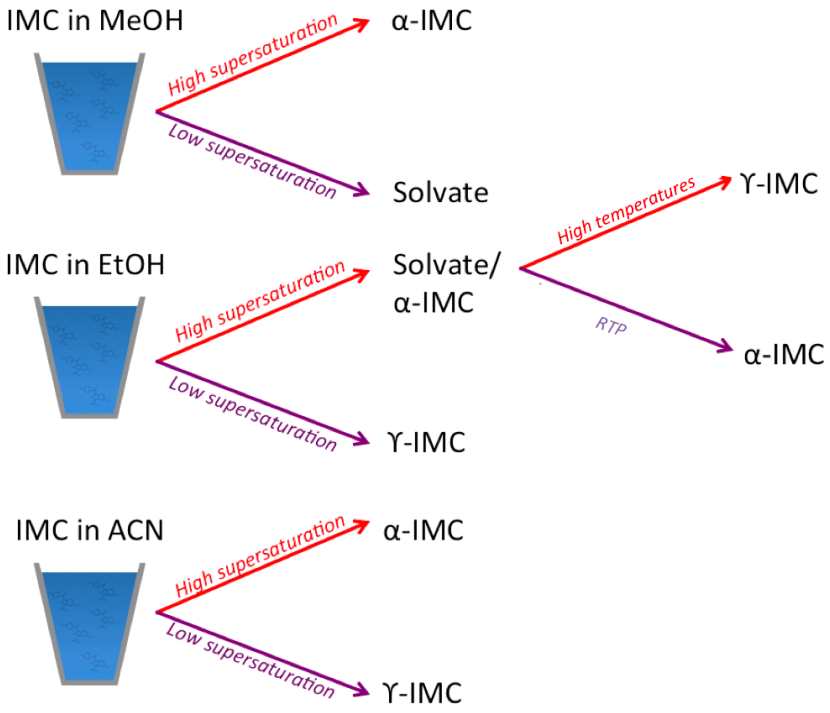


**Figure 5.24:** Summary of concentration dependent crystallisation outcome from methanol, ethanol and acetonitrile solutions [33–35]

## 5.4 Probing miscibility and dynamics of IMC/PVP-VA dispersions with spin-lattice relaxation

### 5.4.1 Detection of miscibility at ambient temperatures

The detection of miscibility of solid dispersions is a vital part of formulation development, as successful production of miscible drug/polymer amorphous dispersions is crucial for maintaining acceptable physical stability during manufacture and storage of pharmaceuticals [62, 108]. The miscibility of solid dispersions has traditionally been studied using DSC, where a single $T_g$ value is thought to indicate molecular level homogeneity [78, 106, 108, 163], with a detection limit of 20-30 nm [46, 164–166], although this can often be misleading [108]. The use of spin-lattice relaxation times (${T_{1\rho}}^H$ and ${T_1}^H$) in the solid-state has proven to be extremely useful in providing additional information about the miscibility and phase separation of solid dispersions, with differences in ${T_{1\rho}}^H$

times allowing estimation of much smaller domains than with DSC; with a demonstrated detection down to *ca.* 2 nm in size [46, 62, 88]

Differences in the relaxation times (($\Delta T_{1\rho}{}^{H}$ and $\Delta T_1{}^{H}$)) of drug and polymer components have been used previously to provide information on miscibility and domain sizes in nifedipine/PVP dispersions [46] (see chapter 4 for detailed explanation). Domain sizes can be estimated as follows [46, 152]:

- $\Delta T_1{}^{H} > 0$ indicates domains of $> 55$ nm
- $\Delta T_1{}^{H} = 0$, but $\Delta T_{1\rho}{}^{H} > 0$ indicates miscibility on the 6 - 24 nm length scale
- $\Delta T_{1\rho}{}^{H} = 0$ indicates miscibility on the 2 - 6 nm length scale

This analysis is based upon the process of spin diffusion within a solid-state sample. Within a homogenous system, common relaxation times will be observed across all sites, due to efficient magnetization transfer *via.* $^{1}$H-$^{1}$H spin diffusion [36, 46].

Small $\Delta T_{1\rho}{}^{H}$ values for the 20/80, 40/40 and 60/40 dispersions (figure 5.25) indicate miscibility on the 2 - 6 nm length scale at 293 K. The 80/20 dispersion showed a larger $\Delta T_{1\rho}{}^{H}$, but small $\Delta T_1{}^{H}$, which indicates immiscibility on the 2 - 6 nm scale, but miscibility on the 6 - 24 nm length scale. For the investigation of the miscibility of nifedipine-PVP solid dispersions, Yuan *et al.* found that dispersions with drug compositions of 25, 40 and 50 wt. % were miscible on a 2 – 6 nm scale, but that dispersions with higher drug content (95 and 90 wt. %) were immiscible on this length scale and borderline miscible on 24 - 55 nm scale [46].

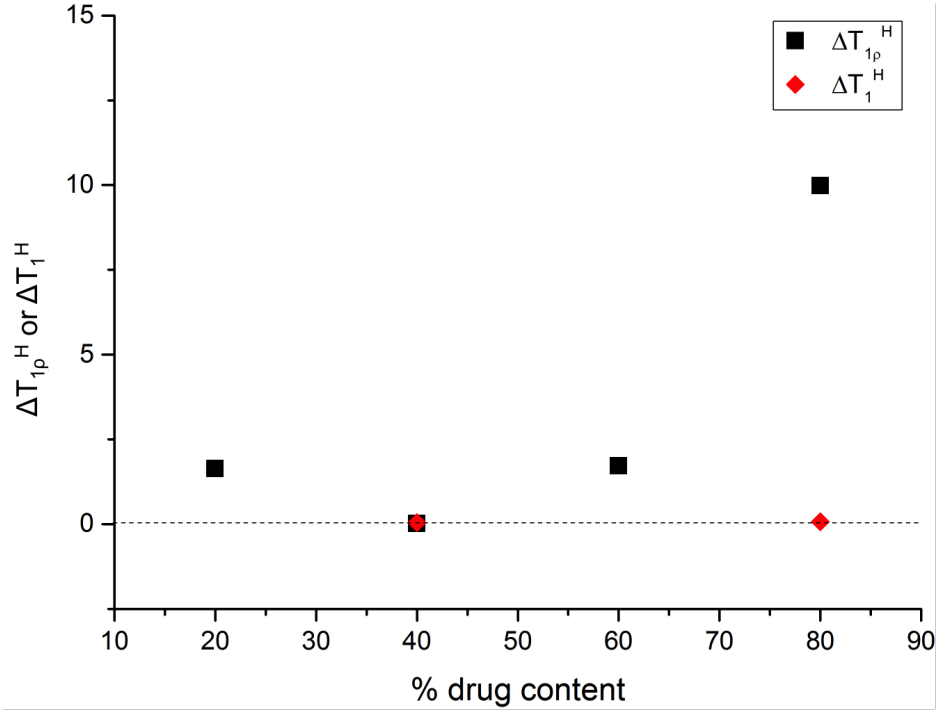


**Figure 5.25:** $\Delta T_{1\rho}{}^{H}$ between IMC and PVP-VA of 20/80, 40/60 60/40 and 80/20 IMC/PVP-VA dispersions. $T_{1\rho}{}^{H}$ values were averaged out for all the non-overlapping $^{13}C$ peaks at 168, 156, 131 and 115 ppm of the drug; and at 171, 68, 43, 37 and 21 ppm for the polymer. These chemical shifts correspond to drug and polymer in the spectra of the amorphous dispersions; and $\Delta T_1{}^{H}$ of 40/60 and 80/20 dispersions at 293 K, displayed as a function of wt. % drug content

### 5.4.2 Variable temperature relaxation studies

Investigating the temperature dependence of relaxation times provides invaluable information about the mobility and dynamics of a system, as outlined in chapter 4. The temperature dependences of $T_{1\rho}{}^{H}$ times for crystalline $\gamma$-IMC and $\alpha$-IMC, amorphous IMC, PVP-VA and the IMC/PVP-VA dispersions were determined. Activation energies were calculated using equation 4.1 (chapter 4).

The $T_{1\rho}{}^{H}$ measurements of $\gamma$-IMC displayed a clear minimum at 293 K with an activation energy of 42.2 kJ mol$^{-1}$ (between 293 and 333 K) (figure 5.26). This shows typical Arrhenius behaviour (analogous with figure 4.8, chapter 4). This was in agreement with the literature where $\gamma$-IMC was found to have a $T_{1\rho}{}^{H}$ minimum at 291 K, with an activation energy for the same regime of 37.7 kJ mol$^{-1}$ [29], or 42 kJ mol$^{-1}$ [59]. Carpentier *et al.* [59] attributed the $T_{1\rho}{}^{H}$ minimum to a relaxation process due to the rotation of the chlorobenzyl group, as the value of $E_A$ was of the same order of magnitude for the similar motions responsible for other structural transformations in aromatic ring systems of $\beta$-estradiol [243].

The $T_{1\rho}{}^{H}$ times for the metastable $\alpha$-polymorph were too long to be measured accurately ($>$ 70 ms) across the full temperature range. The difference in $T_{1\rho}{}^{H}$ times of $\alpha$ and $\gamma$-IMC across a wide temperature range indicates a significant difference in mobility between the two structures.

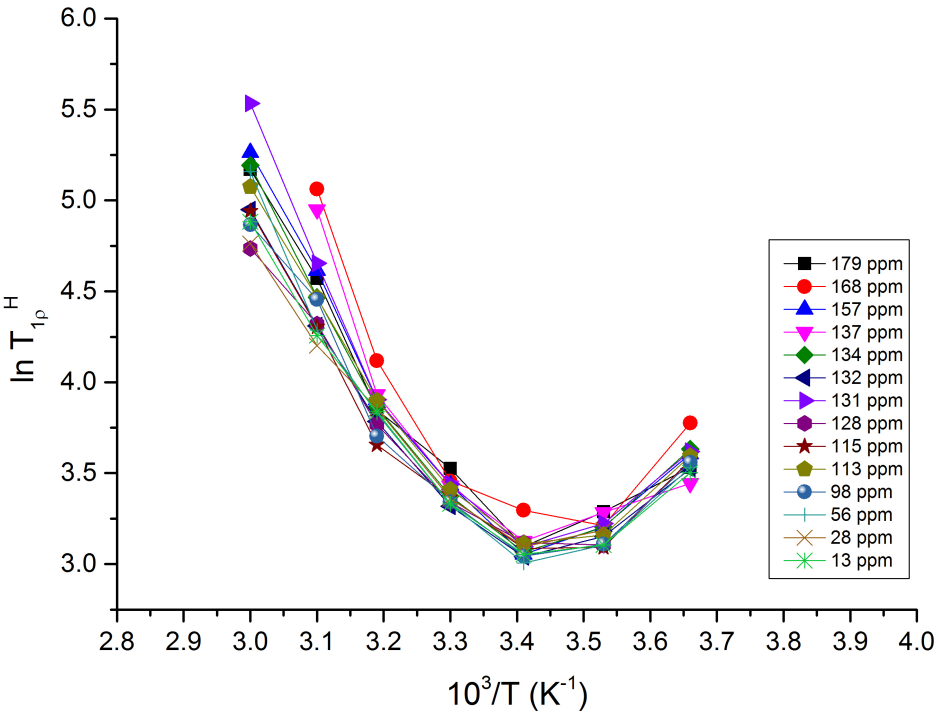


**Figure 5.26:** Temperature dependence of $T_{1\rho}{}^{H}$ time for $\gamma$-IMC (for each $^{13}C$ site). Activation energy calculated from average values at each temperature point, between 293 and 333 K

Carpentier *et al.* [59] also reported a difference in $T_{1\rho}$ relaxation of $\alpha$ and $\gamma$ polymorphs, determining that the lack of a minimum in the $\alpha$-IMC relaxation curve was due to restricted rotation of the chlorobenzyl ring. This was calculated as being a forbidden motion, which was attributed to the additional hydrogen bond (between the carboxylic acid hydroxyl and carbonyl of an amide group) in the more restricted crystal structure (figure 5.27). VT $T_1$ studies additionally highlighted steric hindrance within the $\alpha$-IMC structure .

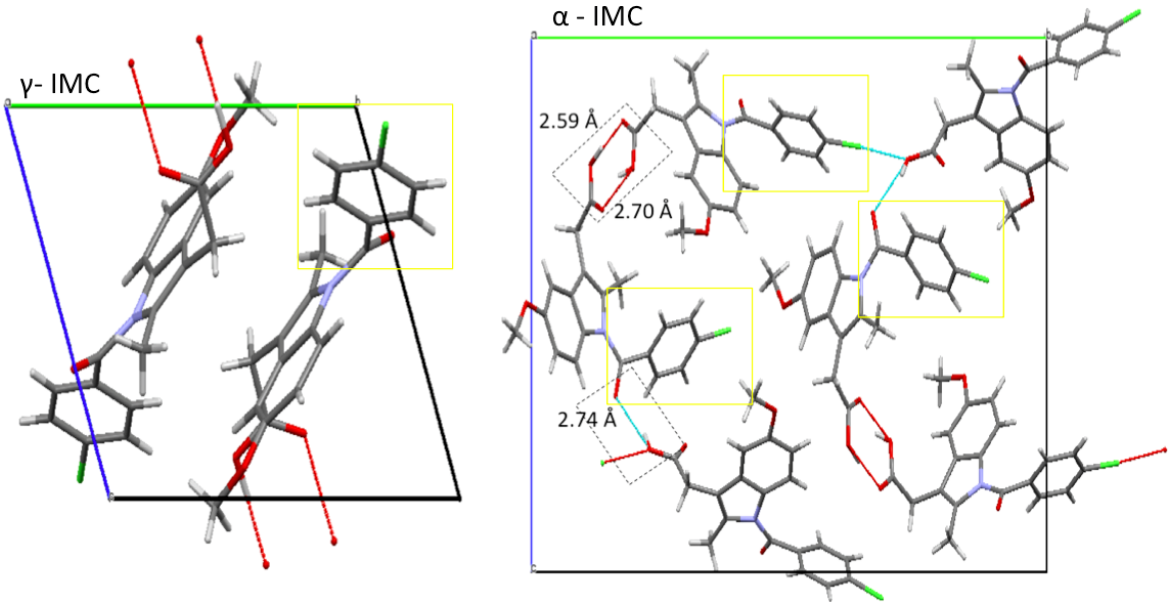


**Figure 5.27:** Crystal structures of $\gamma$ and $\alpha$-IMC, highlighting the differences in hydrogen bonding resulting in the restriction of the chlorbenzoyl ring in the $\alpha$-IMC crystal structure (yellow box)

The $T_{1\rho}{}^{H}$ times of the dispersions, amorphous IMC and PVP-VA did not display the expected minima across the studied temperature range. For our systems of study, the following was generally observed with increasing temperature: Firstly, a slow increase of $T_{1\rho}{}^{H}$ up to a maximum point, $T_{MAX}$, followed by a change in relaxation behaviour, with a dramatic decrease in $T_{1\rho}{}^{H}$. $T_{MAX}$ was below $T_g$ for all systems.

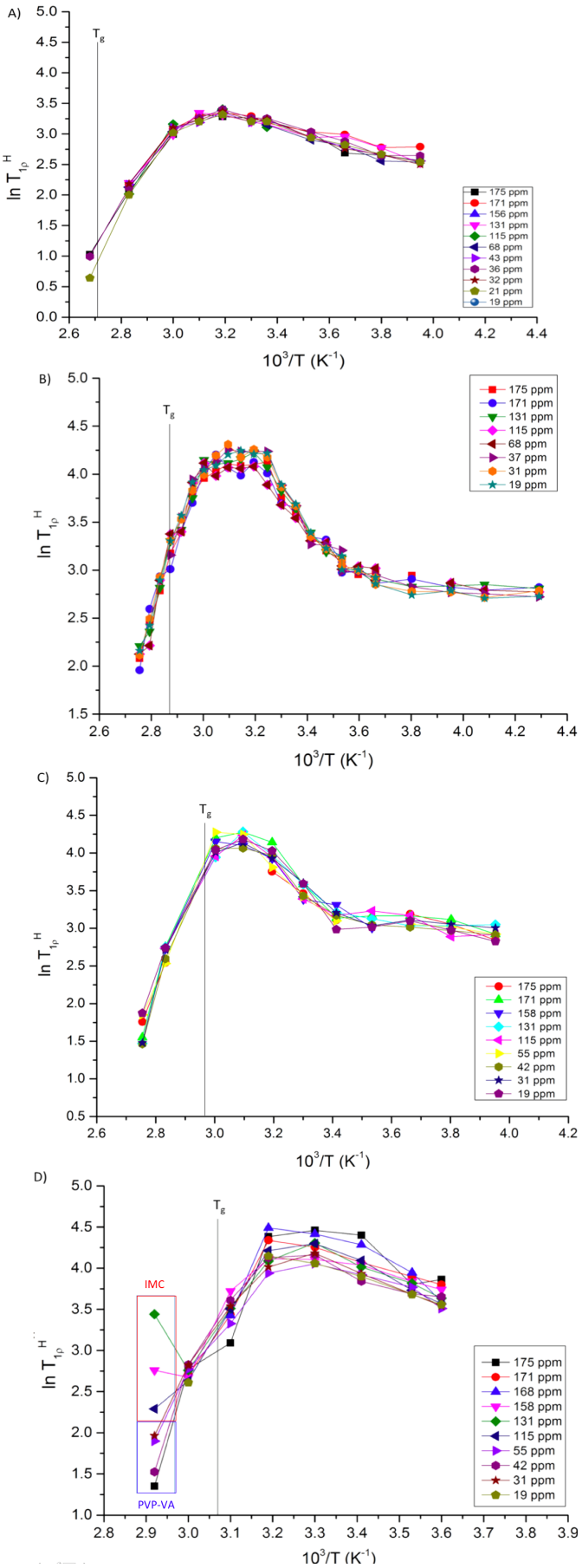


**Figure 5.28:** Temperature dependence of $T_{1\rho}{}^{H}$ time for different $^{13}C$ sites for A) IMC PVPVA 20/80 dispersion B) IMC PVPVA 40/60 dispersion, C) IMC PVPVA 60/40 dispersion, D) IMC PVPVA 80/20

The 40/60 IMC/PVP-VA dispersion was analysed across the widest temperature range. From this detailed temperature dependence curve (figure 5.28 B)), a number of observations can be highlighted. Firstly, across all temperature points, $T_{1\rho}{}^{H}$ times for both drug and polymer were similar, and displayed the same temperature dependence. This indicates we have a homogenous dispersion, due to efficient spin diffusion (see chapter 4 for detailed explanation), which supports the findings of the VT $^{1}$H-$^{13}$C CP/MAS NMR data (section 5.3.2). There are three main components to the temperature dependence of the $T_{1\rho}{}^{H}$ times of the 40/60 dispersion. Initially, at the lowest temperatures (253 – 283 K), there was little change in $T_{1\rho}{}^{H}$, which could indicate the presence of a minimum just outside the temperature range studied. This was followed by an increase in $T_{1\rho}{}^{H}$ times with increasing temperature (283 – 313 K) up to $T_{MAX}$, with an associated $E_A$ of 24.0 kJ mol$^{-1}$. This indicates a motional regime on the fast side of a $T_{1\rho}{}^{H}$ minimum. Finally at temperatures above the $T_{MAX}$, a marked change of gradient occurred, seen by a rapid decrease in $T_{1\rho}{}^{H}$ times with increasing temperature with an $E_A$ of 55.7 kJ mol$^{-1}$.

The $T_{1\rho}{}^{H}$ times of the 60/40 IMC/PVP-VA dispersion (figure 5.28 C) displayed a very similar temperature dependence curve. There was little change in $T_{1\rho}{}^{H}$ times at the lowest temperatures, followed by an increase in $T_{1\rho}{}^{H}$ times up to $T_{MAX}$ ($E_A$ = 26.6 kJ mol$^{-1}$), then a more rapid decrease in $T_{1\rho}{}^{H}$ times with increasing temperature $E_A$ = 65.9 kJ mol$^{-1}$). The $T_{1\rho}{}^{H}$ vs. T curve of the 20/80 dispersion was again similar (figure 5.28 A), but showed only two components: an initial gradual increase in $T_{1\rho}{}^{H}$ up to $T_{MAX}$ ($E_A$ = 8.7 kJ mol$^{-1}$), followed by a more dramatic decrease in $T_{1\rho}{}^{H}$ times with increasing temperature ($E_A$ = 35.3 kJ mol$^{-1}$). Both the dispersions were homogenous, confirmed by similar $T_{1\rho}{}^{H}$ times across all carbon sites. At the higher temperatures, the curve for the 20/80 dispersion shows only the $T_{1\rho}{}^{H}$ times of the polymer, due to reduced intensity of drug peaks on the CP/MAS NMR spectra.

The temperature dependence curve of the highest drug loading dispersion (80/20), provided additional information regarding crystallisation (figure 5.28 D). A temperature dependence similar to the lower loaded dispersions was observed until *ca.* 343 K, but with a larger spread of $T_{1\rho}{}^{H}$ times across all $^{13}$C sites. At 343 K, a clear separation of drug and polymer $T_{1\rho}{}^{H}$ times is detected - IMC peaks displaying a marked increase in $T_{1\rho}{}^{H}$ times, whilst the $T_{1\rho}{}^{H}$ times of the polymer peaks continued to decrease. The separation of $T_{1\rho}{}^{H}$ times occurred at the point of crystallisation of the amorphous form to $\alpha$-IMC, which was previously shown through VT $^{1}$H-$^{13}$C CP/MAS NMR (figure 5.18). At temperatures above 343 K, no $T_{1\rho}{}^{H}$ times could be calculated, as the polymer peaks lost intensity in the CP/MAS spectra due to increased mobility, whilst the $T_{1\rho}{}^{H}$ times of the drug peaks became too long to be measured accurately. At 343 K, the $T_{1\rho}{}^{H}$ times for the drug peaks are much longer than those for the polymer, but still faster than for pure $\alpha$-IMC ($>$ 70 ms), indicating the formation of an intermediate IMC phase, which resembles the $\alpha$-polymorph, but is still influenced by the presence of the polymer within the dispersion.

This can be explained (simply) as follows [36]: Pure $\alpha$-IMC has very long $T_{1\rho}{}^{H}$ times, due to a lack of mobility to transfer magnetization (as energy) to the surrounding environment. Within the 80/20 dispersion at high temperatures, the highly mobile regions of PVP-VA relax quicker than the IMC, seen in the measured short $T_{1\rho}{}^{H}$ times, and also through loss of peak intensity in the VT $^{1}$H-$^{13}$C CP/MAS NMR experiments (section 5.3.2). If a number of small crystalline domains of $\alpha$-IMC were formed within the 'sea' of PVP-VA, magnetization transfer from the slower ($\alpha$-IMC) to the quicker (PVP-VA) relaxing domains would occur through $^{1}$H-$^{1}$H dipolar coupling (spin diffusion). The regions of higher mobility can act as 'relaxation sinks' within a sample (figure 5.29), leading to shorter observed $T_{1\rho}{}^{H}$ times of $\alpha$-IMC within the 80/20 dispersion, as compared to the pure $\alpha$-IMC. Therefore, we hypothesise that the 80/20 dispersion at increased temperatures contains small crystalline 'domains' present within a 'liquid-like' polymer carrier. The approximate maximum domain size, estimated using equation 4.4 and the longest $T_{1\rho}{}^{H}$ time measured at this temperature for the drug in the dispersions ($\delta$ = 131 ppm (31.2 ms) is *ca.* 13 nm. This presence of small crystalline domains in polymeric carrier has previously been reported for paracetamol/Eudragit dispersions, identified through a difference in $T_{1}{}^{H}$ times between crystalline API in the dispersion, and without the presence of polymer [88].

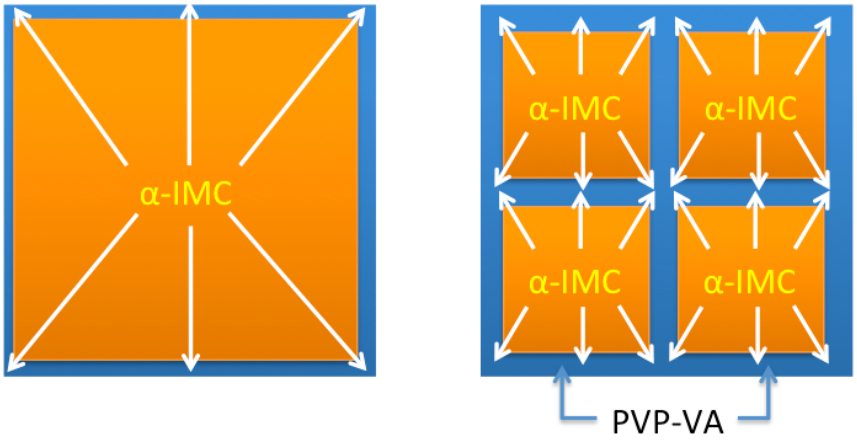


**Figure 5.29:** Representation of the relaxation time differences between pure $\alpha$-IMC (A) and crystallisation of $\alpha$-IMC within the 80/20 dispersion at high temperature (B). The orange squares represent a slow relaxing domain; blue squares represents a fast relaxing domain; white arrows represent transfer of magnetization *via* spin diffusion from orange to blue. Adapted from [36]

Previous studies on the high temperature crystallisation of pure amorphous IMC only detected full crystallisation from amorphous to $\alpha$-IMC at *ca.* 403 K. Andronis *et al.* [32] demonstrated that recrystallisation of amorphous IMC requires a lengthy induction period . Apperley *et al.* [29] also showed that during heating, increased mobility of amorphous IMC occurred around 363 K, and some, but not full, recrystallization occurred at temperatures up to 403 K. The presence of polymer in our study further complicates the recrystallisation process.

We initially hypothesised that the non-typical temperature dependence of $T_{1\rho}{}^{H}$ times of the dispersions was determined mainly by the mobility of the polymer, as $T_{1\rho}{}^{H}$ is known to be sensitive to slower motions associated with backbone polymer motions [161]. However, it can be seen that the $T_{1\rho}{}^{H}$ times of both amorphous IMC and PVP-VA display very similar temperature dependence (figure 5.30).

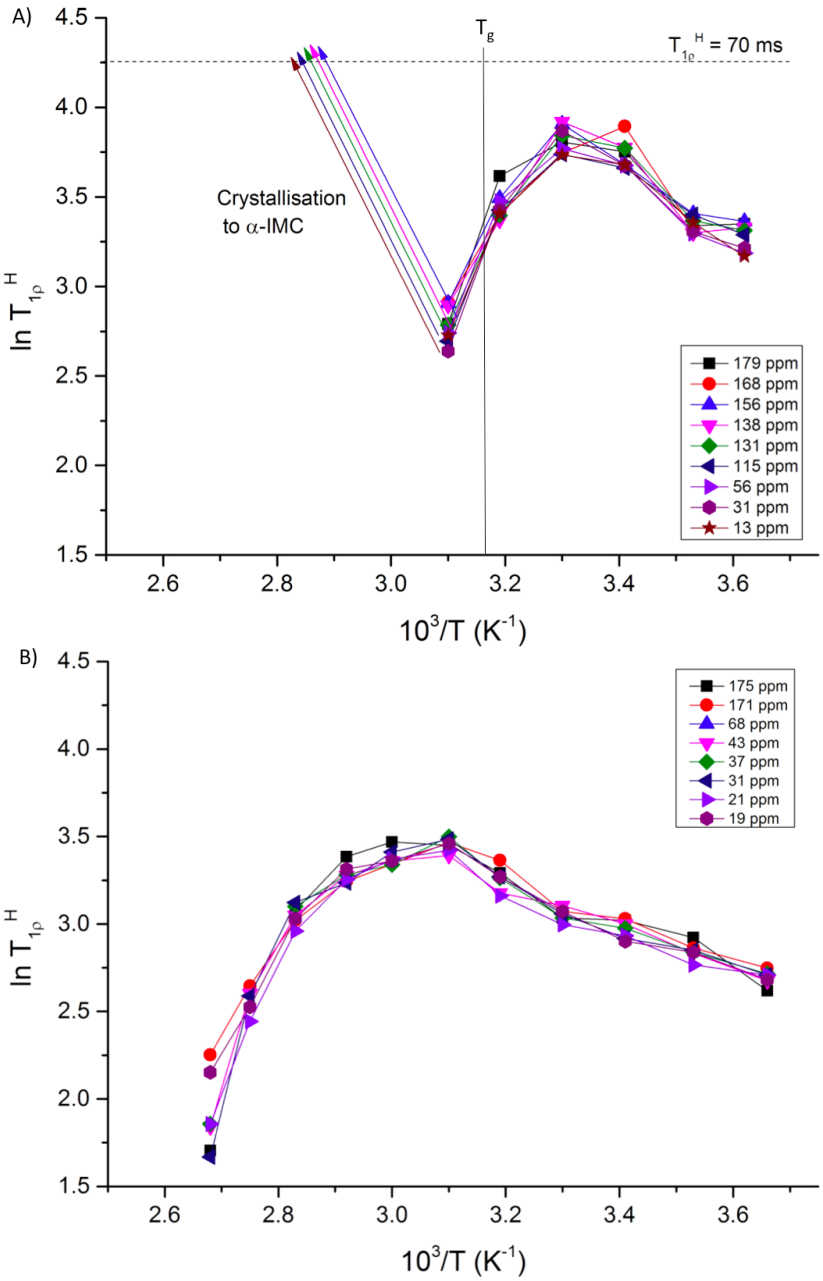


**Figure 5.30:** Temperature dependence of $T_{1\rho}{}^{H}$ times for A) Amorphous IMC and B) PVP-VA

For amorphous IMC, $T_{1\rho}{}^{H}$ times were measurable up to 323 K, above which crystallisation to $\alpha$-IMC occurred (confirmed by VT $^{1}$H-$^{13}$C CP/MAS NMR), hence corresponding relaxation times were too long to be measured accurately. Apperley *et al.* [29] found a similar temperature dependence of $T_{1\rho}{}^{H}$ times of pure amorphous IMC until 333 K, with $T_{MAX}$ occurring around the $T_g$ value, compared to our measurements, where the change in

mobility occurred slightly below $T_g$ at $T_g$ – 10 K.

Similar examples of non-typical temperature dependence of $T_{1\rho}{}^H$ times were observed in a variety of systems, although the literature has not gone far enough to explain this behaviour. From extensive literature searches, there appears to be a lack of understanding regarding the deviation from typical dependence. We therefore constructed a scheme (figure 5.31) which helped form a clearer understanding of the different components of the non-typical temperature dependence curve. In summary, the main explanation for non-typical temperature dependence outlines that $T_{MAX}$ is the result of two different, overlapping motional regimes within the system, each with an associated minimum, and therefore correlation time outside of the measured temperature range [244–246].

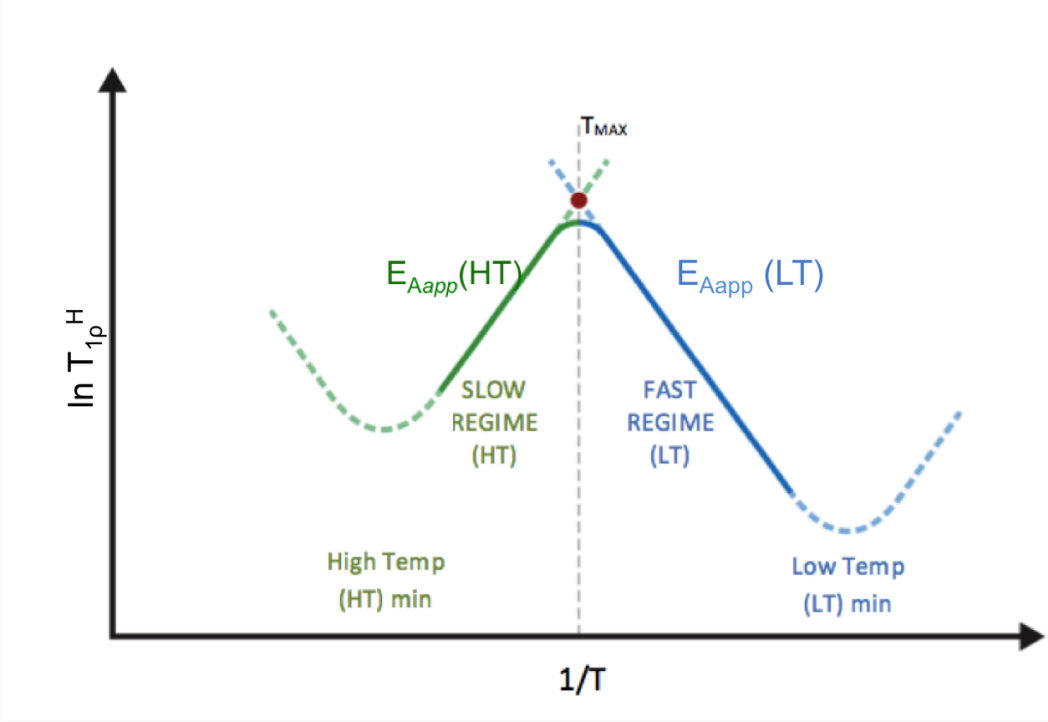


**Figure 5.31:** Explanation for the occurrence of a maximum point on the relaxation temperature dependence curve

The maximum point on the curve ($T_{MAX}$) can be seen as a crossover point between two different, but overlapping motional regimes, each following the expected classical temperature dependence of spin-lattice relaxation times. Each minimum is associated with a *different* correlation time, which describes the nature of the motional regime being observed. $T_{MAX}$ is the point on the curve at which the gradient changes direction, indicating a switch in the dependence of $T_{1\rho}{}^H$ times. It seems feasible to calculate apparent activation energies ($E_{A\,app}$) either side of $T_{MAX}$, representing the kinetic response of the dispersions under the influence of each motional regime: named $E_{A\,app}$(Low Temperature) (to the right of $T_{MAX}$) and $E_{A\,app}$(High Temperature) (to the left of $T_{MAX}$). The $E_{A\,app}$ represent the kinetic response of the dispersions, and therefore provide a comparative measure of stability

between systems. The temperature at which $T_{MAX}$ occurs can be related to $T_g$, giving an indication of whether increased mobility occurs above or below $T_g$. Additionally, the motional correlation times can be calculated across the temperature range of study, using equation 4.2 (chapter 4). Analysing these parameters can help to determine the motions responsible for changes in mobility; and link mobility to physical stability of the dispersions. The main observations of non-typical dependence from figure 5.31 are summarised as follows:

- To the right of $T_{MAX}$ (blue), motions are in a fast regime (increasing ${T_1}^H$ with increasing temperature) associated with the low temperature (LT) minimum. We have named the associated activation energy of this curve $E_{A\,app}$(LT).
- To the left of $T_{MAX}$ (green), motions are within a slow regime (decreasing ${T_{1\rho}}^H$ with increasing temperature) associated with the higher temperature (HT) minimum. The calculated activation energy for this curve is $E_{A\,app}$(HT).
- As mobility always increases with increasing temperature, the mobility of the 'slow HT' regime will still be faster than the 'fast LT' regime within the intermediate kHz timescale of study.

Non-typical temperature dependence of relaxation times of a variety of amorphous pharmaceuticals with and without the stabilization of polymers has been described in the literature [28, 46, 47, 161, 202, 213, 244, 245]. Each study observed the non-typical behaviour we see here with a slow increase in relaxation times with increasing temperature; followed by a rapid decrease in relaxation times, indicating the presence of motions on the slow side of the relaxation minimum above $T_{MAX}$. Studies included investigation of nifedipine/PVP dispersions [46, 160], AZD/PLGA formulations [202], amorphous simvastatin [28], IMC [29], nifedipine [29, 161] and phenobarbital [161] and lyophilized PVP and methylcellulose [245]. The majority of studies reported only the mobility above $T_{MAX}$, where a rapid decrease in relaxation time occurred, as little change was seen below this point.

The temperature of onset of the change in mobility (our $T_{MAX}$) was described in relation to $T_g$. Change in behaviour at temperature substantially below $T_g$ were linked to reduced physical stability [46, 161]. Increased mobility below $T_g$ was linked to instability of systems at these temperatures, indicating that changes in mobility below $T_g$ highlighted by solid-state NMR can play an important role in the prediction of stability of amorphous systems. Yoshioka *et al.* additionally linked the presence of multiple motional regimes to maxima on relaxation temperature dependence curves [244–246].

Aso, Yoshioka and co-workers have published a number of papers investigating molecular mobility using variable temperature $T_{1\rho}$ [47, 161, 244, 245]. They initially studied the temperature dependence of amorphous pharmaceuticals (nifedipine and phenobarbital) and found strong temperature dependence, with a marked decrease in relaxation time with increasing temperature, but no relaxation minimum, which was attributed to increasing

molecular mobility of whole molecule motions on the kHz timescale. Yoshioka *et al.* extended their molecular mobility investigations into protein formulations [244] and polymers [245]. For one formulation (dextran in BGG stored at 60 % RH), they were able to show both a low temperature minimum followed by a higher temperature maximum on the $T_{1\rho}{}^{H}$ temperature dependence curve, and provided evidence for the presence of at least two proton motional regimes (one slow and one faster) with different correlation times [244]. Polymers (PVP and methylcellulose) were also found to follow the same temperature dependence. MC exhibited both a minimum and maximum within the temperature range studied, again attributed to multiple motional regimes. If only a maximum was seen followed by a rapid decrease in $T_{1\rho}{}^{C}$ (PVP), it was thought to be associated with a minimum outside the studied temperature range [245]. More recently, as described below, investigations of drug/polymer solid dispersions have described non-typical temperature dependence. Our group previously demonstrated this dependence with AZD/PLGA formulations [202], and Yuan *et al.* [46] with nifedipine/PVP dispersions. In the temperature ranges studied, the room temperature miscible nifedipine/PVP dispersions (75/25, 60/40 and 50/50) remained homogenous, with relaxation times of drug and polymer varying with temperature in the same (non-typical) manner [46]. For our 80/20 dispersion, which appeared miscible at lower temperatures, we highlighted a phase separation at temperatures above 353K, which was clearly seen through the separation of relaxation times, as the crystalline $\alpha$-IMC has longer relaxation times than the polymer. Nunes *et al.* [28] investigated the effect of temperature on the $T_{1\rho}{}^{C}$ of amorphous simvastatin (without polymer) between 293 and 333 K. They found that the majority of the carbons studied displayed different relaxation behaviour above and below $T_g$; at $T < T_g$, the $^{13}C$ showed similar relaxation times, with a maximum $T_{1\rho}{}^{C}$ below $T_g$; at $T > T_g$, there was a decrease in $T_{1\rho}{}^{C}$ which indicated a liberated molecular motion and possible cooperative motion, possibly due to torsional ring oscillations. They concluded that the variation of $T_{1\rho}{}^{C}$ with temperature indicated that the motions are on the slow-frequency side of the $T_{1\rho}{}^{C}$ minimum, which indicated amorphous simvastatin was in a rigid state [28].

#### 5.4.2.1 Further analysis of $T_{MAX}$, activation energies and correlation times for IMC/PVP-VA dispersions

The calculated activation energies ($E_{A\,app}$ (LT)/(HT)) representing the temperature dependence curves either side of $T_{MAX}$ are shown in table 5.6. $E_{A\,app}$(LT) is particularly useful, as it provides a measure of the mobility behaviour at temperatures below $T_g$. The 40/60 and 60/40 IMC/PVP-VA dispersions had high $E_{A\,app}$s(LT) of 24.0 and 26.6 kJ mol$^{-1}$ respectively. This indicates the systems have a more restricted mobility, and likely suggests that they are the most stable, homogenous systems studied. This is in agreement with the room temperature $^{1}H$-$^{13}C$ WISE NMR; the VT $^{1}H$-$^{13}C$ CP/MAS NMR, which showed no increase in mobility for drug or polymer for the 40/60 dispersion; and the VT relaxation

data which highlighted high homogeneity within the 40/60 dispersion. This activation energy relates to motions occurring well below the $T_g$ of each system and it would be expected therefore, that the $E_{A\,app}$ of a more stable system would be higher, particularly below the $T_g$.

From table 5.6 it can be seen that the higher drug loading dispersions (60/40 and 40/60) again had high $E_{A\,app}$ (HT) values. The amorphous IMC and 20/80 dispersion have lower $E_{A\,app}$(HT), which would indicate that the motion associated with this $E_{A\,app}$ is easier to excite, leading to higher mobility. The $E_{A\,app}$(HT) describes the behaviour of the dispersions at temperatures around and above $T_g$.

**Table 5.6:** Activation energies for amorphous IMC, PVP-VA and IMC/PVP-VA dispersions of different drug loadings. $E_{A\,app}$(HT) could not be calculated for the 80/20 dispersion due to crystallisation to $\alpha$-IMC

| **Formulation** | **$E_{A\,app}$: Fast regime (LT) (kJ mol$^{-1}$)** | **$E_{A\,app}$: Slow regime (HT) (kJ mol$^{-1}$)** |
|---|---|---|
| Amorphous IMC | 16.4 | 42.6 |
| 20/80 | 8.7 | 35.3 |
| 40/60 | 24.0 | 55.7 |
| 60/40 | 26.6 | 65.9 |
| 80/20 | 15.5 | – |
| PVP-VA | 11.0 | 39.7 |

In previous studies, the temperature at which $T_{MAX}$ occurs has been correlated with the $T_g$ for amorphous nifedipine, phenobarbital and IMC, to attempt to relate the change in temperature dependence with stability [29, 46, 161]. The relationship between $T_{MAX}$ and $T_g$ of all **our** IMC/PVP-VA systems can be seen in figure 5.32. We found that all $T_{MAX}$ values occurred at temperatures below $T_g$.Additionally, with increasing polymer content, the difference between $T_g$ and $T_{MAX}$ ($T_g$ - $T_{MAX}$) became larger, with the biggest difference observed for the 20/80 and 40/60 IMC/PVP-VA dispersions.

Aso *et al.* [47,161] found that $T_{MAX}$ occurred at 20 K below $T_g$ for amorphous nifedipine and at a similar temperature to $T_g$ for phenobarbital, indicating amorphous nifedipine had a lower physical stability than phenobarbital, which was in agreement with theoretical calculations of mean relaxation rate (*via* Adam-Gibbs-Vogel (AGV) equation) and crystallisation rate. Yuan *et al.* [46] found a dramatic increase in the molecular mobility of nifedipine/PVP dispersions above temperatures around 20 K below $T_g$, which was thought to be the underlying reason for the increased structural relaxation and crystallization of amorphous systems below $T_g$.. Addtionally, NIF has always been found to be less stable than IMC, identified because increased mobility occurred *ca.* 20 K below $T_g$ for NIF [46], compared to temperatures similar to $T_g$ for IMC [29, 46]. However, our findings do not agree with this analysis method. Here, we have shown that increases in mobility of both amorphous IMC, and dispersions of varying drug/polymer ratio occurred at temperatures below $T_g$ across **all** systems studied. We have

also demonstrated that with increasing polymer content, the change in relaxation times occurred at temperatures further below $T_g$, in the dispersions least likely to have reduced physical stability. The relationship between $T_g$ and $T_{MAX}$ will be further investigated through VT relaxation studies of FFA/PVP-VA (chapter 6) and TLB/PVP-VA (chapter 7) systems.

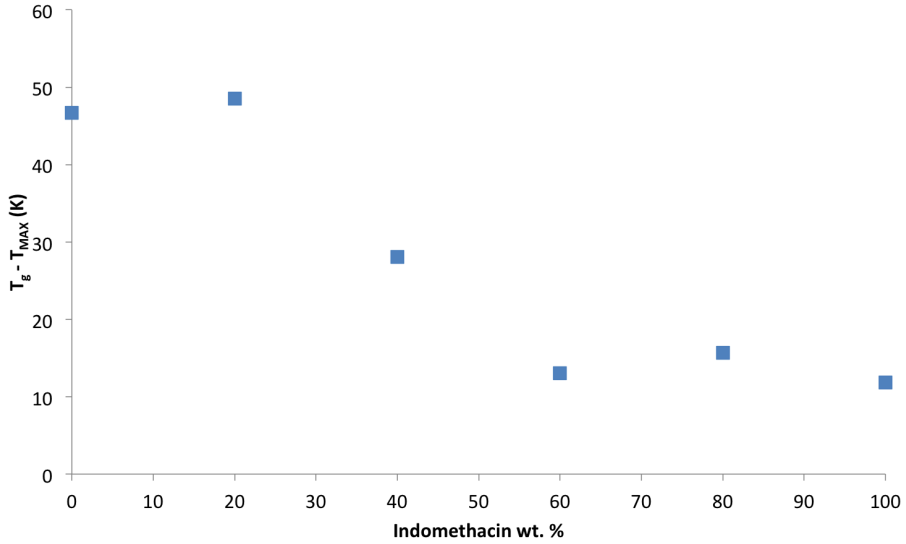


**Figure 5.32:** $T_{MAX}$ calculated by extrapolating the curve either side of the maximum to calculate the crossover temperature

Correlation times ($\tau_c$) were also calculated for the average $T_{1\rho}{}^H$ times at each temperature point, using the relationship with $T_{1\rho}{}^H$ (shown in equation 4.2, chapter 4) for all dispersions, amorphous IMC and PVP-VA. As $T_{1\rho}{}^H$ and $\tau_c$ have a linear relationship, the dependence of $\tau_c$ on temperature is the same as the $T_{1\rho}{}^H$ for each material of study, and therefore doesn't provide much additional information.

### 5.4.3 Stability studies

Throughout the 14 week stability study, all dispersions were monitored for changes in the local ordering using PXRD, mDSC and $^{13}C$ CP/MAS solid-state NMR. No crystallisation was detected for dispersions with IMC content of lower than 70 wt. % across all temperature conditions. For the 80/20 dispersion, crystallisation to $\alpha$-IMC was only detected after 4 days of storage at high temperature (363 K). Crystallisation was identified by the characteristic splitting in the $^1H$-$^{13}C$ CP/MAS NMR spectrum and PXRD pattern (figure 5.33).

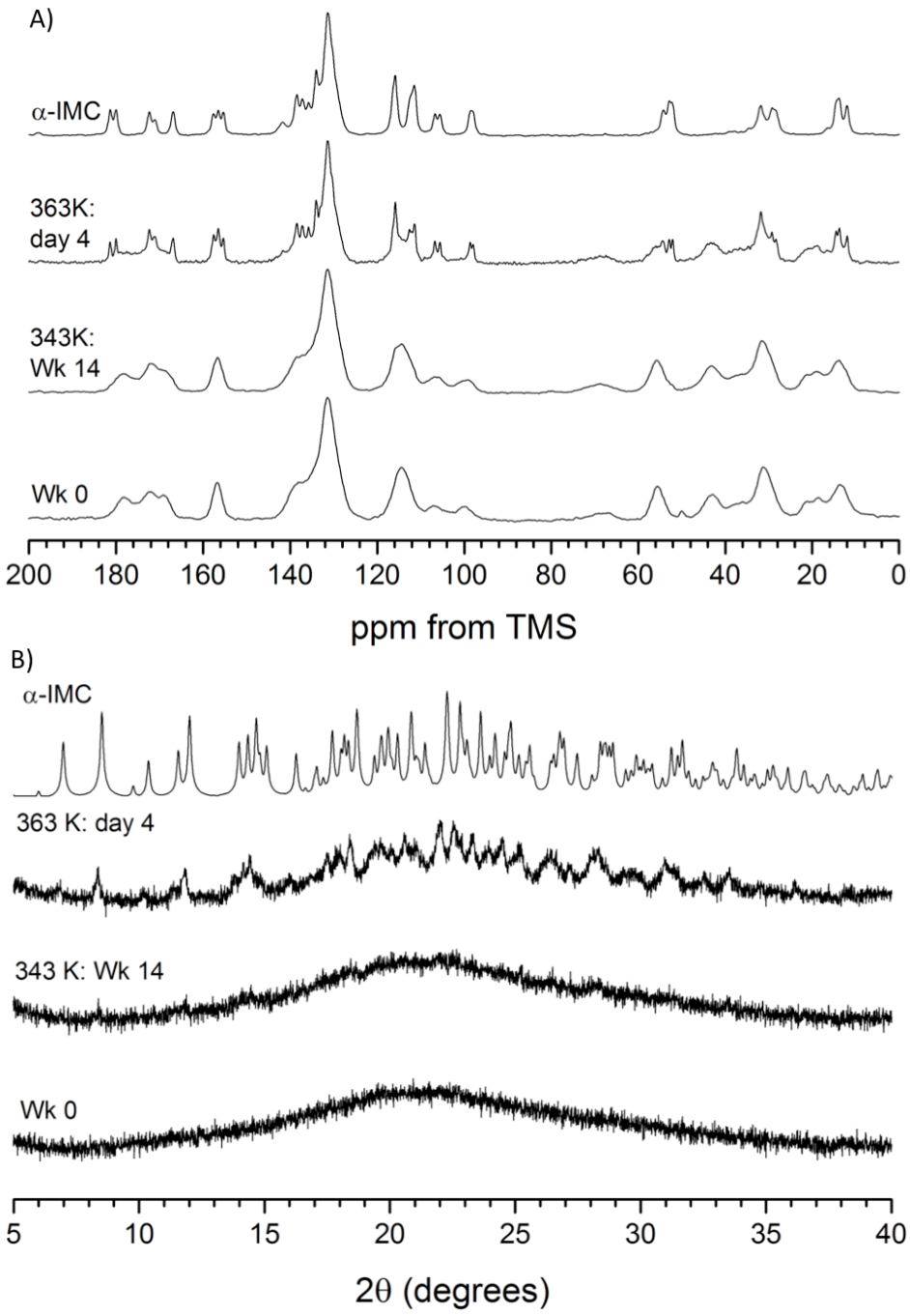


**Figure 5.33:** A) $^{1}$H-$^{13}$C CP/MAS NMR spectra (MAS = 10 kHz) and B) PXRD patterns of IMC/PVPVA 80/20 dispersion before and after storage at 343 and 363 K, with a comparison to $\alpha$-IMC

Crystallisation to $\alpha$-IMC is in agreement with the results seen in the VT CP/MAS NMR study (section 5.3.2), where crystallisation to $\alpha$-IMC was seen by 333 K in the 80/20 dispersion under MAS conditions. Hence, information regarding the stability and crystallisation behaviour of IMC formulations was predicted much more quickly, and at lower temperatures when compared to the more traditional stability study.

## 5.5 Conclusions

IMC was successfully formulated as an amorphous solid dispersion with PVP-VA in a variety of drug/polymer ratios. Initial characterisation with PXRD and $^{1}$H-$^{13}$C CP/MAS NMR indicated the fully amorphous nature of all the dispersions, whilst DSC highlighted a small amount of crystalline IMC in the highest loading dispersions. No deviation from ideal mixing was found, indicating no strong role of hydrogen-bonding in the stabilisation of the dispersions.

The differences in local mobility of drug and polymer at high and low IMC content indicated with $^{1}$H-$^{13}$C WISE spectra at ambient temperature became more apparent at high temperatures with $^{1}$H-$^{13}$C CP/MAS and $^{13}$C{$^{1}$H} MAS NMR. The mobility on the intermediate kHz timescale, through interference with either heteronuclear dipolar coupling during cross-polarisation transfer, or heteronuclear decoupling have been identified. Using VT $^{1}$H-$^{13}$C CP/MAS NMR we were able to mirror the outcome of the accelerated stability study, highlighting the fully amorphous nature of the dispersions up to 60 wt % drug loading, and the crystallisation to $\alpha$-IMC at 80 wt. % drug loading. The use of VT $^{1}$H-$^{13}$C CP/MAS NMR as a predictive tool for outcomes of physical stability will be demonstrated further across the FFA and TLB systems.

A fast mobility regime in the higher drug loading IMC/PVP-VA dispersions, was detected at high temperature. We postulate the high temperature $^{1}$H MAS spectrum of the 80/20 dispersion is dominated by an additional mobile phase, possibly containing amorphous IMC and polymer, alongside small crystallites of $\alpha$-IMC, which was not detected through $^{1}$H-$^{13}$C CP/MAS NMR.

We demonstrated that the mobility on the kHz scale of the IMC/PVP-VA dispersions followed a distinct 'non-typical' temperature dependence, due to the presence of at least two overlapping mobility regimes. We were able to extract two parameters from the temperature dependence curves: $E_{A\,app}$(HT and LT) and ($T_g$ - $T_{MAX}$). The calculation of $E_{A\,app}$ shows the most promise in relating the mobility behaviour detected through $T_{1\rho}{}^{H}$ to physical stability of the amorphous dispersions, and this will be further investigated using the FFA and TLB/PVP-VA systems.

Miscibility between IMC and PVP-VA was probed using $\Delta T_{1\rho}{}^{H}$ measurements which enables detection of domains down to *ca.* 2 nm. This provided a more sensitive analysis tool as compared to more traditional miscibility studies with DSC, where single $T_g$ values indicate miscibility on a 20 - 30 nm lengthscale. At ambient temperature, phase separation in the 80/20 IMC/PVP-VA dispersion was detected: the drug and polymer were found to be miscible on the $T_1{}^{H}$ lengthscale (24 - 55 nm), but immiscible on the $T_{1\rho}{}^{H}$ lengthscale (2 - 6 nm). With increasing temperature, domains of approximately 13 nm were detected, as the crystallisation of $\alpha$-IMC from the amorphous drug content within the dispersion was

observed.

Crystallisation from amorphous IMC was also investigated at different temperatures. Both pure amorphous IMC, and the amorphous content of the 80/20 IMC/PVP-VA dispersion permanently crystallised to the $\alpha$-polymorph above the $T_g$, which is the expected transition based on the thermodynamic stabilities of IMC polymorphs at increased temperature. Both the local structure and dynamics of these systems were affected by the transition. Solvent dependent polymorphic transitions were also shown for the 80/20 IMC/PVP-VA dispersions. $\gamma$-IMC crystallised from the dispersion prepared *via* solvent evaporation with ethanol, as compared to the $\alpha$ polymorph from methanol and acetonitrile. There was some correlation of these crystallisation outcomes with previous solvent studies of IMC in solution, although further investigation to understand the reasons behind the solvent effects is required.

The 40/60 IMC/PVP-VA dispersion was shown to have the lowest drug and polymer mobility. Additionally, the mid-loaded dispersions (40/60 and 60/40) were found to be fully miscible across a wide temperature range, and demonstrated the highest activation barrier (high $E_{A\,app}$). This indicated that the mid-loading dispersions are likely to be the most physically stable across the range of loading levels investigated. The low local mobility, and high miscibility explains the high physical stability of these dispersions confirmed through accelerated stability studies, although further investigation with 2D MAS NMR techniques will be useful in further probing the underlying mechanism of physical stability.

In summary, the numerous methods for probing structure and dynamics employed using the well documented model amorphous IMC, show promise in the provision of useful information regarding local structure and dynamics of amorphous solid dispersions, and will be further investigated with the two lower stability amorphous systems, FFA and TLB.

# Chapter 6

# Variable Temperature Studies of Flufenamic Acid

FFA has not been studied widely in the amorphous form, with only three published studies of FFA amorphous solid dispersions. Aso *et al.* [41] investigated the mobility of FFA as a solid dispersion with PVP and HPMC (at 80/20 w/w) using variable temperature low field $^{19}F$ spin-lattice relaxation studies. They found that FFA formulated with PVP had lower molecular mobility compared its formulation with HPMC, and was therefore more stable when stored at 333 K [41]. Eerdenburgh *et al.* [247] carried out a stability study with a number of poorly soluble drugs (including FFA) formulated with a variety of polymers (including PVP-VA) as solid dispersions and spin coated films. The crystallisation was monitored using polarized light microscopy over seven days at room temperature. Finally, Ibolya *et al.* [248] formulated FFA as solid dispersions with PEG-4000 and PEG-6000 *via* melt cooling (1:5 and 1:10 weight ratios) to demonstrate that dissolution rates of FFA improved as a result of formulating with polymers.

## 6.1 Crystalline Flufenamic Acid (FFA)

FFA exhibits rich polymorphism, with nine known polymorphic forms, eight of which have solved crystal structures [39]. The crystal structure of form III was first published in by McConnell in 1973 [54], followed by form I by Murthy *et al.* in 1982 [55]. Lopez-Meijas *et al.* recently solved the structures of six other polymorphs, meaning FFA has a record number of structurally characterized polymorphs in the Cambridge Structural Database (CSD) [39]. The crystallographic data for all solved structures can be seen in table 6.1 which highlights the large range of molecules present in the asymmetric units.

**Table 6.1:** Crystallographic data for all solved crystal structures of FFA polymorphs, adapted from [39, 54, 55]

| | **Form I** | **Form II** | **Form III** | **Form IV** | **Form V** | **Form VI** | **Form VII** | **Form VIII** |
|---|---|---|---|---|---|---|---|---|
| Crystal system | monoclinic | monoclinic | monoclinic | triclinic | monoclinic | triclinic | monoclinic | triclinic |
| Morphology | needle | plate | needle | prism | prism | | needle | plate |
| Temp (K) | 300 | 95 | 300 | 273 | 95 | 85 | 85 | 85 |
| Space group | $P2_1/c$ | $P2_1/c$ | $C_2/c$ | $P2_1$ | $P2_1/c$ | $P2_1$ | $P2_1/c$ | $P2_1$ |
| $a$ (Å) | 12.523(4) | 10.8813(8) | 39.84 | 8.7589(2) | 26.6592(18) | 8.6485(2) | 14.9687(14) | 17.0047(14) |
| $b$ (Å) | 7.868(6) | 10.2374(7) | 5.10 | 11.6629(3) | 7.9007(2) | 11.5115(2) | 20.641(2) | 19.1941(5) |
| $c$ (Å) | 12.87(3) | 11.7487(10) | 12.24 | 20.0229(14) | 23.2430(5) | 38.895(3) | 7.9486(8) | 19.1941(15) |
| $\alpha$ (°) | 90 | 90 | 90 | 80.632(6) | 90 | 87.914(6) | 90 | 81.321(7) |
| $\beta$ (°) | 95.2(2) | 111.318(8) | 92.47 | 81.041(6) | 94.084(7) | 85.910(6) | 98.316(7) | 89.580(6) |
| $\gamma$ (°) | 90 | 90 | 90 | 73.534(5) | 90 | 72.260(5) | 90 | 78.560(7) |
| V (Å$^3$) | 1263.27 | 1219.21 | 2488.57 | 1922.33 | 4883.20 | 3678.32 | 2430.10 | 5655.09 |
| Z/Z' | 4/1 | 4/1 | 8/1 | 6/3 | 16/4 | 12/6 | 8/2 | 19/9.5 |

Forms I and III are enantiotropically related (Form III → Form I: transition temperature of 315 K [197]), with form I becoming more stable at higher temperatures [249]. Forms I and III

are the most extensively studied of the FFA polymorphs. The transition Form III → form I is particularly important as the temperature of conversion is sufficiently low to occur during manufacturing and/or storage. Forms II and III are also enantiotropically related, with a higher transition temperature of 377 K [37]. The energy-temperature diagram of forms I - III is shown in figure 6.1.

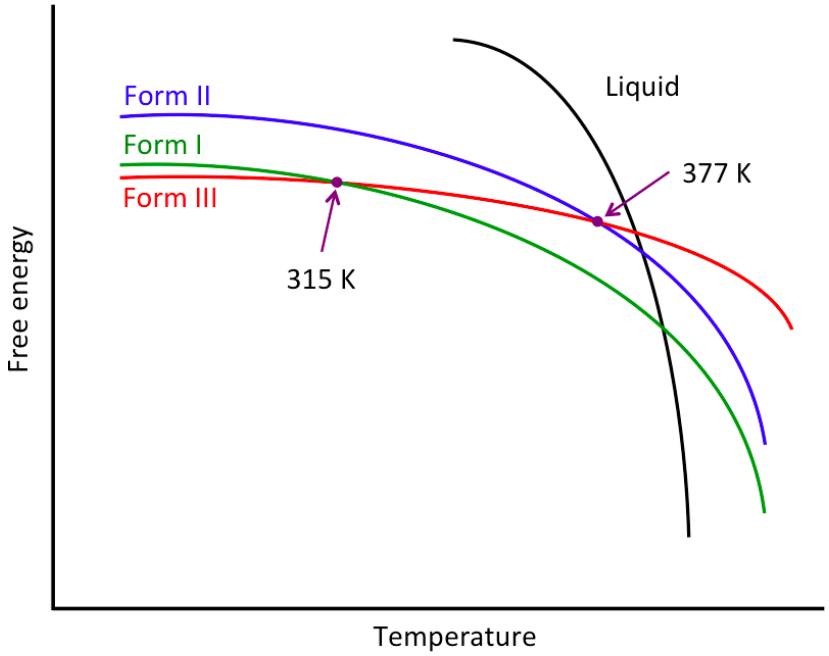


**Figure 6.1:** Energy-temperature diagram for forms I, II and III of FFA. This shows the enantiotropic relationship of forms I and III (transition temperature = 315 K) and forms II and III (transition temperature = 377 K). Adapted from [37]

The crystal structures and hydrogen bonding motifs of the forms I and III FFA can be seen in figures 6.2 and 6.3.

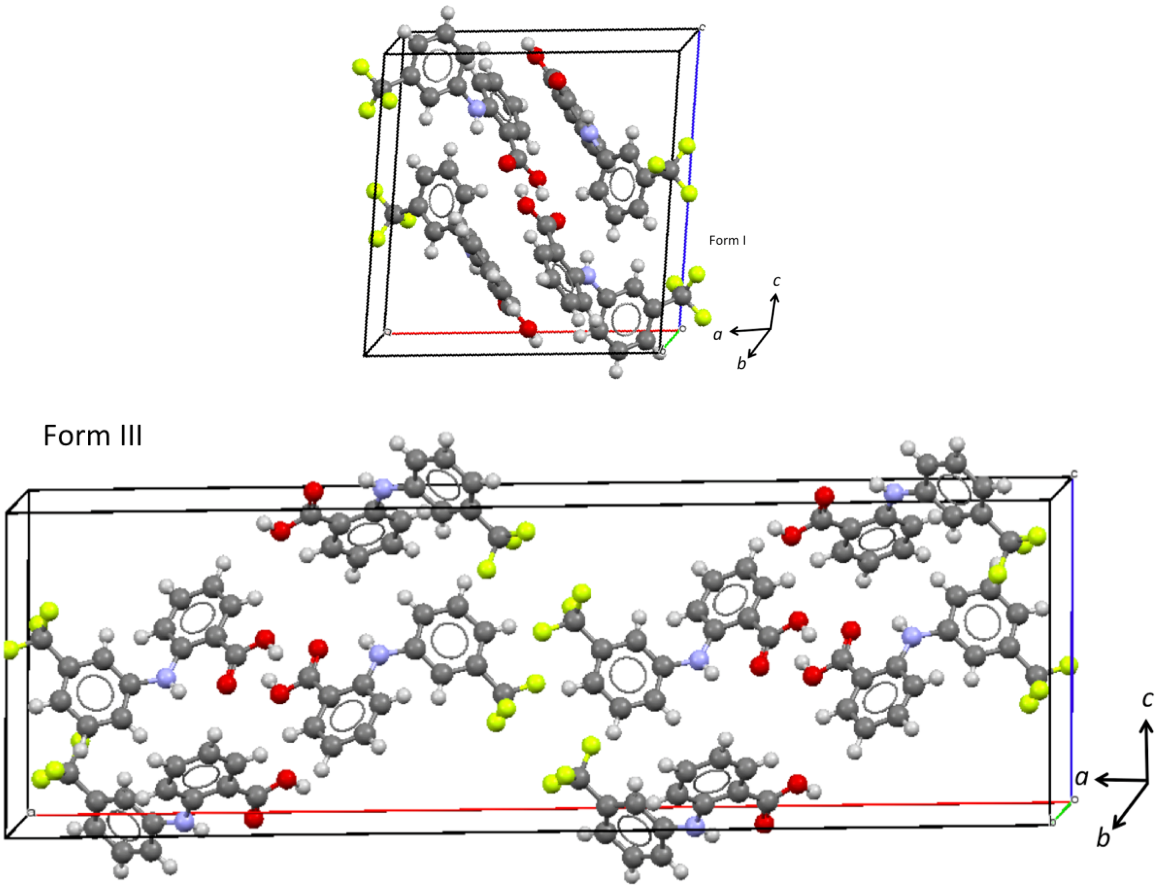


**Figure 6.2:** Unit cell of crystalline structures of form I and form III FFA. Structures extracted from the Cambridge Structural Database (CSD)

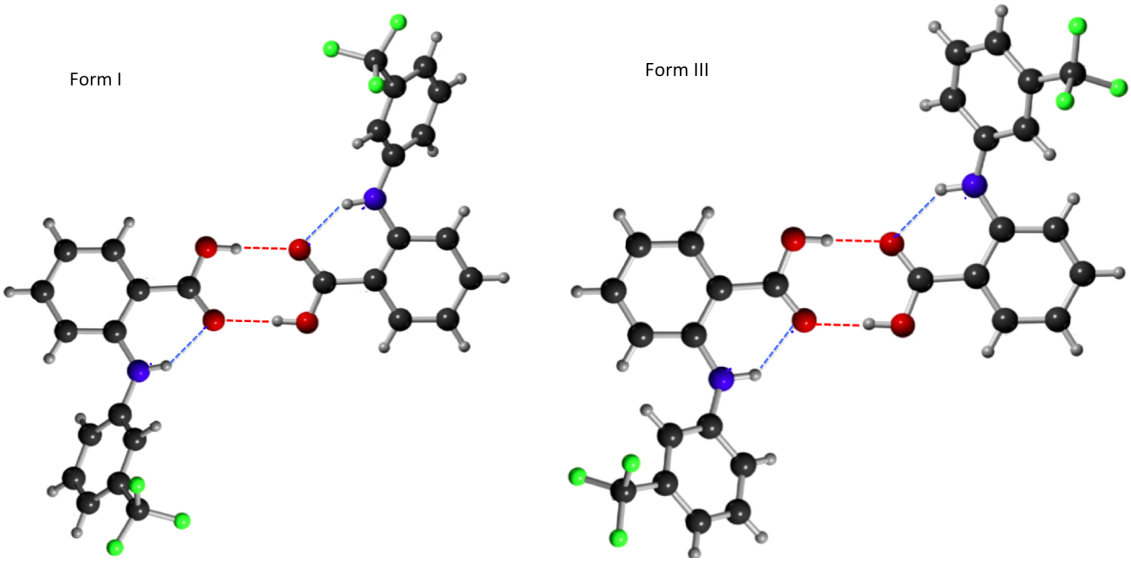


**Figure 6.3:** Different conformations in the molecular structure of FFA forms I and III, adapted from [38]

Both polymorphs have similar hydrogen bonded dimers, with the same overall number of hydrogen bonds. Jabeen *et al.* [250] used Raman and IR spectroscopy alongside density functional theory (DFT) calculations to study conformational differences between forms

I and III FFA. They found subtle differences resulting from differences in conformation from rotation about the N-C bond (figure 6.5) and concluded that the conformation of the whole molecule is dependent on the rotation of these bonds, rather than through differences in hydrogen bonding as previously thought. Delaney *et al.* additionally found that the position of the -$CF_3$ group plays an important role in the difference in overall stability of the two polymorphs [38]. FFA contains both a carboxylic acid and amino group, but it has been suggested that hydrogen bonding interactions can only form with the acid group as a donor [247]. This is because the FFA structure is an ideal candidate for resonance-assisted hydrogen bonding (RAHB) [251], resulting in the formation of a six-membered ring stabilised through intramolecular hydrogen bonding and $\pi$-delocalization [247] (figure 6.4). RAHB commonly occurs in structures of this type, when distances between the N and O are between 2.66 - 2.75 $\AA$ [252]. The distances between these atoms in forms I and III FFA fall within this range [247].

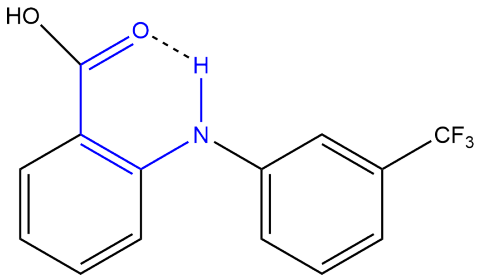


**Figure 6.4:** Example of the formation of a six-membered ring through intramolecular resonance assisted hydrogen-bonding (RAHB) in a FFA molecule

Lopez-Mejias *et al.* [39] characterised polymorphs I - VIII and found unique PXRD patterns for each. They identified different conformers in all polymorphic forms, which resulted in multiple packing modes. Such conformational changes occur around the torsional angles of the biphenyl amine group, highlighted in figure 6.5.

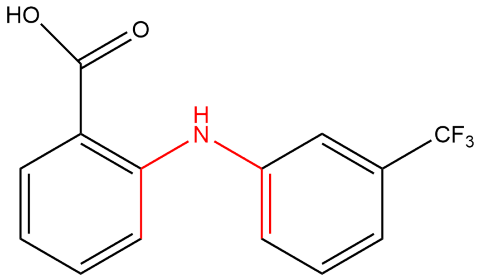


**Figure 6.5:** Molecule of FFA, with the biphenyl amine group highlighted, about which conformational changes between polymorphic forms occur ,adapted from [39]

The melting points and relative stabilities of the polymorphs were also determined (table 6.2). Forms I and II were found to slowly convert to form III at 300 K, in agreement with the E-T diagram in figure 6.1. Forms V, VIII and IX were found to convert to form III almost immediately, during sample preparation. Form III was still identified as the most

stable form of all polymorphs at ambient temperature, through $\Delta H_{fus}$.

**Table 6.2:** Melting points and enthalpy of melting for FFA polymorphs I - VII, adapted from [39]

| **Crystalline Form** | $\mathbf{T}_m$ **K** | $\Delta H_{fus}$ ($J \cdot g^{-1}$) |
|---|---|---|
| I | 407.5 | 98.2 |
| II | 402.6 | 87.8 |
| III | 400.4 | 105.6 |
| IV | 396.9 | 80.4 |
| V | 397.9 | 90.7 |
| VI | 397.2 | 87.8 |
| VII | 393.7 | 83.2 |

### 6.1.1 Solution-state NMR assignment of Flufenamic acid

Solution state $^1$H NMR and $^{13}$C assignments for FFA have been previously published [40] (table 6.3, figure 6.6). The reported $^{13}$C and $^1$H spectra were acquired at 300 MHz $^1$H frequency, therefore only two of the aromatic protons were identified (A and H), with the remaining protons (B - G) assigned as an overlapping multiplet. We had spectrometers at higher fields (500 and 800 MHz) available, therefore we were able to fully assign all aromatic $^1$H nuclei, using previous assignments as an initial guide.

**Table 6.3:** $^1$H and $^{13}$C solution-state assignments, as reported by [40]. m = overlapping multiplet

| $^1$H | $\delta$ (ppm) [40] | $^{13}$C | $\delta$ (ppm) [40] |
|---|---|---|---|
| A | 7.95 | C-2 | 147.73 |
| H | 6.90 | C-13 | 111.38 |
| E | m | C-5 | 132.84 |
| F | m | C-10 | 118.36 |
| D | m | C-4 | 135.48 |
| G | m | C-12 | 114.20 |
| B | m | C-3 | 141.17 |
| C | m | C-11 | 118.84 |
| N-H | 9.68 | C-14 | 131.96 |
| COOH | 13.07 | C-9 | 120.20 |
| | | C-7 | 129.98 |
| | | C-8 | 125.33 |
| | | C-1 | 173.96 |
| | | C-6 | 123.92 |

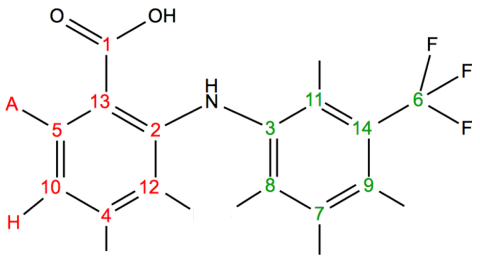


**Figure 6.6:** $^{1}$H and $^{13}$C assignments of FFA available from literature, [40]

The 1D $^{1}$H spectrum acquired at 800 MHz is shown in figure 6.7. Here we observed 5 separate proton signals: three corresponding to single protons: doublet of doublets at 8.02 ppm (proton A), triplet of doublets at 7.32 ppm (assigned to proton E) and a triplet of doublets at 6.84 ppm (proton H). An additional multiplet (protons B, C and D), possibly consisting of an overlapping singlet, doublet and triplet; and two overlapping doublets, *ca.* 7.22 (proton F) and 7.21 (proton G) ppm were also observed.

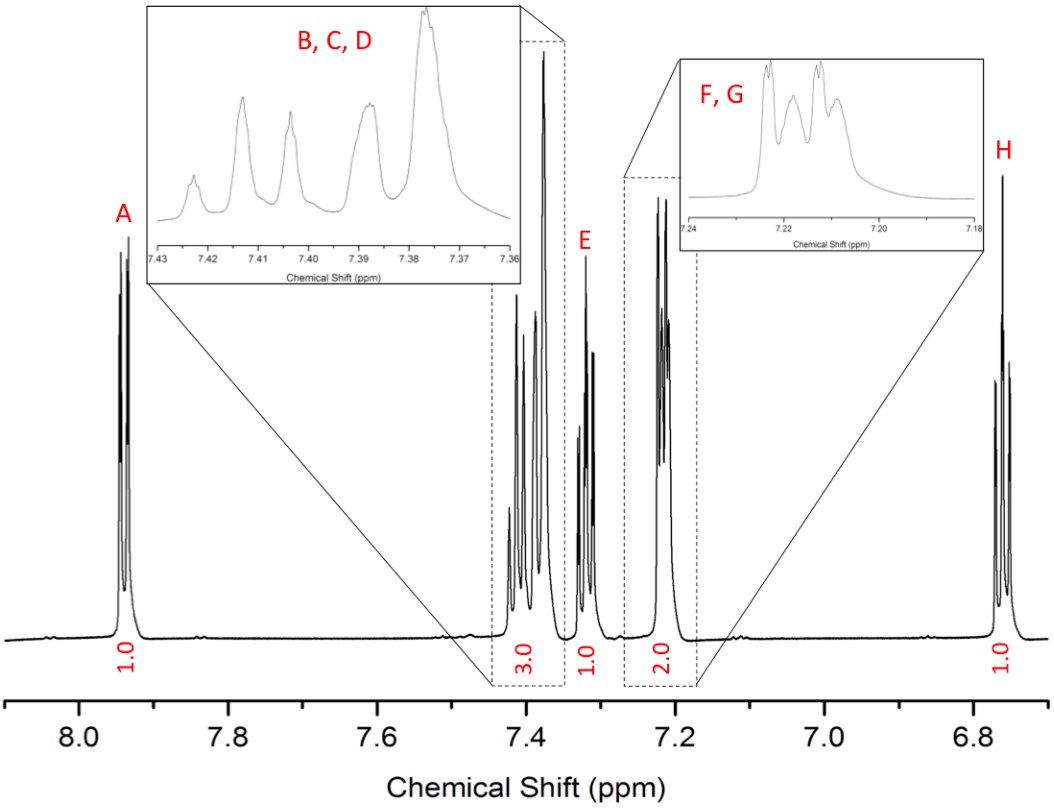


**Figure 6.7:** 800 MHz 1D $^{1}$H NMR spectrum of FFA (0.05 M dissolved in $CD_3OD$) showing the five separate proton peaks

The two proton spin systems of the aromatic rings were separated through $^{1}$H-$^{1}$H COSY (figure 6.8 A) and directly bonded protons were assigned to $^{13}$C nuclei with $^{1}$H-$^{13}$C HSQC and literature $^{13}$C assignments [40] (figure 6.8 B). From these 2D spectra, protons E, and F and G were identified (figure 6.10), but the remaining three protons (B, C and D: multiplet at 7.46 - 7.50 ppm) were too closely overlapped to be distinguished. A 2D J-resolved pulse sequence

was employed to separate coupling constants and chemical shifts into different dimensions of the spectrum, essentially gaining a one-dimensional spectrum, without the complicating presence of multiplets (figure 6.9) [253]. From this spectrum, we were successfully able to identify protons B, C and D (figure 6.10). The full $^{1}$H chemical shift assignments are given in table 6.4.

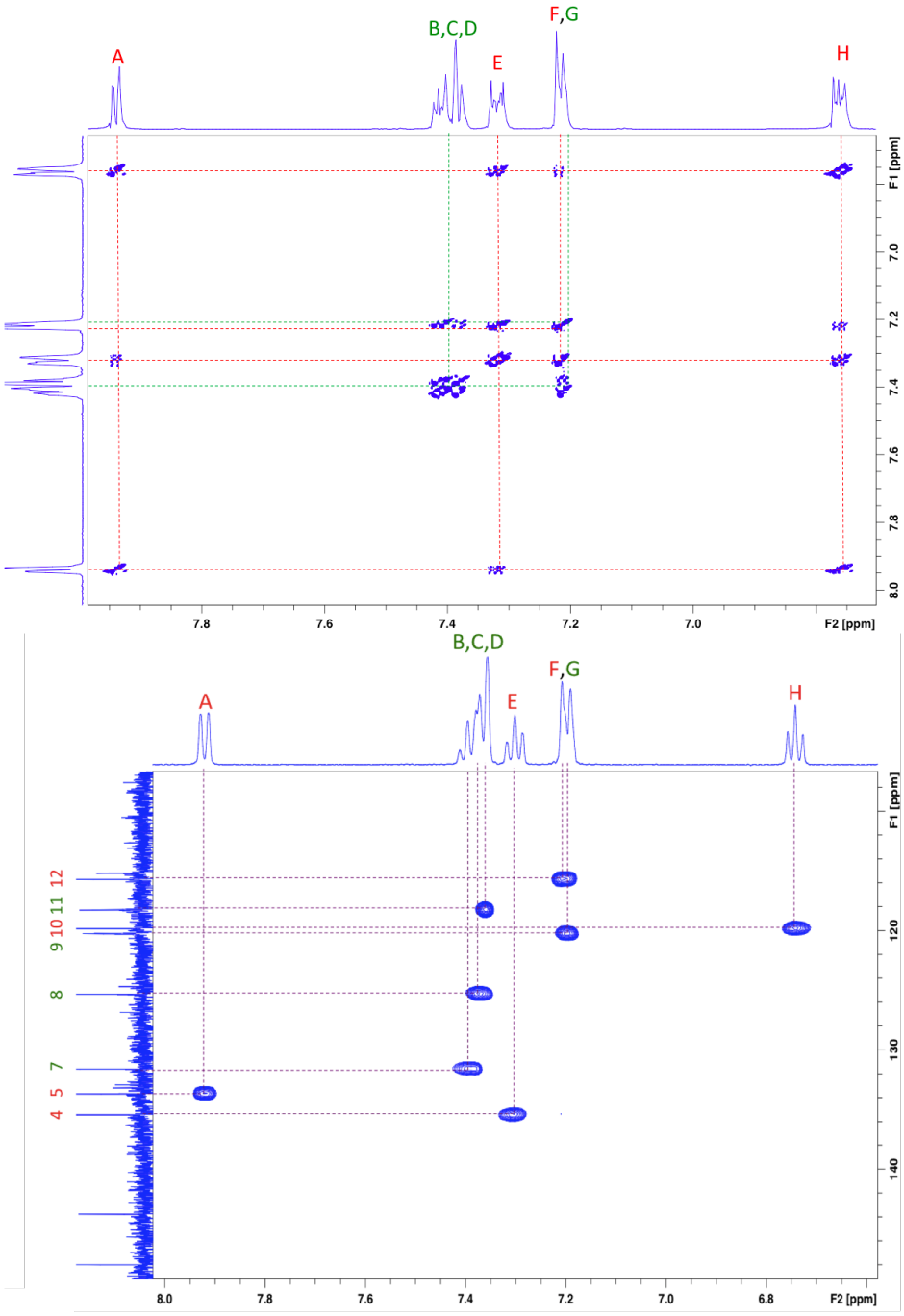


**Figure 6.8:** A) $^{1}$H-$^{1}$H COSY NMR spectrum (800 MHz) of FFA (0.05 M in $CD_3OD$) for the identification of the two proton spin systems: Ring 1: A, E, F, H and Ring 2: B, C, D, G B) $^{1}$H-$^{13}$C HSQC NMR spectrum (500 MHz) of FFA (0.05 M in $CD_3OD$ for the assignment of $^{1}$H-$^{13}$C connectivities

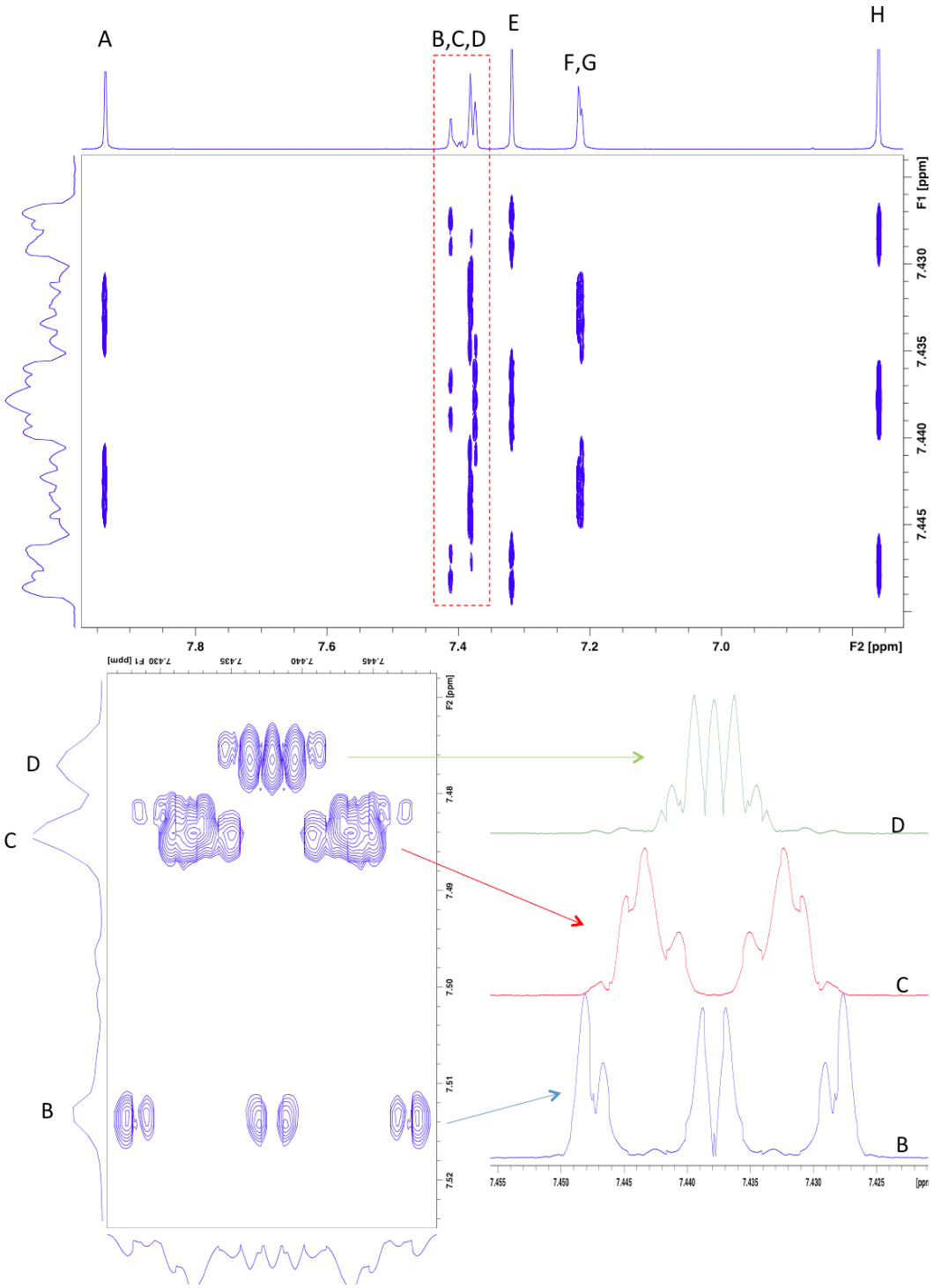


**Figure 6.9:** 2D J-resolved NMR spectrum (800 MHz) of FFA (0.05 M dissolved in $CD_3OD$) with projected coupling constants from the F1 dimension, which allowed the identification of protons B, C and D

**Table 6.4:** $^{1}$H chemical shift assignments of FFA from 2D $^{1}$H-$^{1}$H COSY, $^{1}$H-$^{13}$C HSQC and J-resolved NMR spectra

| $^{1}$H | Chemical Shift (ppm) |
|---|---|
| A | 7.94 |
| B | 7.41 |
| C | 7.39 |
| D | 7.37 |
| E | 7.32 |
| F | 7.22 |
| G | 7.21 |
| H | 6.76 |

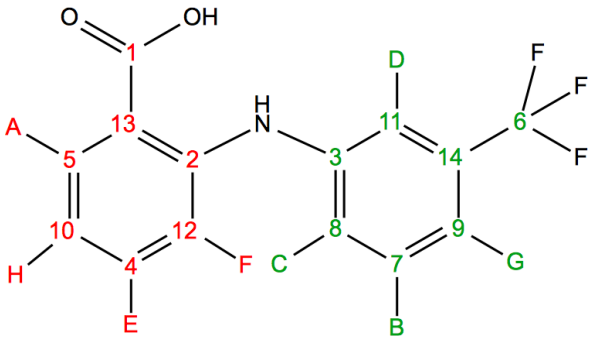


**Figure 6.10:** $^{1}$H and $^{13}$C assignments from 2D $^{1}$H-$^{1}$H COSY, $^{1}$H-$^{13}$C HSQC and J-resolved NMR spectra

### 6.1.2 Initial solid-state characterisation of forms I, III and amorphous FFA

Forms I and III FFA were characterised initially using PXRD, DSC and solid-state NMR. There are currently no reports of the successful preparation of amorphous FFA at ambient temperatures [131], therefore there is no published $T_g$ for comparison. Here we successfully formulated amorphous FFA *via* the quench cool method (figure 6.11 A).

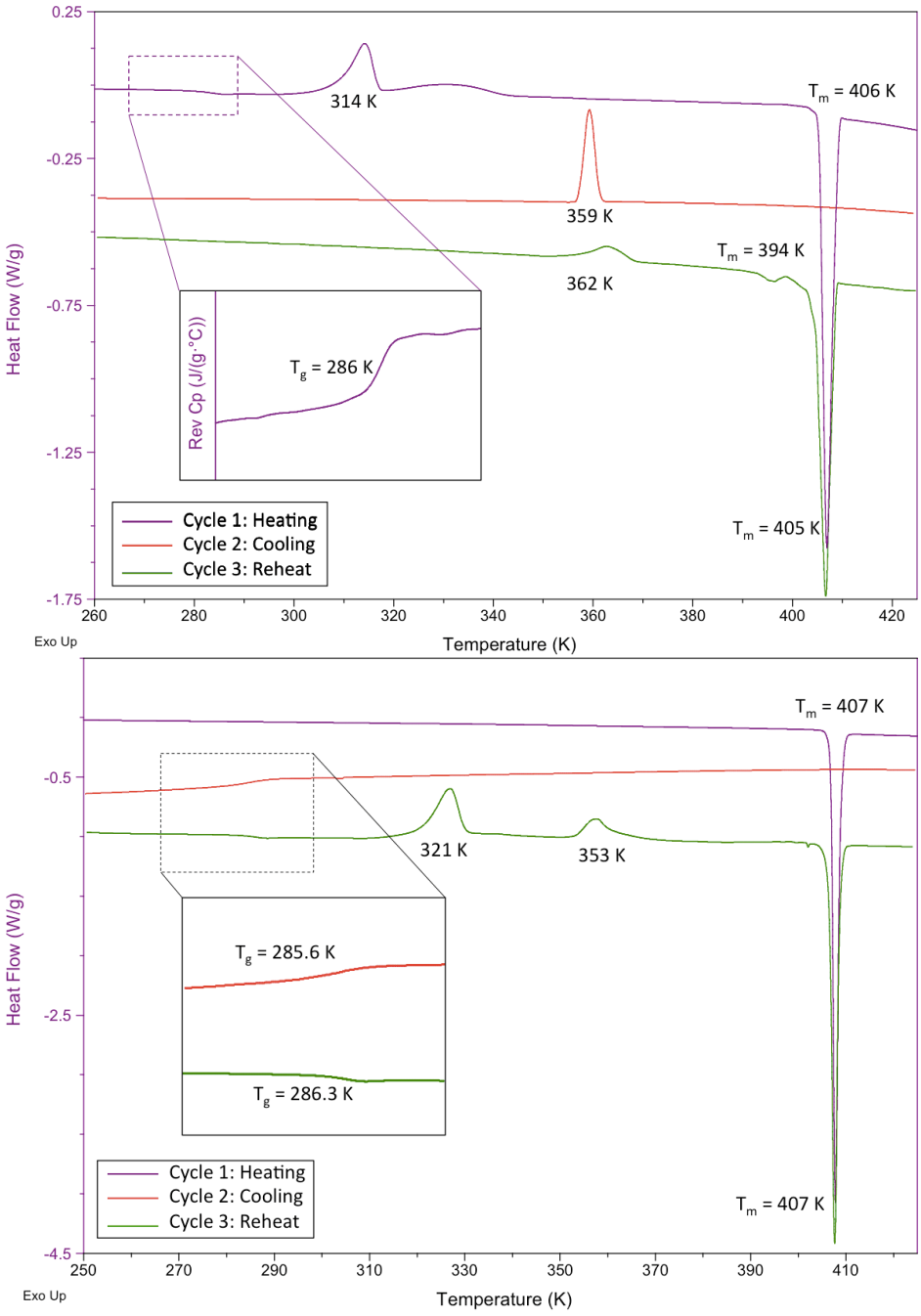


**Figure 6.11:** Modulated DSC heat-cool-reheat cycle of A) quench cooled amorphous FFA and B) form I FFA

A $T_g$ of 286 K was obtained from the initial heating run of the amorphous FFA sample (figure 6.11 A), followed by an exothermic crystallisation event and subsequent melting of form I FFA *ca.* 407 K [55]. Upon cooling and reheating, no $T_g$ was observed, but crystallisation at a higher temperature (359 - 362 K) occurred, followed by melting of both I FFA [54], and an unidentifed form ($T_m$ = 394 K). The presence of crystallisation endotherms upon cooling *and* reheating is consistent with the reversible polymorphic transition between forms I and III. Amorphous FFA produced *in situ* in the DSC pan from FFA-I polymorph (figure 6.11 B), showed the $T_g$ temperature of 286 K, making it unstable at ambient conditions.

When packed in the cold room and cooled to 253 K within the rotor, we were able to acquire the $^{1}$H-$^{13}$C CP/MAS NMR spectrum of amorphous FFA (figure 6.12). The broad $^{13}$C resonances reflect the lack of long range order within the amorphous material, leading to a wide range of carbon environments [29].

There are also significant differences between the $^{1}$H-$^{13}$C CP/MAS NMR spectra of the two crystalline polymorphic forms (forms I and III). The assignment of the solid-state NMR spectra of the different forms of FFA is not straightforward, due to the large number of aromatic carbons. The $^{13}$C spectra of forms I, III and V have been published, but no chemical shift assignments were made [254,255]. Of the few publications on solid dispersions of FFA, none included any solid-state NMR data. Fewer $^{13}$C resonances are observed in the solid-state compared with solution-state spectra: 13 for form I, 11 for form III and only 8 for amorphous FFA. We were able to confirm the resonance positions of the 5 quaternary carbons within the spectrum of form I, *via* NQS CP/MAS NMR (figure 6.13). As all remaining non-quaternary carbons are aromatic, additional $^{13}$C NMR spectral editing experiments would not provide further assignment information [241, 256]. One internet reference describing the assignments of form I *via* CSA amplification measurements and CASTEP calculations was identified, however the assignments of form I were given on the spectrum of form III, therefore this was not deemed to be a reliable source. No peer reviewed references could be identified.

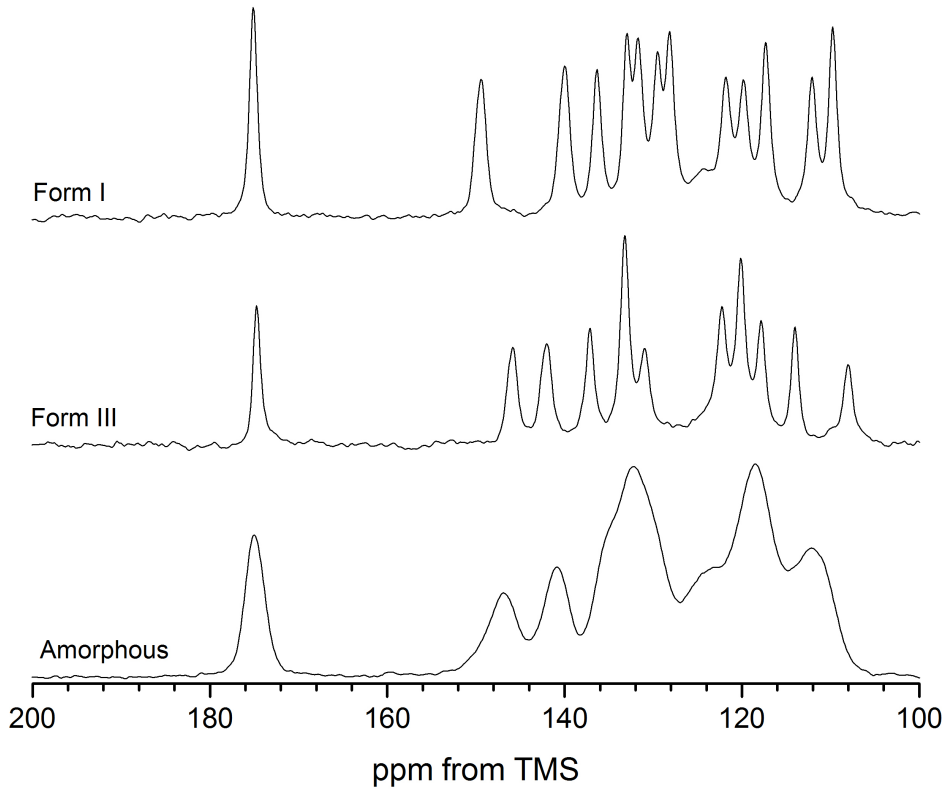


**Figure 6.12:** $^{1}$H-$^{13}$C CP/MAS NMR spectra for forms I, III and amorphous FFA, recorded at an MAS rate of 10 kHz

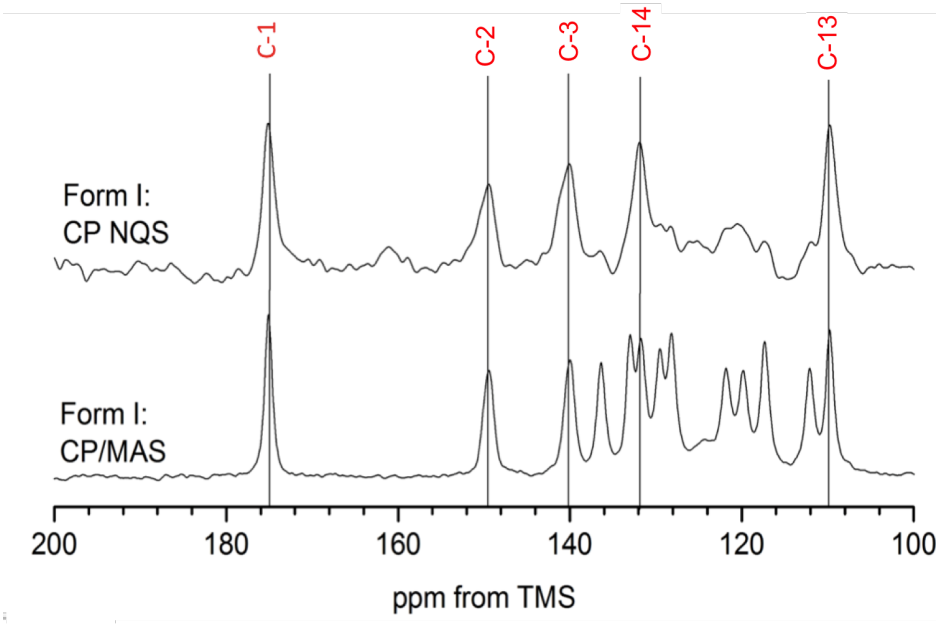


**Figure 6.13:** $^{1}$H-$^{13}$C NQS CP/MAS NMR spectra for FFA form I, highlighting the assignment of quaternary carbons, recorded at an MAS rate of 10 kHz

**Table 6.5:** $^{13}$C Chemical Shift Assignments of Form I, III and amorphous FFA

| $^{13}$C | Form I | Form III | Amorphous |
|---|---|---|---|
| 1 | 175.0 | 174.7 | 175.0 |
| 2 | 149.3 | 145.8 | 146.9 |
| 3 | 140.0 | 142.0 | 140.8 |
| | 136.3 | 137.1 | 135.4 |
| | 132.9 | 133.2 | 132.1 |
| 14 | 131.7 | 130.9 | ” |
| | 129.3 | | ” |
| | 128.2 | | ” |
| | 121.7 | 122.2 | 124.5 |
| | 119.7 | 120.1 | 123.3 |
| | 117.2 | 117.8 | 118.4 |
| | 111.9 | 114.0 | 112.1 |
| 13 | 109.6 | 108.0 | |

Further work with CASTEP calculations to predict the $^{13}$C chemical shifts would be useful in completing the full assignments of forms I and III FFA. Due to time and computer constraints, this was not completed. However, this was not critical, as our study did not depend on the full spectral assignment, with further analysis carried out comparatively between dispersions of different drug loading levels.

### 6.1.3 Initial characterisation of FFA/PVP-VA solid dispersions

In our study, all solid dispersions were initially characterised using modulated DSC, PXRD and $^{1}$H-$^{13}$C CP/MAS NMR. Each dispersion has a single $T_g$ (figure 6.14), intermediate between the $T_g$ values of pure amorphous FFA and PVP-VA, as expected from the Gordon-Taylor relationship [112]. As the amount of polymer increased, the single $T_g$ value increased in a linear manner, which indicates the anti-plasticising property of PVP-VA [257]. Ideal $T_g$ values of the dispersions were calculated using the Gordon-Taylor/Kelley-Bueche (G-T/K-B) and Couchman-Karasz (C-K) equations (equations 2.17 with 2.19 and 2.20 - see chapter 3), and can be seen in figure 6.14.

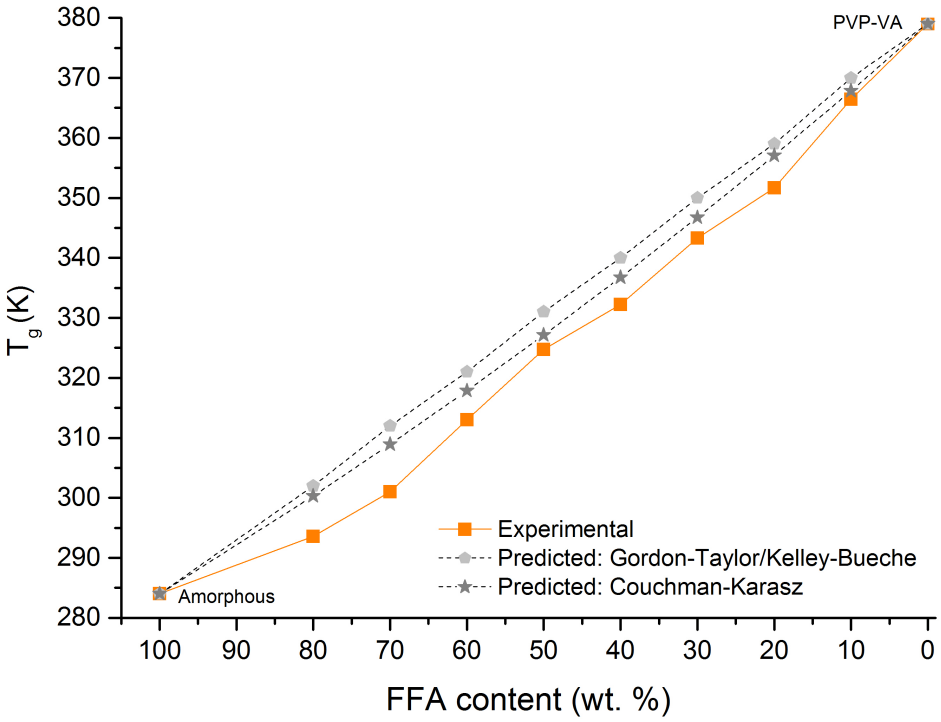


**Figure 6.14:** Glass transition temperatures for FFA/PVP-VA dispersions at different drug loadings, compared to values predicted by the Gordon-Taylor/Kelley-Bueche (G-T/K-B) and Couchman-Karasz (C-K) equations

The FFA/PVP-VA dispersions displayed slight negative deviation from predicted $T_g$ values, especially when compared to the G-T/K-B equation predictions. Negative deviation from ideal indicates dominance of drug/drug interactions within the system and suggests non-ideal mixing between drug and polymer components [193]. However, literature studies only report much larger differences between measured and predicted $T_g$ values as 'deviation' examples [78, 190]. Shamblin *et al.* [179] found negative deviation from predicted values (using the Gordon-Taylor equation) in sucrose/PVP, sucrose/PVP-VA and sucrose/dextran systems, due to hydrogen bonding between sucrose molecules, with differences of up to 40 K. Compared to literature, all deviations observed are negligible, and therefore do not provide information regarding specific interactions in the three systems.

The 10/90 - 60/40 w/w FFA/PVP-VA dispersions were found to be fully amorphous, and miscible on the DSC scale up to 20 - 30 nm due to the absence of melting peaks and presence of a single $T_g$ values. However, the 70/30 and 80/20 dispersions contained both amorphous and crystalline drug phases, highlighted by the presence of several thermal events on the DSC curves (figure 6.15).

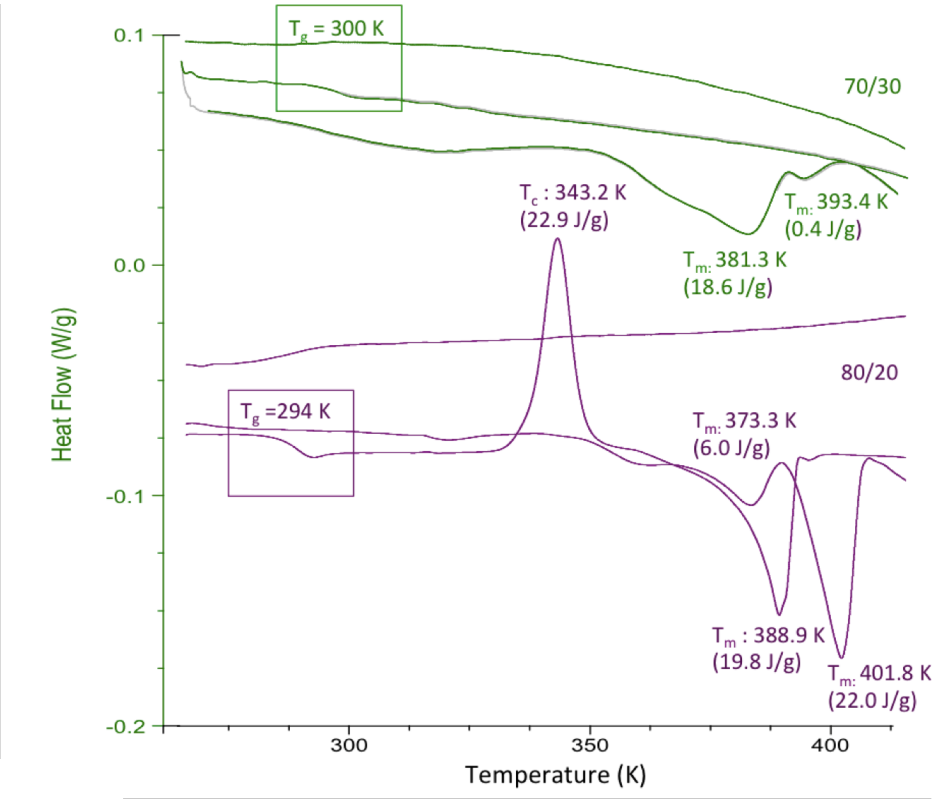


**Figure 6.15:** DSC curve (Heat flow vs. temperature) for 70/30 (green) and 80/20 (purple) dispersions (heat-cool-reheat cycles)

For the 80/20 FFA/PVP-VA dispersion, two broad melting endotherms ($T_m$ = 373 and 402 K) were present in the DSC curve on the initial heating run; upon reheating, a $T_g$ of 294 K was calculated. On the final heating cycle, a crystallisation exotherm was present ($T_c$= 343 K), followed by a single melting endotherm ($T_m$ = 389 K). The DSC curve of the 70/30 FFA/PVP-VA dispersion displayed two broad melting endotherms ($T_m$ = 381 and 393 K) upon the initial heating cycle, and only a glass transition ($T_g$ = 300 K) on the subsequent cooling and reheating cycles. Previous studies of partially crystalline dispersions have also reported the presence of two broad melting endotherms in DSC curves [148, 190, 228, 258]. The lower temperature endotherm is thought to occur due to the melting of a drug/polymer solid solution, formed through the dissolution of crystalline drug in the polymer upon heating [90, 148]. The higher temperature endotherm is thought to occur due to the melting of residual crystalline API formed during manufacture, and is often been reported at lower $T_m$ values compared to the melting observed for pure API [190, 228]. Previously reported high drug loading FFA dispersions (formulated with PVP and HPMC at 80/20 w/w *via*

melt-cooling) were confirmed to be fully amorphous with microscopic observations under polarised light [41]. This difference in stability compared to our dispersions could be due to either differences in formulation method, or in characterisation technique sensitivity.

The fully amorphous nature of the 10/90 - 60/40 w/w FFA/PVP-VA dispersions was confirmed with PXRD. The 80/20 and 70/30 dispersions were found to contain form III FFA at ambient temperatures [255] (figure 6.16). The pale yellow colour of both high drug loaded dispersions was also an indication of the presence of form III FFA [259]. Using this information, the % of the residual crystalline content of the 70/30 and 80/20 was calculated assuming the presence of form III FFA (equation 5.1) as 0.5 % (peak at 393 K) or 25.2 % (peak at 382 K) for the 70/30 dispersion, and 29.8 % for the 80/20 dispersion.

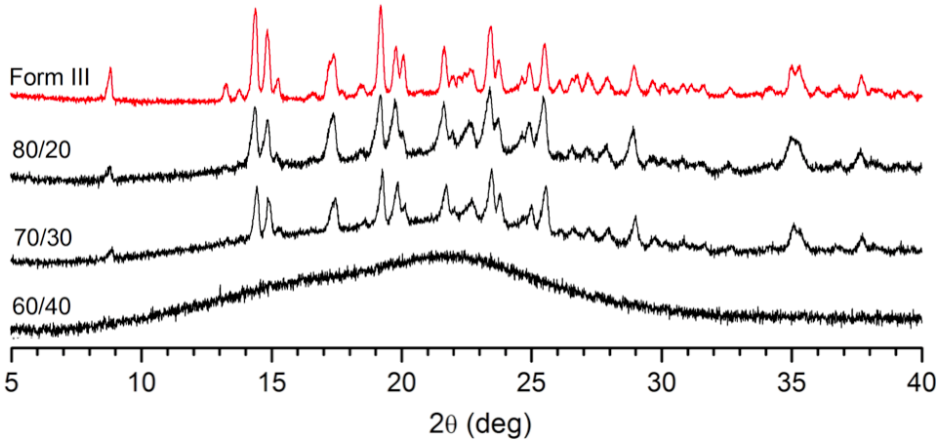


**Figure 6.16:** PXRD patterns for FFA/PVP-VA dispersions at different drug loadings, with crystalline form III for comparison. FFA loadings of below 60 wt. % all displayed broad halo patterns, and were therefore confirmed to be fully amorphous

Figure 6.17 gives the assignment of chemical shifts to FFA, PVP-VA, or both drug and polymer in the FFA/PVPVA 50/50 dispersion. The numerous well separated peaks of drug and polymer enabled us to independently monitor the changes in both components of the dispersion during variable temperature NMR investigations to obtain independent mobility information. The carbonyl region provided additional information about changes in hydrogen-bonding during phase transitions and recrystallisation. There is complete overlap between the FFA and PVP-VA carbonyl peaks at 175.1 and 175.9 ppm respectively, resulting in a broader peak at 175.6 ppm in the dispersion. The shift in the FFA carbonyl peak (of 0.5 ppm for the 50/50 dispersion) indicates a difference in hydrogen-bonding between pure amorphous FFA and FFA in the presence of polymer, and could indicate interaction between the drug and polymer through the carboxylic acid group. The shift of the polymer carbonyl peak is greater with increasing FFA content (figure 6.18).

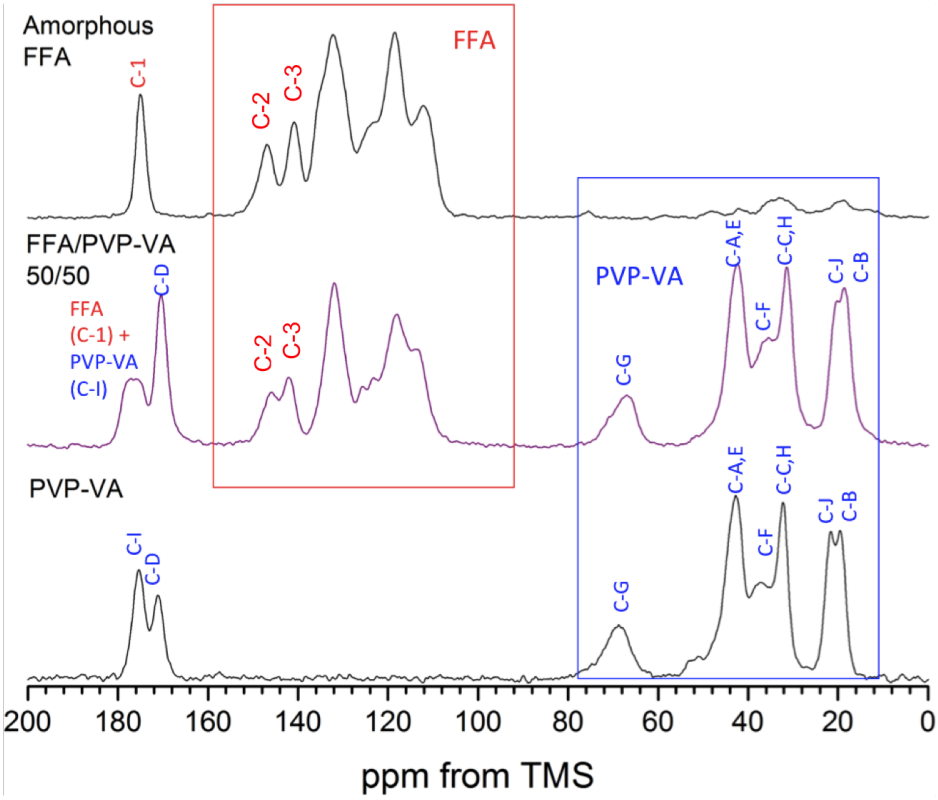


**Figure 6.17:** $^{1}$H-$^{13}$C CP/MAS NMR spectra for FFA/PVP-VA 50/50 solid dispersion compared to amorphous FFA (at 253 K) and PVP-VA recorded at an MAS rate of 10 kHz. Missing FFA chemical shift assignments are unavailable due to overlapping peaks, PVP-VA assignments are the same as in chapter 5

There were additionally some subtle changes to the aromatic region of the FFA in dispersion, compared to amorphous FFA: notably the presence of two peaks at 125.6 and 123.2 ppm; and a shift in the C-N (C-2 and 3) resonances at 145.8 and 142.0 ppm respectively. This could indicate a difference in conformation around the biphenyl amine group.

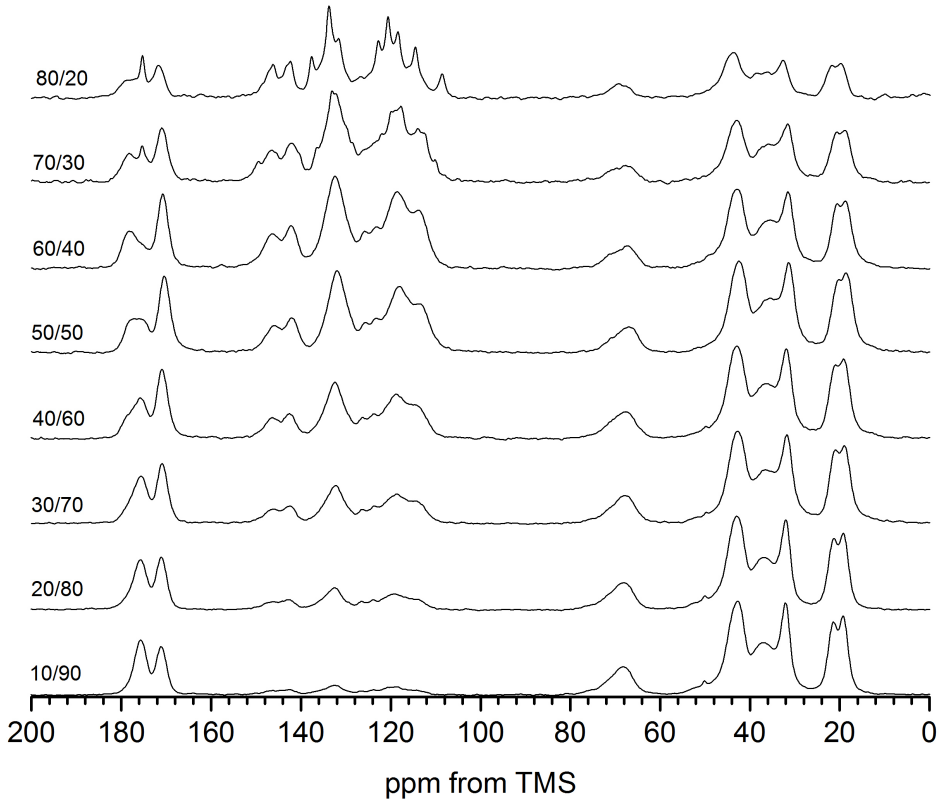


**Figure 6.18:** $^{1}$H-$^{13}$C CP/MAS spectra for amorphous dispersions of various drug loadings, recorded at an MAS rate of 10 kHz

From figure 6.18 it can be seen that the intensity of drug peaks increased proportionally with drug content. The carbonyl peaks change most dramatically as the amount of drug increases, with the drug peak becoming apparent from 40 wt. % drug load and above. The 80/20 and 70/30 dispersions contain both amorphous and crystalline phases, with the 80/20 dispersion being more highly crystalline than the 70/30. The crystalline phase was identified as form III FFA (figure 6.19), in agreement with PXRD.

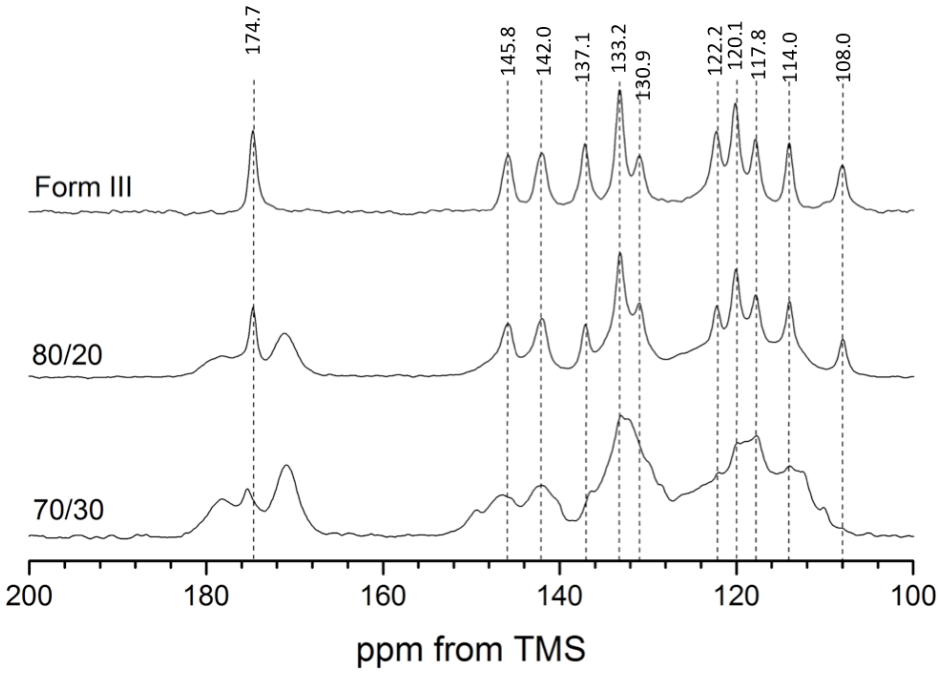


**Figure 6.19:** $^{1}$H-$^{13}$C CP/MAS NMR spectra for 70/30 and 80/20 dispersions with a comparison to form III, recorded at an MAS rate of 10 kHz

The presence of a $CF_3$ group enabled us to use $^{19}$F MAS NMR to probe the mobility and recrystallisation of the amorphous dispersions at increased temperatures. $^{19}$F is a very attractive nucleus in NMR due to its high natural abundance, and therefore much shorter experimental time. This technique also allowed us to focus on the behaviour of the drug alone with increasing temperature.

The values of $^{19}$F chemical shift and full width half-heigh (FWHH) for forms I, III and FFA/PVP-VA dispersions are presented in table 6.6. The amorphous nature of the 40/60 - 60/40 dispersions can be confirmed by the broader isotropic peaks compared to crystalline FFA, due to the wider range of molecular orientations of the $CF_3$ group. The 70/30 and 80/20 dispersions had chemical shift values comparable to form III FFA, with narrower linewidths than the other fully amorphous dispersions, which is in good agreement with the PXRD and $^{1}$H-$^{13}$C CP/MAS NMR results.

**Table 6.6:** $^{19}$F Chemical Shift values and Full Width Half Height (FWHH)at 293 K

| Peak | FFA 8020 | FFA 7030 | FFA 6040 | FFA5050 | FFA 4060 | Form I | Form III |
|---|---|---|---|---|---|---|---|
| Main: $\delta$ (ppm) | -62.2 | -62.2 | -61.9 | -61.8 | -61.7 | -60.0 | -62.0 |
| FWHH (Hz) | 980 | 1102 | 1347 | 1335 | 1334 | 1038.1 | 856.9 |
| SS 1 | -88.9 | -88.9 | -88.6 | -88.5 | -88.4 | -86.9 | -88.7 |

The fully amorphous dispersions (below 60 wt. % of FFA) additionally display lower intensity spinning sidebands (*ca.* - 88 ppm (figure 6.20) compared with the highest drug loaded dispersions and pure crystalline FFA, which indicates a reduction in chemical shift anisotropy

(CSA), due to a combination of the increased local mobility, and reduced structural ordering of the amorphous form as compared to crystalline [6, 7].

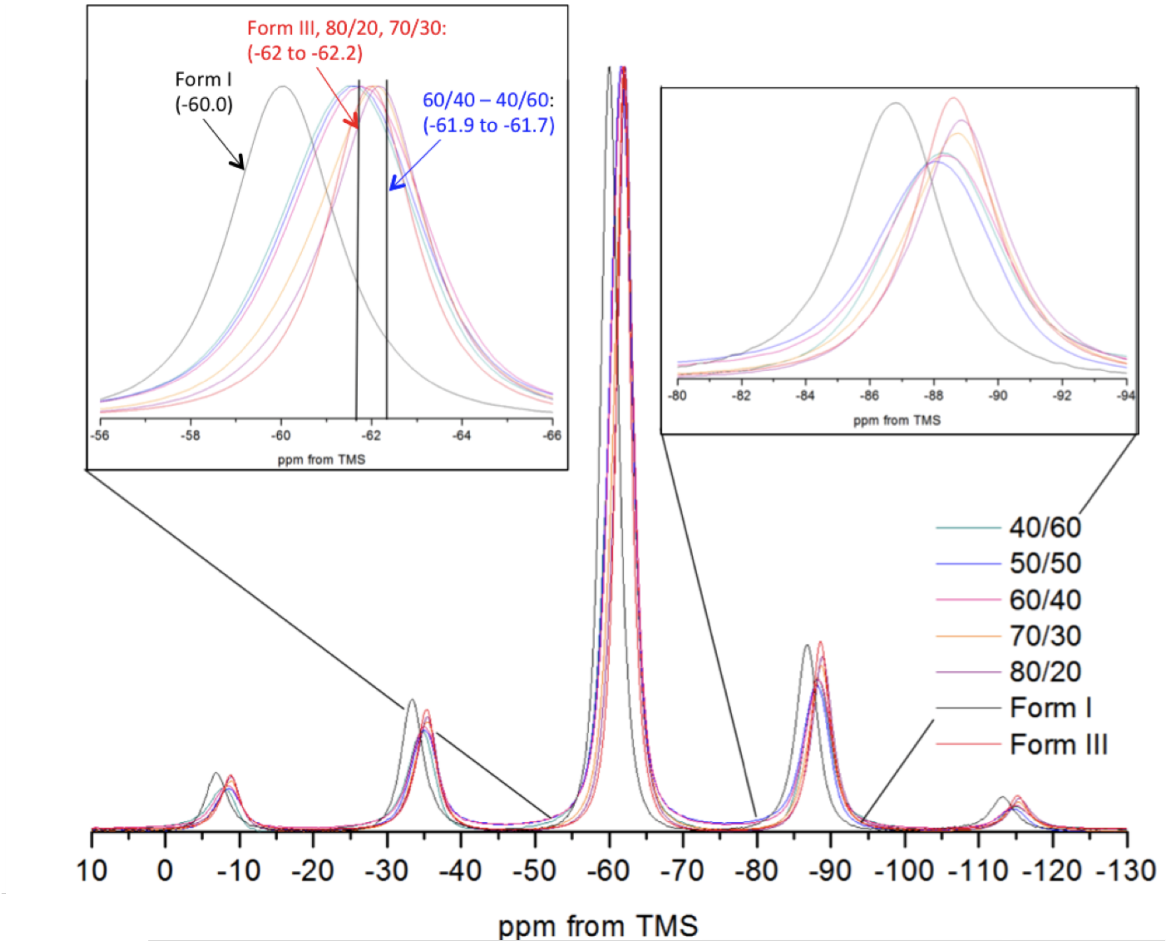


**Figure 6.20:** $^{19}$F MAS NMR spectra of 50/50, 60/40, 70/30 and 80/20 dispersions, with crystalline forms I and III for comparison, recorded at an MAS rate of 10 kHz. Zoomed insets included of the main $^{19}$F peak, and first spinning sideband

## 6.2 Crystalline and Amorphous FFA

### 6.2.1 $^{13}$C and $^{19}$F MAS NMR studies of Crystalline FFA

Upon heating of form I, there were no significant changes to the $^{13}$C or $^{19}$F NMR spectra (figure 6.21), indicating no polymorphic transitions occurred. This is the expected result, as form I is the most stable polymorph at higher temperatures. There was some loss of intensity in the $^{1}$H-$^{13}$C CP/MAS spectra, indicating increased mobility, and a slight change in chemical shift value in the $^{19}$F MAS spectra (-60.1 to -59.8 ppm) with increasing temperature.

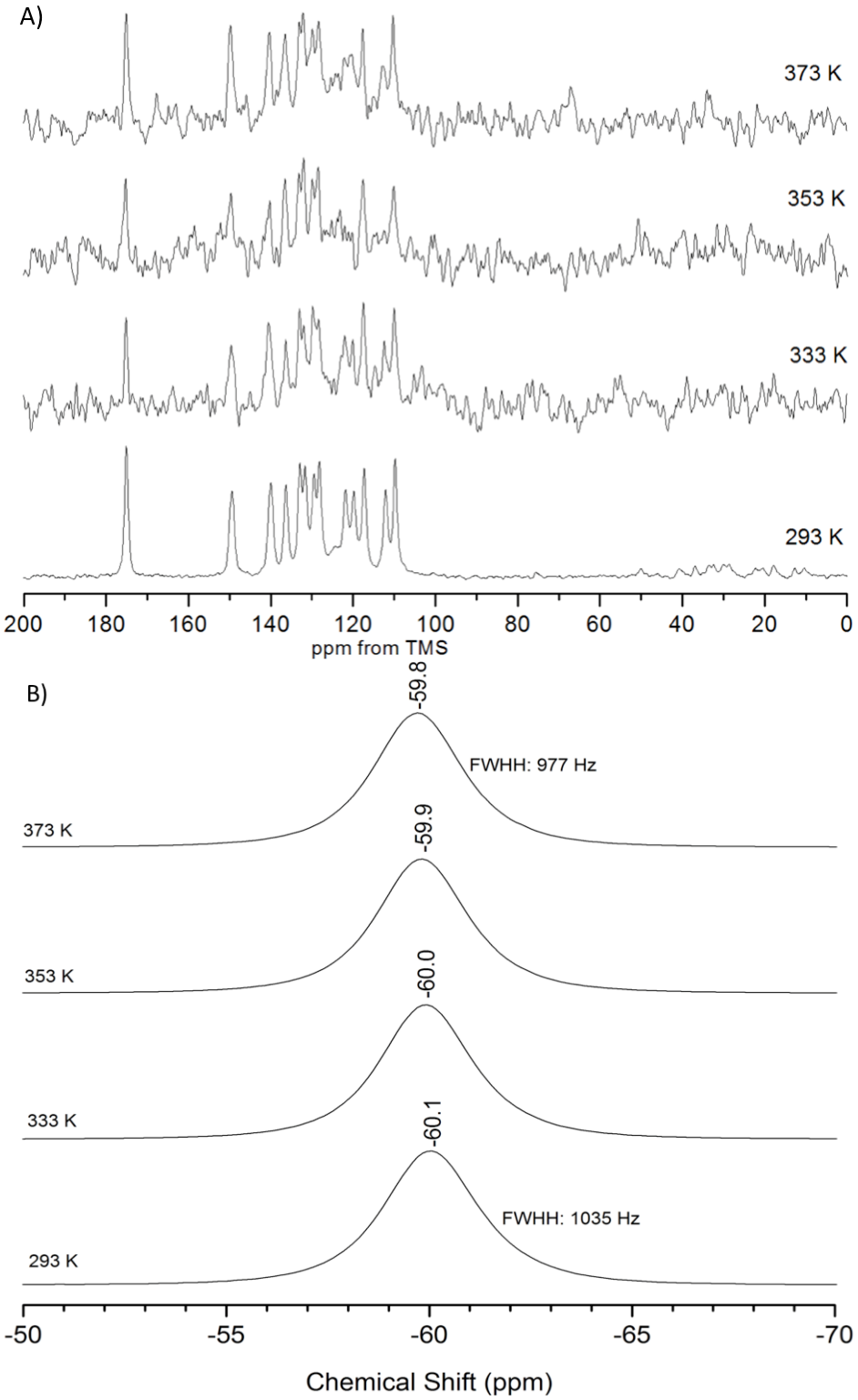


**Figure 6.21:** A) $^{1}$H-$^{13}$C CP/MAS NMR spectra of Form I FFA, heated between 293 and 373 K, at an MAS rate of 10 kHz and B) $^{19}$F MAS NMR spectra of Form I FFA, heated between 293 and 373 K, at an MAS rate of 10 kHz

Upon heating form III FFA, the changes to the $^{1}$H-$^{13}$C CP/MAS NMR and $^{19}$F MAS spectra between 353 and 373 K were consistent with a polymorphic transition to form I FFA (figure 6.22). The $^{13}$C chemical shift values and characteristic peak splitting of each form are very

different (section 6.1.2), therefore it is possible to identify the phase transition temperature between polymorphs; additionally the $^{19}$F chemical shifts of forms I and III differ by *ca.* 2 ppm. Under MAS conditions, form III converted to form I between 353 and 373 K. Upon cooling back to 293 K, the crystalline FFA remained as form I.

Form I and III are well known to be enantiotropic, with a reported transition temperature of 315 K [197]. It has been shown that both forms can occur at the same time under ambient conditions in the solid-state, which is understandable as the free energy and dissolution rate (in water) are very similar below the transition temperature [37, 249].

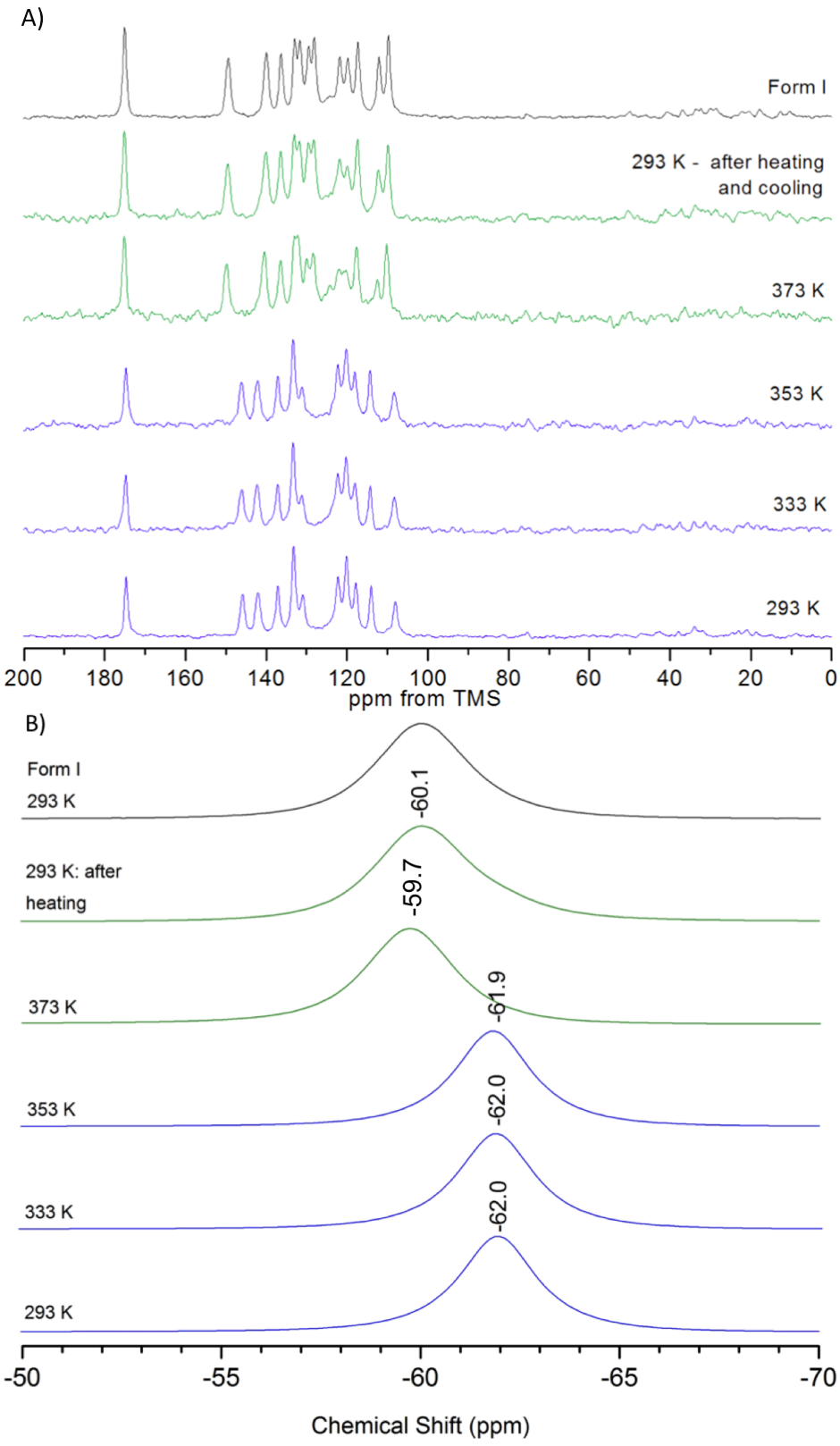


**Figure 6.22:** A) $^{1}$H-$^{13}$C CP/MAS NMR spectra of form III FFA, heated between 293 and 373 K, at an MAS rate of 10 kHz, with form I (293 K) for comparison and B) $^{19}$F MAS NMR spectra of form III FFA, heated between 293 and 373 K, at an MAS rate of 10 kHz, with form I (293 K) for comparison

The transition between forms I and III of FFA has been studied previously using different spectroscopic methods. Gilpin *et al.* [260] applied FT-IR to monitor the conversion of form

III to I, and observed a transition between 358 and 368 K, with a large activation energy of thermal conversion of 212.7 kJ $mol^{-1}$. Hu *et al.* [249] studied the thermodynamic transition between the two polymorphs using *in situ* Raman spectroscopy. The observed transition temperature at 317 K was very close to the originally reported value [197]. To confirm the transition temperature, Van't Hoffs plot of solubility were also constructed, with the solubities of the forms I and III equal at *ca.* 312 K [249]. Hu *et al.* [140] previously studied the transformation kinetics of forms I and III in solution, again with Raman spectroscopy. They determined that in a slurry, rapid conversion from form III to I occurred above the transition temperature, especially at higher temperatures. Upon cooling, the conversion of form I back to III followed much slower kinetics, with forms III and I coexisting for *ca.* 16 hours at 311 K, with full conversion at 298 K after 100 minutes. Li *et al.* [131] further studied the effect of crystal size on the polymorphic transition, and found that larger crystals of form I converted faster to form III, as they had a larger number of surface defects. The slower transformation kinetics of form I $\rightarrow$ form III upon cooling could explain why we did not see the reverse transformation at 293 K under MAS conditions. If left for longer within the rotor, the growth of form III may have become apparent. Additionally, the energy gain from transformation between the polymorphs is low (figure 6.1), therefore under our experimental conditions, it may not have been favourable for the reversible transition to occur.

### 6.2.2 Amorphous Flufenamic Acid

The amorphous drug and amorphous dispersions were analysed using variable temperature solid-state NMR. As discussed previously, there were practically no changes to the $^{1}$H-$^{13}$C CP/MAS spectrum of the polymer alone upon heating.

When amorphous FFA was heated between 253 and 373 K the $^{1}$H-$^{13}$C CP/MAS NMR spectra showed the onset of crystallisation by 273 K, below the $T_g$ of 286 K (figure 6.23). The peaks became narrower and more defined with increasing temperature, and with chemical shifts and peak splitting typical of form I FFA [254]. As with the pure form I at high temperatures, the loss of resolution and signal intensity was observed. This is most probably due to increased mobility.

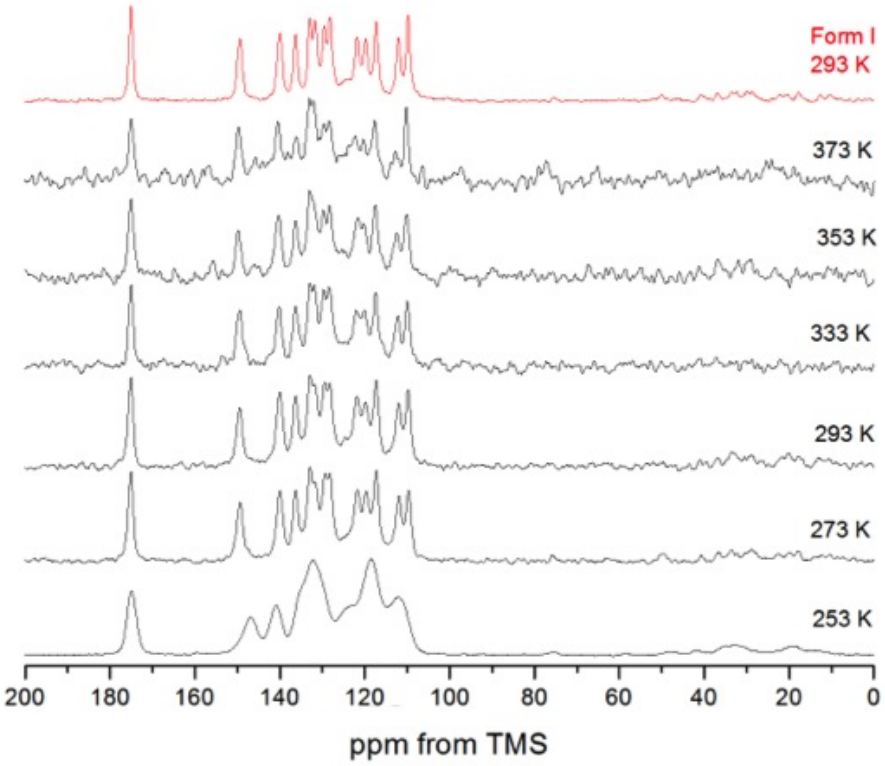


**Figure 6.23:** $^{1}$H-$^{13}$C CP/MAS NMR spectra of amorphous FFA, heated between 253 and 373 K, at an MAS rate of 10 kHz, with Form I (293 K) for comparison

Below the transition temperature, form III would be the expected polymorph to crystallise from the amorphous form, with conversion to form I expected at higher temperatures [255]. However, the possible presence of residual form I seeds formed upon manufacture, may have led to preferential crystallisation over form III. Hu *et al.* [249] demonstrated that rapid crystallisation of form I occurred in the presence of seeds in solution. Therefore, the presence of low quantities of form I within the amorphous sample could favour the transition to form I over form III, as the nucleation sights for crystal growth were already present.

## 6.3 Variable temperature studies of Amorphous FFA/PVP-VA Dispersions

### 6.3.1 Detection of changes in mobility of FFA/PVP-VA dispersions: high drug loaded dispersions

We have extensively characterised dispersions of FFA and PVP-VA, with varying drug/polymer ratios (80 wt. % to 20 wt. %) using a number of variable temperature solid-state NMR techniques, including $^{1}$H-$^{13}$C CP/MAS, $^{13}$C{$^{1}$H} MAS, $^{1}$H MAS and spin-lattice relaxation.

The VT $^{13}$C NMR spectra for FFA/PVP-VA 80/20 dispersion (figure 6.24) illustrates changes

with increasing temperature. At 293 K, the presence of both crystalline (form III) and amorphous FFA (section 6.1.3) can be detected. The $T_g$ of this dispersion is low (293 K), so it is feasible that we observe crystalline FFA at ambient temperatures. With increasing temperature, narrowing of all drug peaks occurred, indicating further crystallisation of the amorphous FFA component to form III. Above 353 K, no polymorphic transition to form I FFA occurred, as would be expected for pure crystalline form III. Additionally, a significant reduction in the intensity of the polymer resonances occurred *ca.* 333 K, with a **complete** loss of CP signal by 373 K, indicating high mobility of both drug and polymer.

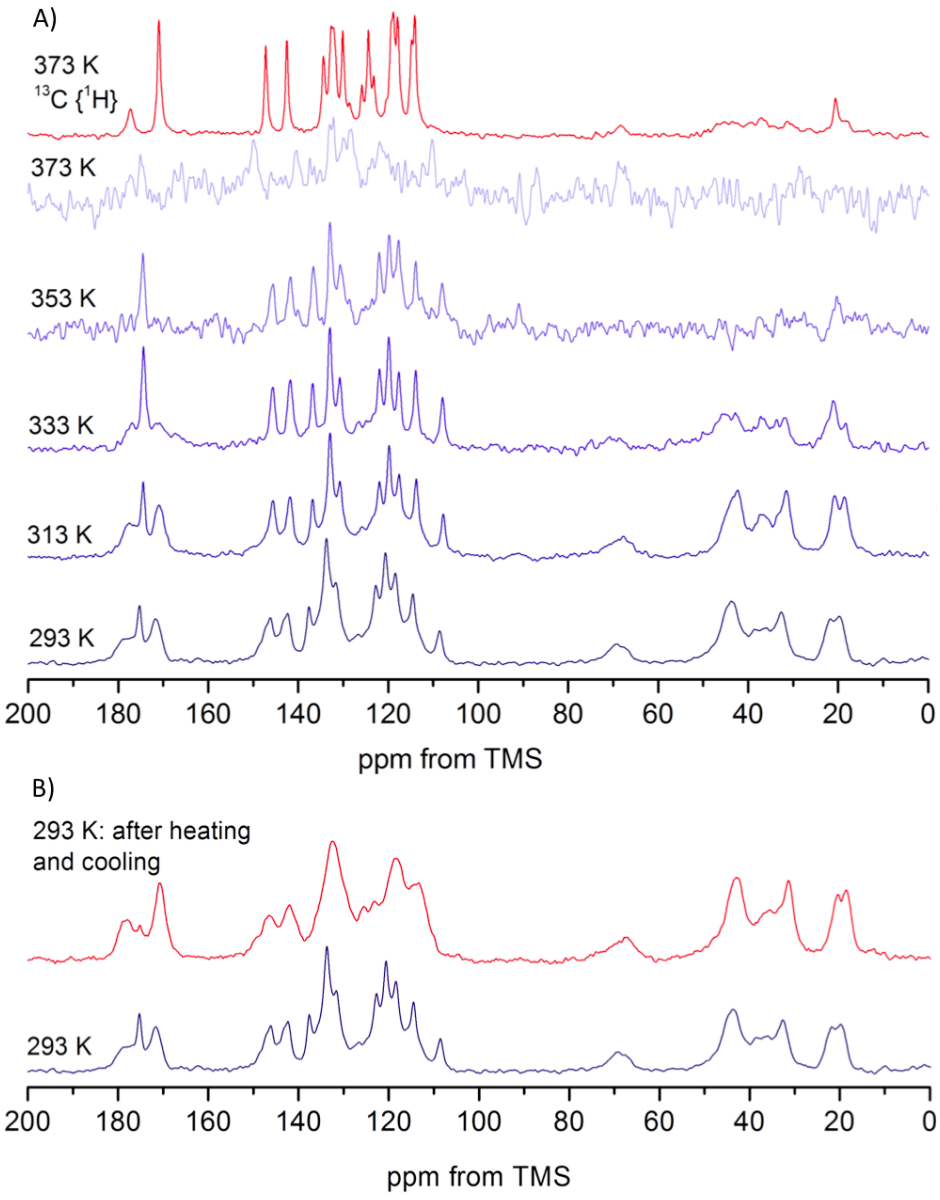


**Figure 6.24:** A) $^{1}$H-$^{13}$C CP/MAS NMR spectra of 80/20 FFA/PVP-VA dispersion (blue) recorded at different temperatures between 293 K and 373 K (MAS rate 10 kHz) and $^{13}$C{$^{1}$H} NMR spectrum at 373 K (red) and B) $^{1}$H-$^{13}$C CP/MAS NMR spectra of 80/20 FFA/PVP-VA dispersion at 293 K, before and after heating to 373 K

The $^{13}$C{$^{1}$H} MAS NMR spectra of FFA/PVP-VA 80/20 at 373 K is completely different as compared to the $^{1}$H-$^{13}$C CP/MAS NMR. Sharp resonances, with chemical shift values

and peak splitting which are not possible to attribute to currently studied polymorphic forms [254, 255], are observed (figure 6.25). Additionally, significantly broadened aliphatic polymer peaks are present, due to increased polymer mobility on an intermediate timescale. However the predominant carbonyl peak at 373 K appears to be related to C-D of PVP-VA.

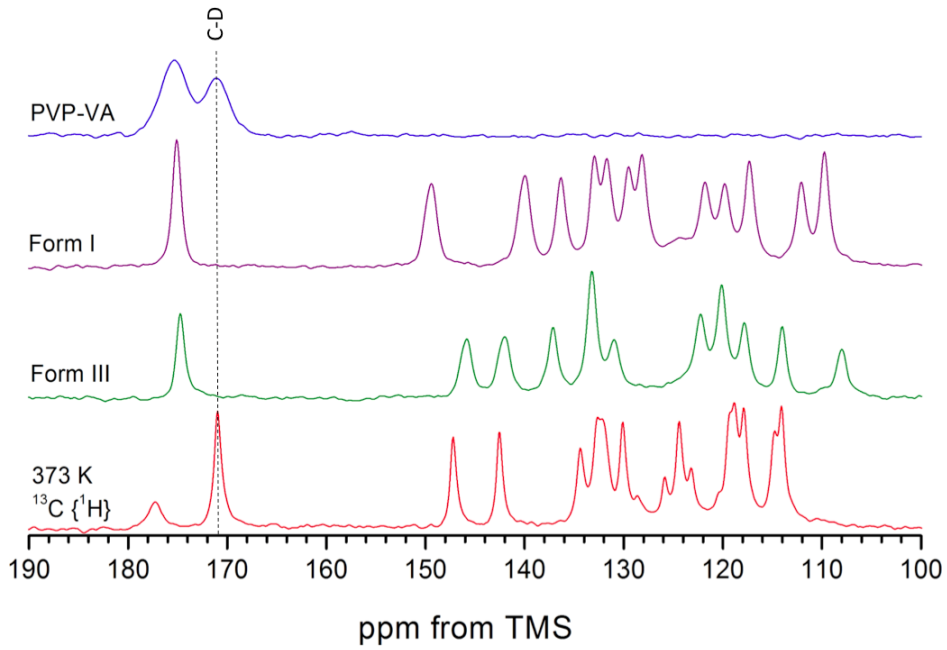


**Figure 6.25:** $^{13}$C{$^{1}$H} MAS NMR spectra of 80/20 dispersion at 373 K (red), with $^{1}$H-$^{13}$C CP/MAS NMR spectra of forms I and III FFA, and PVP-VA provided for comparison, recorded at an MAS rate of 10 kHz

Possible explanations for the observation of line narrowing in $^{13}$C{$^{1}$H} MAS NMR spectra include:

- Line narrowing due to a well defined repeating unit cell as a result of crystallisation to a polymorph not previously characterised with solid-state NMR;
- **OR** line narrowing due to fast mobility, on a timescale faster than 1000 kHz, resulting in the manifestation of isotropic peaks more comparable to a 'liquid-like' state

The presence of a new polymorphic form of FFA can be ruled out, as we would see narrow resonances in **both** the $^{1}$H-$^{13}$C CP/MAS NMR and $^{13}$C{$^{1}$H} MAS NMR spectra respectively. Therefore, the most likely explanation is related to an increased mobility of the FFA component, with both the amorphous and form III FFA phases present before becoming too mobile to detect at high temperatures. The $^{13}$C{$^{1}$H} MAS NMR spectrum at this point clearly indicates a difference in mobility of drug (fast $>$ 1000 kHz) and polymer (intermediate *ca.* 90 kHz).

Upon cooling to 293 K, the presence of drug and polymer was detected with $^{1}$H-$^{13}$C CP/MAS NMR, which highlighted an increased content of the amorphous phase (figure 6.24 B) as compared to the initial ambient temperature characterisation. This indicates that the line

narrowing at high temperatures is a reversible effect. The absence of form III in the dispersion following heating to 373 K could be attributed to the crystalline phase melting, or dissolving in the mobile amorphous and polymer phase, resulting in the presence of predominantly amorphous FFA upon cooling. At high temperature, it is possible we are seeing additional FFA species which are highly soluble and mobile, alongside dissolved amorphous and form III FFA in the polymer phase in the $^{13}C\{^{1}H\}$ MAS NMR spectrum: likely to be small aggregates of pre-nucleation FFA within a viscous polymer 'sea.' These assumptions will be probed further using additional VT solid-state NMR and PXRD methods.

Upon increasing temperature, the 70/30 FFA/PVP-VA dispersion showed behaviour very similar to the 80/20 formulation (figure 6.26). Some further crystallisation of form III was observed at *ca.* 333 K, with the drug and polymer both displaying increased mobility on the intermediate timescale by 353 K, as expected at temperature *ca.* 50 K above the $T_g$. Again, full signal loss in the $^{1}H$-$^{13}C$ CP/MAS NMR spectra occurred by 373 K, with the $^{13}C\{^{1}H\}$ MAS NMR spectrum closely resembling that of the 80/20 dispersion at 373 K. Again, upon cooling back to 293 K, the CP/MAS spectrum showed an increased content of amorphous phase. This indicates the formation of a similar high temperature environment, described for the 80/20 dispersion above.

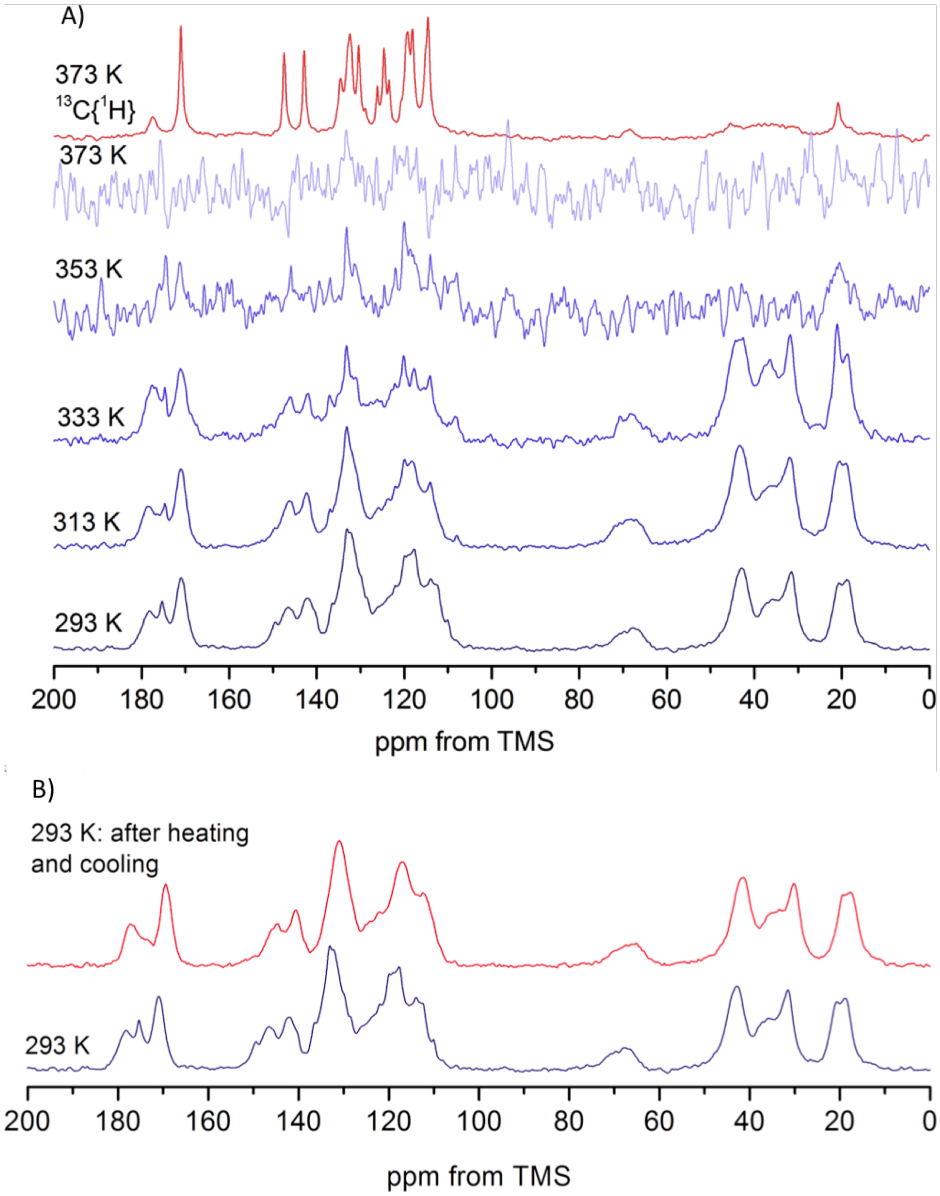


**Figure 6.26:** A) $^{1}$H-$^{13}$C CP/MAS NMR spectra of 70/30 FFA/PVP-VA dispersion (blue) recorded at different temperatures between 293 K and 373 K (MAS rate 10 kHz) and $^{13}$C{$^{1}$H} NMR spectrum at 373 K (red) and B) $^{1}$H-$^{13}$C CP/MAS NMR spectra of 70/30 FFA/PVP-VA dispersion at 293 K, before and after heating to 373 K

The VT $^{13}$C spectra of 60/40, 50/50 and 40/60 FFA/PVP-VA dispersions show similar trends with increasing temperature (figure 6.27 A, B and C). We observe broadening of FFA resonances, followed by broadening of PVP-VA resonances, with complete signal loss in the $^{1}$H-$^{13}$C CP/MAS NMR spectra by 373 K.

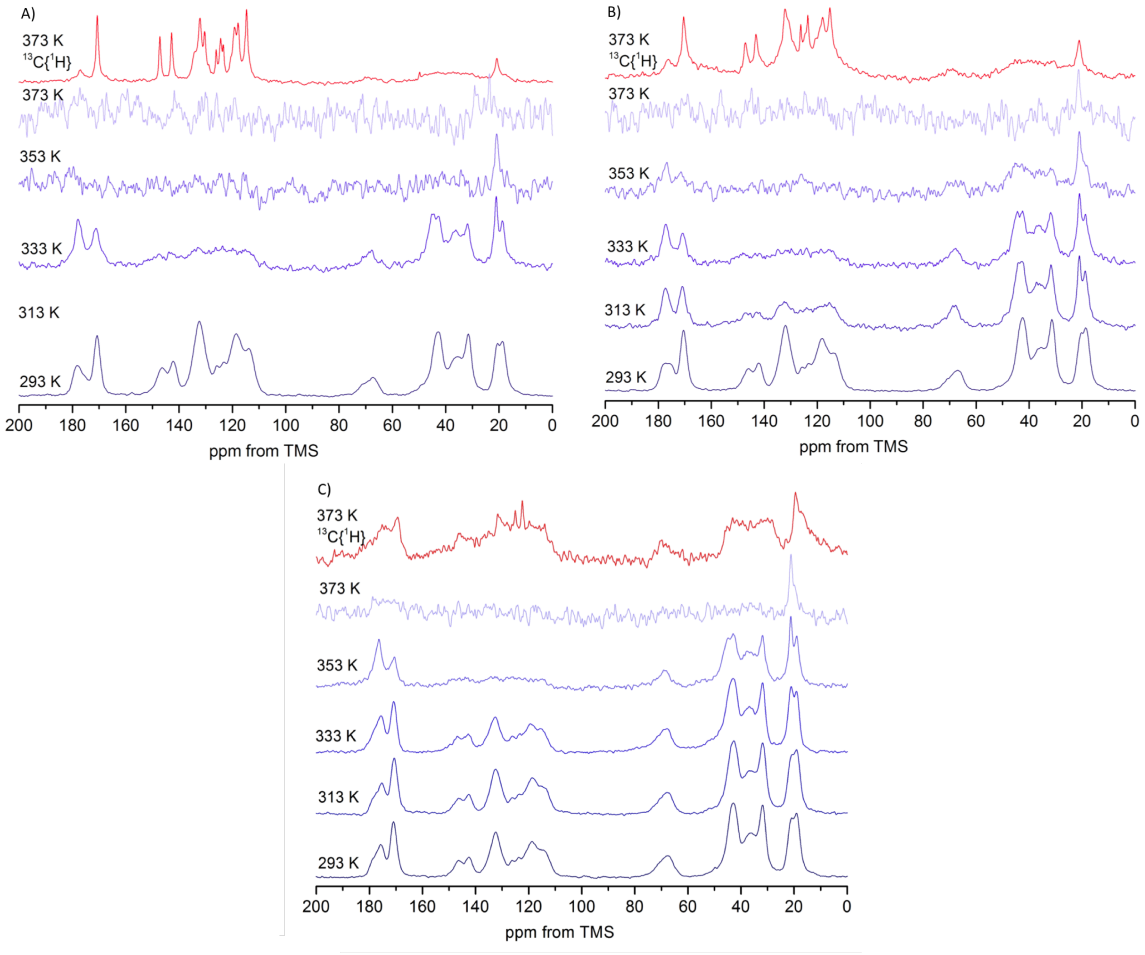


**Figure 6.27:** $^{1}H$-$^{13}C$ CP/MAS NMR spectra of A) 60/40, B) 50/50 and C) 40/60 FFA/PVP-VA dispersion (blue) recorded at different temperatures between 293 K and 373 K (MAS rate 10 kHz) and $^{13}C\{^1H\}$ MAS NMR spectrum at 373 K (red)

The high temperature $^{13}C\{^1H\}$ MAS NMR spectra of the 60/40 and 50/50 dispersions were similar to the spectra of the 80/20 and 70/30 dispersions, with the decoupled spectrum of the 40/60 dispersion showing mostly broad lines at 373 K. However, some peaks *ca.* 131.8, 125.1 and 122.5 ppm were observed, indicating the beginnings of the same high mobility environment described above. The similarity of the high temperature $^{13}C\{^1H\}$ MAS NMR spectra of all five FFA loading levels can be seen in figure 6.28.

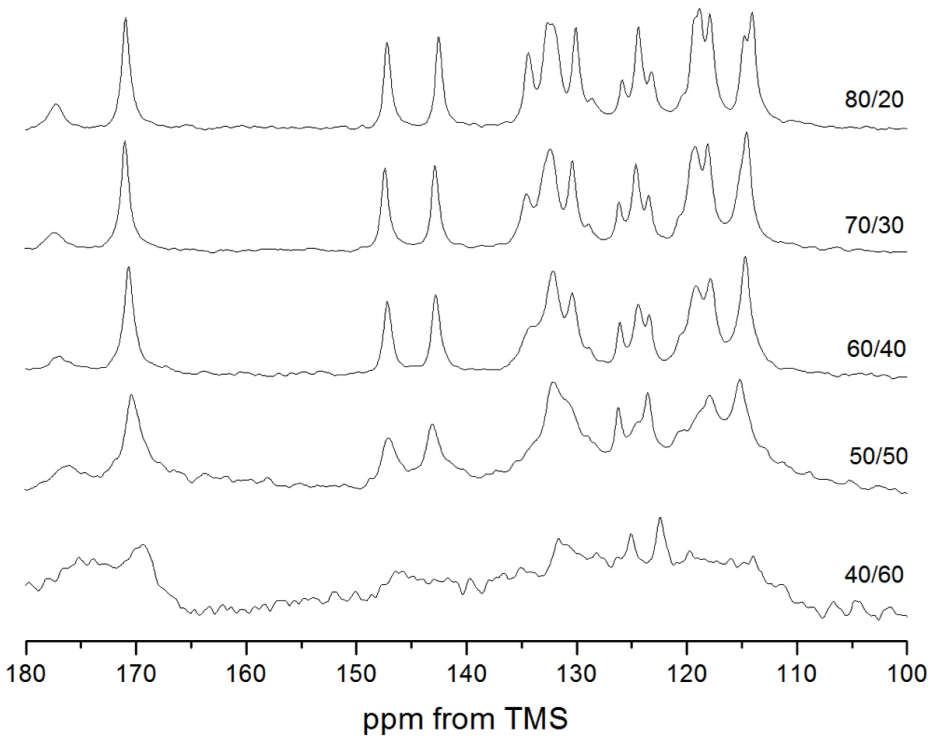


**Figure 6.28:** $^{13}C\{^{1}H\}$ MAS NMR spectra for 40/60, 50/50, 60/40, 70/30 and 80/20 FFA/PVP-VA dispersions recorded at 373 K, with an MAS rate of 10 kHz

### 6.3.2 Detection of changes in mobility of FFA/PVP-VA dispersions: low drug loaded dispersion

The VT $^{13}C$ NMR spectra for FFA/PVP-VA 20/80 dispersion (figure 6.29) show a loss of signal intensity of the FFA peaks with increasing temperature up to 373 K. This effect was especially pronounced above the $T_g$ of 353 K. At 373 K, FFA peaks were broadened significantly in both the $^{1}H$-$^{13}C$ CP/MAS and $^{13}C\{^{1}H\}$ MAS NMR spectra indicating mobility on the intermediate timescale, in comparison to the much faster mobility observed for dispersions of $\geq$ 40 wt. % drug loading. There was little change in the polymer peaks on heating, indicating its lower mobility in comparison to the drug on the observed timescale.

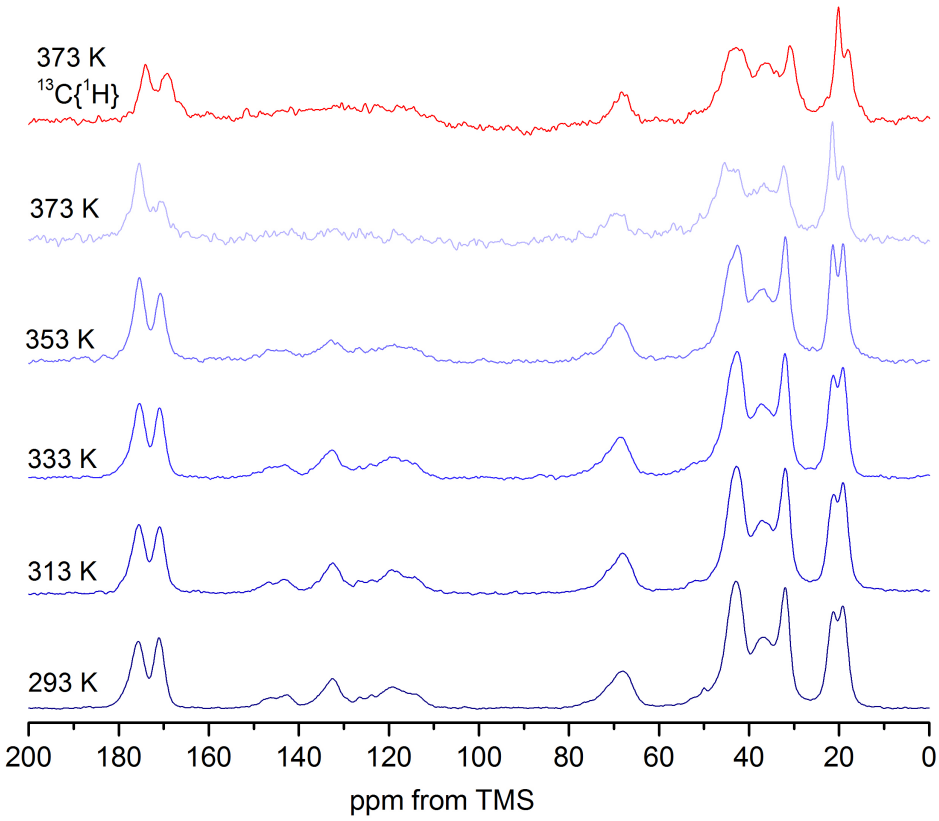


**Figure 6.29:** $^1$H-$^{13}$C CP/MAS NMR spectra of 20/80 FFA/PVP-VA dispersion (blue) recorded at different temperatures between 293 K and 373 K (MAS rate 10 kHz) and $^{13}C\{^1H\}$ spectrum at 373 K (red)

### 6.3.3 Comparison of the high temperature $^{13}C\{^1H\}$ MAS NMR with solution-state NMR

To explore the possibility of the presence of a 'liquid-like' environment at 373 K, the $^{13}C\{^1H\}$ MAS NMR spectra of the dispersions were compared to the $^{13}C$ NMR solution-state spectrum of FFA in $CD_3OD$ (figure 6.30 and table 6.7). It can be seen that the spread of the carbon resonances in the high temperature $^{13}C\{^1H\}$ spectra for each dispersion match closely with those in the solution-state, with $\Delta\delta$ values of less than 1 ppm. This suggests that at high temperature the mobility of the dispersions tends towards a highly mobile, 'liquid-like' environment. Although the FWHH of the solid-state resonances at 373 K are small compared to the lower temperature peaks, they are still much broader than those observed in solution-state spectra. The 'liquid-like' environment described in the solid-state is therefore likely to be of much higher viscosity as compared to a fully isotropic solution.

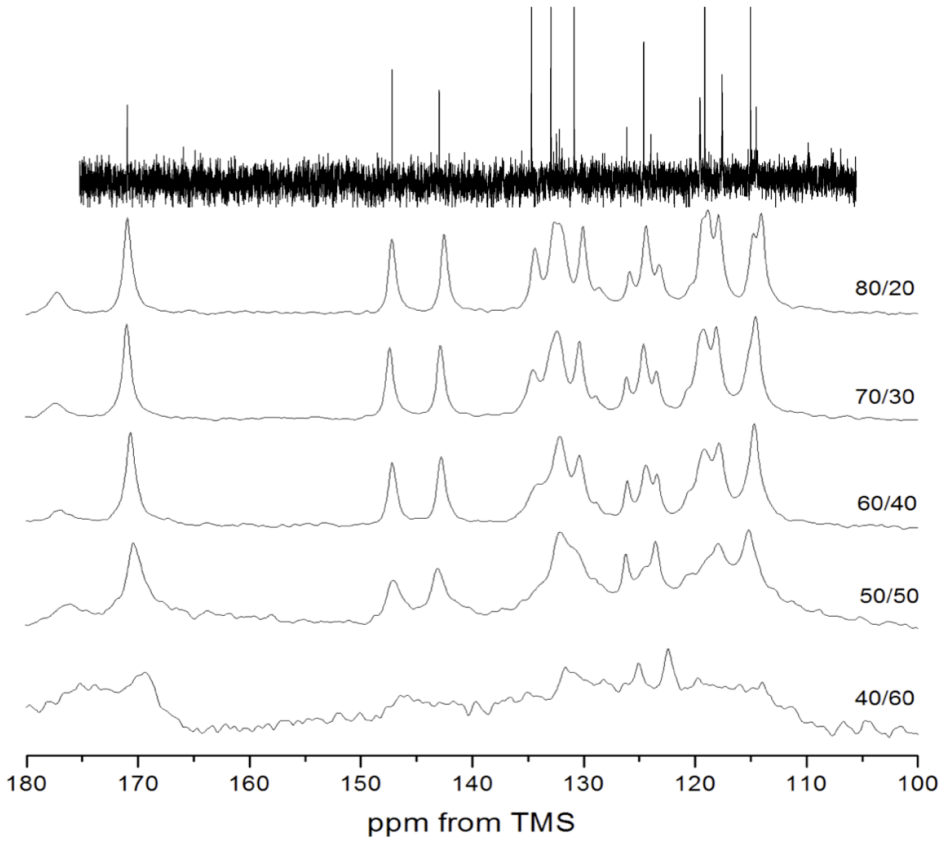


**Figure 6.30:** $^{13}C\{^{1}H\}$ MAS NMR for 40/60, 50/50, 60/40, 70/30 and 80/20 dispersions recorded at 373 K, with an MAS rate of 10 kHz, 400 MHz; compared to the solution-state $^{13}C$ spectrum of FFA 0.05 M in $CD_3OD$ recorded at 500 MHz

**Table 6.7:** $^{13}C$ Chemical Shift Assignment comparison of FFA in $CH_3OD$ (0.05 M) at 293 K and $^{13}C\{^{1}H\}$ MAS NMR of the 80/20 dispersion at 373 K [40]

| $^{13}C$ | Solution-state | 80/20 | $\Delta\delta$ (ppm) |
|---|---|---|---|
| 1 | 171.8 | 171.5 | 0.3 |
| 2 | 148.0 | 147.7 | 0.3 |
| 3 | 143.7 | 143.1 | 0.6 |
| 4 | 135.4 | 134.9 | 0.5 |
| 5 | 133.6 | 133.1 | 0.5 |
| 6 | 133.0 | 132.1 | 0.9 |
| 14 | 131.5 | 130.6 | 0.9 |
| 7 | 125.3 | 124.9 | 0.4 |
| 8 | 124.6 | 123.7 | 0.9 |
| 9 | 120.2 | 119.7 | 0.7 |
| 11 | 119.8 | 119.3 | 0.5 |
| 10 | 118.4 | 118.4 | 0 |
| 12 | 115.7 | 115.2 | 0.5 |
| 13 | 115.1 | 114.6 | 0.5 |

### 6.3.4 Probing the mobility of FFA/PVP-VA dispersions using $^{1}$H MAS NMR Studies

To further investigate the mobility of the FFA/PVPVA dispersions at high temperatures, VT $^{1}$H NMR studies were carried out. $^{1}$H solid-state NMR is very sensitive to faster molecular motions, and therefore provides additional understanding of the VT $^{13}$C MAS NMR.

At ambient temperature, we can distinguish the drug and polymer components of the dispersions with more than 40 wt. % drug loading in the $^{1}$H MAS NMR spectra, as two broad peaks are seen with resonances *ca.* 7.2 ppm (FFA) and *ca.* 1.5 ppm (PVP-VA). The $^{1}$H spectrum of the 20/80 dispersion is dominated by the polymer, with one broad peak at *ca.* 2.8 ppm (figure 6.31).

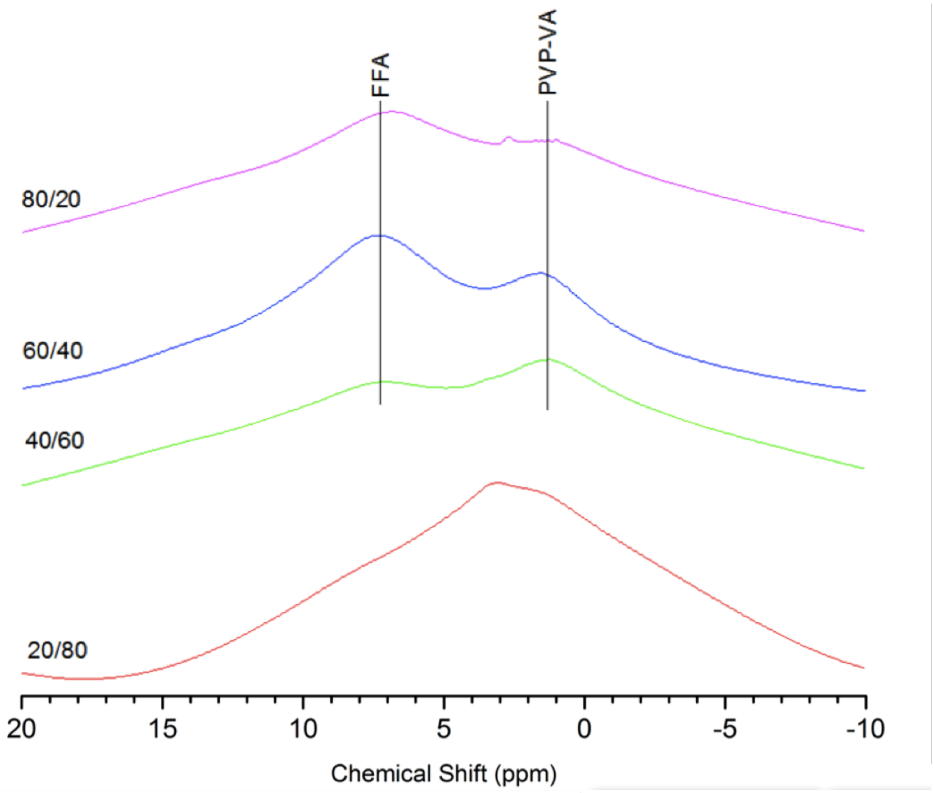


**Figure 6.31:** $^{1}$H MAS NMR spectra for 20/80, 40/60, 60/40 and 80/20 FFA/PVP-VA dispersions at 293 K, measured at an MAS rate of 10 kHz. Highlighted FFA $^{1}$H peak = 7.2 ppm; PVP-VA = 1.6 ppm (80/20, 60/40 and 40/60 FFA/PVP-VA dispersions); 20/80, broad peak = 3.1 ppm

The VT $^{1}$H MAS spectra (figure 6.32) show differences in line widths as a function of temperature and drug loading level. With higher FFA content, resonances become narrower with increasing temperature indicating significantly enhanced mobility, which is especially pronounced at 373 K.

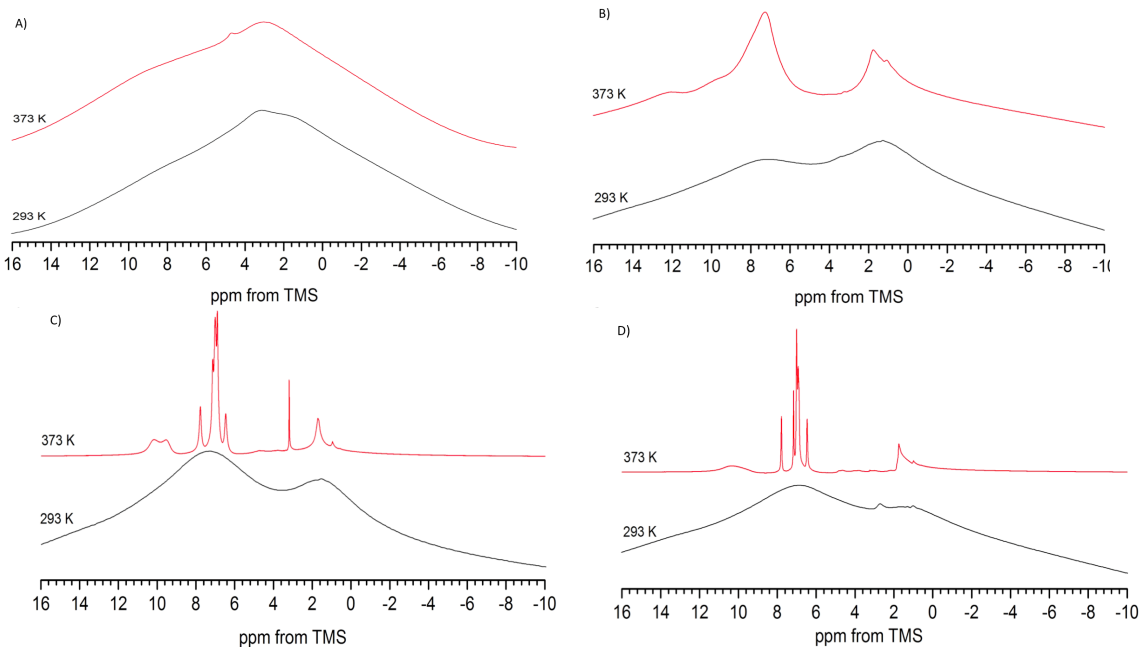


**Figure 6.32:** Variable temperature $^{1}$H MAS NMR spectra for A) 20/80, B) 40/60, C) 60/40 and D) 80/20 FFA/PVP-VA dispersions, measured at an MAS rate of 10 kHz, between 293 and 373 K

The sharply resolved peaks of the higher drug loading dispersions at 373 K are comparable to the solution-state $^{1}$H resonances of FFA, shown in figure 6.34. We can just observe the presence of the polymer in the solid-state at *ca.* 1.9 ppm. At 373 K, broader peaks were observed for the 60/40 dispersion, indicating slightly lower mobility in comparison to the 70/30 and 80/20 dispersions (figure 6.33). Additionally, a peak at *ca.* 9.7 ppm is distinguishable in the high temperature spectra of the 70/30 and 80/20 dispersions, which indicates the presence of hydrogen bonding. The solution state $^{1}$H spectra of the dispersions and FFA alone (dissolved in $CD_3OD$ at 0.05 M) allowed full assignment of FFA protons. There were no downfield peaks ($>$ 10 ppm), so no hydrogen bonding of the carbonyl group was obvious from our solution-state spectra. Munro *et al.* also reported the absence of a hydrogen-bonding resonance for the -COOH proton of FFA dissolved in $CDCl_3$, but observed a downfield peak at *ca.* 13 ppm for FFA dissolved in DMSO-$d_6$ [40], indicating a solvent dependent difference in interactions between FFA molecules in solution.

Figures 6.33 and 6.34 indicate the similarity in peak position for the dispersions at 373 K. The broader peaks observed at lower drug content indicates slightly lower mobility at high temperatures.

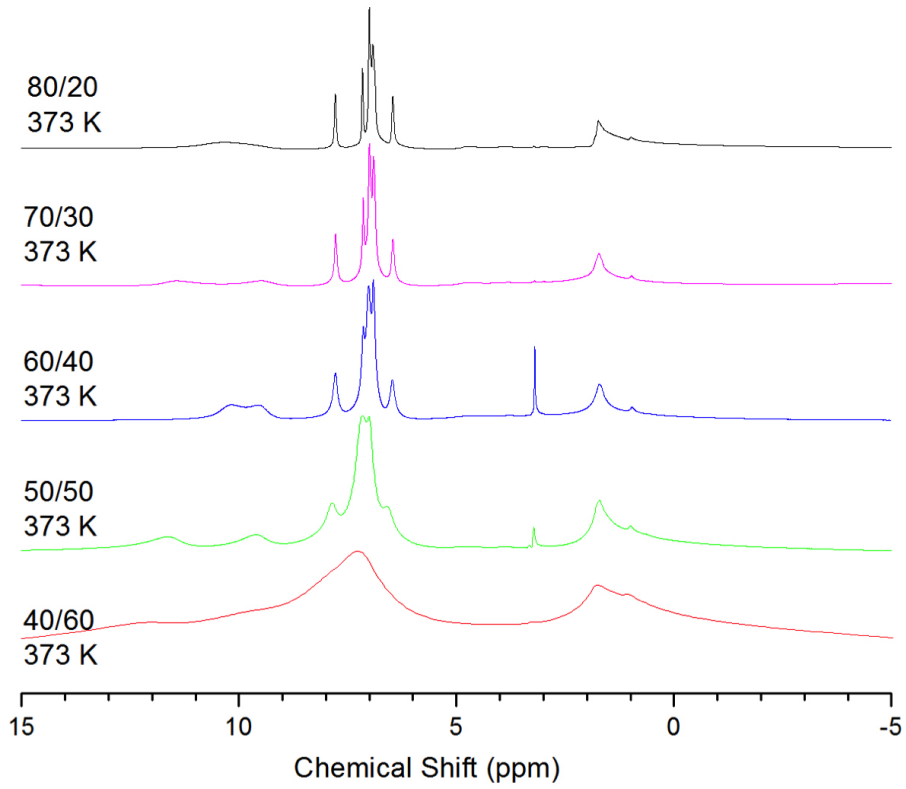


**Figure 6.33:** $^{1}$H MAS NMR spectra for different FFA/PVP-VA dispersions, measured at an MAS rate of 10 kHz at 373 K

In dispersions with the highest drug loading, we observe the same general separation of five $^{1}$H environments as in the solution-state. Assignments of protons 'A' and 'H' were straightforward, with more tentative assignment of 'B,C,D', 'E' and 'F,G' groups made based on the solution state $^{1}$H spectra. Due to the high molecular weight of the polymer, the solution-state resonances were significantly broadened in comparison to the small molecule FFA.

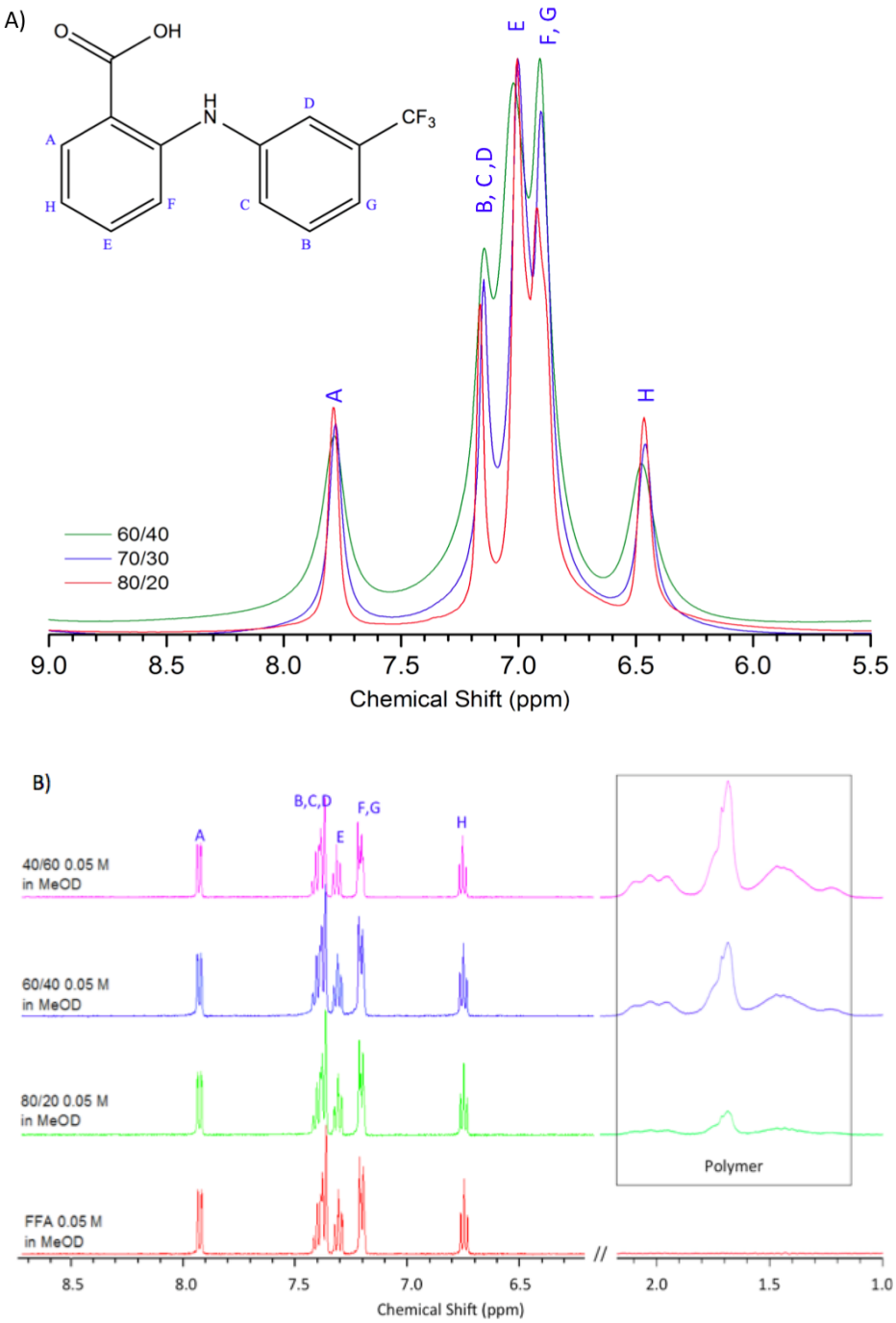


**Figure 6.34:** A) High temperature (373 K) $^{1}$H MAS NMR spectra for 80/20, 70/30 and 60/40 FFA/PVP-VA dispersions (MAS = 10 kHz) with proton chemical shift assignment, B) Solution-state $^{1}$H spectra for different FFA/PVP-VA dispersions and FFA alone dissolved in $CD_3OD$ (0.05 M)

**Table 6.8:** Comparison between $^{1}$H chemical shift values measured in solution and solid state

| $^{1}$**H** | $\delta$ **(ppm) solution-state** | $\delta$ **(ppm) solid-state (80/20)** |
|---|---|---|
| A | 7.94 | 7.78 |
| B | 7.41 | 7.15 |
| C | 7.39 | |
| D | 7.37 | |
| E | 7.32 | 7.00 |
| F | 7.22 | 6.90 |
| G | 7.21 | |
| H | 6.76 | 6.45 |
| Polymer | 2.33-1.45 | 1.7 |

The VT $^{1}$H MAS NMR spectra therefore indicate the presence of a highly mobile 'liquid-like' state at 373 K. The presence of additional FFA polymorphs would be observed in $^{1}$H MAS spectra as much broader peaks. This provides further evidence to support the hypothesis that the dispersions form a highly mobile viscous 'paste' at high temperatures, as discussed in section 6.3.1.

### 6.3.5 Probing the mobility of FFA in FFA/PVP-VA dispersions using $^{19}$F MAS NMR Studies

VT $^{19}$F MAS NMR was applied to elucidate the high temperature mobility behaviour of the FFA/PVP-VA dispersions by focusing solely on the drug component without complication from overlapping polymer signals. Changes to chemical shift, FWHH and spinning sidebands were analysed for the 80/20 - 40/60 dispersions across a range of temperatures from 293 to 373 K.

From figure 6.35 two main changes to the $^{19}$F MAS NMR spectra are apparent with increasing temperature. We see a reduction in both FWHH, as peaks narrowed dramatically with increasing temperature; and spinning sideband intensity for all dispersions, both of which indicate increased mobility within the dispersions.

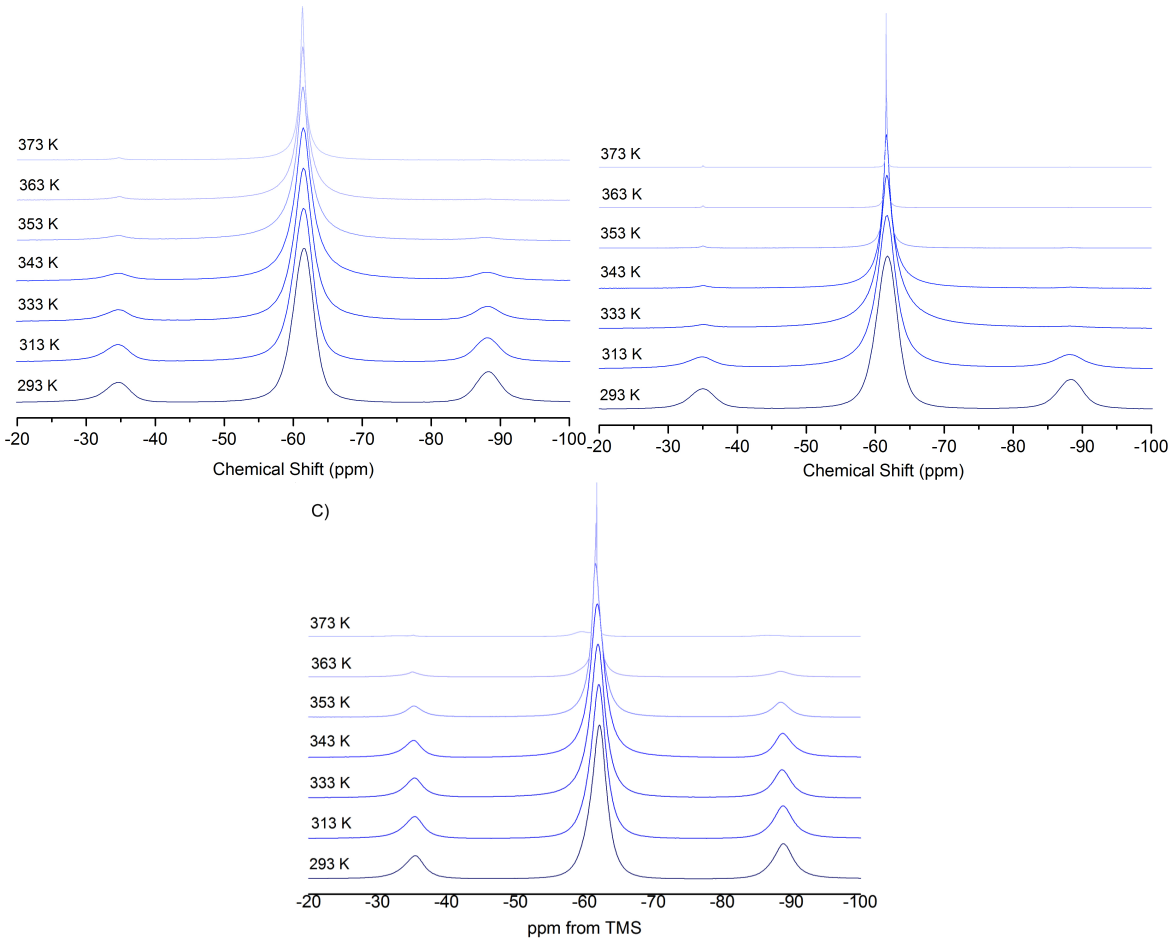


**Figure 6.35:** Variable temperature $^{19}$F MAS NMR spectra for A) 40/60, B) 60/40 and C) 80/20 FFA/PVP-VA dispersions, measured at an MAS rate of 10 kHz, between 293 and 373 K. Spectra are displayed between -20 and -100 ppm to highlight the main isotropic peak, and the two main spinning sidebands

A closer inspection of the $^{19}$F MAS NMR spectra (figure 6.36) indicates further changes to the dispersions dependent on drug loading levels. As with the VT $^{1}$H MAS NMR, the effect was less pronounced with the 40/60 dispersion. Additionally, there was also an upfield shift of the isotropic peak positions, which again was more pronounced for the higher drug loading dispersions (figure 6.38), although this could be due to temperature related changes to chemical shifts, instead of changes to the material properties.

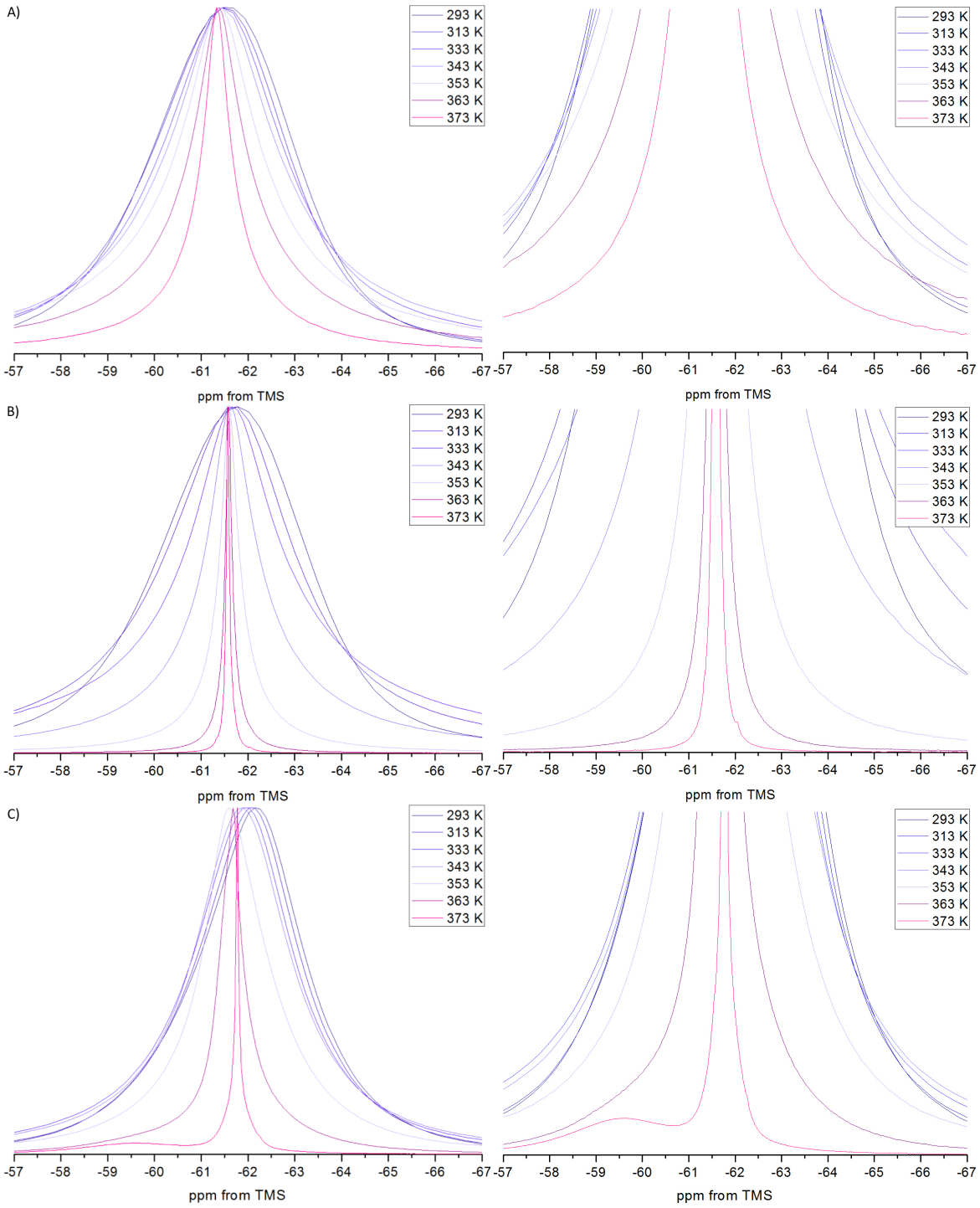


**Figure 6.36:** Variable temperature $^{19}$F MAS spectra for the A) 40/60, B) 60/40 and C) 80/20 dispersions recorded between 293 and 373 K at an MAS rate of 10 kHz. Spectra are displayed between -57 and -67 ppm to highlight the main isotropic peak

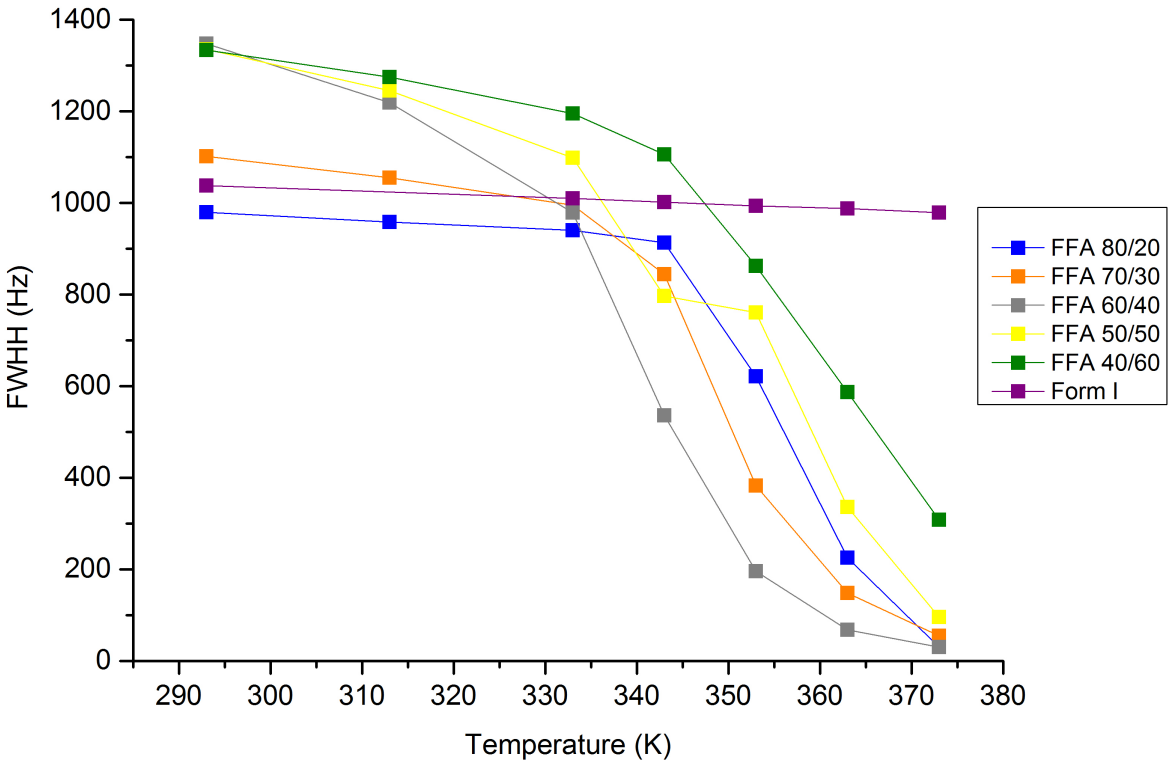


**Figure 6.37:** FWHH of VT $^{19}$F MAS NMR spectra between 293 and 373 K for the 40/60 to 80/20 FFA/PVP-VA dispersions, with form I FFA as a comparison

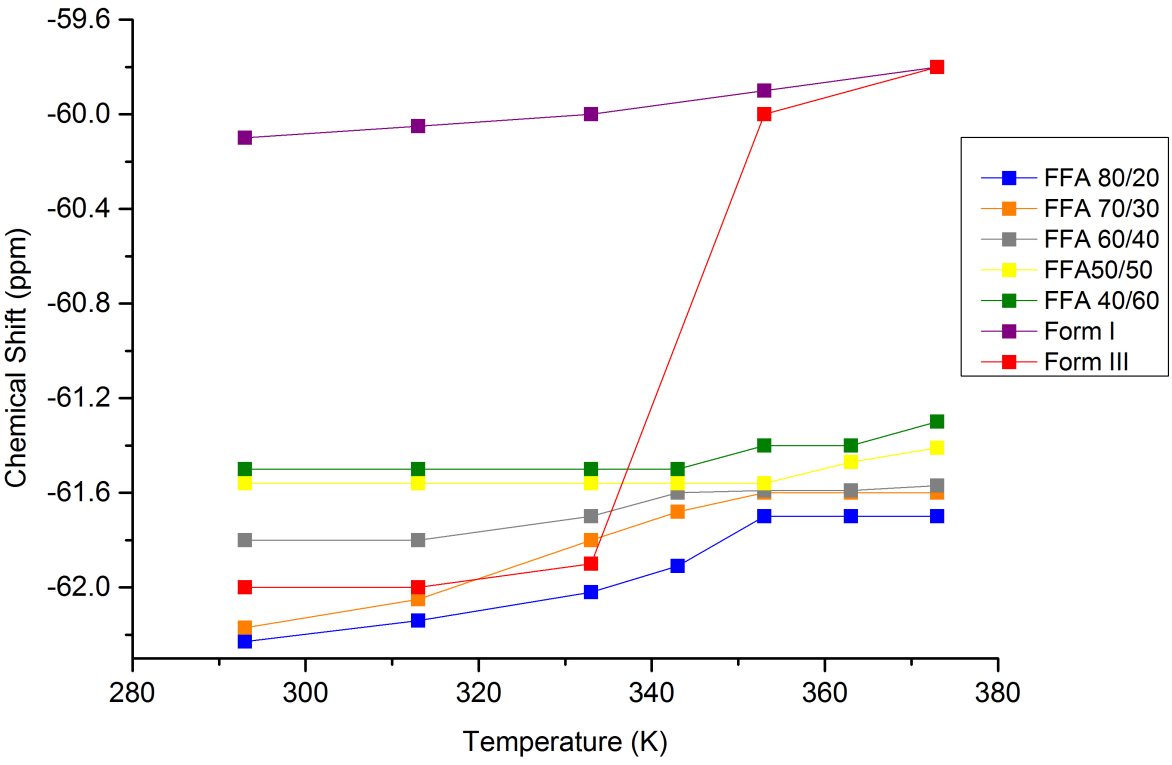


**Figure 6.38:** Chemical Shift values (ppm) of VT $^{19}$F MAS NMR spectra between 293 and 373 K for the 40/60 to 80/20 FFA/PVP-VA dispersions

For the highest loaded dispersions (70/30 and 80/20 w/w), a low intensity $^{19}$F shoulder peak was observed at 373 K, with chemical shift values of *ca.* -59.6 ppm (figure 6.39), which are

comparable to the chemical shift of pure form I at -59.8 ppm. This indicates the presence of two *inequivalent* -$CF_3$ environments: 1) the bulk highly mobile phase, consisting of dissolved FFA in a viscous polymer paste (main isotropic peak); and 2) a small amount of FFA form I, formed through the conversion of residual form III upon heating (shoulder peak). The $^{19}$F $T_1$ relaxation (section 6.5.1 below), show the shoulder peak to have a much longer ${T_1}^F$ time in both the 70/30 and 80/20 dispersions, which is consistent with these assignments. Both dispersions were found to contain form III FFA upon initial characterisation, therefore crystallisation from form III to form I would be thermodynamically favourable, as form I is the more stable polymorph at higher temperatures.

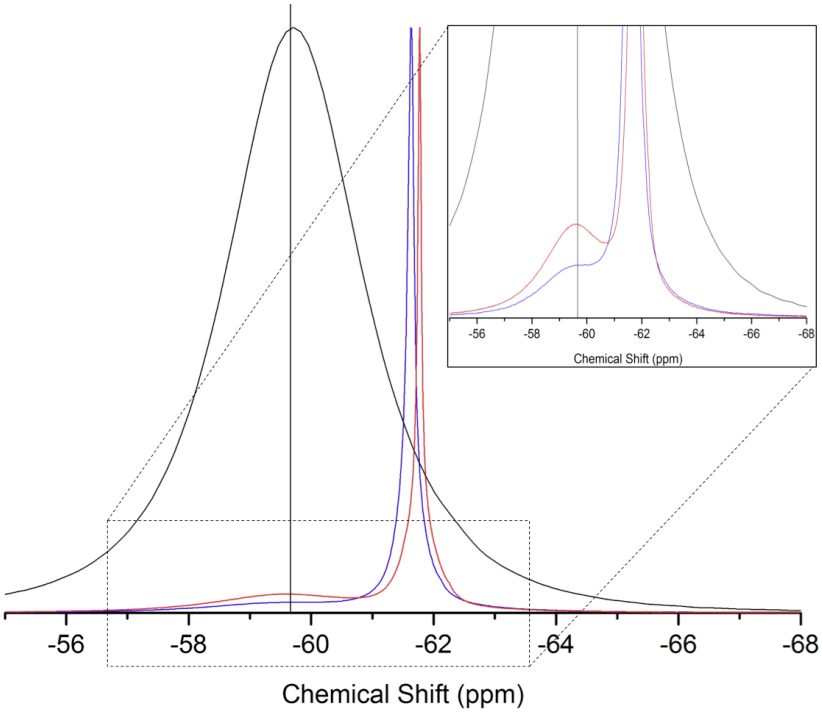


**Figure 6.39:** $^{19}$F MAS NMR spectra for 80/20 (red), 70/30 (blue) and form I FFA (black) recorded at 373 K (MAS = 10 kHz)

Figure 6.40 shows the $^{19}$F MAS NMR spectra for the 80/20 and 70/30 dispersions recorded at 293 K before and after heating to 373 K. Upon cooling, the asymmetrical peaks indicate the presence of two inequivalent $^{19}$F environments in both dispersions, at similar chemical shift values to at 373 K (figure 6.41). These two peaks can be assigned to: 1) amorphous FFA, assigned to the peak at *ca.* -62 ppm, and 2) form I FFA, assigned to the peak at *ca.* -60 ppm. The 70/30 dispersion contains a smaller quantity of crystalline form I FFA than the 80/20 dispersion, following heating. This difference is also reiterated in section 6.5.1, where different relaxation times were calculated for each component of the asymmetrical peaks the 70/30 and 80/20 dispersions, after the heating and cooling cycle. There was no change to the spectra of the 60/40, 50/50 and 40/60 dispersions recorded at 293 K, before and after heating.

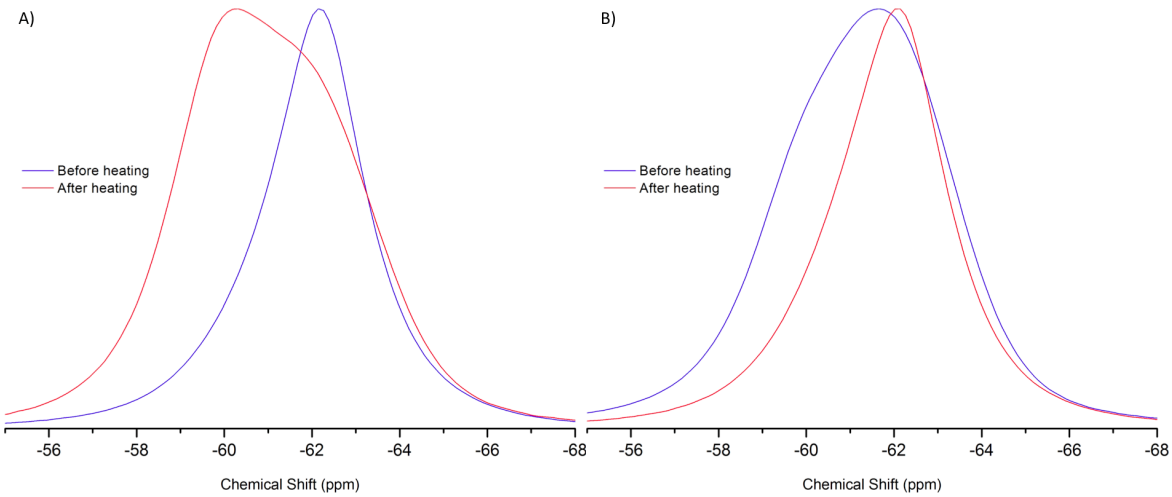


**Figure 6.40:** $^{19}$F MAS spectra of A) 80/20 and B) 70/30 dispersions recorded at 293 K, before and after heating to 373 K, at an MAS rate of 10 kHz

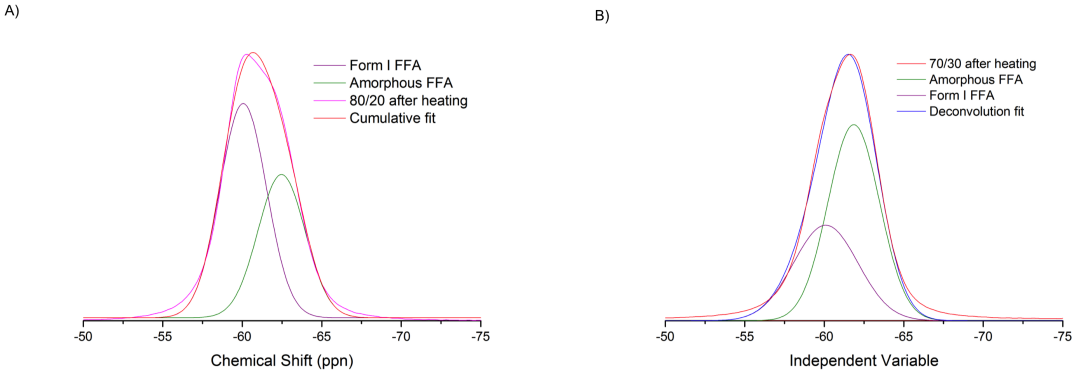


**Figure 6.41:** Gaussian fit deconvolution of the $^{19}$F MAS spectra of A) 80/20 ($R^2 = 0.957$) and B) 70/30 ($R^2 = 0.954$) dispersions recorded at 293 K after heating to 373 K

The VT $^{19}$F analysis of the dispersions helped to clarify two main points. Firstly that the dispersion is highly mobile at high temperatures, which is in agreement with the VT $^{1}$H MAS, and $^{13}$C{$^{1}$H} MAS NMR. Secondly, $^{19}$F MAS was sensitive enough to distinguish two different fluorine environments at 373 K, which remained upon cooling. This likely indicates the permanent presence of crystalline component following heating and cooling in the 70/30 and 80/20 FFA/PVP-VA dispersions, which was not detectable using VT $^{13}$C MAS NMR. Combined, the VT NMR of the three different nuclei become a powerful 'toolkit' for further understanding of the behaviour of the dispersions with increasing temperature.

## 6.4 Clarification of high temperature crystallisation of FFA in high drug loading dispersions with VT PXRD

To help further clarify the crystallisation behaviour of the higher drug loaded dispersions at high temperatures observed in the VT $^{19}$F MAS NMR (form III → form I), the FFA/PVPVA

dispersions were monitored using VT PXRD between 293 and 373 K, at 20 K intervals.

Both the 70/30 and 80/20 dispersions were found to contain a mixture of form III and amorphous FFA at ambient temperatures. Figure 6.42 illustrates the PXRD patterns for the 80/20 dispersion with increasing temperature. After storage at 373 K for *ca.* 30 minutes, peaks corresponding to form I FFA could be identified, with form III peaks reducing in intensity, indicating the polymorphic transition between forms III and I. This occurred at much higher temperatures than the expected literature value of 315 K [197], but is in agreement with the transition we observed upon heating pure form III FFA *in situ* in the NMR rotor, and the temperature of transition determined in the highest loaded dispersions with VT $^{19}$F MAS NMR. Upon cooling back to ambient temperatures, the enantiotropic mixture of forms I and III remained in the 80/20 dispersion.

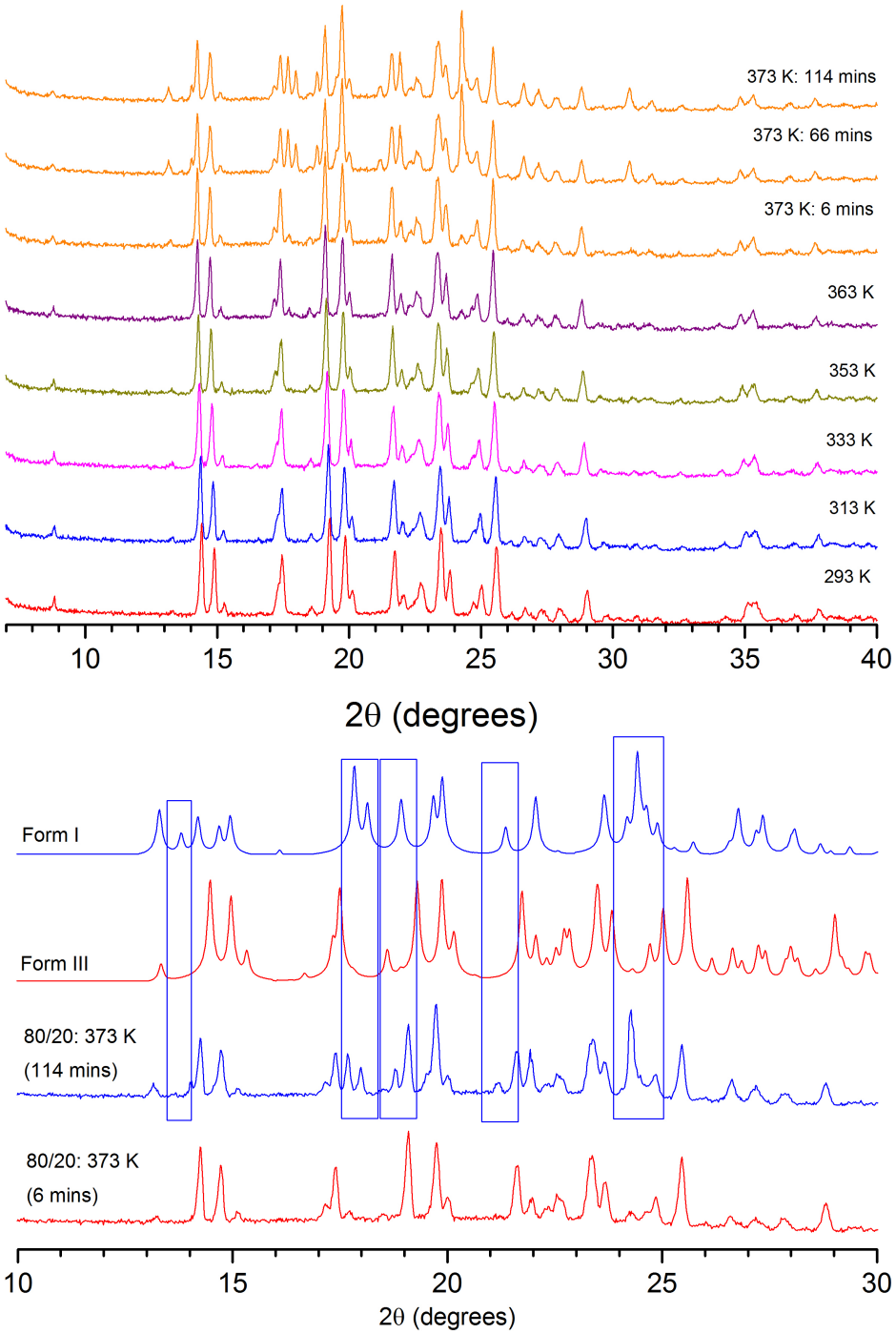


**Figure 6.42:** A) VT PXRD patterns of 80/20 dispersion, recorded between 293 and 373 K in 20 K increments, holding each sample at temperature for 114 minutes and B) Zoomed PXRD patterns of 80/20 dispersion at 373 K, with comparison to pure forms I and III. The conversion to form I is highlighted in blue

Figure 6.43 A) shows the PXRD patterns of the 70/30 dispersion with increasing temperature. When held at 373 K, the growth of new peaks can be clearly seen. After around 40 minutes at 373 K, three main peaks *ca.* 6.9, 14.0 and 21.2 °$2\theta$ greatly increase in intensity compared to the remaining peaks, attributed to the growth of form I. When compared to the 80/20 dispersion after annealing at 373 K (figure 6.43 B), both forms I and III can also be identified in the 70/30 dispersion, with the patterns of each dispersion

displaying peaks in similar positions.

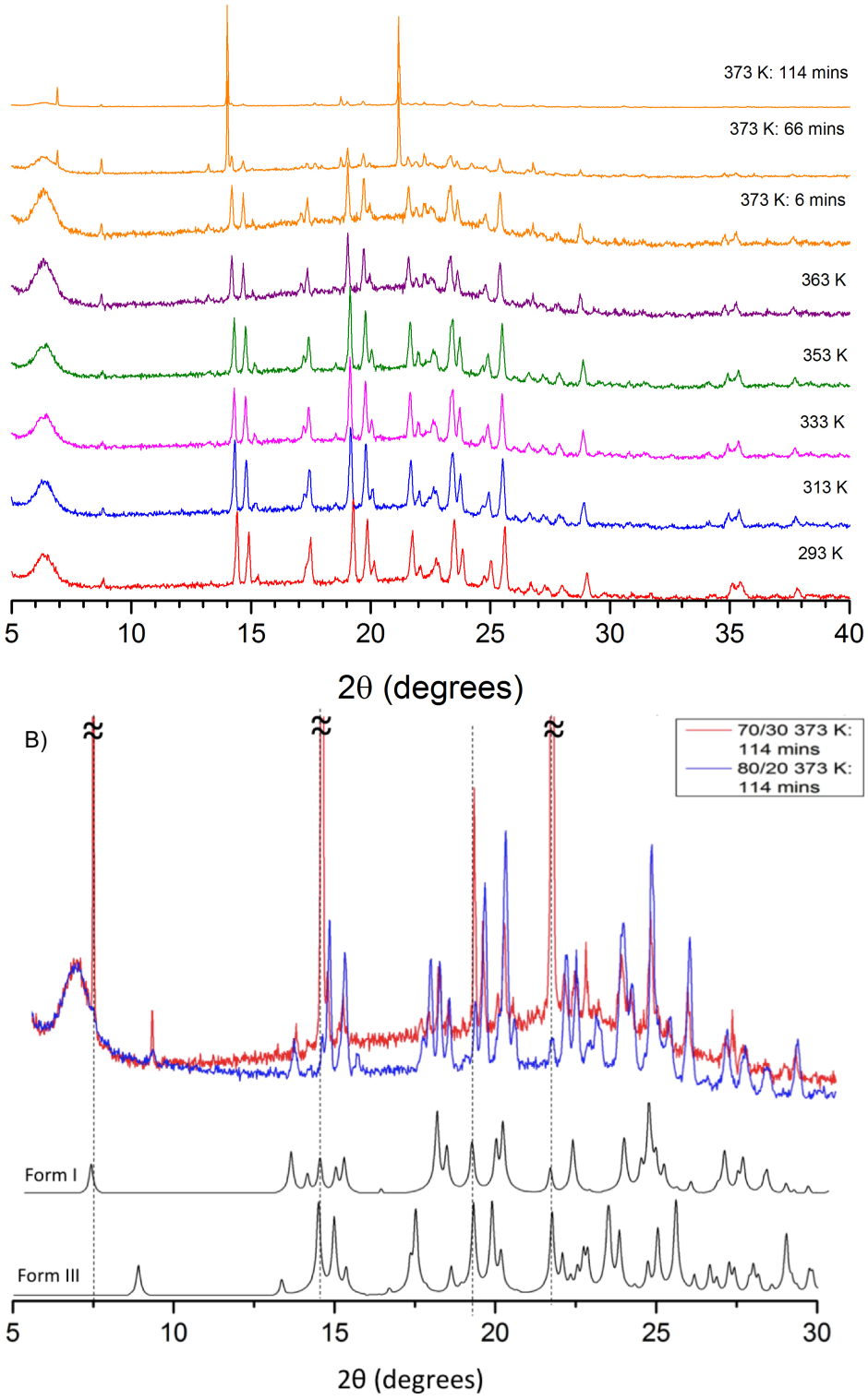


**Figure 6.43:** A) Normalised VT PXRD patterns of 70/30 dispersion, recorded between 293 and 373 K in 20 K increments, holding each sample at temperature for 114 minutes and B) Comparison between 70/30 and 80/20 dispersions after holding at 373 K for 114 minutes, compared with literature forms I and III FFA

Variation in peak intensity of PXRD patterns can occur due to a number of instrumental, inherent and sample preparation factors including crystal morphology, particle size, preferred

orientation, sample homogeneity, size of exposed surface, sample surface characteristics and sample packing [261–263]. It is likely that preferred orientation in one direction is the cause of the increased intensity in the form I diffraction peaks at high temperatures. Preferred orientation is one of the most common causes of changes to peak intensity, especially for acicular (needle-like) crystal morphologies [262, 263], which is the morphology of form I FFA [55]. Here we see preferentially increased intensity of just three characteristic peaks of form I FFA (*ca.* 6.9, 14.0 and 21.2 °2$\theta$). Larger particle size and excess sample packing can lead to preferred orientation effects [42,262,263]. Sample preparation/packing may have lead to preferred orientation in this case, as the same effect was not observed with the 80/20 dispersion, which at high temperatures contained the same FFA polymorphs. Sample rotation can be carried out to confirm preferred orientation effects [262], and may become part of further VT PXRD investigations of the high temperature effects on the crystallisation of FFA within dispersions.

Upon cooling, the 70/30 FFA/PVP-VA dispersion remained crystalline, with a combination of forms I and III detected at ambient temperatures. Interestingly, when the sample was removed from the holder, it had a hard, glassy surface. The PXRD pattern after scratching the surface (black pattern in figure 6.44) shows the reduction in intensity of the 'preferred orientation' high intensity peaks, which suggests a preferential *surface* orientation effect, reversible through reorientation by mechanical impact.

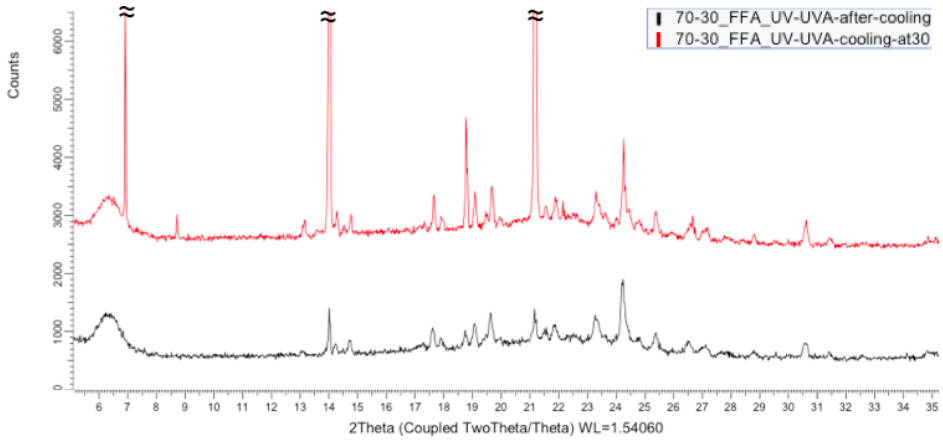


**Figure 6.44:** PXRD patterns of 70/30 dispersion, recorded at 293 K after the heat and cool cycle, before (red) and after (black) scratching the sample surface

The 60/40 dispersion remained amorphous with heating up to 363 K, where some recrystallisation occurred after *ca.* 18 minutes, with peaks at positions 8.8, 13.2, 17.6, 22.2 and 26.8 ° 2$\theta$ starting to grow (figure 6.45). All peaks completely disappeared again, with the sample becoming amorphous once more. The crystallisation event was short-lived, lasting only for *ca.* 40 minutes. Following this when heated to 373 K and upon subsequent cooling, the sample remained amorphous.

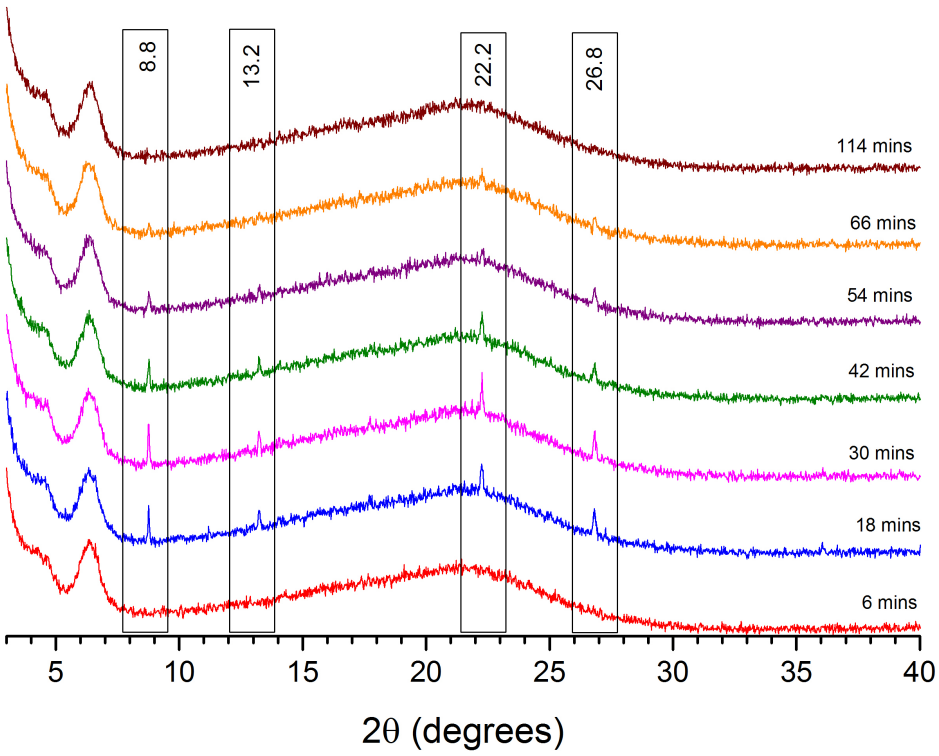


**Figure 6.45:** VT PXRD patterns of 60/40 FFA/PVP-VA dispersion during annealing at 363 K

The peaks observed at 363 K can be attributed to either form I or form III, and are all present in the 80/20 and 70/30 dispersions after annealing at 373 K. The beginnings of crystallisation from amorphous FFA therefore likely occurs at 363 K in the 60/40 dispersion as conditions become favourable. However, the higher polymer content in the 60/40 dispersion prevents further crystallisation, instead dissolving the crystallites as increased drug solubility dominates. This explanation is in agreement with our current hypothesis, which describes the presence of a viscous 'liquid like' environment at high temperatures.

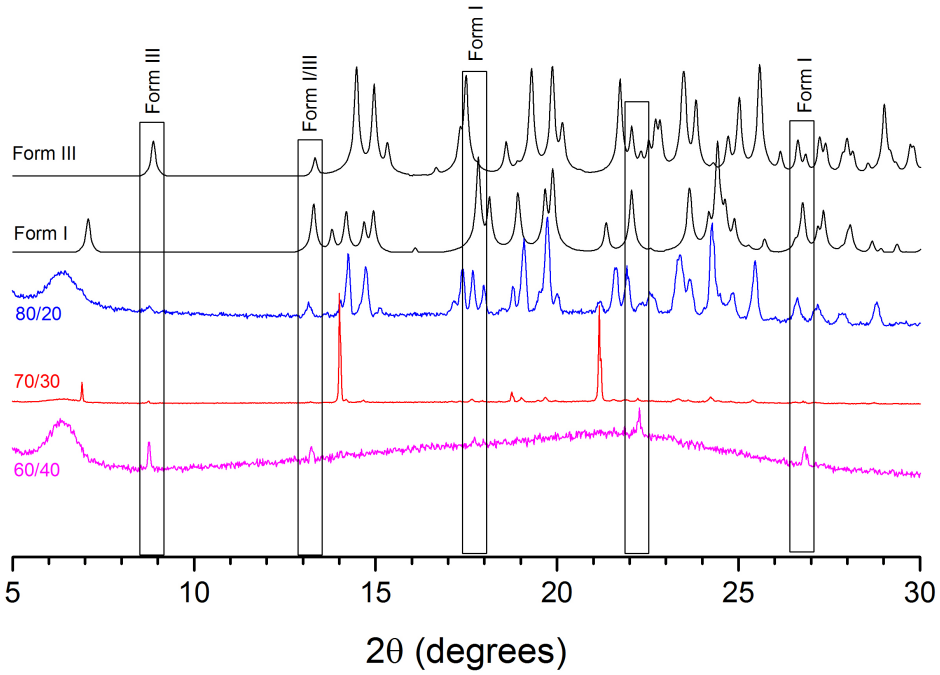


**Figure 6.46:** Comparison of high temperature crystallisation in the 80/20, 70/30 and 60/40 FFA/PVP-VA dispersions, with reference to forms I and III FFA

The 40/60 dispersion remained amorphous throughout the VT PXRD.

The VT PXRD studies therefore confirmed the permanent polymorphic transition from existing form III to form I at 373 K in the 70/30 and 80/20 FFA/PVP-VA dispersions, detected with VT $^{19}$F MAS NMR, but not VT $^{13}$C and $^{1}$H MAS NMR. Again this transition occurred at much higher temperature than expected from previous literature studies [197, 249], although there is some inconsistency in the the literature [260]

## 6.5 Probing miscibility and dynamics of FFA/PVP-VA dispersions with spin-lattice relaxation

### 6.5.1 Variable Temperature $T_1{}^F$

The investigation of variable temperature $^{19}$F spin-lattice relaxation times was used to further probe the faster motions and crystallisation of the drug detected in the FFA/PVP-VA dispersions at high temperatures. A difference in the temperature dependence of the $T_1{}^F$ times with increasing drug content was observed (figure 6.47).

There was little change in the $T_1{}^F$ times of the 40/60 - 60/40 dispersions with increasing temperature, with slight reduction in $T_1{}^F$ times of the 50/50 and 60/40 dispersions at the highest temperatures. At lower temperatures, the 70/30 and 80/20 dispersions had longer relaxation times, due to the presence of form III FFA. With increasing temperature, a gradual increase in $T_1{}^F$ occurred, followed by a more dramatic reduction in $T_1{}^F$ times,

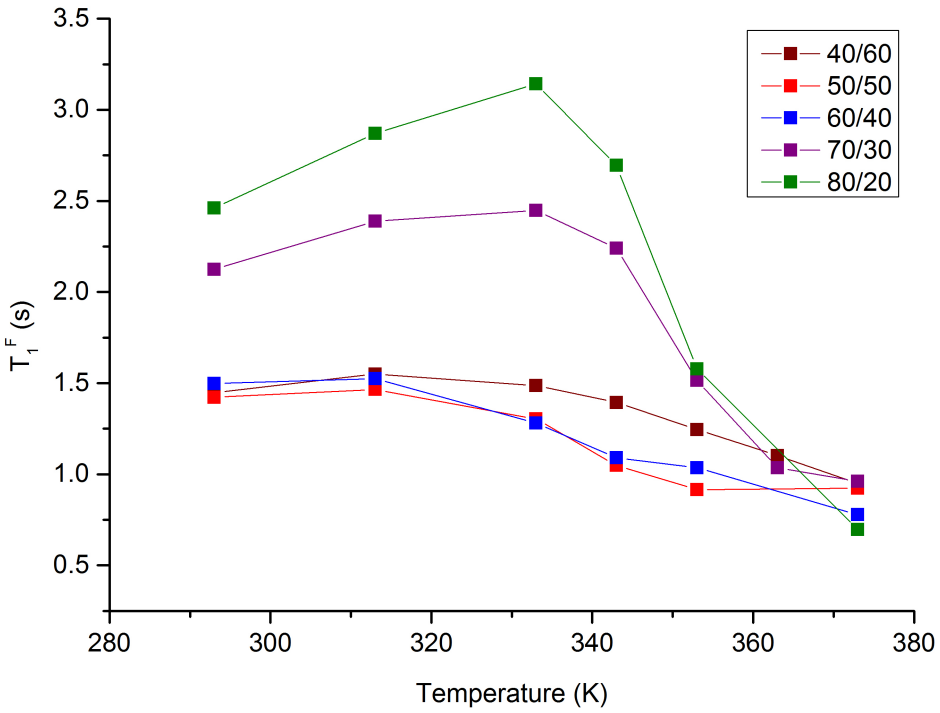


**Figure 6.47:** $T_1{}^F$ times (s) for the 80/20, 70/30, 60/40, 50/50 and 40/60 dispersions with increasing temperature (293 K to 373 K)

with the absence of a $T_1{}^F$ minimum. For the 70/30 dispersion, a further change in $T_1{}^F$ times at *ca.* 373 K indicates the possible beginnings of a minimum, which is in agreement with Aso *et al.* [41] who detected a $T_1{}^F$ minimum in their FFA/PVP 70/30 dispersion at 363 K. Temperature dependence of this kind can be attributed to the overlapping of multiple motional regimes within the system. At high temperatures, the FFA/PVP-VA dispersions have been shown to be complex, with possible melting, liquefaction, crystallisation and high mobility occurring concurrently; making it difficult to fully interpret the changes in relaxation times. At temperatures below *ca.* 333 K, relaxation times are most likely dominated by the presence of form III crystalline material. However, above this temperature, a more rapid reduction in $T_1{}^F$ times occurs indicating an increased mobility, as the dispersion begins to change to a more liquid-like state, identified previously. This correlates with the VT $^{19}$F MAS data, which showed the dramatic reduction of linewidth, occurring at temperatures *ca.* 343 K (figure 6.37).

To gain additional information about the high-drug loaded dispersions, the apparent activation energies were calculated above and below $T_{MAX}$, by assuming $\tau_c$ follows an Arrhenius law. The $E_A$ values calculated above $T_{MAX}$ were greater by a factor of ten for both dispersions, therefore different motional process are clearly being represented above and below 333 K.

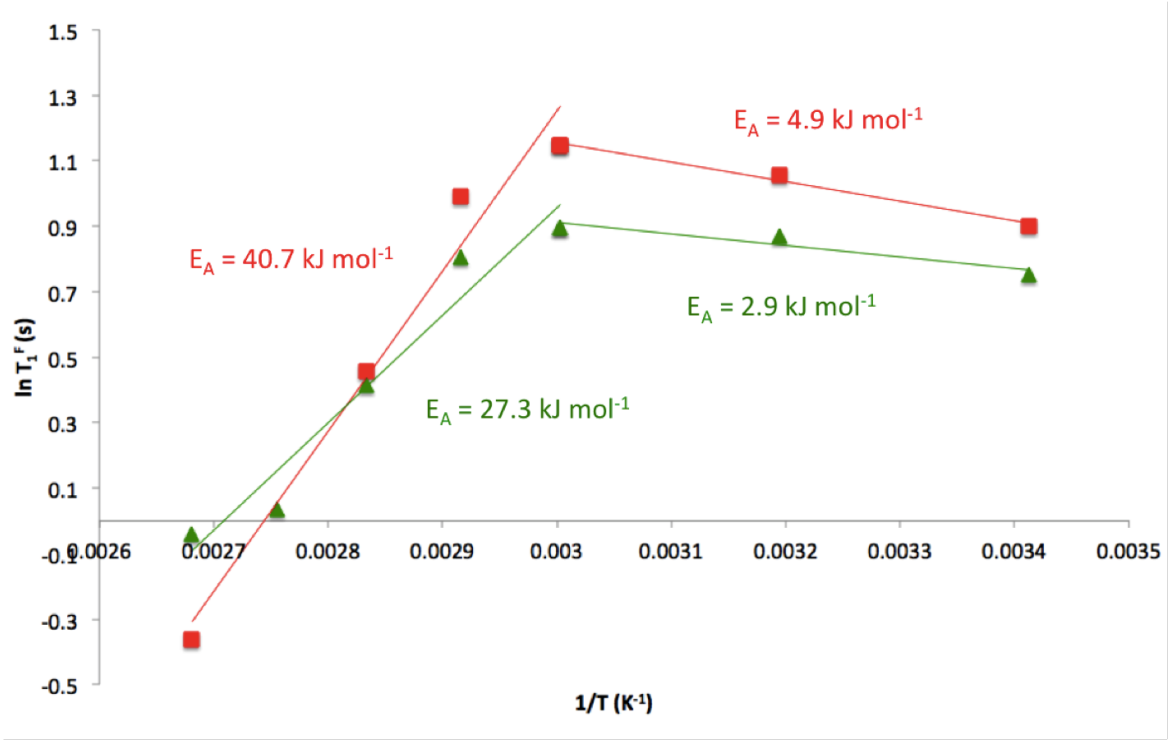


**Figure 6.48:** Arrhenius plots of $\ln(T_1{}^F)$ vs. inverse temperature for the -$CF_3$ functional group of the 70/30 and 80/20 FFA/PVP-VA dispersions. Activation energies are shown, as calculated from the gradient

The $T_1{}^F$ times of the two inequivalent fluorine sites assigned to amorphous FFA (*ca.* -62 ppm) and form I FFA (*ca.* -60 ppm) (see section 6.3.5) in the 80/20 and 70/30 dispersions were calculated at 373 K; and upon cooling back to 293 K (figure 6.49). Two distinct $T_1{}^F$ times were calculated for each $^{19}F$ environment, which indicates the presence of two different FFA phases, both at 373 K, which remain present upon cooling to 293 K. At 373 K, there was a large difference in $T_1{}^F$ between the two sites in both dispersions: the shoulder peak had a much longer $T_1{}^F$ time than the main peak, which provides further evidence for the presence of crystalline FFA at high temperature. Upon cooling, we continue to see separation of the two components within the dispersions *via* $T_1{}^F$ times: the peak *ca.* - 60 ppm (corresponding to the crystalline component) has a longer $T_1{}^F$ than the amorphous peak *ca.* - 62 ppm.

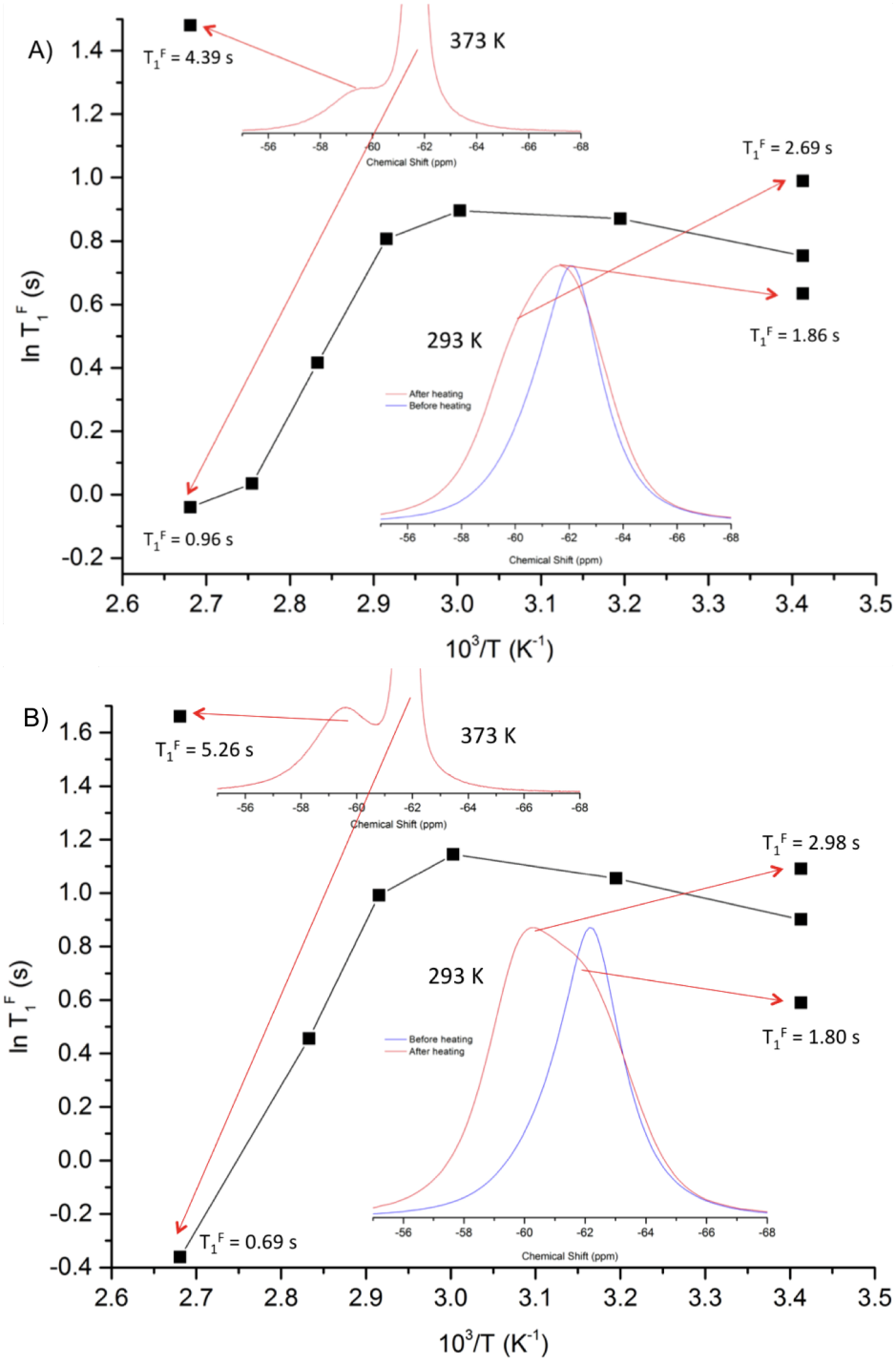


**Figure 6.49:** Arrhenius plots outlining the temperature dependence of $T_1{}^F$ times of A) 80/20 and B) 70/30 dispersions, heated between 293 K and 373 K, then cooled back to 293 K. Relevant $^{19}$F MAS NMR spectra for 373 K and upon cooling back to 293 K are shown to highlight the origins of phase separation

There are very few studies in the literature which use $^{19}$F MAS NMR to assess the mobility of drug/polymer dispersions. Aso *et al.* [41] used variable temperature low field $^{19}$F NMR to assess the mobility of FFA/PVP and FFA/HPMC dispersions at 70 and 80 wt. % drug loading, by determining $T_1{}^F$ and $T_{1\rho}{}^F$ times. For $T_1{}^F$, they observed a minimum for the FFA/PVP 70/30 dispersion *ca.* 363 K, but no minimum for the 80/20 dispersion due to rapid crystallisation above 343 K, where no $T_1$ times could be calculated (figure 6.50).

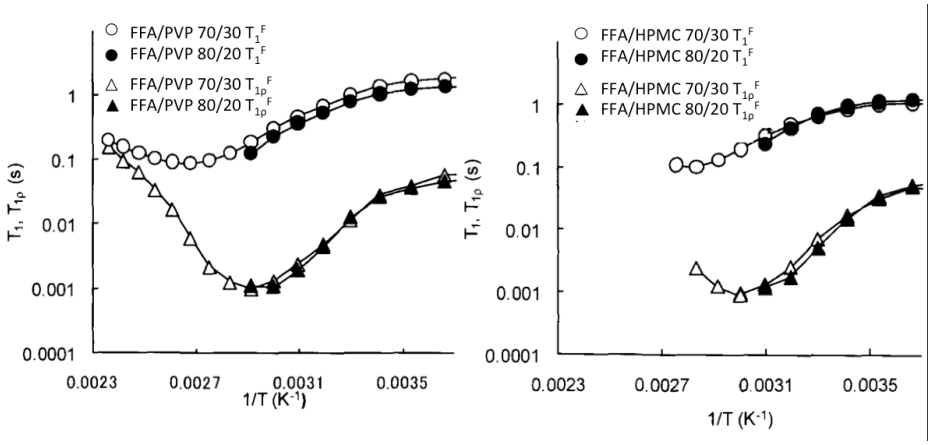


**Figure 6.50:** Temperature dependence of $T_1{}^F$ and $T_{1\rho}{}^F$ for FFA/PVP and FFA/HPMC 70/30 and 80/20 dispersions [41]

No information was provided to identify the polymorphic form of the crystalline FFA [41]. It is therefore highly likely that the minimum for the mobile phase in our experiments is just outside the covered temperature range.

### 6.5.2 Variable Temperature $T_{1\rho}{}^H$

The temperature dependence of $T_{1\rho}{}^H$ times of the FFA/PVP-VA dispersions (40/60 - 80/20), amorphous FFA and forms I and III FFA were investigated. The relaxation times of form I FFA were too long to be determined accurately (longer than 70 ms) across the full temperature range. $T_{1\rho}{}^H$ times of amorphous FFA could only be recorded below 273 K, as following crystallisation to form I (detected *via* VT $^1$H-$^{13}$C CP/MAS NMR at *ca.* 273 K), relaxation times were also too long for accurate determination.

The 40/60, 50/50 and 60/40 FFA/PVP-VA dispersions were found to be homogenous across the full temperature range, as indicated by the very similar $T_{1\rho}{}^H$ times measured for both drug and polymer, due to efficient spin diffusion (figure 6.51). For the 40/60 FFA/PVP-VA dispersion, the non-typical temperature dependence described in chapter 5, was observed. Firstly an initial increase in $T_{1\rho}{}^H$ times with increasing temperature was identified, indicating a fast motional regime with $E_A$ of 12.87 kJ mol$^{-1}$ up to a $T_{MAX}$ at ($T_g$ - 19 K). Following $T_{MAX}$, a marked change in temperature dependence occurred, seen by a rapid decrease in $T_{1\rho}{}^H$ times with increasing temperature ($E_A$ = 61.7 kJ mol$^{-1}$). The difference in activation energies above and below $T_{MAX}$ indicates the presence of two different motions, likely associated with two different $T_{1\rho}{}^H$ minima, at opposite temperature extremes outside the studied temperature range. No $T_{MAX}$ was observed for the 50/50 and 60/40 FFA/PVP-VA dispersions, with $T_{1\rho}{}^H$ times decreasing with increasing temperature across the full range, indicating a motional regime on the slow side of a $T_{1\rho}{}^H$ minimum. A change in gradient occurred again *ca.* 19 K below $T_g$, representing an increased mobility, with an $E_A$ of 55.4 kJ mol$^{-1}$.

The similarity of the high temperature apparent activation energies between the dispersions indicates the same motional environment with increasing temperature, likely to be a combination of a number of overlapping motional regimes. The nature of the FFA/PVP-VA dispersions at high temperatures has been shown to be complex, with possible overlapping melting, liquefaction, crystallisation and high mobility occurring concurrently, as highlighted with VT $^{1}$H, $^{19}$F and $^{13}$C MAS NMR experiments.

An increased molecular mobility *ca.* 19 K below $T_g$ has been observed in the literature with amorphous nifedipine and nifedipine/PVP dispersions, with a number of separate studies showing that $T_{1\rho}$ times were dramatically reduced *ca.* 20 K below $T_g$, which was linked to instability due to increased molecular mobility [46, 47].

A difference in the relaxation behaviour of drug and polymer indicative of phase separation can be seen across the whole temperature range for the 70/30 and 80/20 FFA/PVP-VA dispersions; and was especially pronounced for the 80/20 dispersion (figure 6.52). At 70 wt. % drug loading, the $T_{1\rho}{}^{H}$ temperature dependence was comparable to that seen for the 60/40 and 50/50 FFA/PVP-VA dispersions. Both drug and polymer components displayed similar temperature dependence, with very little change below $T_g$, followed by a more dramatic increase in $T_{1\rho}{}^{H}$ above $T_g$, until the point where signal disappeared from the CP/MAS spectra. The $T_{1\rho}{}^{H}$ times of FFA in the dispersion were consistently longer than for PVP-VA throughout, however still shorter than pure crystalline FFA. This behaviour is comparable to the 80/20 IMC/PVP-VA dispersion at temperatures prior to full crystallisation to the $\alpha$-polymorph, where regions of higher mobility polymer act as 'relaxation sinks' for small crystalline 'domains'. This leads to shorter observed $T_{1\rho}{}^{H}$ times of crystalline material within the dispersion, as compared to pure crystalline material. By 80 wt. % drug loading, we can clearly see a greater separation of drug and polymer, despite very few points on the temperature dependence curve, with $T_{1\rho}{}^{H}$ times of FFA consistently longer than 70 ms, indicating the presence of a high level of crystalline FFA.

The relaxation curves of the highest drug loading dispersions are extremely useful visual tools to identify phase separation and homogeneity in solid dispersions. At high drug loading levels, the phase separation is obvious, even without further calculation of differences between $T_{1\rho}{}^{H}$ times, often employed as a technique to determine miscibility in solid dispersions [90]. This could become an important technique to initially determine miscibility limits when first investigating drug loading levels within a formulation.

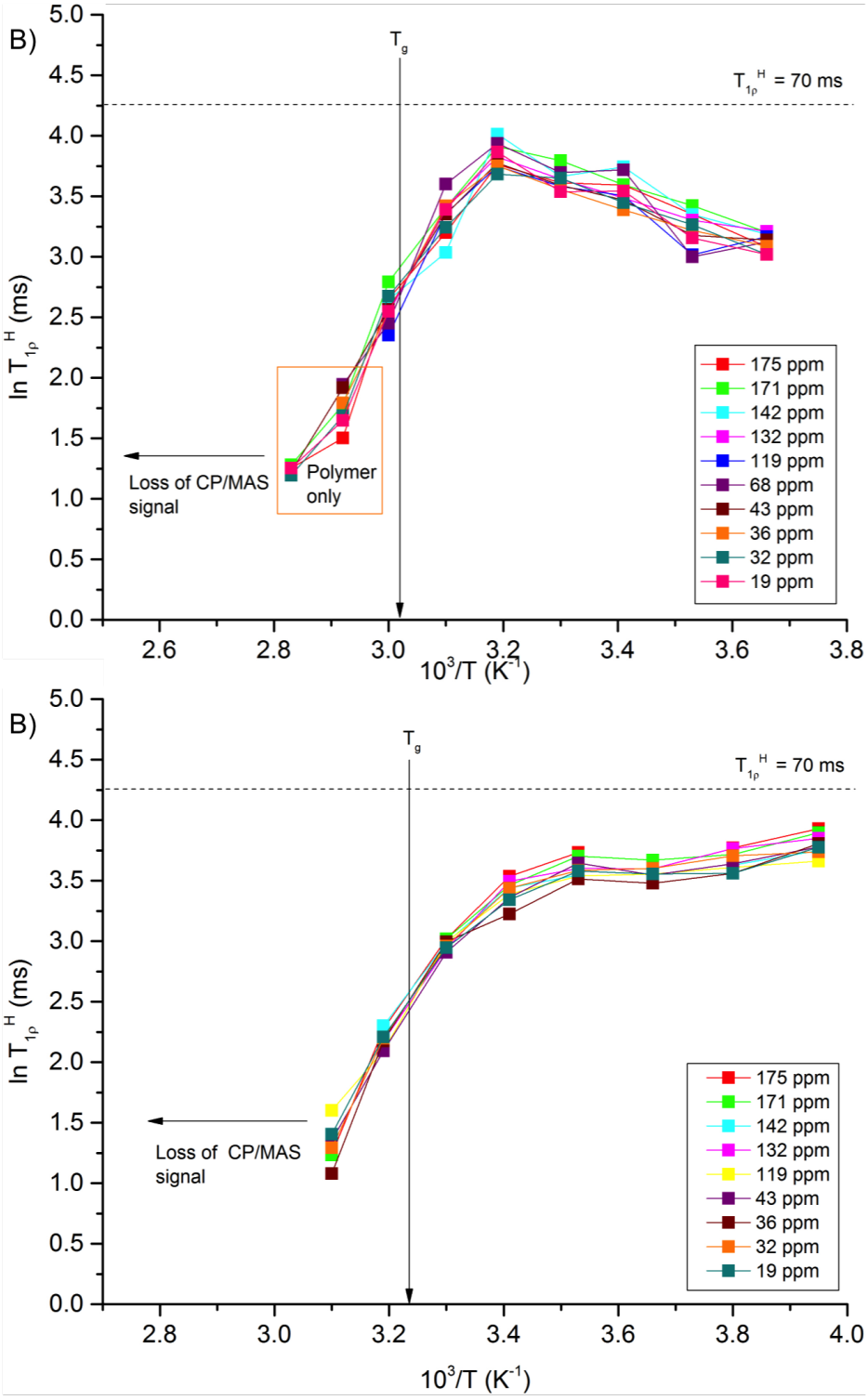


**Figure 6.51:** Temperature dependence of $T_{1\rho}{}^{H}$ times for different $^{13}C$ sites for A) 40/60 and B) 60/40 FFA/PVP-VA dispersions. The 50/50 dispersion displayed a similar temperature dependence to the 60/40 dispersion

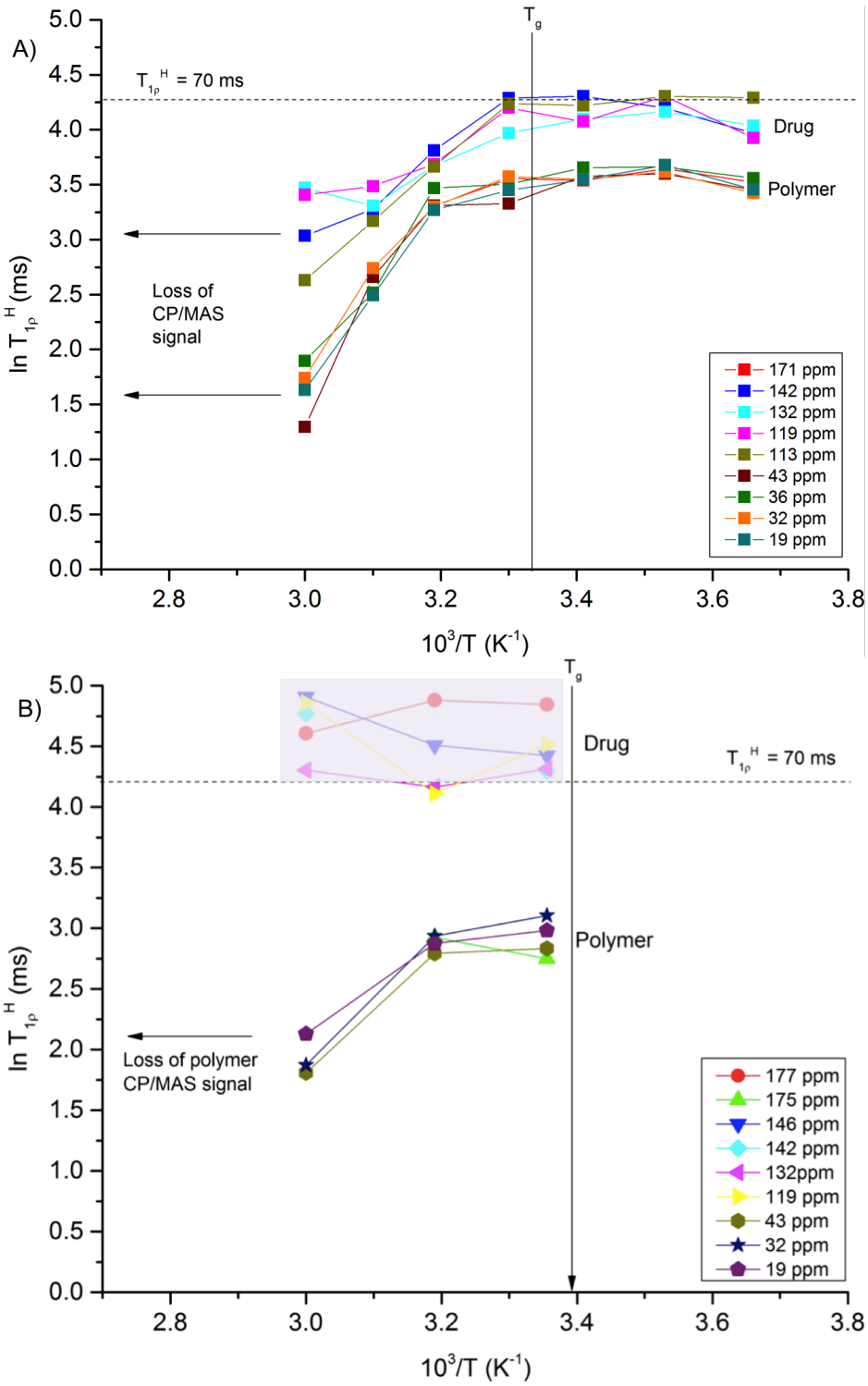


**Figure 6.52:** Temperature dependence of $T_{1\rho}{}^H$ times for different $^{13}C$ sites for A) 70/30 and B) 80/20 FFA/PVP-VA dispersions

### 6.5.2.1 Detection of miscibility on the $T_{1\rho}{}^H$ timescale

The $\Delta T_{1\rho}{}^H$ (between FFA and PVP-VA) of each dispersion at 293 K can be seen in figure 6.53. As demonstrated in the previous temperature dependence curves, there were no differences in $T_{1\rho}{}^H$ times for 20 - 60 wt. % FFA/PVP-VA dispersions, indicating

miscibility on the 2 - 6 nm length scale. The 70/30 and 80/20 dispersions displayed a large $\Delta T_{1\rho}{}^{H}$ well above the zero line, indicating the presence of obvious domains larger than 6 nm in size. Due to time constraints, we were unable to carry out VT $T_1{}^{H}$ time measurements to further investigate the larger domains present in the 70/30 and 80/20 dispersions.

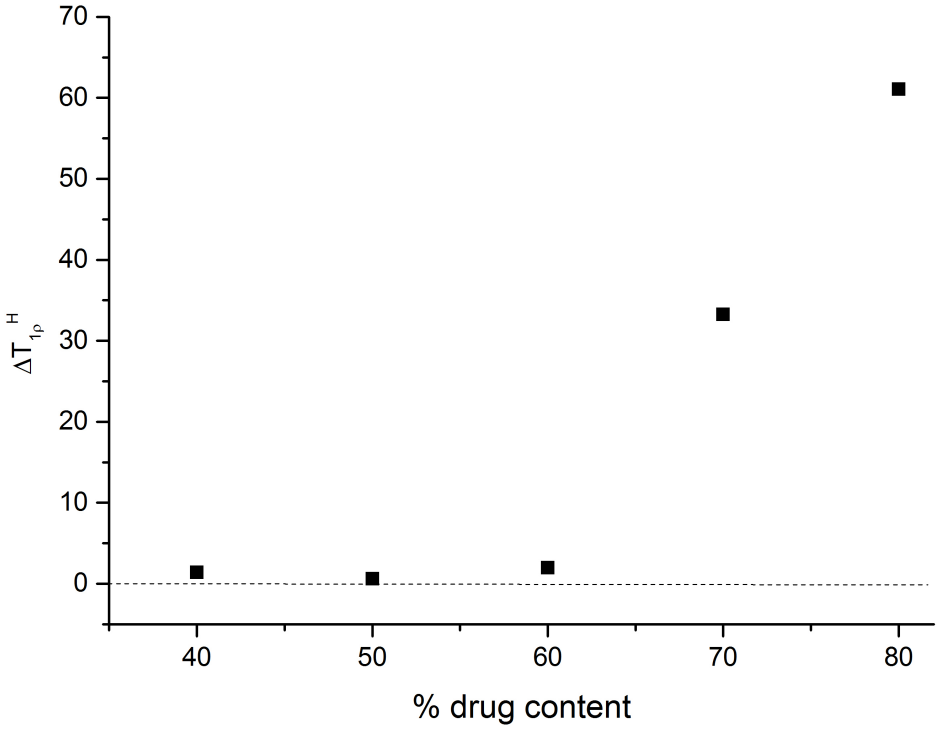


**Figure 6.53:** $\Delta T_{1\rho}{}^{H}$ (ms) between FFA and PVP-VA in the solid dispersions, at 293 K, displayed as a function of wt. % drug content

## 6.6 Stability Studies

Throughout the 8 week stability study, all dispersions were monitored for changes in the local ordering using PXRD, mDSC and $^{13}$C CP/MAS solid-state NMR. FFA/PVP-VA dispersions with drug content $\leq$ 50 wt. % remained amorphous in each storage condition throughout, indicating high physical stability (figure 6.54).

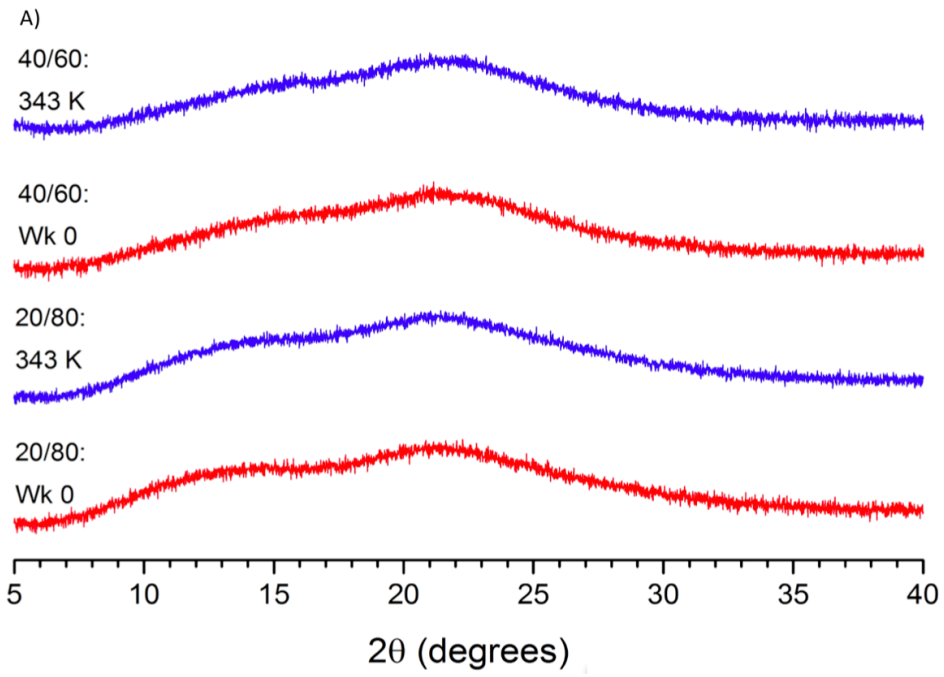


**Figure 6.54:** PXRD pattern recorded before (red) and after (blue) 8 weeks storage at 343 K for the 20/80 and 40/60 FFA/PVP-VA dispersions

The 60/40 FFA/PVP-VA dispersion remained amorphous throughout the study at room temperature (0 % RH), with some crystallisation to form III detected after 6 weeks storage at all other conditions (figure 6.55). Unusually, no endothermic melting was observed in the DSC curves in any 60/40 stability study samples, despite form III being identified with both PXRD and $^{1}$H-$^{13}$C CP/MAS NMR. This may be linked to the higher solubility of the small crystallites of form III at increased temperature in the polymer which was thought to be the reason for the lack of crystallisation observed *via.* VT PXRD. No crystallisation was identified in the previously discussed $^{13}$C, $^{19}$F or $^{1}$H MAS NMR studies.

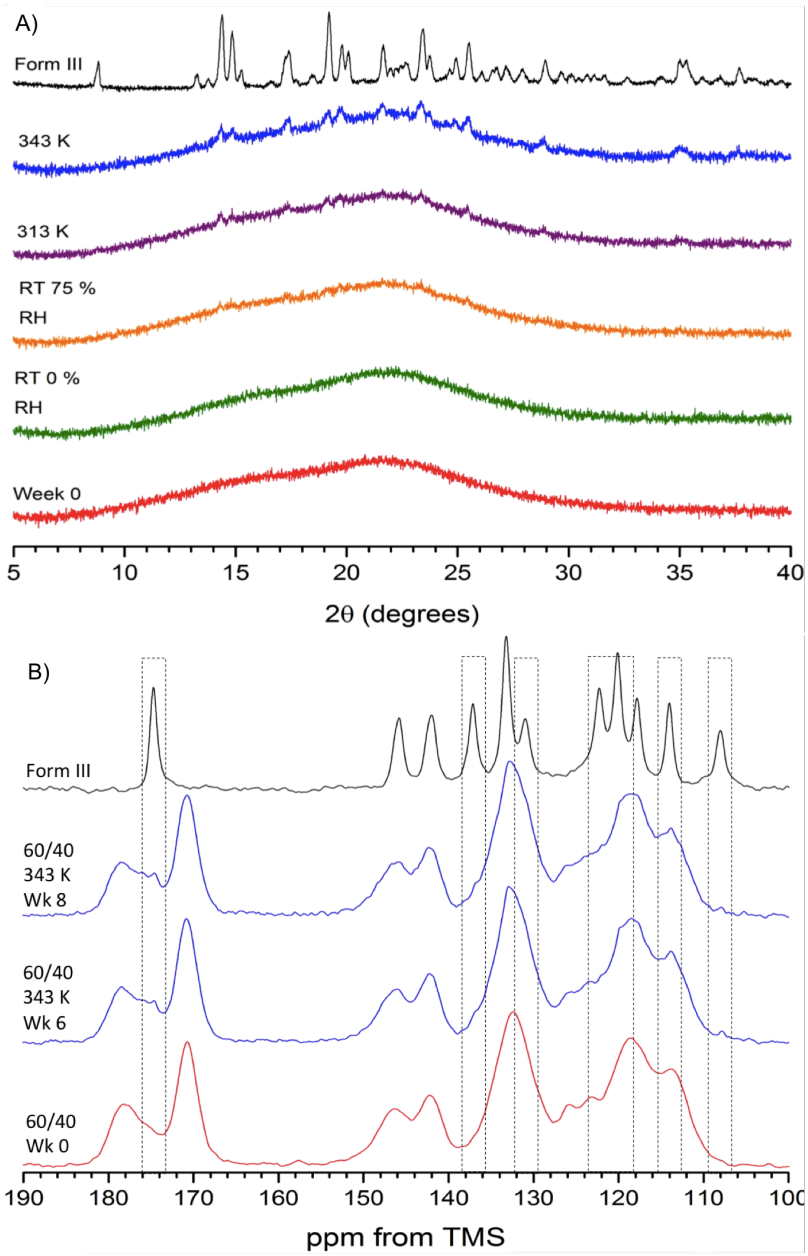


**Figure 6.55:** A) PXRD patterns recorded before (red) and after 8 weeks storage at room temperature (0 and 75 % RH), 313K and 343 K for the 60/40 FFA/PVP-VA dispersions, with a comparison to form III FFA and B) $^{1}$H-$^{13}$C CP/MAS NMR spectra acquired before (red) and after storage at 343 K, with a comparison to form III FFA

No further polymorphic transitions were observed in the 70/30 and 80/20 FFA/PVP-VA dispersions stored up to temperatures of 343 K, with only form III FFA detected throughout the 8 week stability study (figure 6.56). This is in agreement with the crystallisation observed *via* VT PXRD, as the transition from form III → form I only occurred at 373 K, *ca.* 60 K above the reported transition temperature [197].

The three highest loading dispersions were stored at in the oven at 373 K for 2 weeks, to investigate the high temperature transition from form III → form I detected through VT $^{19}$F MAS NMR and VT PXRD studies. Unfortunately, under these conditions, the dispersions

formed hard glass melts, which proved unsuitable for further analysis.

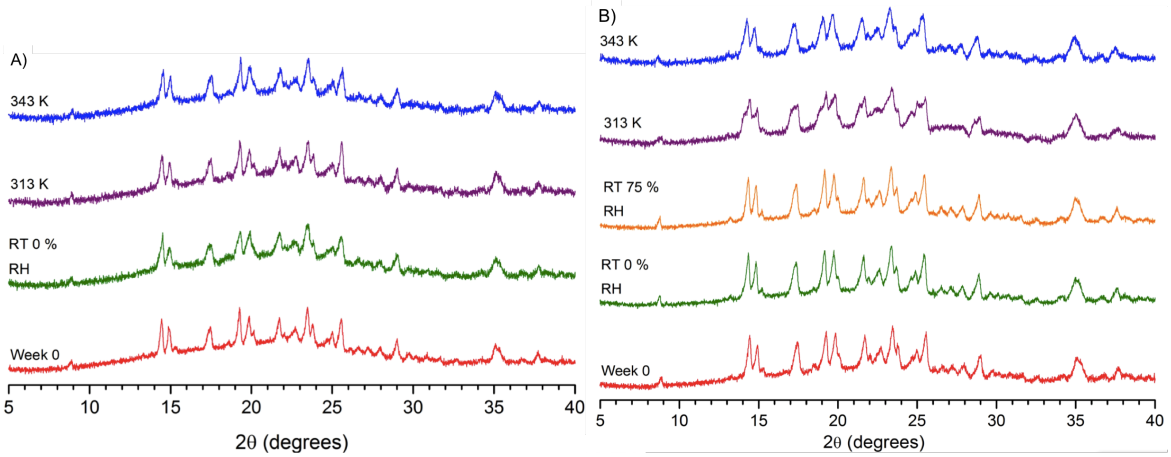


**Figure 6.56:** PXRD pattern recorded before (red) and after 8 weeks storage at room temperature (0 and 75 % RH), 313K and 343 K for the A) 70/30 and B) 80/20 FFA/PVP-VA dispersions

Aso *et al.* [41] stored 80/20 FFA/PVP and FFA/HPMC dispersions at 333 K for 10 hours. They found crystallisation in both samples within this time, with faster crystallisation in the HPMC dispersion compared to the PVP, which was linked to the higher local mobility of the sample, confirmed through VT $\tau_c$ calculations from $T_1{}^F$ and $T_{1\rho}{}^F$ studies. The polymorphic form of FFA was not identified. Van Eerdenbrugh and Taylor [247] studied the ability of a number of polymers to inhibit crystallisation in 8 model drug compounds, including FFA and PVP-VA. Spin coated samples with drug content between 10 - 95 wt. % were monitored over 7 days storage under dry conditions at ambient temperature. For FFA/PVP-VA, crystallisation only occurred in the 75/25 and 90/10 dispersions over the 7 day period, in agreement with our stability study results.

## 6.7 Conclusions

FFA was successfully formulated as an amorphous solid dispersion with PVP-VA in a variety of drug/polymer ratios. Initial characterisation indicated the fully amorphous nature of the dispersions up to the maximum drug loading of 60 wt. %, above which varying levels of form III, alongside amorphous FFA were detected. The previously unreported full $^1$H assignment of FFA and solid-state characterisation of amorphous FFA was presented, with the $T_g$ was calculated to be 286 K.

In comparison to IMC, the local mobility of the FFA/PVP-VA dispersions proved more complex. The 40/60 - 80/20 FFA/PVP-VA dispersions showed a similar mobility behaviour at high temperatures, which was more pronounced with increasing drug loading. Upon cooling back to 293 K, broad amorphous FFA peaks were detected in all dispersions. We postulate that at high temperatures, a highly mobile, 'liquid-like' environment exists in these

dispersions, described as consisting of an amorphous (or 'melted') FFA component, dissolved in a viscous polymer 'paste.' The timescale of dominant processes in FFA molecular mobility is likely to be *ca.* 1000 kHz. At the highest drug loadings, an additional crystalline phase is likely present, which was further probed using VT $^{19}$F MAS and PXRD techniques.

The fully amorphous FFA/PVP-VA dispersions followed the 'non-typical' temperature dependence observed with IMC/PVP-VA, due to the presence of at least two overlapping mobility regimes, although the loss of CP signal hindered the measurements at high temperatures. $E_{A\,app}$(LT) and ($T_g$ - $T_{MAX}$) measurements extracted from the temperature dependence curves provided further data to relate the mobility behaviour detected through $T_{1\rho}{}^H$ to physical stability, which is further discussed in chapter 8.

Miscibility between FFA and PVP-VA was additionally probed, with $\Delta T_{1\rho}{}^H$ measurements allowing the investigation of domains down to *ca.* 2 nm. Phase separation was shown across all temperatures for the 70/80 and 80/20 dispersions. These curves are extremely useful visual tools for the identification of phase separation in solid dispersions. This could become an important technique to initially determine miscibility limits during initial drug formulation.

Crystallisation from amorphous FFA, and polymorphic transitions of forms I and III FFA, were also studied. FFA is known to exhibit complex polymorphism [39], having the highest number of solved polymorphic structures in the Cambridge Structural Database. Pure amorphous FFA was shown to crystallise to form I FFA; and Form III was shown to undergo an enantiomeric polymorphic transition to form I, at *ca.* 373 K, with both $^1$H-$^{13}$C CP/MAS NMR and $^{19}$F MAS NMR. Monitoring the crystallisation behaviour of the high drug loaded dispersions was hampered due to the high mobility at high temperatures. However, $^{19}$F provided an alternative way to detect and characterise the drug *via* $^{19}$F MAS NMR and $T_1{}^F$. This method clearly highlighted two distinct fluorine environments, corresponding to crystalline (form I) and amorphous FFA, both at 373 K, and upon cooling to ambient temperatures. There are no previously reported examples of the detection of phase separated drug phases with $T_1{}^F$.

The enantiomeric transition from form III $\rightarrow$ form I in the 70/30 and 80/20 dispersions was confirmed using VT PXRD studies. This enantiomeric polymorphic transition (form III $\rightarrow$ I) was found to occur at a much higher temperature than the expected literature transition temperature.

In summary, the numerous solid-state NMR techniques employed have provided a large amount of information regarding the local structure and dynamics of FFA solid dispersions, which have not previously been reported. We have shown that FFA dispersed in PVP-VA displays complex high temperature mobility behaviour, which therefore proved to be a difficult system to investigate. However the presence of a $^{19}$F nucleus extended the NMR analysis options, with the combination of numerous techniques allowing further

understanding of these systems.

# Chapter 7

# Variable Temperature Studies of Tolbutamide

Previous literature studies of TLB have focussed mainly on studying polymorphism and the crystalline form [42–44, 264]. Amorphous TLB has been shown to have low stability - Graeser *et al.* [100] found it to be stable at 258 K after 30 days storage, but unstable at ambient temperatures. There have been some studies of TLB solid dispersions: TLB has been most widely studied as a cyclodextrin (CD) inclusion complex, using a variety of techniques including PXRD, DSC and IR-spectroscopy [265] and molecular dynamics simulations [266]; with only one study applying solid-state NMR to investigate crystallisation behaviour [264]. TLB has also been shown to form amorphous solid dispersions with PVP: characterised using PXRD and dissolution [267], DSC [175] and as part of the same solid-state NMR study to investigate crystallisation behaviour [264]; and PEG-4000 [176]. Additionally, TLB solid dispersions (formulated with a number of polymers) were included in a small scale stability study, which used polarized light microscopy to monitor physical stability [247].

## 7.1 Crystalline Tolbutamide

Tolbutamide has six reported polymorphic forms (forms $I^L$, $I^H$, II-V) [42–44, 172–174], with its ability to crystallize into different forms due to the flexibility of rotatable alkyl bonds [42]. Form $I^H$ has the highest melting point, and is the most stable form at high temperatures: forms II and III are known to undergo a transition to form I upon heating [58, 171]. Form V was most recently formed by Nath *et al.* [44], through the crystallisation of TLB in methanol with a trace of $HNO_3$. Following slow evaporation over 48 hours, single crystals of form V were isolated, which were found to be unstable with conversion to form I occurring within 2 hours at room temperature [44]. The published crystal packing data of forms I-V can be seen in table 7.1.

**Table 7.1:** Crystallographic data on forms I-V tolbutamide [42–44, 56]

| | **Form $I^L$** | **Form $I^H$** | **Form II** | **Form III** | **Form IV** | **Form V** |
|---|---|---|---|---|---|---|
| Crystal habit | Prism | | Plate | Needle | Needle | Plate |
| Colour | Colourless | | Colourless | Colourless | White | Colourless |
| Crystal system | Orthorhombic | Orthorhombic | Monoclinic | Monoclinic | Monoclinic | Orthorhombic |
| Temp. of structure determination (K) | 153 | 363 | 153 | 153 | 298 | 298 |
| Space group | $Pna2_1$ | $Pna2_1$ | $Pc$ | $P2_1/n$ | $P2_1/c$ | $Pbcn$ |
| $a$ (Å) | 20.223(1) | 20.8095(4) | 9.087(8) | 11.735(2) | 10.091 | 15.851(6) |
| $b$ (Å) | 7.831(9) | 7.9323(2) | 17.228(3) | 9.052(8) | 15.646 | 9.288(4) |
| $c$ (Å) | 9.090(10) | 9.0610(2) | 17.951(4) | 13.732(3) | 9.261 | 19.691(8) |
| $\alpha$ (°) | 90 | 90 | 90 | 90 | 90 | 90 |
| $\beta$ (°) | 90 | 90 | 95.01(3) | 103.57(3) | 100.49 | 90 |
| $\gamma$ (°) | 90 | 90 | 90 | 90 | 90 | 90 |
| V (Å$^3$) | 1439.55(11) | 1494.67(5) | 2799.8(10) | 1416.4(5) | 1438.9 | 2899.2(19) |
| Z/Z' | 4/1 | 4/1 | 8/4 | 4/1 | 4/1 | 8/1 |
| CSD Code | ZZZPUS02 | | ZZZPUS05 | ZZZPUS06 | ZZZPUS07 | ZZZPUS10 |

Due to the conformational flexibility of TLB, the effect of low temperature on crystal structure was investigated (simultaneously by Drebushchak *et al.* [57] and Nath *et al.* [44]) in 2011, as torsional rotations of flexible molecules are known to become frozen at low temperatures [268]. There were no changes to forms I and II upon cooling, (to 100 K) [57], but changes to the unit cell structure of form III were determined (table 7.2) [44, 57]. At 100 K, a high Z' form III was described (named form III$^2$), with 3 molecules in the asymmetric unit, and elongation of the *b* axis, which was fully reversible upon heating. The higher temperature form III was found to have disorder in the butyl chain [57]. There is discrepancy between the two groups regarding the volume of form III$^2$, with Drebushchak *et al.* reporting no change as compared to form III [57], and Nath *et al.* reporting a much larger volume [44]. Nath *et al.* additionally attempted to investigate the effect of reduced temperature on form V, but found it immediately converted to form I upon cooling, due to rapid uptake of moisture [44].

**Table 7.2:** Crystallographic data at different temperatures for form III and III$^2$ tolbutamide [42, 44, 57]

| | **Form III** | **Form III** | **Form III** | **Form III$^2$** | **Form III$^2$** |
|---|---|---|---|---|---|
| Reference | [42] | [57] | [44] | [57] | [44] |
| Temp. of structure determination (K) | 153 | 295 | 298 | 100 | 100 |
| Space group | $P2_1/n$ | $P2_1/n$ | $P2_1/n$ | $P2_1/n$ | $P2_1/n$ |
| *a* (Å) | 11.735(2) | 11.8100(6) | 11.787(5) | 11.5671(1) | 11.5613(17) |
| *b* (Å) | 9.052(8) | 9.0587(3) | 9.043(4) | 27.1703(3) | 27.189(4) |
| *c* (Å) | 13.732(3) | 13.9713(6) | 13.955(6) | 13.5558(2) | 13.556(2) |
| $\alpha$ (°) | 90 | 90 | 90 | 90 | 90 |
| $\beta$ (°) | 103.57(3) | 104.491(5) | 104.644(7) | 102.746(1) | 102.803(2) |
| $\gamma$ (°) | 90 | 90 | 90 | 90 | 90 |
| V (Å$^3$) | 1438.9 | 1447.12(3) | 1439.2(10) | 1385.1169(7) | 4155.2(11) |
| Z/Z' | 4/1 | 4/1 | 4/1 | 12/4 | 12/4 |
| CSD Code | ZZZPUS06 | ZZZPUS13 | ZZZPUS08 | ZZZPUS11 | ZZZPUS09 |

The thermal behaviour of form I crystalline tolbutamide is illustrated in figure 7.1. On the initial heating run (green), the conversion of form I$^L$ to I$^H$ at 313.3 K is observed, followed by the melting of form I$^H$ at 401.8 K. Upon cooling, we observe the $T_g$ of amorphous TLB at 278.0 K. Upon subsequent reheating, a number of polymorphic transitions occur due to the crystallisation of form IV, form III and form II to form I$^H$ at 358.7, 377.8 and 391.3 K respectively, which indicates an enantiotropic relationship between each polymorph and form I$^H$. All thermal events observed agree with the literature values, shown in table 7.3.

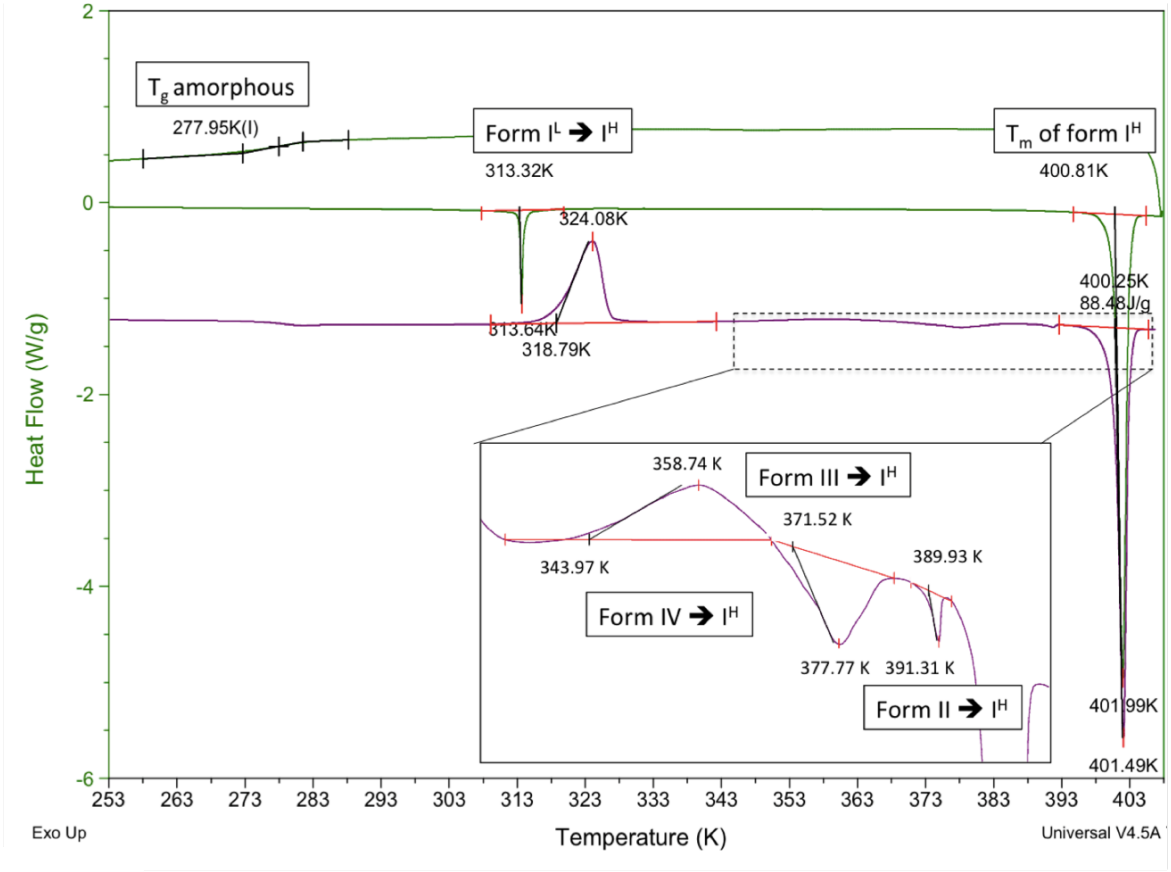


**Figure 7.1:** DSC trace of form I tolbutamide, heated between 253 and 408 K. The initial heat and cool cycles are displayed in green, with the subsequent reheat cycle in purple

**Table 7.3:** DSC data of TLB polymorphs, adapted from [42, 44, 56]

| TLB Polymorph | $T_m$ (K) | Transition Point (K) | $\Delta H_{trs}$ J · g$^{-1}$ | $\Delta H_{fus}$ J · g$^{-1}$ |
|---|---|---|---|---|
| Form I$^H$ | 401 | | | 88.0 |
| Form I$^L$ | | 313 | +7.0 (I$^L$ to I$^H$) | 95.1 |
| Form II | 390 | | +8.1 (II to I$^H$) | 97.2 |
| Form III | | 379 | +6.4 (III to I$^H$) | 94.7 |
| Form IV | | 361 | -4.8 (IV to I$^H$) | 73.2 |
| Form V | | Unknown | | |

There is some discrepancy in the literature around the correct order of thermodynamic stability of the TLB polymorphs. Kimura *et al.* [58] initially reported the thermodynamic order at room temperature as form III < form II < form I. However, this was disputed by Hasegawa *et al.* [43], when they determined that form I displayed enantiotropic behaviour, with a transition temperature of 311 K; and named the two polymorphs form I$^L$ and form I$^H$. They additionally disputed Kimura's stability order, as the solubility of form III at room temperature was found to be higher than that of form I. The revised thermodynamic stability was published as Form III < Form I$^L$ < Form II below the I$^L$ → I$^H$ transition

temperature of 311 K; and Form $I^H$ < Form III < Form II above the transition temperature. Therefore form II was determined to be the most stable polymorph, *via* investigations of heat of solution ($\Delta$H) and solubility [43].

Thirunahari *et al.* [42] revisited the crystal structures of forms I-IV, providing refined single crystal structures (forms I-III) and updated information on packing, molecular conformation and thermodynamic stability. They extensively characterised the polymorphs using solid-state NMR, FT-IR, DSC, hot stage microscopy and SEM and found that below *ca.* 353 K, form II was indeed the most thermodynamically stable polymorph, but above 353 K, form $I^H$ was more stable [42]. Thirunahari constructed an E-T diagram of the tolbutamide polymorphs, based on the DSC data collected (melting point, transition point, heat of transition, heat of fusion) (figure 7.2). This indicates that at an increased temperature, all polymorphs undergo a transition to the most stable high temperature form $I^H$. They showed that forms III/$I^H$ and II/$I^H$ are enantiotropically related; and IV/$I^H$ monotropically related. Additionally, from the E-T diagram, form IV was suggested to be monotropically related to all other polymorphic forms, and the transition from form III to $I^L$ was enantiotropic below 311 K [42]. Form V was only isolated recently, so was not included in the energy-temperature diagram. It is known to be metastable, converting to form I within two hours at room temperature [44].

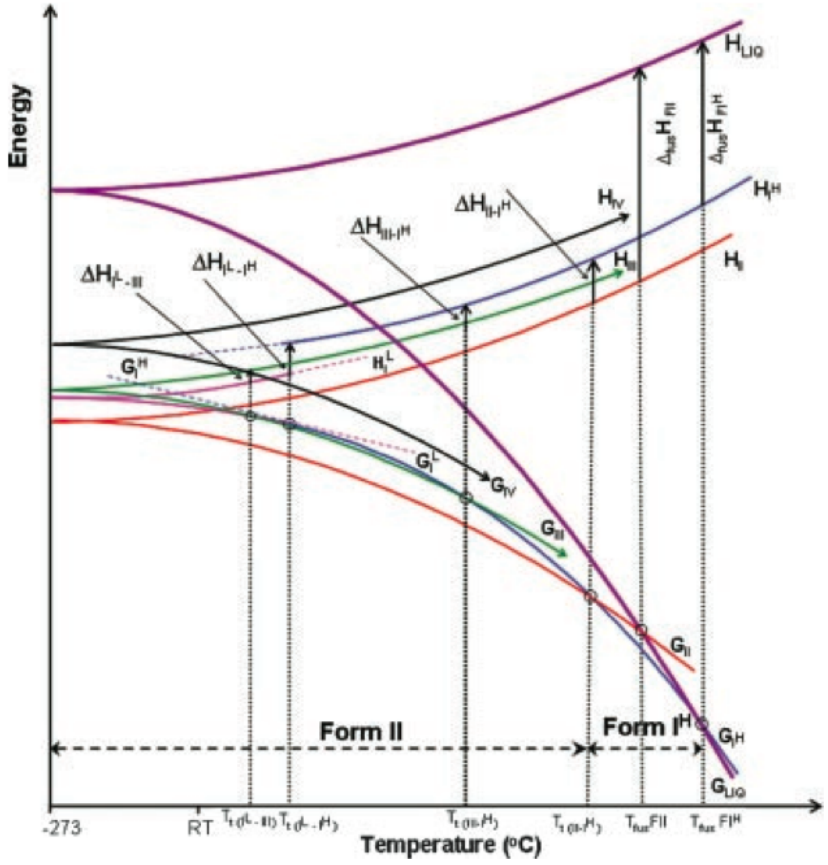


**Figure 7.2:** Schematic energy-temperature diagram of TLB polymorphs, adapted from [42]

In each polymorphic form, different conformations of TLB molecules are present, divided into two types of conformational polymorphs: U (same side) and chair (opposite sides), with reference to the position of the tolyl and butyl groups either side of the central S-N-C-N plane (figure 7.3) [42]. Forms $I^L$ and III follow packing scheme A (U-type), form II has a combination of schemes C and D (chair-type) and forms IV and V follow scheme B (U-type) [42,44]. The main hydrogen bonding within each polymorph occurs *via* the 'urea tape' motif between N-H donor and C=O acceptor groups (figure 7.3) [42,44].

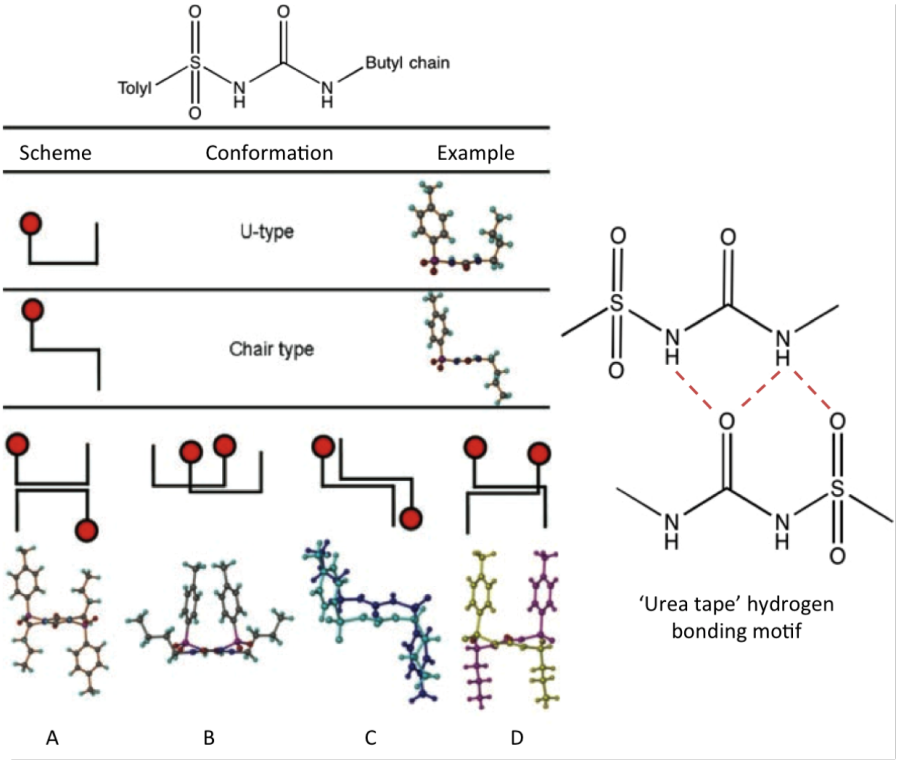


**Figure 7.3:** Types of packing schemes around the central S-N-C-N plane in TLB polymorphs, as described by [42]

Additional information about the enantiotropic transition of forms $I^L$ and $I^H$ was published by Hasegawa *et al.* in 2009 [43]. Using the DSC data, they demonstrated that the transition was reversible. Changes to the crystal structure were observed above and below the enantiotropic transition temperature, using both PXRD and solid-state NMR. Form $I^L$ was found to convert to form $I^H$ upon heating over 311 K, with an enthalpy of 2 kJ $mol^{-1}$. Both polymorphs had the same space group, with isomorphic molecular packing.

The structural difference between forms $I^L$ and $I^H$ was shown to be small: a conformational change of the terminal butyl group (figure 7.4), with additional movement of the S-N bond (figure 7.5).

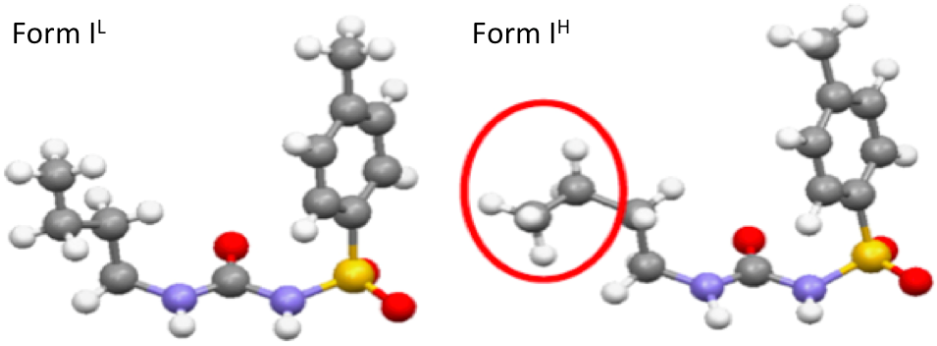


**Figure 7.4:** Molecular structure of form $I^L$ and form $I^H$ TLB, adapted from [43]

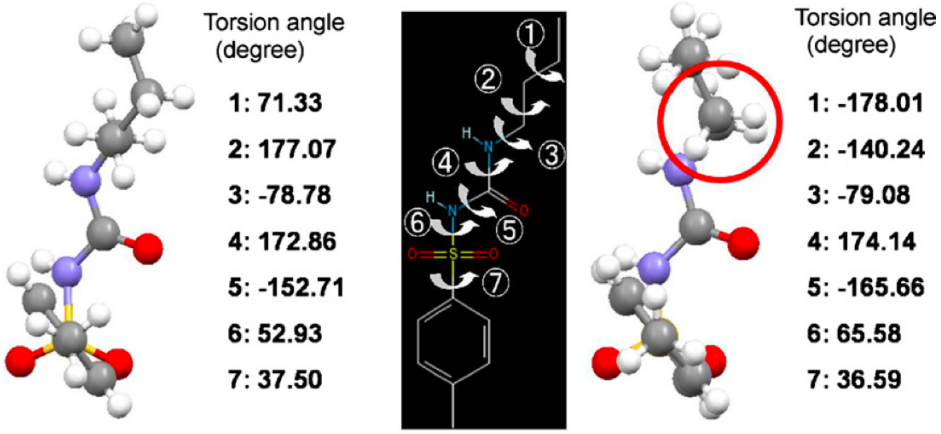


**Figure 7.5:** Torsion angles (degrees) in tolbutamide for A) form $I^L$ and B) form $I^H$, adapted from [43]

The solid-state $^{1}$H-$^{13}$C CP/MAS NMR spectra of forms $I^L$ and $I^H$ can be seen in figure 7.6. The chemical shift assignments of each form are detailed in table 7.4, which are in agreement with literature values [43]. The main changes to the $^{13}$C chemical shifts upon heating form $I^L$ occur within the aliphatic region, due to the rearrangement of the butyl chain (figure 7.6). Further downfield, the only significant change occurs to C-8 (C=0), which is positioned between the S-N bond and butyl chain, and undergoes a change in torsion angle. All differences observed upon conversion of form $I^L$ to form $I^H$ agree with those found by Thirunahari *at al.* [42].

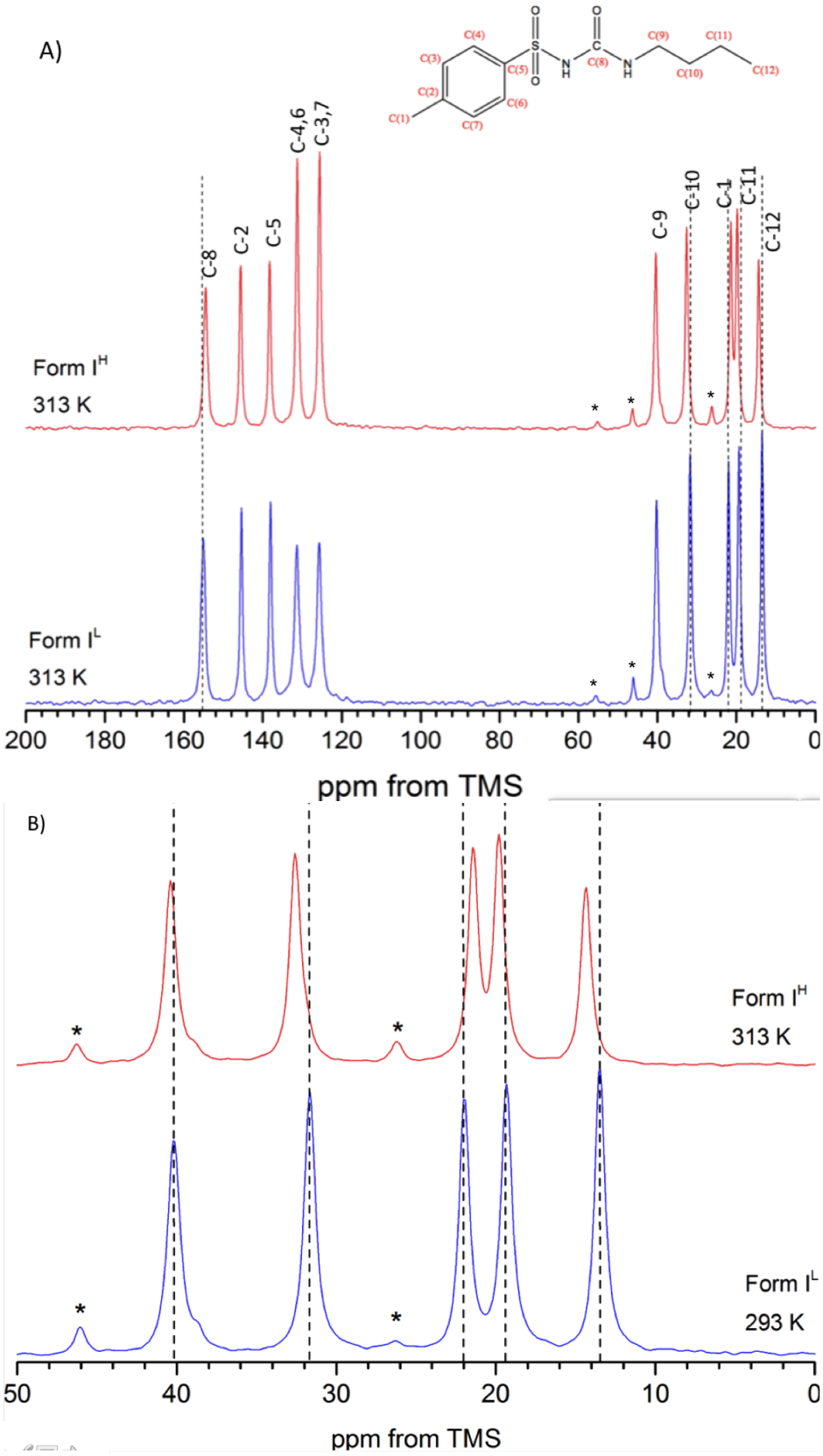


**Figure 7.6:** A) $^{1}$H-$^{13}$C CP/MAS NMR spectra of form I TLB at 293 and 313 K, recorded with an MAS rate of 10 kHz. $^{13}$C chemical shift assignments are indicated alongside the molecular structure of TLB. B) Zoomed aliphatic region, to highlight the temperature dependent enantiotropic transition between form $I^L$ and form $I^H$ (* denotes spinning sideband peaks)

**Table 7.4:** $^{13}$C NMR chemical shifts ($\delta$) of forms $I^L$ and $I^H$ tolbutamide, compared to literature values [43, 58]

| Carbon | Measured | | | Literature [43] |
|---|---|---|---|---|
| | Form $I^L$ | Form $I^H$ | $\Delta\delta$ (ppm) | $\Delta\delta$ (ppm) |
| 12 | 13.4 | 14.3 | 0.9 | 0.8 |
| 11 | 19.3 | 19.8 | 0.5 | 0.4 |
| 1 | 21.9 | 21.4 | 0.5 | 0.5 |
| 10 | 31.6 | 32.5 | 0.9 | 1.0 |
| 9 | 40.1 | 40.3 | 0.2 | 0.2 |
| 3,7 | 125.6 | 125.5 | 0.1 | 0 |
| 4,6 | 131.3 | 131.2 | 0.1 | 0.1 |
| 5 | 138.0 | 138.2 | 0.2 | 0.3 |
| 2 | 145.4 | 145.6 | 0.2 | 0.2 |
| 8 | 155.1 | 154.5 | 0.4 | 0.4 |

Although the $^1$H-$^{13}$C CP/MAS NMR spectra of forms II-IV have been reported (figure 7.7 [42, 58]), their quality is not sufficient to use as a reliable comparison. The spectra can at best be used as a visual qualitative reference for polymorph identification.

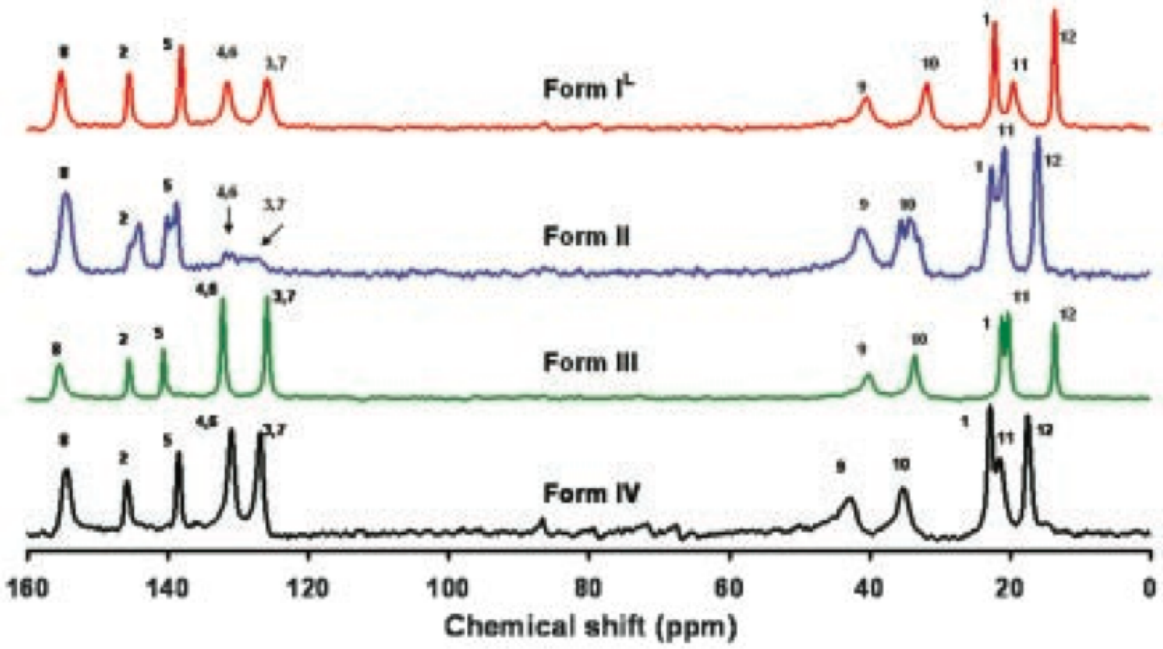


**Figure 7.7:** $^1$H-$^{13}$C CP/MAS NMR spectra of forms I-IV TLB polymorphs, recorded at 400 MHz, as reported by [42]

## 7.2 Initial Characterisation of Amorphous TLB, and TLB/PVP-VA solid dispersions

All solid dispersions were characterised using modulated DSC, PXRD and $^{1}$H-$^{13}$C CP/MAS NMR. Each dispersion has a single $T_g$ (figure 7.8), intermediate between the $T_g$ values of pure amorphous TLB and PVP-VA, as expected from the Gordon-Taylor relationship [112]. The value of $T_g$ increases with increasing polymer content for all dispersions. Ideal $T_g$ values of the dispersions were calculated using the Gordon-Taylor/Kelley-Bueche (G-T/K-B) and Couchman-Karasz (C-K) equations (equations 2.17 with 2.19 and 2.20 - see chapter 3), and can be seen in figure 7.8.

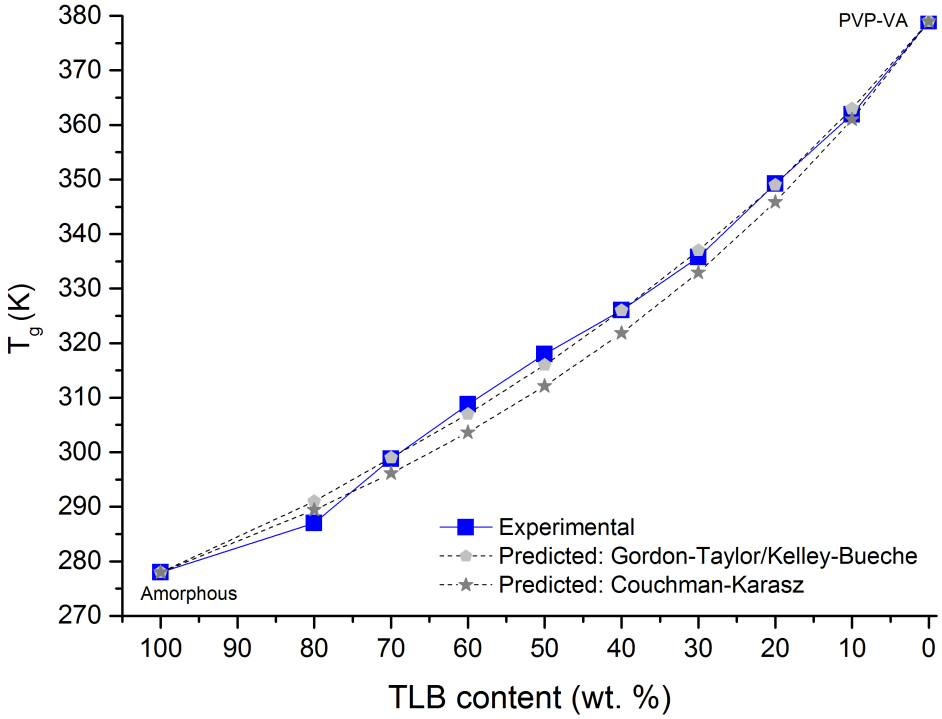


**Figure 7.8:** Glass transition temperatures for TLB/PVP-VA dispersions at different drug loadings, compared to values predicted by the Gordon-Taylor/Kelley-Bueche (G-T/K-B) and Couchman-Karasz (C-K) equations

The $T_g$ values of the TLB/PVP-VA dispersions showed very little deviation from predictions, indicating relatively ideal mixing between the drug and polymer, with the absence of strong intermolecular interactions. The experimental values were closer to predictions by the G-T/K-B over the C-K equation. In previous studies, deviations of $\pm$ 5 K were considered to be good agreement for 'ideal' mixing [78, 190]

The initial heating run for the highest drug loaded dispersions (60/40 - 80/20 TLB/PVP-VA) showed both endothermic melting peaks, and a glass transition event, highlighting the presence of both crystalline and amorphous TLB (figure 7.9). For the 70/30 and 80/20 dispersions, the transition of form $I^L$ to $I^H$ can be observed at 313 K [42]. Additional melting endotherms were also observed: at 80 wt. % drug loading, a small endothermic transition

peak at 370 K followed by a large, broad endothermic melt at 396 K ($\Delta H_f = 35.8$ J·g$^{-1}$); and for 70 wt. % drug loading, a broad endothermic peak at 389 K ($\Delta H_f = 23.4$ J·g$^{-1}$). There were also very slight exothermic transition points observed in both dispersions at 340 and 346 K for 80/20 and 70/30 respectively, which could indicate crystallisation from amorphous TLB upon heating. The DSC curve for the 60/40 dispersion showed a small endothermic peak at *ca.*380 K. As discussed in chapter 6, the presence of broad melting endotherms in DSC curves is attributed to either 1) the melting of a drug/polymer solid solution, formed through the dissolution of crystalline drug in the polymer upon heating [90, 148]; or 2) the melting of residual crystalline API formed during manufacture, which is often reported at lower $T_m$ values compared to the pure drug in the absence of polymer [148, 190, 228]. As we observe the transition of form $I^L$ to $I^H$ in the DSC curve of the 70/30 and 80/20 dispersions, let us assume that they contain residual form $I^L$, formed during manufacture. In this case, the melting endotherms at 389 and 396 K respectively can be assumed to be due to the melting of form $I^H$, which has a lower than expected $T_m$ value. The content of residual crystalline material can therefore be calculated with equation 5.1 (see chapter 5) using $\Delta H_f$ for form $I^H$ (88.5 J·g$^{-1}$ - figure 7.3) as 37.8 % and 50.6 % for the 70/30 and 80/20 dispersions respectively. If we calculate assuming the presence of form I TLB for the 60/40 dispersion in the same way, the crystalline content is much lower: only 5.7 % of the TLB content.

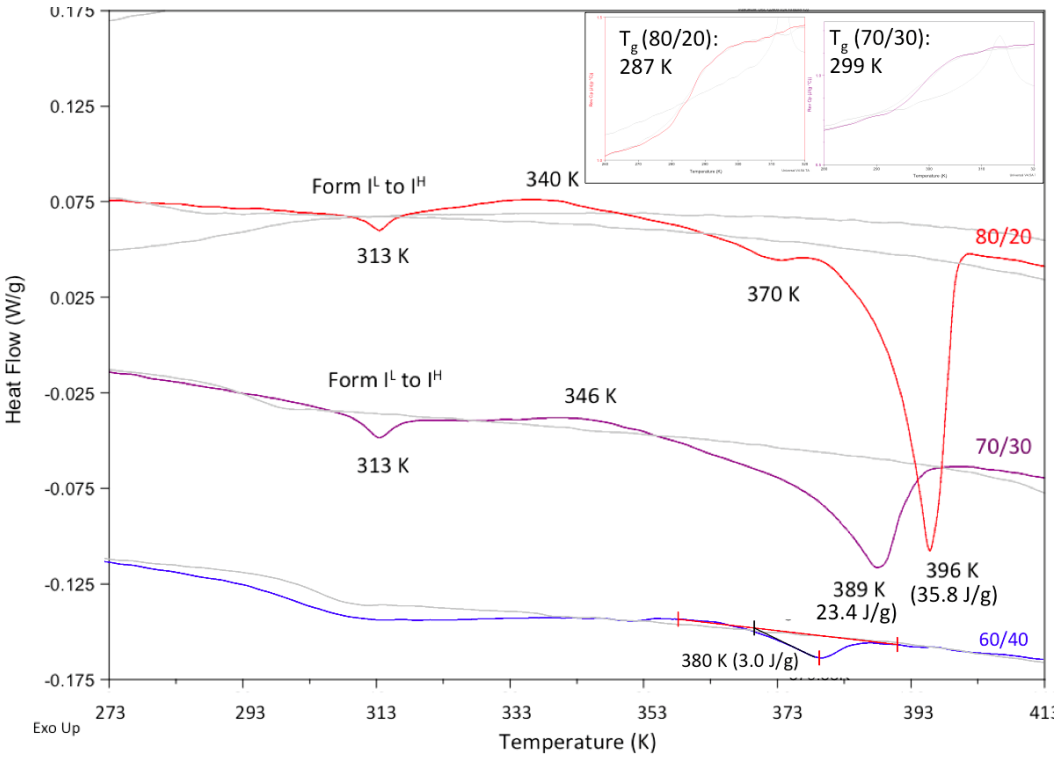


**Figure 7.9:** DSC data for 60/40, 70/30 and 80/20 dispersions (initial heat run only). $T_g$ events are shown inset (Rev. $C_p$ vs. temperature curves)

PXRD analysis at ambient temperature (figure 7.10) also indicated the presence of crystalline material in the highest drug loading dispersions. The dispersions with drug loadings lower

than 50 wt. % were fully amorphous.

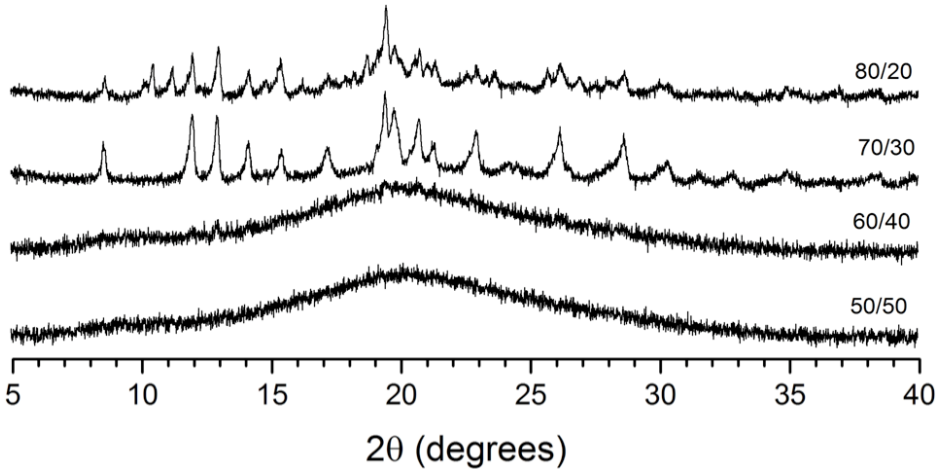


**Figure 7.10:** PXRD patterns of TLB/PVP-VA dispersions at different drug loadings. TLB loadings of greater than 50 wt. % all displayed broad halo patterns, and were therefore confirmed to be fully amorphous

Here we see the presence of *multiple* polymorphs of TLB in the 80/20 dispersion, which can be identified as mainly form $I^L$ (dashed black lines), alongside some form II (green lines) and V (blue lines) ((figure 7.11)) [42, 44]. The crystalline TLB in the 70/30 dispersion was confirmed to be form $I^L$ ((figure 7.11)). There are some slight peaks in the PXRD pattern of the 60/40 dispersion, which could indicate form $I^L$, although the amount is very low.

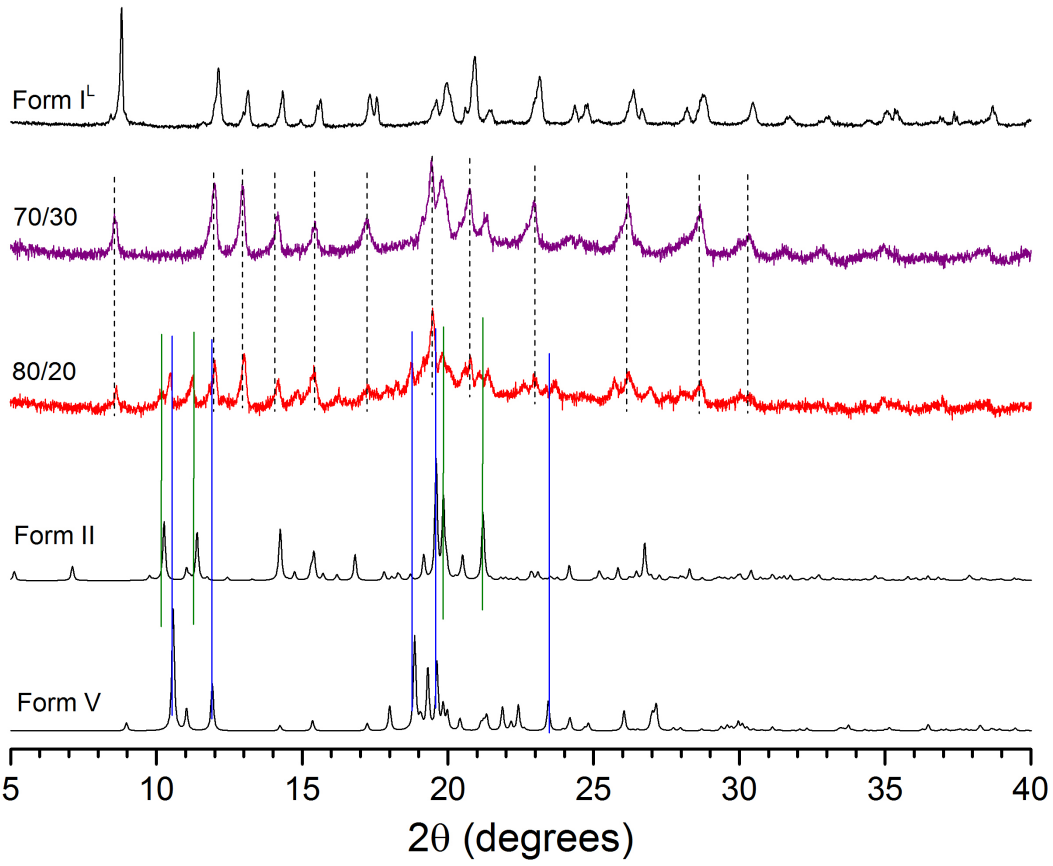


**Figure 7.11:** PXRD patterns of 70/30 and 80/20 dispersions at ambient temperature, compared to form $I^L$ (Sigma Aldrich, UK), form II [42] and form V [44] TLB polymorphs.

$^{1}$H-$^{13}$C CP/MAS NMR confirmed the amorphous nature of dispersions up to 50 % drug loading (figure 7.12), which was in agreement with DSC and PXRD analysis. Crystalline TLB was not detected in the $^{1}$H-$^{13}$C CP/MAS NMR spectrum for the 60/40 dispersion, in comparison to DSC and PXRD. The change in intensity of the drug/polymer peaks reflects the ratio of the two components within each dispersion. $^{13}$C chemical shift assignments of the amorphous TLB can be seen in table 7.5, with the additional peaks assigned to the polymer.

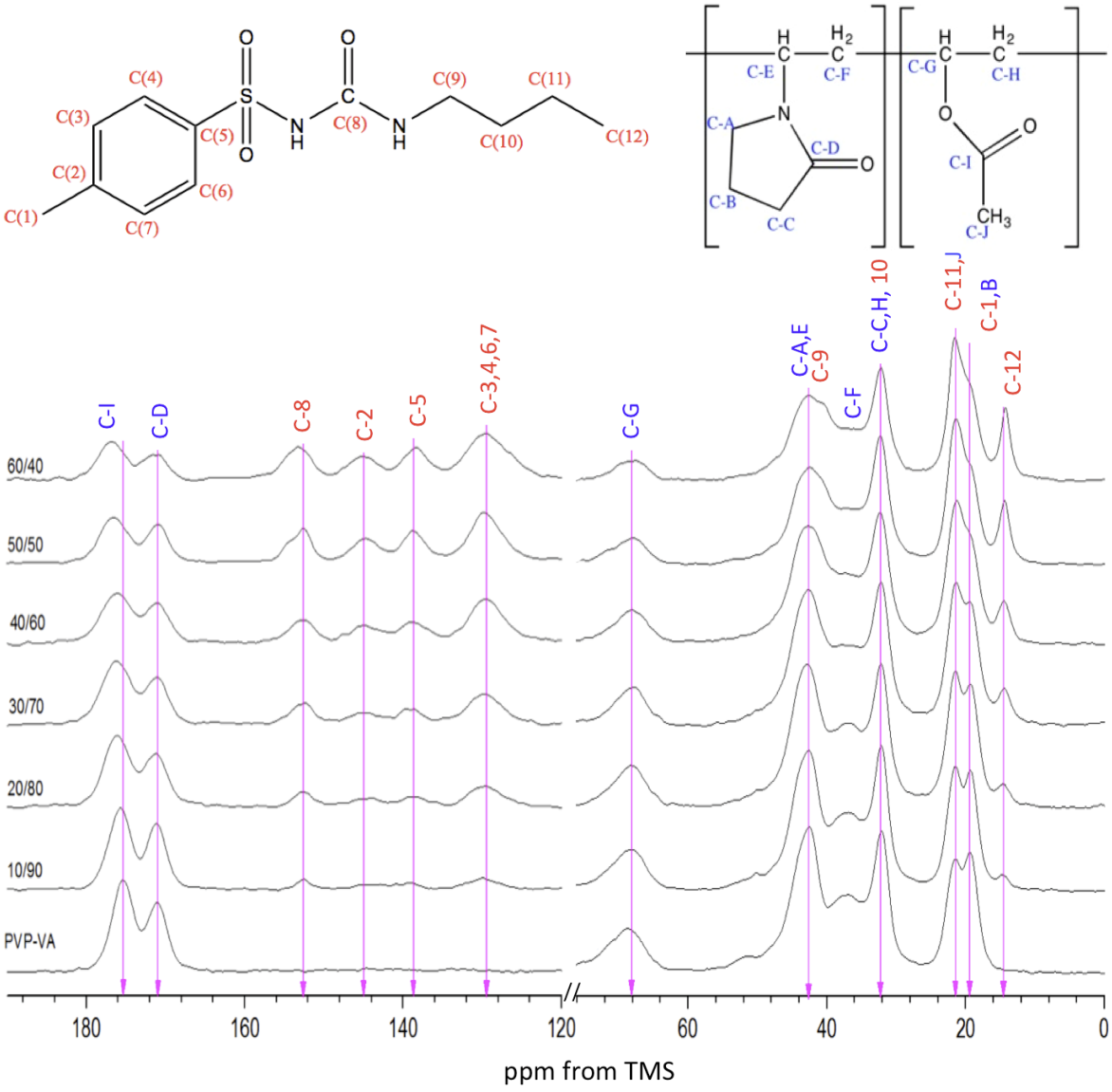


**Figure 7.12:** $^{1}$H-$^{13}$C CP/MAS NMR spectra for all amorphous dispersions: TLB/PVP-VA 10/90 - 60/40 compared to PVP-VA, recorded at an MAS rate of 10 kHz, with the molecular structure of TLB and PVP-VA to indicate chemical shift assignment

**Table 7.5:** $^{13}$C NMR chemical shifts ($\delta$) of amorphous TLB and and PVP-VA for dispersions of drug content between 10 and 60 %

| $^{13}$C assignment | Amorphous TLB | $^{13}$C assignment | PVP-VA |
|---|---|---|---|
| C-12 | 14.4 | | |
| | | C-B | 19.3 |
| C-1, C-11 | 21.5 | C-J | 21.5 |
| C-10 | 32.1 | C-C, C-H | 32.1 |
| | | C-F | 36.5 |
| C-9 | 40.4 | | |
| | | C-A, C-E | 42.6 |
| | | C-G | 68 |
| C-3,4,6,7 | 129.9 | | |
| C-5 | 138.0 | | |
| C-2 | 144.5 | | |
| C-8 | 152.7 | | |
| | | C-D | 171.0 |
| | | C-I | 175.7 (10/90) - 176.9 (60/40) |

Figure 7.13 shows the ambient temperature $^{1}$H-$^{13}$C CP/MAS NMR spectra for the 70/30 and 80/20 dispersions. The narrower resonances, with broadening around the base indicate the presence of both crystalline and amorphous TLB. The crystalline component of the 70/30 dispersion can clearly be identified as form I$^{L}$, in agreement with PXRD. The 80/20 dispersion contains a more complex mixture of polymorphs. Using the CP/MAS spectrum, we confirmed the presence of forms I$^{L}$, II and V in the 80/20 dispersion, in agreement with PXRD. The assignments of resonances to each polymorph within the dispersion can be seen in table 7.6. Form V was concurrently obtained in our research group through encapsulation of TLB within mesoporous silica at 50 % drug loading (which was confirmed by comparison with the literature PXRD pattern for form V [44]), hence the unreported $^{13}$C NMR spectrum was used here for identification purposes. Following PXRD and $^{1}$H-$^{13}$C CP/MAS NMR analysis, the calculation of residual crystalline content from the DSC curve can be considered a good estimation for the 70/30 dispersion, but most likely an underestimate for the 80/20 dispersion. The broad endotherm observed for the 80/20 dispersion at 396 K, is likely due to the combined melting of forms I$^{H}$, II and V, which were not fully accounted for in the calculation. The constituent parts of the high drug loading dispersions have been further clarified through variable temperature experiments (see section 7.3.2).

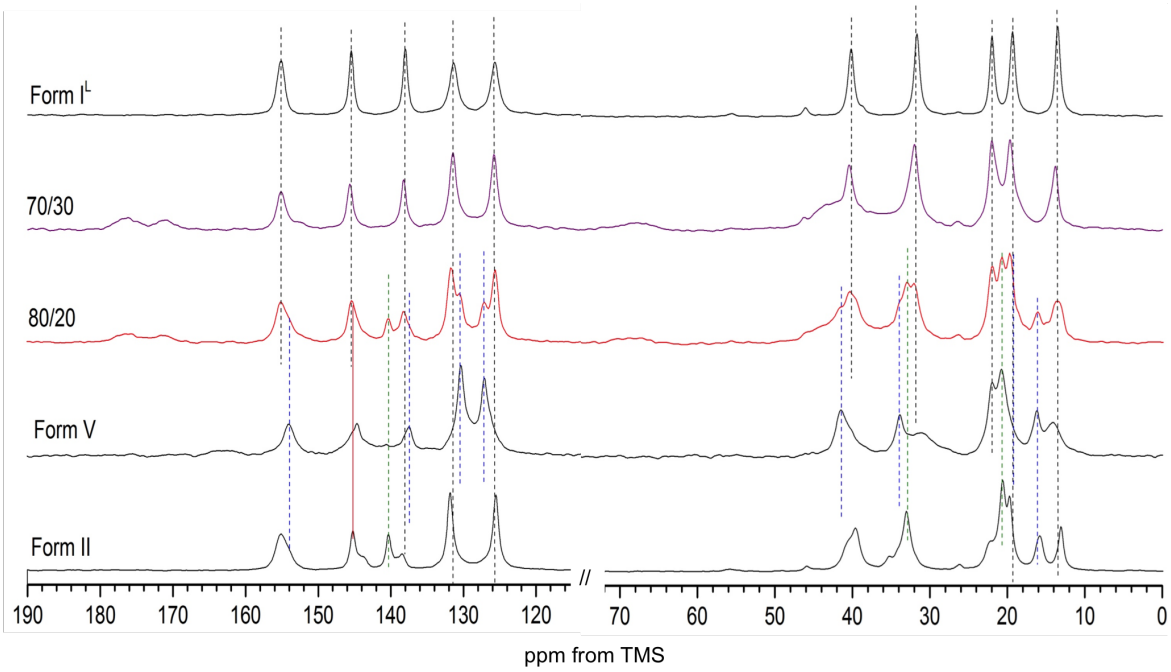


**Figure 7.13:** $^{1}$H-$^{13}$C CP/MAS NMR spectra for 70/30 and 80/20 dispersions compared to forms I$^L$ II and V, recorded at an MAS rate of 10 kHz at 293 K. Splitting of the peaks at *ca.* 145.4 and 138.1 ppm for form II TLB may be due to the increased Z' value of this polymorph (Z' = 4, see table 7.1). Unfortunately, due to time constraints, this was not investigated further

**Table 7.6:** $^{13}$C NMR chemical shifts ($\delta$, ppm) of forms I$^L$, form II and form V tolbutamide, and PVP-VA within the 80/20 dispersion, recorded at ambient temperature. Note, the level of amorphous TLB in this dispersion was too low to detect specific chemical shift values

| $^{13}$C assignment | Form I$^L$ | Form II | Form V | $^{13}$C assignment | PVP-VA |
|---|---|---|---|---|---|
| C-12 | 13.4 | 13.4, 15.9 | 13.4, 15.9 | | |
| C-11 | 19.5 | 19.5 | 20.6 | C-B | 19.5 |
| C-1 | 21.9 | 20.3 | 21.9 | C-J | 21.9 |
| C-10 | 31.7 | 32.9 | 33.9 | C-H | 31.7 |
| | | | | C-C, | 32.8 |
| C-9 | 40.2 | 39.6 | 41.5 | | |
| | | | | C-A, C-E | 43.4 |
| | | | | C-G | 68.0 |
| C-3,7 | 125.6 | 125.6 | 127.1 | | |
| C-4,6 | 131.5 | 131.5 | 130.2 | | |
| C-5 | 138.1 | 140.0 | 138.1 | | |
| C-2 | 145.5 | 145.5 | | | |
| C-8 | 155.0 | 155.0 | 153.9 | | |
| | | | | C-D | 170.9 |
| | | | | C-I | 176.2 |

We were able to deconvolute the C-8 peak for the 70/30 dispersion to estimate the relative

contribution of form $I^L$ and amorphous TLB (figure 7.14). Unfortunately, the level of amorphous TLB in the 80/20 dispersion was too low for accurate deconvolution of this spectrum.

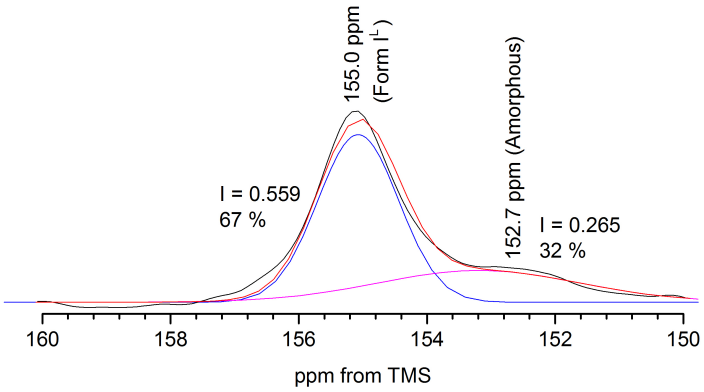


**Figure 7.14:** $^1$H-$^{13}$C CP/MAS NMR spectrum of the C-8 peak for the 70/30 dispersion. Peak integrals obtained from Gaussian dseconvolution are shown, alongside the calculated % contribution to the peak from form $I^L$ ($\delta$ = 155.0 ppm) and amorphous TLB ($\delta$ = 152.7 ppm)

This estimation of 67 % form $I^L$ at 293 K is much higher than the value calculated using the melting enthalpies detected in the DSC curve (37.8 %), although this technique may underestimate the amorphous form due to the broadening effect.

Changes to the chemical shift of one carbonyl for PVP-VA (C-I) were observed across all dispersions (figure 7.15). The gradual downfield shift of the carbonyl peak from 175.4 ppm in pure PVP-VA to 176.9 ppm in the 60/40 dispersion indicates a change in drug-polymer hydrogen bonding within the fully amorphous dispersions with increasing drug content [30]. The 70/30 and 80/20 dispersions show a change in hydrogen bonding behaviour compared to the 60/40 dispersion, indicating that the amorphous TLB content in the 60/40 dispersion is dominant over the small amount of crystalline material present.

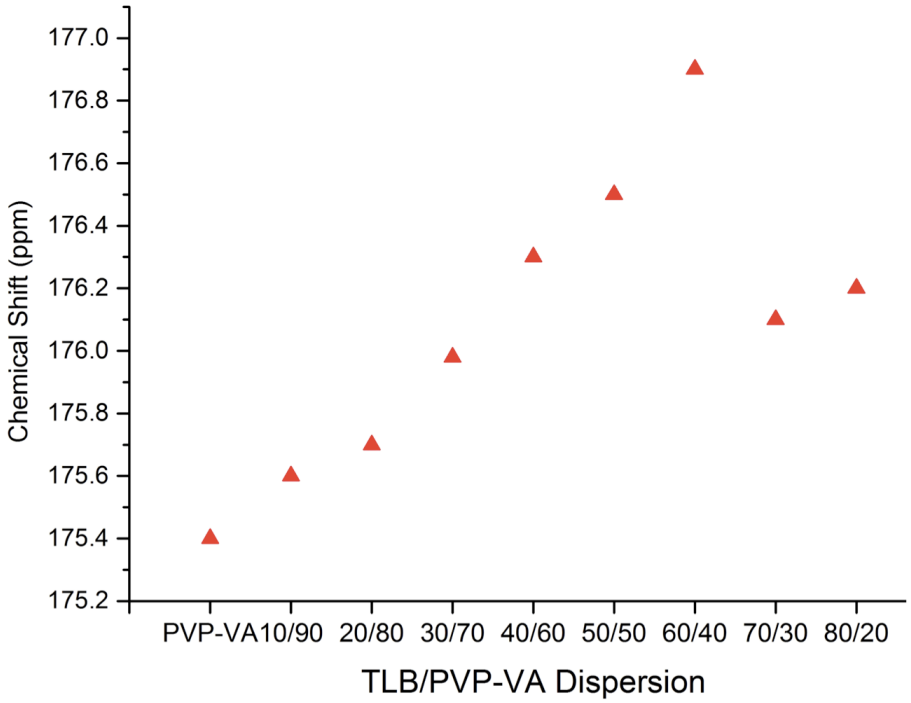


**Figure 7.15:** Changes to the polymer carbonyl group chemical shift values for C-I across all TLB/PVP-VA dispersions

From the initial characterisation, we have determined that the dispersions with drug content up to 50 % are fully amorphous, the 60/40 and 70/30 dispersions contain a mixture of amorphous and form $I^L$ TLB, and the 80/20 dispersion is a more complex mixture of amorphous, form $I^L$, form II and form V TLB.

## 7.3 Variable temperature NMR studies of TLB

The VT $^{1}$H-$^{13}$C CP/MAS NMR acquisition for crystalline TLB, and TLB/PVP-VA solid dispersions followed the temperature cycle as follows:

1. Cooling from room temperature to 253 K over *ca.* 30 minutes
2. Samples were equilibrated at the target temperature for 15 minutes prior to acquisition
3. Heating, in 20 K intervals, with temperature equilibration prior to acquisition
4. Step 3 was repeated up to the maximum temperature of 373 K
5. Following acquisition at 373 K, samples were cooled back to 293 K, followed by equilibration and acquisition

Spectra acquired at 293 K during the initial characterisation (section 7.2) were used as a comparison to determine changes upon cooling to 253 K, and following heating to 373 K.

### 7.3.1 Polymorphic transitions of form I TLB

The polymorphic transition of form I TLB (form $I^L \rightarrow I^H$) at *ca.* 311 K was shown in section 7.1. Here we investigated the variable temperature behaviour of form I TLB further by cooling to 253 K (figure 7.16). At lower temperatures, the resonances for aromatic carbons C-4,6 and C-3,7 are broadened significantly, and appear not to be present within the spectra. Similar effects have been shown in the spectra for form II TLB at ambient temperature by Thirunahari *et al.* (figure 7.7), although an explanation for the broadening of the resonances was not provided [42].

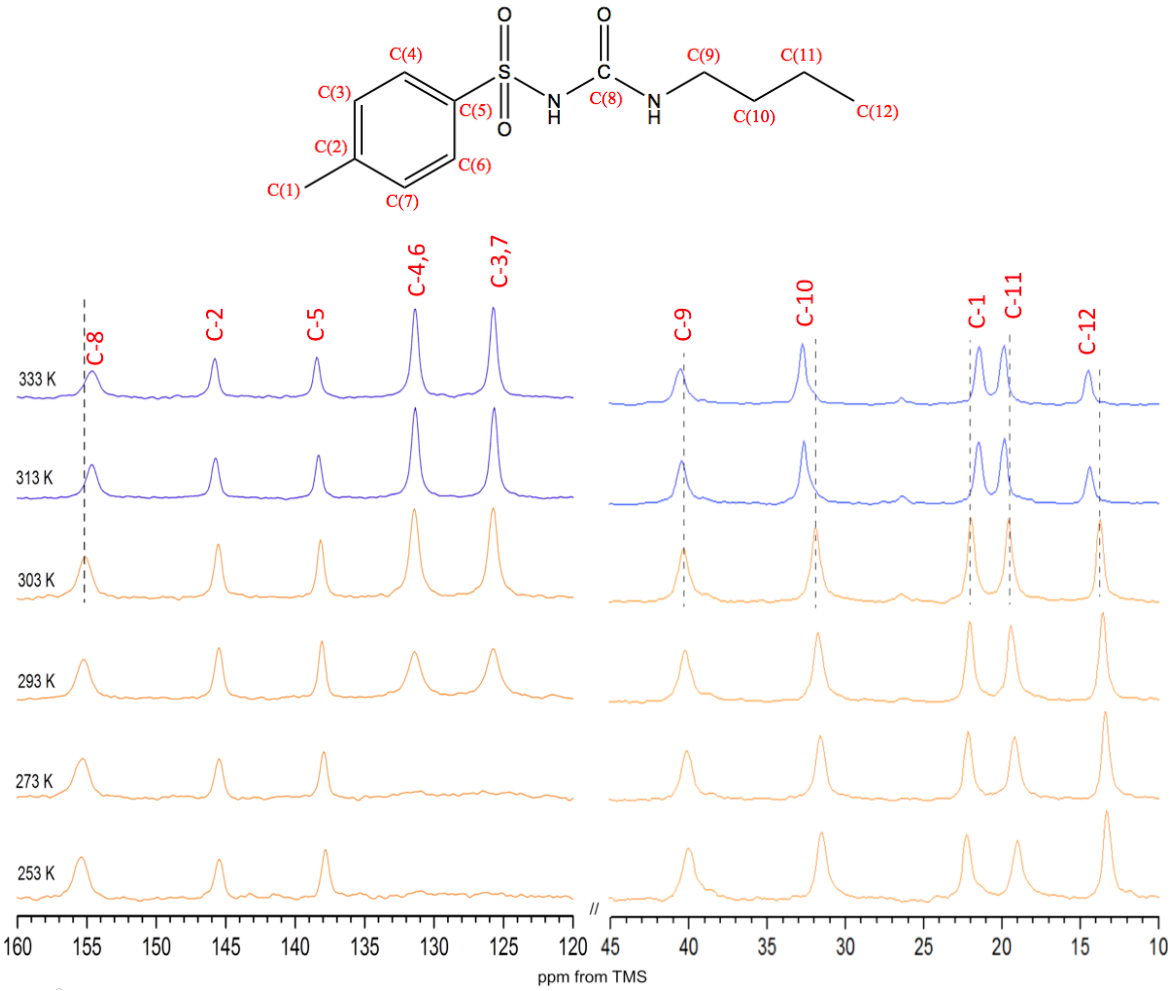


**Figure 7.16:** $^{1}$H-$^{13}$C CP/MAS NMR spectra of form I TLB, recorded at different temperatures between 253 K and 373 K, at an MAS rate of 10 kHz. The polymorphic transition between form $I^L$ and $I^H$ is highlighted by dashed lines

There is no evidence of disorder around the aromatic ring of TLB form I from crystallographic structural information. Low temperature crystallographic investigations show no significant changes in the crystal structure of form $I^L$ upon temperature, with good overlap between aromatic ring positions at 295 and 153 K [57]. Additionally, the ORTEP (Oak Ridge Thermal-Ellipsoid Plot) diagram of the aromatic ring thermal

ellipsoids also shows very low disorder for form $I^L$, as compared to form III, which is known to undergo temperature dependent disorder effects (figure 7.17) [42].

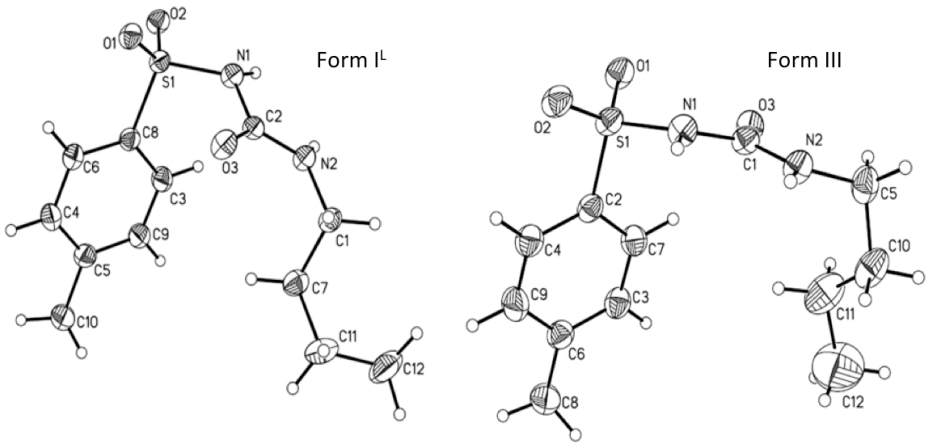


**Figure 7.17:** ORTEP diagrams of forms $I^L$ and III TLB, adapted from the supporting information of [42]

Disorder in the crystal structure does not explain the broadening of the resonances in the CP/MAS spectra. The broadening is therefore likely due to a motional freezing of the aromatic ring, observable on the kHz timescale at low temperature.

At ambient temperatures, the effect of aromatic ring oscillations are averaged between the carbon positions, leading to two distinct $^{13}$C peaks at 125.6 and 131.3 ppm for carbons C-3,7 and C-4,6 respectively. Upon cooling, slightly slower mobility could lead to an increase in the number of aromatic ring positions. This would result in the loss of chemical equivalence of the four aromatic carbons (C-4,6 and C-3,7). The broadening effect in the spectra can be thought of in terms of chemical exchange between a two symmetrical $^{13}$C environments, in dynamic equilibrium [1]. In this case, dynamic equilibria between carbons $4 \rightleftharpoons 6$ and carbons $3 \rightleftharpoons 7$ must be imagined (figure 7.18 B)). These effects could be further investigated using other methods, for example $^2$H NMR, which has been shown to be sensitive to the identification of mobility of similar systems [269].

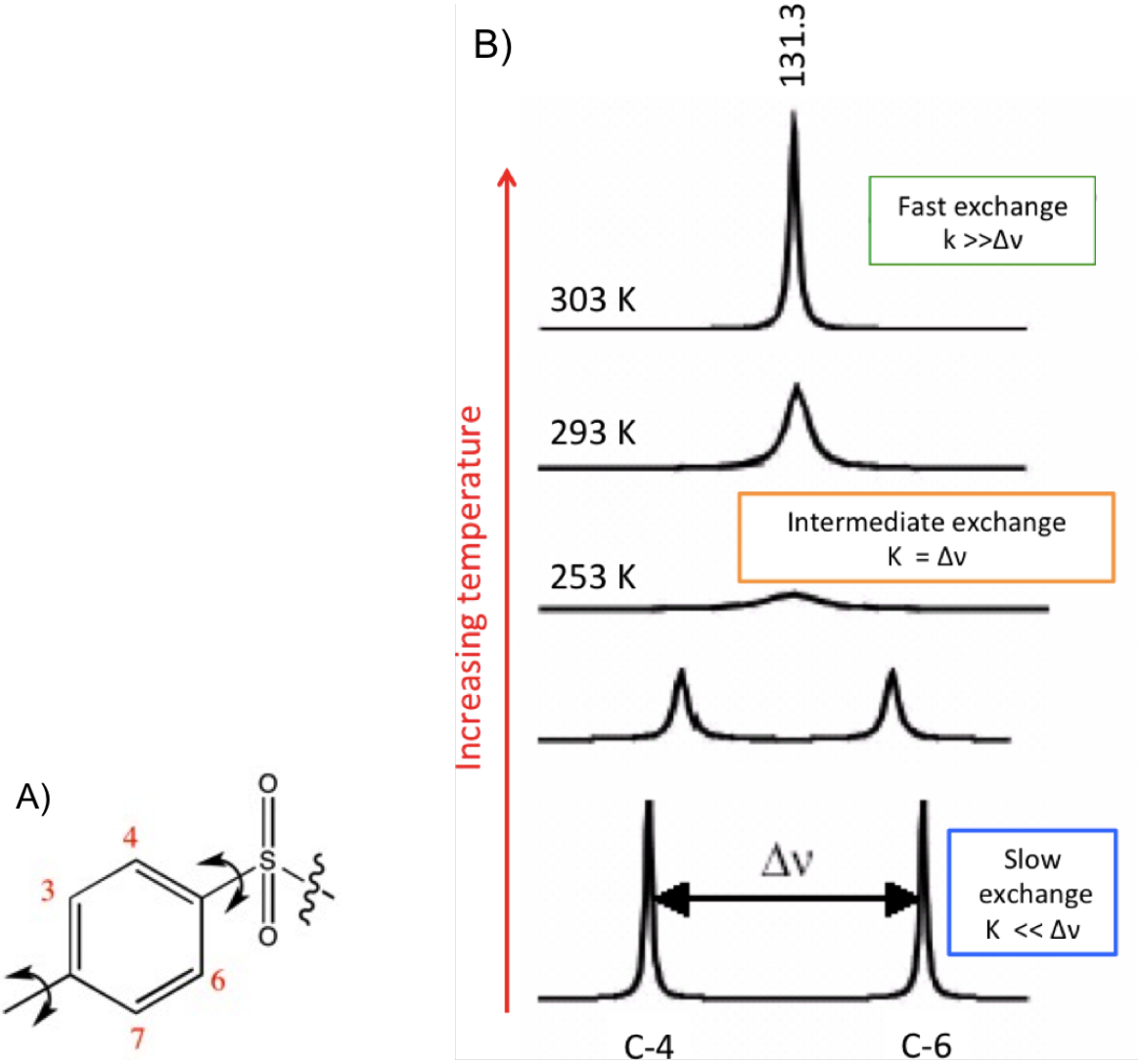


**Figure 7.18:** A) Representation of the possible oscillation of TLB aromatic ring and B) Example of the effect of chemical exchange in a NMR spectrum with increasing temperature adapted from [45]

### 7.3.2 Detection of changes in mobility and polymorphic transitions in high drug loading TLB/PVP-VA dispersions

The focus of literature on TLB in recent years has been the characterisation of pure polymorphic forms. There is little evidence of NMR studies of TLB amorphous dispersions, especially regarding mobility and crystallisation behaviour so far. Here we have extensively characterised dispersions of TLB and PVP-VA, with varying drug/polymer ratios (80 % to 20 %) using a number of variable temperature solid-state NMR techniques, including $^{1}$H-$^{13}$C CP/MAS, $^{13}$C{$^{1}$H} MAS, $^{1}$H MAS and spin-lattice relaxation.

Across a range of temperatures, we were able to observe a number of polymorphic transitions in the $^{1}$H-$^{13}$C CP/MAS NMR spectra of the 80/20 dispersion (figure 7.19). From the initial characterisation, the 80/20 dispersion was found to contain a polymorphic mixture of forms $I^{L}$, II and V at ambient temperature. There is considerable overlap of peaks between the

three polymorphs (and polymer), especially within the aliphatic region of the spectrum. To monitor the changes in polymorphic composition with increasing temperature, the non-overlapping peaks at 140.0 ppm (C-5: form II) and 127.1 and 130.2 ppm (C-3,7 and C-4,6: form V) will be used.

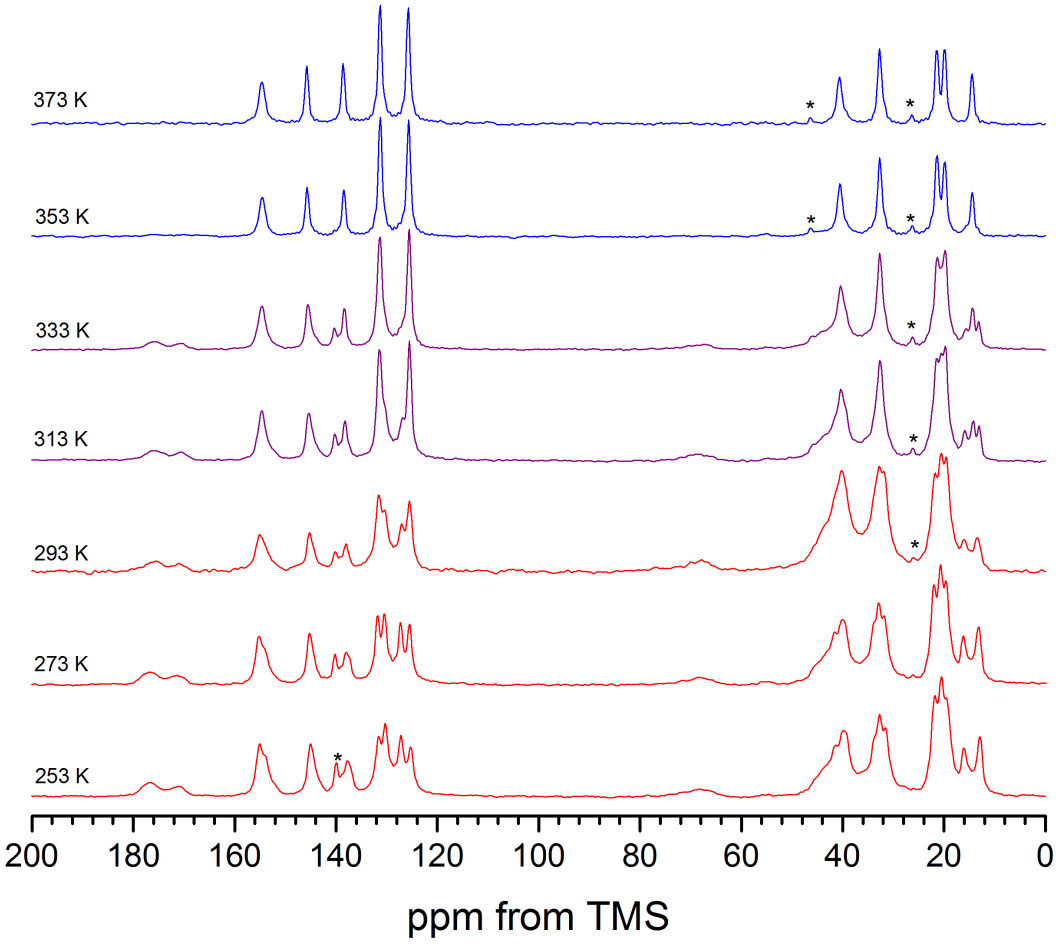


**Figure 7.19:** $^{1}$H-$^{13}$C CP/MAS NMR spectra of 80/20 dispersion recorded at different temperatures between 253 K and 373 K, at an MAS rate of 10 kHz (* denotes spinning sideband peaks)

Upon cooling from 293 to 253 K, an increased presence of form V is observed, through the growth of the resonances at 127.1 (C-3,7) and 130.2 (C-4,6) ppm, and the shoulder peak at 153.9 ppm (C-8), consistent with an enantiotropic transition. All three polymorphs can still be identified at 253 K, although forms V and II appear to dominate over the form $I^L$ (figure 7.20). The broadening of the C-3,7: C-4,6 resonances observed for pure form $I^L$ did not occur in the dispersion, hence uncertainty of assignment of these resonances to form $I^L$, form II, or a combination of both at low temperatures remains.

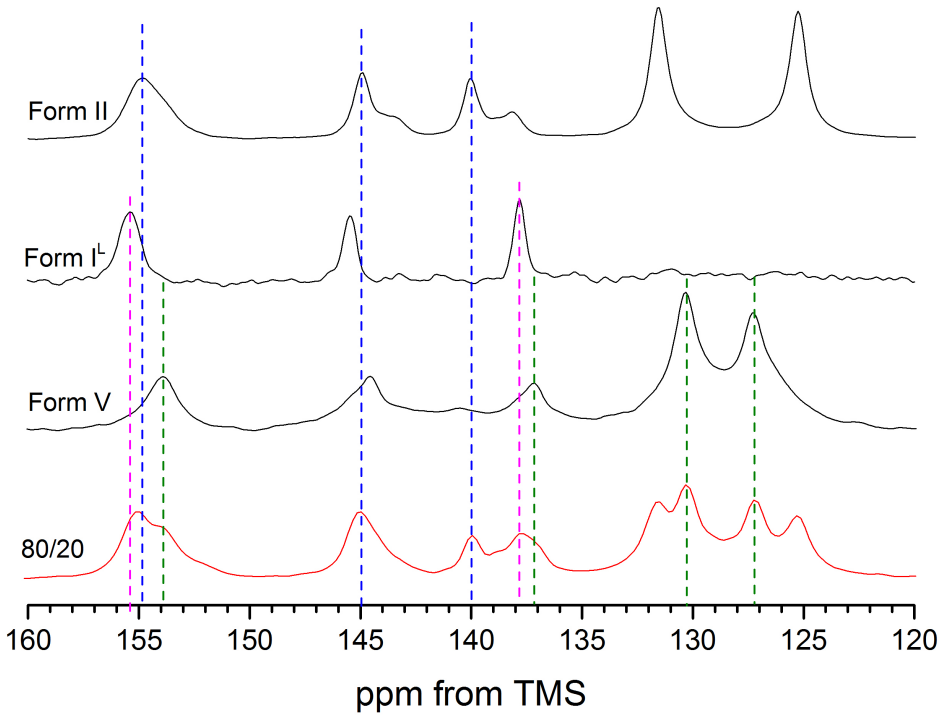


**Figure 7.20:** Aromatic region of the $^{1}$H-$^{13}$C CP/MAS NMR spectra of 80/20 dispersion, form I$^{L}$ and form V recorded at 253 K, with a comparison to form II recorded at 293 K, at an MAS rate of 10 kHz

It is difficult to determine which polymorph converts to form V, although it is likely to be form I$^{L}$, as we observe a reduction in the intensity of the peaks attributable to form I$^{L}$ at 253 K. Additionally, in the published characterisation study of form V, Nath *et al.* [44] found form V crystallised to form I$^{L}$ within two hours at room temperature, demonstrating the presence of an enantiotropic relationship. Here we observe this transition in the opposite direction at lower temperatures, indicating this relationship is reversible and that form V is the more stable polymorph at low temperatures.

Despite the 80/20 dispersion containing a complex mixture of polymorphs, we were able to observe a number of interesting polymorphic transitions with increasing temperature, seen in more detail in figure 7.21.

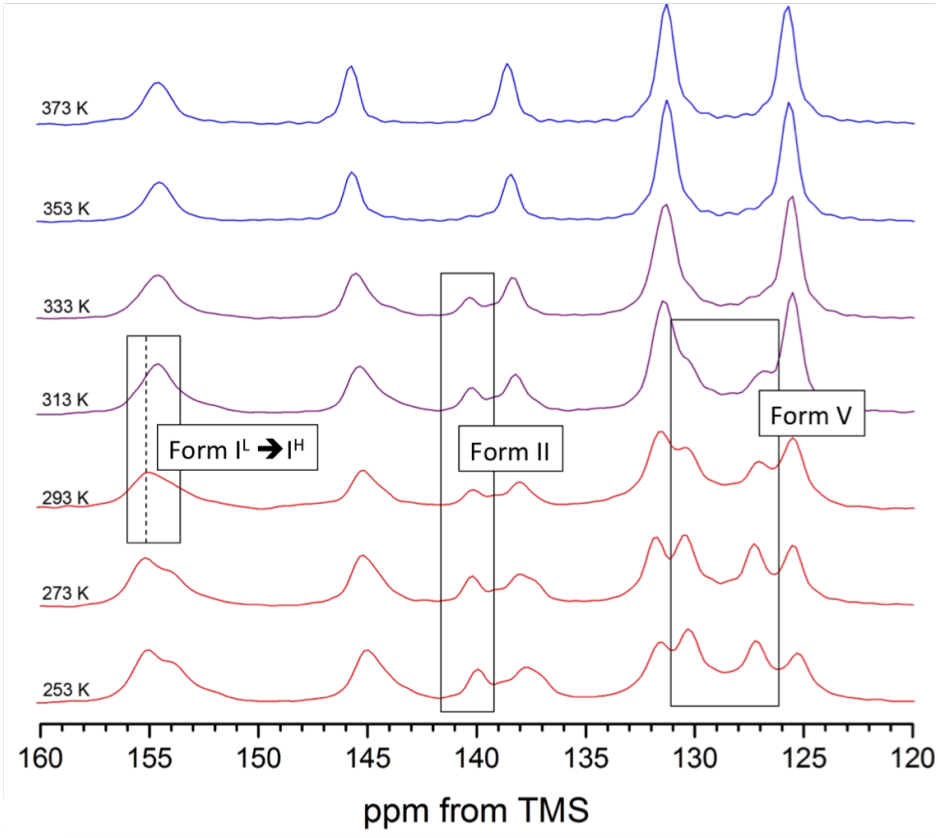


**Figure 7.21:** Aromatic region of the $^{1}$H-$^{13}$C CP/MAS NMR spectra of 80/20 dispersion recorded at different temperatures between 253 K and 373 K, at an MAS rate of 10 kHz

- 253 - 313 K: The conversion of form V to form I occurs, observed through the reduction of the resonance intensity for form V, and the increase of the resonance intensity of form I for carbons C-4,6 and C-3,7.
- 293 - 313 K: Spectral changes in the aromatic (figure 7.22) and aliphatic (figure 7.21) regions are attributed to the polymorphic transition from form $I^L$ to form $I^H$ (figure 7.22), which is in agreement with the known transition temperature of 311 K [43].
- Above 333 K: The presence of form II TLB (C-5: 140 ppm) can be observed until 333 K. At 353 K and above the $^{1}$H-$^{13}$C CP/MAS spectrum shows only the presence of one phase: form $I^H$, as form II becomes metastable and undergoes crystallisation to the more stable form (figures 7.21 and 7.23).

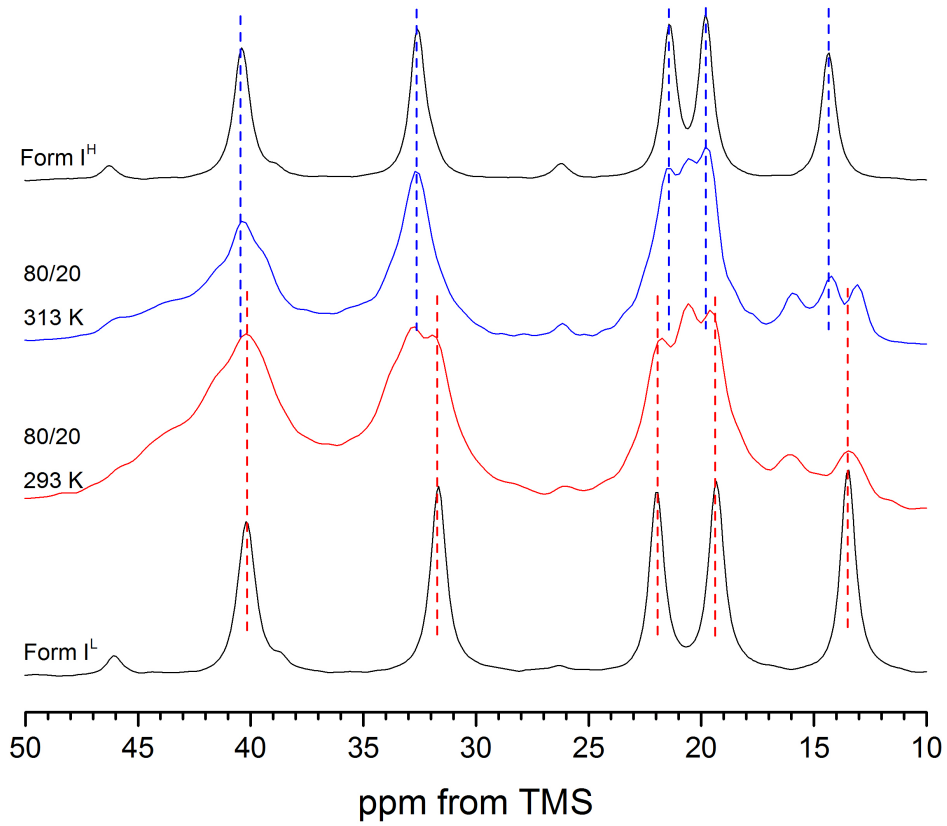


**Figure 7.22:** Aliphatic region of the $^{1}$H-$^{13}$C CP/MAS NMR spectra of 80/20 TLB/PVP-VA dispersion at 293 (red) and 313 K (blue), with a comparison to forms $I^{L}$ (pink) and $I^{H}$ (green), recorded at an MAS rate of 10 kHz

These observations agree well with the trend of thermodynamic stabilities of the polymorphs, as form $I^{H}$ is the most stable polymorph at temperatures above 353 K, with form II being the most stable at temperatures below 353 K [42]. The thermodynamic stability of form V is currently unknown, but from this work we can suggest it has a higher stability than form $I^{L}$ at low temperatures, with an enantiotropic relationship existing between form V/$I^{L}$.

By 353 K and above, we additionally observe the complete disappearance of all polymer peaks, and the loss of broadening around the peak base due to amorphous TMB (figures 7.19 and 7.23). This is likely due to the increased mobility of this phase, indicating a degree of phase separation between crystalline drug and polymer/remaining amorphous TLB at high temperatures.

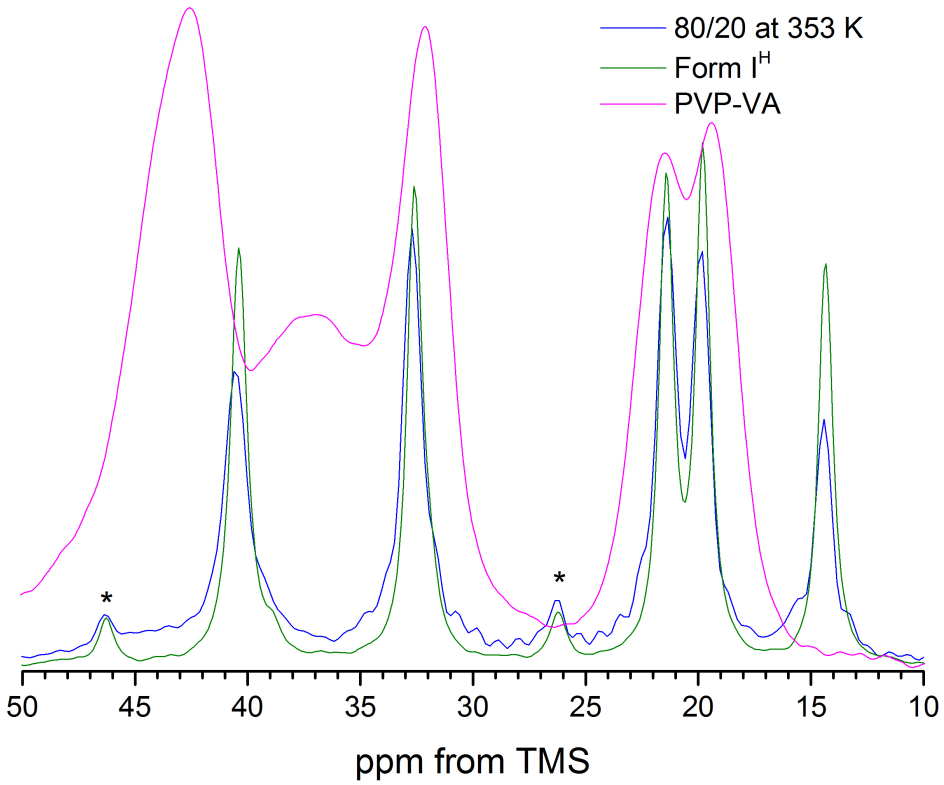


**Figure 7.23:** Aliphatic region of the $^{1}$H-$^{13}$C CP/MAS NMR spectra of 80/20 TLB/PVP-VA dispersion at 353 K (blue), with a comparison to form $I^{H}$ (green) and PVP-VA (pink), recorded at an MAS rate of 10 kHz. Spinning sidebands are denoted by asterisks

Figure 7.24 provides a schematic representation of the crystallisation behaviour of TLB in the 80/20 dispersion with increasing temperature. Although important observations have been made through the VT $^{1}$H-$^{13}$C CP/MAS NMR spectra of the 80/20 dispersion, future work should focus on variable temperature PXRD analysis to provide confirmation of the exact transition temperatures between each polymorph.

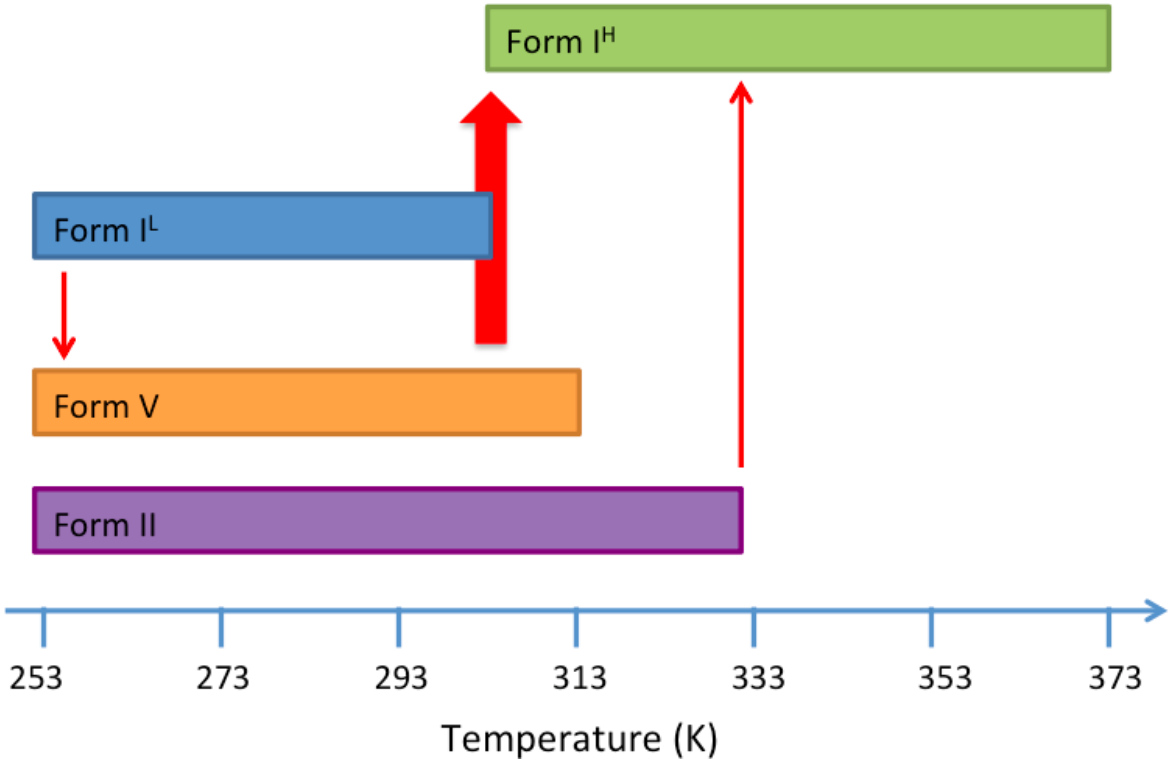


**Figure 7.24:** Schematic representation of the polymorphic changes within the 80/20 TLB/PVP-VA dispersion with increasing temperature

Reducing the drug loading of the dispersion to 70 % simplified the polymorphic behaviour. Initial DSC characterisation of the 70/30 dispersion indicated the presence of amorphous material ($T_g$ = 299 K), which was also seen through broadening around the base of the ambient temperature $^{1}$H-$^{13}$C CP/MAS NMR spectrum.

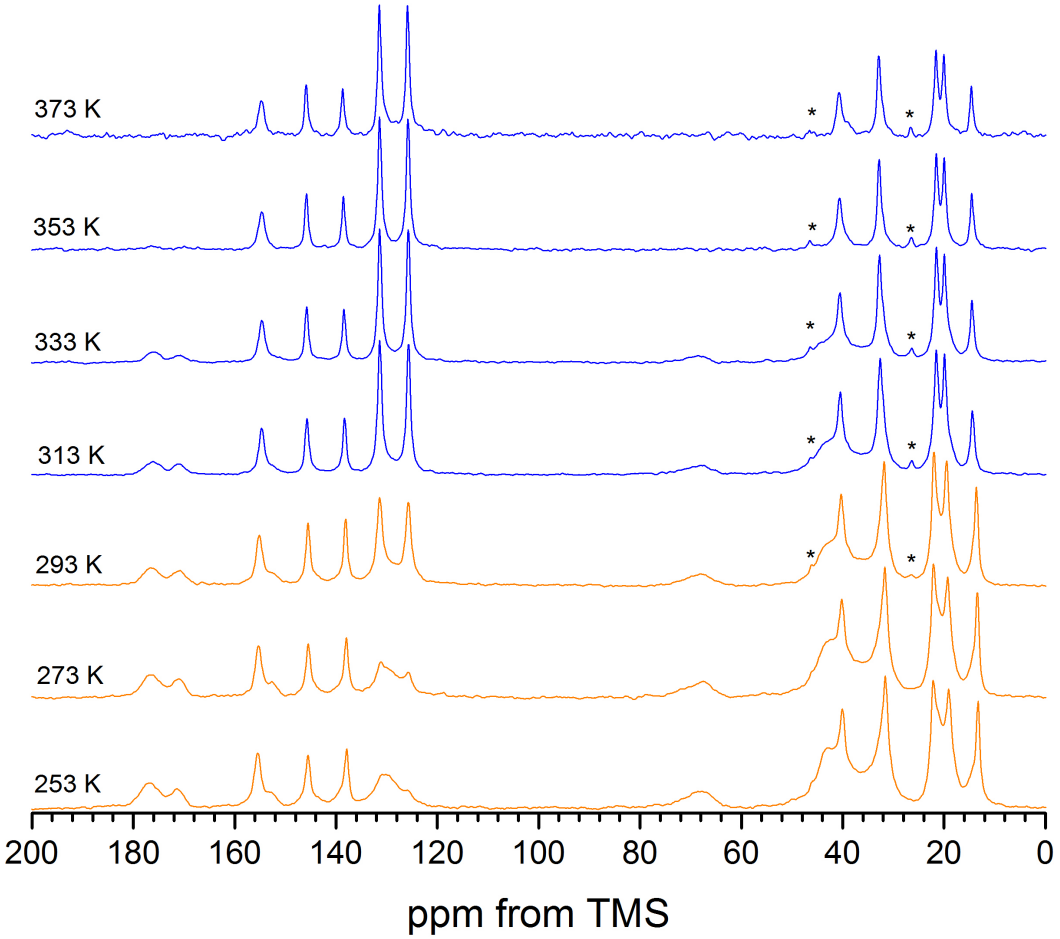


**Figure 7.25:** $^{1}$H-$^{13}$C CP/MAS NMR spectra of 70/30 dispersion recorded at different temperatures between 253 K and 373 K, at an MAS rate of 10 kHz. Spinning sidebands are denoted by asterisks

Upon cooling from 293K to 253 K (figures 7.25 and 7.26), the presence of amorphous TLB within the dispersion becomes more visible in the spectra for the resonances of carbons C-3,4,6,7 (132 - 124 ppm), due to the significant broadening of the aromatic ring signals of the crystalline form $I^L$ TLB component, which was observed at lower temperatures in the pure form $I^L$ (figure 7.6). There is some additional broadening around the base of the central aromatic peaks (138 and 145.5 ppm) (figure 7.26), with a broad shoulder peak apparent *ca.* 155 ppm (C-8), both also highlighting the amorphous component. When heated from 253 to above the $T_g$ of 299 K (figure 7.25), the broadening reduced as the amorphous component crystallised to form I, with the most significant difference being to the peak for C 3-7, which clearly resolved into two separate peaks, as would be expected for form $I^L$ upon heating.

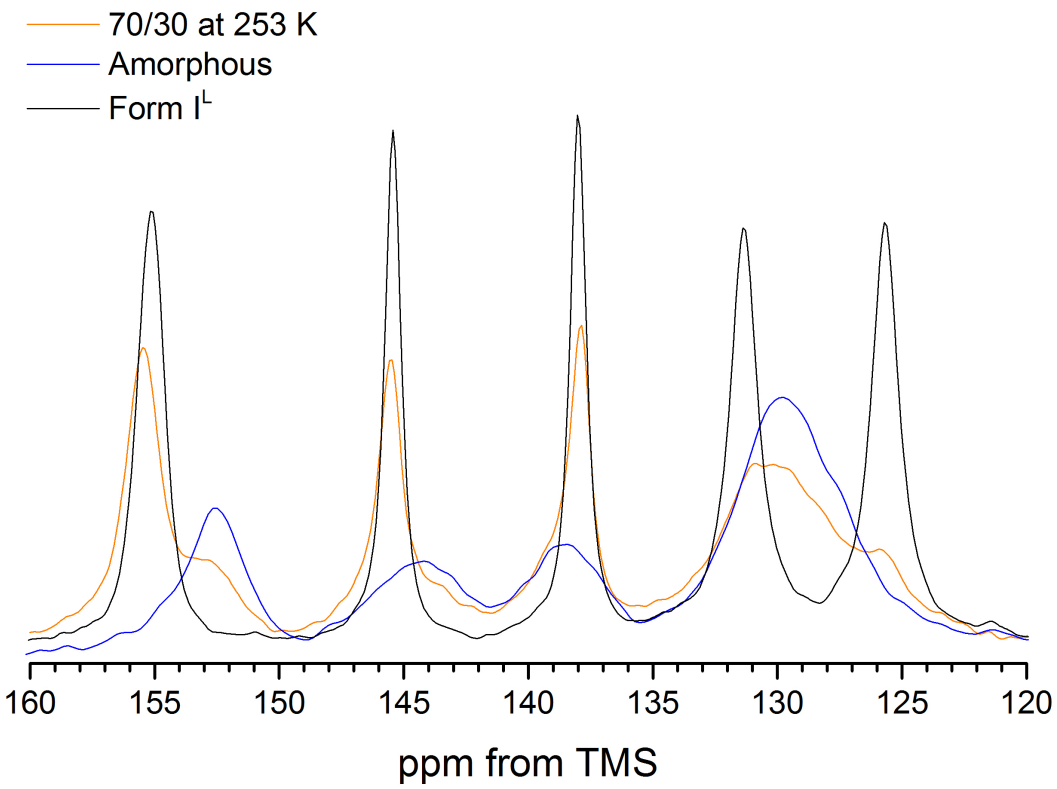


**Figure 7.26:** Aromatic region of the $^{1}$H-$^{13}$C CP/MAS NMR spectra of the 70/30 dispersion, compared to form $I^L$ and amorphous TLB, all recorded at 253 K, at an MAS rate of 10 kHz

Above 293 K, the expected polymorphic transition between form $I^L$ and $I^H$ occurs close to the known transition temperature of the two polymorphs (311 K [42]) (figure 7.27). As with the 80/20 dispersion, the polymer peaks, and amorphous TLB peaks, disappear by 353 K, again due to increased mobility leading to phase separation of crystalline drug and polymer/amorphous drug (figure 7.25).

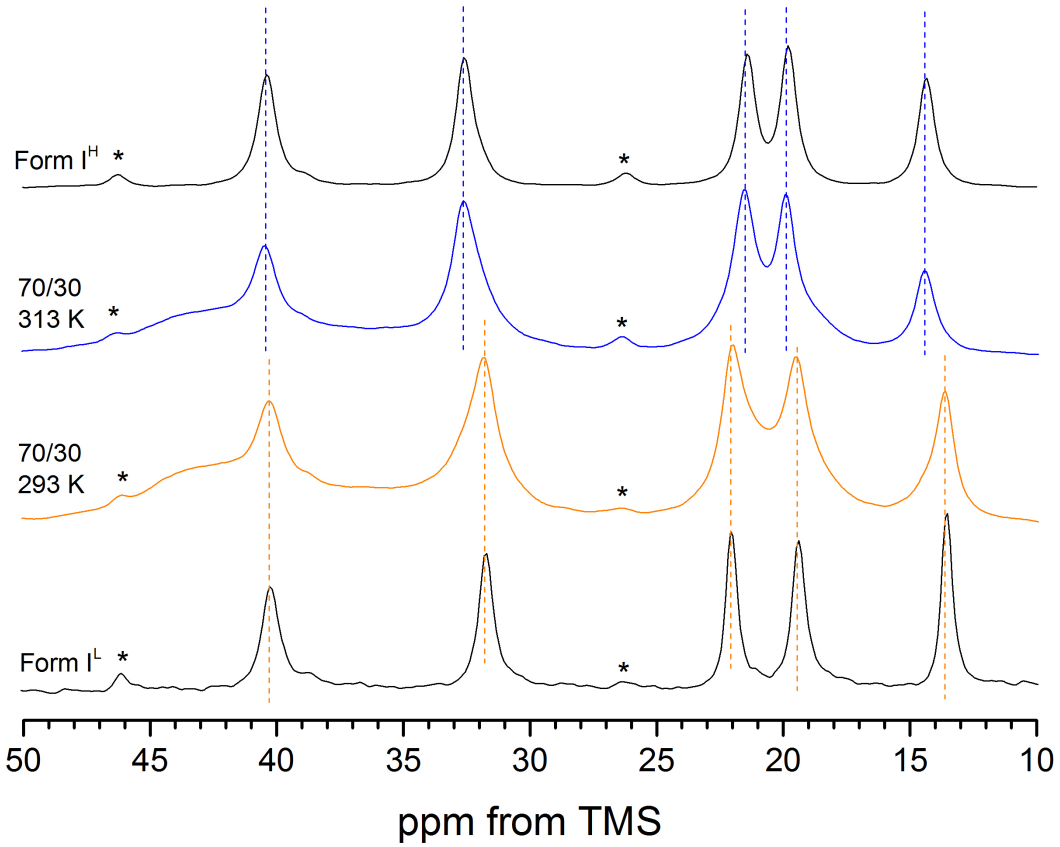


**Figure 7.27:** Aliphatic region of the $^{1}$H-$^{13}$C CP/MAS NMR spectra of 70/30 dispersion at 293 and 313 K compared to form $I^L$ and form $I^H$ TLB, at an MAS rate of 10 kHz. Spinning sidebands are denoted by asterisks

The 60/40 dispersion was found to contain a small amount of crystalline TLB, (alongside mainly amorphous TLB) upon formulation, which was below the detection limit of $^{1}$H-$^{13}$C CP/MAS NMR. The TLB in the dispersion remained predominantly in the amorphous form with increasing temperature up to the $T_g$ value of 309 K (figure 7.28). Partial crystallisation to form $I^H$ around 313 K was observed, with form $I^H$ identified though the appearance of resonances at 131 and 125 ppm, for carbons C-4,6 and C-3,7 respectively.

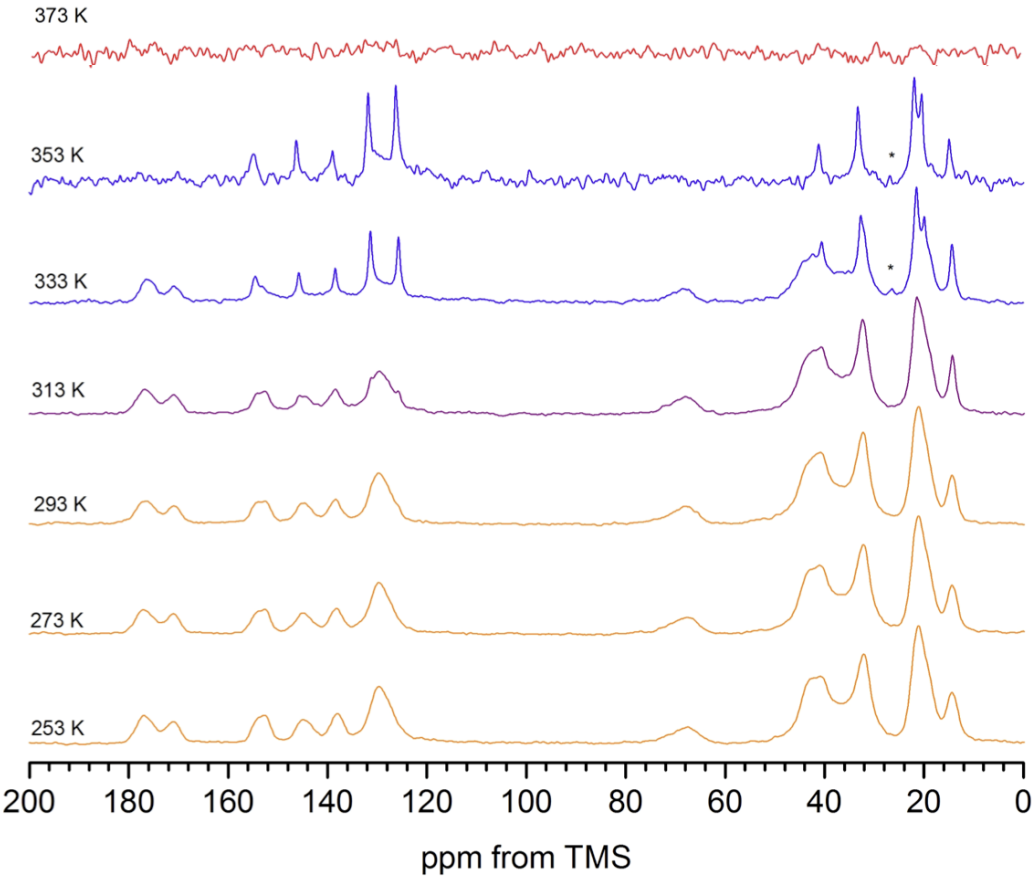


**Figure 7.28:** $^{1}$H-$^{13}$C CP/MAS NMR spectra of 60/40 dispersion recorded at different temperatures between 253 K and 373 K, at an MAS rate of 10 kHz. Spinning sidebands are denoted by asterisks

Between 313 K and 353 K, we see an increase in the content of form $I^H$ TLB as amorphous TLB continues to crystallise. As with the 80/20 and 70/30 TLB/PVP-VA dispersions, the intensity of the PVP-VA and amorphous TLB peaks reduced considerably by 353 K, indicating higher amorphous TLB/polymer mobility. By 373 K, complete loss of CP signal indicates the presence of a highly mobile 'liquid-like' state, seen for many of the FFA/PVP-VA dispersions at high temperatures, but which did not occur for the 80/20 or 70/30 TLB dispersions. This indicates that the solubility of the crystalline TLB at this temperature favours it's dissolution in the mobile phase, which is thought to consist of remaining amorphous TLB, plus polymer.

All high drug loading dispersions were therefore found to crystallise to form $I^H$ at high temperatures through a variety of polymorphic 'routes.' The current proven stability order of the tolbutamide polymorphs is as follows:

- Between absolute zero and 311 K: Form IV < Form III < Form $I^L$ < Form II [42, 43]
- 311 - 353 K: Form IV < Form $I^H$ < Form III < Form II [43]
- Above 353 K: Form IV <Form III < Form II < Form $I^H$ [42]

There are a number of enantiotropic relationships between the polymorphic forms of TLB. Alongside forms $I^L/I^H$, forms $III/I^L$, $III/I^H$ and $II/I^H$ have also been shown to be enantiotropically related. All polymorphs have been shown to undergo transitions to form $I^H$, as outlined in table 7.3, apart from form V, which has not been published. The tolbutamide polymorphs are therefore a complex system to study, as transitions between forms can easily occur, due to the low energy barriers and abundance of enantiotropic relationships.

Through VT analysis of the higher drug loading solid dispersions using solid-state NMR, we were able to closely monitor the crystallisation behaviour of TLB. For the 60/40 and 70/30 dispersions, we observed crystallisation of amorphous TLB to form I ($I^L$: 70/30 and $I^H$: 60/40) at temperatures above the $T_g$ values. For both the 70/30 and 80/20 dispersions, form $I^L$ crystallised to form $I^H$ above the transition temperature of 311 K. The 80/20 dispersion contained a complex mixture of forms I, II and V which allowed the observation of a number of additional polymorphic transitions and highlighted the reversible enantiotropic relationship of forms $I^L$ and V at lower temperatures, and the conversion of form II to $I^H$ at high temperatures, as form $I^H$ became the most stable thermodynamic form. Ultimately, at temperatures above 353 K, all three dispersions showed crystallisation to form $I^H$.

These results indicate that the presence of polymer (up to 40 %) did not affect either the polymorphic stability order, or polymorphic transitions between forms. The transition between $I^L$ and $I^H$ occurred within the expected temperature range, and as expected, the most stable form of tolbutamide (form $I^H$) was the only form present at high temperatures. This indicates that drug-drug interactions (urea tape hydrogen bonding motif - see figure 7.3) were not hindered by the presence of polymer; and that the thermodynamic stability order of the different polymorphs of TLB is the same both in the presence and absence of polymer. Formulating solid dispersions at high concentrations therefore widens the field of crystallisation study, with us being able to predict the crystalline behaviour of the drug once in formulation, clarifying whether transitions between polymorphs occur in the same way in presence of excipients. Being able to predict the recrystallisation behaviour of pharmaceutical APIs from amorphous dispersions accurately is of paramount importance, as this affects the long term efficacy of the formulation. The more information and understanding we have about polymorphic changes and recrystallisation behaviour, the more robust and predictable the long term stability of the formulation.

Following heating to 373 K, all three high drug loaded dispersions were cooled to 293 K within the rotor. After the cooling and reheating cycle was complete, the three resulting dispersions (80/20, 70/30 and 60/40) had a similar composition: form $I^L$ and amorphous TLB; alongside PVP-VA (figure 7.29). The polymorphic transition between forms $I^L$ and $I^H$ is reversible [43], and is again seen here upon cooling past the transition temperature of 311 K.

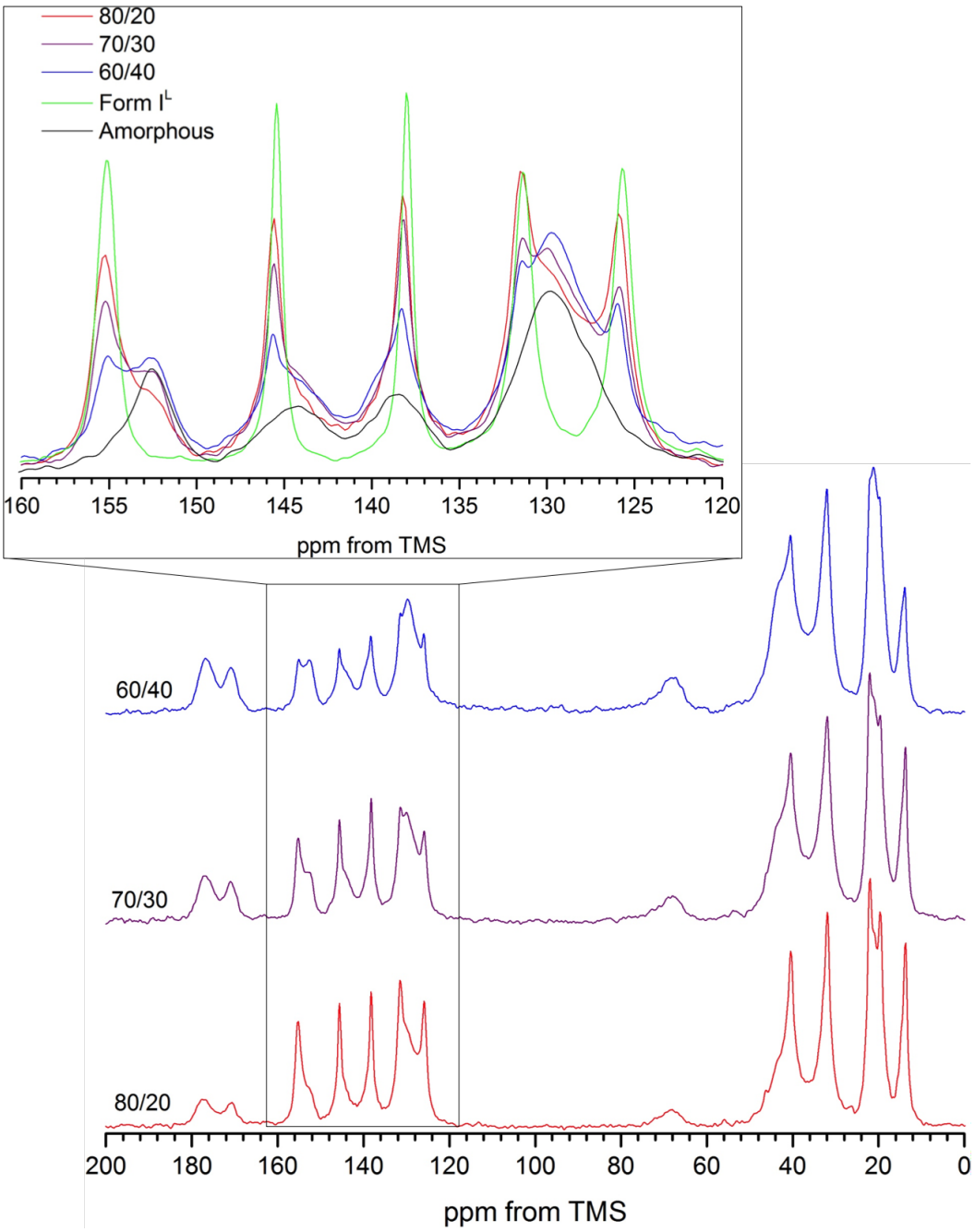


**Figure 7.29:** $^{1}$H-$^{13}$C CP/MAS NMR spectra of 80/20, 70/30 and 60/40 dispersions measured at 293 K following cooling from 373 K, at an MAS rate of 10 kHz. Inset provides a comparison of Form $I^{L}$ and amorphous tolbutamide

Although the $^{1}$H-$^{13}$C CP/MAS spectra are not strictly quantitative, Gaussian deconvolution of the peaks upon cooling to 293 K allowed the approximation of the ratios of form $I^{L}$:amorphous TLB as 25:75 (80/20), 19:81 (70/30) and 10:90 (60/40).

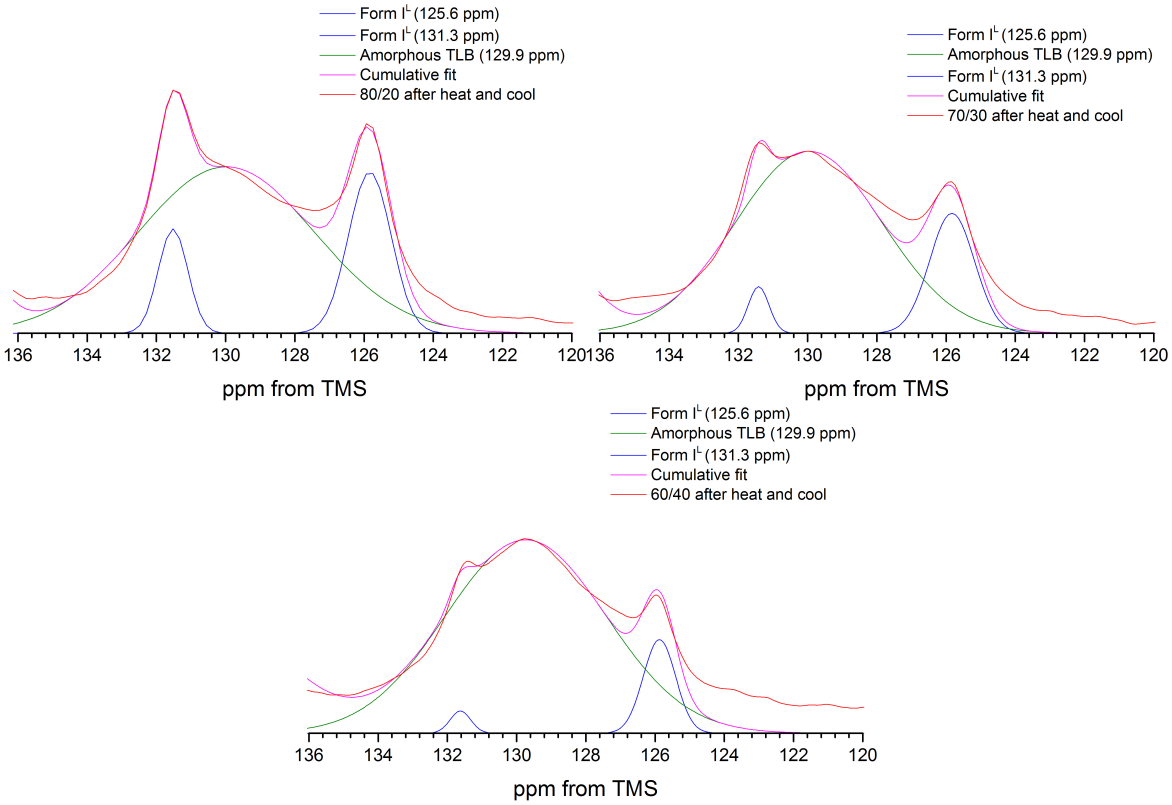


**Figure 7.30:** $^{1}$H-$^{13}$C CP/MAS NMR spectrum of the C-3,7 and C-4,6 resonances for the 60/40, 70/30 and 80/20 dispersion following cooling from 373 K to 283 K. Peak integrals obtained from Gaussian deconvolution are shown

**Table 7.7:** Summary of the % integrals for amorphous TLB and form I$^L$ TLB in the 60/40, 70/30 and 80/20 dispersions following the heating and cooling cycle. Calculated through Gaussian deconvolution peak fitting. Standard error is included in brackets after each integral (I) value

| Dispersion | I for $\delta$ = 125.6 ppm | I for $\delta$ = 129.9 ppm | I for $\delta$ = 131.3 ppm | % Amorphous | % Form I$^L$ |
|---|---|---|---|---|---|
| 60/40 | 0.268 (0.01163) | 2.756 (0.02794) | 0.040 (0.00982) | 89.9 | 10.1 |
| 70/30 | 0.475 (0.02043) | 2.372 (0.02984) | 0.085 (0.02654) | 80.9 | 19.1 |
| 80/20 | 0.609 (0.02646) | 2.603 (0.06127) | 0.272 (0.02453) | 74.7 | 25.3 |

The additional polymorphic forms present in the 80/20 dispersion throughout the VT study (forms II and V) were not recrystallised upon cooling to 293 K, indicating the transitions of form I$^H$ to II, or I$^L$ to V were not reversible under the conditions employed. The 80/20 dispersion was further cooled to 253 K, where the amorphous TLB content became more visible in the $^{1}$H-$^{13}$C CP/MAS spectrum (figure 7.31). This is due to the loss of signal through broadening of form I$^L$ $^{13}$C resonances (C-3,4,6,7) at low temperature, as previously discussed.

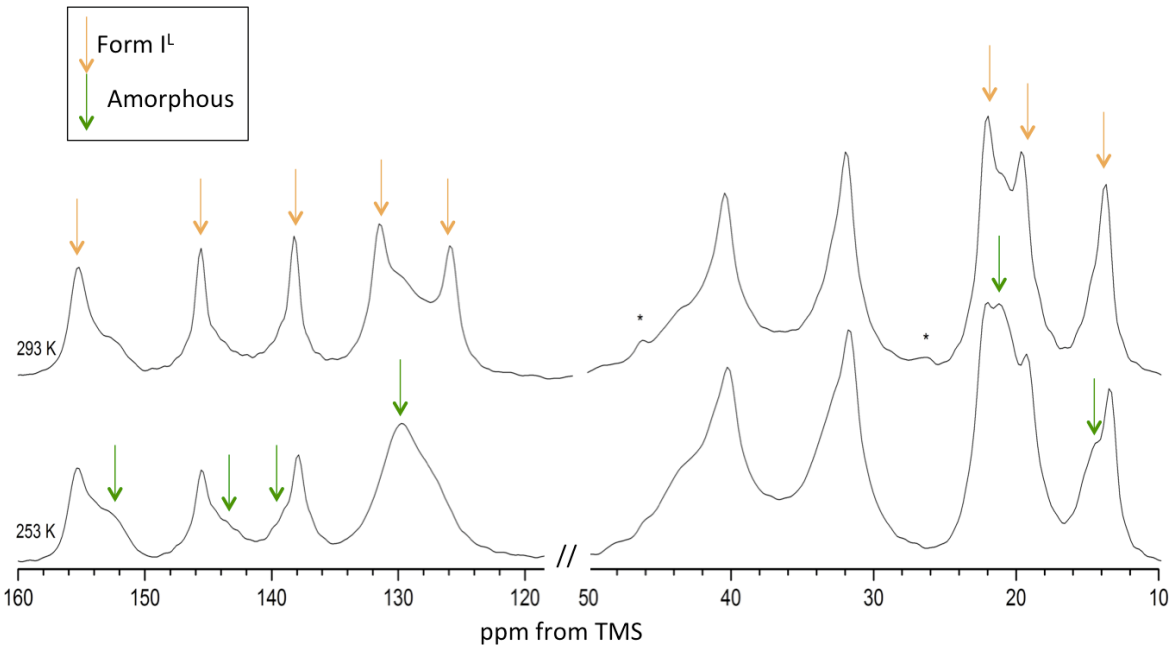


**Figure 7.31:** $^{1}$H-$^{13}$C CP/MAS NMR spectra of 80/20 dispersion measured at 293 K and 253 K following cooling from 373 K, at an MAS rate of 10 kHz. Orange arrows - form $I^{L}$ peaks; Green arrows - amorphous peaks

These results indicate that at 373 K, the remaining amorphous content of the 60/40, 70/30 and 80/20 dispersions must be contained in the highly mobile phase, alongside the PVP-VA. In the VT $^{1}$H-$^{13}$C CP/MAS NMR spectra, this phase is 'invisible' due to increased mobility. Therefore, at high temperatures, it is likely that phase separation occurs for high drug loaded dispersions, with one phase consisting of of form $I^{H}$ crystalline material, which has lower mobility and is therefore detectable *via.* CP/MAS NMR; and a second more mobile phase consisting of amorphous TLB and PVP-VA, which only becomes visible in the spectra upon cooling back to 293 K. The phase separation behaviour of these dispersions has been probed further using variable temperature measurements of $T_{1\rho}{}^{H}$ and $T_{1}{}^{H}$ relaxation times (see section 7.5).

### 7.3.3 Detection of changes in mobility of TLB/PVP-VA dispersion: mid to low drug loading

At drug content below 50 wt. %, no crystallisation of amorphous TLB was detected at high temperatures. However, the VT $^{13}$C NMR spectra for TLB/PVP-VA 40/60 and 20/80 dispersions (figure 7.32) enabled us to detect changes in mobility with increasing temperature. The drug was monitored using the non-overlapping peaks (with polymer) of carbons C-2, C-5, C-4,6 C-3,7 and C-12 (152.5, 144.2, 138.5, 129.8 and 14.8 ppm), as the increased polymer content dominated the aliphatic region.

For both dispersions, the VT CP spectra showed a loss of signal intensity of the aromatic and carbonyl TLB peaks with increasing temperature and was especially pronounced above the

$T_g$: 326 K for 40/60 and 349 K for 20/80. This indicates an increased mobility of carbons 2-7 of tolbutamide within the dispersion on an intermediate timescale at higher temperatures. At 373 K, the 40/60 dispersion showed similar behaviour to the 60/40 dispersion, with high mobility of drug and polymer within a 'liquid-like' state consisting of highly mobily drug and polymer, leading to loss of signal across the spectrum. Slight line narrowing across all visible peaks of the 20/80 showed increased mobility of drug and polymer components.

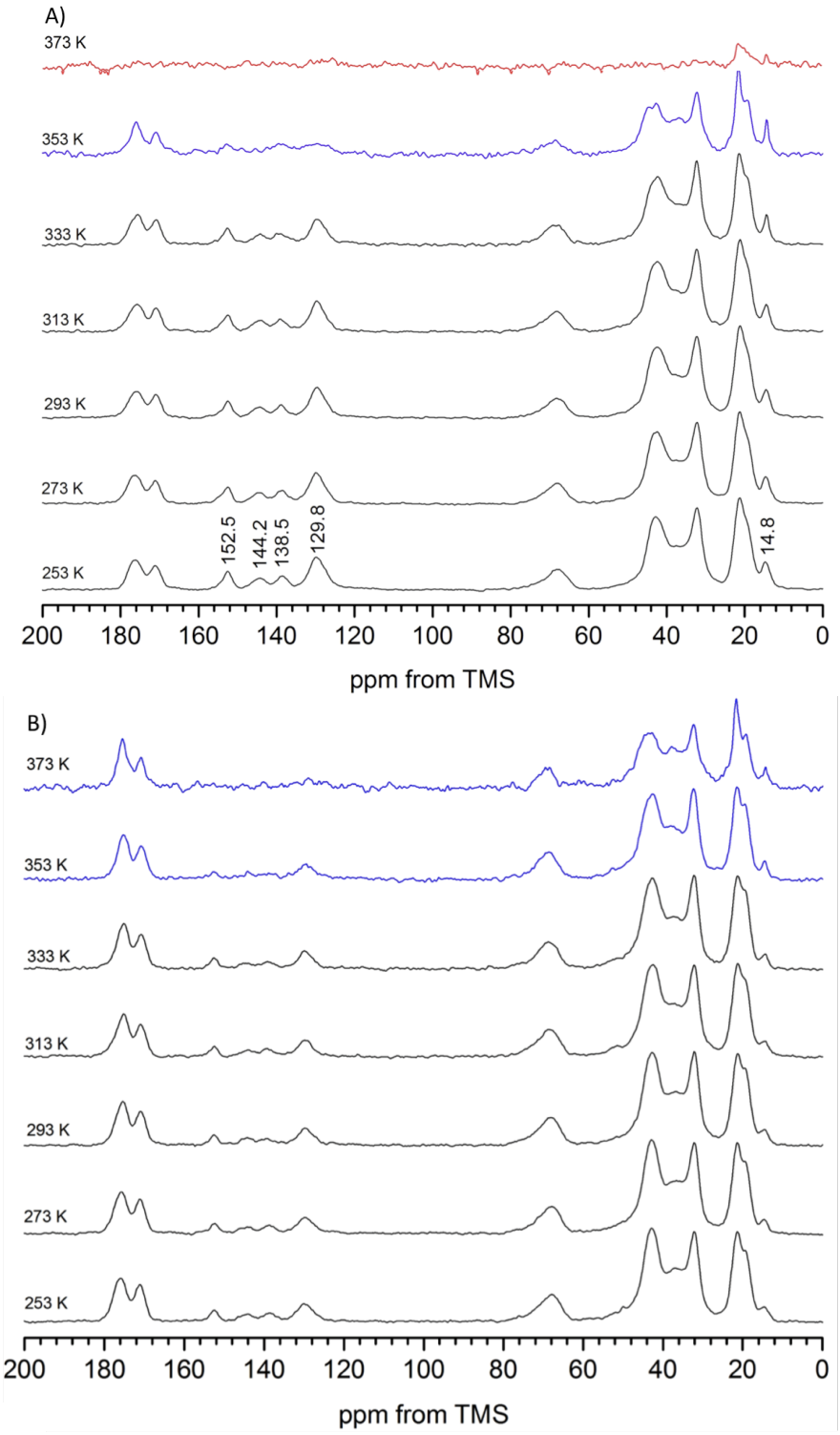


**Figure 7.32:** $^{1}$H-$^{13}$C CP/MAS NMR spectra of A) 40/60 and B) 20/80 dispersions recorded at increasing temperatures between 253 K and 373 K, at an MAS rate of 10 kHz

Following heating to 373 K, both dispersions were cooled gradually to 293 K within the rotor. Upon cooling, they appeared fully amorphous, with no evidence of crystallisation, or other significant changes to the $^{1}$H-$^{13}$C CP/MAS spectra (figure 7.33).

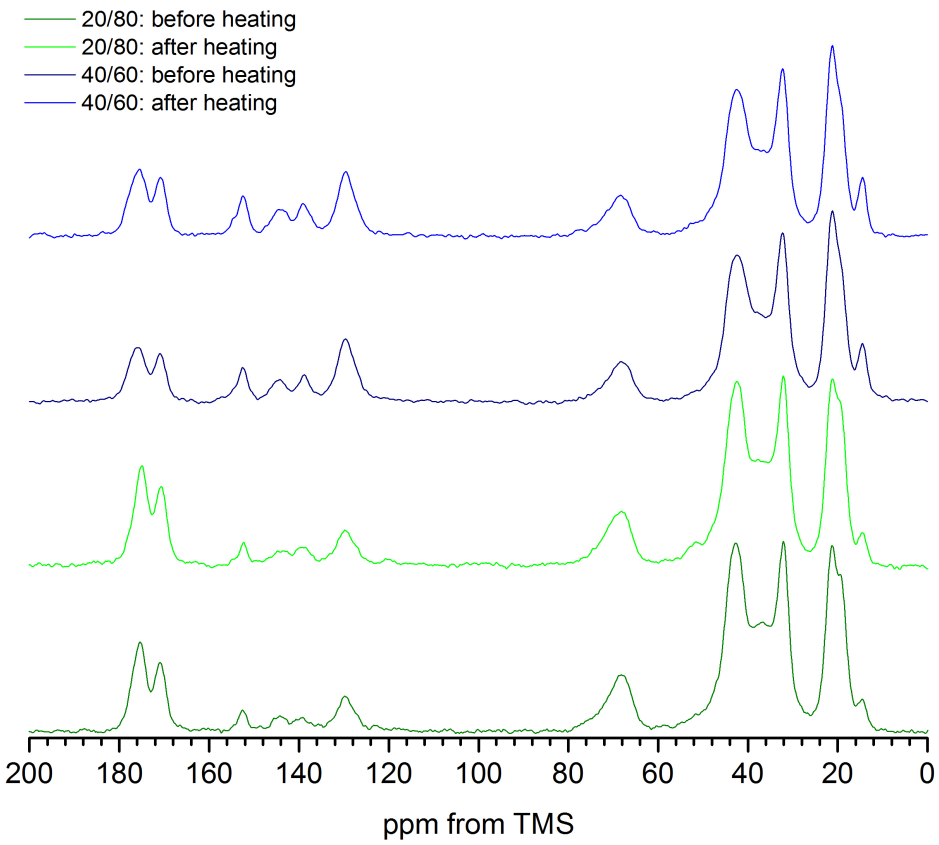


**Figure 7.33:** $^{1}$H-$^{13}$C CP/MAS NMR spectra of 40/60 and 20/80 dispersions before and after heating to 373 K, recorded at 293 K, at an MAS rate of 10 kHz

To further explore the loss of signal at 373 K for the 40/60 TLB/PVP-VA dispersion, $^{13}$C{$^{1}$H} MAS NMR spectra were acquired. Although some significantly broadened peaks were just about visible, these spectra largely showed the same mobility behaviour as the $^{1}$H-$^{13}$C CP/MAS NMR spectra between 353 and 373 K, (figure 7.34).

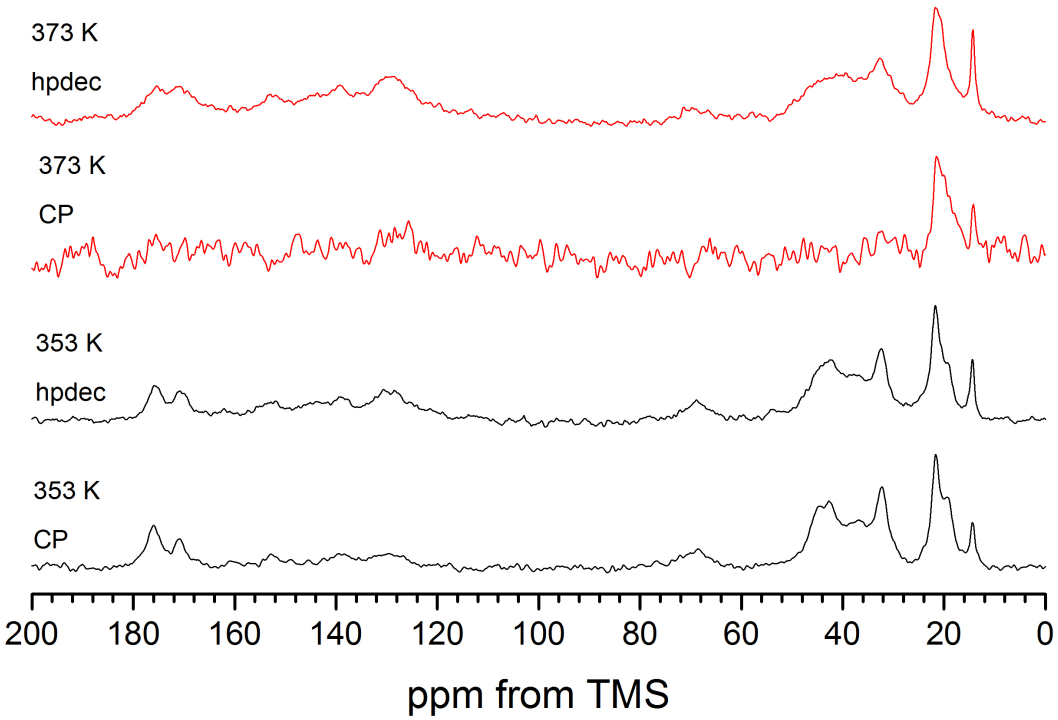


**Figure 7.34:** Comparison of $^{1}$H-$^{13}$C CP/MAS and $^{13}$C{$^{1}$H} MAS NMR spectra of 40/60 dispersion recorded at 353 K and 373 K, at an MAS rate of 10 kHz

## 7.4 Detection of changes in mobility and crystallisation of TLB/PVP-VA dispersions with VT $^{1}$H NMR MAS Studies

The enantiomeric transition between form $I^{L}$ and $I^{H}$ TLB was detectable in the VT $^{1}$H MAS NMR spectra, although the changes were more subtle as compared to the $^{1}$H-$^{13}$C CP/MAS NMR spectra (figure 7.35). Form $I^{L}$ has a broad aliphatic resonance at *ca.* 1.9 ppm, which reduced in intensity with increasing temperature, eventually disappearing above the transition temperature of 311 K. The one aliphatic resonance observed for form $I^{H}$ TLB is seen at *ca.* 0.6 ppm. There is little change in the aromatic $^{1}$H peak between the two forms.

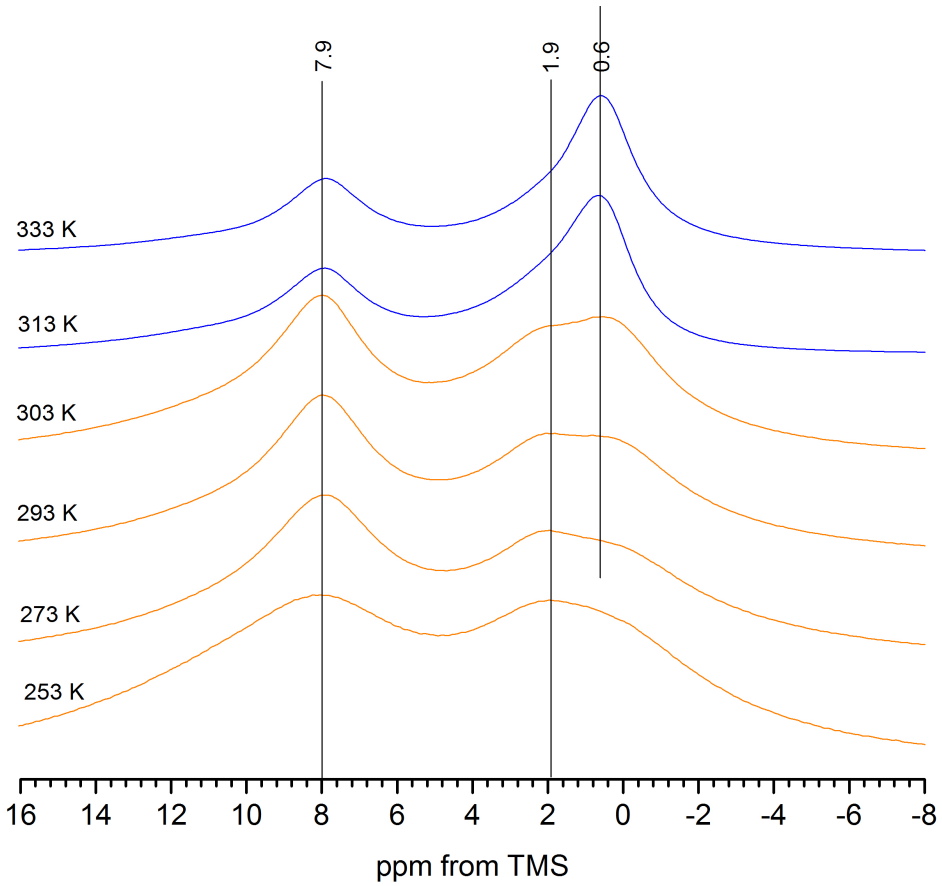


**Figure 7.35:** Variable temperature $^{1}$H MAS NMR spectra for forms $I^{L}$ and $I^{H}$ enantiomeric polymorphs measured at an MAS rate of 10 kHz, between 253 and 333 K

To further investigate the mobility of the TLB/PVPVA dispersions at high temperatures, variable temperature $^{1}$H NMR studies were carried out. Figure 7.36 shows the change in $^{1}$H resonances and line widths as a function of temperature, highlighting the mobility differences dependent on drug loading. With higher TLB content, resonances become narrower with increasing temperature indicating a significantly enhanced mobility at 373 K.

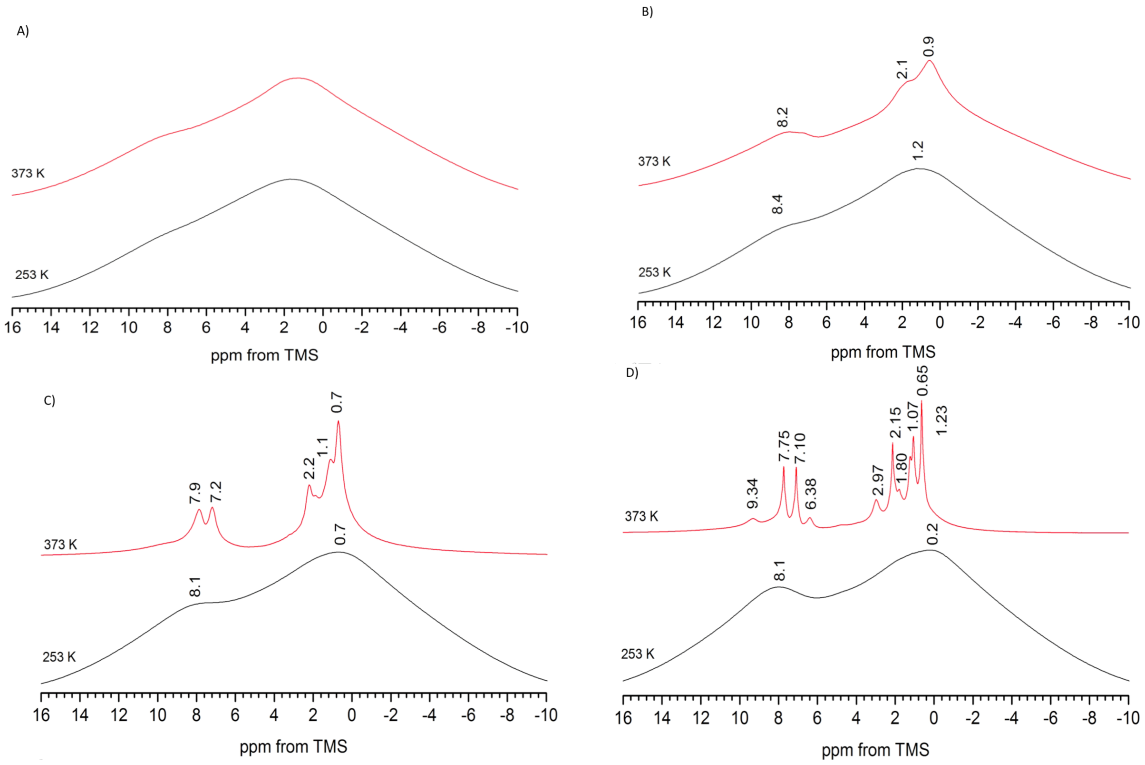


**Figure 7.36:** Variable temperature $^{1}$H MAS NMR spectra for A) 20/80, B) 40/60, C) 60/40, D) 80/20 TLB/PVPVA dispersions, measured at an MAS rate of 10 kHz, between 253 and 373 K

The sharply resolved peaks of the higher drug loading dispersions (60/40 - 80/20 TLB/PVP-VA) at 373 K are comparable to the solution-state $^{1}$H resonances of TLB, shown in figure 7.37, indicating a highly mobile 'liquid-like' environment. We can just observe the presence of the polymer in the solid-state at *ca.* 1.8 ppm. Broader peaks were observed for the 60/40 dispersion, indicating slightly lower mobility in comparison to the 70/30 and 80/20 dispersions. The solution state $^{1}$H spectra of the dispersions and TLB alone (dissolved in $CD_3OD$ at 0.05 M) allowed full assignment of TLB protons.

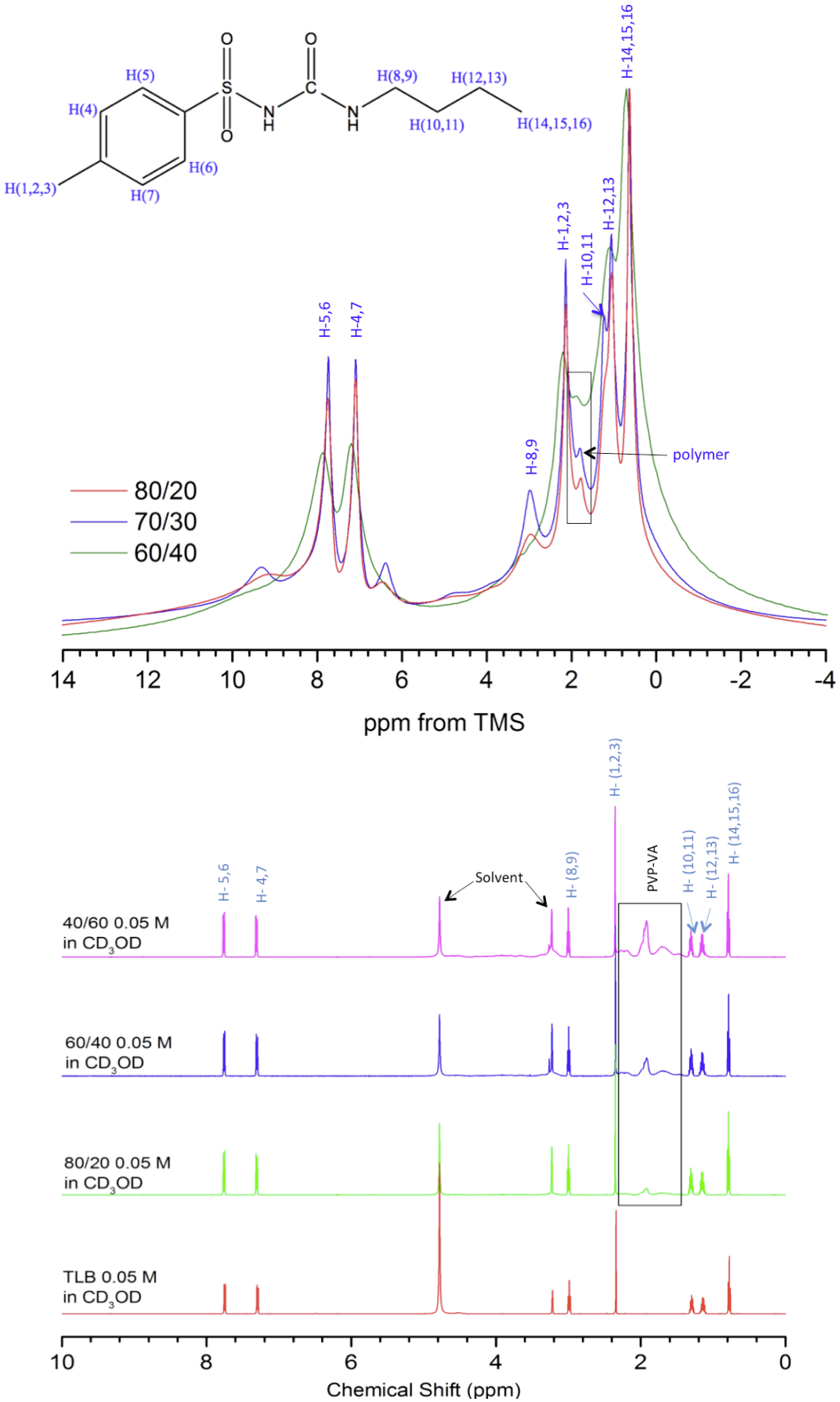


**Figure 7.37:** A) High temperature (373 K) $^{1}$H MAS NMR spectra for 80/20, 70/30 and 60/40 TLB/PVP-VA dispersions (MAS = 10 kHz) with full chemical shift assignment; B) Solution-state $^{1}$H spectra for different TLB/PVP-VA dispersions and TLB alone dissolved in $CD_3OD$ (0.05 M)

## 7.5 Probing miscibility and dynamics of TLB/PVP-VA dispersions with spin-lattice relaxation

### 7.5.1 The mobility regimes of form I TLB

NMR relaxation behaviour, for any TLB systems has not been previously reported in the literature. Here we report the variable temperature spin-lattice relaxation of crystalline form I TLB. We observed changes to the mobility of forms $I^L$ and $I^H$ across a range of NMR timescales, with increasing temperature. For the $T_{1\rho}{}^H$ measurements (figure 7.38) a clear $T_{1\rho}{}^H$ minimum at *ca.* 263 K is observed, with a calculated $\tau_c$ of 5.6 x $10^{-4}$ s. The slope above the minimum (263 - 303 K) gave an activation energy of 56.6 kJ $mol^{-1}$, which reflects the mobility of form $I^L$ TLB. This is most likely associated with the slow oscillation of the aromatic ring, as changes in this temperature region were additionally highlighted with VT $^1$H-$^{13}$C CP/MAS (see section 7.3.1). This type of aromatic ring motion is expected to be observable on the kHz timescale [269]. The increase in $T_{1\rho}{}^H$ times with increasing temperature above the minimum indicates that we are observing the high-temperature side of the minimum (associated with a faster regime). Upon crystallisation to form $I^H$ above 303 K, $T_{1\rho}{}^H$ times became too long to accurately measure (longer than 70 ms); indicating forms $I^L$ and $I^H$ have very different spin-lattice relaxation behaviour, which is unexpected, as structurally these forms are very similar [43].

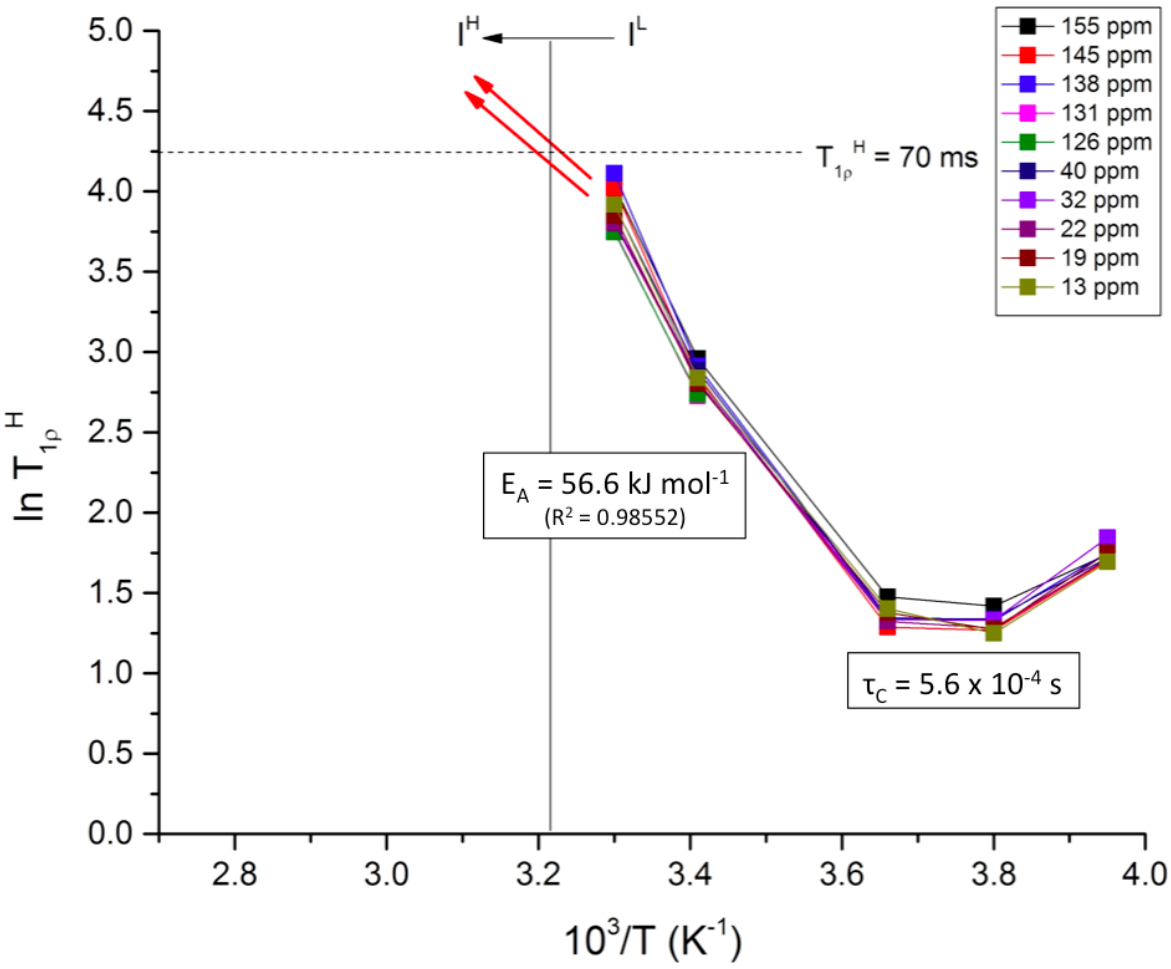


**Figure 7.38:** Temperature dependence of $T_{1\rho}{}^{H}$ time for different $^{13}C$ sites for form I TLB

The $T_1{}^{H}$ measurements for form I TLB (figure 7.39) also showed a clear minimum, this time at a higher temperature of 313 K, with an $E_{A\,app}$ of 6.77 kJ mol$^{-1}$ calculated between 253 and 313 K. The minimum occurs at a similar temperature to the transition between forms $I^L$ and $I^H$ (311 K) [43], and likely describes mobility of the butyl chain, which should be observable on the MHz timescale. The significant difference in activation energies calculated for $T_{1\rho}{}^{H}$ and $T_1{}^{H}$ times for form I TLB is consistent with different motional processes being observed *via* each technique.

Combining the two analysis methods indicates that:

- At low temperatures, form $I^L$ TLB undergoes a slower kHz timescale motion, likely due to the oscillation of the aromatic ring comparable to the frozen (solid II) rotational motion of benzene 7.3.1. This motion is described by the $T_{1\rho}{}^{H}$ minimum at *ca.* 263 K
- At higher temperatures, a faster MHz timescale motion is observed as form $I^L$ converts to $I^H$. This motion is described by the $T_1{}^{H}$ minimum at *ca.* 313 K, likely due to the conformational change of the terminal butyl group associated with the transition [43]. Isobutyl rotations have previously been shown to be observable on the MHz timescale in other systems [206].

By extending the temperature range to 253 K, we observed previously unreported changes to the $^{13}C$ spectrum, attributed to a low temperature motional freezing of the aromatic ring resulting in the loss of chemical equivalence of carbons C-4,6 and C-3,7. We further investigated both the kHz and MHz motional regimes of form I TLB with VT spin-lattice relaxation studies. Minima were observed for both the $T_1{}^H$ and $T_{1\rho}{}^H$ temperature dependence curves, associated with motions on two different timescales. Additionally, forms $I^L$ and $I^H$ were found to have very different $T_{1\rho}{}^H$ times, which is unexpected as structurally the forms are extremely similar. The combination of variable temperature $T_{1\rho}{}^H$ and $T_1{}^H$ relaxation alongside $^1H$-$^{13}C$ CP/MAS NMR highlighted the different motional regimes experienced across the full temperature range for form I TLB.

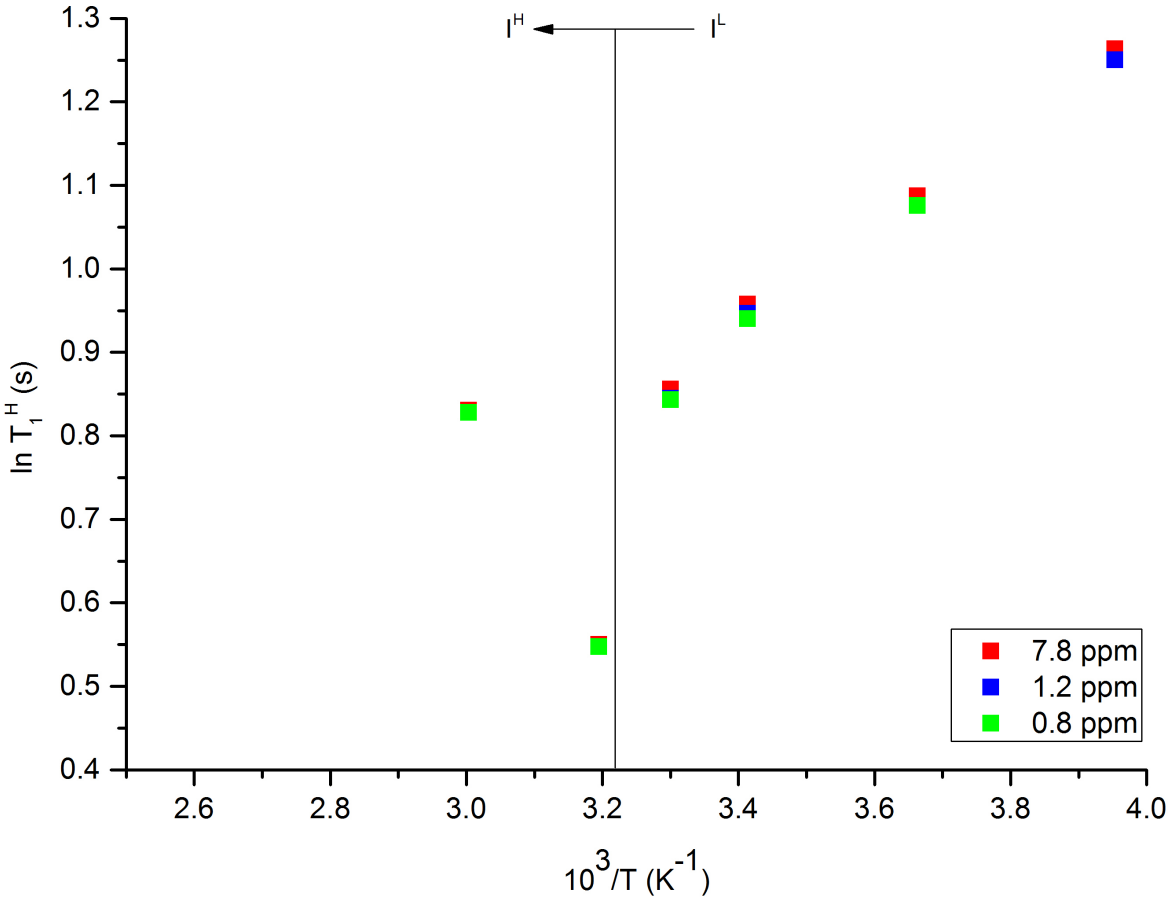


**Figure 7.39:** Temperature dependence of $T_1{}^H$ times for different $^1H$ sites of form I TLB

### 7.5.2 Variable temperature relaxation studies of TLB/PVP-VA dispersions

The TLB/PVP-VA dispersions display two distinct types of relaxation behaviour, dependent on drug loading. The lower drug loaded dispersions (20 - 40 wt. %) remained amorphous and miscible throughout, displaying non-typical temperature dependence comparable to the fully amorphous IMC and FFA/PVP-VA dispersions. For the higher drug loaded dispersions (60 - 80 wt. % drug loading) we were able to detect and monitor phase separation and

crystallisation with increasing temperature.

#### 7.5.2.1 Detection of polymorphic transitions and phase separation using VT relaxation studies: high drug loaded dispersions

Figure 7.40 shows that for the 60/40 dispersion, we observed similar relaxation across all $^{13}C$ sites until *ca.* 303 K, indicating homogeneity between drug and polymer. Above this temperature, a wider spread of $T_{1\rho}{}^{H}$ times was measured. Differences in relaxation times show heterogeneity within the system, due to the presence of processes with different $^{1}H$-$^{1}H$ spin diffusion rates. At 313 K, above the $T_g$ of 309 K, the amorphous TLB within the dispersion began to crystallise to form $I^H$, with full crystallisation by *ca.* 333 K (section 7.3.2). These changes are reflected in the $T_{1\rho}{}^{H}$ times. The TLB protons show a difference in relaxation behaviour in two steps. Firstly, at 313 K, longer $T_{1\rho}{}^{H}$ times are associated with the aromatic ring and carbonyl group of tolbutamide ($\delta$ = 153, 138 and 130 ppm). Secondly, above 333 K, the $T_{1\rho}{}^{H}$ times of the remaining aliphatic drug peaks (40, 32, 21 and 15 ppm) also increase. Above 333 K, the $T_{1\rho}{}^{H}$ times of the drug resonances were too long to be measured accurately (greater than 70 ms), which indicates crystallisation to form $I^H$ TLB. The phase separation of drug and polymer is therefore mapped by the changing $T_{1\rho}{}^{H}$ times with increasing temperature: homogenous relaxation of the whole dispersion occurs at lower temperatures, with drug and polymer displaying completely different relaxation times above $T_g$. This clearly indicates phase separation of the dispersion, with a different mobility behaviour seen for the crystalline TLB compared to PVP-VA.

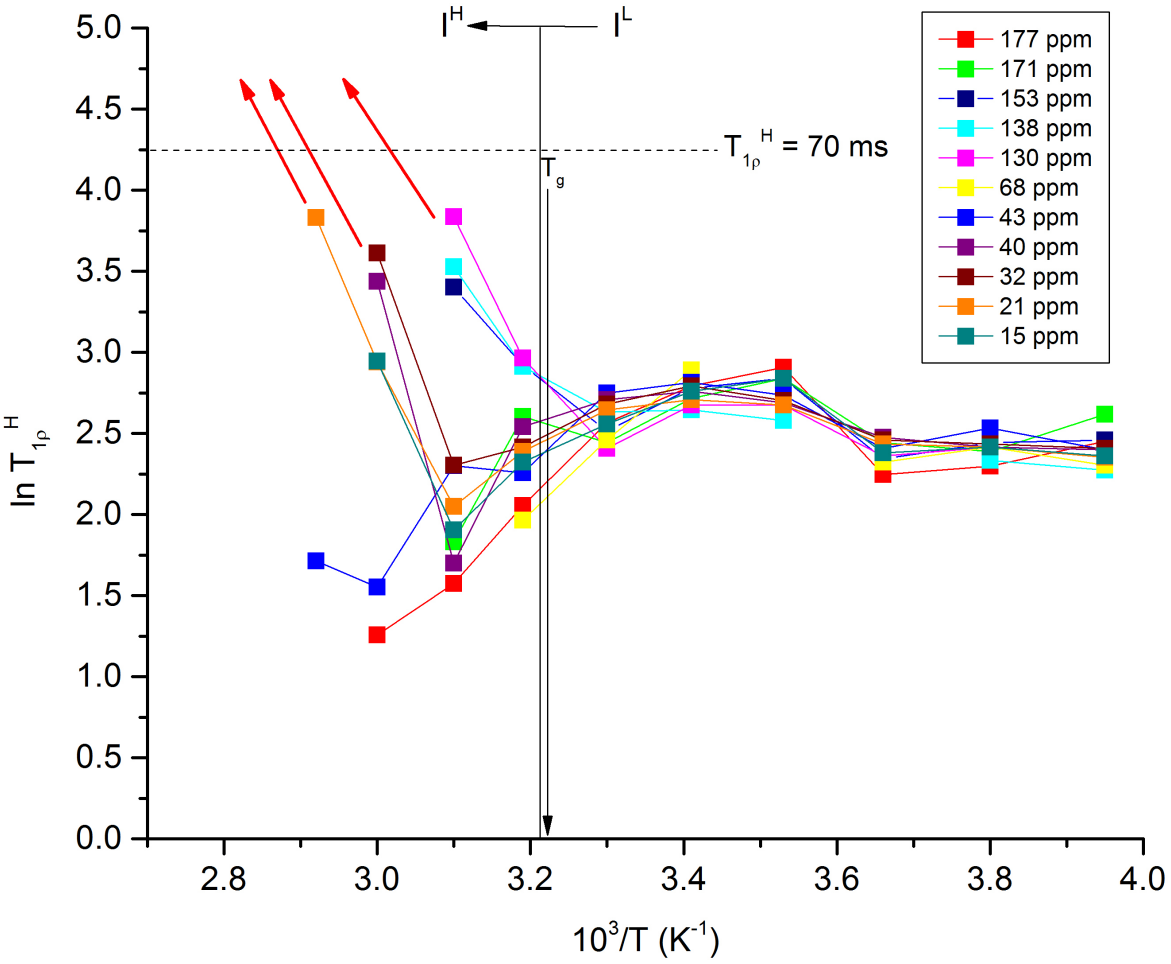


**Figure 7.40:** Temperature dependence of $T_{1\rho}{}^{H}$ time for different $^{13}C$ sites for TLB PVPVA 60/40 dispersion

The VT $T_{1\rho}{}^{H}$ relaxation curve of the 70/30 dispersion can be seen in figure 7.41. A difference in $T_{1\rho}{}^{H}$ times of TLB and PVP-VA occurs across the whole temperature range. A $T_{1\rho}{}^{H}$ minimum was observed at *ca.* 263 K for the TLB peaks, which is associated with a $\tau_c$ of 5.48 x $10^{-4}$ s. Above the minimum, the slope gave an activation energy of 46.05 kJ $mol^{-1}$ (273 - 303 K). The temperature and $\tau_c$ of this minimum is comparable to that seen for pure form $I^L$ (figure 7.38), associated with the oscillation of the aromatic ring. Again, we can clearly see the polymorphic transition between form $I^L$ and $I^H$ within the dispersion. A difference in the relaxation behaviour of drug and polymer can be seen across all temperatures, which agrees with the phase separation observed in the VT $^{1}H$-$^{13}C$ CP/MAS NMR (section 7.3.2). Due to the dominance of the crystalline TLB in the $^{1}H$-$^{13}C$ CP/MAS NMR spectrum, we were unable to calculate $T_{1\rho}{}^{H}$ times for the amorphous component of the dispersion.

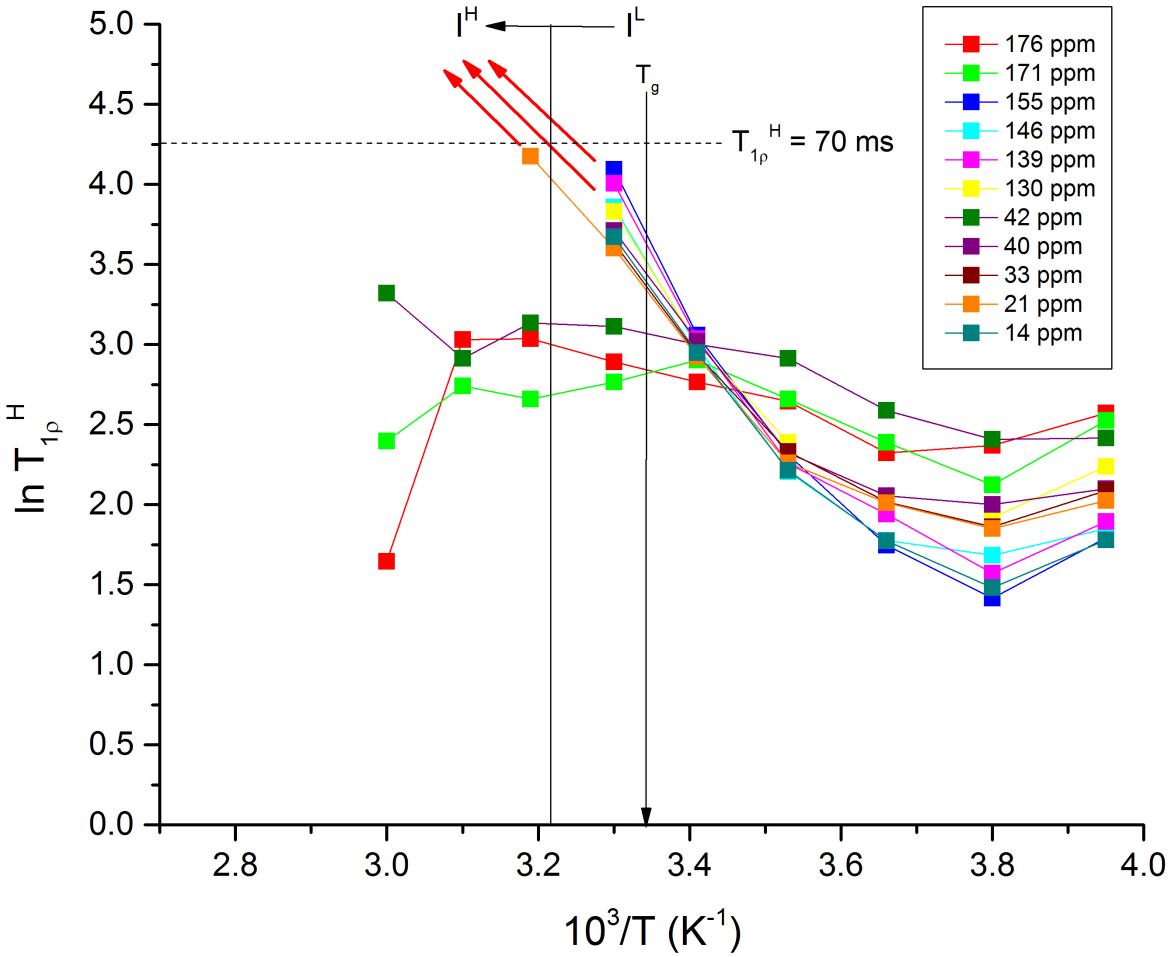


**Figure 7.41:** Temperature dependence of $T_{1\rho}{}^{H}$ time for different $^{13}C$ sites for TLB PVPVA 70/30 dispersion

The $T_1{}^{H}$ temperature dependence curve for the 70/30 dispersion (figure 7.42) shows a $T_1{}^{H}$ minimum at *ca.* 313 K, at the same temperature as for pure form I TLB, with a marked change in relaxation behaviour occurring either side. Above 313 K, the motion has an activation energy of 12.88 kJ $mol^{-1}$. The increase in $T_1{}^{H}$ with increasing temperature indicates we are on the high-mobility side of the minimum. At temperatures below the minimum, there was little change in $T_1{}^{H}$ times with increasing temperature, indicating a difference in mobility between the TLB in the dispersion, and pure form I. It is likely the dispersion is dominated by the polymer presence at this point.

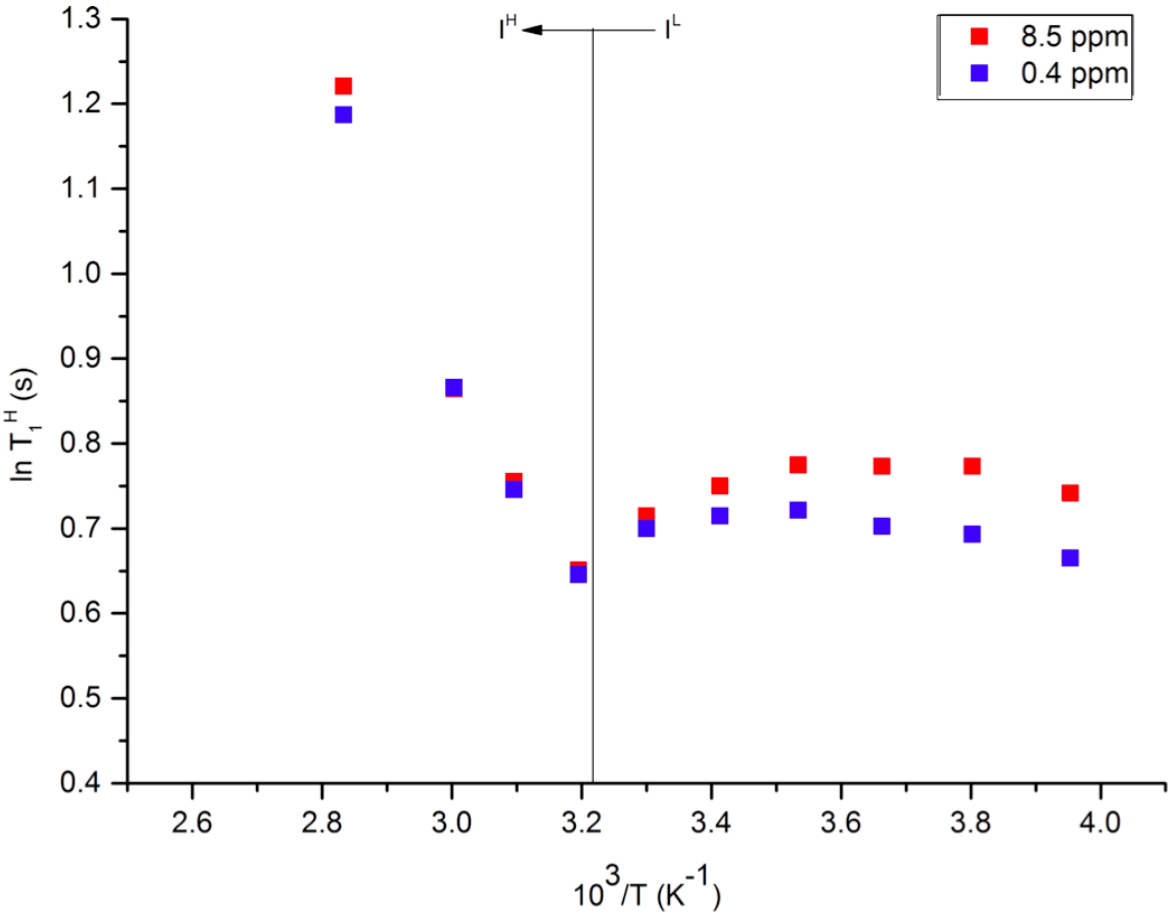


**Figure 7.42:** Temperature dependence of $T_1{}^H$ time for different $^1$H sites for TLB PVPVA 70/30 dispersion

The VT $T_{1\rho}{}^H$ relaxation curve for the 80/20 dispersion reflects the more complex mixture of polymorphs, amorphous TLB and polymer present, displaying a wide range of relaxation times across the different chemical shift sites. Unfortunately, this curve was too complex to analyse. The variable temperature $T_1{}^H$ dependence of the 80/20 dispersion can be seen in figure 7.43. Unlike the 70/30 dispersion, the $T_1{}^H$ minimum is outside of the measured temperature range. An increase in $T_1$ times for all protons is observed with increasing temperature, indicating the presence of a fast regime. At low temperatures, the relaxation dependence describes the cumulative behaviour of the three polymorphs, amorphous TLB and PVP-VA. We do however observe a change in the gradient of the $T_1{}^H$ behaviour at 313 K, which indicates the crystallisation of forms $I^L$ and V to the more thermodynamically stable form $I^H$.

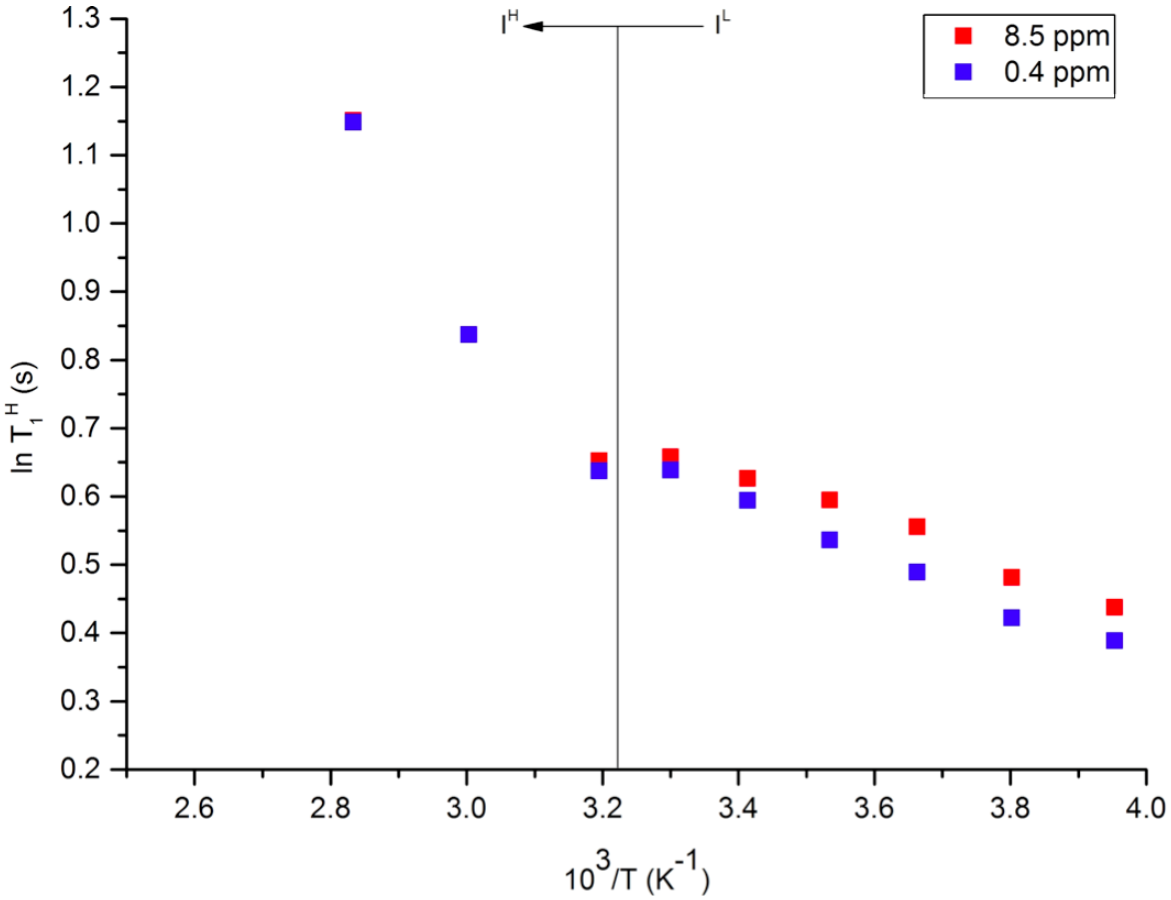


**Figure 7.43:** Temperature dependence of $T_1{}^H$ time for different $^1$H sites for TLB PVPVA 80/20 dispersion

#### 7.5.2.2 A non-typical temperature dependence: 20/80 and 40/60 dispersions

The $T_{1\rho}{}^H$ times of the 20/80 and 40/60 dispersions displayed non-typical temperature dependence, comparable to the lower loaded IMC and FFA dispersions (figure 7.44). We observed homogenous relaxation behaviour across all carbon sites for both dispersions. Initially, between 253 and 333 K, there was a slight but steady increase in $T_{1\rho}{}^H$ time with increasing temperature, with similar $E_{A\,app}$(LT) of 8.0 and 6.8 kJ mol$^{-1}$ for 20/80 and 40/60 respectively. Above $T_{MAX}$, a more marked change of $T_{1\rho}{}^H$ times occurred, with $E_{A\,app}$(HT) values of 54.7 and 22.2 kJ mol$^{-1}$ for 20/80 and 40/60 respectively. $T_{MAX}$ occurred the same point with respect to $T_g$ for each dispersion: 311 K ($T_g$ - 15 K) for 40/60 and 349 K ($T_g$ - 16 K) for 20/80. No phase separation or crystallisation was observed in these dispersion across the measured temperature range.

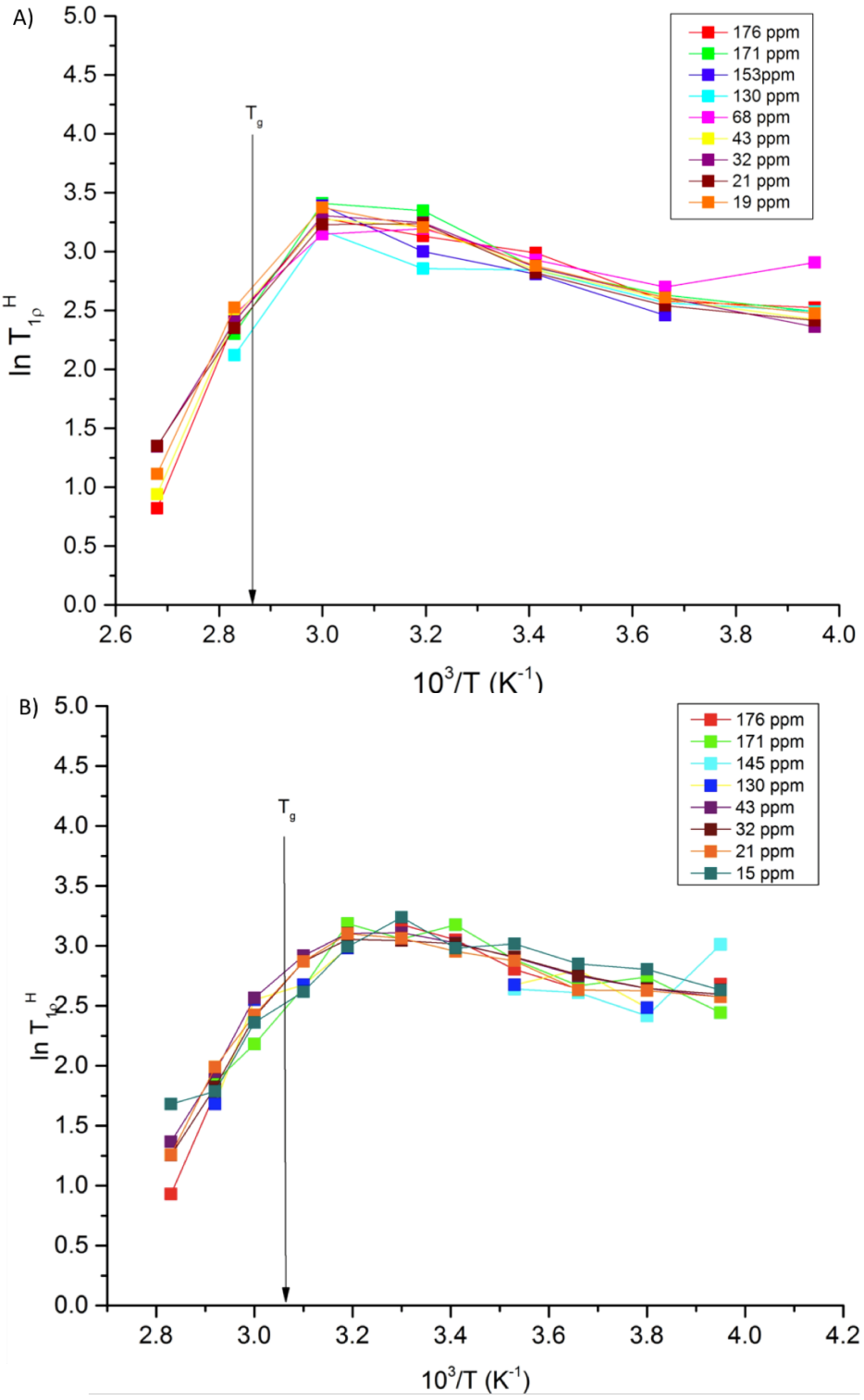


**Figure 7.44:** Temperature dependence of $T_{1\rho}{}^{H}$ time for different $^{13}C$ sites for TLB/PVPVA A) 20/80 and B) 40/60 dispersions

#### 7.5.2.3 Miscibility of dispersions, determined through spin-lattice relaxation times

Differences in the relaxation time of drug and polymer components within a dispersion have been used previously to assess miscibility of drug/polymer dispersions (see chapters 4

and 5 for detailed explanation). To calculate the difference in $T_{1\rho}{}^{H}$ for the TLB/PVP-VA dispersions, the peaks at 177, 171 and 68 ppm were chosen for PVP-VA, as these were the only non-overlapping polymer peaks. For the drug component, the four peaks between 160 and 120 ppm were used.

The differences in relaxation time ($\Delta T_{1\rho}{}^{H}$) at 293 K can be seen in figure 7.45. At 293 K, $\Delta T_{1\rho}{}^{H}$ was 0 for all dispersions except the 80/20 TLB/PVP-VA, indicating miscibility on the 2 - 6 nm length scale. The 80/20 dispersion showed a large $\Delta T_{1\rho}{}^{H}$ well above the zero line, indicating the presence of domains larger than 6 nm in size.

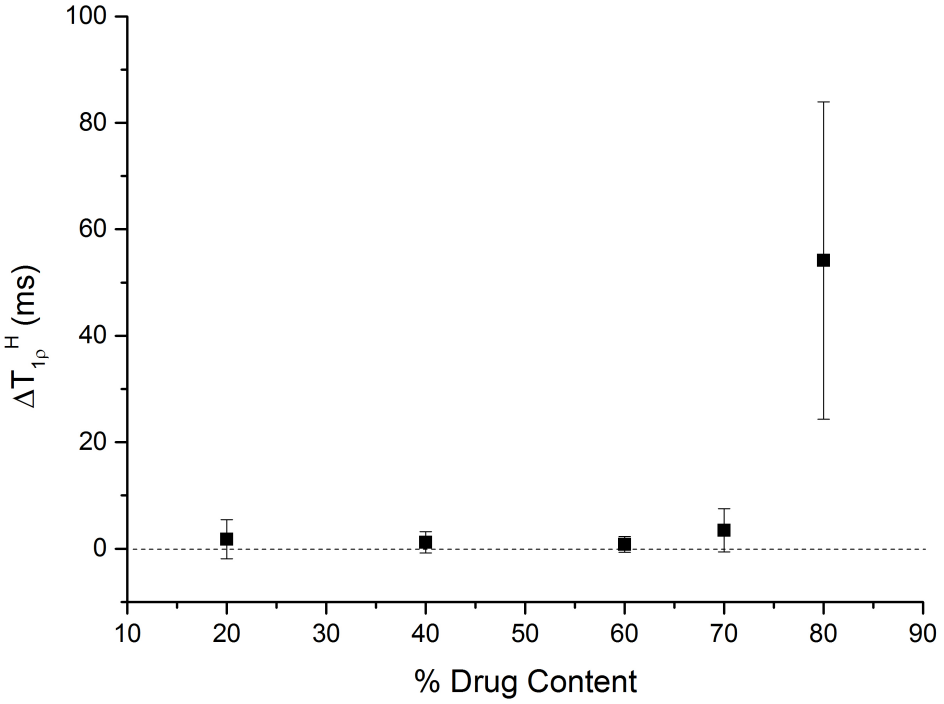


**Figure 7.45:** $\Delta T_{1\rho}{}^{H}$ (ms) between tolbutamide and PVP-VA in the solid dispersions, at 293 K, displayed as a function of wt. % drug content. Error bars represent 95 wt. % confidence intervals of the difference between means

The temperature dependence of the $\Delta T_{1\rho}{}^{H}$ for the 60/40 and 70/30 dispersions were investigated further (figure 7.46). It was not possible to include the 80/20 dispersion, due to the complexity of the temperature dependence curve. Both dispersions show no difference in relaxation between drug and polymer at the lower temperatures, indicating miscibility on the 2 - 6 nm length scale. However, above 293 K, we see a substantial increase in $\Delta T_{1\rho}{}^{H}$, indicating phase separation of drug and polymer, and the formation of domains greater than 6 nm. The difference between form I and polymer becomes much greater above 303 K, where we observed the polymorphic transition between form $I^{L}$ and $I^{H}$.

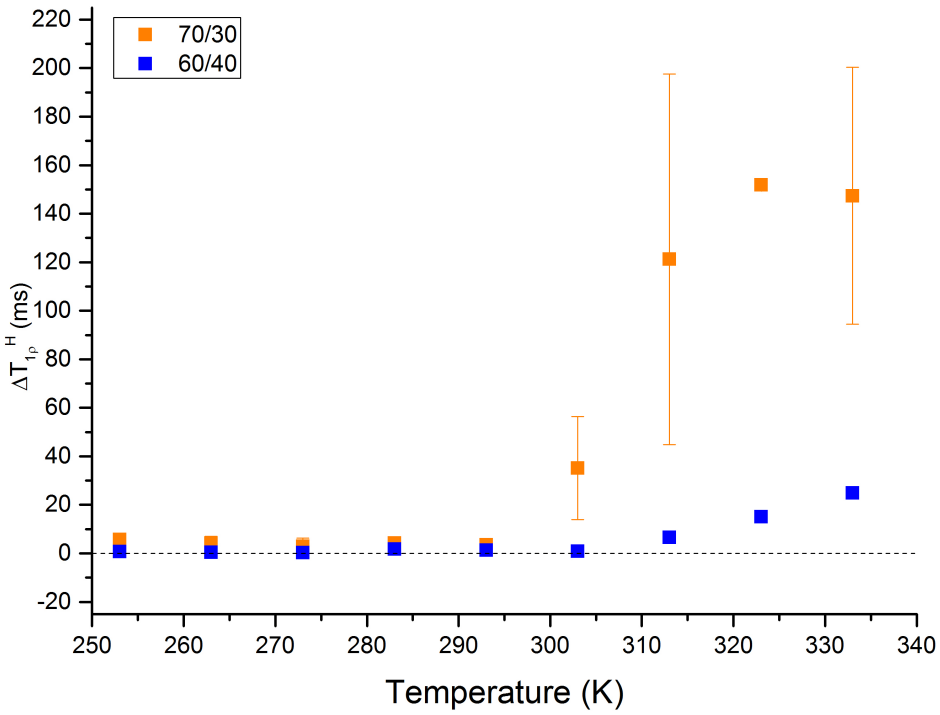


**Figure 7.46:** $\Delta T_{1\rho}{}^{H}$ (ms) between TLB and PVP-VA in the 60/40 and 70/30 solid dispersions, between 253 and 333 K. Error bars represent 95 % confidence intervals of the difference between means

To further investigate the miscibility of the highest loaded dispersions on a faster timescale, the differences in $T_1{}^{H}$ times between the two $^{1}$H peaks of the 70/30 and 80/20 dispersions with increasing temperature were calculated. Although there were some slight differences in $T_1{}^{H}$ times at the lower temperatures for both dispersions, these are considered to be negligible ($\delta T_1{}^{H} \approx 0$), indicating miscibility on the 6 - 24 nm length scale. Previous studies found $\Delta T_1{}^{H}$ of $> 0.5$ s to be indicative of phase separation on the 24 - 55 nm scale [46].

## 7.6 Stability Studies

Throughout the 8 week stability study, all dispersions were monitored for changes in the local ordering using PXRD, mDSC and $^{13}$C CP/MAS solid-state NMR. The TLB/PVP-VA dispersions behaved in two ways: dispersions with drug content $\leq$ 50 wt. % remained amorphous in each storage condition throughout; dispersions with drug content $\geq$ 60 wt. % crystallised to various TLB polymorphs at certain storage conditions, as detailed below. Unfortunately, upon storage above 333 K, the majority of the higher drug loading dispersions formed hard glass melts, which proved unsuitable for further analysis.

The small amount of crystalline TLB in the 60/40 dispersion did not increase throughout the study at room temperature (0 % RH) (figure 7.47). With increased humidity (75 % RH), further crystallisation to form $I^{L}$ TLB occurred by week 4, indicating that the rate of crystallisation of amorphous TLB to form I is increased by the presence of moisture, due to the plasticizing effect of water [122]. Above 313 K, crystallisation to form I occurred more

quickly, by week 2. The PXRD and solid-state NMR results were carried out at ambient temperature following removal from storage, hence all form I material is identified as form $I^L$. Above 311 K, we expect crystallisation to form $I^H$ occurred within storage, as seen in the VT $^1$H-$^{13}$C CP/MAS NMR spectra, only converting to form $I^L$ upon removal. This crystallisation behaviour is in agreement with the results seen in the VT CP/MAS, where amorphous TLB converted to form $I^H$ at temperatures $\geq$ 313 K under MAS conditions.

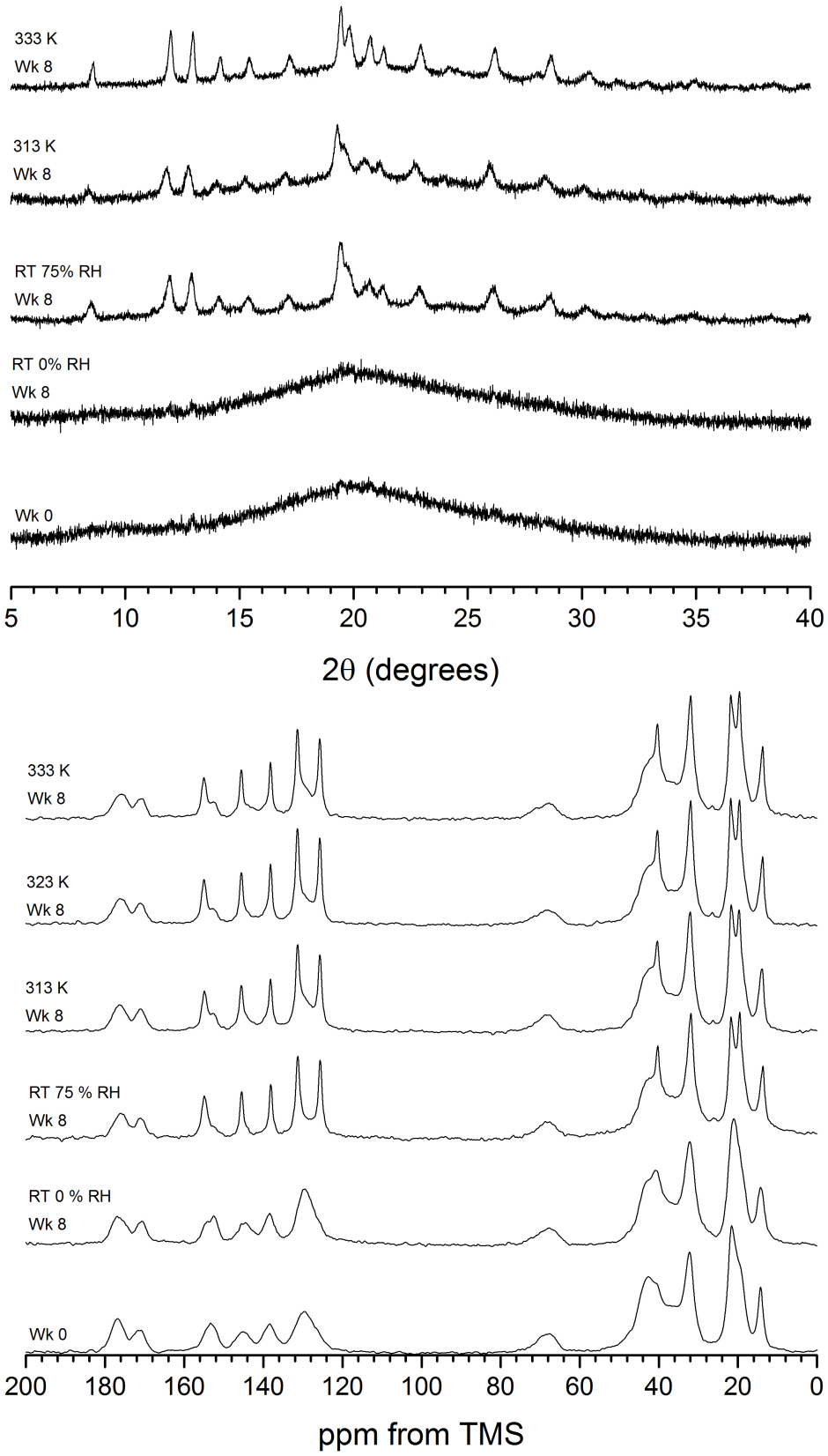


**Figure 7.47:** A) PXRD patterns and B) $^{1}$H-$^{13}$C CP/MAS NMR spectra (MAS = 10 kHz) of TLB/PVP-VA 60/40 dispersion, before and after storage at RT (0 and 75 % RH), 313, 323 and 333 K

No further polymorphic changes were observed for the 70/30 dispersion, which was found to contain form I TLB throughout the stability study (figure 7.48). Upon storage at higher

temperatures, the content of amorphous TLB was reduced, identified with the $^{1}$H-$^{13}$C CP/MAS NMR spectra, due to the reduction in intensity of the shoulder peak at *ca.* 153 ppm. This behaviour is in agreement with the results seen in the VT CP/MAS, where the amount of amorphous TLB reduced at temperatures greater than 313 K, with form I being the only detected crystalline material.

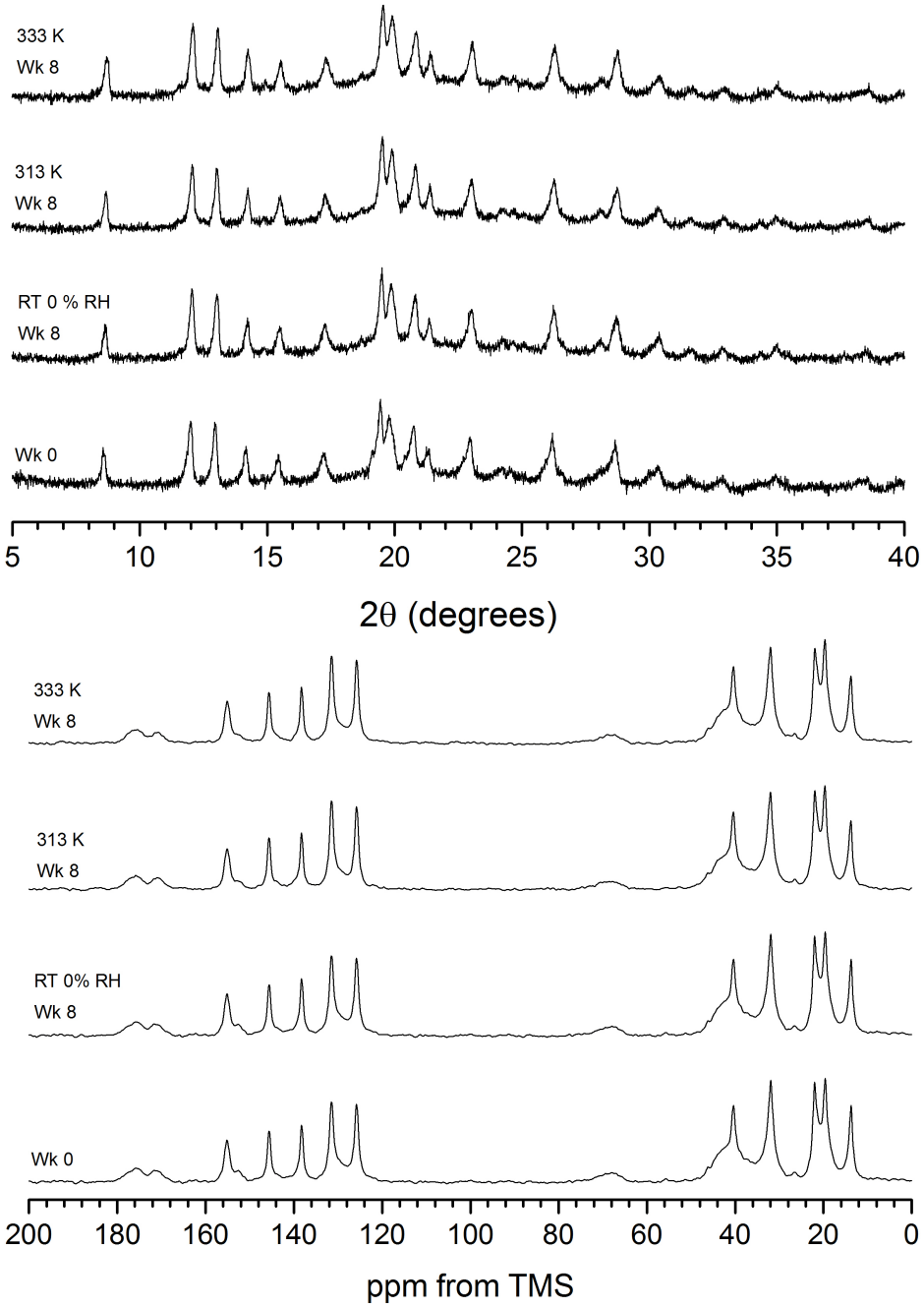


**Figure 7.48:** A) PXRD patterns and B) $^{1}$H-$^{13}$C CP/MAS NMR spectra (MAS = 10 kHz) of TLB/PVP-VA 70/30 dispersion, before and after storage at RT (0 % RH), 313 and 333 K

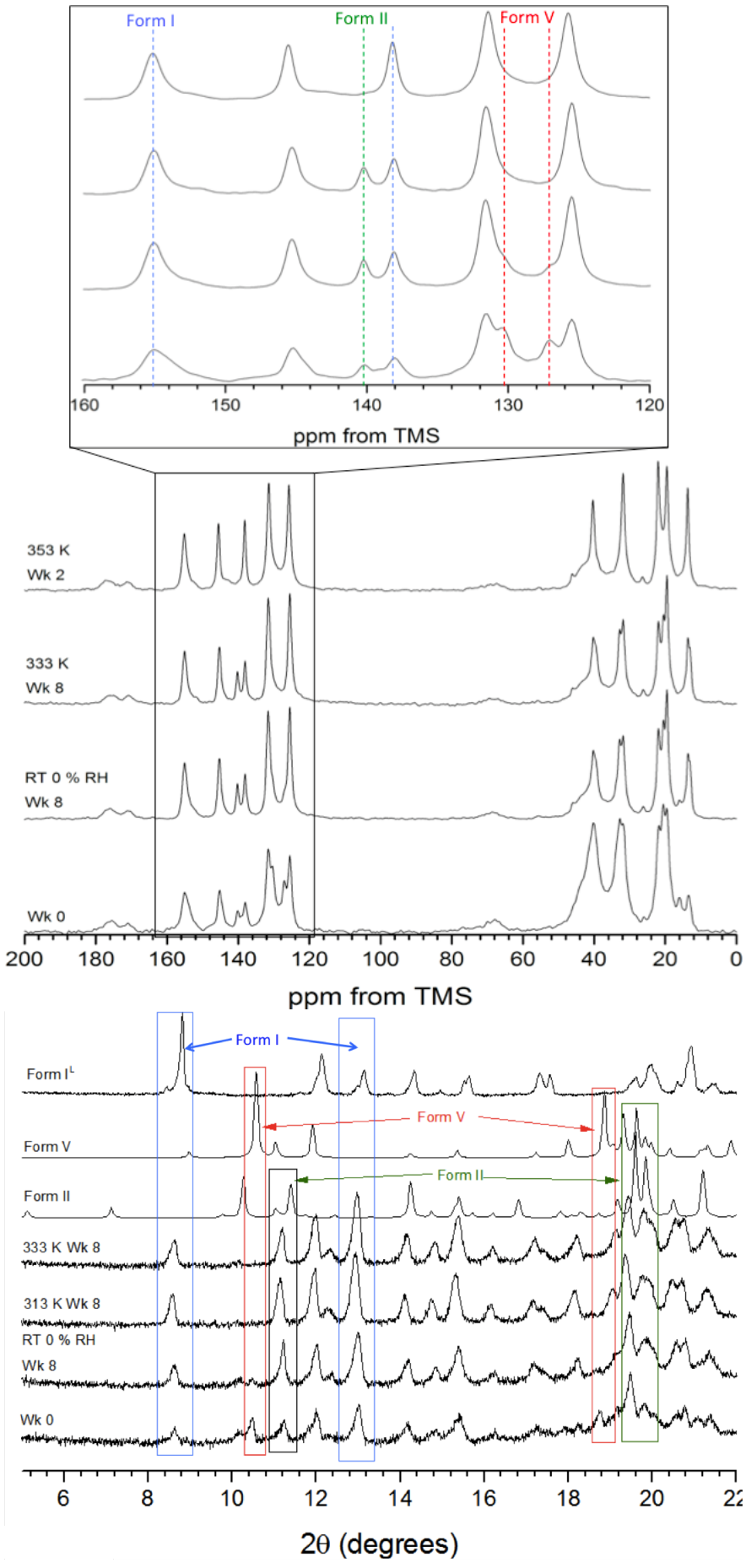


**Figure 7.49:** A) $^{1}$H-$^{13}$C CP/MAS NMR spectra (MAS = 10 kHz) and B) PXRD patterns of TLB/PVP-VA 80/20 dispersion, before and after storage at RT (0 % RH), 313 333 K and 353 K, with identification of forms $I^{L}$, II and V TLB

The 80/20 dispersion was initially characterised as containing a mixture of forms $I^L$, II and V TLB, as well as some amorphous material. The polymorphic mixture makes it difficult to study, but some changes to the composition were observed over the 8 week period (figure 7.49)). Stored under dry conditions at room temperature, a reduction in the content of form V was observed, with the presence of forms $I^L$ and II remaining constant. At higher temperatures (313 K and above) no form V was detectable by after 2 weeks of storage, with the presence of form I greater than form II, see by the changing C-11 resonances *ca.* 20 ppm. It is difficult to detect changes in the PXRD traces due to overlapping peaks, but forms I and II can be detected after storage at 313 K and above, with the majority of peaks corresponding to those of form I. Additionally, we were able to analyse the 80/20 dispersion following 2 weeks storage at 353 K, where the presence of only form I TLB was detected. This indicates the transition of form II to form I, and is in agreement with the polymorphic transitions mapped with VT $^{1}$H-$^{13}$C CP/MAS NMR studies (section 7.3.2).

Figure 7.50 shows the effect of moisture on the composition of the 80/20 dispersion when stored at room temperature. As highlighted, we observed an increase in presence of form II (peak = 10.5 °2$\theta$), and a decrease in form V (peaks = 10.2 and 18.8 °2$\theta$). This indicates a polymorphic transition between form V and II, accelerated by the presence of moisture.

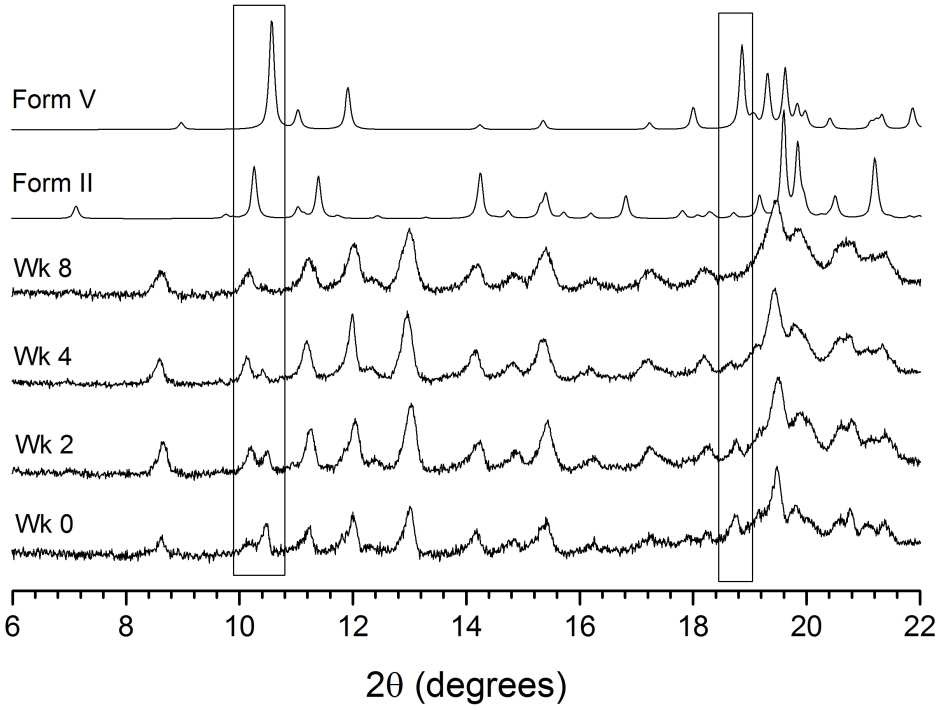


**Figure 7.50:** PXRD patterns of the TLB/PVP-VA 80/20 dispersion before and after storage at 75 % RH over the 8 week period

The advantage of using VT $^{1}$H-$^{13}$C CP/MAS NMR to predict crystallisation behaviour is time constraints, as we were able to observe the same crystallisation behaviour in a much shorter time period, as compared to the conventional stability study.

## 7.7 Conclusions

TLB was successfully formulated as an amorphous solid dispersion with PVP-VA in a variety of drug/polymer ratios. The fully amorphous nature of the dispersions was confirmed up to a maximum drug loading level of 50 wt. %, above which varying levels of a number of different polymorphic forms of TLB were identified. The 70/30 dispersion contained amorphous form, alongside form $I^L$ TLB; with the 80/20 dispersion containing a small amount of amorphous TLB, alongside three different crystalline polymorphs: forms $I^L$, II and V.

The combined use of different spectroscopic, structural and thermal methods, allowed successful investigation of the local mobility of the TLB/PVP-VA dispersions across a range of timescales. Crystallisation from amorphous TLB; and various polymorphic transitions dominated the analysis of the higher drug loading dispersions, providing an interesting, if slightly deviated study of the crystallisation behaviour of TLB in polymeric carriers.

As with IMC and FFA, solid-state $^1$H MAS NMR highlighted the presence of a fast mobility regime in the higher drug loading TLB/PVP-VA dispersions, which was able to more effectively average out strong $^1$H-$^1$H dipolar couplings. This technique provides further insight into the mobility behaviour of the amorphous drug content, as the high temperature $^1$H spectra are likely dominated by a mobile amorphous TLB phase, alongside PVP-VA, which was not detected through $^1$H-$^{13}$C CP/MAS NMR.

We demonstrated that the $T_{1\rho}{}^H$ times of the fully amorphous (20/80 and 40/60 TLB/PVP-VA dispersions) followed the same 'non-typical' temperature dependence as IMC and FFA, allowing the extraction of $E_{A\,app}$. This provided further data to relate the mobility behaviour detected through $T_{1\rho}{}^H$ to physical stability, which is further discussed in chapter 8.

Miscibility between TLB and PVP-VA was additionally probed, with $\Delta T_{1\rho}{}^H$ measurements allowing the investigation of domains down to *ca.* 2 nm. A change in miscibility behaviour was only observed at temperatures above 303 K for the 60/40 and 70/30 dispersions, which highlights the important role of studying miscibility at a variety of temperatures. Throughout formulation and storage, components of solid dispersions can be exposed to a variety of different temperature conditions, which need to be fully understood in the development process. Although a dispersion may appear to be intimately mixed at ambient temperature, a small change can lead to phase separation, and ultimately changes in properties affecting dissolution rate and physical stability.

Using VT $^1$H-$^{13}$C CP/MAS NMR we were able to accurately predict the crystallisation outcome of the TLB/PVP-VA dispersions occurring during the stability study, including highlighting the physically stable dispersions which remained amorphous (greater than 50 wt. % TLB content); the lower stability dispersions which showed crystallisation at increased temperature (60/40 TLB/PVP-VA); and the complex polymorphic transitions occurring

in the partially crystalline dispersions. VT $^{1}$H-$^{13}$C CP/MAS NMR therefore shows great promise as a tool for the prediction of stability study outcome of solid dispersions, achieving reliable results in around 8 hours *in situ*, compared to up to 8 - 12 weeks in the oven.

Due to the high crystalline content in the 70/30 and 80/20 TLB/PVP-VA dispersions, this system provided a useful probe of polymorphic behaviour, allowing the mapping of numerous enantiomeric transitions of crystalline drug **in the presence of polymer**, which has not previously been demonstrated with solid-state NMR. Using VT $^{1}$H-$^{13}$C CP/MAS NMR we were able to monitor the complex polymorphic transitions between forms I, II and V in the 80/20 TLB/PVP-VA dispersion (figure 7.24). Temperature dependent enantiotropic transitions of TLB polymorphs were detected in the 80/20 dispersion: form $I^{L} \rightarrow$ V upon cooling below 293 K; which indicated form V has higher stability at low temperatures; form $I^{L} \rightarrow I^{H}$ at the expected transition temperature; and form II $\rightarrow I^{H}$ above 353 K.

The presence of different motional regimes across a range of timescales, associated with transitions between forms $I^{L}$ and $I^{H}$ were demonstrated: 1) A low temperature kHz timescale motion *ca.*263 K (kHz timescale), thought to be associated with slow oscillations of the aromatic ring; and 2) A higher temperature MHz timescale motion at *ca.* 313 K, associated with the butyl chain rotation of the form $I^{L} \rightarrow I^{H}$ transition. The same motional regimes were clearly observed in both the pure crystalline form I, and the 70/30 and 80/20 TLB/PVP-VA dispersion which contained both form I and amorphous TLB alongside PVP-VA.

In summary, the numerous solid-state NMR techniques employed have provided a large amount of information regarding the local structure and dynamics of TLB solid dispersions, which have not previously been reported. The inclusion of high drug dispersions in the study, led to a number of interesting findings surrounding the polymorphic behaviour of TLB at different temperatures, which are previously not reported in the literature.

# Chapter 8

# General Discussion and Conclusions

In formulating solid dispersions of amorphous drugs with polymers, the ultimate aim is to prepare a **fully amorphous**, **fully miscible** drug/polymer system which remains **physically stable** upon storage for the full shelf-life duration.

Here we describe our investigation of these factors using three different drug systems: IMC, FFA and TLB, formulated at a variety of drug loadings with PVP-VA *via* solvent evaporation to investigate the terms:

- Fully amorphous
- Fully miscible
- Physically stable upon storage

We explored a number of different solid-state NMR methodologies to provide local molecular level information, comparing them to standard bulk characterisation techniques. We especially focussed on stressing the systems with variable temperature studies, in order to achieve a more comprehensive understanding of the structural organisation and mobility behaviour of amorphous solid dispersions, in relation to physical stability. We formulated a large number of dispersions, encompassing three different drugs, and eight different drug/polymer loading levels ranging from 10/90 - 80/20 w/w. This is the first time such a study across different drug systems has focussed on utilising *variable temperature* solid-state NMR to study local mobility, in combination with more commonly used bulk characterisation techniques.

## 8.1 Deducing properties of formulations based on different drug content

### 8.1.1 Determination of maximum drug loading level of amorphous solid dispersions

During initial formulation development processes, it is crucial for the maximum drug loading level of the API in the chosen polymeric carrier to be determined in order to consistently formulate physically stable dispersions. The maximum drug loading for a stable amorphous dispersion is dependent on properties of both the drug and polymer [147]. Inadvertently manufacturing a solid dispersion at drug loadings close to the maximum loading level would be detrimental to the physical stability of the system, as slight changes in storage temperatures could drive nucleation, leading to crystallisation. One difficulty of this is to identify techniques with sufficient sensitivity to reliably identify the successful formulation of fully amorphous dispersions, which are also able to detect, identify and quantify the presence of coexisting crystalline phases in lower stability dispersions. Identification of such techniques is integral to the successful design of

amorphous pharmaceutical dispersions [69, 192]. Understanding the possible polymorphic crystallisation behaviour around and above the maximum drug loading level in dispersions is additionally important, as polymorphic behaviour may not necessarily be predictable from available resources describing the pure crystalline materials [270], especially in drugs with complex polymorphism. Investigation of crystallisation behaviour in high drug loaded dispersions is often neglected in literature studies [41, 147].

Initial characterisation demonstrated that dispersions formulated at 60 wt. % (IMC and FFA) and 50 wt. % (TLB) drug content and below were found to be **fully amorphous** by all three characterisation methods employed: DSC, PXRD and solid-state NMR. Fully amorphous dispersions were identified through the concomitant presence of a broad halo in PXRD, broad peaks in $^{1}$H-$^{13}$C CP/MAS NMR spectra, and absence of crystallisation and melting events in DSC curves. This initially suggests the suitability of PVP-VA as a polymeric carrier for formulating solid dispersions with IMC, FFA and TLB, as *ca.* 60 wt. % is an extremely high drug loading as compared to the majority of commercially available amorphous formulations, which tend to contain much lower drug loading levels.

Of the higher drug loading level dispersions (60/40, 70/30 and 80/20 w/w) varying levels of crystalline drug were detected, highlighting the difference in maximum drug loading level for each drug/polymer system. Additionally, the three techniques differed in their ability to identify, characterise and quantify the presence of crystalline API.

In partially crystalline/amorphous dispersions, two different thermodynamic states exist, which can lead to both structural inhomogeneities, and variation in physical properties between batches [192], creating difficulties with reproducibility. The presence of crystalline seeds in a dispersion can act as an initial point for nucleation, in turn leading to crystallisation [271–273]. Additionally, depending on the level of miscibility between the phases, the behaviour of one phase may influence the other [192]. Partially ordered systems have been described by two models [192, 271, 274]:

- "One-state" - domains of partial crystalline phase with a semi-ordered structure are present in the amorphous carrier. This occurs due to motional restriction during crystallisation
- "Two-state" - domains of fully amorphous or crystalline phases exist next to each other in a molecularly mixed state

The "one-state" model is thought to provide a more realistic model of partially crystalline dispersions [192].

Using PXRD and $^{1}$H-$^{13}$C CP/MAS NMR, IMC/PVP-VA dispersions were found to be fully amorphous up to the highest drug loading of 80 %. In contrast, some crystalline drug was detected in the 70/30 and 80/20 FFA/PVP-VA and 60/40, 70/30 and 80/20 TLB/PVP-VA dispersions, with the techniques allowing the identification of the particular polymorphs

present (table 8.1). One very low intensity peak was identified in the PXRD pattern of the 60/40 TLB/PVP-VA dispersion, Crystalline FFA was identified as form III in both the 70/30 and 80/20 dispersions; and TLB as form $I^L$ in the 70/30 and forms $I^L$, II and V in the 80/20 dispersion. The percentage of crystalline content increased as follows: TLB/PVP-VA 60/40 < FFA/PVP-VA 70/30 < FFA/PVP-VA 80/20 ≈ TLB/PVP-VA 70/30 < TLB/PVP-VA 80/20. The TLB/PVP-VA 80/20 dispersion was found to be highly crystalline, with the presence of three polymorphs identified upon formulation. The ability of PVP-VA to prevent crystallisation in these systems appears to follow their physical stability order as predicted by the $T_g$ values of the amorphous drugs, with IMC being the most stable ($T_g$ = 315 K) and TLB the least stable ($T_g$ = 278).

**Table 8.1:** Composition of IMC/PVP-VA, FFA/PVP-VA and TLB/PVP-VA dispersions upon initial characterisation at ambient temperatures by PXRD and solid-state NMR Amorphous → Crystalline, with darker colour representing higher crystalline content

| | 10/90 | 20/80 | 30/70 | 40/60 | 50/50 | 60/40 | 70/30 | 80/20 |
|---|---|---|---|---|---|---|---|---|
| IMC | A | A | A | A | A | A | A | A |
| FFA | A | A | A | A | A | A | A + C (form III) | A + C (form III) |
| TLB | A | A | A | A | A | A + C | A + C (form $I^L$) | A + C (forms $I^L$, II, V) |

Therefore in using PXRD and solid-state NMR, the maximum drug loading levels for the formulation of fully amorphous dispersions for our three drug systems were determined to be > **80 % for IMC; 60 % for FFA and 50 % for TLB**.

DSC was the final technique employed in the initial characterisation of the dispersions. In previous studies of pharmaceutical dispersions, DSC curves tend to be interpreted to determine maximum drug loading for amorphous dispersion formation in two ways:

1. Presence of an **exothermic crystallisation event** indicates spontaneous crystallisation of the amorphous drug. This indicates the mobility of the drug in the dispersion is not completely restricted by the polymer, allowing nucleation to occur, which has increased likelihood in partially crystalline dispersions with higher initial crystalline content [190, 275].

2. Presence of an **endothermic melting peak** indicating presence of residual crystalline drug formed during manufacture [276, 277]. Melting endotherms in partially crystalline dispersions are reported as being broad, with lower $T_m$ values than for pure crystalline drug [148, 190, 258].

Table 8.2 indicates the dispersions with an exothermic crystallisation event ($T_c$) detected in the DSC curve (method 1), where the absence of a crystallisation exotherms indicates the formation of a fully amorphous dispersion [190]. $T_c$ values were identified for the 80/20 FFA/PVP-VA and 70/30 and 80/20 TLB/PVP-VA dispersions, with the exotherms having lower $\Delta H_C$ values compared to amorphous drug without polymer, demonstrating the ability of PVP-VA to inhibit some but not all crystallisation of the amorphous

content [190]. Therefore with this analysis method, the maximum drug loading levels for the formulation of fully amorphous dispersions for our three drug systems were above 80 % for IMC; *ca.* 70 % for FFA and *ca.* 60 % for TLB.

**Table 8.2:** Presence of $T_c$ in the DSC curve of IMC, FFA and TLB/PVP-VA dispersions with increasing drug loading level. * $\Delta H_c$ values scaled to account for the presence of polymer. $\Delta H_c$ of pure amorphous FFA and TLB = 27.78 and 51.10 $J{\cdot}g^{-1}$ respectively

| | **50/50** | **60/40** | **70/30** | **80/20** |
|---|---|---|---|---|
| IMC | N | N | N | N |
| FFA | N | N | N | Y ($\Delta H_c$ = 17.47 $J{\cdot}g^{-1}$) |
| TLB | N | N | Y ($\Delta H_c$ = 3.13 $J{\cdot}g^{-1}$) | Y (($\Delta H_c$ = 11.36 $J{\cdot}g^{-1}$)) |

Method 2 identified the presence of melting endotherms of all three systems in the 70/30 and 80/20 dispersions, alongside the 60/40 for TLB/PVP-VA; indicating the presence residual crystalline drug formed during manufacture (table 8.3). The presence of crystalline drug in formulations can affect the physical stability, therefore this is important to identify. The quantification of the crystalline content of the IMC/PVP-VA high loaded dispersions; and 60/40 TLB/PVP-VA dispersion highlighted a very low level of crystalline API, with the majority of the drug in the amorphous form. In this case, the absence of an exothermic crystallisation peak indicates PVP-VA was able to stabilise the remaining amorphous drug. Such a low content of crystalline material was below the detection limit for PXRD and/or $^{1}$H-$^{13}$C CP/MAS NMR.

**Table 8.3:** Presence of melting endotherms in the DSC curve of IMC, FFA and TLB/PVP-VA dispersions with increasing drug loading level

| | **50/50** | **60/40** | **70/30** | **80/20** |
|---|---|---|---|---|
| IMC | N | N | Y | Y |
| FFA | N | N | Y | Y |
| TLB | N | Y | Y | Y |

Much broader endotherms, with higher $\Delta H_f$ were identified in DSC curves of the FFA/PVP-VA and TLB/PVP-VA 70/30 and 80/20 dispersions. All endotherms occurred at lower temperatures than the known $T_m$ of pure crystalline drug, which indicates 1) the melting of a drug/polymer solid solution formed of crystalline API dissolved in the polymeric carrier upon heating [148, 190] and 2) melting of residual crystalline drug formed during manufacturing [276, 277]. These two melting events can be observed as two separate endotherms [90], which can merge into one broad peak. Similar broad melting endotherms have been previously reported in high drug loaded celecoxib/PVP dispersions [190], phenobarbitone/PVP dispersions [258] and ebselen/PVP-VA dispersions [148]. We were unable to identify the specific polymorph formed *via* DSC, as broad endotherms were present with decreased $T_m$ values. With this analysis method, the maximum drug loading levels for the formulation of fully amorphous dispersions for our three drug systems were

larger than 60 % for IMC/PVP-VA and FFA/PVP-VA and 50 % for TLB/PVP-VA dispersions.

All dispersions which were partially crystalline had $T_g$ values around or below ambient temperature; with the lowest $T_g$ dispersions containing the highest levels of crystalline drug. The presence of residual crystalline drug upon formulation and characterisation at ambient conditions in these dispersions is therefore not surprising.

**Table 8.4:** Experimental $T_g$ values of partially crystalline dispersions of IMC, FFA and TLB with PVP-VA

| | IMC $T_g$ (K) | FFA $T_g$ (K) | TLB $T_g$ (K) |
|---|---|---|---|
| 60/40 | | | 309 |
| 70/30 | 335 | 300 | 298 |
| 80/20 | 325 | 294 | 287 |

Van Eerdenbrugh and Taylor [247] formulated a number of different solid dispersions with model compounds and PVP-VA, at a variety of drug loadings. The FFA/PVP-VA dispersions, formulated at drug loading levels between 10 - 90 wt. % *via* spin coating with EtOH, provide a direct comparison to our dispersions. Crystalline FFA was only detected in the 90/10 dispersion, as compared to the 70/30 dispersion in our study. The likelihood of nucleation during formulation leading to a partially crystalline dispersion is formulation method specific. Van Eerdenbrugh's dispersions were formulated *via* spin coating, which employs faster evaporation kinetics as compared to standard solvent evaporation. The slower evaporation allows more time for nucleation and growth to occur in solution, increasing the likelihood of the presence of crystalline drug upon formulation. Tobyn *et al.* [78] compared BMS-488043/PVP dispersions prepared *via* solvent evaporation and spray drying, and found a much higher maximum drug loading in spray dried dispersions (80 % as compared to 50 %), indicating this was a more effective method of stabilising the amorphous drug. Formulating fully amorphous dispersions is therefore dependent on a combination of factors, including the ability of the polymer to stabilise the amorphous drug, drug loading level and formulation method [78, 247].

In summary, the maximum drug loading level identified in the three different drug/ polymer systems differed slightly depending on the characterisation technique employed. Additionally, we were only able to identify the different polymorphic forms of the partially crystalline dispersions using PXRD and solid-state NMR. Whilst DSC could highlight the presence of both amorphous and crystalline phases, we could not extend to the identification of polymorphs.

The partially crystalline dispersions can be further categorised into:

- Those with **low** crystalline content, with properties likely to be dominated by the amorphous phase and behave as more standard amorphous solid dispersions

- Those with **high** crystalline content, with properties likely to be dominated by further crystallisation and polymorphic transitions

The range of crystalline content dispersions allowed us an additional opportunity for the investigation of polymorphic transitions in solid dispersions with variable temperature, alongside the standard fully amorphous solid dispersions.

### 8.1.2 Detection of changes in local mobility in dispersions upon changes in temperature

Increased knowledge of molecular mobility is fundamental to the understanding of stabilisation mechanisms of amorphous APIs, both alone and in drug/polymer dispersions [69, 187]. Considerable studies have focussed on improving research and understanding in this area. Traditionally, $T_g$, as measured with DSC is used as an indicator for changes in molecular mobility of amorphous systems and correlated with amorphous stability, with research particularly focusing on changes around and below the $T_g$. Higher $T_g$ values should indicate increased physical stability [187] although literature examples do exist where $T_g$ has not proven to be an accurate indicator of amorphous stability [67].

There are an increasing number of literature examples where solid-state NMR has been used to study molecular mobility [59, 278–280], using variable temperature MAS techniques focusing on a variety of nuclei, and spin-lattice relaxation studies. This approach can provide information about local molecular mobility of different components and phases for multi-component systems across a wide range of timescales [41, 146, 160, 245, 281] (see chapter 4). Relaxation studies are used as a complimentary technique alongside DSC and DRS [146].

#### 8.1.2.1 Changes in local mobility of amorphous dispersions

Spin-Lattice ${T_{1\rho}}^H$ temperature dependence curves were collected for the three drug/ polymer systems across a range of temperatures. ${T_{1\rho}}^H$ probes the slower motions on a kHz timescale times, providing information about overall molecular mobility [146], representing the 'freeing up' of mobility as the properties of the sample change with increasing temperature [187]. These mobility processes are of particular interest around and below the $T_g$, which allows the possibility of a relationship with the likelihood of crystallisation and therefore physical stability of amorphous dispersions [146, 161].

We found that the ${T_{1\rho}}^H$ times of all fully amorphous dispersions across the IMC, FFA and TLB/PVP-VA systems exhibited a distinct 'non-typical' temperature dependence in the the VT relaxation curves. We consistently observed the presence of at least two overlapping mobility regimes, with a crossover point ($T_{MAX}$), and represented by a dramatic change in temperature dependence with increasing temperature. A clear explanation for the

non-typical behaviour was difficult to find in the literature. Similar examples of such relaxation behaviour were observed for the following systems: polymers [245]; protein lyophilized formulations [279]; amorphous APIs, and drug/polymer dispersions [46, 47]. From this literature, we constructed a unified scheme which helped form a clearer understanding of the different components of the non-typical relaxation curve (figure 8.1), relating to changes of mobility in the dispersions with increasing temperature.

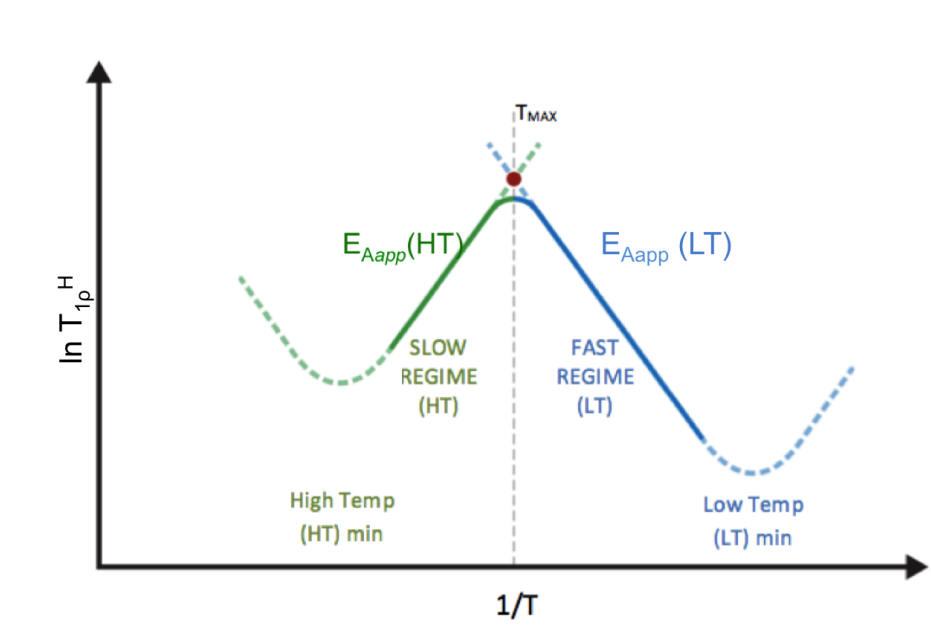


**Figure 8.1:** Explanation for the occurrence of a maximum point on the relaxation temperature dependence curve

In previous literature, $T_{MAX}$ was not specifically named, instead referred to as the temperature at which a 'break in the Arrhenius plots' was observed [47]. It is clearer to see by studying figure 8.1 that the non-typical behaviour occurs as a result of two overlapping motional regimes, each following the expected classical temperature dependence of relaxation times (chapter 4, figure 4.8). $T_{MAX}$ therefore represents the point at which the two regimes coincide. Using this approach, it seems feasible to calculate apparent activation energies ($E_{A\,app}$) either side of $T_{MAX}$, representing the kinetic response of the dispersions under the influence of each motional regime. The values of $E_{A\,app}$ therefore allows a comparative measure of stability across the different amorphous drug/polymer systems, with $E_{A\,app}$(LT) being particularly informative of the mobility behaviour at temperatures below $T_g$.

An example of the calculated $E_{A\,app}$ for our three drug/polymer systems can be seen in table 8.5. Only the dispersions found to be fully amorphous upon initial characterisation with PXRD and solid-state NMR were included, as the presence of differing quantities of crystalline material in the highest drug loading dispersions further complicated the temperature dependence curves.

**Table 8.5:** Comparison of $E_{A\,app}$ in kJ mol$^{-1}$ (LT and HT) for all amorphous IMC, FFA and TLB/PVP-VA dispersions. *HT $E_{A\,app}$ measurements were excluded if crystallisation occurred with increased temperature. PC = partially crystalline

| | IMC | | FFA | | TLB | |
|---|---|---|---|---|---|---|
| | $E_{A\,app}$ (LT) | $E_{A\,app}$ (HT) | $E_{A\,app}$ (LT) | $E_{A\,app}$ (HT) | $E_{A\,app}$ (LT) | $E_{A\,app}$ (HT) |
| 20/80 | 8.7 | 35.3 | N/A | N/A | 8.0 | 54.7 |
| 40/60 | 24.0 | 55.7 | 12.9 | 61.7 | 6.8 | 22.2 |
| 60/40 | 26.6 | 65.9 | 4.8 | 55.4 | – | X (*) |
| 80/20 | 15.5 | X (*) | PC | PC | PC | PC |

The mid-loading IMC/PVP-VA dispersions (40/60 and 60/40) had much higher LT $E_{A\,app}$ values than the other systems. High $E_{A\,app}$ indicates a more restricted mobility, requiring a higher input of energy to excite. This correlates well with the VT $^{1}$H-$^{13}$C CP/MAS NMR studies, as the IMC/PVP-VA mid-loading dispersions showed no change in mobility with increasing temperature of either drug or polymer, indicating the formation of a highly stable dispersion. Additionally, no crystallisation was detected in the stability study across the range of temperature conditions employed.

The IMC, FFA and TLB systems where LT $E_{A\,app}$ was measurable had similar values of between 5 - 13 kJ mol$^{-1}$, indicating that the motion associated with this $E_{A\,app}$ is easier to excite, leading to higher mobility in the system. This again correlated well with the VT $^{13}$C MAS NMR, as at these drug concentrations, higher mobility of the drug phase was detected as compared to the mid-loading IMC systems. This indicates that at lower drug concentration, the likelihood of high molecular mobility was greater. This does not necessarily correlate directly to the deterioration of physical stability resulting in crystallisation, as crystallisation is also dependent on drug concentration, as nucleation is more likely to occur with increasing drug content. However, the difference in molecular mobility demonstrated through analysis of VT relaxation curves could be an important part of the initial assessment of amorphous forms, and provides insight through an additional parameter not detectable using other thermal analysis techniques.

As discussed above, the kHz regime probed by VT $T_{1\rho}{}^{H}$ studies is sensitive to increases in mobility associated with the glass transition. The temperature at which $T_{MAX}$ (or the 'break in Arrhenius behaviour') occurs has been correlated with the $T_g$ of amorphous APIs [29, 47, 161] and amorphous dispersions [46, 187] in a handful of studies *via* NMR relaxation times. The general consensus is that detection of increased mobility below $T_g$ could be a useful tool in the prediction of physical stability of amorphous systems. $T_{MAX}$ represents the point of change in relaxation behaviour in the system, therefore it makes sense that an increase in molecular mobility at temperatures below $T_g$ could indicate reduced physical stability.

In all our systems studied, a dramatic change in mobility behaviour at temperatures below

$T_g$ was detected for fully amorphous dispersions. It was found that $T_{MAX}$ occurred at temperatures below $T_g$, independent of physical stability highlighted by our accelerated stability study. For example, the difference between $T_g$ and $T_{MAX}$ of the IMC/PVP-VA 40/60 and 60/40 dispersions suggests increased mobility should occur from *ca.*313 and 326 K respectively. However, despite being exposed to temperatures up to 373 K *in situ* in the rotor and in the accelerated stability study, no recrystallisation was detected. Additionally, the 60/40 FFA/PVP-VA dispersion had lower physical stability in the stability study, crystallising to form III after storage at 313 K, but the $T_g$-$T_{MAX}$ for this system was 19 K, much closer to the $T_g$ value than for higher stability dispersions which remained stable up to 373 K in VT $^{1}$H-$^{13}$C CP/MAS NMR and the stability study. The largest difference between $T_{MAX}$ and $T_g$ occurred in the IMC 20/80 and 40/60 dispersions, with $T_{MAX}$ occurring *ca.* 50 and 40 K below $T_g$ respectively. It would therefore appear that increased molecular mobility below $T_g$ is not a straightforward indication of reduced physical stability for our dispersions.

Two previous literature studies have been carried out to apply this method to amorphous dispersions. Forster *et al.* [187] investigated NIF/PVP and IMC/PVP 50/50 dispersions, which have similar $T_g$ values. They found that $T_{MAX}$ occurred at a lower temperature for the NIF/PVP dispersion compared to IMC/PVP dispersion, which correlated with the lower physical stability after 5 weeks storage at 303 K/75 % RH. However, in a more recent study of the effect of drug loading level in NIF/PVP dispersions by Yuan *et al.* [46], the correlation was not obvious. They again observed a change in mobility in 50/50, 60/40 and 75/25 NIF/PVP dispersions at temperatures below $T_g$ through analysis of VT $T_{1\rho}{}^{H}$ times. The difference between $T_{MAX}$ and $T_g$ was slightly greater with *decreasing* drug content. Unfortunately no stability data, or VT $^{13}$C solid-state NMR data were included to relate this to likelihood of crystallisation, although the trend of physical stability would be expected in the opposite direction: lower stability with *increasing* drug content. Additionally all three dispersions were found to be fully miscible on the $T_{1\rho}{}^{H}$ timescale (2 - 6 nm).

A comparison of the difference between $T_g$ and $T_{MAX}$ values for our IMC, FFA and TLB dispersions, amorphous IMC and PVP-VA alone; and literature nifedipine/PVP [46] dispersions and amorphous nifedipine [47, 187] can be seen in figure 8.2. The majority of systems, covering a variety of different drug loadings, appear to fall into a narrow range, with $T_{MAX}$ occurring *ca.*15 - 20 K below the $T_g$.

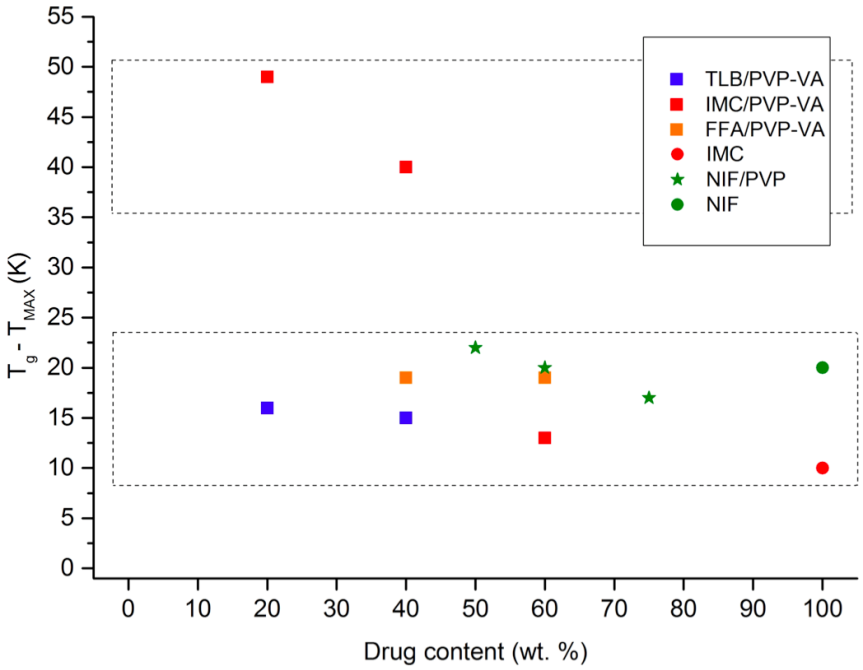


**Figure 8.2:** Comparison of the difference between $T_{MAX}$ and $T_g$ for IMC/PVP-VA, FFA/PVP-VA, TLB/PVP-VA and NIF/PVP [46] dispersions; and for amorphous IMC and NIF [47]

It is possible that the prediction of stability based on difference between $T_g$ and $T_{MAX}$ may be relevant for amorphous drugs without polymer stabilisation, with correlation found for indomethacin, nifedipine and phenobarbital [29, 47, 161]. However, our larger scale study compared to previous literature suggests this prediction does not translate for use in drug/polymer dispersions, instead the calculation of $E_{A\,app}$ may be more useful as a predictive tool. The best example of this hypothesis being that the IMC/PVP-VA 40/60 dispersion showed no crystallisation or increased mobility in VT $^{1}$H-$^{13}$C CP/MAS, $^{1}$H MAS and no crystallisation in the accelerated stability study, but still $T_{MAX}$ occurred at 40 K below $T_g$. Conversely the $E_{A\,app}$ predicted this dispersion to be highly stable.

VT spin-lattice relaxation time measurements have proven to give a different insight into mobility of drug/polymer dispersions, compared to the measurement of $T_g$ with DSC. The calculation of $E_{A\,app}$ shows promise as a technique to assess the likelihood of molecular mobility, as a comparative technique between drug/polymer systems. This could be especially useful in assessing how much of an impact a potential change to the formulation, or manufacturing process has on mobility, and therefore physical stability risk. Further research is required in this area, through investigation of $E_{A\,app}$ analysis across a wider range of systems.

## 8.2 Detection of miscibility in drug/polymer dispersions

Phase separation in drug/polymer solid dispersions generally occurs due to amorphous or crystalline drug domains occurring in the polymer matrix [11]. Such domains are not always evenly distributed, with the presence of drug concentration gradients between drug and polymer-rich domains in paracetamol/EUDRAGIT dispersions previously demonstrated by Qi *et al.* [103]. The detection of miscibility and phase separation of solid dispersions is therefore a vital part of formulation development, as successful formulation of miscible drug/polymer amorphous dispersions is crucial for maintaining acceptable physical stability during manufacture and storage of pharmaceuticals [62, 108]. The miscibility of solid dispersions has traditionally been studied using DSC, where a single $T_g$ value (intermediate between the $T_g$s of the individual components) is thought to indicate molecular level homogeneity [78, 106, 108, 163], with a detection limit of 20-30 nm [46, 164–166].

However, the detection of miscibility using DSC has been shown to be unreliable, with phase separation of amorphous dispersions detected, despite the presence of single $T_g$ values [67, 108, 144]. Therefore, a distinctive single $T_g$ value can often be a misleading identifier of physical stability of amorphous drug/polymer systems [108]. The use of spin-lattice relaxation times ($T_{1\rho}{}^H$ and $T_1{}^H$) in the solid-state has proven to be extremely useful in providing additional information about the miscibility and phase separation of solid dispersions, with differences in $T_{1\rho}{}^H$ times allowing estimation of much smaller domains than with DSC; with a demonstrated detection down to *ca.*2 nm in size [46, 62, 88].

### 8.2.1 Thermal Analysis

The experimental and predicted $T_g$ values for our three drug/polymer systems can be seen in figure 8.3. Density measurements of the three amorphous drugs were not possible, therefore predictions were made using the Gordon-Taylor/Kelley-Bueche (G-T/K-B) and Couchman-Karasz (C-K) equations only (equations 2.17 with 2.19 and 2.20 respectively - see chapter 3).

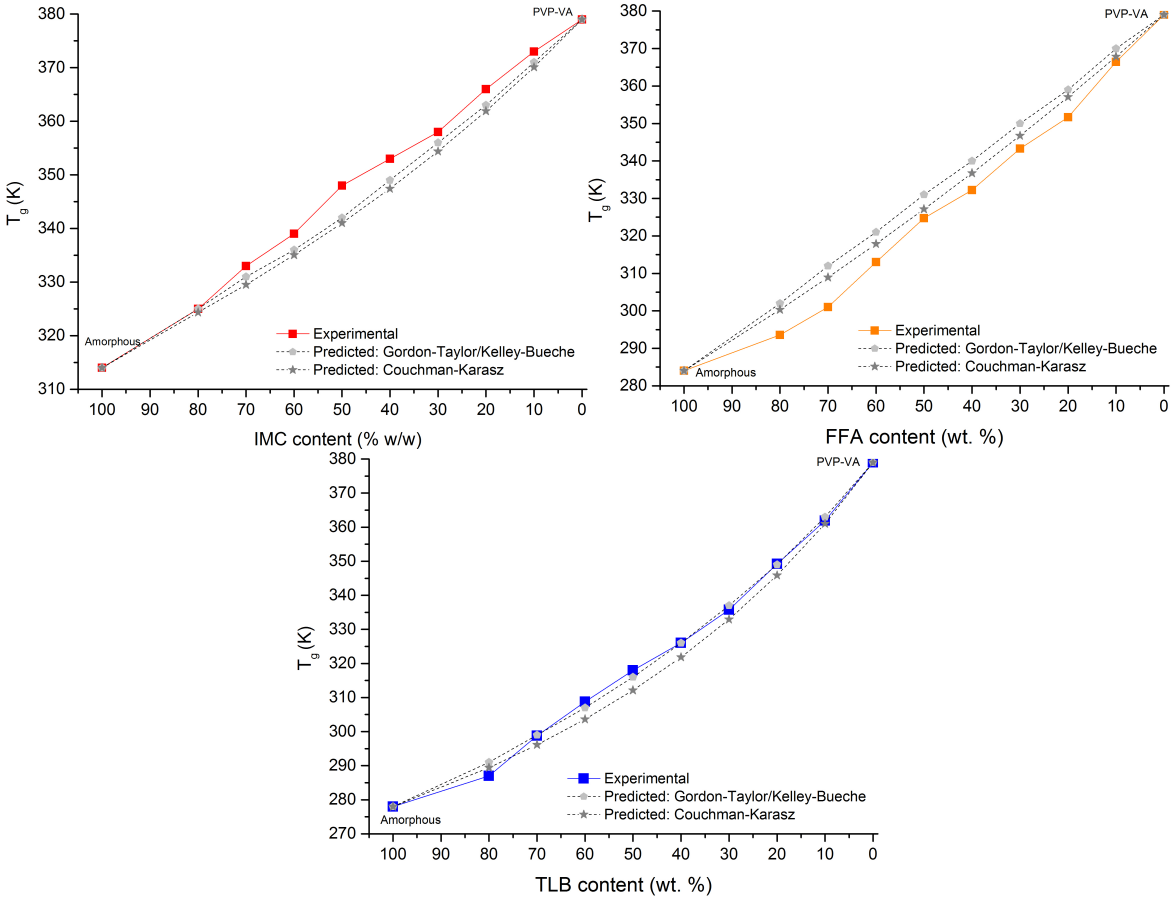


**Figure 8.3:** Glass transition temperatures for IMC/PVP-VA, FFA/PVP-VA and TLB/PVP-VA dispersions at different drug loadings, compared to values predicted by the Gordon-Taylor/Kelley-Bueche (G-T/K-B) and Couchman-Karasz (C-K) equations

For fully amorphous solid dispersions, deviation from predicted $T_g$ values can indicate the presence of immiscible, or incompatible components [192]. Deviations of ± 5 - 8 K between theoretical and experimental $T_g$ values is considered to be good agreement for 'ideal' mixing [78, 108]. Using this approach, all three drug/polymer systems showed negligible deviation from predicted values across all drug/polymer ratios. This method indicates that these systems are not dominated by intermolecular interactions, and instead are considered to be 'ideally' mixed from the DSC perspective. Additionally, the presence of one single $T_g$ value was found in all our fully amorphous dispersions, at an intermediate temperature between the drug and polymer $T_g$ values. This indicates miscibility between amorphous drug and polymer, with a domain size detection limit of 20-30 nm [165].

### 8.2.2 Detection of miscibility using relaxation times studies

Variable temperature solid-state NMR relaxation studies have highlighted a number of important observations with regard to the miscibility and phase separation of the IMC, FFA and TLB/PVP-VA drug/polymer systems, including not using $T_{1\rho}{}^H$ times to detect phase separation between drug and polymer upon heating fully miscible dispersions; but

also using $T_1{}^F$ times to identify phase separation between different drug phases (crystalline and amorphous) at high temperatures.

The majority of literature studies employing spin-lattice relaxation times to detect miscibility in drug/polymer systems have focussed on measurements at ambient temperatures. We demonstrated in section 8.1.2.1 that relaxation time is highly dependent on temperature. The detection of miscibility and phase separation based upon relaxation times is therefore also highly temperature dependent. Additionally, it is crucial to fully investigate the behaviour of amorphous dispersions across the full range of temperatures likely to be experienced throughout manufacture and storage, in order to identify and understand changes to miscibility occurring in formulations.

#### 8.2.2.1 Drug/polymer miscibility

Firstly, changes in relaxation times ($T_{1\rho}{}^H$ and $T_1{}^H$) were used for the detection of phase separation between drug and polymer components in solid dispersions. At ambient temperatures, all dispersions with drug loadings of 60 wt. % and below were found to be miscible (down to 2-6 nm domain sizes) using $\Delta T_{1\rho}{}^H$ times, which correlated with the amorphous nature of these dispersions shown through DSC, PXRD and $^1$H-$^{13}$C CP/MAS NMR. Of the highest drug loadings (70 % and above), the IMC/PVP-VA dispersions showed the smallest level of phase separation with $\Delta$ $T_{1\rho}{}^H$ of 10 ms, compared to *ca.* 50 ms (FFA) and 60 ms (TLB) at 80 wt. % drug loading (figure 8.4), which again correlates well with the level of crystalline drug detected upon initial characterisation: the larger the proportion of crystalline drug present within the dispersion, the larger the separation of $T_{1\rho}{}^H$ times detected though $T_{1\rho}{}^H$ time analysis. No significant differences in $\Delta T_1{}^H$ were detected for all dispersions studied, suggesting miscibility on the 6 - 24 nm lengthscale, despite the presence of crystalline drug in the higher drug loading dispersions.

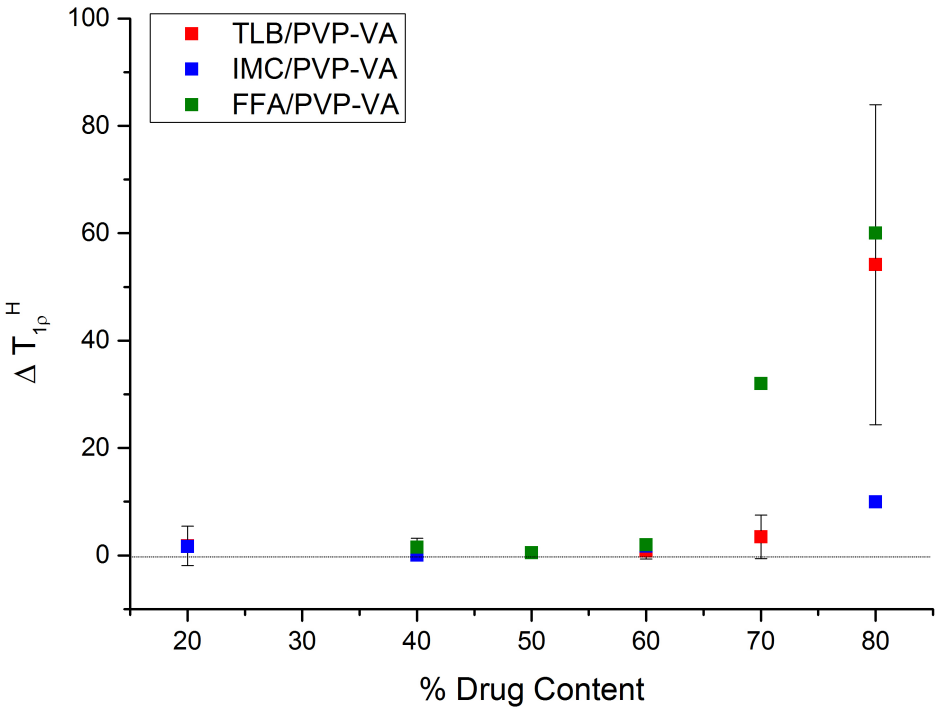


**Figure 8.4:** Miscibility of drug and polymer at 293 K, as predicted through $\Delta T_{1\rho}{}^{H}$ times for IMC, FFA and TLB/PVP-VA dispersions at varying drug loadings

Solid-state NMR was first used to demonstrate miscibility in polymer blends and alloys [282, 283]. Pignatello *et al.* [90] demonstrated this method to be useful for the detection of homogeneity in pharmaceutical solid dispersions with diflusinal and Eudragit, formulated *via* solvent evaporation. A large separation of $T_1{}^{H}$ between drug and polymer was observed for physical mixtures, as compared to one common $T_1{}^{H}$ time for each component within the solid dispersion, indicating intimate mixing. Aso *et al.* [152] further expanded the method, to assess the sensitivity of spin-lattice relaxation in detecting miscibility in nifedipine solid dispersions, as compared to DSC. Relaxation decay curves were used to detect miscibility, where mono-exponential decay described homogeneity to the detection limit of $T_{1\rho}{}^{H}$ (less than 5 nm) and $T_1{}^{H}$ (smaller than 50 nm), with larger domains described by bi-exponential equations. Nifedipine/PHPA (40/60 and 50/50 w/w) contained domains 5-50 nm in size, despite displaying a single $T_g$ values, demonstrating that NMR provides a more detailed level of miscibility information compared to DSC.

Pham *et al.* [88] studied a range of pharmaceutical formulations extensively with a variety of solid-state NMR techniques, including the detection of phase separation through spin-lattice relaxation. Trehalose/Dextran solid dispersions were found to be miscible with domains of less than 82 nm (50/50 w/w) and 55 nm (30/70 w/w) *via* $T_1{}^{H}$ relaxation time measurements at 273 K. Both dispersions were found to be miscible by DSC [144]. Kojima *et al.* [86] found one common $T_1{}^{H}$ time in mefenamic acid/Eudragit EPO (24/76 w/w) cryogenically ground dispersions, which indicated domains of less than 100 nm. Litvinov *et al.* [101] used $T_{1\rho}{}^{H}$ times to demonstrate the formation of 1.6 nm amorphous nanoclusters

dispersed within the polymer phase of miconazole/PEG-gPVA (10/90 w/w) dispersions. The most extensive studies to detect molecular level miscibility in solid dispersions *via* spin-lattice relaxation (combining analysis of both $\Delta\ T_{1\rho}{}^{H}$ and $T_1{}^{H}$) were carried out by Yuan *et al.* [46] and Song *et al.* [62]. Both groups investigated the effect of drug loading on miscibility at ambient temperature, probing a range of dispersions of nifedipine/PVP and lapatinib/HPMC-P respectively (figure 8.5).

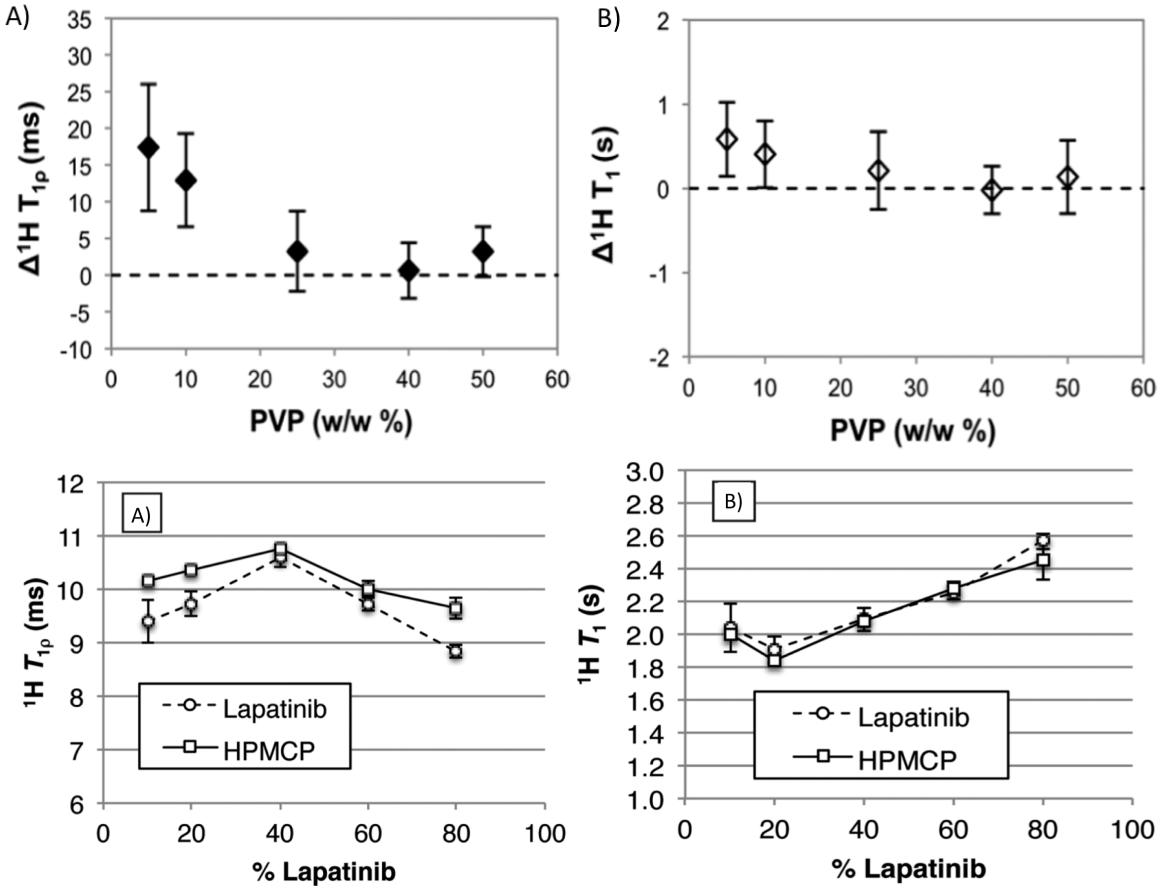


**Figure 8.5:** Differences in A) $T_{1\rho}{}^{H}$ and B) $T_1{}^{H}$ between nifedipine and PVP in melt quenched solid dispersions, adapted from [46] and Differences in A) $T_{1\rho}{}^{H}$ and B) $T_1{}^{H}$ between lapatinib and HPMC-P in spray dried solid dispersions, adapted from [46]

Nifedipine/PVP melt quenched dispersions were found to be homogenous at 75/25, 60/40 and 50/50 (w/w) loadings, with domains of less than 4.5 nm. Only extremely high drug loadings (90 - 95 wt. %) displayed immiscibility on this scale, with estimated domain sizes between 20 - 50 nm. Spray dried dispersions showed an even higher level of mixing, with 90 % drug loading showing no difference in $T_{1\rho}{}^{H}$ between drug and polymer [46]. Lapatinib/HPMC-P spray dried dispersions were miscible by $T_1{}^{H}$ up to 80 % drug loading, but $\Delta T_{1\rho}{}^{H}$ times highlighted the separation of drug and polymer at both low and high drug loadings. $\Delta T_{1\rho}{}^{H}$ was smallest for the 40/60 lapatinib/HPMC-P dispersion, enabling them to choose this as the optimum drug loading level for formulation in terms of miscibility. The multiple phases in the low (10/90 and 20/80) and high (80/20) loading dispersions were attributed to the

presence of excess amorphous drug/polymer salt alongside un-ionized excess polymer and some drug/polymer salt alongside excess un-ionized drug respectively [62].

By combining both $T_1{}^H$ and $T_{1\rho}{}^H$ measurements with DSC analysis we gain a more complete picture of the level of homogeneity within solid dispersions, allowing detection of miscibility to *ca.* 2 nm lengthscale. Measuring differences in spin-lattice relaxation times to detect miscibility in solid dispersions has therefore been shown to be an effective tool, with higher detection sensitivity than DSC in our results and in previous literature studies.

However, the in-depth analysis of the miscibility of different drug/polymer dispersions with **varying temperature** is still lacking. This is extremely important, as throughout formulation and storage, components of solid dispersions can be exposed to a variety of different temperature conditions. Here we demonstrate the importance of probing the miscibility of drug/polymer dispersions across a temperature range, as although a dispersion may appear to be intimately mixed at ambient temperature, a small change in temperature can lead to phase separation, crystallisation, and ultimately changes in properties affecting dissolution rate and physical stability. To the best of our knowledge, our work presents the first comprehensive studies of changes in miscibility (under 30 nm) of polymer/drug dispersions across different temperatures.

Both the 60/40 and 70/30 TLB/PVP-VA dispersions were found to be miscible on the lengthscale sensitive to $T_{1\rho}{}^H$ times at 293 K (figure 8.6). Above 293 K, a clear phase separation of drug and polymer was detected for the 70/30 dispersion, as the temperature induced crystallisation to form $I^H$ TLB occurred. The 60/40 dispersion was also fully miscible at ambient temperatures, with phase separation detected as the dispersion was heated through $T_g$ (*ca.*313 K: $T_g$ + 4 K). At this point, crystallisation from amorphous to form $I^H$ TLB was identified through VT $^1$H-$^{13}$C CP/MAS NMR.

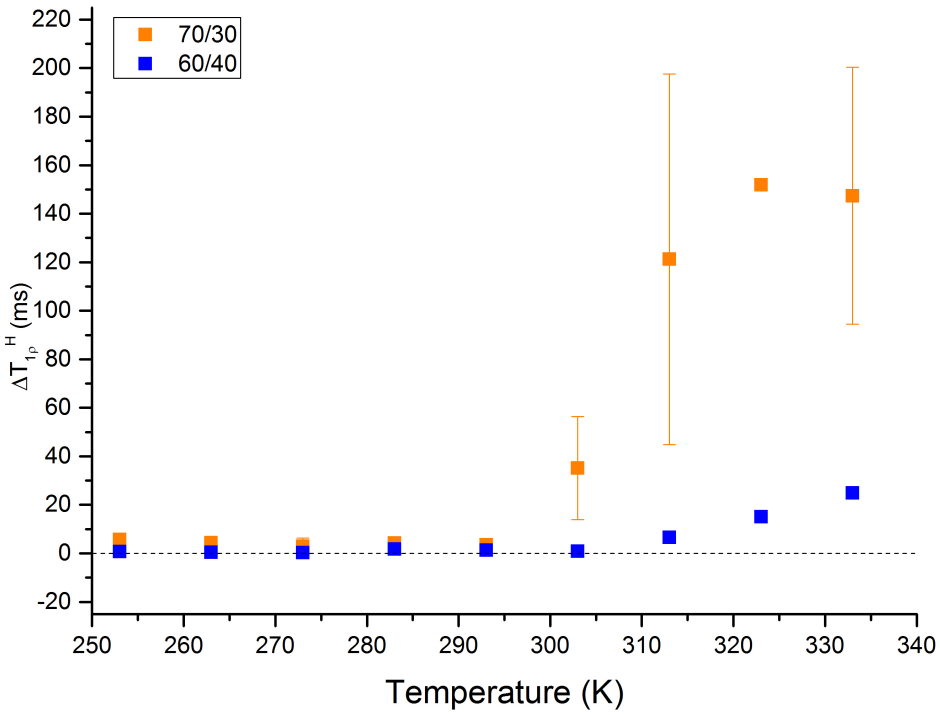


**Figure 8.6:** Difference in $T_{1\rho}{}^{H}$ times between TLB and PVP-VA in the 60/40 and 70/30 dispersions between 253 and 343 K. Error bars represent 95 % confidence intervals of the difference between means

For the IMC/PVP-VA 80/20 dispersion, partial phase separation was detected at ambient temperatures ($\Delta T_{1\rho}{}^{H}$ *ca.*10 ms), but increased at higher temperature, particularly *ca.* 343 K ($T_g$ + 18 K), when crystallisation from amorphous to $\alpha$-IMC was detected. The highest loading FFA/PVP-VA dispersions (70/30 and 80/20) were immiscible (*via* $T_{1\rho}{}^{H}$ times) across the entire temperature range, with clear phase separation identified, and a greater separation of $T_{1\rho}{}^{H}$ times with increasing crystalline content.

The measurement of $T_{1\rho}{}^{H}$ times has been shown to be a very sensitive technique as compared to DSC and $T_1{}^{H}$, as it enabled the estimation of domain sizes down to as little as 2 nm. The combination of relaxation time difference measurements alongside temperature dependence relaxation curves and VT $^{1}$H-$^{13}$C CP/MAS NMR, provides an extremely useful visual tool to identify phase separation, homogeneity and crystallisation behaviour in solid dispersions. Identification of these attributes is important during initial formulation development to identify both ideal and maximum drug loading levels.

#### 8.2.2.2 Understanding solid forms of drugs within dispersions at high temperatures

Solid-state NMR can additionally be used for the identification and quantification of different solid forms of API present in dispersions. We observed the presence of both amorphous and crystalline forms in the TLB/PVP-VA and FFA/PVP-VA 70 and 80 wt. % dispersions through DSC and $^{1}$H-$^{13}$C CP/MAS NMR at ambient temperatures, and monitored the

crystallisation and polymorphic behaviour with increasing temperature. However, due to the high mobility of both FFA and PVP-VA at high temperatures, this method proved more challenging for the FFA/PVP-VA dispersions.

At high temperatures, we were able to detect form $I^H$ TLB in the 60, 70 and 80 wt. % dispersions; and $\alpha$-IMC in the wt. 80 % dispersion with $^1$H-$^{13}$C CP/MAS NMR, however the FFA/PVP-VA dispersions proved more problematic to characterise. As the FFA/PVP-VA dispersions crossed to a high mobility regime, the $^{13}$C signal was undetectable, but the presence of $^{19}$F provided an alternative way to detect and characterise the drug *via* $^{19}$F MAS NMR and $T_1{}^F$.

This method clearly highlighted two distinct fluorine environments, corresponding to crystalline (form I) and amorphous FFA, both at 373 K, and upon cooling to ambient temperatures (figure 8.7). There are no previously reported examples of the detection of phase separated drug phases with $T_1{}^F$, although Pham *et al.* [88] identified two drug phases in high drug loaded paracetamol/Eudragit dispersions *via* $^{13}$C detected $T_1{}^H$ analysis.

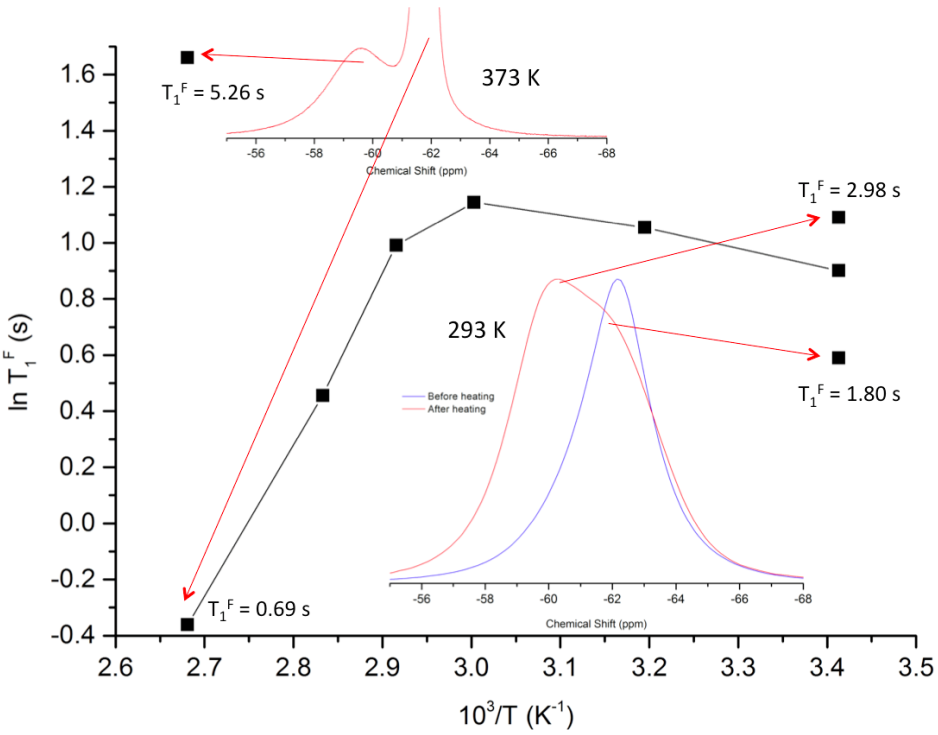


**Figure 8.7:** Arrhenius plots outlining the temperature dependence of $T_1{}^F$ times of 80/20 dispersion, heated between 293 K and 373 K, then cooled back to 293 K. Relevant $^{19}$F MAS NMR spectra for 373 K and upon cooling back to 293 K are shown to highlight the origins of phase separation

#### 8.2.2.3 Limitations of the detection of miscibility with $\Delta T_{1\rho}{}^H$

The 70/30 TLB/PVP-VA dispersion was found to contain form $I^L$ TLB, alongside amorphous TLB upon formulation *via* DSC, PXRD and solid-state NMR. However, within experimental

error at 293 K, there was no difference in $T_{1\rho}{}^{H}$ between crystalline drug and polymer, with the level of amorphous TLB too low to accurately measure $T_{1\rho}{}^{H}$ times. Therefore it would be incorrect to apply $\Delta T_{1\rho}{}^{H}$ time measurements in this case. This method is highly dependent on different phases having different individual $T_{1\rho}{}^{H}$ times, so that a difference of zero gives a meaningful result. In this case, the individual $T_{1\rho}{}^{H}$ times of the crystalline form $I^{L}$ and PVP-VA were highly similar at 293 K. The possibility of $T_{1\rho}$ times which are statistically indistinguishable between components is therefore a limitation of this technique [146]. In this case, more complex 2D solid-state NMR techniques such as multinuclear HETeronuclear Correlation (HETCOR) could be employed to provide additional miscibility information [88, 284, 285].

Measuring the difference in $T_{1\rho}{}^{H}$ times across a range of temperatures provides a more complete picture of the level of phase separation under different conditions. In the 70/30 TLB/PVP-VA dispersion, increasing the temperature uncovered a difference in $T_{1\rho}{}^{H}$ times of the drug (form $I^{L}$) and polymer, as they display completely different temperature dependencies at higher temperatures. Relying on one temperature point measurement provides only a snapshot of the behaviour of the individual components *under one specific environment*. When the temperature dependence relaxation curves of TLB and PVP-VA in the 70/30 dispersion were studied separately, it became clear that the two phases had completely different temperature dependencies, despite appearing to have similar relaxation times at 293 K. This highlights the importance of studying the temperature dependence of relaxation.

VT $^{1}$H-$^{13}$C CP/MAS NMR did show an increased level of form $I^{L}$ TLB within the 70/30 dispersion with increasing temperature, followed by a polymorphic transition to form $I^{H}$. Despite having similar crystal structures, it has been demonstrated here that the enantiomeric polymorphs have very different $T_{1\rho}{}^{H}$ times. It is unlikely that upon conversion from form $I^{L}$ $\rightarrow$ form $I^{H}$ the domain sizes of crystalline TLB drastically changed, but the difference in $T_{1\rho}{}^{H}$ times between drug and polymer was only detectable following the polymorphic transition.

This observation highlights the importance of investigating the miscibility information gained through $\Delta T_{1\rho}{}^{H}$ and $\Delta T_{1}{}^{H}$ analysis, alongside the full temperature dependence relaxation curves, and VT $^{1}$H-$^{13}$C CP/MAS NMR to provide a more comprehensive understanding of the behaviour of the different solid dispersion components, particularly when drug loading approaches the maximum loading limit, increasing the likelihood of the presence of more complex phase transitions.

### 8.2.3 Mapping polymorphic transitions in dispersions with high drug loadings

Both IMC and TLB proved to be interesting systems at high drug loading levels, with both amorphous, and partially crystalline dispersions enabling the mapping of crystallisation and polymorphic transitions with VT $^{1}$H-$^{13}$C CP/MAS NMR and $T_{1\rho}{}^{H}$ relaxation studies.

IMC was a useful proof of concept system. We were able to clearly observe the crystallisation of amorphous to $\alpha$-IMC from the amorphous drug by acquiring $^{1}$H-$^{13}$C CP/MAS NMR spectra with increasing temperature. Amorphous IMC has been shown to convert to $\alpha$-IMC when stored at temperatures above $T_g$, as this is the more thermodynamically stable polymorph at high temperatures. We also found that the same polymorphic transition occurred from amorphous IMC dispersed in low levels of PVP-VA (80/20 dispersion), showing that polymorphic phase diagrams are still relevant to predict transitions in drug/polymer systems under conditions where crystallisation can occur. Additionally, the transition was clearly observed in both VT $^{1}$H-$^{13}$C CP/MAS NMR and relaxation studies, which demonstrates the usefulness of both solid-state NMR techniques.

Using the TLB system, we were able to clearly monitor a number of different polymorphic transitions in both the pure crystalline form and in the highest drug loaded dispersions. The transition of form $I^{L} \rightarrow I^{H}$ is known to occur reliably upon heating and cooling through *ca.* 311 K due to a conformational change to the butyl chain associated with an enthalpy of *ca.* 2 kJ mol$^{-1}$ [43]. The changes to the structure were clearly seen in the $^{13}$C solid-state NMR spectrum, through changes in chemical shift in the aliphatic region. Heating and cooling form I TLB *in situ* in the rotor reliably induced these changes in the chemical shift positions, in agreement with the study by Hasegawa *et al.* [43].

Throughout the full temperature range, we observed the presence of two different motional regimes, *via* spin-lattice relaxation and $^{1}$H-$^{13}$C CP/MAS NMR studies.

- **Low temperature motional regime *ca.*263 K, on the kHz timescale**, which has not been reported before and is thought to be associated with slow oscillations of the aromatic ring
- **Higher temperature motional regime *ca.*313 K on the MHz timescale**, associated with the motion of the butyl chain during the form $I^{L} \rightarrow I^{H}$ transition.
- The same motional regimes were clearly observed in both the pure crystalline form I, and the 70/30 TLB/PVP-VA dispersion which contained both form I and amorphous TLB alongside PVP-VA

Using VT $^{1}$H-$^{13}$C CP/MAS NMR we were able to monitor the more complex polymorphic transitions between forms I, II and V in the 80/20 TLB/PVP-VA dispersion (figure 8.8). Form V has been described previously, but was found to be very unstable, converting to

form I within two hours at ambient temperature [44, 57]. Cooling to low temperatures resulted in conversion of form $I^L \rightarrow$ V, which was reversible upon heating back to ambient temperatures, indicating this is a temperature dependent *reversible* polymorphic transition. Form V also appeared to be more stable in the dispersion under dry conditions at room temperature in comparison to pure form V. Slow conversion from form V $\rightarrow$ to form $I^L$ did occur, but form V was still detectable *via* PXRD after 8 weeks of storage.

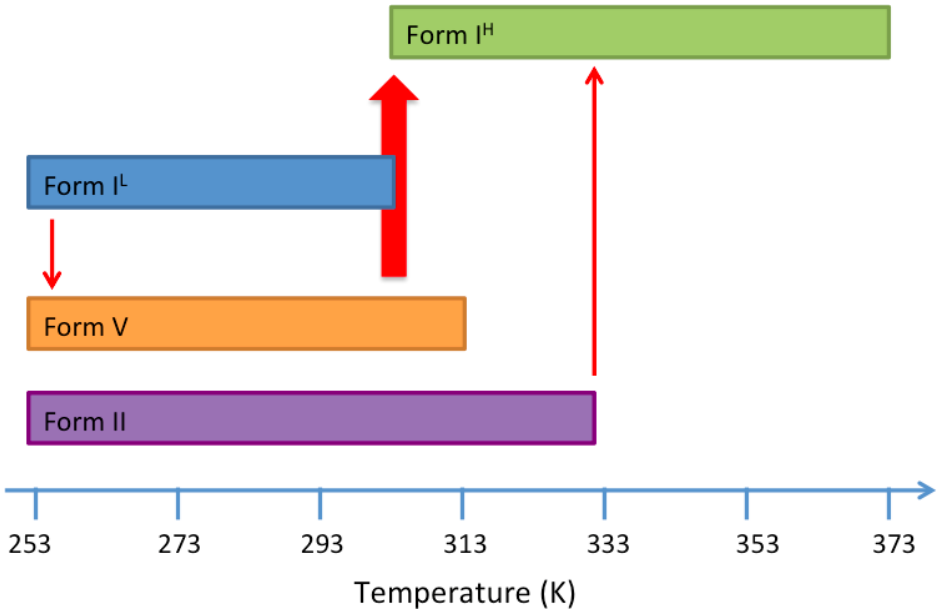


**Figure 8.8:** Schematic representation of the polymorphic transitions mapped in 80/20 TLB/PVP-VA dispersion

The FFA system proved much more difficult to study, especially in terms of polymorphic transitions. FFA is known to exhibit complex polymorphism [39], having the highest number of solved polymorphic structures in the Cambridge Structural Database. Through heating pure form III FFA, we were able to detect the transition from form III $\rightarrow$ form I *via* VT $^{1}$H-$^{13}$C CP/MAS and $^{19}$F MAS NMR. The highest drug loading dispersions contained form III on formulation alongside amorphous FFA, but the same transition to form I was not detectable in VT $^{1}$H-$^{13}$C CP/MAS NMR, due to loss of signal through high mobility of drug and polymer. The VT $^{19}$F MAS NMR identifed the presence of form I FFA in the dispersions at 373 K, which was confirmed with VT PXRD studies. In all three systems, the polymorphic transition (form III $\rightarrow$ I) occurred at a much higher temperature than the expected literature transition temperature.

This extends work done in previous studies of crystallisation from high drug loaded dispersions, by identifying and characterising different polymorphic forms. Currently, polymorphic screening of API is carried out from solvent, but not in the presence of polymer. Therefore, unidentified polymorphs can sometimes be missed in early development, only appearing at later stages, which can cause huge problems in terms of physical stability and dissolution of formulations.

Here we have three different systems, where we see crystallisation and phase separation at high drug loading levels. Through application of VT solid-state NMR techniques, we were able to sensitively monitor a number of polymorphic transitions which agreed with known thermodynamic stabilities; identify different polymorphs within complex polymorphic mixtures; and observe the stabilisation of previously unstable polymorphs within dispersions.

## 8.3 Prediction of outcomes of accelerated stability studies

The physical stability of the amorphous and partially crystalline solid dispersions was monitored at elevated temperatures over a period of 8 - 12 weeks. We aimed to predict the outcome of the stability study, in terms of physical stability, crystallisation of amorphous API, and occurrence of polymorphic transitions between crystalline phases of the various solid dispersions with variable temperature $^{1}$H-$^{13}$C CP/MAS NMR.

The majority of the fully amorphous dispersions remained physically stable upon storage at elevated temperature and humidity, throughout the study period. Crystallisation was detected in the IMC/PVP-VA 80/20, FFA/PVP-VA 60/40 and TLB/PVP-VA 60/40 dispersions after storage at 363 K, 313 K and RT 75 % RH respectively. Further polymorphic transitions of the partially crystalline high loading dispersions were also detected, providing useful additional data relating to polymorphism within solid dispersions.

The crystallisation outcomes of the dispersions in the accelerated stability study and *in situ* in the NMR rotor *via* VT $^{1}$H-$^{13}$C CP/MAS NMR can be seen in tables 8.6 and 8.7 respectively. These results demonstrate that VT NMR accurately predicted the crystallisation outcome of the IMC/PVP-VA, FFA/PVP-VA and TLB/PVP-VA dispersions occurring in the stability study, unless the $^{13}$C signal was absent through high sample mobility. This was a particular problem at higher temperatures with FFA/PVP-VA dispersions above 40 wt. % drug loading. In this case, we were able to use a multinuclear approach to detect crystallisation outcomes with $^{19}$F MAS NMR.

The $^{13}$C VT MAS NMR method was therefore able to identify:

1. The stable dispersions which remained amorphous
2. Lower stability dispersions which showed crystallisation at increased temperature
3. Further polymorphic transitions of the partially crystalline dispersions

These findings mirror both the stability study and VT PXRD. VT $^{1}$H-$^{13}$C CP/MAS NMR therefore shows great promise as a toolset for the prediction of stability study outcome of solid dispersions, achieving reliable results in around 8 hours *in situ*, compared to up to 8 - 12 weeks in the oven, provided signal does not break down through increased sample mobility.

**Table 8.6:** Composition of IMC/PVP-VA, FFA/PVP-VA and TLB/PVP-VA dispersions before and after storage at various conditions in the accelerated stability study (12 weeks) as detected by PXRD and solid-state NMR. Amorphous → Crystalline Dispersion was considered to be crystalline if crystalline peaks of the drug were detectable by PXRD and $^{1}$H-$^{13}$C CP/MAS NMR

| | Start | RT 0 % | RT 75 % | 313 K | 333 K | 353 K | 363 K |
|---|---|---|---|---|---|---|---|
| IMC 20 | A | A | A | A | A | | |
| IMC 40 | A | A | A | A | A | | |
| IMC 60 | A | A | A | A | A | | |
| IMC 70 | A | A | | A | A | A | |
| IMC 80 | A | A | A | A | A | | $\alpha$-IMC |
| | | | | | | | |
| FFA 20 | A | A | A | A | A | | |
| FFA 40 | A | A | A | A | A | | |
| FFA 60 | A | A | A | III | III | | |
| FFA 70 | III | III | | III | III | | |
| FFA 80 | III | III | III | III | III | | |
| | | | | | | | |
| TLB 20 | A | A | A | A | A | | |
| TLB 40 | A | A | A | A | A | | |
| TLB 60 | A | A | $I^L$ | $I^L$ | $I^L$ | | |
| TLB 70 | $I^L$ | $I^L$ | | $I^L$ | $I^L$ | | |
| TLB 80 | V, II, $I^L$ | V ($\downarrow$), II, $I^L$ | II, $I^L$ | II, $I^L$ | II, $I^L$ | $I^L$ | |

**Table 8.7:** Composition of IMC/PVP-VA, FFA/PVP-VA and TLB/PVP-VA dispersions with increasing temperature *in situ* in the NMR rotor detected *via* $^{1}$H-$^{13}$C CP/MAS NMR Amorphous → Crystalline

| | 293 K | 313 K | 333 K | 353 K | 373 K | |
|---|---|---|---|---|---|---|
| | | | | | $^{13}$C | $^{19}$F |
| IMC 20 | A | A | A | A | A | |
| IMC 40 | A | A | A | A | A | |
| IMC 60 | A | A | A | A | No signal | |
| IMC 80 | A | A | A | $\alpha$ | $\alpha$ | |
| | | | | | | |
| FFA 20 | A | A | A | A | A | A |
| FFA 40 | A | A | A | A | No signal | A |
| FFA 60 | A | A | A | No signal | No signal | A |
| FFA 70 | III | III | III | No signal | No signal | I |
| FFA 80 | III | III | III | III | No signal | I |
| | | | | | | |
| TLB 20 | A | A | A | A | A | |
| TLB 40 | A | A | A | A | No signal | |
| TLB 60 | A | $I^H$ | $I^H$ | $I^H$ | No signal | |
| TLB 70 | $I^L$ | $I^H$ | $I^H$ | $I^H$ | $I^H$ | |
| TLB 80 | V, II, $I^L$ | V, II, $I^H$ | II, $I^H$ | $I^H$ | $I^H$ | |

## 8.4 Overall Conclusions

1. Amorphous solid dispersions were successfully formulated with PVP-VA for three contrasting amorphous pharmaceuticals: IMC, FFA and TLB. Differences in maximum drug loading level were identified for each. The combined use of different spectroscopic, structural and thermal methods allowed successful, and varied investigations of the local structure and mobility of the drug/polymer systems across a range of timescales. Such a combined approach is essential in understanding the complexities of polymer drug dispersions.

2. Each drug/polymer system proved valuable to this study in a different way. **IMC** proved to be a useful proof of concept system; providing a high stability comparison against the FFA and TLB systems. The use of $^{19}$F NMR spectroscopy enabled us to gain a unique insight in the very complex behaviour of **FFA**/PVP-VA dispersions at high temperature. **TLB** provided a useful probe of polymorphic transitions in the presence of polymer, due to the high crystalline content, and complex polymorphic behaviour of these dispersions. Additionally, the presence of motional regimes across a range of timescales were demonstrated in this system.

3. All fully amorphous dispersions followed similar 'non-typical' relaxation time temperature dependence, which we clarified through creation of a unified scheme. The calculation of apparent activation energies $E_{Aapp}$ showed the most promise as a tool to relate local mobility with the prediction of physical stability of amorphous solid dispersions, as some correlation between these parameters was demonstrated. This requires further study across a wider range of drug/polymer dispersions to increase the dataset with which more definite conclusions can be drawn. The use of $T_{MAX}$ - $T_g$ to assess physical stability should be taken with more caution.

4. Variable temperature studies highlighted changes in miscibility for a number of dispersions, reinforcing the importance of studying local structure and mobility at a **range of temperatures**. Throughout manufacturing and storage, solid formulations can be exposed to a variety of different temperature conditions: although a dispersion may appear to be intimately mixed at ambient temperatures, a small change can lead to phase separation, and ultimately changes in dissolution rate and physical stability.

5. The combination of relaxation time difference measurements, temperature dependence relaxation curves and VT $^{1}$H-$^{13}$C CP/MAS NMR provided a clear visual tool to identify phase separation and crystallisation behaviour in solid dispersions, Early identification of these attributes is important during initial formulation development to identify both ideal, and maximum drug loading levels. VT $^{13}$C MAS NMR has additionally shown great promise as a tool for the prediction of crystallisation outcomes of high temperature stability studies. This could also prove

to be a useful technique in highlighting unusual polymorphic behaviour of early development compounds, essentially eliminating problem APIs from further development at the earliest possible stage.

# Bibliography


[1] Hore, P. J., 1995, Nuclear Magnetic Resonance, Oxford Chemistry Primers

[2] Levitt, M. H., 2001, Spin Dynamics: Basics of Nuclear Magnetic Resonance, Wiley

[3] Keeler, J., 2006, Understanding NMR Spectroscopy, Wiley

[4] Duer, M. J., 2002, Solid-State NMR Spectroscopy, Wiley, Cambridge

[5] Laybourn, A., 2012, Ph.D. thesis, University of Liverpool

[6] Laws, D. D., Bitter, H.-M. L. and Jerschow, A., 2002, *Angew Chem Int Ed Engl*, 41, 3096–3129

[7] Levitt, M. H., 2008, Spin Dynamics: Basics of Nuclear Magnetic Resonance, Wiley

[8] Kolodziejski, W. and Klinowski, J., 2002, *Chem Rev*, 102, 613–28

[9] Duer, M., 2004, Introduction to Solid-State NMR Spectroscopy, Blackwell Publishing Ltd.

[10] Tarasov, V. A., Bogdanovich, A. S., Litvinov, A. I. and Larin, I. A., 2012, *Klin Med (Mosk)*, 90, 26–30

[11] Qi, S., Belton, P., Nollenberger, K., Clayden, N., Reading, M. and Craig, D., 2010, *Pharmaceutical Research*, 27, 1869–1883

[12] Giernoth, D., Bankmann, D. and Schlorer, N., 2005, *Green Chemistry*, 7, 279–282

[13] Atkins, P. and De Paula, J., 2002, Physical Chemistry, Oxford University Press

[14] Schwarzenbach, D., 1996, Crystallography, John Wiley and Sons, Inc.

[15] University, A. N., 2011, Amorphous semiconductors, http://physics.anu.edu.au/eme/research/amorphous.php

[16] Angell, C. A., 1995, *Proc Natl Acad Sci U S A*, 92, 6675–82

[17] Paudel, A., Geppi, M. and Van den Mooter, G., 2014, *Journal of Pharmaceutical Sciences*, 1–28

[18] Hancock, B. C. and Zograf, G., 1997, *Journal of Pharmaceutical Sciences*, 86, 1–12

[19] Guo, Y., Shalaev, E. and Smith, S., 2013, *Trends in Analytical chemistry*, 49, 137–144

[20] Edwards, J. C., 2008, Principles of nmr, http://www.process-nmr.com/nmr1.htm

[21] Wiper, P., 2012, Phd thesis, University of Liverpool

[22] Cropper, C., 2011, Phd thesis, University of Liverpool

[23] Collins, S., 2015, Differential scanning calorimetry, https://community.dur.ac.uk/n.r.cameron/.../DSC

[24] Harris, R. K., 1985, *Analyst*, 110, 649–655

[25] Fyfe, C. A., Lyeria, J. R., Volksen, W. and Yannoni, C. S., 1979, *Macromolecules*, 12 (4), 757–761

[26] Takegoshi, K. and Hikichi, K., 1991, *Journal of Chemical Physics*, 94, 3200–3206

[27] Lyerla, J. R. and Yannoni, C. S., 1983, *IBM Journal of Research and Development*, 27, 302–312

[28] Nunes, T. G., Viciosa, M. T., Correia, N. T., Danede, F., Nunes, R. G. and Diogo, H. P., 2014, *Mol Pharm*, 11 (3), 727–737

[29] Apperley, D. C., Forster, A. H., Fournier, R., Harris, R. K., Hodgkinson, P., Lancaster, R. W. and Rades, T., 2005, *Magnetic Resonance in Chemistry*, 43, 881–892

[30] Schachter, D. M., Xiong, J. and Tirol, G. C., 2004, *Int J Pharm*, 281, 89–101

[31] Chen, X., Morris, K. R., Griesser, U. J., Byrn, S. R. and Stowell, J. G., 2002, *J Am Chem Soc*, 124, 15012–9

[32] Andronis, V. and Zografi, G., 2000, *Journal of Non-Crystalline Solids*, 271, 236–248

[33] Slavin, P. A., Sheen, D. B., Shepherd, E. E., Sherwood, J. N., Feeder, N., Docherty, R. and Milojevic, S., 2002, *Journal of Crystal Growth*, 237-239 (1), 300–305

[34] Lohani, S., Grant, D. and Suryanarayanan, R., 2006, Doctoral thesis, University of Minnesota

[35] Okumura, T., Ishida, M., Takayama, K. and Otsuka, M., 2006, *Journal of Pharmaceutical Sciences*, 95, 689–700

[36] Lubach, J. W., Xu, D., Segmuller, B. E. and Munson, E. J., 2007, *J Pharm Sci*, 96, 777–787

[37] Lee, D. C. and Webb, M. L., 2003, Pharmaceutical Analysis, Blackwell Publishing

[38] Delaney, S. P., Smith, T. M. and Korter, T. M., 2014, *Journal of Molecular Structure*, 1978, 83–89

[39] Lopez-Mejias, V., Kampf, J. and Matzger, A. J., 2012, *Journal of the American Chemical Society*, 134 (24), 9872–9875

[40] Munro, S. L. and Craik, D. J., 1994, *Magnetic Resonance in Chemistry*, 32, 335–342

[41] Aso, Y., Yoshioka, S., Miyazaki, T. and Kawanishi, T., 2009, *Chem Pharm Bull (Tokyo)*, 57, 61–4

[42] Thirunahari, S., Aitipamula, S., Chow, P. S. and Tan, R. B. H., 2010, *J Pharm Sci*, 99, 2975–2990

[43] Hasegawa, G., Komasaka, T., Bando, R., Yoshihashi, Y., Yonemochi, E., Fujii, K., Uekusa, H. and Terada, K., 2009, *Int J Pharm*, 369, 12–18

[44] Nath, N. K. and Nangia, A., 2011, *Cryst Eng Comm*, 13, 47–51

[45] Parella, T., 2015, enmr parameters: Chemical exchange, http://triton.iqfr.csic.es/guide/eNMR/restraints/exchange.html

[46] Yuan, X., Sperger, D. and Munson, E. J., 2014, *Molecular Pharmaceutics*, 11, 329–337

[47] Aso, Y., Yoshioka, S. and Kojima, S., 2001, *J Pharm Sci*, 90, 798–806

[48] Lee, E. H., 2014, *Asian Journal of Pharmaceutical Sciences*, 9, 163–175

[49] Kistenmacher, T. J. and Marsh, R. E., 1972, *J. Am. Chem. Soc.*, 94, 1340

[50] Borka, L., 1974, *Acta Pharmaceutica Suecica*, 11, 295–303

[51] Crowley, K. J. and Zografi, G., 2002, *Journal of Pharmaceutical Sciences*, 91, 492–507

[52] Surwase, S. A., Boetker, J. P., Saville, D., Boyd, B. J., Gordon, K. C., Peltonen, L. and Strachan, C. J., 2013, *Molecular Pharmaceutics*, 10, 4472–4480

[53] Joshi, V., Morris, K. R., Byrn, S. R. and Carvajal, M. T., 2009, *Crystal Growth & Design*, 9, 3359–3366

[54] McConnell, J., 1973, *Cryst. Struct. Commun.*, 3, 439

[55] Murthy, K., 1982, *Acta Cryst.*, 38, 315

[56] Donaldson, J., Leary, J., Ross, S., Thomas, M. and Smith, C., 1981, *Acta Crystallogr. Sect. B: Struct. Crystallogr. Cryst. Chem.*, 37, 2245–2248

[57] Drebushchak, T. N., Pankrushina, N. A. and Boldyreva, E. V., 2011, *Doklady Physical Chemistry*, 437, 61–64

[58] Kimura, K., Hirayama, F. and Uekama, K., 1999, *J Pharm Sci*, 88 (4), 385 – 391

[59] Carpentier, L., Decressain, R., De Gusseme, A., Neves, C. and Descamps, M., 2006, *Pharm Res*, 23, 798–805

[60] Dictionary.com, 2015, Dictionary.com, unabridged, http://dictionary.reference.com/browse/crystal

[61] O'Donnell, K. and Woodward, W., 2014, *Drug Development and Industrial Pharmacy*, 1, 1–10

[62] Song, Y., Yang, X., Chen, X., Nie, H., Byrn, S. and Lubach, J. W., 2015, *Mol Pharm*, 12, 857–866

[63] Kawabata, Y., Wada, K., Nakatani, M. and Onoue, S., 2011, *International Journal of Pharmaceutics*, 420, 1–10

[64] Yu, L., 2001, *Advanced Drug Delivery Reviews*, 48, 27–42

[65] Mullins, J. D. and Macek, T. J., 1960, *Journal of Pharmaceutical Sciences*, 49 (4), 245–248

[66] Haleblian, J., 1975, *Journal of Pharmaceutical Sciences*, 64 (8), 1269–1288

[67] Fukuoka, E., Makita, M. and Yamamura, S., 1986, *Chemical & Pharmaceutical Bulletin*, 34, 4314–4321

[68] Yoshioka, M., Hancock, B. C. and Zografi, G., 1994, *J Pharm Sci*, 83, 1700–5

[69] Hancock, B. C., Shamblin, S. L. and Zografi, G., 1995, *Pharmaceutical Research*, 12, 799–806

[70] Masuda, K., Tabata, S., Sakata, Y., Hayase, T., Yonemochi, E. and Terada, K., 2005, *Pharmaceutical Research*, 22, 797–805

[71] Taylor, L. S. and Zografi, G., 1997, *Pharmaceutical Research*, 14, 1691–1698

[72] Tong, P. and Zografi, G., 2003, *AAPS PharmSciTech*, 5 (2), 1 – 8

[73] Savolainen, M., Kogermann, K., Heinz, A., Aaltonen, J., Peltonen, L., Strachan, C. and Yliruusi, J., 2009, *European Journal of Pharmaceutics and Biopharmaceutics*, 71, 71–79

[74] Van Den Mooter, G., Van Den Brande, J., Augustijns, P. and Kinget, R., 1999, *Journal of Thermal Analysis and Calorimetry*, 57, 493–507

[75] Hancock, B. C. and Zografi, G., 1994, *Pharm Res*, 11, 471–477

[76] Kearney, A. S., Gabriel, D. L., Mehta, S. C. and Radebaugh, G. W., 1994, *International Journal of Pharmaceutics*, 104, 169–174

[77] Guilbaud, J. B., Cummings, L. and Khimyak, Y., 2007, *Macromol. Symp.*, 251, 41 – 46

[78] Tobyn, M., Brown, J., Dennis, A., Fakes, M., Gao, Q., Gamble, J., Khimyak, Y., McCeorge, G., Patel, C., Sinclair, W., Timmins, P. and Yin, S., 2009, *J Pharm Sci*, 98, 3456–68

[79] Tao, J., Sun, Y., Zhang, G. and Yu, L., 2009, *Pharmaceutical Research*, 26, 855–864

[80] Van Den Mooter, G., Craig, D. and Royall, P., 2001, *Journal of Pharmaceutical Sciences*, 90, 996 – 1003

[81] Yoshioka, M., Hancock, B. C. and Zografi, G., 1995, *J Pharm Sci*, 84, 983–6

[82] Tanno, F., Nishiyama, Y., Kokubo, H. and Obara, S., 2004, *Drug Dev Ind Pharm*, 30, 9–17

[83] Xiang, T.-X. and Anderson, B. D., 2014, *Mol Pharm*, 11, 2400–2411

[84] Matsumoto, T. and Zografi, G., 1999, *Pharmaceutical Research*, 16, 1722–1728

[85] Sun, Y., Tao, J., Zhang, G. G. Z. and Yu, L. A., 2010, *Journal of Pharmaceutical Sciences*, 99, 4023–4031

[86] Kojima, T., Higashi, K., Suzuki, T., Tomono, K., Moribe, K. and Yamamoto, K., 2012, *Pharm Res*, 29, 2777–2791

[87] Neervanna, S., 2006, *Expert Opinion on Drug Metabolism and Toxicology*, 2, 715–731

[88] Pham, T. M., Watson, S. A., Edwards, A. J., Manisha, C., CLawson, J. S., Strohmeier, M. and Vogt, F. G., 2010, *Molecular Pharmaceutics*, 7, 1667 – 1691

[89] Pignatello, R., Bucolo, C., Ferrara, P., Maltese, A., Puleo, A. and Puglisi, G., 2002, *European Journal of Pharmaceutical Sciences*, 218, 27–42

[90] Pignatello, R., Ferro, M., De Guidi, G., Salemi, G., Vandelli, M. A., Guccione, S., Geppi, M., Forte, C. and Puglisi, G., 2001, *Int J Pharm*, 218, 27–42

[91] Crowley, K. J. and Zografi, G., 2003, *Pharmaceutical Research*, 20, 1417–1422

[92] Takeuchi, H., Nagira, S., Yamamoto, H. and Kawashima, Y., 2005, *International Journal of Pharmaceutics*, 293, 155–164

[93] Dong, Z., Chatterji, A., Sandhu, H., Choi, D. S., Chokshi, H. and Shah, N., 2008, *Int J Pharm*, 355, 141–149

[94] Mokarram, A. R., Zadeh, A. K., Keshavarz, M., Ahmadi, A. and Mohtat, B., 2010, *Daru-Journal of Pharmaceutical Sciences*, 18, 185–192

[95] Gong, K., Viboonkiat, R., Rehman, I. U., Buckton, G. and Darr, J. A., 2005, *Journal of Pharmaceutical Sciences*, 94, 2583–2590

[96] Serajuddin, A. T., 1999, *Journal of Pharmaceutical Sciences*, 88, 1058–1066

[97] Habib, M. J., Venkataram, S. and Hussain, M. D., 2001, Fundamentals of solid dispersions - Pharmaceutical Solid Dispersion Technology, Technomic Publishing

[98] Desai, J., Alexander, K. and Riga, A., 2006, *International Journal of Pharmaceutics*, 308, 115–123

[99] VandenMooter, G., 2012, *Drug Discov Today*, 9, 79–85.

[100] Graeser, K. A., Patterson, J. E., Zeitler, J. A., Gordon, K. C. and Rades, T., 2009, *European Journal of Pharmaceutical Sciences*, 37, 492–498

[101] Litvinov, V. M., Guns, S., Adriaensens, P., Scholtens, B. J. R., Quaedflieg, M. P., Carleer, R. and Van den Mooter, G., 2012, *Molecular Pharmaceutics*, 9, 2924–2932

[102] Marsac, P. J., Konno, H. and Taylor, L. S., 2006, *Pharm Res*, 23, 2306–16

[103] Qi, S., Gryczke, A., Belton, P. and Craig, D., 2008, *International Journal of Pharmaceutics*, 354, 158–167

[104] Janssens, S. and Van den Mooter, G., 2009, *Journal of Pharm. Pharmacol.*, 61, 1571–1586

[105] Chiou, W. L. and Riegelman, S., 1971, *J Pharm Sci*, 60, 1281–302

[106] Rumondor, A. C. F., Marsac, P. J., Stanford, L. A. and Taylor, L. S., 2009, *Molecular Pharmaceutics*, 6, 1492–1505

[107] Gao, P., 2008, *Mol Pharm*, 5 (6), 903–904

[108] Qian, F., Huang, J., Zhu, Q., Haddadin, R., Gawel, J., Garmise, R. and Hussain, M., 2010, *International Journal of Pharmaceutics*, 395, 232–235

[109] Prudic, A., Ji, Y. and Sadowski, G., 2014, *Mol Pharm*, 11, 2294–2304

[110] Elliott, S. R., 1990, Physics of amorphous materials, Longman Scientific and Technical

[111] Tong, P. and Zografi, G., 1999, *Pharmaceutical Research*, 16, 1186 – 1192

[112] Gordon, M. and Taylor, J. S., 1952, *Journal of applied Chemistry*, 2, 493–498

[113] Kelley, F. N. and Bueche, F., 1961, *Journal of Polymer Science*, 50, 549–556

[114] Couchman, P. R. and Karasz, F. E., 1978, *Macromolecules*, 11, 117–119

[115] Mansfield, M. L., 1995, *Journal of Chemical Physics*, 103, 8124–8129

[116] Ediger, M. D., Angell, C. A. and Nagel, S. R., 1996, *Journal of Physical Chemistry*, 100, 13200–13212

[117] Bhugra, C. and Pikal, M. J., 2008, *J Pharm Sci*, 97, 1329–49

[118] Bhattacharya, S. and Suryanarayanan, R., 2009, *J Pharm Sci*, 98, 2935–53

[119] Angell, C. A., 1995, *Science*, 267, 1924–35

[120] Alie, J., Menegotto, J., Cardon, P., Duplaa, H., Caron, A., Lacabanne, C. and Bauer, M., 2004, *J Pharm Sci*, 93, 218–233

[121] Williams, G. and Watts, D. C., 1970, *Trans. Faraday Soc.*, 66, 80

[122] Roos, Y. and Karel, M., 1991, *Journal of Food Science*, 56, 38 – 43

[123] Pajula, K., Wittoek, L., Lehto, V.-P., Ketolainen, J. and Korhonen, O., 2014, *Mol Pharm*, 11, 2271–2279

[124] Andronis, V., Yoshioka, M. and Zografi, G., 1997, *Journal of Pharmaceutical Sciences*, 86, 346–351

[125] Zhou, D., Grant, D. J., Zhang, G. G., Law, D. and Schmitt, E. A., 2007, *J Pharm Sci*, 96, 71–83

[126] Chieng, N., Rades, T. and Aaltonen, J., 2011, *J Pharm Biomed Anal*, 55, 618–644

[127] Rodríguez-Spong, B., Acciacca, A., Fleisher, D. and Rodríguez-Hornedo, N., 2008, *Mol Pharm*, 5, 956–967

[128] McCrone, A. W., 1965, *Science*, 148, 167

[129] Bernstein, J., 2002, Polymorphism in Molecular Crystals, New York : Clarendon Press ; Oxford University Press

[130] Ukmar, T., Kaucic, V. and Mali, G., 2011, *Acta Chimica Slovenica*, 58, 425–433

[131] Li, H., Wen, H., Stowell, J. G., Morris, K. R. and Byrn, S. R., 2010, *J Pharm Sci*, 99, 3839–48

[132] Bauer, J., Spanton, S., Henry, R., Quick, J., Dziki, W., Porter, W. and Morris, J., 2001, *Pharm Res*, 18, 859–66

[133] Morissette, S. L., Soukasene, S., Levinson, D., Cima, M. J. and Almarsson, O., 2003, *Proceedings of the National Academy of Sciences of the United States of America*, 100, 2180–2184

[134] Lehmann, O., 1891, Die Krystallanalyse oder die chemische Analyse durch Beobachtung der Krystallbildung mit Hulfe des Mikroskps, Wilhelm Engelmann

[135] Ostwald, W. F., 1897, *J Phys Chem*, 22, 289 – 330

[136] Zhang, G., Law, D. and E., S., 2004, *Advanced Drug Delivery Reviews*, 56, 371–90

[137] Patel, J. R., Carlton, R. A., Yuniatine, F., Needham, T. E., Wu, L. and Vogt, F. G., 2012, *J Pharm Sci*, 101, 641–663

[138] Baird, J. A. and Taylor, L. S., 2012, *Adv Drug Deliv Rev*, 64, 396–421

[139] Ivanisevic, I., 2010, *J Pharm Sci*, 99, 4005–12

[140] Hu, Y., Liang, J. K., Myerson, A. S. and Taylor, L. S., 2005, *Industrial & Engineering Chemistry Research*, 44, 1233–1240

[141] Jachowicz, R., Nurnberg, E., Pieszczek, B., Kluczykowska, B. and Maciejewska, A., 2000, *International Journal of Pharmaceutics*, 206, 13–21

[142] Blasi, P., Schoubben, A., Giovagnoli, S., Perioli, L., Ricci, M. and Rossi, C., 2007, *AAPS PharmSciTech*, 8, Article 37

[143] Aso, Y., Yoshioka, S. and Kojima, S., 2004, *J Pharm Sci*, 93, 384–91

[144] Newman, A., Engers, D., Bates, S., Ivanisevic, I., Kelly, R. C. and Zografi, G., 2008, *J Pharm Sci*, 97, 4840–4856

[145] Ito, A., Watanabe, T., Yada, S., Hamaura, T., Nakagami, H., Higashi, K., Moribe, K. and Yamamoto, K., 2010, *Int J Pharm*, 383, 18–23

[146] Vogt, F. G., 2015, Pharmaceutical Amorphous Solid Dispersions: Solid-State Characterization of Amorphous Dispersions, John Wiley and Sons, Inc

[147] Martinez-Oharriz, M. C., Rodriguez-Espinosa, C., Martin, C., Goni, M. M., Tros-Ilarduya, M. C. and Sanchez, M., 2002, *Drug Development and Industrial Pharmacy*, 28, 717–725

[148] Vogt, F. G. and Williams, G. R., 2012, *Pharm Res*, 29, 1866–81

[149] Johari, G. P., Kim, S. and Shanker, R. M., 2007, *J Pharm Sci*, 96, 1159–75

[150] Andronis, V. and Zografi, G., 1998, *Pharmaceutical Research*, 15, 835–842

[151] Geppi, M., Mollica, G., Borsacchi, S. and Veracini, C., 2008, *Applied Spectroscopy Reviews*, 43, 202 – 302

[152] Aso, Y., Yoshioka, S., Miyazaki, T., Kawanishi, T., Tanaka, K., Kitamura, S., Takakura, A., Hayashi, T. and Muranushi, N., 2007, *Chem Pharm Bull (Tokyo)*, 55, 1227–31

[153] Harris, R. K., 2007, *J Pharm Pharmacol*, 59, 225–39

[154] Koga, A., Yonemochi, E., Machida, M., Aso, Y., Ushio, H. and Terada, K., 2004, *Int J Pharm*, 275, 73–83

[155] Nath, R. and Bohmer, R., 2007, *J. Non. Cryst.-Solids*, 353, 3788–3795

[156] Di Martino, P., Joiris, E., Gobetto, R., Masic, A., Palmieri, G. F. and Martelli, S., 2004, *Journal of Crystal Growth*, 265, 302 – 308

[157] Geppi, M., Guccione, S., Mollica, G., Pignatello, R. and Veracini, C. A., 2005, *Pharm Res*, 22, 1544–1555

[158] Watanabe, T., Hasegawa, S., Wakiyama, N., Kusai, A. and Senna, M., 2002, *International Journal of Pharmaceutics*, 248, 123–129

[159] Schantz, S., Hoppu, P. and Juppo, A. M., 2009, *J Pharm Sci*, 98, 1862–70

[160] Aso, Y. and Yoshioka, S., 2006, *J Pharm Sci*, 95, 318–25

[161] Aso, Y., Yoshioka, S. and Kojima, S., 2000, *J Pharm Sci*, 89, 408–416

[162] Schachter, D., Mitchell, S., Schmitt, R. and Xiong, J., 2003, *30th Annual Meeting of the Controlled Release Society*, Glasgow, Scotland, July 19–23

[163] Rumondor, A. C. F., Ivanisevic, I., Bates, S., Alonzo, D. E. and Taylor, L. S., 2009, *Pharm Res*, 26, 2523–2534

[164] Kaplan, D. S., 1976, *Journal of Applied Polymer Science*, 20, 2615–2629

[165] Krause, M., S.; Iskandar, 1977, *Polymer Science and Technology*, 10, 231–243

[166] Ando, I. and Asakura, T., 1998, Solid-state NMR of Polymers, Elsevier Science

[167] Bhugra, C., Shmeis, R., Krill, S. L. and Pikal, M. J., 2008, *Journal of Pharmaceutical Sciences*, 97, 4498–4515

[168] Imaizumi, H., Nambu, N. and Nagai, T., 1983, *Chemical & Pharmaceutical Bulletin*, 31, 2510–2512

[169] Kaneniwa, N., 1985, *Chemical & Pharmaceutical Bulletin*, 33, 2632–2632

[170] Kawakami, K., Usui, T. and Hattori, M., 2012, *Journal of Pharmaceutical Sciences*, 101 (9), 3239–48

[171] Rowe, E. L. and Anderson, B. D., 1984, *J Pharm Sci*, 73, 1673–1675

[172] Burger, A., 1975, *Sci. Pharm.*, 43, 161–168

[173] Simmons, D., Ranz, R. J., Gyanchandani, N. D. and Picotte, P., 1972, *Can J Pharm Sci*, 7, 121–123

[174] Leary, J., Ross, S. and Thomas, M., 1981, *Pharm. Weekblad. Sci. Ed.*, 3, 62–66

[175] Yoshihashi, Y., Iijima, H., Yonemochi, E. and Terada, K., 2006, *Journal of Thermal Analysis and Calorimetry*, 3, 689–692

[176] Vasa, D. M., Dalal, N., Katz, J. M., Roopwani, R., Nevrekar, A., Patel, H., Buckner, I. S. and Wildfong, P. L. D., 2014, *J Pharm Sci*, 103, 2911–2923

[177] Oksanen, C. A. and Zografi, G., 1990, *Pharmaceutical Research*, 7, 654–657

[178] Van den Mooter, G., Wuyts, M., Blaton, N., Busson, R., Grobet, P., Augustijns, P. and Kinget, R., 2001, *Eur J Pharm Sci*, 12, 261–9

[179] Shamblin, S. L., Taylor, L. S. and Zografi, G., 1998, *J Pharm Sci*, 87, 694–701

[180] Zhao, Y. Y., Inbar, P., Chokshi, H. P., Malick, A. W. and Choi, D. S., 2011, *Journal of Pharmaceutical Sciences*, 100, 3196–3207

[181] Bloch, F., 1958, *Physical Review Letters*, 111, 841

[182] Scholz, I., Hodgkinson, P., Meier, B. H. and Ernst, M., 2009, *J Chem Phys*, 130, 114510

[183] Fung, B. M., Khitrin, A. K. and Ermolaev, K., 2000, *Journal of Magnetic Resonance*, 142, 97–101

[184] Cobo, M. F., Malinakova, K., Reichert, D., Saalwaechter, K. and DeAzevedo, E. R., 2009, *Physical Chemistry Chemical Physics*, 11, 7036–7047

[185] Lesage, A., Sakellariou, D., Hediger, S., Eléna, B., Charmont, P., Steuernagel, S. and Emsley, L., 2003, *J Magn Reson*, 163, 105–113

[186] Hartmann, S. R. and Hahn, E. L., 1962, *Physical Review*, 128, 2042–2053

[187] Forster, A., Apperley, D., Hempenstall, J., Lancaster, R. and Rades, T., 2003, *Pharmazie*, 58, 761–762

[188] Schaefer, J., Stejskal, E. and Sefcik, M., 1980, *Macromolecules*, 13, 1121

[189] Simha, R. and Boyer, R., 1962, *Journal of Chemical Physics*, 37, 1003–1007

[190] Gupta, P., Thilagavathi, R., Chakraborti, A. K. and Bansal, A. K., 2005, *Mol Pharm*, 2, 384–391

[191] Liu, Y., Bhandari, B. and Zhou, W., 2006, *Journal of Agricultural and Food Chemistry*, 54, 5701–5717

[192] Hancock, 1997, *Transplantation*, 64, 1225–1225

[193] Brekner, M., Schneider, H. C. and Cantow, H. J., 1988, *Polymer*, 29 (1), 78–85

[194] Schneider, H. A., 1988, *Makro. Chem*, 189, 1941–1955

[195] Clark, C. M. and Dutrow, B. L., 2015, Single-crystal x-ray diffraction, http://serc.carleton.edu/research_education/geochemsheets/techniques/SXD.html

[196] Flohr, J. K., 2014, X-ray powder diffraction, http://pubs.usgs.gov/info/diffraction/html/

[197] Krc, J., 1977, *Microscope*, 25, 31–45

[198] Yan, B. and Stark, R. E., 1998, *Macromolecules*, 31, 2600–2605

[199] Rothwell, W. P. and Waugh, J. S., 1981, *Journal of Chemical Physics*, 74, 2721–2732

[200] McBrierty, V. J. and Packer, K. J., 1993, Nuclear Magnetic Resonance in Solid Polymers, Cambridge University Press

[201] Fülber, C., Demco, D. E. and Blümich, B., 1996, *Solid State Nucl Magn Reson*, 6, 213–223

[202] Guilbaud, J. B., Clark, B. C., Meehan, E., Hughes, L., Saiani, A. and Khimyak, Y. Z., 2010, *J Pharm Sci*, 99, 2681–96

[203] Zhang, X. Q., Takegoshi, K. and Hikichi, K., 1991, *Macromolecules*, 24, 5756–5762

[204] Nowacka, B., Lubiński, W. and Karczewicz, D., 2010, *Klin Oczna*, 112, 247–252

[205] Lyerla, J. R., Yannoni, C. S. and Fyfe, C. A., 1982, *Acc Chem Res*, 15 (7), 208–216

[206] Carignani, E., Borsacchi, S. and Geppi, M., 2011, *J Phys Chem A*, 115, 8783–90

[207] Brus, J., Urbanova, M., Sedenkova, I. and Brusova, H., 2011, *International Journal of Pharmaceutics*, 409, 62–74

[208] Urbanova, M., Brus, J., Sedenkova, I., Policianova, O. and Kobera, L., 2013, *Spectrochimica Acta Part A-Molecular and Biomolecular Spectroscopy*, 100, 59–66

[209] Abraham, A. and Crull, G., 2014, *Mol Pharm*, 11, 3754–3759

[210] Calahan, J. L., Zanon, R. L., Alvarez-Nunez, F. and Munson, E. J., 2013, *Molecular Pharmaceutics*, 10, 1949–1957

[211] Barry, S. J., Pham, T. N., Borman, P. J., Edwards, A. J. and Watson, S. A., 2012, *Analytica Chimica Acta*, 712, 30–36

[212] Wenslow, R. M., 2002, *Drug Development and Industrial Pharmacy*, 28, 555–561

[213] Lim, A. R. and Kim, J. S., 2000, *Solid State Communications*, 115, 179–183

[214] Kwak, S. Y., Kim, J. H. and Lee, J. C., 2001, *Journal of Polymer Science Part B-Polymer Physics*, 39, 993–1000

[215] Lim, A. R., Schueneman, G. T. and Novak, B. M., 1999, *Solid State Communications*, 109, 465–470

[216] Cai, R., Yang, H., He, J. and Zhu, W., 2009, *Journal of Molecular Structure*, 938, 15–19

[217] Lee, C. H., Spano, J., McGrath, J. E., Cook, J., Freeman, B. D. and Wi, S., 2011, *The Journal of Physical Chemistry B*, 115, 6876–6884

[218] Zhang, Y. H., Xu, H. S., Litvinov, Y. A., Tu, X. L., Yan, X. L., Typel, S., Blaum, K., Wang, M., Zhou, X. H., Sun, Y., Brown, B. A., Yuan, Y. J., Xia, J. W., Yang, J. C., Audi, G., Chen, X. C., Jia, G. B., Hu, Z. G., Ma, X. W., Mao, R. S., Mei, B., Shuai, P., Sun, Z. Y., Wang, S. T., Xiao, G. Q., Xu, X., Yamaguchi, T., Yamaguchi, Y., Zang, Y. D., Zhao, H. W., Zhao, T. C., Zhang, W. and Zhan, W. L., 2012, *Phys Rev Lett*, 109, 102501

[219] Dickinson, L. C., Yang, H., Chu, C. W., Stein, R. S. and Chien, J. C. W., 1987, *Macromolecules*, 20, 1757–1760

[220] McBrierty, V. J., Douglass, D. C. and Kwei, T. K., 1978, *Macromolecules*, 11, 1265–1267

[221] Bovey, F. A. and Mirau, P. A., 1996, NMR of Polymers, Academic Press, San Diego

[222] Vyazovkin, S. and Dranca, I., 2005, *Journal of Physical Chemistry B*, 109, 18637–18644

[223] Vyazovkin, S. and Dranca, I., 2007, *Journal of Physical Chemistry B*, 111, 7283–7287

[224] Karmwar, P., Boetker, J. P., Graeser, K. A., Strachan, C. J., Rantanen, J. and Rades, T., 2011, *European Journal of Pharmaceutical Sciences*, 44, 341–350

[225] Brettmann, B. K., Myerson, A. S. and Trout, B. L., 2012, *J Pharm Sci*, 101, 2185–93

[226] Masuda, K., Tabata, S., Kono, H., Sakata, Y., Hayase, T., Yonemochi, E. and Terada, K., 2006, *International Journal of Pharmaceutics*, 318, 146–153

[227] Lin, S., 1992, *Journal of Pharmaceutical Sciences*, 81, 572–576

[228] Ali, W., Williams, A. C. and Rawlinson, C. F., 2010, *Int J Pharm*, 391, 162–168

[229] Williams, A. C., Timmins, P., Lu, M. and Forbes, R. T., 2005, *Eur J Pharm Sci*, 26, 288–294

[230] Rawlinson, C. F., Williams, A. C., Timmins, P. and Grimsey, I., 2007, *International Journal of Pharmaceutics*, 336, 42–48

[231] Legendre, B. and Feutelais, Y., 2004, *Journal of Thermal Analysis and Calorimetry*, 76, 255–264

[232] Aceves-Hernandez, J. M., Nicolas-Vazquez, I., Aceves, F. J., Hinojosa-Torres, J., Paz, M. and Castanoz, V. M., 2009, *Journal of Pharmaceutical Sciences*, 98, 2448–2463

[233] Bradley, J. P., Velaga, S. P., Antzutkin, O. N. and Brown, S. P., 2011, *Crystal Growth & Design*, 11, 3463–3471

[234] Schmidt-Rohr, K., Clauss, J. and Spiess, H. W., 1992, *Macromolecules*, 25, 3273–3277

[235] Werkhoven, T. M., Mulder, F. M., Zune, C., Jerome, R. and De Groot, H. J. M., 2003, *Macromolecular Chemistry and Physics*, 204, 46–51

[236] Mowery, D. M., Harris, D. J. and Schmidt-Rohr, K., 2006, *Macromolecules*, 39, 2856–2865

[237] Guilbaud, J. B., 2007, Ph.D. thesis, University of Liverpool

[238] Foumier, R., 2006, Ph.D. thesis, Durham University

[239] Alonzo, D. E., Zhang, G. G. Z., Zhou, D., Gao, Y. and Taylor, L. S., 2010, *Pharmaceutical Research*, 27, 608–618

[240] Hess, S., Teubert, U., Ortwein, J. and Eger, K., 2001, *European Journal of Pharmaceutical Sciences*, 14, 301–311

[241] Brown, S. P., 2012, *Solid State Nucl Magn Reson*, 41, 1–27

[242] Lohani, S., Nesmekova, I., Grant, D. and Suryanarayanan, R., 2011, *Crystal Growth & Design*, 11, 2368–2378

[243] Andrew, E. R., Kempka, M., Radomski, J. M. and Szczesniak, E., 1999, *Solid State Nucl Magn Reson*, 14, 91–94

[244] Yoshioka, S., Aso, Y. and Kojima, S., 2002, *J Pharm Sci*, 91, 2203–10

[245] Yoshioka, S., Aso, Y. and Kojima, S., 2003, *Chem Pharm Bull (Tokyo)*, 51, 1289–92

[246] Ren, P., Reichert, D., He, Q., Zhang, L. and Tang, H., 2011, *J Phys Chem B*, 115, 2814–23

[247] Van Eerdenbrugh, B. and Taylor, L. S., 2010, *Mol Pharm*, 7, 1328–1337

[248] Ibolya, F., Gyeresi, A., Szabo-Revesz, P. and Aigner, Z., 2011, *Farmacia*, 59, 60 – 70

[249] Hu, Y., Wikström, H., Byrn, S. R. and Taylor, L. S., 2007, *J Pharm Biomed Anal*, 45, 546–551

[250] Jabeen, F., Hussain, D., Fatima, B., Musharraf, S. G., Huck, C. W., Bonn, G. K. and Najam-ul Haq, M., 2012, *Anal Chem*, 84, 10180–5

[251] Gilli, P., Bertolasi, V., Ferretti, V. and Gilli, G., 2000, *Journal of the American Chemical Society*, 122, 10405–10417

[252] Bilton, C., Allen, F. H., Shields, G. P. and Howard, J. A., 2000, *Acta Crystallogr B*, 56 (5), 849–856

[253] Beckonert, O., Coen, M., Keun, H. C., Wang, Y., Ebbels, T. M. D., Holmes, E., Lindon, J. C. and Nicholson, J. K., 2010, *Nat Protoc*, 5, 1019–1032

[254] Tishmack, P. A., Bugay, D. E. and Byrn, S. R., 2003, *Journal of Pharmaceutical Sciences*, 92, 441–474

[255] Lee, A. K., 2008, *Crystal Growth & Design*, 8, 91–97

[256] Wu, X. L. and Zilm, K. W., 1993, *Journal of Magnetic Resonance*, 102, 205 – 213

[257] Van den Mooter, G., Wuyts, M., Blaton, N., Busson, R., Grobet, P., Augustijns, P. and Kinget, R., 2001, *Eur J Pharm Sci*, 12, 261–269

[258] Corrigan, O., Sabra, K. and Holohan, E. M., 1983, *Drug Development and Industrial Pharmacy*, 9, 1–20

[259] Chen, X., Stowell, J. G., Morris, K. R. and Byrn, S. R., 2010, *J Pharm Biomed Anal*, 51, 866–874

[260] Gilpin, R. K. and Zhou, W., 2005, *J Pharm Biomed Anal*, 37, 509–15

[261] Bugay, D. E., Newman, A. W. and Findlay, W. P., 1996, *J Pharm Biomed Anal*, 15, 49–61

[262] Hurst, V. J., Schroeder, P. A. and Styron, R. W., 1997, *Analytica Chimica Acta*, 337, 233–252

[263] Campbell Roberts, S. N., Williams, A. C., Grimsey, I. M. and Booth, S. W., 2002, *J Pharm Biomed Anal*, 28, 1149–1159

[264] Kimura, K., Hirayama, F., Arima, H. and Uekama, K., 1999, *Pharmaceutical Research*, 16, 1729–1733

[265] Kedzierewicz, F., Villieras, F., Zinutti, C., Hoffman, M. and Maincent, P., 1995, *International Journal of Pharmaceutics*, 117, 247–251

[266] Suihko, E., Poso, A., Korhonen, O., Gynther, J., Ketolainen, J. and Paronen, P., 2000, *Pharmaceutical Research*, 17, 942–948

[267] Kimura, K. and Hirayama, F., 2000, *Chem Pharm Bull*, 48, 646–650

[268] Drebushchak, T. N., Chesalov, Y. A. and Boldyreva, E. V., 2009, *Acta Crystallogr B*, 65, 770–781

[269] Buntkowsky, G., Breitzke, H., Adamczyk, A., Roelofs, F., Emmler, T., Gedat, G. B., E., Xu, Y., Limbach, H.-H. and Shenderovich, I., 2007, *Phys Chem Chem Phys*, 9, 4843–4853

[270] Martinez-Oharriz, M. C., Martin, C., Goni, M. M., Rodriguez-Espinosa, C., Tros-Ilarduya, M. C. and Zomoza, A., 1999, *European Journal of Pharmaceutical Sciences*, 8, 127–132

[271] Saleki-Gerhardt, A., 1993, Ph.D. thesis, University of Wisconson, Madison

[272] Saleki-Gerhardt, A., Ahlneck, C. and Zografi, G., 1994, *International Journal of Pharmaceutics*, 101, 237–247

[273] Saleki-Gerhardt, A. and Zografi, G., 1994, *Pharmaceutical Research*, 11, 1166–1173

[274] Huttenrauch, R., 1978, *ActaPharm.Technol.,Suppl.*, 6, 55–127

[275] Nordwall, H. J. and A., S. L., 1956, *Trans. Faraday Soc.*, 52, 1207–1215

[276] Mura, P., Faucci, M. T., Parrini, P. L., Furlanetto, S. and Pinzauti, S., 1999, *International Journal of Pharmaceutics*, 179, 117–128

[277] Mura, P., Faucci, M. T., Manderioli, A. and Bramanti, G., 1999, *International Journal of Pharmaceutics*, 193, 85–95

[278] Oksanen, C. A. and Zografi, G., 1993, *Pharmaceutical Research*, 10, 791–799

[279] Aso, Y., Yoshioka, S., Zhang, J. and Zografi, G., 2002, *Chem Pharm Bull*, 50, 822–826

[280] Shamblin, S. L. and Zografi, G., 1998, *Pharm Res*, 15, 1828–1834

[281] Yoshioka, S., Aso, Y., Kojima, S., Sakurai, S., Fujiwara, T. and Akutsu, H., 1999, *Pharm Res*, 16, 1621–5

[282] Cheung, M. K., Wang, J., Zheng, S. and Mi, Y., 2000, *Polymer*, 41 (4), 1469–1474

[283] Ando, I. and Asakura, T., 1998, Solid State NMR of Polymers, Elsevier, Amsterdam

[284] Meier, B. H., 1994, *Advanced Magnetic Optical Resonance*, 18, 1–116

[285] Cheung, T., 1996, The encyclopedia of NMR, Wiley, New York